JPL Publication 02-1

Proceedings of the Tenth JPL Airborne Earth Science Workshop

Robert O. Green
Editor
California Institute of Technology
Jet Propulsion Laboratory

National Aeronautics and Space Administration

Jet Propulsion Laboratory
California Institute of Technology
Pasadena, California

December 2001

This publication was prepared at the Jet Propulsion Laboratory, California Institute of Technology, under a contract with the National Aeronautics and Space Administration.

Contents

Introduction

This publication contains the proceedings of the AVIRIS Earth Science and Applications Workshop—a forum held to report science research and applications results with spectral images measured by the NASA Airborne Visible/Infrared Imaging Spectrometer (AVIRIS). These papers were presented at the Jet Propulsion Laboratory on February 27 and 28 and March 1 and 2, 2001. Electronic versions of these papers may be found at the AVIRIS Web site noted below.

Note

Our budget this year allows for only a few color reproductions, even though they now often prove necessary for a complete understanding of figures presented here in black and white. For full color versions of the papers, please go to the AVIRIS Web site at http://makalu.jpl.nasa.gov/docs/workshops/toc.htm

SHADOW-INSENSITIVE MATERIAL DETECTION/CLASSIFICATION WITH ATMOSPHERICALLY CORRECTED HYPERSPECTRAL IMAGERY

Steven M. Adler-Golden,[1] Robert Y. Levine,[1] Michael W. Matthew,[1] Steven C. Richtsmeier,[1]
Lawrence S. Bernstein,[1] John Gruninger,[1] Gerald Felde,[2] Michael Hoke,[2] Gail Anderson,[2] and Anthony Ratkowski[2]

1. INTRODUCTION

Hyperspectral imaging (HSI) from airborne or space-based platforms, currently conducted mainly in the 0.4 - 2.5 μm wavelength region, is a valuable technique for detection and classification of materials and objects on the Earth's surface. In a typical analysis, the spectral radiance data are "corrected" or compensated for the atmospheric and illumination conditions to yield spectral reflectance, and the results are processed with any of a variety of algorithms, which may, for example, compare the contents of each pixel with reference spectra for classification, search the scene for a desired material spectrum, or calculate a terrain property such as a vegetation cover index. Atmospheric correction algorithms include several based on first-principles radiation transport models (e.g., Gao *et al.*, 1996; Green *et al.*, 1996; Richter, 1996; Matthew *et al.*, 2000) as well as the Empirical Line Method (ELM), which utilizes known materials in the scene. An alternative approach is to work with the original radiance data; this is effective for identifying scene anomalies and for supervised processing, where the scene elements can be identified visually by an analyst.

Regardless of the analysis method, varying illumination of the ground caused by shadowing or uneven terrain poses problems for detection and classification. The radiance spectra can vary in both shape and amplitude, since the ground-reflected light is altered while the atmospherically scattered components, consisting of backscattering and forward-scattered surface-reflected light ("adjacency" scattering), remain unchanged. To account for the spectral variation, Healey and Slater (1999) developed a simulation-based detection method that involves a 9-dimensional projection spanning combinations of material spectra, atmosphere models, and direct-sun and sky radiance levels. Alternatively, one can work with the spectra output by an atmospheric correction algorithm, which have the atmospheric scattering removed and thus have a much more constant shape. With such processed spectra, a brightness-normalized algorithm such as the Spectral Angle Mapper (SAM) (Kruse *et al.*, 1993) can largely compensate for reduced sunlight. However, even the SAM loses effectiveness in shadows, where typically the dominant illumination is from skylight, which is skewed to short (blue-violet) wavelengths. The spectral skewing effect is illustrated in the reflectance data shown in Figure 1.

In this paper we present and compare some simple, new algorithms for classification and whole-pixel material detection using atmospherically corrected data. These include the SAM, an extension of the SAM that accounts for the different spectral shapes of sunlight and skylight, and algorithms that use a Euclidean distance rather than a spectral angle difference metric. The most effective algorithm in this study computes the distance between the pixel spectrum and a best-fit combination of direct-sun-illuminated and sky-illuminated apparent reflectance spectra of the desired material or endmember. Another, simpler algorithm computes an analogous distance using the SAM's assumption of an invariant spectral shape. As an initial demonstration the algorithms are applied to an atmospherically corrected HYDICE (Basedow et al., 1995) image from the Forest Radiance I set studied by Healey and Slater and to a HYDICE image of the DOE ARM (Atmospheric Radiation Measurement) Site in Lamont, Oklahoma.

---

[1] Spectral Sciences, Inc., Burlington, Massachusetts (sag@spectral.com)
[2] Air Force Research Laboratory, Space Vehicles Directorate, Hanscom AFB, Massachusetts

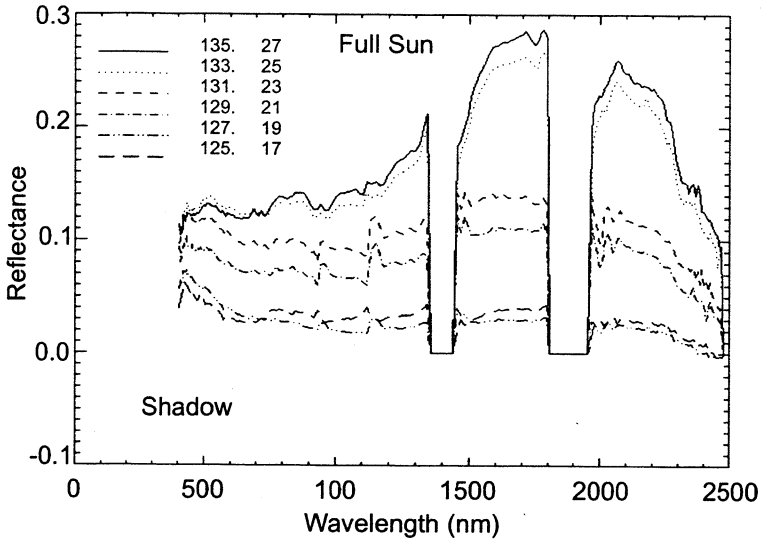

Figure 1. Apparent reflectance spectra of gravel road pixels across the edge of a tree line cast shadow (curve labels are pixel x,y coordinates). Data are from Run 7 of the HYDICE Forest Radiance I experiment. Atmospheric correction includes adjacency effect compensation. Note the relative emphasis of the short wavelengths as the shadowing increases.

2. DESCRIPTION OF APPROACH

The basic procedure involves atmospherically correcting the data to generate apparent surface spectral reflectance, calculating a skylit-to-fully-illuminated spectral ratio, applying the ratio to a fully illuminated reflectance spectrum of a chosen material to simulate its spectrum in shadow, and finally incorporating both the original and the shadowed spectrum in a detection or classification algorithm. The details are described below.

2.1 Atmospheric Correction Method

The standard equation for spectral radiance L* measured above the surface may be written as (Matthew *et al.*, 2000)

$$L^* = (A\rho + B\rho_e)/(1 - \rho_e S) + L^*_a \qquad (1)$$

for ultraviolet through near-infrared wavelengths, where thermal emission is negligible. Here ρ is the pixel surface reflectance, ρ_e is a spatially convolved surface reflectance for a region surrounding the pixel, S is the spherical albedo of the atmosphere, L^*_a is the radiance backscattered by the atmosphere, and A and B are coefficients that depend on atmospheric and geometric conditions. All of these quantities are spectrally dependent. The A term in Equation (1) represents radiance from the surface that travels directly into the sensor, while the B term represents radiance from the surface that is scattered by the atmosphere into the sensor. The distinction between ρ and ρ_e accounts for the adjacency effect.

Using calculations from a radiation transport model (for example, MODTRAN (Berk *et al.*, 1989)), the values of A, B, S and L^*_a can be determined and combined with a suitable point-spread function (kernel) for the ρ_e spatial convolution to iteratively solve Equation (1) for ρ. A simple method for extracting A, B, S and L^*_a from MODTRAN calculations with surface reflectances of 0, 0.5, and 1 has been described by Adler-Golden *et al.* (1999). To account for variations in the atmospheric water vapor column over the scene, a separate set of parameters is tabulated for each of a series of water amounts spanning the scene. The water amount for each pixel is retrieved using shape information from one or more water absorption bands, and the result is used to interpolate among the tabulated parameters.

2.2 Effect of Reduced Direct Solar Illumination

Equation (1) assumes full sun and sky illumination. We now consider the case where the direct sun is partially or fully blocked but the sky illumination remains. Denoting α as the fractional direct sun, Equation (1) becomes

$$L^* = (A\rho + B\rho_e)/(1 - \rho_e S) + L^*_a - (1 - \alpha)D\rho \quad (2)$$

Here $D\rho$ is the radiation that would travel along the L-shaped path from the sun to the surface to the sensor without scattering (the "direct reflected" radiance in MODTRAN).

Equations (1) and (2) together allow one to calculate the apparent reflectance spectrum ρ_p of a partially sunlit surface that is returned by a standard atmospheric correction algorithm that assumes full illumination. To do this, we replace ρ with ρ_p in Equation (1) and equate the spectral radiance to that of Equation (2). This leads to the following relationship between the two reflectance spectra:

$$\rho_p = \rho[1 - (1 - \alpha)D(1 - S\rho_e)/A] \quad (3)$$

According to Equation (3), the observed spectrum ρ_p can be written as a linear combination of a shadow spectrum ($\alpha = 0$), given by $\rho[1 - D(1 - S\rho_e)/A]$, and either the ordinary full-illumination spectrum ρ or the spectrum $\rho D(1 - S\rho_e)/A$ that is attributable to direct sun illumination only (no skylight). The quantity $R = 1 - D(1 - S\rho_e)/A$ is the spectral ratio between the shadowed spectrum and the fully illuminated spectrum, and depends only on quantities that are calculated during the atmospheric correction process.

In strict terms, R is not constant over the scene because of variation in the spatially convolved reflectance ρ_e. However, in most situations this variation can be neglected. At the shortest visible wavelengths, where S is largest, the atmospheric scattering is dominated by Rayleigh scattering, for which the range of the convolution kernel is typically of order 1 km. With a kernel of this size, ρ_e tends to vary little over the scene as long as the different surfaces types are reasonably well distributed spatially. At longer wavelengths the kernel range is shorter, but here $S << 1$ for typical aerosol loadings, so that any ρ_e variation will have only a small effect. Therefore, to a good approximation, we may replace ρ_e with the scene-average reflectance ρ_a. This results in a simple expression for the shadow (full sky-illuminated) to full illumination spectral ratio,

$$R = 1 - D(1 - S\rho_a)/A \quad (4)$$

that is independent of both location in the scene and the spectral properties of the surface. R is of course dependent on the atmospheric properties, particularly the aerosol amount and type, as well as the solar and viewing geometries.

A typical calculation of R using MODTRAN appears in Figure 2. Since the Equation (4) result is close to the simpler expression 1-D/A that neglects $S\rho_a$, the replacement of ρ_e with the scene-average ρ_a should be a negligible source of error. The absorption band structure in R, which is mainly from water vapor, arises because the skylight takes a somewhat longer average path through the atmosphere than the direct sun. With typical atmospheric correction codes, this structure tends not to appear in shadows because the code adjusts the retrieved water amount to compensate. To account for this adjustment, R may be computed using slightly different water amounts in D and A so as to minimize the band structure.

2.3 Shadow-Invariant Detection and Classification

A variety of hyperspectral algorithms exist for the detection of desired materials at the sub-pixel or whole-pixel levels. Unconstrained subspace projection (Chang *et al.*, 1998), constrained unmixing (Keshava *et al.*, 2000), and the matched filter (MF) and Constrained Energy Minimization (CEM) (Farrand and Harsanyi, 1997) algorithms are suitable for sub-pixel detection. Classification algorithms, which assign each pixel to an "endmember" spectrum, work well for whole-pixel detection if the desired material is taken as an endmember. The simplest of these algorithms, which require definitions of endmember spectra but not their statistics, use either Euclidean distance or spectral angle as a spectrum difference metric. The spectrum is assigned to the endmember that gives the minimum distance or angle, or equivalently the maximum angle cosine.

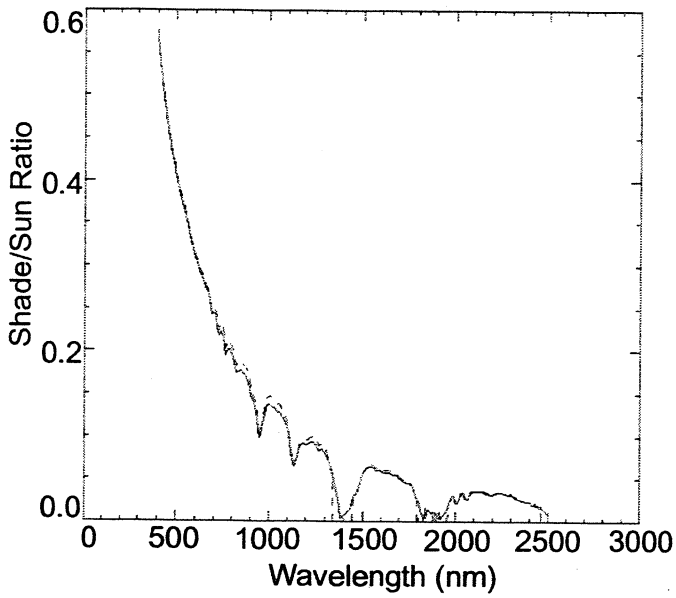

Figure 2. MODTRAN-calculated shadow to full illumination reflectance ratio for the HYDICE Forest Radiance Run 7 scene (56° solar zenith angle, 25 km urban haze, 2200 atm-cm water vapor). Solid line is 1-D/A; dashed line is from Equation (4).

One can envision generalizing the above methods to accommodate the sky-versus-sun spectral difference by representing the desired or endmember material spectrum as some linear combination of the skylit spectrum and the direct sun-illuminated spectrum (the fully illuminated spectrum minus the skylit spectrum). Examples of generalized classification algorithms are given below. *If the sky is considered as a spectrally uniform source, then all combinations of sky and sun illumination can be represented by some positive linear combination of those two spectra,* even when there is less than full sky illumination. As a special case, if one imposes a full-sky illumination constraint the linear combination is defined simply by the direct-sun fraction α.

2.3.1 Algorithms Based on Spectral Angle

The SAM computes the spectral angle between the unknown pixel spectrum and the endmember (or desired) spectrum, a quantity that is amplitude independent. The angle cosine is given by

$$p = \boldsymbol{r}_i^T \boldsymbol{d} \,/\, |\boldsymbol{r}_i||\boldsymbol{d}| \tag{5}$$

where $\boldsymbol{r}_i^T$ is the pixel spectrum, $\boldsymbol{d}$ is the endmember (or desired) spectrum; bold font is used to denote vector quantities and operations.

We may write a generalization of the SAM that explicitly accounts for the spectral variation caused by reduced direct sun:

$$p_L = \boldsymbol{r}_i^T \boldsymbol{d}_p \,/\, |\boldsymbol{r}_i||\boldsymbol{d}_p| \tag{6}$$

Here $\boldsymbol{d}_p$ is the least-squares best-fit linear combination of direct sun-illuminated and sky-illuminated endmember reflectance spectra for each pixel and p_L is the cosine of the spectral angle between the pixel spectrum and $\boldsymbol{d}_p$. If we assume full sky illumination, $\boldsymbol{d}_p$ is written as

$$\boldsymbol{d}_p = \alpha \boldsymbol{d}_1 + \boldsymbol{d}_2 \tag{7}$$

where $\boldsymbol{d}_2$ is the spectrum of the endmember in shadow (*i.e.*, $\boldsymbol{d}$ scaled by R) and $\boldsymbol{d}_1$ is the direct-sun spectrum $\boldsymbol{d} - \boldsymbol{d}_2$. The best-fit direct sun fraction α for the pixel is given by

$$\alpha = (\boldsymbol{r}_i - \boldsymbol{d}_2)^T \boldsymbol{d}_1 / (\boldsymbol{d}_1^T \boldsymbol{d}_1) \tag{8}$$

To keep α physically meaningful it should be restricted to values between 0 and 1. This enhanced version of the SAM is referred to in this paper as *SAM-IM*, for *Spectral Angle Mapper with Illumination Matching*.

2.3.2 Algorithms Based on Distance

The simplest distance metric for detection or classification is the Euclidean distance between the desired or endmember spectrum and the unknown pixel spectrum,

$$D = |\boldsymbol{r}_i - \boldsymbol{d}| \tag{9}$$

A corresponding distance may be defined in which the endmember illumination is best fit to the pixel spectrum:

$$D_L = |\boldsymbol{r}_i - \boldsymbol{d}_p| \tag{10}$$

We have found that the full-sky constraint used to define $\boldsymbol{d}_p$ in Equation (7) is very limiting with the distance metric, since it does not allow brightness matching when the shadows are only partially illuminated by the sky. To overcome this problem $\boldsymbol{d}_p$ is redefined by including β as an effective sky illumination fraction:

$$\boldsymbol{d}_p = \alpha \boldsymbol{d}_1 + \beta \boldsymbol{d}_2 \tag{11}$$

α and β are determined from a least-squares fit to the pixel spectrum. The unconstrained solutions, obtained by 2-dimensional projection, are

$$\alpha = (\boldsymbol{r}_i^T \boldsymbol{u}_1 - w \boldsymbol{r}_i^T \boldsymbol{u}_2) / |\boldsymbol{d}_1|(1 - w^2) \tag{12}$$

$$\beta = (\boldsymbol{r}_i^T \boldsymbol{u}_2 - w \boldsymbol{r}_i^T \boldsymbol{u}_1) / |\boldsymbol{d}_2|(1 - w^2) \tag{13}$$

where $\boldsymbol{u}_1$ and $\boldsymbol{u}_2$ are the unit vectors $\boldsymbol{d}_1/|\boldsymbol{d}_1|$ and $\boldsymbol{d}_2/|\boldsymbol{d}_2|$, respectively, and $w = \boldsymbol{u}_1^T \boldsymbol{u}_2$. If either α or β lie outside the physically plausible 0 to 1 interval, the results are replaced with a constrained solution, which is omitted here for brevity. The classification algorithm based on Equations (10)-(13b) is referred to in this paper as *MD-IM*, for *Minimum Distance with Illumination Matching*.

An alternative, simpler distance metric can be generated by assuming that the spectral shape is illumination-independent, as in the SAM. This leads to a definition of $\boldsymbol{d}_p$ as the projection of the pixel spectrum onto the fully illuminated endmember material,

$$\boldsymbol{d}_p = \boldsymbol{u}\, \boldsymbol{r}_i^T \boldsymbol{u} \tag{14}$$

where $\boldsymbol{u}$ is the endmember unit vector $\boldsymbol{d}/|\boldsymbol{d}|$. The projection magnitude $\boldsymbol{r}_i^T \boldsymbol{u}$ can be limited to a maximum of $|\boldsymbol{d}|$, the length of the endmember, to insure that the illumination does not exceed that of the full sun and sky. This constraint effectively prevents the pixel from being classified with a dimmer endmember, as can happen with the SAM and SAM-IM. We refer to the classification algorithm based on Equations (10) and (14) as *PD*, for *Projection Distance*. While not as accurate as the MD-IM algorithm, a practical advantage is that no information on the shadow-to-full-illumination reflectance ratio is required, making it suitable with atmospheric correction methods such as the ELM that do not use radiation transport calculations.

3. ILLUSTRATIONS

3.1 Shadowed Material Detection

To test the effectiveness of the SAM in cast shadows and assess the importance of the different spectral shapes of sunlight and skylight, the SAM and SAM-IM algorithms were exercised on an early morning image, Run 7, from the 1995 HYDICE Forest Radiance I data. Figure 3 shows a portion of the image where an L-shaped loop

of gravel road (dotted line) runs along a tree line. The short side of the L is in the open but is shadowed by the tree line to the left. The long side of the L is both shaded and partly obscured by overhanging trees. On the opposite side of the road is a line of test objects. The purpose of the demonstration was to find all non-obscured gravel road pixels, including the parts of the road in shadow, using spectral information only (i.e., no spatial filtering). This detection problem is a fairly challenging one, because the actual road spectrum varies over the scene and also because it lacks obvious unique spectral features.

The hyperspectral image was atmospherically corrected using the code developed by Matthew *et al.* (2000), which is based on MODTRAN4 (Berk *et al.*, 1998) and includes an adjacency effect compensation and aerosol retrieval capability. The code was modified to output the D coefficient in Equation (2). A visible range of around 25 km was retrieved with the urban aerosol model. For simplicity we assumed that the sunlit road could be represented by the spectrum from a single pixel. The SAM and SAM-IM angle cosine outputs were calculated and used as the road detection metric; a pixel was identified as road if a threshold was exceeded.

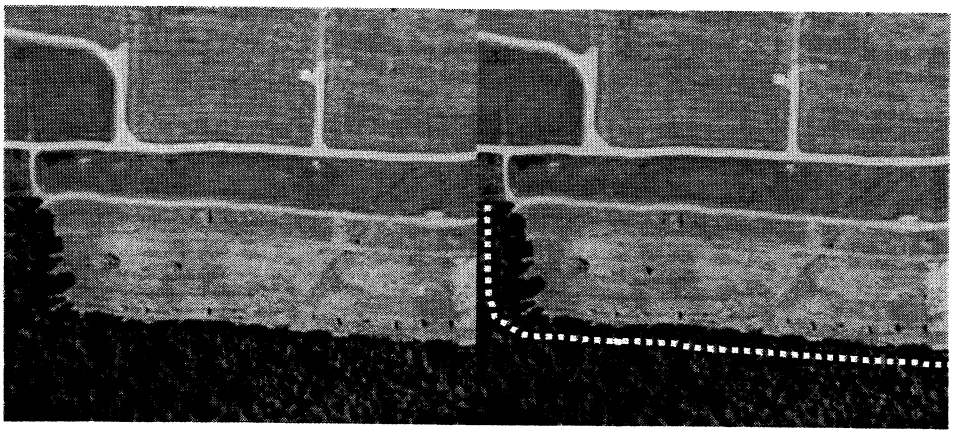

Figure 3. Forest Radiance I Run 7 scene. The right hand image shows the location of a gravel road at the tree line.

The results are summarized in Figure 4, which depicts the output amplitudes as gray scale images in the left-hand column (white = maximum) and the results after thresholding in the right-hand column. In the top two images, the sunlit road spectrum is input, and the SAM yields a strong response to the sunlit road pixels but a very poor response to the shadowed road pixels. In the middle four images, a shadowed road spectrum is input. Here the SAM responds well to the shadowed road and almost as well to shadows cast on the field by the tree line and the test objects, but the response to the sunlit road is poor. Nearly identical results are obtained using an actual shadowed road spectrum (second row) and a spectrum simulated from the sunlit spectrum and the spectral ratio R (third row).

As shown in the bottom two images in Figure 4, the SAM-IM essentially combines the detection capabilities of the sunlit and the shadowed SAM runs. Compared to the ordinary SAM there is some sacrifice in the ability to reject false positives, which, as seen from Figure 3, are mainly from shadows and dead grass. However, this is more than compensated by the new capability to detect the road in shadow.

3.2 Shadow-Invariant Classification

As a second demonstration, we compare the angle metrics of the SAM and SAM-IM with the distance metrics of the PD and MD-IM algorithms for surface classification. The algorithms were applied to an image of the Lamont, Oklahoma DOE ARM site taken by HYDICE in June 1997 (Figure 5) with a very low sun angle (around 15° elevation), resulting in long shadows cast by trees and buildings. The image was atmospherically corrected, and seven representative spectra were manually selected as endmembers. The spectra are grass, dirt (from the furrowed field at the lower left), building roof (from one of the brighter building pixels), pond, black panel (the nominal 3% reflective panel at the upper right corner of the array), road, and driveway (a pixel in the open area between the buildings). These spectra all have distinct shapes, except for the road and driveway, which differ somewhat in brightness but otherwise are very similar. The distinction between the road and driveway classes turns out not to be meaningful, so these classes have been lumped together in the presentation of results.

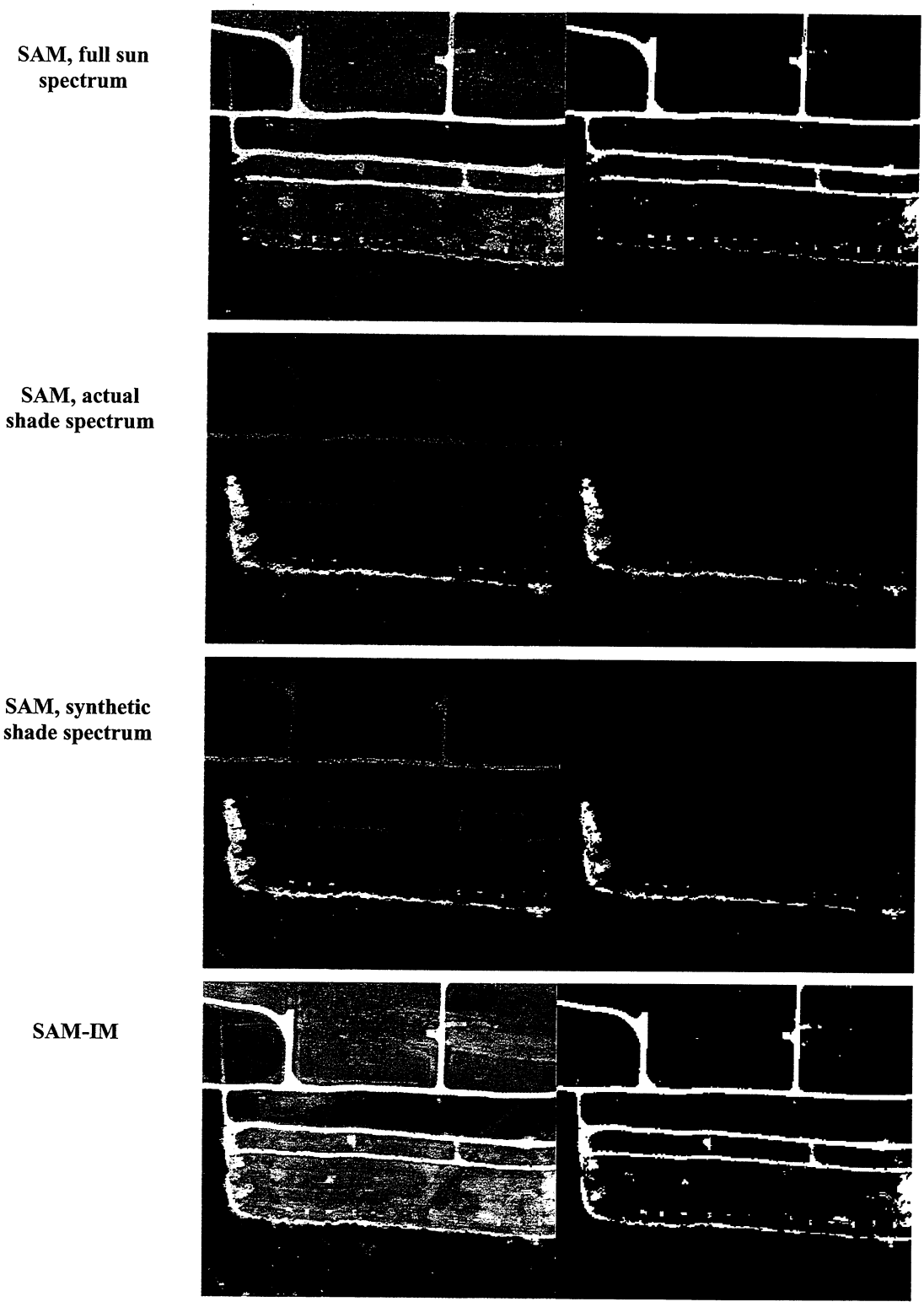

Figure 4. Road detection results. Left-hand images are the angle cosine outputs; right-hand images are the results after thresholding.

The classification results are shown in Figures 6a-d. Enlargements of Figures 5 and 6a-d that focus on the main cluster of buildings appear in Figures 7 and 8a-d. The color scheme in the classification maps is green = grass, ochre = dirt, pink = roof, dark blue = pond, black = panel, gray-blue = road/driveway.

Figure 5. HYDICE ARM Site scene, Run 22.

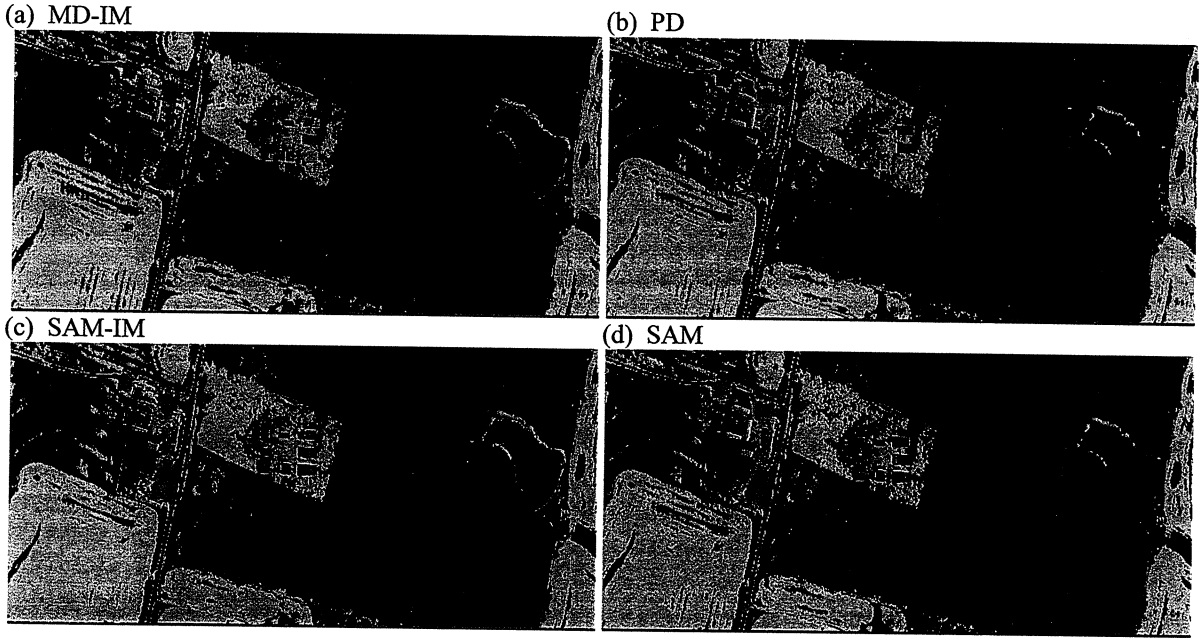

Figure 6a-d. ARM site classification maps.

The main differences among the classifications revolve around the black panel, road/driveway and building classes. The algorithms that do not include the blue-skewing effect of the sky (PD and SAM) classify the shadows on the road/driveway with the black panel, while those that include the skewing correctly assign nearly all of them to the road/driveway class. On the other hand, shadows on the grass are correctly classified as grass by all of the algorithms, including the SAM. The building pixels are classified well by all algorithms except the SAM-IM, which mis-classifies the building roofs that face away from the sun.

The two spectral angle-based algorithms assign a large number of the calibration panels to the black panel class, even those that are much brighter than the black panel. In contrast, the distance-based algorithms assign only portions of the two darkest panels to the black panel class. These results are consistent with the discussion in Section 2.3.2. The MD-IM black panel class is actually a bit too restricted; many of the black panel pixels are assigned to the soil class, apparently because the difference in brightness and color can together be compensated by reduced illumination.

The MD-IM algorithm was also run with different constraints on the sky fractional illumination β. With a lower limit of 0.5 most shadows were properly classified. However, raising the limit to 1.0 gave very poor results; even shadowed grass was mis-classified. The problem may be that the skylight is very anisotropic, increasing strongly near the sun especially when it is low; thus, even a small obscuration of the sky around the sun can reduce the illumination to well below the full sky total. The SAM-IM algorithm performs better than the MD-IM with $\beta =$ 1 because the spectral angle is insensitive to the illumination intensity.

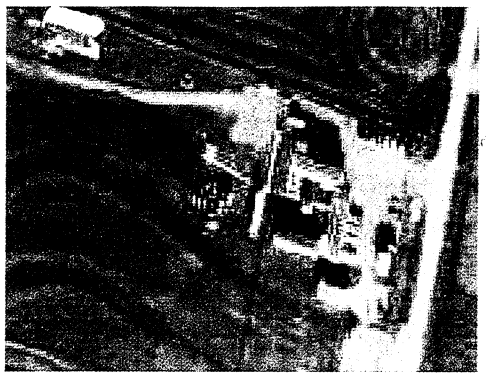

Figure 7. Enlargement of Figure 5.

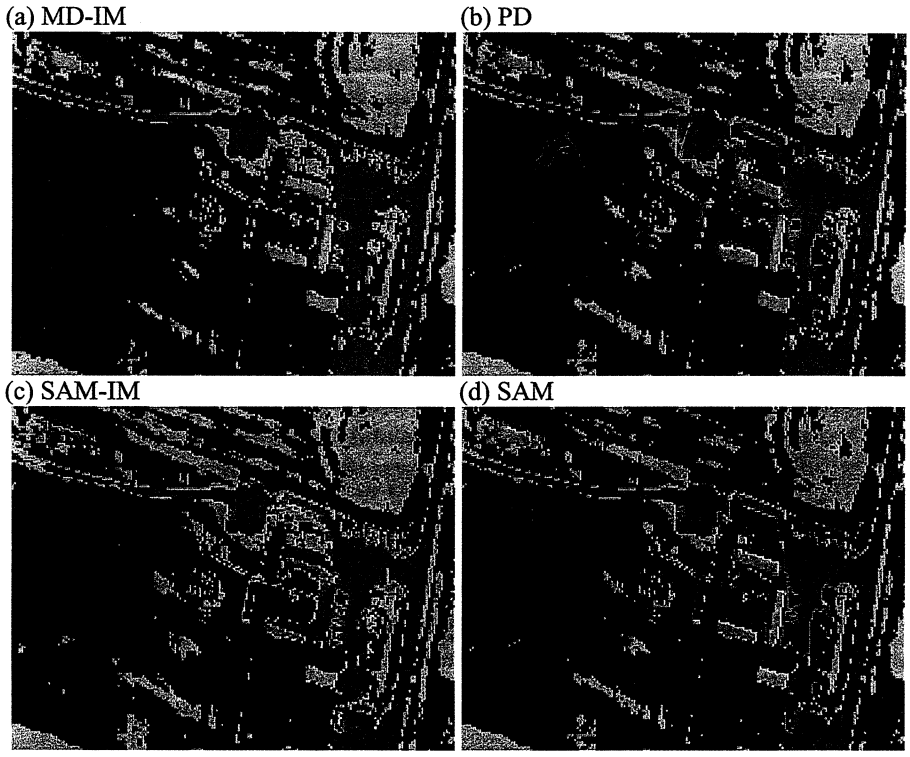

Figures 8a-d. Enlargements of Figures 6a-d.

4. CONCLUSIONS

Starting from radiation transport equations and spectral angle or Euclidean distance metrics, some simple algorithms for illumination-invariant detection or classification of surface materials in atmospherically corrected hyperspectral images have been formulated. In initial demonstrations on HYDICE data the new algorithms performed significantly better in shadow than the Spectral Angle Mapper (SAM). The most successful algorithm, MD-IM, uses a constrained 2-dimensional projection of the pixel spectrum onto apparent endmember reflectance spectra that correspond to illumination by direct sun and by the sky. The sky-illuminated spectrum is simulated from the ordinary reflectance spectrum using a spectral ratio calculated from the MODTRAN radiation transport model. Another algorithm, PD, does not use this ratio but still outperformed the SAM in our tests. Both the PD and MD-IM algorithms generate a spectral distance metric that incorporates a maximum illumination constraint. The SAM has no such constraint, and thus can assign a pixel to the class of a dimmer endmember, which is not physically justifiable for horizontal Lambertian surfaces. For situations where such an assignment may be sensible (for example, when the target brightness is inherently variable due to specular behavior and varying orientation), the allowable maximum illumination could be increased. The sky illumination in the MD-IM algorithm can be constrained with a lower bound; however, the current study did not find this to be helpful.

Further work is needed to evaluate of the performance of the new [illegible]ithms and metrics on a broader range of data and to compare the results with the radiance simulation approach of Healey and Slater (1999). We anticipate that the best performance may be attainable with algorithms, such as the MD-IM, that use a low-dimensional projection, incorporate physical constraints, and take advantage of state-of-the-art radiation transport codes and processing algorithms t[illegible]move sensor-related artifacts (Boardman, 1998). In addition to detection and classification, the PD and MD-IM distance metrics may prove valuable in clustering or other methods for endmember selection. Finally, we note that with either an atmospheric correction or simulation-based approach, inclusion of the adjacency effect is essential for the accurate treatment of dark surfaces and shadows (see Figure 5 of Adler-Golden et al. (1999)).

5. ACKNOWLEDGEMENTS

The authors greatly thank the US Air Force for support under Contract Nos. F19628-99-C-0031 and F19628-00-C-0022 and the Spectral Information Technical Application Center (Fairfax, VA) for providing the HYDICE data.

References

Adler-Golden, S. M., M.W. Matthew, L. S. Bernstein, R. Y. Levine, A. Berk, S. C. Richtsmeier, P. K. Acharya, G. P. Anderson, G. Felde, J. Gardner, M. Hoke, L. S. Jeong, B. Pukall, A. Ratkowski and H.-H Burke, 1999, "Atmospheric Correction for Short-wave Spectral Imagery Based on MODTRAN4," *SPIE Proc. Imaging Spectrometry V*, **3753**, pp. 61-69.

Basedow, R.W., D.C. Armer, and M.E. Anderson, 1995, "HYDICE System: Implementation and Performance," *SPIE Proc. Imaging Spectrometry V*, **2480**, pp. 258-267.

Berk, A., L. S. Bernstein, G. P. Anderson, P. K. Acharya, D. C. Robertson, J .H. Chetwynd and S. M. Adler-Golden, 1998, "MODTRAN Cloud and Multiple Scattering Upgrades with Application to AVIRIS," *Remote Sens. Environ.*, Vol. **65**, pp. 367-375.

Berk, A., L. S. Bernstein and D. C. Robertson, 1989, "MODTRAN: a moderate resolution model for LOWTRAN7," *GL-TR-89-0122*, Air Force Geophys. Lab., Hanscom AFB, MA, 38 pp.

Boardman, J.W., 1998, "Post-ATREM Polishing of AVIRIS Apparent Reflectance Data using EFFORT: a Lesson in Accuracy versus Precision," *Summaries of the Seventh JPL Airborne Earth Science Workshop,* JPL Publication 97-21, Vol. 1, p. 53.

Chang, C-I., Xiao-Li Zhao, M. L. G. Althouse and J. J. Pan, "Lease Squares Subspace Projection Approach to Mixed Pixel Classification for Hyperspectral Images," *IEEE Trans. on Geosci. Remote Sensing*, Vol. **36**, No. 3, (1998).

Farrand, W. H. and J.C. Harsanyi, 1997, "Mapping the Distribution of Mine Tailings in the Coeur d'Alene River Valley, Idaho, Through the Use of a Constrained Energy Minimization Technique," *Remote Sens. Environ.*, Vol. **59**, pp. 64-76.

Gao, B. -C., K. B. Heidebrecht, and A. F. H. Goetz, 1996, "Atmospheric Removal Program (ATREM) Version 2.0 Users Guide," Center for the Study of Earth from Space/CIRES, University of Colorado, Boulder.

Green, R. O., D. A. Roberts, and J. E. Conel, 1996, "Characterization and Compensation of the Atmosphere for Inversion of AVIRIS Calibrated Radiance to Apparent Surface Reflectance," *Summaries of the 6th Annual JPL Earth Science Workshop, JPL Publication 96-4*, Vol. **1**, pp. 135-146.

Healey, G. and D. Slater, "Models and Methods for Automated Material Identification in Hyperspectral Imagery Acquired Under Unknown Illumination and Atmospheric Conditions," *IEE Trans. Geosci. Remote Sensing*, Vol. **37**, pp. 2706-2717 (1999).

Keshava, N., J. Kerekes, D. Manolakis, and G. Shaw, 2000, "An Algorithm Taxonomy for Hyperspectral Un-mixing," *SPIE Proc. Algorithms for Multispectral, Hyperspectral, & Ultraspectral Imagery VI*, **4049**, pp. 42-63.

Kruse, F.A. *et al.*, 1993, "The Spectral Image Processing System (SIPS)--Interactive Visualization and Analysis of Imaging Spectrometer Data," *Remote Sens. Environ.*, Vol. **44**, pp. 145-163.

Matthew, M.W., S.M. Adler-Golden, A. Berk, S.C. Richtsmeier, R.Y. Levine, L.S. Bernstein, P.K. Acharya, G.P. Anderson, G.W. Felde, M.P. Hoke, A. Ratkowski, H.-H. Burke, R.D. Kaiser, and D.P. Miller, 2000, "Status of Atmospheric Correction Using a MODTRAN4-based Algorithm," *SPIE Proceeding, Algorithms for Multispectral, Hyperspectral, and Ultraspectral Imagery VI*, **4049**, pp. 199-207.

Richter, R., 1996, "Atmospheric Correction of DAIS Hyperspectral Image Data," *SPIE Proc. Algorithms for Multispectral and Hyperspectral Imagery II,* **2758**, pp. 390-399.

Results from the Vicarious Calibration of ADEOS/AVNIR and the Visible and Near-Infrared Channels of OCTS with AVIRIS

Kohei Arai
arai@is.saga-u.ac.jp
Dept. of Information Science, Saga University
1 Honjo, Saga 840-8502 Japan

Abstract

A field campaign for the vicarious calibration of the instruments ADEOS/AVNIR (Advanced Earth Observing Satellite/Advanced Visible and Near-Infrared Radiometer) and the visible to near-infrared channels of the Ocean Color and Temperature Scanner (OCTS) was conducted based on the reflectance-based method. The results show a not so small difference between the estimated top of atmosphere (ToA) radiance and the instruments' data-derived radiance, i.e., 3.5 to 20%. In order to confirm the validity of the difference, vicarious calibration based on the radiance-based method was conducted using Airborne Visible/Infrared Imaging Spectrometer (AVIRIS) data. Also, an effect due to the spectral refractive index of aerosol on the estimation of the ToA radiance was confirmed, together with smear-like image defect in the AVNIR imagery data.

1. Introduction

There are two well-defined methods for vicarious calibration of spectral radiometers onboard satellites: (1) reflectance-based and (2) radiance-based [1–4]. The Advanced Earth Observing Satellite/Advanced Visible and Near-Infrared Radiometer (ADEOS/AVNIR) and the visible to near-infrared channels of Ocean Color and Temperature Scanner (OCTS) were calibrated using the reflectance-based method [5–7]. The results show a significant discrepancy—5 to 12%—between the estimated top of atmosphere (ToA) radiance and the instruments' data-derived radiance [8]. From an error budget analysis, it is clear that the vicarious calibration accuracy of the radiance-based method is better than that of the reflectance-based method, in general, if well-calibrated airborne instrument spectral radiometer data is acquired simultaneously with satellite data as well as ground-based measurements. In order to confirm the significant discrepancy, ADEOS/AVNIR and the visible to near-infrared channels of OCTS were re-calibrated using the radiance-based method with well-calibrated AVIRIS data, which was provided by the U. S. National Aeronautics and Space Administration/Jet Propulsion Laboratory (NASA/JPL) through Japan's National Space Development Agency (NASDA) under a contract between NASA and NASDA.

There are many factors influencing vicarious calibration accuracy. It is not so difficult to accurately estimate molecule optical depth (Rayleigh Scattering), optical depth of ozone, and water vapor compared to that for aerosol optical depth (Mie Scattering). One of the largest error sources is estimation of the refractive index of aerosol, which depends on aerosol type and size distribution of aerosol particles, and vertical profile in the atmosphere. Moreover, the refractive index of aerosol has spectral characteristics, so it is better to take into account the spectral refractive index in the estimation of aerosol optical depth.

First, the results from the vicarious calibration of ADEOS/AVNIR and the visible to near-infrared channels of OCTS is briefly described, followed by the results from the radiance-based vicarious calibration. Then the influence due to the spectral refractive index is followed together with the other error sources, in particular, bidirectional reflectance distribution function (BRDF) effect. Also, a smear-like image defect observed in the ADEOS/AVNIR is described.

2. A Brief Description of Previous Vicarious Calibration Results Based on the Reflectance-Based Method

2.1 Major Characteristics of ADEOS/AVNIR and OCTS

The wavelength coverage of ADEOS/AVNIR and the visible and near-infrared channels of OCTS are shown in Table 1.

Table 1. Major Characteristics of ADEOS/AVNIR and the Visible to Near Infrared Channels of OCTS

Center Wave-length	AVNIR	460 (Mu1)	560 (Mu2)	650 (Mu3)	825 (Mu4)	605 (Pa)			
	OCTS	412	443	490	516	565	667	765	862
Band-Width	AVNIR	80	80	80	130	170			
	OCTS	18	20	23	15	19	21	41	39

Mux: Multi-spectral band x, Pa: Panchromatic band

AVNIR is 18 m of spatial resolution of multi-spectral visible to near-infrared radiometer while OCTS is 800 m of spatial resolution of ocean color and temperature scanner.

2.2 Field Campaign

The field campaign was conducted at Ivanpah Playa, California, situated on the border with Nevada, on March 4, 1997. The conditions of the field campaign are shown in Table 2.

Table 2. The Conditions for the Field Campaign for Vicarious Calibration of ADEOS/AVNIR and the Visible to Near-Infrared Channels of OCTS

Date	Location	Lat/Lon	Sunrise	Overpass	Solar Noon
1997/3/4	Ivanpah Playa	35N/115W	6:07	10:49:59	11:52
Surface Pressure	Humidity	Air Temperature	Solar Azimuth	Solar Zenith	Pointing Angle
930 (hPa)	48 (%)	284 (K)	156.8 (deg)	45.0 (deg)	3.6 (deg)

Two days before the field campaign, it rained, so the surface of the test site was dry and the reflectance high. The atmosphere was so clear that curve fitting results between the measured optical depth (368-, 500-, 675-, 778-, 862-nm channels of sun-photometer were used), and the MODTRAN 4.0 derived optical depth shows that the meteorological range is better than 50 km. The sun-photometer used was well calibrated through Langley plots in clear sky conditions, in particular, at the top of the Mauna Loa mountain in Hawaii. Meanwhile, the spectral radiometer used for surface reflectance measurements was also well calibrated, with higher than 1% stability of the gain for short-term measurements (more than 1 hour). The radiometer covers from 500 nm to 999 nm for the visible to near-infrared, with 10 nm of spectral resolution and 1300 nm to 2599 nm for the short-wave infrared region, with 20 nm of spectral resolution. On the other hand, Spectralon® was used for the reference plaque. In the calculation of surface reflectance, the BRDF of the Spectralon was taken into account [9].

2.3 Comparisons of ToA Radiance from the ADEOS/AVNIR- and OCTS-Derived Data and the Field Campaign Data

The results from the field campaign are shown in Tables 3 and 4.

Table 3. A Comparison Between Estimated with Field Campaign Data and Derived from ADEOS/AVNIR Data

Band	Estimated ToA	Digital Number Derived ToA	% Difference
1	89.46	86.33	-3.5
2	140.40	130.29	-7.2
3	112.90	90.09	-20.2
4	93.82	75.43	-19.6

Table 4. A Comparison Between Estimated with Field Campaign Data and Derived from ADEOS/OCTS Data

Band	Estimated ToA	Digital Number Derived ToA	% Difference
1	87.60	75.84	-15.5
2	95.73	86.09	-11.2
3	102.54	93.05	-10.2
4	94.36	86.25	-9.4

3. Vicarious Calibration Using the Radiance-Based Method

3.1 AVIRIS Data Used

Figure 1 shows the AVIRIS-derived AVNIR and the real AVNIR data. The instantaneous field of view (IFOV) and spectral response are adjusted to the AVNIR. A smear-like image defect is seen in all the bands of the real AVNIR images.

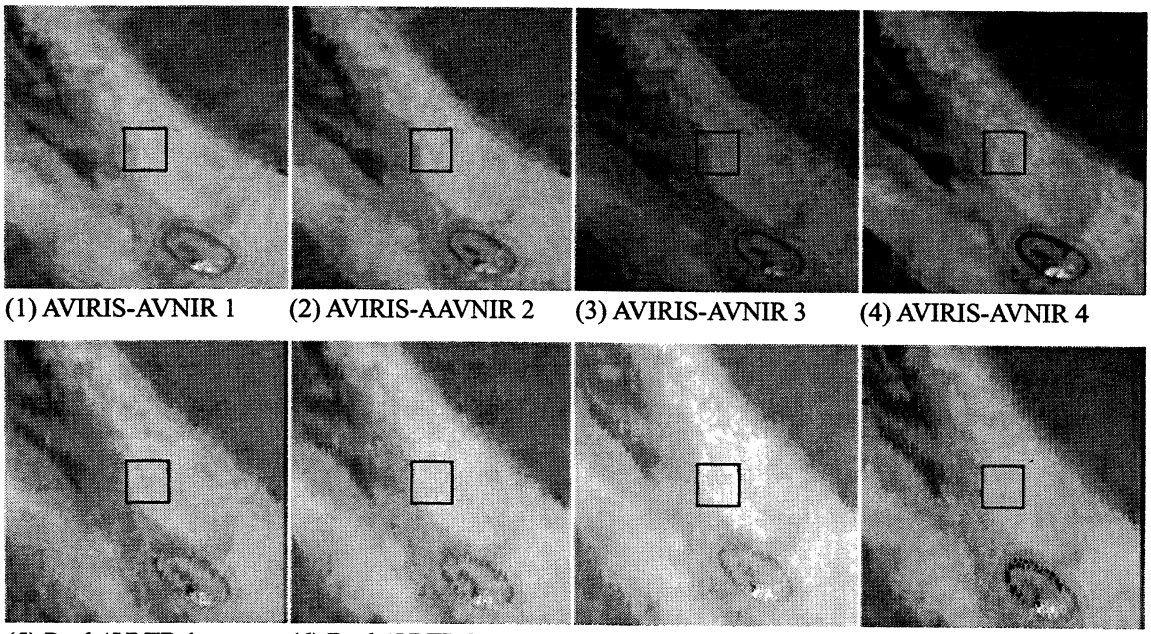

(1) AVIRIS-AVNIR 1 (2) AVIRIS-AAVNIR 2 (3) AVIRIS-AVNIR 3 (4) AVIRIS-AVNIR 4

(5) Real AVNIR 1 (6) Real AVNIR 2 (7) Real AVNIR 3 (8) Real AVNIR 4

Figure 1. The AVIRIS-Derived AVNIR and the Real AVNIR Data (Bands 1 to 4, From the Top to the Bottom) of Ivanpah Playa, California, on March 4, 1997.

3.2 Estimation of ToA Radiance Using the Radiance-Based Method

There are many factors influencing vicarious calibration accuracy. It is not so difficult to accurately estimate molecule optical depth (Rayleigh Scattering), optical depth of ozone, and water vapor compared to that for aerosol optical depth (Mie Scattering). One of the largest error sources is estimation of the refractive index of aerosol, which depends on aerosol type and size distribution of aerosol particles,

vertical profile in the atmosphere. Moreover, the refractive index of aerosol has spectral characteristics, so it is better to taken into account the spectral refractive index in the estimation of aerosol optical depth.

From Total Ozone Mapping Spectrometer (TOMS) data, the total ozone (column) was estimated. By using spectral absorption coefficients provided by World Meteorological Organization (WMO), optical depth due to ozone was estimated. Also, optical depth due to water vapor was estimated, with relative humidity measured at the surface. By using MODTRAN 4.0, a vertical profile of the water vapor was estimated, based on a scaling with the relative humidity on the ground, in accordance with the Mid-Latitude Summer model of MODRAN 4.0.

Using an empirical model of the aerosol, the refractive index of the test site, Ivanpah Playa, in this season was assumed to be 1.44-i0.005, while 3.622 of the Junge parameter was estimated from the optical depth measurement. Then, a ToA radiance was estimated using the Gauss-Seidel Model based atmospheric code (plane parallel atmosphere) as a radiative transfer model, taking multiple scattering in the atmosphere into account.

3.3 Spectral Characteristics of the Refractive Index

Meanwhile, the refractive index has spectral characteristics. The value 1.44-i0.005 implies mixed aerosol particles between water soluble and oceanic aerosols, with the mixing ratio of 0.5 and 0.5, respectively, based on Maxwell-Garnet Mixing Model. Figures 2 and 3 show the characteristics of the real and the imaginary parts of the refractive index for five typical aerosol types: soot, oceanic, water soluble, dust and 75% H_2SO_4. As is shown in the figure, the imaginary part of the water-soluble aerosol has enough of this spectral characteristic to be taken into account. Figure 4 shows the real and imaginary parts of the refractive index of 50 by 50 of oceanic and water soluble.

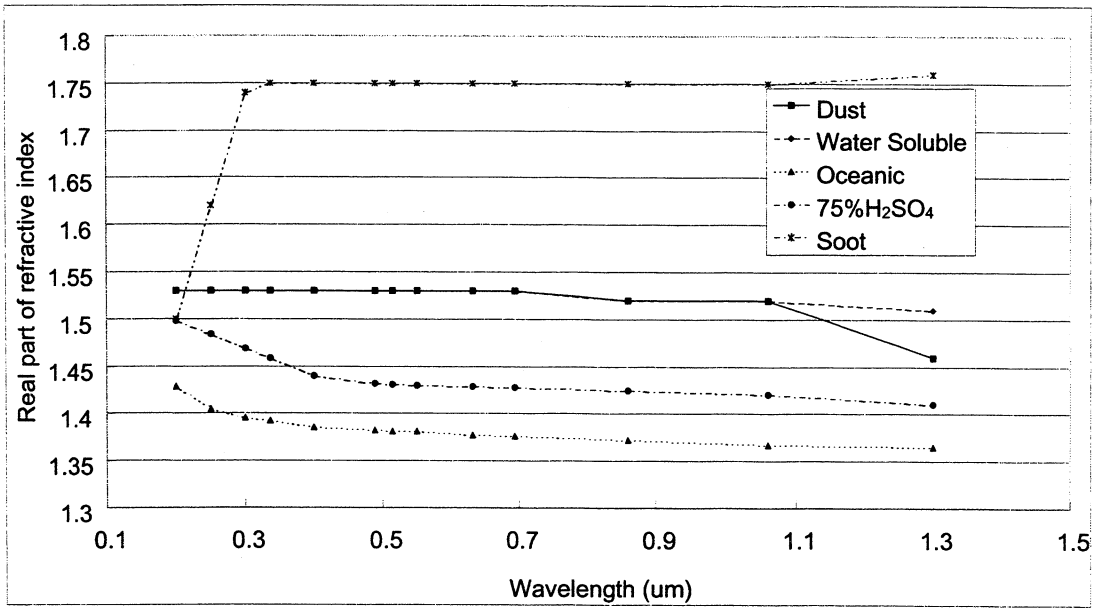

Figure 2. Spectral Characteristics of the Real Part of the Refractive Index.

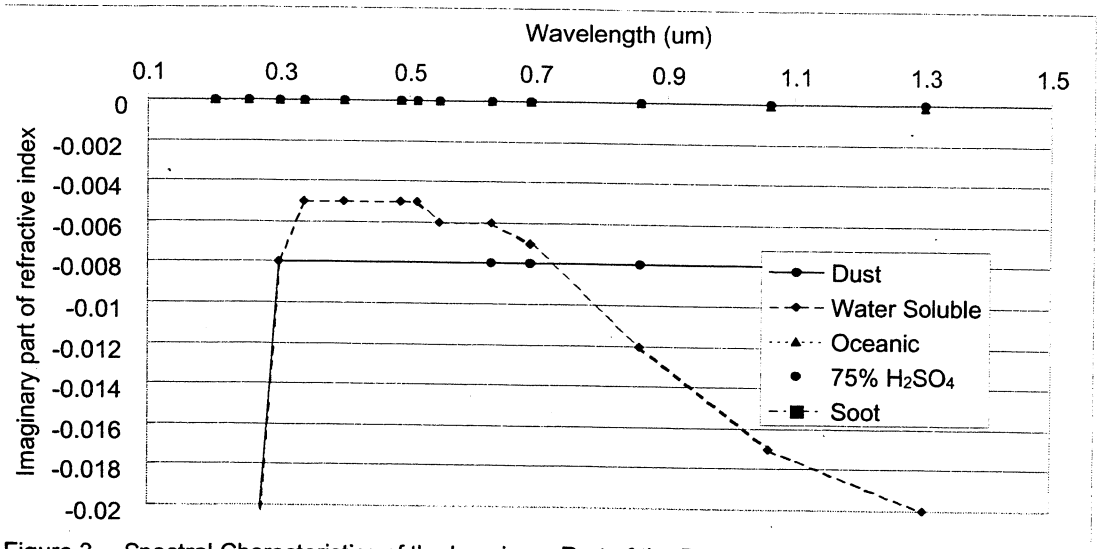

Figure 3. Spectral Characteristics of the Imaginary Part of the Refractive Index.

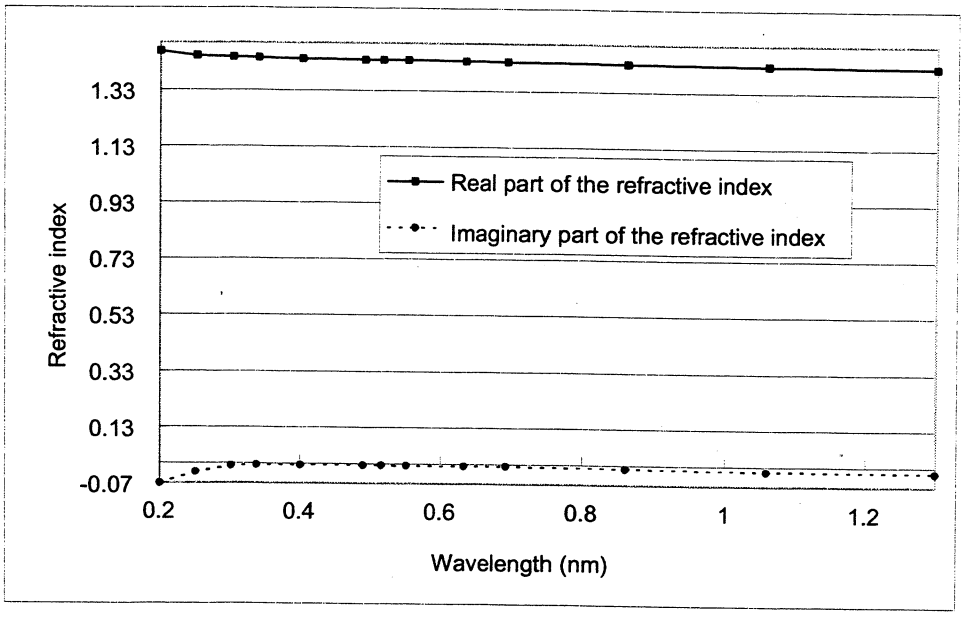

Figure 4. The Refractive Index of 50 by 50 of Mixed Aerosol Between Oceanic and Water Soluble Aerosols.

At the center of the square is the location of test site. In the square, the reflectance in the 36 x 36 m of area was measured. From the estimated parameters with the measured optical depth, atmospheric pressure, relative humidity, TOMS derived column ozone in unit of Dobson unit (DU) and assumed refractive index and size distribution as well as meteorological range from the curve fitting with MODTRAN 4.0, ToA radiance was estimated together with the up-welling radiance at the altitude of 20 km (AVIRIS altitude) based on MODTRAN 4.0. Table 5 shows the single scattering albedo (Omega), path radiance (PathRad.), up-welling radiance of direct component (Direct) and gaseous transmittance (Gaseous) for the ToA radiance under the assumption of the Junge parameter of 3.0 and refractive index of 1.44-i0.005 (first part of the table), for the up-welling radiance at the altitude of 20 km (AVIRIS altitude) (second part of the table), for the ToA radiance taking into account the spectral characteristics of the refractive index (third part of the table) and for the up-welling radiance at the altitude of 20 km (AVIRIS altitude) (bottom part of the table).

3.4 Comparison of ToA Radiance

Results from the comparison of the estimated radiance with and without consideration of the spectral characteristics of the refractive index of aerosol are shown in Figures 5 and 6. In accordance with the change of the transparency above 20-km atmosphere, which is shown in Figure 5, the path radiance, in particular, affects ToA radiance. In the radiance-based method, the difference between actual AVIRIS-derived AVNIR radiance and the estimated up-welling radiance with MODTRAN 4.0 is adjusted in the ToA radiance calculation.

Table 5. The single scattering albedo (Omega), path radiance (PathRad.), up-welling radiance of direct component (Direct) and gaseous transmittance (Gaseous)

ToA		3 1.44-0.005i			
AVNIR Band	ToA	Omega	PathRad.	Direct	Gaseous
1	89.46	0.943681	33.10494	47.15204	0.897127
2	140.4	0.943162	35.47947	104.8832	0.999734
3	112.9	0.942481	10.3049	94.8752	0.931622
4	93.82	0.938002	4.891018	84.38399	0.951556
20-km		3 1.44-0.005i			
AVNIR Band	20-km	Omega	PathRad.	Direct	Gaseous
1	88.43348	0.943681	31.38323	47.73283	0.894639
2	142.7767	0.943162	22.23247	107.7011	0.910047
3	114.3207	0.942481	9.929993	96.52892	0.93123
4	93.84546	0.938002	4.660277	84.62563	0.951414
ToA		3 Spectral			
AVNIR Band	ToA	Omega	PathRad.	Direct	Gaseous
1	89.46214	0.943787	33.10765	47.15204	0.897136
2	140.2458	0.943787	35.34943	104.8832	0.999906
3	112.7916	0.930559	10.24988	94.8752	0.932029
4	93.36738	0.859744	4.680581	84.38396	0.953915
20-km		3 Spectral			
AVNIR Band	20-km	Omega	PathRad.	Direct	Gaseous
1	88.43537	0.943787	31.3858	47.73283	0.894649
2	142.6199	0.943787	22.15099	107.7013	0.910478
3	114.2112	0.930559	9.876302	96.52892	0.931653
4	93.39988	0.859744	4.457769	84.62563	0.953785

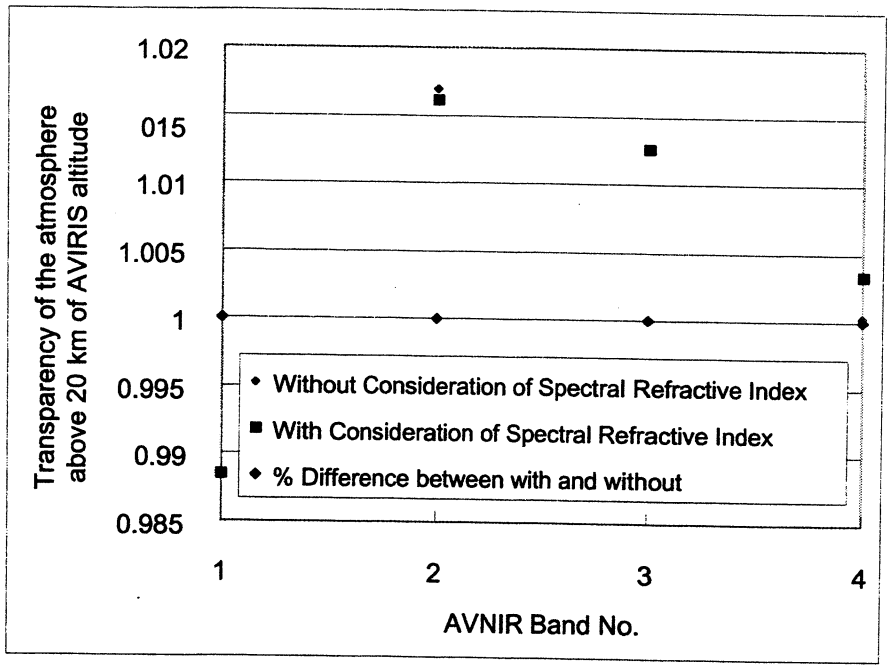

Figure 5. Transparency of the atmosphere from the 20 km altitude (AVIRIS altitude) to the top of the atmosphere.

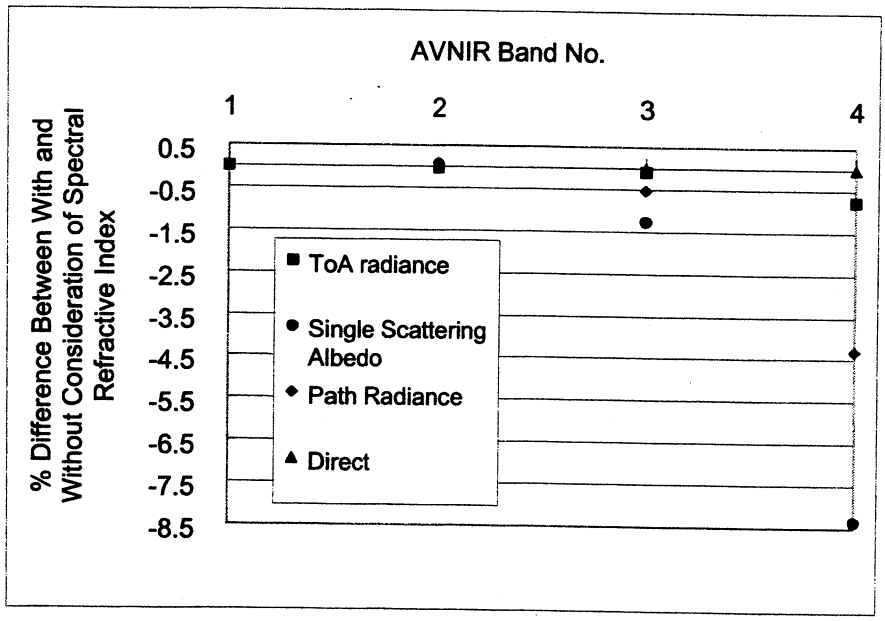

Figure 6. Percent Difference of ToA Radiance With and Without Consideration of Spectral Characteristics of the Refractive Index of Aerosol.

4. Concluding Remarks

It was found that the influence due to the spectral refractive index to ToA radiance was around 0.5% in maximum (AVNIR Band 4). It was also found that the difference between the estimated ToA and AVNIR DN-derived radiance was still large—3 to 18%—even when the radiance-based method was employed. The AVIRIS-derived AVNIR radiance and the estimated ToA radiance showed a good coincidence so that it may concluded that AVIRIS provides a qualified radiance. Moreover, smear-like image defect observed in the real AVNIR imagery data is significant.

Acknowledgements

The author would like to thank Dr. Stuart Biggar and Kutis Thome of the University of Arizona for their valuable discussions. The AVIRIS data used is provided by NASA/JPL through NASDA so that the author would also like to express his deep thanks to Dr. R. Green of NASA/JPL and Dr. S. Shimada of NASDA/EORC (Earth Observation Research Center).

References

[1] P. Slater, S. Biggar, R. Holm, R. Jackson, Y. Mao, M. Moran, J. Palmer and B. Yuan, Reflectance and radiance based methods for the in-flight absolute calibration of multispectral sensors, Remote Sensing of Environment, 22, 11-37, 1987.

[2] K. Arai, Fundamental Theory for Remote Sensing, Gakujutsu Tosho Shuppan Pub.Co., Ltd., 144, 2001.

[3] K. Arai and K. Thome, Error Budget Analysis of Vicarious Calibration Based on Reflectance Based Method, Journal of Japan Society of Photogrammetry and Remote Sensing, 39, 2, 74-81, 2000.

[4] K. Arai, K. Thome, S. Tsuchida, T. Takashima, S. Machida and H. Tonooka, A Field Experiment at Tsukuba Test Site for Vicarious Calibration of ASTER (Visible to Shortwave Infrared Wavelength Region), Journal of Remote Sensing Society of Japan, 20, 1, 55-62, 2000.

[5] K. Arai and Y. Terayama, An Experimental Approach for Vicarious Calibration of ADEOS/AVNIR and the Visible Channels of OCTS, Journal of Japan Society of Photogrammetry and Remote Sensing, 38, 6, 34-40, 2000.

[6] K. Arai, N. Ebuchi, G. Jaross and M. Moriyama, The Results from the Cross Calibration and Validation of the Instruments Onboard ADEOS Satellite, Journal of Remote Sensing Society of Japan, 17, 5, 19-25, 1997.

[7] M. Naka, I. Sato, S. Tsuchida, Y. Kawata, A. Yamazaki, M. Imanaka and K. Arai, An Interim Report on CAL/VAL Study for the ADEOS/AVNIR, Journal of Remote Sensing Society of Japan, 17, 5, 32-40, 1997.

[8] K. Thome, S. Shiller, J. Cornel, K. Arai and S. Tsuchida, Results of the 1996 EOS vicarious calibration joint field campaign at Lunar Lake Playa, Nevada (USA), Metrologia, 35, 631-638, 1999.

[9] K. Thome, F. Palluconi, K. Arai, S. Hook, H. Tonooka and S. Tsuchida, Inflight Radiometric Calibration of ASTER, American Geophysics Union, Spring, Boston, May, 2001.

SPECTRAL UNMIXING OF VEGETATION, SOIL AND DRY CARBON IN ARID REGIONS: COMPARING MULTISPECTRAL AND HYPERSPECTRAL OBSERVATIONS

Gregory P. Asner[1] and Kathleen B. Heidebrecht[1]

1. Introduction

Remote sensing of vegetation cover and condition is critically needed to understand the impacts of land use and climate variability in arid and semi-arid regions. However, remote sensing of vegetation change in these environments is difficult for several reasons. First, individual plant canopies are typically small and do not reach the spatial scale of typical Landsat-like satellite image pixels. Second, the phenological status and subsequent dry carbon (or non-photosynthetic) fraction of plant canopies varies dramatically in both space and time throughout arid and semi-arid regions. Detection of only the "green" part of the vegetation using a metric such as the normalized difference vegetation index (NDVI) thus yields limited information on the presence and condition of plants in these ecosystems. Monitoring of both photosynthetic vegetation (PV) and non-photosynthetic vegetation (NPV) is needed to understand a range of ecosystem characteristics including vegetation presence, cover and abundance, physiological and biogeochemical functioning, drought severity, fire fuel load, disturbance events and recovery from disturbance.

Many approaches have been devised to analyze PV, NPV and bare soil cover in arid and semi-arid regions. A wide variety of studies have attempted to correlate vegetation indices (e.g., NDVI) to the fractional coverage of PV and bare soil (e.g., Duncan et al. 1993, Carlson and Ripley 1997). The typical spectral regions used to detect PV – the visible and near-infrared wavelengths (0.4-1.3 um) – do not easily separate the individual contribution of NPV and bare soil to the measurement (van Leeuwen and Huete 1996, Asner 1998, Roberts et al. 1998, Asner et al. 2000). More recently, spectral mixture analysis (SMA) was developed to decompose image pixels into constituent PV, NPV and bare soil covers. Many SMA efforts have now been applied in arid and semi-arid ecosystems using airborne and spaceborne sensors (e.g., Smith et al. 1990, Sohn and McCoy 1997, Wessman et al. 1997, Elmore et al. 2000). Most SMA approaches assume that image pixels contain endmember cover fractions that are linearly summed:

$$\rho(\lambda)_{pixel} = \Sigma [C_e \bullet \rho(\lambda)_e] = [C_{pv} \bullet \rho(\lambda)_{pv} + C_{soil} \bullet \rho(\lambda)_{soil} + C_{npv} \bullet \rho(\lambda)_{npv}] \quad (1)$$

where $\rho(\lambda)_e$ is the reflectance of each land-cover endmember (e) at wavelength λ. The sub-pixel cover fraction (C_e) of each land-cover endmember may be PV, NPV, bare soil or other constituents. Solving for the sub-pixel cover fractions (C_e) therefore requires that the observations (in this case, reflectance or $\rho(\lambda)_{pixel}$) contain enough information to solve a set of linear equations, each of the form of equation (1) but at a different wavelength (λ).

The selection of reflectance endmembers ($\rho(\lambda)_e$) for equation (1) is also critical to the accurate estimation of the sub-pixel cover fractions (C_e). These endmembers are usually selected either from the image data (e.g., Wessman et al. 1997) or from spectral libraries built from field surveys (e.g., Roberts et al. 1998). Each approach has distinct advantages and disadvantages. Image-based endmembers are ideal because they are drawn from the population of data points to be analyzed, which increases the likelihood that image pixels will be decomposed using endmembers that actually exist in the area. However, selection of image endmembers often requires the availability of pixels comprised purely of each dominant cover type. Pure image pixels are rarely available in images of ecosystems, especially in arid and semi-arid regions. A very unique method for addressing this issue has been developed by Bateson and Curtiss (1996) and Bateson et al. (2000). Nonetheless, no automated, fully objective methods have been developed for dealing with sub-pixel heterogeneity in image endmember selection.

The alternative approach of spectral endmember libraries has its advantages and problems as well. The major advantages are that endmembers can be readily collected from large field-based surveys and that the quality and interpretation of the endmembers are easy to control. The potential problems in using spectral libraries relate to endmember generality and scalability. Spectral endmembers collected in one area may not be applicable to another

[1] Carnegie Institution, Stanford, California, 94305.

area, depending on the spatial and temporal variability of vegetation, soils, rocks and other features. Equally important, vegetation spectral properties collected at the leaf or branch level, or very close to the top of a plant canopy, usually do not well represent the spectral properties of the entire plant canopy, which includes all of the tissues, their architectural orientation, and within-crown gaps (Asner 1998, Asner in press).

Of the many spectral mixture modeling methods presented in the literature, all have either used multi-spectral or hyperspectral observations to decompose image pixels into constituent endmember cover fractions (C_e of eq. 1). To our knowledge, no studies have objectively compared the capabilities of multi-spectral and hyperspectral observations with spectral mixture analysis to estimate PV, NPV and bare soil extent in arid and semi-arid ecosystems. To do so requires: (1) that the generality and scalability of the endmember spectra are controlled for in the experiment; (2) that the spectral resolution of the endmember spectra and image data are adjusted between multi-spectral and hyperspectral cases in a consistent manner; and (3) that the spectral mixture model is general, fully automatic and thus resistant to subjective decision-making, such as in the determination of spectral endmembers.

In this paper, we present a study that quantitatively compares the ability of various multi-spectral and hyperspectral observations to decompose remotely sensed optical data into sub-pixel photosynthetic vegetation (PV), non-photosynthetic vegetation (NPV) and bare soil covers. We employed five different spectroscopic sampling schemes available from the NASA Airborne Visible-Infrared Imaging Spectrometer (AVIRIS) as well as with these data convolved to Landsat Thematic Mapper (TM), Terra Moderate Resolution Imaging Spectrometer (MODIS), and Terra Advanced Spaceborne Thermal Emission and Reflection Radiometer (ASTER) optical channels. The analysis using the six optical Landsat TM channels was selected to represent one of the most commonly available satellite data sets for land-cover monitoring. The ASTER analysis was selected because of its relatively dense 5-channel sampling of the shortwave-IR2 (SWIR2) region between 2.1 and 2.4 μm. We tested MODIS because it is available on a daily basis, and it provides a 15-channel sampling of the visible and NIR spectral regions.

2. Study Region

The study area was located in the northeast Chihuahuan Desert, New Mexico, USA at the U.S. Department of Agriculture (USDA) Jornada Experimental Range (Figure 1). Mean annual precipitation is 210 mm yr^{-1}, and mean annual temperature is 16°C (min: -7°C, max: 38°C). The area is also a U.S. National Science Foundation (NSF) Long-term Ecological Research (LTER) site, and has been the focus of many hydrologic and ecological studies associated with land use in arid ecosystems (Schlesinger and Pilmanis 1998). Long-term grazing and fire suppression have been factors in the observed conversion of desert grasslands to shrublands (Buffington and Herbel 1965, Schlesinger et al. 1990). Some areas remain dominated by *Boutelua eriopoda* (black grama) grasslands, while other areas have been transformed into *Prosopis glandulosa* (mesquite) shrublands. The grasslands are also sparsely populated by *Prosopis* shrubs and occasional yucca plants (*Yucca elata*). The shrublands are comprised of a two-phase landscape containing dune-like mesquite clusters imbedded in a bare soil surface.

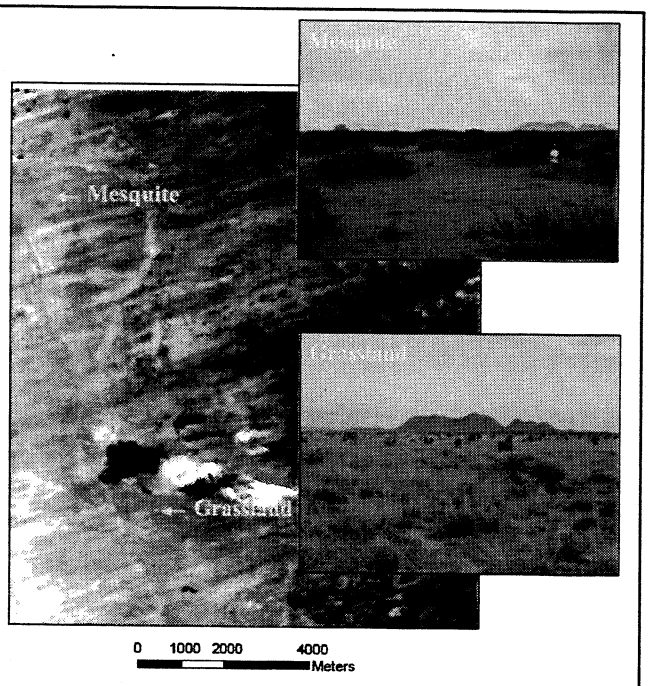

Figure 1. AVIRIS (Red: 0.80 μm, Green: 0.68 μm, Blue: 0.54 μm) showing the Jornada Experimental Range and locations of field sites. Photographs of the shrubland and grassland sites illustrate the differences in photosynthetic vegetation (PV), non-photosynthetic vegetation (NPV), and bare soil covers in each study area.

3. Site Selection and Field Sampling

For this study, the biophysical and geochemical requirements of an experimental grassland and shrubland site included: (1) low species diversity, (2) strong differences in PV cover between sites, (3) pronounced differences in NPV between sites, and (4) nearly constant soil type. These requirements were used to maximize differences in the physical setting between two arid ecosystem sites while minimizing biogeophysical variability within each site. We also selected sites that had few cryptobiotic soil crusts, which can play an important role in determining the "green" reflectance properties of arid ecosystems (Karnieli et al. 1999) and thus confuse our study. Using these requirements, we selected one shrubland and one grassland area, each of 8 ha (200 m x 400 m) in size (Figure 1). A 300 m transect was established in each area running directly north-south (azimuth = 0); geo-location of each transect was achieved using differentially-corrected global position system (GPS) measurements. The following field measurements were made at the two sites in June 2000, coincident with an airborne imaging spectroscopy acquisition using the NASA AVIRIS sensor: (1) species presence-absence, (2) PV, NPV and bare soil cover fraction, and (3) spectroscopy of PV, NPV and bare soil covers.

The vascular plant composition of each site was determined using a presence-absence tabulation of species every 5 m along the 300 m transect. At the grassland site, the fractional cover of PV and NPV was determined using a visible/near-infrared digital camera (Agricultural Digital Camera - ADC; Dycam, Inc.). The camera was mounted 3 m above the ground in the downward nadir-viewing position from a portable boom, yielding an image field-of-view of 1.5 m x 2.5 m. The camera uses visible and near-infrared filters to isolate the fractional cover of PV and bare soil as described by White et al. (2000). Here, we imaged the grassland canopy every 10 m along the centerline of the 300 m transect.

Vegetation cover fraction at the shrubland site could not be adequately determined using the ADC camera because the shrub clusters (~ 5-15 m dia.) are much larger than the field-of-view of the ADC camera (~ 1.5 x 2.5 m). Therefore, we acquired a pan-chromatic IKONOS image with spatial resolution of 1m on July 2, 2000, which was within two weeks of the field sampling and AVIRIS data acquisitions. This imagery was co-located with the AVIRIS data to facilitate comparisons of PV cover along the 300 m transect. Because NPV cover was near zero in the shrubland area, the IKONOS data isolate PV from the soil background.

Canopy and soil spectroscopic measurements were collected using a field spectroradiometer (Fieldspec FR-Pro, Analytical Spectral Devices, Inc.) along each transect in the shrubland and grassland sites and at eight other shrubland and grassland locations throughout the area. The spectroradiometer collects upwelling radiance measurements in the 0.4-2.5 μm wavelength range; the sampling interval is 1.4 μm in the visible and near-IR (0.4-1.0 μm) and 2.0 μm in the shortwave-IR (1.0-2.5 μm). The spectral radiance measurements were collected at 5 m intervals along the 300 m transects and were converted to reflectance using a calibration panel (Spectralon, Labsphere, Inc.). All plant canopies within 5 m radius of the sampling point were measured. At the time of the field survey, the grassland canopies were nearly fully senescent and the shrubland canopies were fully green, allowing us to separate the spectra both by species and by PV-NPV category. In addition, the spectral reflectance properties of bare soil patches were measured at each sampling location along each transect.

4. Airborne Imaging Spectroscopy

AVIRIS imaging spectroscopy data were collected over the field sites on June 10, 2000, coincident with the field measurement campaign. The AVIRIS sensor was flown on a NASA ER-2 aircraft at an altitude of 20 km, which resulted in image pixels of 19 m x 19 m. The flightlines were oriented in the north-south direction (azimuth = 0°). The imagery was geo-located using roads matched to GPS points in a geographic information system (GIS). The GIS data were provided by the USDA and Jornada LTER staff (courtesy of B. Nolen); the geo-location accuracy of the roads was less than 1 m. The AVIRIS data were converted from radiance to apparent surface reflectance using the ATREM atmospheric calibration code (Gao et al. 1993) and further refined using a field spectral measurement of a bare soil area.

5. Spectral Mixture Analysis

We developed a general, probabilistic model for decomposing optical reflectance measurements into sub-pixel estimates of PV, NPV and bare soil covers. This model is fully automated and uses a Monte Carlo approach to

derive uncertainty estimates of the sub-pixel cover fraction values (Figure 2). The model, *AutoMCU*, is based on a code first developed only for the shortwave-IR spectral region (*AutoSWIR*; Asner and Lobell 2000), but it is more general in that any combination of optical wavelengths can be used in the unmixing process. *AutoMCU* uses three spectral endmember "bundles", derived from field measurements, to decompose each image pixel using equation (1).

We used the spectra collected in the grassland and shrubland field sites to execute the unmixing code. Our intent was to minimize errors and uncertainty that can arise when unmixing image pixels with spectral endmembers not present in the specific study area. This strategy was critical to comparing the accuracy of sub-pixel cover fraction estimates from different combinations of spectral channels and signature types.

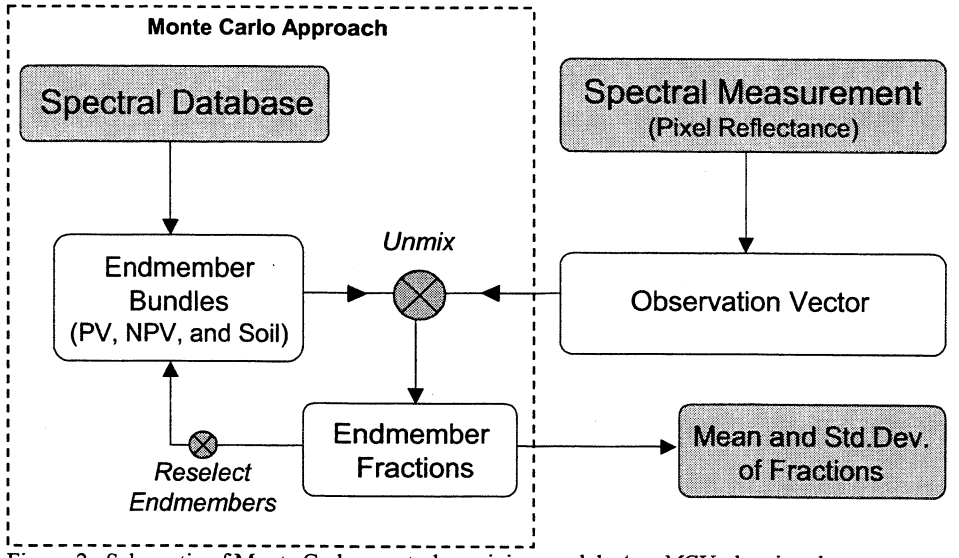

Figure 2. Schematic of Monte Carlo spectral unmixing model, *AutoMCU*, showing that any spectral measurement (in any number of wavelength channels) forms an observation vector. This observation vector is decomposed using eq. 1 (text) with spectral endmember bundles of photosynthetic vegetation (PV), non-photosynthetic vegetation (NPV), and bare soil. The unmixing algorithm is iteratively run using endmembers randomly selected from these sets (n = 50). The algorithm produces sub-pixel cover fraction values with uncertainty estimates that arise from variability in the endmember bundles.

After the three spectral endmember bundles (PV, NPV, soil) were collected from the field, they were sub-sampled to AVIRIS, Landsat TM, ASTER, and MODIS wavelength channels using published spectral response functions. The AVIRIS imagery was also convolved to the wavelength channels provided by the four satellite instruments. This provided a means to spectrally unmix the same ecological area using the same field spectra and *AutoMCU* code. The only difference between each spectral unmixing was the wavelength sampling. In addition, we tested the accuracy of spectrally decomposing image pixels using only the visible and near-IR (0.4-1.3 μm) and only the shortwave-infrared (SWIR: 1.3-2.5 μm) hyperspectral measurements from AVIRIS.

The SWIR2 (2.0-2.3 μm) spectral unmixing algorithm of Asner and Lobell (2000) was also tested against the other spectral sampling schemes. This algorithm uses SWIR2 spectra that are "tied" at 2.03 μm to isolate the shapes of the PV, NPV and bare soil spectra, which are very distinct in this wavelength region. Based on both field and radiative transfer studies (Asner 1998, Asner et al. 2000), tied-SWIR2 spectra of PV and NPV should be less susceptible to variation in canopy biomass, architecture and leaf biochemistry. Tied-SWIR2 spectral bundles of bare soils accommodate variation in geochemical properties that cause the distinctive 2.2 μm soil hydroxyl (OH^-) absorption feature to shift in width, shape, and depth (Ben-dor et al. 1999). Therefore by developing bundles of these tied-SWIR2 spectra for use in the Monte Carlo unmixing model, *in situ* variations in biochemical and geochemical properties are propagated to the sub-pixel cover fraction estimates.

Some studies have divided the spectral reflectance values within a given wavelength region by the reflectance value at the first wavelength. This is analogous to tying at 2.03 μm, but dividing is often used to accentuate the distinctive absorption features of various materials (Clark 1999). We therefore also test the spectral unmixing model using divided SWIR2 data. In addition, the SWIR2 data in five ASTER channels provide a means to test both the tying and dividing approaches using an available multi-spectral satellite instrument. This comparison is especially pertinent here since the ASTER and AVIRIS instruments have similar spatial resolutions of

15-30m and ~20m, respectively. All of the spectral wavelength sampling and signature permutations compared in this study are presented in Table 1.

6. Results and Discussion

Species Composition

The vascular plant presence-absence survey yielded the following information verifying that the first criterion for site selection (low plant diversity) was successfully met. At the shrubland site, 98.9% of the species present was *Prosopis glandulosa*, and 1.1% was comprised of small, fully senescent herbaceous grasses and forbs (species undetermined). At the grassland site, the species present were *Boutelua eriopoda* and other graminoids (99.3% of the time), *Prosopis* (4.7%), and *Yucca* spp. (3.3%).

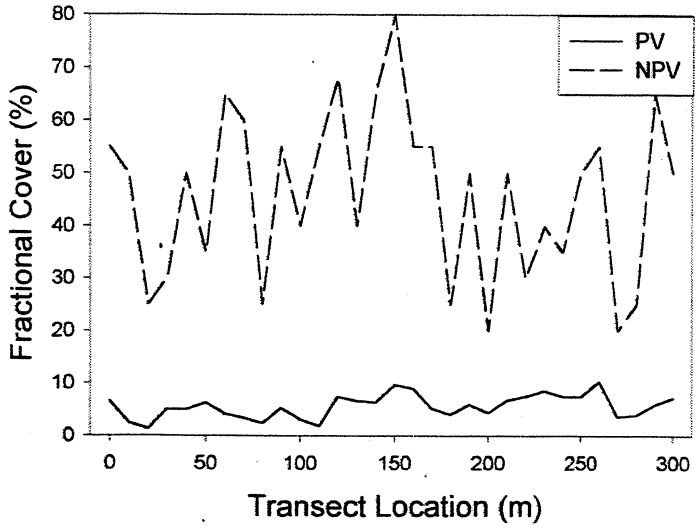

Figure 3. Photosynthetic vegetation (PV) and non-photosynthetic vegetation (NPV) cover along a 300 m transect cutting through the 8 ha grassland study site. PV and NPV fractions were calculated using the method described in detail by White et al. (2000).

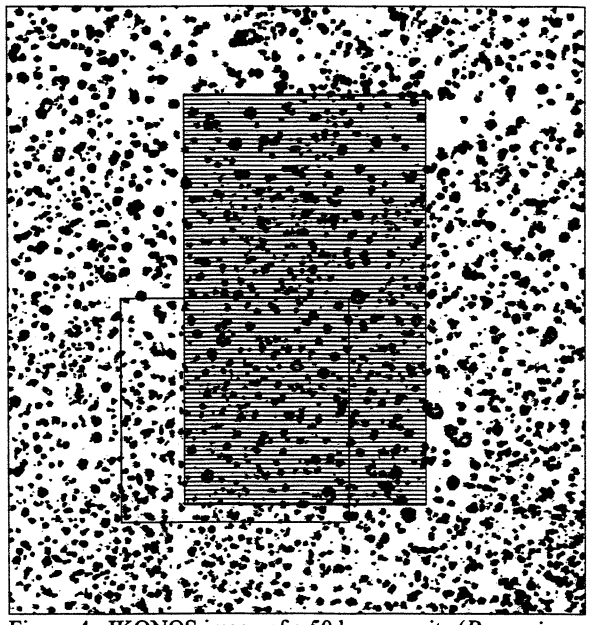

Figure 4. IKONOS image of a 50 ha mesquite (*Prosopis glandulosa*) shrubland area. Large shrub-dunes are visible throughout this region. The rectangular box indicates extent of 200 x 400 m (8 ha) study area, showing the photosynthetic vegetation (PV) cover of 18%. The square box shows the extent and overlap of the 200 x 200 m study area from Rango et al. (2000), which indicated a PV cover of 19%.

PV, NPV and Bare Soil Cover

At the grassland site, the ADC camera results yielded a mean PV cover of 6.9% (std. dev. = 3.3%), with a range of 1% to 18% (Figure 3). Bare soil fraction estimates yielded mean (s.d.) values of 58.6 (17.3) %, with a range of 20% to 80%. Asner et al. (2000) had estimated PV fractional cover of 4-11% along a neighboring grassland transect in May 1997. Those values were determined independently from our values reported here, by measuring total vegetation cover and multiplying it by the NPV:PV ratio of 1m sub-plots in the area.

At the shrubland site, the high spatial resolution IKONOS imagery indicated a PV and bare soil cover fraction of 18% and 82%, respectively, throughout the 8 ha area surrounding our 300m transect (Figure 4). This concurs with recent laser altimetry data that yielded PV and bare soil cover estimates of 19% and 81%, respectively (Rango et al. 2000). These estimates also agree with those reported by Schlesinger et al. (1996) and Asner et al. (2000).

NPV was extremely low (< 2%) at the shrubland site as is evident in our field transect of plant

presence-absence as well as in our visual surveys of the area (Figure 1). NPV was extremely high at the grassland site (mean = 36.7%, s.d. = 13.3%), with values ranging from 10-70% along the 300m transect. These estimates concur with recent studies conducted in the same or similar areas (Schlesinger et al. 1996, Asner et al. 2000).

Field Spectroscopy

Field spectral data collections yielded distinct spectral endmember bundles for PV, NPV and bare soil (Figure 5). The PV spectra from shrubland and grassland sites were not statistically different (t-tests by wavelength), and thus they were combined into a single PV endmember set for all subsequent spectral mixture analyses (Figure 5a). The PV spectra showed typical value ranges for the visible, NIR, and SWIR wavelength regions as found in many arid ecosystems (Asner 1998). The greatest spectral variation occurred in the NIR (0.7-1.3 μm) and was the lowest in the SWIR2 region from 2.1-2.4 μm. The strong NIR spectral variation is indicative of highly varying leaf area index (LAI) at the scale of individual plant canopies (Asner et al. 2000). While the SWIR2 region did show some variability in the magnitude of reflectance, the spectral shapes were highly consistent (Figure 5d).

The NPV spectra were collected only from the grassland site, as very little NPV was present or exposed at the shrubland site. These NPV spectra were used in all mixture modeling analyses of both sites. Consistent with previous studies, the NPV spectra showed almost constant monotonic-increasing reflectance in the visible-NIR region (Figure 5b). Several dry carbon spectral absorption features in the SWIR2 region are clearly apparent. The features near 2.1 and 2.4 μm are associated with the presence of cellulose, starch and oils (Curran 1989). While the magnitude of reflectance varied strongly in the SWIR2 region, the shapes of the spectra were highly consistent (Figure 5e).

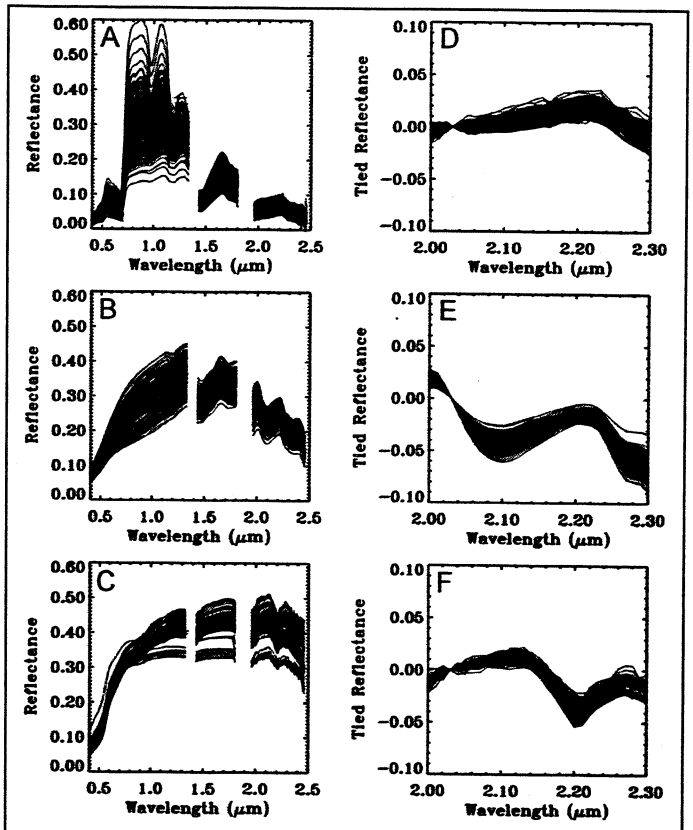

Figure 5. Field spectra from shrubland and grassland sites throughout the area: (A) photosynthetic vegetation (PV), (B) non-photosynthetic vegetation (NPV), (C) bare soil. The spectral shapes in the shortwave-IR2 region (2.0-2.3 μm) are shown in panels D-F to highlight the distinctiveness and relative consistency of endmembers when "tied" at 2.03 μm.

The soil spectra were similar between sites (t-tests by wavelength), thus they were combined into a single endmember set for spectral mixture analyses. The well-described OH^- absorption feature near 2.2 μm is apparent (Figure 5c), as are the visible wavelength features associated with the presence of iron (Ben-dor et al. 1999). Again, the shapes of the soil spectra in the SWIR2 region were distinct from PV and NPV, and they were relatively consistent (Figure 5f).

AVIRIS and AVIRIS-Convolved Spectra

The AVIRIS spectra from the shrubland and grassland sites are shown in Figure 6a-b. Subtle differences between sites can be seen in the AVIRIS spectroscopy throughout the visible-NIR transition, the SWIR1 (1.5-1.8 μm) and the SWIR2 (2.0-2.4 μm) wavelength regions. The magnitudes of reflectance values from each site were statistically similar at nearly all wavelengths (t-tests by wavelength). Visual inspections also showed the shapes of the spectra in the visible, NIR and SWIR1 regions to be very similar. However, the shapes of the reflectance continuum in the SWIR2 region were unique between the shrubland and grassland sites (Figure 6c-d). Tied-SWIR2

spectra visually indicate that the shrubland site contained high bare soil cover due to well-defined 2.2 μm OH^- absorption features (Figure 6c). The grassland site displayed weaker OH^- features in the tied-SWIR2 spectra (Figure 6d). Tied SWIR2 spectra in the 2.02-2.12 μm region from the grassland site indicated the presence of significantly more NPV than in the shrubland site. The convex shapes of the tied-SWIR2 data from the grassland site were distinct from the concave shapes of the data from the shrubland site.

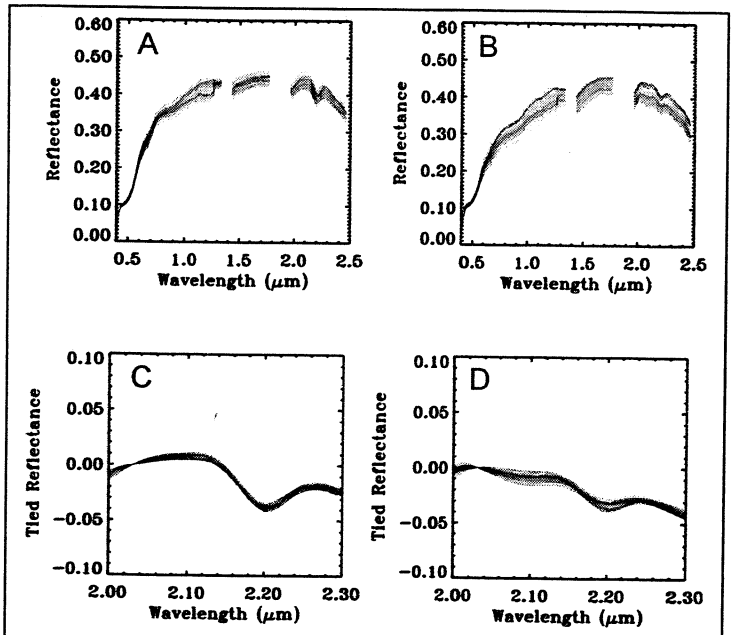

Figure 6. AVIRIS spectra from the (A) shrubland and (B) grassland sites. The 2.03-μm tied spectral shapes in the shortwave-IR2 region (2.0-2.3 μm) are shown in panels C-D.

The Landsat TM-convolved data showed little difference between the shrubland and grassland sites (Figure 7a), with only a slight difference in albedo in the NIR and SWIR wavelengths. The MODIS data provided an increased sampling of the visible and NIR spectral regions (Figure 7b), yet the two field sites were spectrally indistinguishable using these channels. This was the case for the visible-NIR channels in the AVIRIS data as well (Figure 6a-b). Previous studies have shown that bare soil and NPV cannot be easily separated in visible-NIR wavelength channels (Huete 1988, van Leeuwen and Huete 1996, Asner et al. 2000). The ASTER data provided a unique multi-spectral

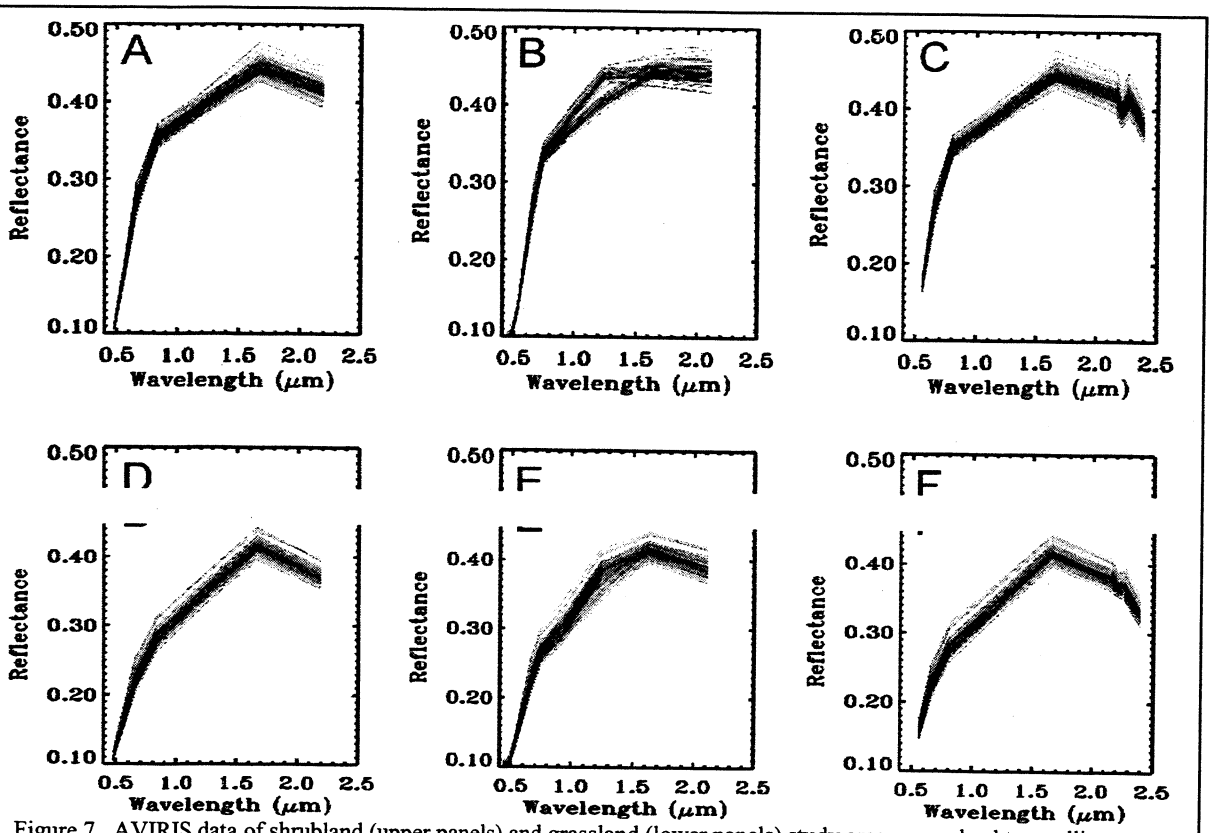

Figure 7. AVIRIS data of shrubland (upper panels) and grassland (lower panels) study areas convolved to satellite sensor channels: (A) Landat TM, (B) MODIS, (C) ASTER, (D) Landsat TM, (E) MODIS, (F) ASTER.

sampling of the SWIR2 (Figure 7c), indicating some differences between sites. The tied-SWIR2 ASTER data are provided in Figure 8, showing the distinctive OH^- absorption feature at 2.2 μm for the shrubland site, and less so for the grassland area. ASTER's sampling of the SWIR2 region does not resolve the 2.0-2.12 μm wavelengths that are needed for detection of NPV (Figure 5).

Monte Carlo Spectral Mixture Analyses

The Monte Carlo spectral unmixing provided two pieces of information important to this study: (1) the accuracy of PV, NPV, and bare soil estimates and (2) the uncertainty or precision of these estimates. Table 2 shows the spectral decomposition results for the shrubland and grassland sites using the ten different wavelength permutations. The summary of field and IKONOS results are also shown under "Field Measurements" in Table 2.

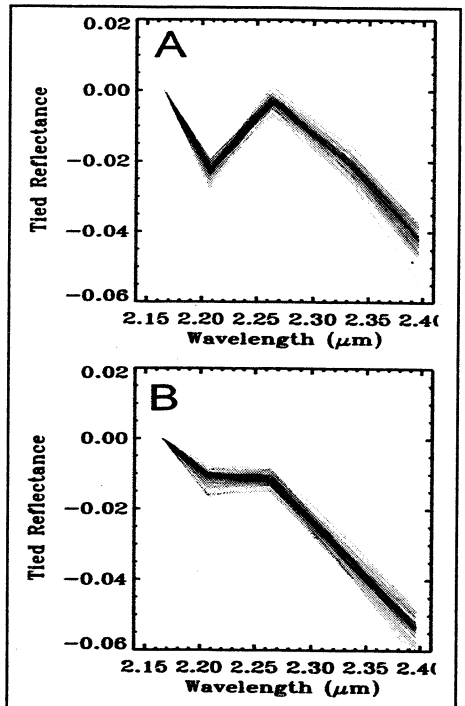

Figure 8. Tied (normalized to 2.16 μm) spectra in the five ASTER shortwave-IR2 channels for the (A) shrubland and (B) grassland sites.

The full-range AVIRIS unmixing resulted in negative PV fractions, and the bare soil fractions were consistently over-estimated by about 20% (Table 2). However, the estimated NPV fractions were very close to the field NPV values, and within the statistical uncertainty of the two methods (ANOVA, $p < 0.05$). The data show that full spectral range (0.4-2.4 μm) analyses may provide some measure of NPV presence, but they grossly under-estimate PV and over-estimate bare soil extent. These results concur with other studies in arid regions, where very low green vegetation cover and very bright soils often preclude an accurate unmixing of image pixels using full-range AVIRIS data (van Leeuwen et al. 1997, Okin and Roberts 2000). The PV fractions from Monte Carlo unmixing were also far under-estimated at both field sites when using only the visible-NIR (VNIR) spectral region (0.4-1.3 μm) of the AVIRIS data (Table 2). This is also likely due to the presence of very bright soil, which saturates this wavelength region and leads to over-estimates of soil cover. The NPV fraction was also significantly over-estimated using the VNIR-only AVIRIS data. This results from the known confusion when separating NPV and soils using this spectral region (van Leeuwen and Huete 1996, van Leeuwen et al. 1997, Asner et al. 2000).

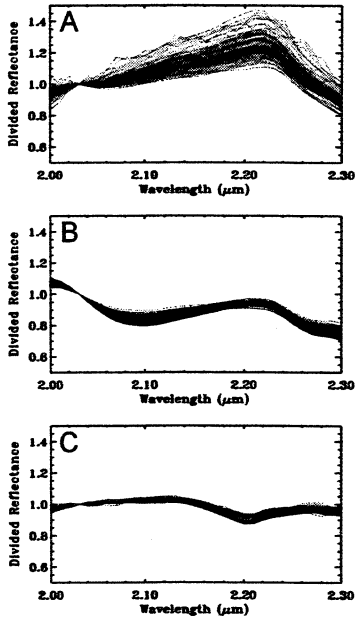

Figure 9. Field spectra normalized by dividing the reflectance value at each wavelength by the value at 2.03 μm for photosynthetic vegetation or PV (panel A), non-photosynthetic vegetation or NPV (panel B), and bare soil (panel C).

Spectral unmixing using the un-normalized SWIR2 (2.0-2.3 μm) region of the AVIRIS data yielded similarly poor results that were comparable to the VNIR unmixing (Table 2). In arid and semi-arid regions, SWIR2 spectra are dominated by extremely bright soils and NPV (Figure 5b-c). Like the VNIR, this can lead to a substantial under-estimate of PV cover in these environments.

Spectral unmixing with the "tied" SWIR2 region of the AVIRIS imagery yielded accurate estimates of all three land surface covers (Table 2). The field-measured PV, NPV and bare soil fractions in the shrubland site were well within the statistical uncertainty range of the *AutoMCU* results. While the PV fraction was slightly over-estimated at the grassland site (not statistically significant; ANOVA, $p = 0.09$), both the NPV and bare soil fractions were estimated with high accuracy. These results corroborate the

work presented by Asner and Lobell (2000), and indicate that the tied-SWIR2 spectra are a means for estimating the three dominant surface constituents in two dramatically different arid ecosystems.

It is common practice in the spectroscopy community to analyze specific absorption features via spectral normalization by division (Clark 1999). Spectral unmixing with divided-SWIR2 spectra resulted in moderate over-estimates of bare soil extent and major under-estimates of PV (Table 2). The reason for this can be seen in the divided-SWIR2 spectra (Figure 9): normalization by division accentuated the shape of the endmembers relative to the tied-SWIR2 values (Figure 5 d-f). This led to under-estimates of PV and over-estimates of bare soil as the unmixing algorithm attempted to compensate for overly accentuated PV endmembers (Table 2). Moreover, it is mathematically inappropriate to use division-normalized spectra for linear mixture modeling. The diagnostic spectral shapes of each land cover type are exploited by using tied spectra, which remove differences in overall albedo while preserving the linear relation in equation (1). For example, subtracting the reflectance at one wavelength (ρ_0) is valid because a spectrum can still be expressed as the properly weighted sum of endmembers:

$$\begin{aligned}\rho - \rho_0 &= C_{veg} \bullet \rho_{veg} + C_{soil} \bullet \rho_{soil} + C_{litter} \bullet \rho_{litter} - (C_{veg} \bullet \rho_{veg,0} + C_{soil} \bullet \rho_{soil,0} + C_{litter} \bullet \rho_{litter,0}) \\ &= C_{veg} \bullet (\rho_{veg} - \rho_{veg,0}) + C_{soil} \bullet (\rho_{soil} - \rho_{soil,0}) + C_{litter} \bullet (\rho_{litter} - \rho_{litter,0})\end{aligned} \quad (2)$$

However, a nonlinear spectral transformation, such as dividing by ρ_0, cannot be done within the SMA framework:

$$\frac{\rho}{\rho_0} = \frac{C_{veg} \bullet \rho_{veg} + C_{soil} \bullet \rho_{soil} + C_{litter} \bullet \rho_{litter}}{C_{veg} \bullet \rho_{veg,0} + C_{soil} \bullet \rho_{soil,0} + C_{litter} \bullet \rho_{litte,0}} \neq C_{veg} \frac{\rho_{veg}}{\rho_{veg,0}} + C_{soil} \frac{\rho_{soi\,lg}}{\rho_{soi\,lg,0}} + C_{litter} \frac{\rho_{litter}}{\rho_{litter\,g,0}} \quad (3)$$

This analysis shows, both mathematically and experimentally, that the use of division-normalized spectra is not appropriate for linear spectral mixture analysis.

The ASTER sensor holds some promise for extending the tied-SWIR2 AVIRIS capability to the multi-spectral spaceborne level, but our results indicated less than ideal estimates of the three cover fractions. The tied-SWIR2 ASTER unmixing did estimate bare soil and PV to within 10% of the field-measured values at the shrubland site (Table 2). However, the NPV fraction was substantially under-estimated at this site. Estimates of bare soil were similarly accurate at the grassland site, while the retrieved PV values were 4-5 times too high and the NPV values were 50% too low. These results can be explained by comparing tied-SWIR2 spectra in AVIRIS (Figure 6c-d) and ASTER (Figure 8a-b) wavelengths. The dense spectral sampling of the 2.0-2.15 μm region by AVIRIS allows for the NPV to be better separated from the bare soil. ASTER's spectral sampling does not begin until 2.16 μm, and thus it does not easily resolve the presence of NPV (only soil via the OH^- absorption feature).

Of all wavelength permutations attempted in the Monte Carlo spectral mixture analysis, only the tied-SWIR2 data in AVIRIS channels 2.03-2.30 μm yielded accurate results with low statistical uncertainty (Table 2). The tied-SWIR2 ASTER results showed some promise for estimating bare soil cover; however, additional analysis at more sites is needed to verify the value of ASTER's SWIR2 sampling for this purpose. Based on these findings, the AVIRIS tied-SWIR2 unmixing was extended over the entire Jornada Experimental Range (Figure 10). The shrubland site is located near the western edge of the larger shrubland region, which occupies the upper third of the image. This region has PV cover values ranging from 0-30% and very low NPV cover values of 0-10%. It has very high bare soil cover of greater than 70%. The grassland site is located within a larger black grama grassland in the lower third of these images. This region has very high NPV (>30%), low to moderate PV (0-15%), and relatively low bare soil cover (<60%). The analysis will be extended in future efforts to understand the full variability of vegetation and bare soil extent and its linkages to biogeochemical processes at the regional scale. For now, this study, combined with the study presented by Asner and Lobell (2000), indicates that the tied-SWIR2 spectral mixture analyses using high quality AVIRIS spectroscopic data can be used to estimate the relative and absolute fractional coverages of photosynthetic vegetation, non-photosynthetic vegetation (dry carbon), and bare soil in this arid region.

7. Conclusions

This study considered the accuracy and precision of linear spectral mixture analysis for estimating sub-pixel coverage of photosynthetic vegetation (PV), non-photosynthetic vegetatation (NPV), and bare soils in arid regions. The study employed two contrasting arid ecosystems and directly compared a wide variety of spectral sampling schemes in a controlled spectral unmixing or decomposition experiment. This experiment utilized a dense sampling of field spectroscopic endmembers for PV, NPV and bare soil along with a general, probabilistic linear mixture model based on Monte Carlo analysis. Concomitant imaging spectroscopy measurements from the NASA AVIRIS sensor provided a means to test five hyperspectral sampling schemes. The field spectral endmembers and AVIRIS data were also convolved to the optical wavelength channels provided by Landsat TM, MODIS and ASTER.

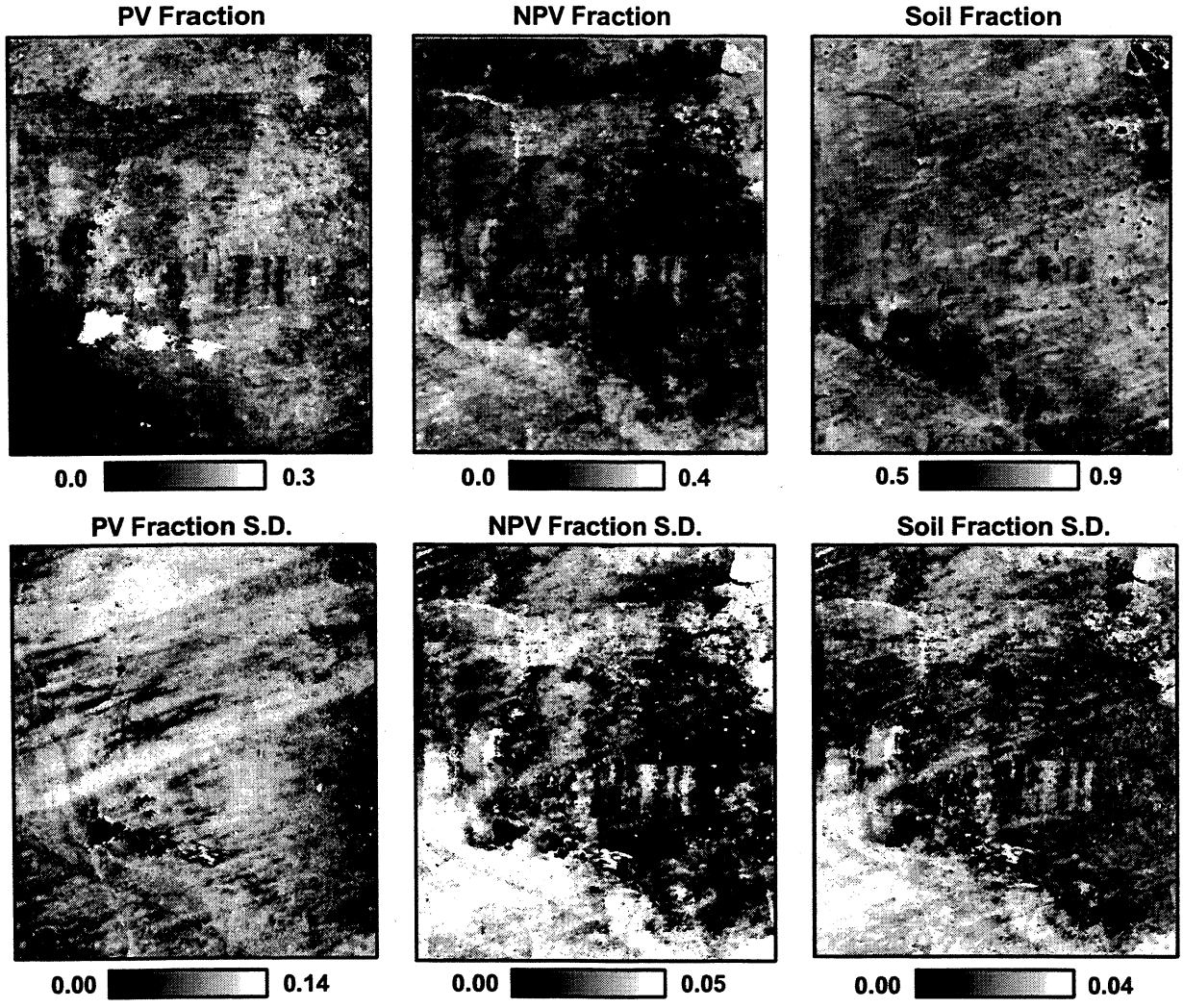

Figure 10. Monte Carlo spectral unmixing results for the Jornada Experimental Range, New Mexico, USA, using tied-SWIR2 AVIRIS imagery. Top panels show mean cover fractions for PV, NPV and bare soil. Bottom panels show standard deviation images for the three endmembers.

The comparison indicated clear limitations in using the full optical range (0.4-2.5 μm) or visible-NIR (0.4-1.3 μm) to decompose image pixels into PV, NPV and bare soil covers in an arid shrubland and grassland ecosystem (Table 2). Shortwave-IR2 (SWIR2) measurements in the 2.0-2.3 μm range showed the distinctive differences in PV,

NPV and bare soil spectral properties. When the SWIR2 spectra are normalized by tying each value to that of the first wavelength (2.03 μm), the distinctive shapes of the three endmembers are isolated and the effect of changing albedo is minimized. These tied-SWIR2 endmembers provided verifiably accurate estimates of PV, NPV and bare soil in the shrubland and grassland study areas. No other spectral combination or approach tested in this study could provide similar performance. The tied-SWIR2 sampling provided by ASTER (5 channels; Table 1), provided some useful information on bare soil extent, but poor spectral coverage in the 2.0-2.15 μm range precluded an accurate NPV or a better bare soil estimate.

In general, we believe that the SWIR2 spectral region is one of the best ways to estimate the fractional cover of photosynthetic vegetation, non-photosynthetic vegetatation, and bare soils in arid regions. To date, only a few instruments, such as the AVIRIS, provide the SWIR2 spectral sampling with sufficiently high signal-to-noise ratio for use in our Monte Carlo mixture model. Further testing and analysis of the SWIR2 region for analyzing the presence and abundance of these land surface materials will continue in our future efforts. Ecological and biogeochemical research efforts at the landscape and regional scale require detailed information on the spatial and temporal variability of live vegetation, dry carbon, and bare soils. Based on our studies thus far conducted, the SWIR2 spectral region continues to stand out as a potential means for providing these needed data.

8. Acknowledgements

We thank B. Sawtelle, C. Cody, and B. Nolen for their invaluable assistance in the field studies presented in this paper. We thank two anonymous reviewers of the manuscript and A. Karnieli for providing editorial guidance. We also thank the personnel from Jornada Long-term Ecological Research program, the USDA Jornada Experimental Range office, and the NASA AVIRIS Program. This work was supported by NASA NIP grant NAG5-8709 and NASA New Millenium (EO-1) Program grant NCC5-480 to G. Asner.

9. References

ASNER, G.P., 1998, Biophysical and biochemical sources of variability in canopy reflectance, Remote Sensing of Environment, 64, 234-253.

ASNER, G.P., Biophysical remote sensing signatures of arid and semi-arid ecosystems, Manual of Remote Sensing, S.L. Ustin ed., John Wiley & Sons, New York, in press.

ASNER, G.P. and LOBELL, D.B., 2000, A biogeophysical approach for automated SWIR unmixing of soils and vegetation. Remote Sensing of Environment, 66, 99-112.

ASNER, G.P., WESSMAN, C.A., BATESON, C.A., and PRIVETTE, J.L., 2000, Impact of tissue, canopy and landscape factors on reflectance variability of arid ecosystems. Remote Sensing of Environment, 66, 69-84.

BATESON, C.A., ASNER, G.P., and WESSMAN, C.A., 2000, Endmember bundles: A new approach to incorporating endmember variability in spectral mixture analysis, IEEE Transactions on Geoscience and Remote Sensing, 38, 1083-1094.

BATESON, C.A., and CURTISS, B., 1996, A method for manual endmember selection and spectral unmixing. Remote Sensing of Environment, 55, 229-243.

BEN-DOR, E., IRONS, J.R., and EPEMA, G.F., 1999, Soil reflectance, in Remote Sensing for the Earth Sciences: Manual of Remote Sensing, A.N. Rencz ed., John Wiley & Sons, New York, pp. 111-188.

BUFFINGTON, L.C. and HERBEL, C.H., 1965, Vegetation changes on a semidesert grassland range from 1858 to 1963, Ecological Monographs, 35, 139-163.

CARLSON, T.N., and RIPLEY, D.A., 1997, On the relationship between NDVI, fractional vegetation cover, and leaf area index, Remote Sensing of Environment, 62, 241-252.

CLARK, R.N., 1999, Spectroscopy of rocks and minerals, and principles of spectroscopy, in Remote Sensing for the Earth Sciences: Manual of Remote Sensing, A. N. Rencz ed., John Wiley & Sons, New York, pp. 3-58.

CURRAN, P.J., 1989, Remote sensing of foliar chemistry, Remote Sensing of Environment, 30, 271-278.

DUNCAN, J., STOW, D., FRANKLIN, J., and HOPE, A., 1993, Assessing the relationship between spectral vegetation indices and shrub cover in the Jornada Basin, New Mexico, International Journal of Remote Sensing, 14, 3395-3416.

ELMORE, A.J., MUSTARD, J.F., MANNING, S.J., and LOBELL, D.B., 2000, Quantifying vegetation change in semiarid environments, Remote Sensing of Environment, 73, 87-102.

GAO, B.-C., HEIDEBRECHT, K.B., and GOETZ, A.F.H., 1993, Derivation of scaled surface reflectance from AVIRIS data. Remote Sensing of Environment, 44, 145-163.

HUETE, A.R., 1988, A soil-adjusted vegetation index (SAVI), Remote Sensing of Environment, 25, 295-309.

KARNIELI, A., KIDRON, G., GHASSLER, C., and BEN-DOR, E., 1999, Spectral characteristics of cyanobacteria soil crust in the visible, near-infrared, and shortwave infrared (400-2500 nm) in semiarid environment, International Journal of Remote Sensing, 69, 67-77.

OKIN, G.S., and ROBERTS, D.A., 2000, Linear unmixing of simulated noisy spectra: Vegetation detection limits in areas of low cover, in Proceedings of the 9th JPL Airborne Earth Science Workshop, R.O. Green ed., Jet Propulstion Laboratory, Pasadena, CA.

RANGO, A., CHOPPING, M., RITCHIE, J., HAVSTAD, K., KUSTAS, W., and SCHMUGGE, T., 2000, Morphological characteristics of shrub coppice dunes in desert grasslands of Southern New Mexico derived from scanning LIDAR, Remote Sensing of Environment, 74, 26-44.

ROBERTS, D.A., GARDNER, M., and GREEN, R.O., 1998, Mapping chaparral in the Santa Monica Mountains using multiple endmember spectral mixture models, Remote Sensing of Environment, 65, 267-279.

SCHLESINGER, W.H., and PILMANIS, A.M., 1998, Plant-soil interactions in deserts, Biogeochemistry, 42, 169-184.

SCHLESINGER, W.H., RAIKES, J.A., and CROSS, A.F., 1996, On the spatial pattern of soil nutrients in desert ecosystems, Ecology, 77, 364-376.

SCHLESINGER, W.H., REYNOLDS, J. F., CUNNINGHAM, G. L., HUENNEKE, L. F., JARRELL, W.M., VIRGINIA, R.A., and WHITFORD, W.G., 1990, Biological feedbacks in global desertification, Science, 247, 1043-1048.

SMITH, M.O., USTIN, S.L., ADAMS, J.B., and GILLESPIE, A.R., 1990, Vegetation in deserts: I. A regional measure of abundance from multispectral images, Remote Sensing of Environment, 31, 1-26.

SOHN, Y., and McCOY, R.M., 1997, Mapping desert shrub rangeland using spectral unmixing and modeling spectral mixtures with TM data, Photogrammetric Engineering and Remote Sensing, 63, 707-716.

VAN LEEUWEN, W.J.D., and HUETE, A.R., 1996, Effects of standing litter on the biophysical interpretation of plant canopies with spectral indices, Remote Sensing of Environment, 55, 123-138.

VAN LEEUWEN, W.J.D., HUETE, A.R., WALTHALL, C.L., PRINCE, S.D., BEGUE, A., and ROUJEAN, J.L., 1997, Deconvolution of remotely sensed spectral mixtures for retrieval of LAI, fAPAR and soil brightness, Journal of Hydrology, 188/189, 697-724.

WESSMAN, C.A., BATESON, C.A., and BENNING, T.L., 1997, Detecting fire and grazing patterns in tallgrass prairie using spectral mixture analysis, Ecological Applications, 7, 493-512.

WHITE, M.A., ASNER, G.P., NEMANI, R.R., PRIVETTE, J.L., and RUNNING, S.W., 2000, Monitoring fractional cover and leaf area index in arid ecosystems: digital camera, radiation transmittance, and laser altimetry results, Remote Sensing of Environment, 74, 45-57.

Table 1. Permutations of AVIRIS data used in Monte Carlo spectral mixture analysis of shrubland and grassland sites. The Landsat TM, MODIS and ASTER satellite instruments were simulated using the AVIRIS data convolved to actual sensor response functions. Special treatment for bad bands and for normalizing various wavelength regions (tying and dividing) are also shown.

Technique/Instrument	Wavelength Region(s)	Special Treatment
AVIRIS	Contiguous 0.4-2.5 μm, 168 channels	Atmospheric water absorption bands (1.3-1.5 μm and 1.8-2.0 μm) are ignored.
AVIRIS VNIR	Contiguous 0.4-1.3 μm, 98 channels	---
AVIRIS SWIR2	Contiguous 2.0-2.3 μm, 45 channels	---
AVIRIS Tied-SWIR2	Contiguous 2.0-2.3 μm, 45 channels	The value at the first wavelength at 2.03 μm is subtracted from the reflectance value at each wavelength.
AVIRIS Divided-SWIR2	Contiguous 2.0-2.3 μm, 45 channels	The reflectance value at each wavelength is divided by value at the first wavelength at 2.03 μm.
Landsat 5 TM	0.48, 0.57, 0.66, 0.84, 1.68, 2.22 μm	---
MODIS	0.41, 0.44, 0.46, 0.49, 0.52, 0.54, 0.55, 0.66, 0.67, 0.74, 0.85, 0.90, 0.93, 0.94, 1.2, 1.6, 2.1 μm	---
ASTER	0.56, 0.66, 0.80, 1.7, 2.16, 2.21, 2.26, 2.33, 2.39 μm	---
ASTER Tied-SWIR2	2.16, 2.21, 2.26, 2.33, 2.39 μm	The value at the first wavelength at 2.16 μm reflectance is subtracted from the value at each wavelength.
ASTER Divided-SWIR2	2.16, 2.21, 2.26, 2.33, 2.39 μm	The reflectance value at each wavelength is divided by value at the first wavelength at 2.16 μm.

Table 2. Summary of estimated photosynthetic vegetation (PV), non-photosynthetic vegetation (NPV), and bare soil cover fractions from 10 different wavelength sampling analyses using *AutoMCU*. Fractional cover results from field measurements are also given. Sums of the three fractions are also shown for each set of estimates.

Permutation		Study Site			
		Shrubland	Std Dev	Grassland[$]	Std Dev
FIELD MEASUREMENTS	**PV**	**0.181***	**0.010***	**0.069**	**0.033**
		0.010**	**0.010****	**0.367**	**0.133**
	Soil	**0.820***	**0.020***	**0.586**	**0.173**
	SUM	**1.01**	---	**1.01**	---
AVIRIS Full-range	PV	-0.006	0.060	-0.176	0.036
	NPV	0.019	0.043	0.325	0.031
	Soil	1.053	0.036	0.795	0.036
	SUM	1.06	---	0.94	---
AVIRIS VNIR	PV	0.006	0.044	-0.074	0.028
	NPV	0.147	0.063	0.694	0.066
	Soil	0.953	0.069	0.404	0.078
	SUM	1.11	---	1.02	---
AVIRIS SWIR2 (No tying)	PV	-0.531	0.107	-0.124	0.088
	NPV	0.162	0.042	0.433	0.041
	Soil	1.081	0.035	0.736	0.037
	SUM	0.71	---	1.05	---
AVIRIS Tied SWIR2	**PV**	**0.148**	**0.062**	**0.129**	**0.057**
	NPV	**0.013**	**0.034**	**0.326**	**0.038**
	Soil	**0.839**	**0.050**	**0.548**	**0.060**
	SUM	**1.0**	---	**1.01**	---
AVIRIS Divided SWIR2	PV	0.026	0.011	0.029	0.011
	NPV	0.036	0.020	0.264	0.029
	Soil	0.94	0.016	0.707	0.026
	SUM	1.0	---	1.01	---
Landsat TM	PV	0.375	0.028	0.139	0.030
	NPV	0.242	0.059	0.807	0.062
	Soil	0.836	0.057	0.285	0.285
	SUM	1.45	---	1.23	---
MODIS	PV	-0.049	0.051	-0.222	0.032
	NPV	0.234	0.040	0.570	0.053
	Soil	0.947	0.041	0.642	0.038
	SUM	1.13	---	0.99	---
ASTER Full-range	PV	0.023	0.041	-0.163	0.023
	NPV	-0.002	0.053	0.295	0.046
	Soil	1.066	0.041	0.822	0.031
	SUM	1.09	---	0.95	---
ASTER Tied SWIR2	PV	0.271	0.195	0.271	0.205
	NPV	-0.187	0.172	0.127	0.167
	Soil	0.916	0.068	0.609	0.072
	SUM	1.0	---	1.01	---

* From a combination of IKONOS (Figure 4) - uncertainty values given as ranges and not standard deviations; ** From field observations; [$] From Figure 3.

APPLICATION OF RADIATIVE TRANSFER THEORY TO ATMOSPHERIC CORRECTION OF AVIRIS Data

Sima Bagheri,[1] Knut Stamnes,[2] Wei Li[3]

1. Introduction

The aim of an algorithm based on Radiative Transfer Theory (RTT) is a physical-bio-optical description of the radiative transfer process in the entire system from the solar source to the remote sensor via the hydrosols. The quantitative description provides a sound basis for the inversion of remotely sensed signals to retreive the optical water quality parameters. AVIRIS records the integrated effects of the solar source, the atmosphere and the targeted surface. To compensate for the atmospheric effects in the AVIRIS data, an air water interface atmospheric correction algorithm based on DISORT was applied to infer the water-leaving radiance. The spectral absorption and backscattering defined as the inherent optical properties (IOP) are physically related to subsurface irradiance reflectance R(0-). The subsurface irradiance reflectance links the optical properties to the water signals recorded by AVIRIS. This paper reports on the application of physically-based algorithms for retrieval of optical properties of the coastal waters for which the near-infrared black pixel approximation is invalid. To test the retrieval algorithm the configuration of the AVIRIS bands are used. In conjunction with bio-optical models these optical properties are used to characterize such waters in terms of chlorophyll concentration, colored dissolved organic matter and inorganic material.

The study area is the Hudson/Raritan Estuary located south of the Verrazano Narrows and bordered by western Long Island, Staten Island and New Jersey. Fresh water flows into the estuary mainly from the Hudson and Raritan Rivers and ocean waters enter tidally across the Sandy Hook-Rockaway transect. The tidal water is mixing with fresh water inflows, in highly dynamic environments where there are major conflicting interests on the use of these waters. This shallow (< 8 m) and eutriphicated interface of the Hudson and Raritan Rivers and Atlantic Ocean was cruised during the field seasons in 1998-2000 with RV Walford (NJMSC) and Blue Sea (MAST). Table 1 shows the sample locations and local observations recorded during the field campaigns.

2. Materials and Methods

2.1 AVIRIS Data and Atmospheric Correction

On May 15, 2000, the AVIRIS, was flown over the study area. The AVIRIS images the earth's surface in 224 spectral bands approximately 10 nm covering the region 400-2500 nm from a NASA ER-2 aircraft at an altitude of 20 km. The ground resolution is 20m * 20m. AVIRIS records the integrated effects of the solar source, the atmosphere and the targeted surface. To compensate for the atmospheric effects in the AVIRIS data, an atmospheric and air-water interface correction algorithm based on DISORT was utilized.

DISORT is a forward radiative transfer model for the coupled atmosphere-ocean system (Jin and Stamnes, 1994; Thomas and Stamnes, 1999) which is used to determine the water constituents as well as the atmospheric parameters that in combination give rise to the reflected radiance spectra measured by the AVIRIS spectrometers. Currently, Most of the atmospheric correction algorithms are designed for case 1 (clean deep ocean) waters. Those algorithms are based on the assumption that the water-leaving radiances are close to zero in the spectral range 760 - 870 nm. Thus, an aerosol/aerosol optical depth model can be derived from the channels located in that region of the spectrum. Subsequently, the aerosol information can be extrapolated into the visible range for retrieval of the water-leaving radiance and the water constituent concentration. Unfortunately, these algorithms are not directly applicable to case 2 (turbid coastal) waters because of the presence of suspended materials which cause strong scattering in the spectral range of 760 - 870nm.

Figure 1 depicts the atmospheric reflectance ratio spectra produced from the selected pixels within the subset of the AVIRIS imagery. It is evident that the shape of these spectra covering 60 channels of AVIRIS data varied considerably; the first two spectral lines show that the two pixels provide very different information about the ocean. In the bay area, the water is very turbid due to strong absorption at 660 nm and strong scattering in the NIR region. This implies that the concentration of suspended matter is high there. On the right side of the image, the

1 New Jersey Institute of Technology, Newark, New Jersey (sima@klimt.njit.edu)
2 & 3 Stevens Institute of Technology, Hoboken, New Jersey

ocean water is of different spectral characteristics. The ratio changes smoothly with wavelength, which indicates that the difference between the two pixels is mainly due to the atmosphere. The spectra are consistently higher at the blue wavelength as is the characteristic of the molecular (Rayleigh) reflectance. At the bottom right of the image, the aerosol optical depth is much larger than the area to the top. Furthermore, we noted that ratio lines 3 and 5 are parallel, but ratio line 4 is anomalous. It is evident that pixels (523,342) and (510,49) have the same aerosol absorption and scattering characteristics, but different optical depths, while pixel (26,66) has different aerosol absorption and scattering characteristics altogether. It should be mentioned that the raw image contained distinctive patterns recognizable as surface features--e.g., swell and slicks--indicating some degree of sunglint. In addition, rough waters were observed from the shipboard and recorded by the field spectroradiometer at the time of the AVIRIS overflight. The aerosol information obtained from the ratio image were extrapolated for retrieval of water leaving radiance and estimation of water quality parameters (Table 2).

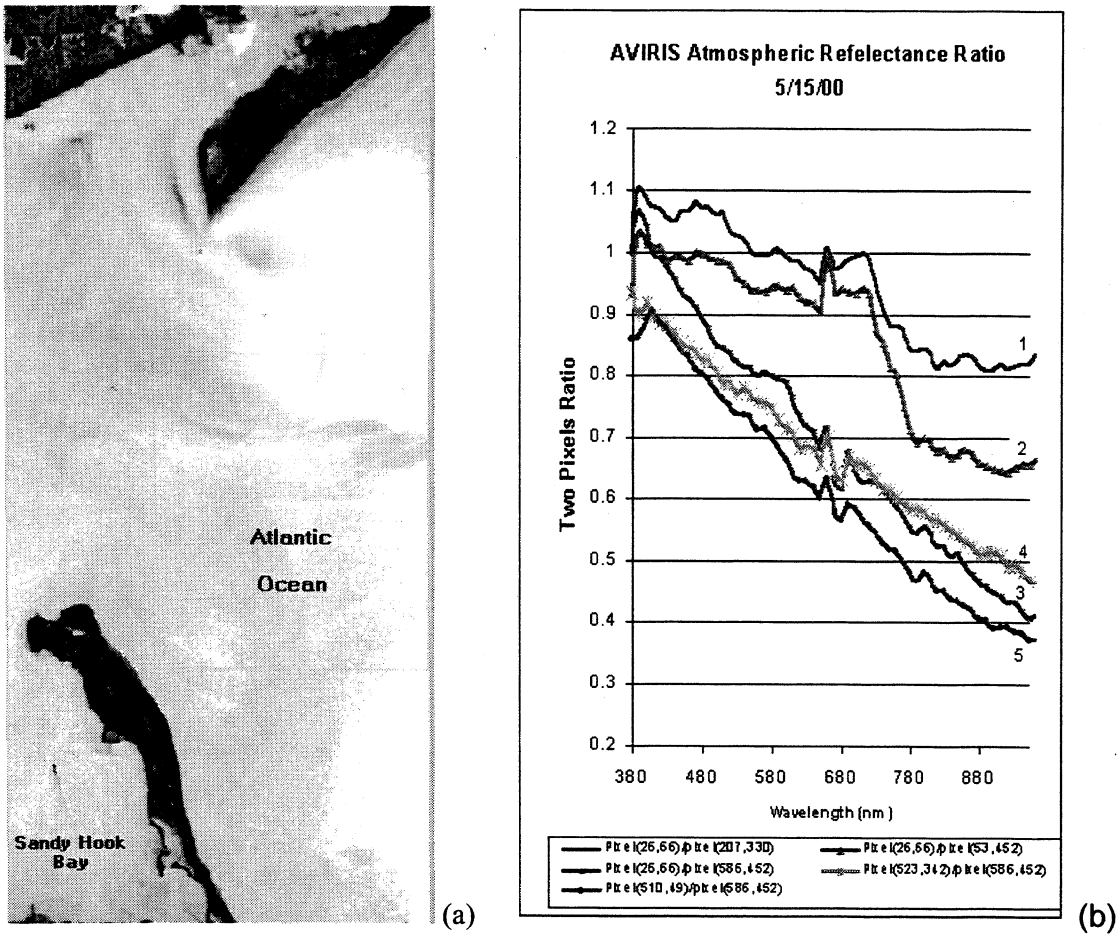

Figure 1(a) AVRIS ratio image (13/20) of transect 1 acquired on 5/15/2000 and (b) two pixels ratio spectra of the AVIRIS showing the atmospheric variations

2.2 Subsurface Irradiance Reflectance R(0-)

Spectral subsurface irradiance reflectance R(0-) as a ratio of upwelling to downwelling irradiance for all stations listed in Table 1 were obtained using the submersible field spectroradiometers--OL754 (Bagheri et. al., 2000). The goal is to parameterize the bio-optical model relating the colored dissolved organic matter (CDOM), total suspended matter (TSM) and algal pigment concentrations, to the light absorption and scattering and to the water leaving radiance, through direct and laboratory based optical measurements. In short, the link between remotely sensed upwelling radiance and underwater inherent optical properties is made through R(0-) (Dekker, 1993).

2.3 Inherent optical properties (IOP)

The spectral absorption and backscattering are the inherent optical properties (IOP). The spectral absorption causes reduction in R(0-) and the spectral scattering causes an increase in R(0-). Laboratory based spectrophotometric measurements of spectral attenuation and spectral absorption was performed. From these measurements spectral scattering was deduced. Absorption spectra of seston (phytoplankton and tripton) and tripton (suspended particles excluding phytoplankton) were determined using the filterpad method (Truper & Yentsch, 1967) with 0.45 μm Whatman GF/F filters. The absorption was calculated on a basis of a calibrated relationship between the optical density of a suspension in a sample cell and the optical density on a filter (Weidemann & Cleveland, 1993). The absorption spectra of CDOM and the seston beam attenuation were determined spectrophotometrically according to the methods described in Rijkeboer et al., 1998.

2.4 Water quality Parameters (WQP)

To estimate optical water quality concentrations coinciding with the spectral reflectance measurements, subsurface water samples (0.2 to 0.5-m depth) were collected in 1-l bottles for laboratory analysis. Standard procedures as described by Rijkeboer *et al.* 1998 was used to determine the concentrations of total chlorophyll-a (TCHL) defined as the sum of chlorophyll-a and phaeopigment (as indication of concentration of phytoplankton) and total suspended matter (TSM). The TCHL and TSM concentrations were determined according to the Dutch standard norm (NEN 6520, 1981 and NEN 6484, 1982) respectively.

Table 1. Sample locations and water conditions as recorded on board R/V Walford and Blue Sea

Date	St	Location	Lat	Long	S.D. (m)	TCHL ($mg\ m^{-3}$)	TSM (gm^{-3})
8/14/1999	1	Comptons/PewsCreek	40.45	74.08	1.3	15	6
	2	Keyport Harbor	40.47	74.19	0.8	32	26
	3	Traid Bridge	40.50	74.28	0.9	17	13
	4	Crookes Pt State Isl.	40.54	74.14	0.6	37	15
	5	Coney Isl. Pt.	40.57	74.02	1.8	6	11
	6	Sandy Hook Tip	40.49	74.02	0.9	22	12
	7	Shrewsbury River	40.38	73.98	0.5	48	21
5/15/2000	1	Buoy 2	40.42	74.01	1.25	31	8
	2	Atlantic Highlands	40.47	74.03	1.25	46	11
	3	Horseshoe Cove	40.59	74.03	1.37	22	7

3. Bio-Optical Model Development

To develop analytical algorithms for these case 2 waters it is necessary to develop an appropriate bio-optical model linking the water constituents to the inherent optical properties (IOP) and to link the IOP to the subsurface irradiance reflectance. In this study, we used the linear backscattering albedo model (Gordon et. al., 1975), which is being considered the most appropriate model for case 2 waters (Dekker et. al. 1994).

$$R = r_1(b_b/(a+b_b)) \quad (1)$$

The use of this model implies knowledge of the IOP:

$$a = a_w + a^*_{dw}DW + a^*_{ph}CHL + a^*_{CDOM440}\,CDOM \quad (2)$$

$$b_b = 0.5\, b_w + b_{b\,dw}DW$$

Where a is the total absorption coefficient, b_b is the total backscatter coefficient and r is a factor that is dependent on geometry of the incoming light and the volume scattering in the water body. a and b_b are assumed to be linear functions of the constituent concentrations. This allows the introduction of the specific inherent optical properties, i.e. the IOP per unit concentration: e.g. the specific inherent absorption by phytoplankton, a^*ph, is the amount of absorption caused by 1 mg m^{-3} CHL. Utilizing Beer's law enables to write the total absorption coefficient a as a superposition of the absorption by phytoplankton, tripton, CDOM and water. The concentrations of the constituents are given by CHL, DW and $CDOM_{440}$ (the absorption of coloured dissolved organic matter at 440 nm).

The asterisks denote that a and b_b are specific inherent optical properties (SIOP), i.e. per unit concentration denoted by the subscript. The factors for calculating backscattering for water itself and samples were taken from Bukata (1995) and Dekker (1997) respectively. The backscattering b_b is used here to convert the scattering coefficient to the backscattering coefficient. For pure water this ratio is 0.5 but for seston measurements depends on the composition of the water and is measured as the difference between beam attenuation and seston absorption (Pasterkamp et.al., 2000).

The absorption and scattering coefficients of the main water quality parameters collected for all stations were averaged to produce a set of representative values (Figure 2) and were used as input for calculating R(0-) for different dates. No significant changes in concentrations of water quality parameters were observed in the field data collected in 1999 and 2000. The shapes of the absorption curves reflect the composition and concentration of different optical water quality parameters (i.e., phytoplankton).

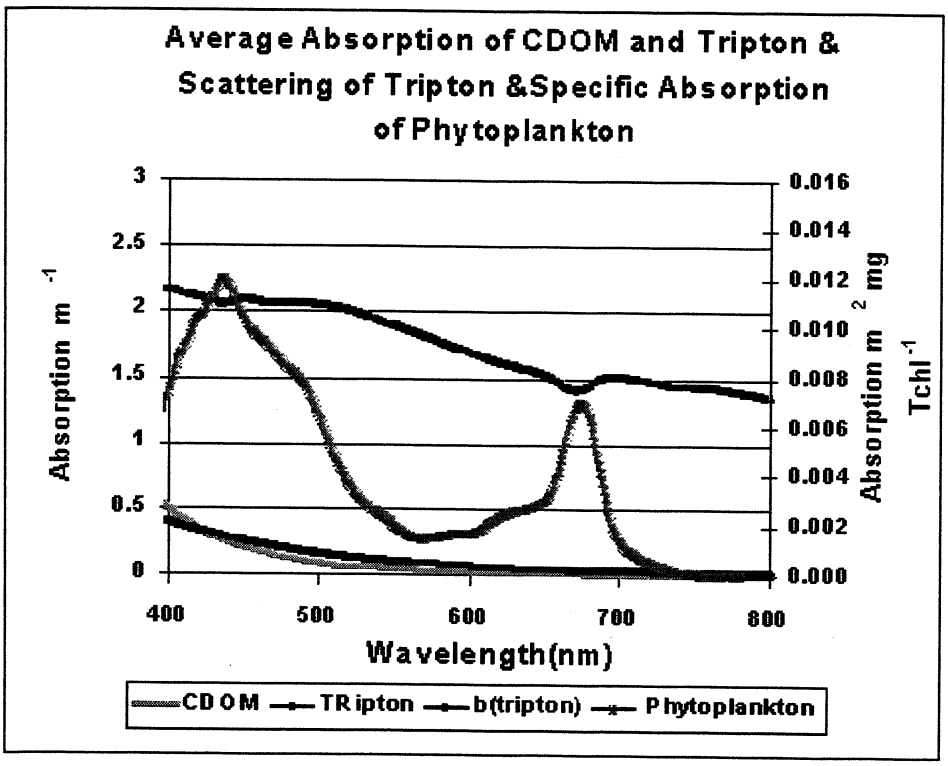

Figure 2. The average spectral absorption, specific absorption and scattering for all stations sampled

Using equation 1, the modeled R(0-) were generated to represent the spectra for the range of chlorophyll-a concentrations calculated in the laboratory for the individual station sampled on May 15'00. Figure 3 depicts the modeled R(0-) versus measured R(0-) for station 2 (Atlantic Highlands) sampled simultaneously with the AVIRIS

overflight on May 15'00. The figure demonstrates that a reasonable fit could be obtained between calculated and measured R(0-) spectra using the bio-optical model. Several reflectance features are prominent in the modeled/measured spectra. These features are the absorption by humus, tripton and the first chlorophyll_a absorption peak causing low reflectance. Beyond 500nm overall absorption decreases and reflectance increases allowing a better discrimination on local spectral features in the spectra, such as the red chlorophyll_a absorption peak at 676 nm.

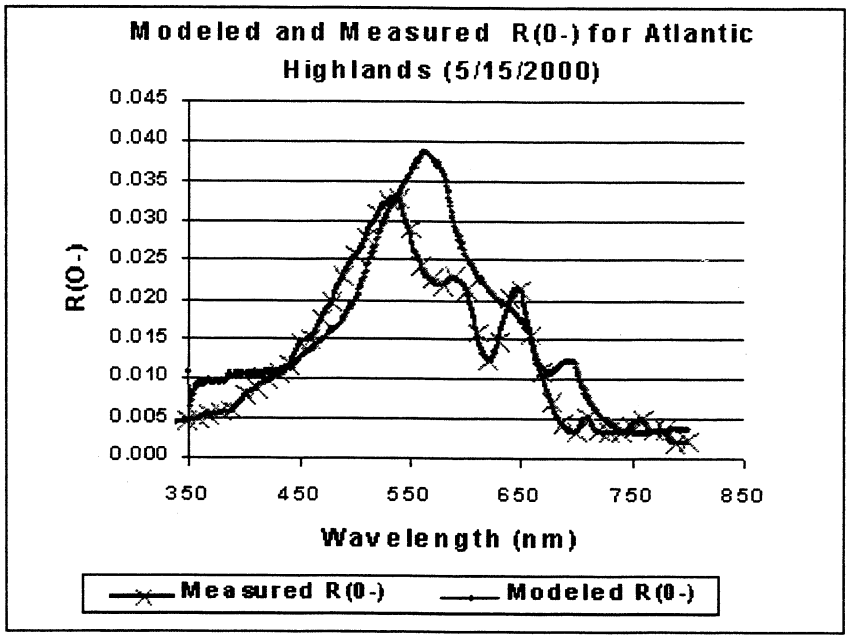

Figure 3. Modeled R(0-) vs measured R(0-) for Horseshoe Cove sampling station

Note that the discrepancy between the measured and modeled R(0-) at the 615-645 nm region is due to the fact that the water-soluble phycobiliprotein pigments are not extracted in the pigment extraction. Thus there are cyanobacteria absorbing through cyanobacterial pigment phycocyanin (cpc) at 615-645 nm visible in the measured R(0-) detected by the field spectroradiometer and not visible in the modeled R(0-).

Use of all the ancillary data recorded during the flight led to a "reasonable" agreement between R(0-) derived from the spectral irradiance data recorded by the field spectroradiometer and computed by the radiative transfer model. In the radiative transfer model we used a mid-latitude summer atmospheric model with an aerosol optical thickness τ=0.12. Subsequently these atmospheric parameters were applied to spectra from several sampling locations where in situ measurements were collected during the AVIRIS overflight and the results are given in Table 2. The table presents a good match between the insitu measurements and the retrieved water constituents concentrations from the atmospherically corrected AVIRIS data.

Table 2. AVIRIS Retrieved Chlorophyll and Suspended Solids vs Insitu Measurements

Chlorophyll (mg m^{-3})	31-46	34-41
TSM (g m^{-3})	7-11	7-8

4. Conclusion

We conclude that the AVIRIS spectral data provides the opportunity to distinguish the atmospheric effect from the ocean effect, and to set the estimated turbidity for chlorophyll concentration retrieval. Development of a robust algorithm for simultaneous retrieval of atmospheric aerosol optical properties, chlorophyll concentration and colored dissolved organic matter is a very challenging task. Nevertheless, such an algorithm is needed to make progress in this area. Future work will continue in this collaborative effort aimed at tying the bio-optical model derived from the field measurements to a reliable algorithm for simultaneous retrieval of water constituents and aerosol optical properties using the information content of the AVIRIS data.

Acknowledgment

This project is funded by the National Science foundation (Grant # 9806982). Support of the NASA/Headquarters-Biology and Geochemistry Program and the AVIRIS Experiment Team is greatly appreciated.

References

Bagheri, M. Rijkeboer, R. Pasterkamp, A. Dekker, *Comparison of Field Spectroradiometers in Preparation of Bio-Optical Modeling,* 9th JPL AVIRS Workshop. Pasadena, CA, Feb. 23-27, 2000.

Bukata, R. P.; Jerome, J.H.; Konratyev, K. Ya.; Pozdnyakov, D.V. *Optical Properties and Remote Sensing of Inland and Coastal Waters*, CRC Press: Boca Raton, 1995.

Dekker, A.G., 1993. *Detection of Optical Water Quality Parameters for Eutrophic Waters by High Resolution Remote Sensing*. Ph. D. Thesis (published). Proeschrift Vrije University, Amsterdam. The Netherlands, 1-240.

Dekker, A.G. and M. Donze, 1994. *Imaging Spectrometry as a Research Tool for Inland Water Resources Analysis*. Edited by J.Hill, Dordrecht, The Netherlands: Kluwer AP.

Dekker, A.G., H.J. Hoogenboom, L.M. Goddijn and T.J.M.Malthus, 1997. *The Relation between Inherent Optical Properties and Reflectance Spectra in Turbid Inland Waters, Remote Sensing Reviews*, Vol. 15, PP.59-74.

Gordon, H. R., O. B. Brown and M. M. Jacobs, 1975. *Computed Relationships between Inherent and Apparent Optical Properties of a Flat Homogeneous Ocean*. Appl. Optics, 14:417-427.

Jin, Z., and Stamnes, K., 1994 Radiative transfer in nonuniformly refracting media such as the atmosphere/ocean system, Appl. Opt., 33, 431-442.

NEN 6484, 1982, Water: *Determination of the Content of Not Dissolved Material and Its Ignition Residue*, Nederlands Normalisatie instituut, Delft, The Netherlands (in Dutch).

NEN 6520, 1981, Water: *Spectrophotometric Determination of Chlorophyll a Content*, Nederlands Normalisatie instituut, Delft, The Netherlands (in Dutch).

Pasterkamp, R., Peters, S. W. M., and A.G. Dekker, 2000, *Environmental Baseline Mapping of TSM Concentration*. 6 th ERIM Conference 1:260-267.

Rijkeboer, M., Dekker, A.G., and Hoogenboom, H.J., 1998, *Reflectance Spectra with Associated Water Quality Parameters Measured in Dutch Waters (Speclib-TK-database),* Institute for Environmental Studies, E98/12, The Netherlands.

Thomas, G. E., and Stamnes, K., 1999. *Radiative Transfer in the Atmosphere and Ocean*, Cambridge University Press.

Truper, H.G., and Yentsch, C.S., 1967, *Use of Glass Fiber Filters for the Rapid Preparation of in vivo Absorption Spectra of Photosynthetic Bacteria*, J. Bact'94:1255-1256.

Weidemann, A. D., and Cleveland J. S., 1993, *Quantifying Absorption by Aquatic Particles: A Multiple Scattering Correction for Glass-Fiber Filters,* Limnol. Oceanogr. 38:1321-1327.

RCGb INDEX: A TOOL FOR MAPPING THE DEGREE OF WEATHERING IN THE TROPICAL SOILS IN BRAZIL

Gustavo Macedo de Mello Baptista[1] and José da Silva Madeira Netto[2]

[1]União Pioneira de Integração Social – UPIS Faculdades Integradas, Departamento de Geografia
E-mail: gmbaptista@uol.com.br

[2]Centro de Pesquisas Agropecuárias dos Cerrados (Embrapa / CPAC)

1. INTRODUCTION

In the Cerrado region the presence of classes of soils that possess perceptible mineralogical variations is common. Those classes cannot be separated with the methods adopted in the usual soil surveys.

The mineralogical variation of the soils is studied by means of the analysis of samples collected in the field. For mapping, the extrapolation of the punctual values used morphologic approaches of correlation with the topography, with the origin material, etc.

The discrimination of the soils with various contents of kaolinite and gibbsite is not reliable for field approaches. Though the variability of these two minerals can be assayed, a systematic sampling with high density of points would be necessary. This procedure would increase the cost of the projects.

That limitation has led to a search for new techniques and resources to increase the understanding of the pedologic covering. Recent progress in the acquisition of images of remote sensing has been introduced as an alternative to the usual method.

Now the studies related to the remote sensing change the actual paradigm, with the appearance of the hyperspectral systems sensor. The main difference between those two types of sensor systems is in the spectral resolution.

The hyperspectral sensor now in operation is AVIRIS (Airborne Visible/InfraRed Imaging Spectrometer), property of the Jet Propulsion Laboratory (JPL/NASA). It is an airborne system composed of four spectrometers that give images continually scan the reflected optical spectrum from 0.4 to 2.5 μm, in 224 bands, with widths of 10 nm approximately.

The obtained data by that sensor system allow the analysis of the reflectance spectra of the different targets that compose the scene. In these spectra they meet spectral features or absorption bands of the main mineral components of the soils. Those features result of quantum events, the interactions of the discreet electromagnetic radiation with the particles, the atoms and the molecules, in certain wavelengths.

The spectral analysis and the multispectral remote sensing data has been used for the detection of the occurrence of some of the main components of the tropical soils, as shown by Hlavay et al. (1977); Madeira Netto (1993); Madeira Netto et al. (1997) and others.

Those studies however have shown the possibility of the use of radiometric spectra for the definition of occurrences and mineral content variations.

One of the most important aspects in the understanding of the pedologic environments is the different weathering degrees of the soils. The knowledge of space variation of the mineralogy is important for different reasons: it permits to elucidate processes of genesis of the soils; it helps in the definition of more appropriate management systems; and it is an important factor for classification and mapping.

The present work presents the RCGb spectral index (Relation Kaolinite/Gibbsite), based on the method of three bands ratio (Gao et al., 1993). The method uses the spectra of pure minerals of the JPL spectral library (Grove

et al., 1992) and validated the same spectra adopted by Madeira Netto being used (1993) for the construction of the IKi index. This method represents a new tool for mapping the weathering degrees of Brazilian tropical soils.

2. SPECTRAL CHARACTERISTICS OF THE MAIN MINERALS OF TROPICAL SOILS

Tropical soils are usually highly weathered, due mainly to warm and wet climate. Their mineralogy is characterized by a reduced number of components with kaolinite, iron and aluminum oxides as the most frequent minerals in the clay fraction and quartz in the sand and silt fractions. The amounts and proportions of these components are important for soil classification and management. The knowledge of reflectance spectra of these components is important for utilization of image spectroscopy for soil studies applications.

2.1 Kaolinite ($Al_2Si_2O_5(OH)_4$)

Kaolinite is the most frequent clay mineral found in tropical soils. Its reflectance spectra have characteristic sharp features in the reflected infrared region. The kaolinite presents its main spectra features associated to the molecular vibrations of the OH^- of its crystalline net. In the near infrared the most perceptible features are associated to the overtones of fundamental OH- stretching mode (2s) in 1400 nm and to combinations involving OH- stretching and Al-OH bending modes (d + s), in 2200 nm (Hlavay et al, 1977). Figure 1 presents the diffuse reflectance spectra of a kaolinite sample from Mesa Alta (New Mexico).

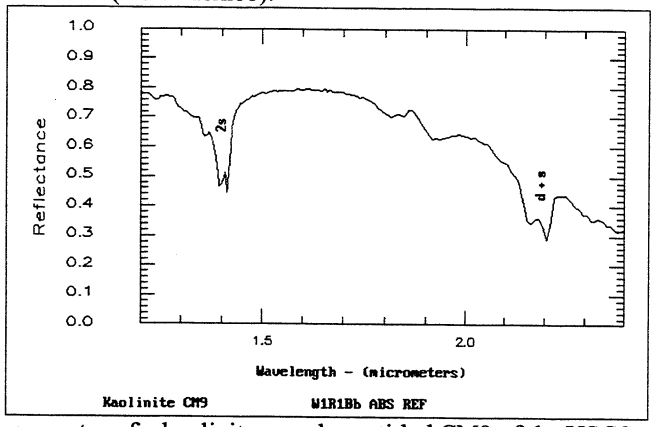

Figure 1. Diffuse reflectance spectra of a kaolinite sample, entitled CM9 of the USGS spectral library (Clark et al., 1993), from Mesa Alta (New Mexico), show absorption's band.

2.2 Gibbsite ($Al_2O_3\,3H_20$)

Soils, which have been subject to pronounced alteration, like the oxisols located in the old erosion surfaces, may present a large amount of gibbsite on their composition. In some cases it may be the most important mineral in the clay fraction.

Gibbsite, as kaolinite, presents spectral features due to OH^- vibrations. In the near infrared gibbsite presents harmonic molecular vibrations (2s) close to 1550 nm and the combinations of the type d + s close to 2300 nm (Hunt et al, 1971). The bands of absorption of the water are shown to 1400 nm (2s) and to 1900 nm (d + s). Figure 2 presents the characteristic features of a gibbsite sample (HS423 of the library of USGS, Clark et al., 1993), from Brazil.

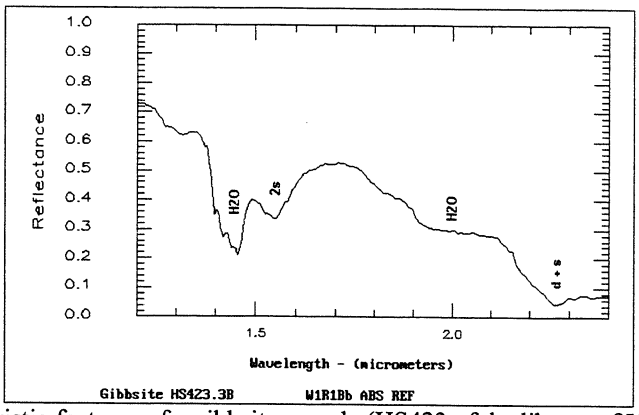

Figure 2. Characteristic features of a gibbsite sample (HS423 of the library of USGS), from Brazil.

3. DEVELOPMENT OF THE RCGb INDEX

For the development of RCGb we search for the spectral features of kaolinite and gibbsite to find an index that represents a Y scale similar or close to the Ki values. We used the spectra of the pure minerals of the JPL spectral library (Grove et al., 1992) entitled Kaolinite Well Ordered PS-1A and Gibbsite Synthetic OH-3A. Those spectra were resampling to the AVIRIS bands resolution. Later on, the spectra were integrated, by means of module spectral math, using 50% of each mineral for the formation of a spectrum, as it can be seen in Figure 3.

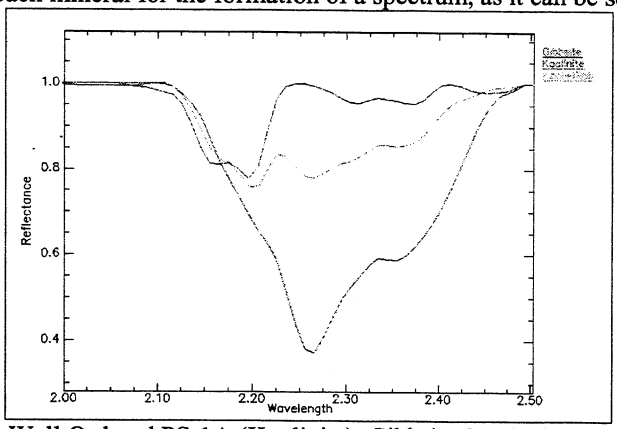

Figure 3. Spectra Kaolinite Well Ordered PS-1A (Kaolinite), Gibbsite Synthetic OH-3A (Gibbsite) (Grove et al., 1992) and the integration of 50% of each one to generate the spectrum Kaol+Gibb.

The proposed method is based on three points: the point at the beginning of spectral feature; the minimum reflectance point; and the point at the end of the spectral feature. To determine those points we used the procedure of continuum removed. The intensity of the spectral feature is directly proportional to the mineral content (Clark et al., 1990; Madeira Netto, 1993; Baptista et al., 1998).

For the elaboration of the index RCGb we also used the IKi index methodology (Madeira Netto, 1993), as can be seen in the equation 1.

$$RCGb = \frac{I_{kaol}}{I_{kaol} + I_{gibb}} \tag{1}$$

Therefore the procedure for the determination of Ikaol and Igibb was altered using the three band ratio procedure proposed by Gao et al. (1993). To determine the intensity of the mineral spectral features we use the average of the reflectance values at the beginning and at the end of feature minus the average of absorption points at the minimum reflectance. It's worth noting that the kaolinite presents two points of minimum reflectance or an absorption doublet, which was used two points of minimum reflectance. Therefore Ikaol is determined in agreement with the equation 2.

$$I_{kaol} = \frac{(R_{2,127} + R_{2,226})}{2} - \frac{(R_{2,176} + R_{2,196})}{2} \tag{2}$$

where Ikaol is a value regarding intensity of the feature of the kaolinite, and R it is the reflectance value in the several wavelengths, adapted to AVIRIS bands.

The same procedure was adopted for the determination of the intensity of the absorption's feature of gibbsite, or Igibb, we just used a single point of minimum, as it can be visualized in equation 3.

$$I_{gibb} = \frac{(R_{2,226} + R_{2,335})}{2} - R_{2,266} \quad (3)$$

The reflectance value to 2,335 μm, was adopted as the terminal point of the gibbsite feature. It was determined by means of a heuristic method looking for the best adjustment. As can be seen in Figure 3 the gibbsite feature presents some internal inflection points before its end. These inflections are influenced by other elements or by the intensity of the noise.

An adjustment was also made to observe the determination of Igibb for laboratory spectra and for the AVIRIS data. Due to intensity of the noises in the final portion of the spectrum, we propose the use as the final point of the feature, the reflectance value at the first inflection at 2,286 μm for the AVIRIS data.

The model RCGb writing in the format ENVI® is presented in equation 4.

$$RCGb = (((b_1 + b_4)/2) - ((b_2 + b_3)/2))/((((b_1 + b_4)/2) - ((b_2 + b_3)/2)) + (((b_4 + b_6)/2) - b_5)) \quad (4)$$

Where b1, b2, b3, b4, b5 and b6 correspond respectively to the reflectance values in the wavelengths of 2,127 μm (band 186), of 2,176 μm (band 191), of 2,196 μm (band 193), of 2,226 μm (band 196), of 2,266 μm (band 200) and of 2,286 μm (band 202) (in the case AVIRIS data) or 2,335 μm (equivalent the band 207) (if laboratory spectra are used). The use of three band ratio procedure, besides the best Y scale adjustment, minimizes the noise found in the AVIRIS spectra.

Figure 4 presents the two integrated spectra, with the continuum removed, showing the six bands used in the RCGb spectral index.

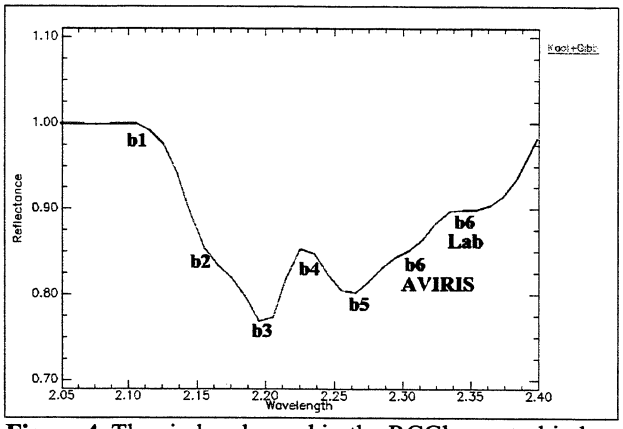

Figure 4. The six bands used in the RCGb spectral index.

4. SPECTRAL INDEX VALIDATION

To validate the RCGb spectral index we used the same spectra adopted by Madeira Netto (1993) for the construction of the IKi index, for 56 soil samples that corresponds to the surface and deeper horizons of 27 profiles of two main sources:

a) 25 samples, of the National Service of Survey and Conservation of Soils (SNLCS), corresponding to 14 profiles of representative Brazilian soils.
b) 31 samples of 13 profiles that belong to four toposequences studied in the area of Brasilia (Madeira Netto, 1993).

Of the 56 spectra. we removed four that presented opaque minerals. The influence of those minerals in the determination of the RCGb spectral index was discussed by Baptista et al. (2000a), using samples of the municipal

district of Niquelândia, Goiás. The 52 diffuse reflectance spectra obtained in laboratory were resampled to the AVIRIS bands.

We performed the calculation for Ikaol and Igibb (equations 2 and 3) to test whether the same ones can be used for an individual analysis of the mineral contents. As shown by Madeira Netto (1993), those results indicate a linear relationship between kaolinite and gibbsite contents and the intensities of the absorption features.

For the kaolinite several factors influence the analysis, because Ikaol presents a low correlation coefficient (r=0,53) with the mineral contents. Madeira Netto (1993) accomplished a multiple lineal regression between Ikaol and the kaolinite and gibbsite contents that presented a high correlation coefficient (r=0,88), which shows that the gibbsite content affects the measures of intensity of absorption of the kaolinite.

On the other hand, for the gibbsite, inclusion of the kaolinite content in the regression didn't modify the correlation. As the clay fraction of the soils under heavy weathering consists mainly of kaolinite and gibbsite, we find a better degree of adjustment (r=0,91) considering the kaolinite contents in relation to the clay fraction. The hypothesis proposed by Madeira Netto (1993) is that gibbsite absorption interferes with the measure of Ikaol explaining such a low correlation coefficient.

For the gibbsite, Madeira Netto (1993) points out that Igibb can be used to calculate the content of that mineral in the latosols. The use of Igibb for determination of the gibbsite content was also tested and it presents a high correlation coefficient (r=0,81), as it can be seen in Figure 5.

Ikaol allows only estimating the kaolinite contents in relation to the fraction clay in a satisfactory way. The inclusion and the analysis of another parameters can drive a more precise estimate method for the kaolinite content of the latosols, by means of reflectance spectra (Madeira Netto, 1993).

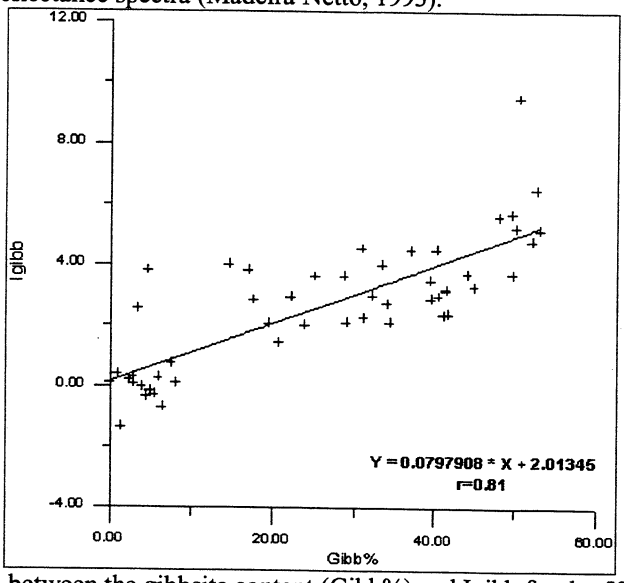

Figure 5. Linear regression between the gibbsite content (Gibb%) and Igibb for the 52 samples of Madeira Netto (1993).

We determined the values of band reflectance used in the determination of the RCGb spectral index, for each one of the 52 spectra. In addition, linear regressions were accomplished between the values obtained with the spectral index, when it is used as the dependent variable and the values of Ki as the independent variable. Table 1 presents the values obtained in the 52 spectra of reflectance of RCGb, with the values of Ki for each sample.

An important aspect to be understood in the analysis of the data is the correlation coefficients found. In the regression between the results of RCGb index and Ki values, the found correlation coefficient was quite high (r=0,93). Figure 6 presents the results of the linear regression.

Table 1. Values of RCGb and Ki for the 52 samples of Madeira Netto (1993)

Sample	RCGb	Ki
I1Ap	0.95	1.58
I1Bo4	1.00	1.56
I4Ap	1.08	1.58
I4Bo1	0.96	1.49
I3A2	0.94	1.55
I9A2	0.30	0.47
I9BA	0.32	0.51
I10A	0.45	1.03
I10BA	0.42	0.99
I11A2	0.42	0.22
I11Bo4	0.31	0.23
I13BA	0.95	1.91
I13Bo4	0.95	1.91
I17AB	0.43	0.74
I17Bo5	0.56	0.86
I20A	0.51	0.63
I20Bo1	0.51	0.53
I22Ap	1.02	1.45
I22Bo1	1.16	1.70
I23Ap	1.04	1.69
I23Bog2	1.09	1.65
A1Ap1	0.50	0.63
A1BA	0.57	0.68
A1Bo3	0.47	0.68
A2Ap2	0.71	1.12
A2BA	0.70	0.98
A2Bo2	0.64	0.92
A3Ap1	0.52	0.70
A3BA	0.61	0.68
A3Bo2	0.57	0.69
B1Ap1	0.47	0.52
B1BA	0.54	0.51
B1Bo3	0.42	0.51
B2Ap1	0.44	0.50
B2BA	0.48	0.63
B2Bo2	0.45	0.48
B3Ap1	0.55	0.82
B3BA	0.58	0.83
B3Bo2	0.44	0.71
C1Ap1	0.49	0.58
C1BA	0.55	0.53
C1Bo2	0.47	0.52
C2Ap1	0.65	1.00
C2BA	0.71	0.94
C2Bo2	0.62	0.91
C3Ap1	0.70	1.18
C3BA	0.75	1.15
C3Bo2	0.72	1.15
D1Ap	0.90	1.48
D2Ap	0.98	1.67
D3Ap	0.94	1.84
D4Ap	0.96	1.65

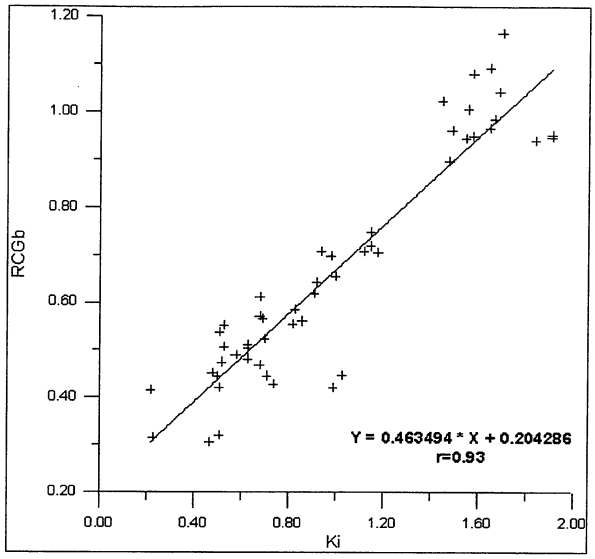

Figure 6. Linear regression between RCGb and Ki values.

5. RCGb INDEX TEXT IN AVIRIS DATA

The original radiance data was used in this stage, because, as it was pointed out by Baptista et al. (2000b), the radiance images present such good results as images corrected by the Green's method or by ATREM.

The RCGb spectral index was applied on two concatenated scenes of the AVIRIS data (Figure 7). This data was obtained on the same day with a difference of less than ½ hour between the acquisitions. The flight over Niquelândia (950816L3 - 10) was preceded by that over São João D'Aliança (950816L2 - 03).

The two images don't present clouds, and it was assumed that the atmospheric conditions would not have varied in a significant way between the images.

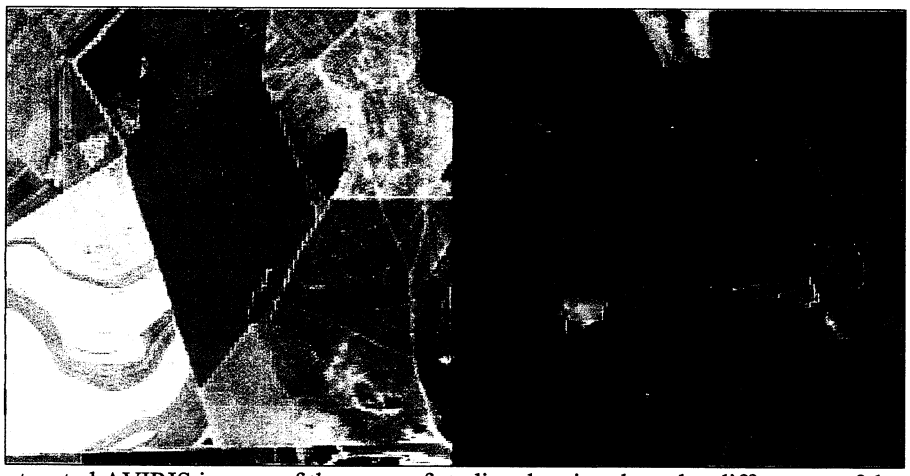

Figure 7. Concatenated AVIRIS images of the areas of studies showing the color differences of the soils due to the non-presence and the presence of opaque minerals respectively.

Figure 8 presents the gradual variation of RCGb for the two concatenated study areas.

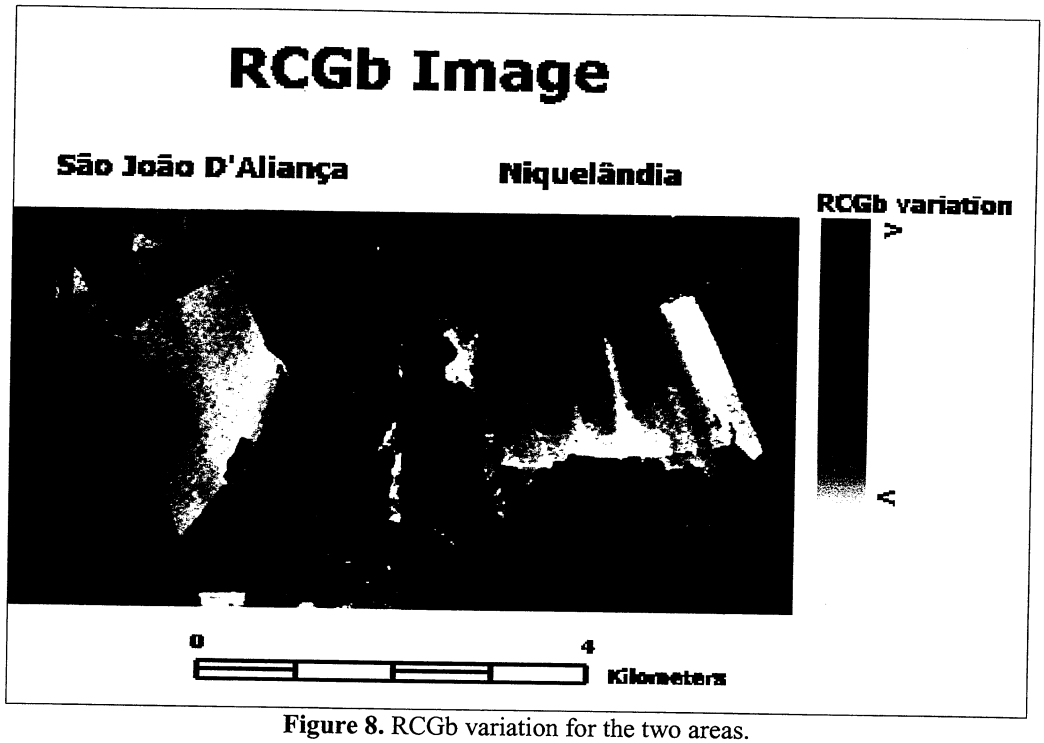

Figure 8. RCGb variation for the two areas.

For the analysis of Figure 8 it is important to know that for the kaolinite/(kaolinite+gibbsite) ratio, larger values, indicates more abundance of kaolinite and smaller values indicates a tendency of elevated gibbsite contents. It can be noticed that is a space variability of RCGb and not the homogeneity of soil classes as Figure 7 suggests.

This kind of processing of the AVIRIS data allows one a better slicing of the areas, because the result is not just based on color or on the morphology of the land but on a relationship of minerals by means of spectral analysis. It is noticed that the area of São João D'Aliança presents smaller variation of the kaolinite/(kaolinite+gibbsite) ratio, because it presents a less intense tonal variation than in the portion of Niquelândia.

In São João D'Aliança the clearest part of the studied area comes as a prolonged micro-dome that can be a structure slightly preserved of erosion processes. The darkest part of the area is a small concave depression, therefore more eroded and that can be a place of larger accumulation of water. This depression presents a small alteration, with less silicon and more aluminum. This is just a hypothesis to explain the difference of RCGb, but that is not the study object of this paper.

The clearest parts that appear in the Niquelândia scene indicate a higher local relief and present an inclination of those areas towards the darkest ones. They are higher either because a depositional process happens, since that area meets in Ultramafic's Unit and among them a altimetric significant variation happens in approximately 500 m, or for a process of differential erosion that exposed the areas with larger gibbsite contents.

6. CONCLUSIONS

The RCGb index has the advantage of generating very compatible Y scale values to Ki results, which facilitates the preliminary understanding of the soils stains exposed even before a field trip. Besides, once based on the three band ratio method (Gao et al., 1993), the RCGb spectral index minimizes the noises that happen in the laboratory spectra or of the AVIRIS images.

As the latosols genesis process is characterized by the removal of the Si and of exchangeable bases and posterior concentration of Al. The kaolinite represents the remains of silicon in those soils, and the gibbsite presents aluminum in its structures, the RCGb index allows an understanding of the weathering degree of the Brazilian tropical soils.

This work showed that the RCGb index could minimize the time expended in the analysis and in the recognition process and mapping soils. To perform those two study areas in the traditional way it would be necessary to adopt a sampling matrix with regular spacing covering the whole area, which would increase the costs of the project.

It is also worthy of note that index works for exposed soils and that any covering types can obliterate the features turning it inefficient.

The use of the laboratory radiometry is fundamental for the construction of the spectral indexes and for posterior validation. That is the most fundamental methodological aspect used in this paper. If the study's objective is to derive indexes starting from the analysis of AVIRIS data or of any other spectroscopy data, the spectral analysis of the data obtained in the laboratory can be used in the study of themes for which no image data yet exists.

7. ACKNOWLEDGMENT

We would like to thank Dr. Robert Green for his valuable assistance during this work.

8. REFERENCES

Baptista, G.M.M.; J.S., Madeira Netto; P.R , Meneses, 1998, "Determinação da Relação Sílica - Alumina a partir dos Dados do Sensor AVIRIS (JPL/NASA), para Discretização Espacial do Grau de Intemperismo de Solos Tropicais". Proceedings of the IX Brazilian Symposium of Remote Sensing, CD-ROM, INPE.

Baptista, G.M.M.; J.S., Madeira Netto; P.R , Meneses, 2000a, "Influência de minerais opacos na determinação do índice espectral RCGb em dados AVIRIS e em espectros de laboratório de solos derivados do complexo máfico e ultramáfico de Niquelândia, Goiás, Brasil", IX Simposio Latinoamericano de Percepción Remota, Puerto Iguazú, Argentina, 6 –10 de novembro.

Baptista, G.M.M.; J.S., Madeira Netto; P.R , Meneses, 2000b, "Análise de métodos de correção atmosférica na determinação do índice espectral RCGb dos solos tropicais por meio dos dados do sensor hiperspectral AVIRIS", IX Simposio Latinoamericano de Percepción Remota, Puerto Iguazú, Argentina, 6 –10 de novembro.

Clark, R.N., A.J. Gallagher and G.A. Swayze, 1990, "Material Absorption Band Depth Mapping of Imaging Spectrometer Data using a Complete Band Shape Least-Squares Fit with Library Reference Spectra", Summaries of the Third Airborne Visible/Infrared Imaging Spectrometer (AVIRIS) Workshop, JPL Publication 90-54, pp. 176-186.

Clark, R.N.; G.A., Swayze; A., Gallagher; T.V.V., King; W.M., Calvin, 1993, "The U.S. Geological Survey Digital Spectral Library: Version 1: 0.2 to 3.0 μm", U.S.G.S. Open File Report, vol. 93-592, 1340.

Gao, B.C.; K.B., Heidebrecht; A.F.H., Goetz, 1993, "Derivation of scaled surface reflectances from AVIRIS data", Remote Sensing of Environment, vol. 44, pp. 165-178.

Grove, C. I.; S. J., Hook; E. D., Paylor II, 1992, "Laboratory reflectance spectra of 160 minerals, 0.4 to 2.5 micrometers", JPL Publications, vol. 92-2.

Hlavay, H., K. Jonas, S. Elek and J. Inczedy, 1977, "Characterization of the Particle Size and Christallinity of Certain Minerals by Infrared Spectrophotometry and Other Instrumental Methods – I. Investigations on clay minerals", Clays and Clay Minerals, vol. 25, pp. 451-456.

Hunt, G.R., J.W. Salisbury and C.J. Lenhoff, 1971, "Visible and Near-Infrared Spectra of Minerals and Rocks: III. Oxides and hydroxides", Modern Geology, vol. 2, pp. 195-205.

Madeira Netto, J. da S., 1993, "Étude Quantitative des Relations Constituants Minéralogiques – Réflectance Diffuse des Latosols Brésiliens: Application à l'utilisation pédologique des données satellitaires TM (Région de Brasilia)", Éditions de l'ORSTOM, Paris, 236p.

Madeira Netto, J. da S., A. Bédidi, B. Cervelle, M. Pouget, N. Flay, 1997, "Visible Spectrometric Indices of Hematite (Hm) and Goethite (Gt) Content in Lateritic Soils: the application of a Thematic Mapper (TM) image for soil-mapping in Brasília, Brazil", Int. J. Remote Sensing, vol. 18, pp. 2835 – 2852.

Intimate and Macroscopic Mixture Analysis by Linear and Nonlinear Regression. Study Case: Garnerite x Goethite and Garnerite x Asbolan

OSMAR ABÍLIO DE CARVALHO JÚNIOR[1]
ANA PAULA FERREIRA DE CARVALHO[2]
RENATO FONTES GUIMARÃES[1]
PAULO ROBERTO MENESES[3]

[1]Departamento de Geografia - Universidade de Brasília (UnB)- Campus Universitário Darcy Ribeiro, Asa Norte, 70910-900, Brasília, DF, Brazil
osmana@tba.com.br
[2]Departamento de Ecologia - Universidade de Brasília (UnB)- Campus Universitário Darcy Ribeiro, Asa Norte, 70910-900, Brasília, DF, Brazil
[3]Instituto de Geociências - Universidade de Brasília (UnB)- Campus Universitário Darcy Ribeiro, Asa Norte, 70910-900, Brasília, DF, Brazil

Abstract: This paper evaluates the abundance of minerals estimate from spectral mixtures behavior, both macroscopically and microscopically (intimate). The analyzed mixture comes from a lateritic nickel deposit: pimelite, goethite and Mn laterite (*Fazenda* Mine, Niquelândia, GO). Mixture simulations were made as in laboratory, from the intimate mixture of the minerals powder followed by the radiometric mensuration, as from mathematical simulation using a linear function to describe the macroscopic mixtures. The calculation of the mineral abundance is estimated by indexes that compare morfometric values of the spectrum of the pure mineral with relationship to the spectrum of the mixture. In order to define the abundance of the mixture models was used the unmixed partial and scale coefficient. The abundance estimate in the intimate and macroscopic mixture can generate errors and should be corrected by mathematics adjustments with experimental data.

Key Words: macroscopic mixtures, intimate mixtures, lateritic nickel.

1 Spectral Mixture

Two types of spectral mixture can be distinguished: the macroscopic mixture and the intimate mixture. The macroscopic mixture considers that the probability of a photon's being spread among the representatives of a mixture is dependent only on the contribution area of each constituent specimen and not on a previous photon spread (Johnson *et al.*, 1983). This fact turns the spectral reflectance of a certain surface a linear combination of its individuals that makes its estimate easier.

In the intimate mixture, the components are randomly distributed within the field of view of an instrument and light is multiply scattered between mineral species (Singer, 1981; Mustard & Pieters, 1989). The spectral behavior of the intimate mixture is a nonlinear function of its components. Among the minerals intimate mixture methods of analysis there are physical models (Hapke 1981, 1984, 1986; Hapke & Wells, 1981, Lumme & Bowell, 1981) and empirical models (Adams, 1974; Singer, 1981; Cloutis *et al.*, 1986).

The physical models are based on the interaction of the electromagnetic energy with the mixture under study. Among the physical models the Hapke Model stands out. It is based on the bi-directional reflectance of intimate mixtures (Hapke & Wells, 1981). However the Hapke model requires multiple viewing geometries, which are not commonly obtained by current and planned imaging spectrometers (Mustard and Pieters, 1989).

The empirical models relate the measurable properties of the absorption features to the material abundance. It is specific for a certain mixture in study where a calibration is requested in laboratory with a systematic of mineral proportions (Adams, 1974; Singer, 1981; Cloutis *et al.*, 1986).

2 Methodology

For the analysis of a spectral mixture it was accomplished simulations as macroscopic mixture as of intimate mixture, generating a continuous series among the endmembers. The macroscopic mixtures were computational simulated using linear proportions. The intimate mixtures were simulated in a laboratory from the powder of the minerals mixture followed by the radiometric measurement. However in the intimate mixture, several conditions alter its final behavior such as the particle size and the rough.

For the mixture models the following indexes were calculated: angular and linear coefficients related to the linear regression (Harsanyi and Chang, 1994) and the scale coefficient (Clark & Roush, 1984). In order to evaluate the correlation interference of the pure spectra, was also calculated the similarity index Spectral Correlation Mapper (SCM) (Carvalho & Meneses, 2000). The methodology was tested for the mixtures garnerite x goethite and garnerite x typical asbolan of the lateritic Ni profile of the *Fazenda* mine (Niquelândia, GO).

3 Analysis of the Garnerite Abundance when Mixed with Goethite

The mixture of the garnerite and goethite is very common in lateritic Ni mineralization, as the macroscopic form as in the intimate one. For the calculation of garnerite abundance the feature used was 2.29 μm, regarding pimelite feature (Mg-OH) its main mineral composed.

The macroscopic mixture series is shown in **Figure 1** in 10% intervals abundance. A linear behavior of the angular and linear coefficient is observed in relation to garnerite abundance (**Figure 2**). However, the angular coefficient without the pimelite doesn't reach zero. That is due to the correlation among the spectra in analysis that is demonstrated by SCM that reaches values of 0.90 even in the absence of the mineral (**Figure 3**). The coefficient scale presents a nonlinear behavior; even so it is not so affected by the correlation of the spectra, obtaining values close to zero in the garnerite absence.

In the intimate mixtures series among the goethite and the pimelite accomplished in a laboratory a 10% intervals abundance was also used (**Figure 4**). The SCM in the pimelite absence also presents high values demonstrating a high correlation among the spectra. The coefficients have linear behavior (**Figure 5, 6, 7, and 8**).

4. Abundance of Garnerite Analysis when Mixed with Asbolan

The garneritic facie of the mine has asbolan veins. In spite of the presence of the asbolan being restricted to a specific area, the use of that mixture is interesting to demonstrate another type of spectral mixture behavior.

Figure 9 presents the macroscopic mixtures series between the garnerite and the asbolan. The angular coefficient establishes a linear relationship that corresponds to the amount of garnerite due to the low correlation among the spectra (**Figure 10**). The coefficient scale doesn't obtain the same result.

In the intimate mixture a reduction of the mixture reflectance is observed due to the asbolan presence (**Figure 11**). Those results are consistent with previous studies of mineral assemblies mixture of opaque with not opaque (Pieters, 1973; Nash & Conel, 1974; Singer, 1981; Ribeiro *et al.*, 2000). The coefficients present a distribution according to a logarithmic function (**Figure 12**). The logarithmic function can be applied to the hyperspectral image providing a better estimate of the pimelite amount for areas.

5 Conclusion

The index values should be confirmed in a laboratory for the intimate mixture and the macroscopic mixture. In the macroscopic mixture the coefficient can present overestimation in the spectra correlation. The garnerite abundance in the mixture with the goethite was harmed due to that correlation. In the intimate mixture the indexes are also shown vulnerable mainly, when an albedo difference exists. The use of the logarithmic function presented excellent results for the mixture calibration. Other simulations for intimate mixture varying the particle size and rough are also necessary for a better process control. The quantification of intimate mixture in the spectroscopy image still presents a lot of problems, constituting a vast field for research.

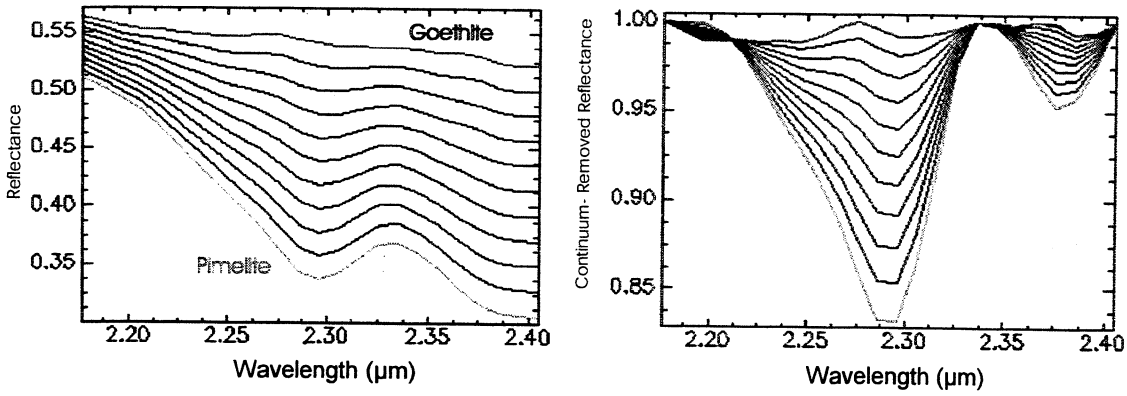

Figure 1–Simulation of the macroscopic mixtures between the pimelite and the goethite with abundance interval of 10%: a) without normalization (removal of the continuous) and b) with normalization.

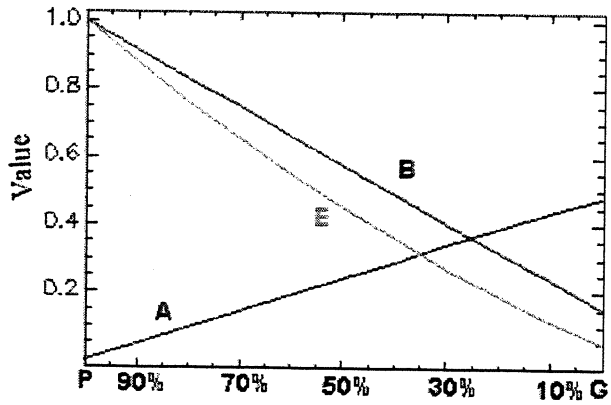

Figure 2–Angular coefficient (B), linear (A) and scale (E) behavior for the macroscopic mixtures models between the pimelite and goethite

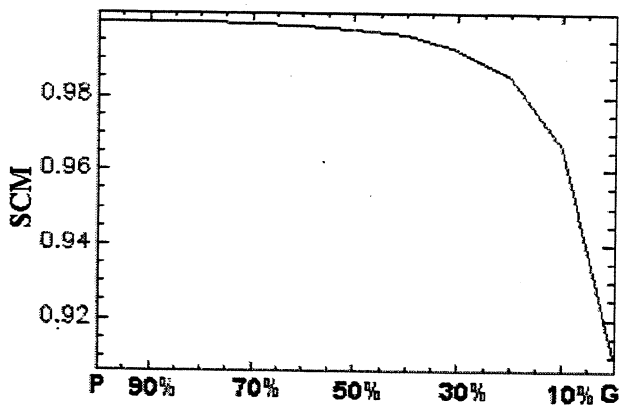

Figure 3–SCM among the pimelite and the relative curves to the macroscopic mixture among the pimelite and goethite

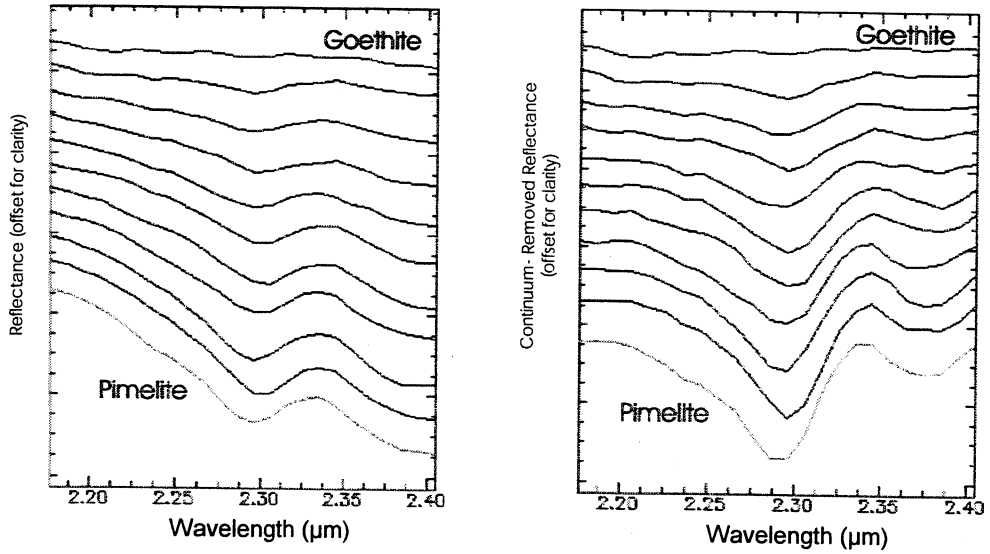

Figure 4–Simulation of intimate mixture between the pimelite and the goethite with interval abundance among the curves of 10%: a) reflectance (offset for clarity) and b) continuum remove reflectance.

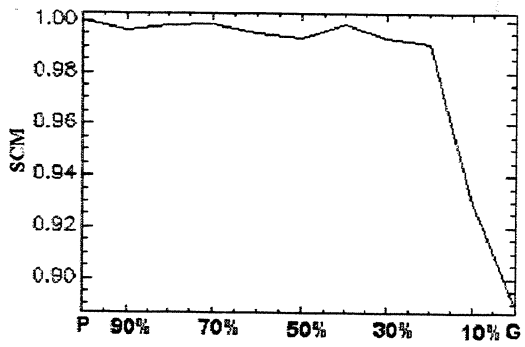

Figure 5–Values of SCM between the pimelite and the relative curves to the mixture with the goethite.

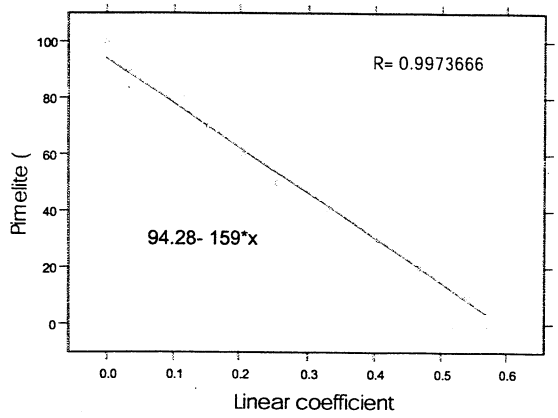

Figure 6–Linear coefficient behavior for the intimate mixture between pimelite and goethite

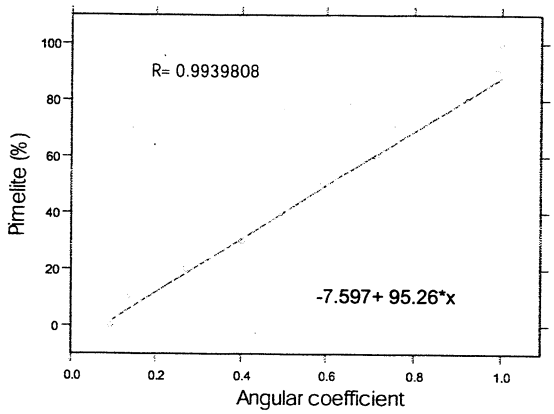

Figure 7–Angular coefficient behavior for the intimate mixture between pimelite and goethite

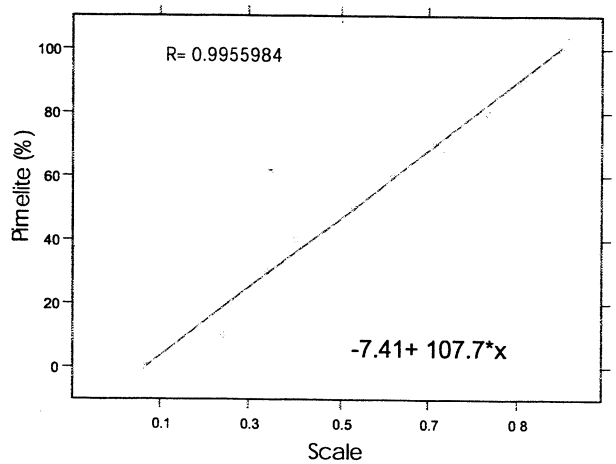

Figure 8–Coefficient scale behavior for the intimate mixture between pimelite and goethite presenting a linear distribution.

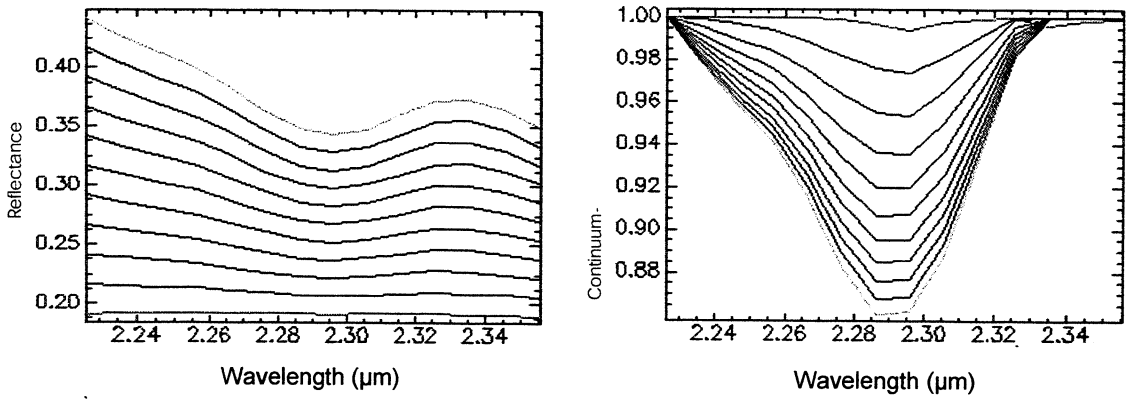

Figure 9–Macroscopic mixture simulation among the pimelite (green) and the asbolan (red), with interval of 10%: a) reflectance and b) continuum remove reflectance.

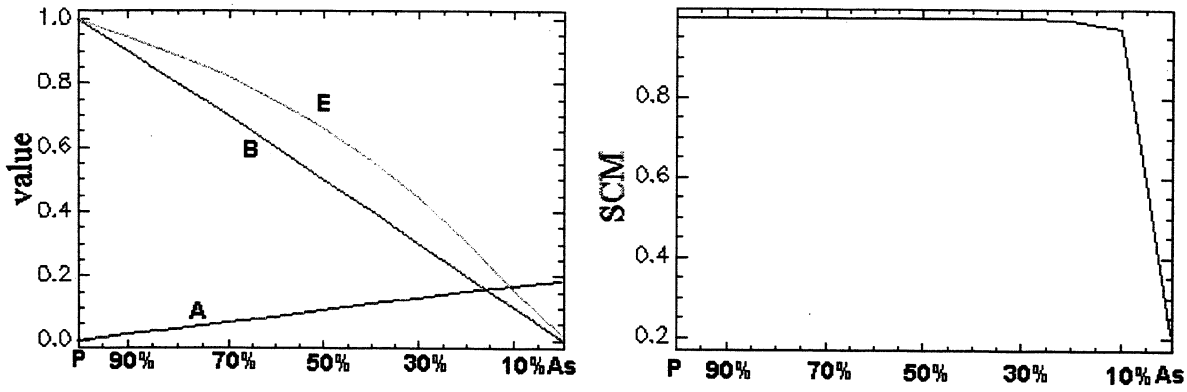

Figure 10–a) Angular coefficient (B), linear (A) and it scale (E) behavior for the macroscopic mixtures simulation between pimelite and asbolan b) SCM among pimelite and the relative curves to the macroscopic mixtures between pimelite and goethite

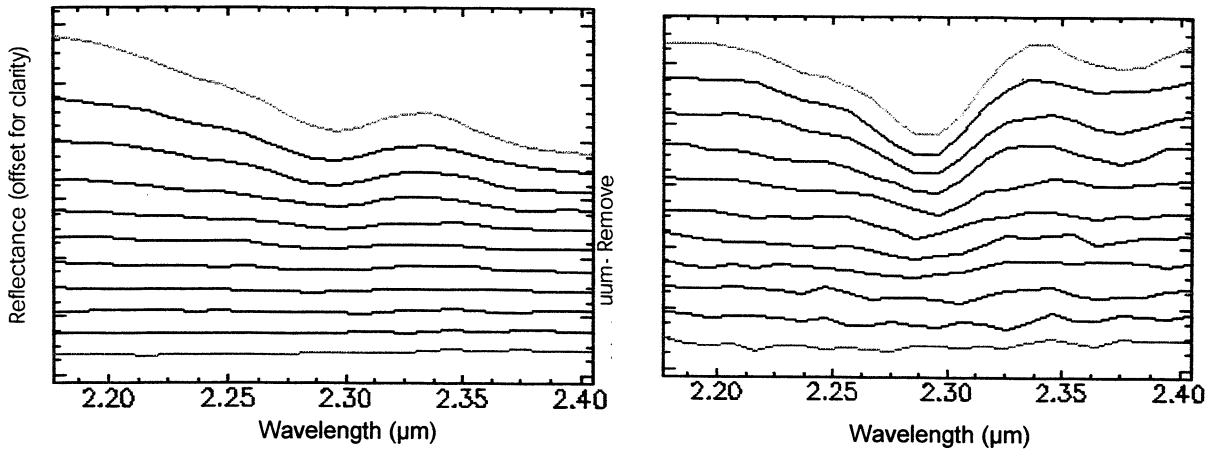

Figure 11–Intimate mixture simulation of pimelite (green) and asbolan (magenta) in interval of 10% a) reflectance (offset for clarity) and b) continuum remove reflectance.

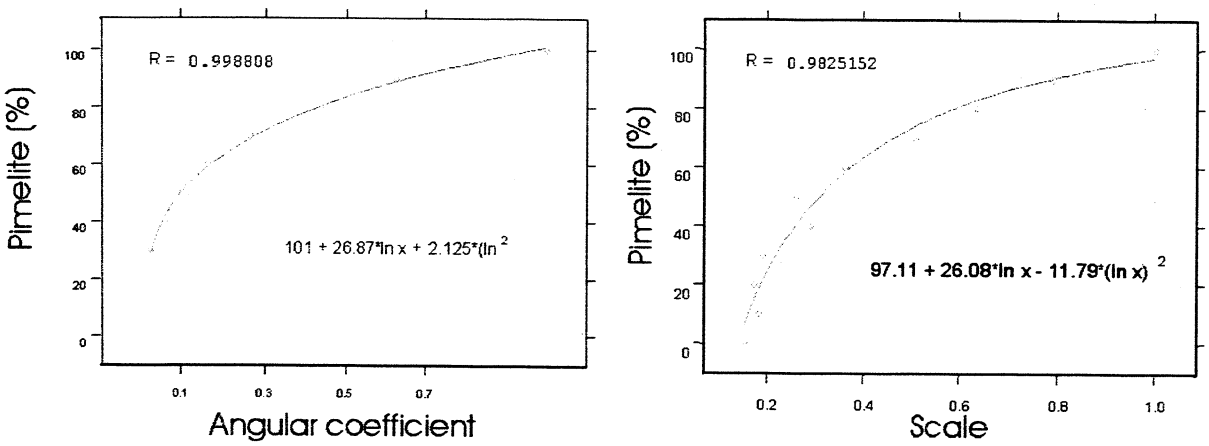

Figure 12–Logarithmic behavior of the angular coefficient, and scale for the intimate mixture between pimelite and asbolan.

References

Adams, J. B., 1974. Visible and near-infrared diffuse reflectance: Spectra of pyroxenes as applied to remote sensing of solid objects in the solar system. *J. Geophys. Res.*, 79, 4829–4836.

Carvalho Jr., O. A. & Meneses, P. R., 2000. Spectral Correlation Mapper (SCM): an Improving Spectral Angle Mapper, *Proceedings of the Ninth JPL Airborne Earth Science Workshop*, Jet Propulsion Laboratory, Pasadena, California, JPL Publication 00-18.

Clark, R. N. & Lucey, P. G., 1984. Spectral properties of ice-particulate mixture and implications for remote sensing 1. Intimate Mixtures. *J. Geophys. Res.*, 89, 6341–6348

Clark, R. N. & Roush, T. L., 1984. Reflectance Spectroscopy: Quantitative analysis techniques for remote sensing applications. *J. Geophys. Res.*, 89, 6329–6340.

Cloutis, E. A., Gaffey, M. J., Jackowski, T. L., Reed, K. L., 1986. Calibrations of Phase Abundance, Composition, and Particle Size Distribution for Olivine—Orthopyroxene Mixtures from Reflectance Spectra, *J. Geophys. Res.*, vol. 91, NO. B11, pg. 11641–11653.

Hapke, B., 1981. Bi-directional reflectance spectroscopy, 1, Theory, *J. Geophys. Res.*, 86, 3.039–3.054.

Hapke, B., 1984. Bi-directional reflectance spectroscopy, 3, Correction for macroscopic roughness, *Icarus*, 59, 41–59.

Hapke, B., 1986. Bi-directional reflectance spectroscopy, 4, The extinction coefficient and the opposition effect, *Icarus*, 67, 264–287.

Hapke, B. & Wells, E., 1981. Bi-directional reflectance spectroscopy, 2, Experiments and observations, *J. Geophys. Res.*, 86, pp. 3.055–3.060.

Harsanyi and Chang, 1994, Hyperspectral image classification and dimensionality reduction: An orthogonal subspace projection approach: *IEEE Trans. Geosci. and Remote Sens.*, v.32, p.779–785.

Johnson, P. E., Smith, M. O., Taylor-George, S. & Adams, J. B., 1983. A semi-empirical method for analysis of the reflectance spectra of binary mineral mixtures, *J. Geophys. Res.*, 88, 3557–3561.

Lumme, K. & Bowell, E., 1981. radiative transfer in the surfaces of atmosphereless bodies, I, Theory, *Astron. J.*, 86, 1.694–1.704.

Mustard, J. F. & Pieters, C. M., 1989. Photometric phase functions of common geologic minerals and applications to quantitative analysis of mineral mixture reflectance spectra. *J. Geophys. Res.*, Vol. 94, No B10, pp. 13.619–13.634.

Nash, D. B. and Conel, J. E., 1974. Spectral reflectance systematics for mixtures of powdered hypersthene, labradorite, and ilmenite, *J. Geophys. Res.*, 79, 161–1621.

Pieters, C. B., 1973. Polarization in mineral absorption band, in *Planets, Stars and Nebulae Studied with Photopolarimetry*, edited by T. Gehrels, pp. 405–418, University Arizona Press, Tucson, 1973.

Ribeiro, M. N. C., Carvalho Jr., O. A., Guimarães, E. M. & Meneses, P. R., 2000. Integral Spectral Analysis (ISA) applied to AVIRIS data for manganese mineralized laterites in São João da Aliança /GO, Brazil, *Proceedings of the Ninth JPL Airborne Earth Science Workshop*, Jet Propulsion Laboratory, Pasadena, California, JPL Publication 00-18.

Singer, R. B., 1981. Near-infrared reflectance of mineral mixtures: Systematic combinations of pyroxenes, olivine, and iron oxides, *J. Geophys. Res.*, 86, 7967–7982.

Analysis Absorption Band Positioning: A New Method for Hyperspectral Image Treatment

OSMAR ABÍLIO DE CARVALHO JÚNIOR[1]
ANA PAULA FERREIRA DE CARVALHO[2]
PAULO ROBERTO MENESES[3]
RENATO FONTES GUIMARÃES[1]

[1]Departamento de Geografia - Universidade de Brasília (UnB)- Campus Universitário Darcy Ribeiro, Asa Norte, 70910-900, Brasília, DF, Brazil
osmana@tba.com.br
[2]INCRA – SBN Ed. Palácio do desenvolvimento, sala 1205, 70057-900, Brasília, DF, Brazil
[3]Instituto de Geociências - Universidade de Brasília (UnB)- Campus Universitário Darcy Ribeiro, Asa Norte, 70910-900, Brasília, DF, Brazil

Abstract This work demonstrates a new program for the spectral classification of hyperspectral images based on the positioning of the absorption band. The program generates an image where the value of the pixel is the wavelength of the absorption band after the continuum removal. This program, when used with similar spectral features, provides a classification with better results than the usual procedures (i.e., SAM, SCM, SFF, correlation coefficient R used by Tricorder). This program was tested in AVIRIS hyperspectral images obtaining excellent results as much in mineralogical as vegetation discrimination.

Keywords: spectral classifier, absorption band, hyperspectral, remote sensing.

1. Method of the Analysis Absorption Band Positioning (AABP)

The main spectra classifiers SAM (Kruse *et al.* 1992, Kruse *et al.* 1993a and b), MCE (Carvalho & Meneses, 2000), SFF and the correlation coefficient R used by Tricorder (Clark & Swayze, 1995) have problems in separating near and similar absorption features due to the high correlation between the features. This problem increases when they are mixed, as in the case of goethite and hematite, which generate intermediary features. For those minerals and their mixtures, the identification can be better determined by the absorption band position. Therefore, a program was developed to determine the absorption band from continuum analysis of reflectance spectra and generates an image relative to its wavelength. This method was named Analysis of the Absorption Band Positioning (AABP).

The continuum removal can alter the absorption band value in relation to the spectrum without continuum removal. Thus, it is always necessary to analyze the absorption positioning before and after the continuum removal.

2. The Use of AABP in Hyperspectral Images

AABP can be used for two purposes: a) previous image segmentation and b) the discrimination of specific absorption bands. The first case is characterized as an exploratory stage used in a wider spectral range. In the second case, the use of the method should be restricted to specific absorption bands.

AABP was tested in the AVIRIS image obtained during the SCAR-B mission (Smoke, Clouds and Radiation - Brazil) done in 1995 in Brazil. The study area is the lateritic nickel mine located in Niquelândia (GO). The image was corrected for the atmospheric effect, using the Green method.

First, AABP was used in the 0,46-μm to 0,74-μm spectral range. The image on gray levels shows a strong contrast among the vegetation areas and the exposed soil area (Figure 1). The visualization of the histogram demonstrates the data distribution. Due to the low contrast, an interactive density slicing is necessary according to the absorption band. The use of a profile in the image highlights the differentiated nature of the pixels. In Figure 2, the areas with vegetation cover are well discriminated from the areas with exposed soil and saprolite in the *Fazenda* mine.

To obtain a better visualization of the two segments previously selected, AABP was used in the spectral range relative to the vegetation and exposed soil. The vegetation was analyzed in the 0,65-μm to 0,70-μm spectral range, which can be separated into areas with predominance of green vegetation (0,6754 μm) and nonphotosynthetic vegetation (0,6849 μm) (Figure 3). The relative spectra for the two classes are presented in Figure 4.

The Fe^{+3} band is well defined in the 0,46-μm to 0,62-μm spectral range. Figure 5 presents the AABP classified image. A gradation of iron minerals behavior can be seen, more goethite in the base of the weathering profile is observed and more hematite is observed on the top, as was verified in the field. The class with the feature positioning in 0,4995 μm in the mine represents areas with silica impregnated with goethite and limonite.

Figure 6 presents the mean spectrum of the Fe^{+3} band among the goethite and hematite mineral from the USGS spectral library (Clark *et al.*, 1993). That procedure is effective in separating these two minerals indicating the relative mixture degree.

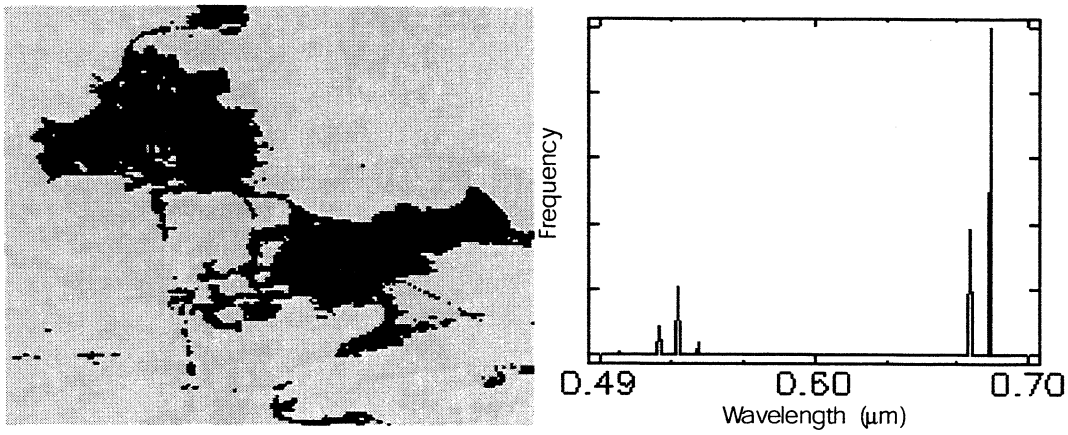

Figure 1 - Wavelength image of the absorption band.

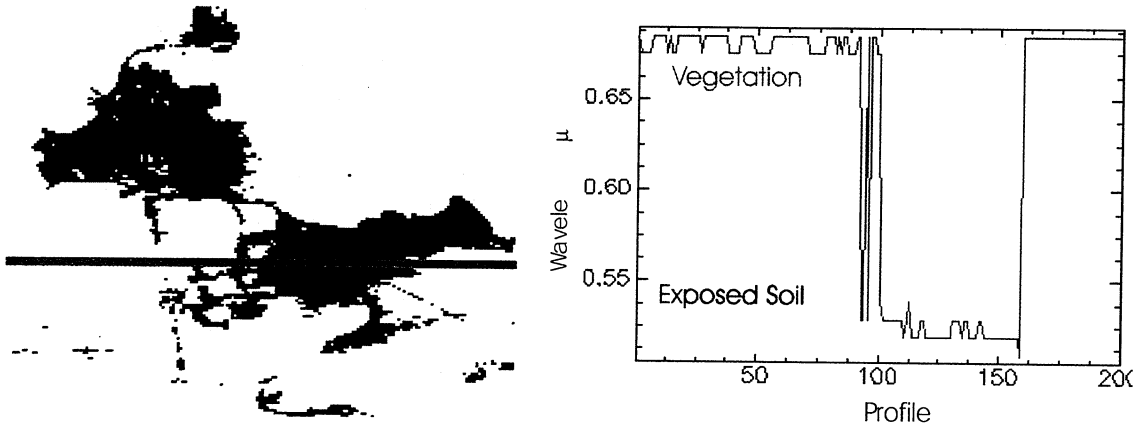

Figure 2 - Horizontal profile in the wavelength image of the absorption band.

Figure 3 -Image regarding the wavelength image of the absorption band in the 0,65-μm to 0,70-μm spectral range highlighting the areas with vegetation cover.

a) b)

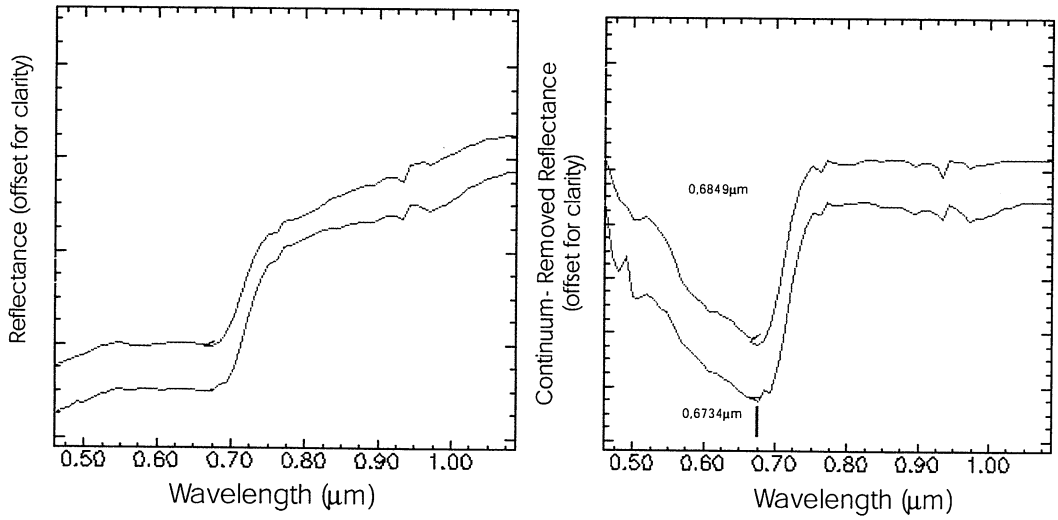

Figure 4 - Spectral curves refer to green vegetation (0,6849 μm) and nonphotosynthetic vegetation (0,6754 μm): a) reflectance and b) continuum removed reflectance.

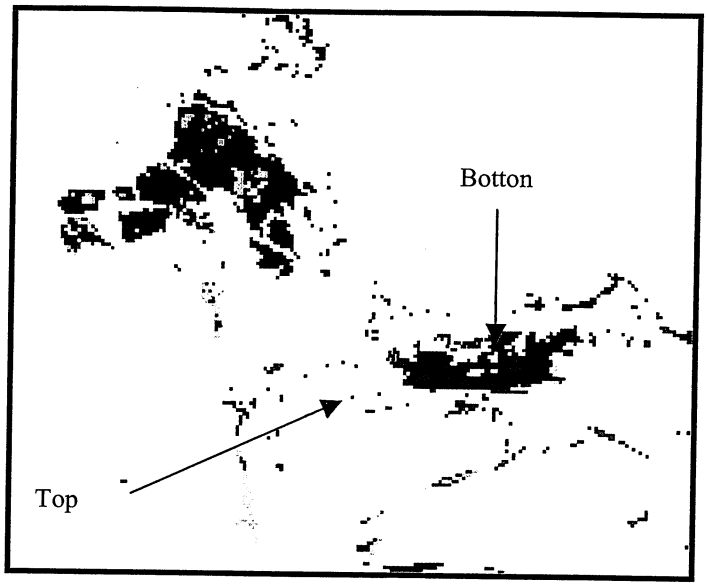

Figure 5 - Image regarding the wavelength image of the absorption band in the 0,46-μm to 0,62-μm spectral range.

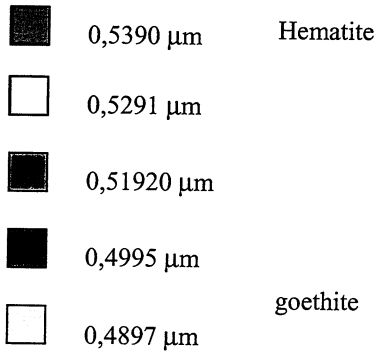

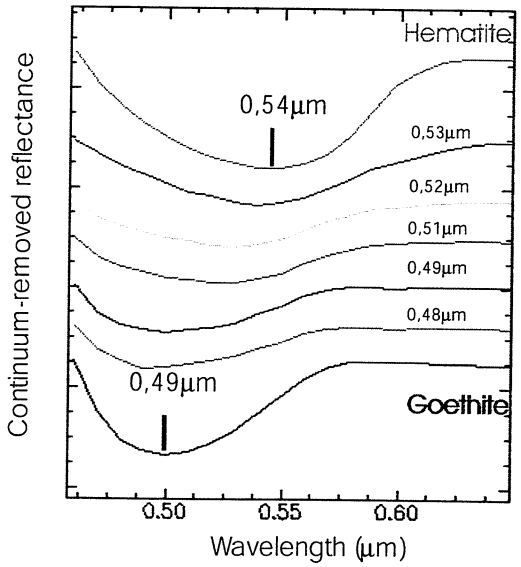

Figure 6 –Spectral curve sequence between goethite and hematite (0,46 μm and 0,62 μm).

Another interesting application of AABP in the study area is in the characterization of the garnerite main spectra representative of the facies with a concentration of nickelliferous silicated minerals. The term garnerite has a generic connotation to define a mixture of hydrated silicate of Ni-Mg from the montmorilonite group (Trecasses *et al.*, 1980; Brindley & Pham, 1973). In the mine area, pimelite and saponite with serpentine (antigorite) are mainly constituted of garnerite. The garnerite coloration varies from green at the base, to brown on the top, due to the presence of goethite .

The garnerite is characterized by the Mg-OH band that presents a small displacement in conformity with the preponderant mineral, varying between 2,22 μm and 2,36 μm. The AABP method allows detection of the dominant minerals: pimelite/saponite, saponite and antigorite (Figure 7). The differences between each one of those minerals correspond to an interval of little bands for the AVIRIS sensor.

Figure 8 presents the AABP image where the wavelength values of the absorption bands are characterized. The antigorite and the saponite are seen to be limited to restricted areas. The differentiation of the antigorite can also be obtained using the absorption band at 2,11 μm.

3. Conclusion

This new method (AABP) aims to generate an image relative to the wavelength of the absorption band. This method can be used as an exploratory stage and as in the analysis refinement stage. This method presents advantages in the spectra discrimination with high similarity and proximity. Therefore, AABP can be used as a refinement after the employment of others spectral classifiers. In the *Fazenda* mine, the use of AABP method made easier the identification of the vegetation patterns and also the discrimination of the soil mineralogy. In the vegetation, it was possible to separate areas with a prevalence of green vegetation and those with non-photosynthetic vegetation. In the soil mineralogy, it was possible to distinguish gradations of soils hematitics for goethitics as well as garnerite types.

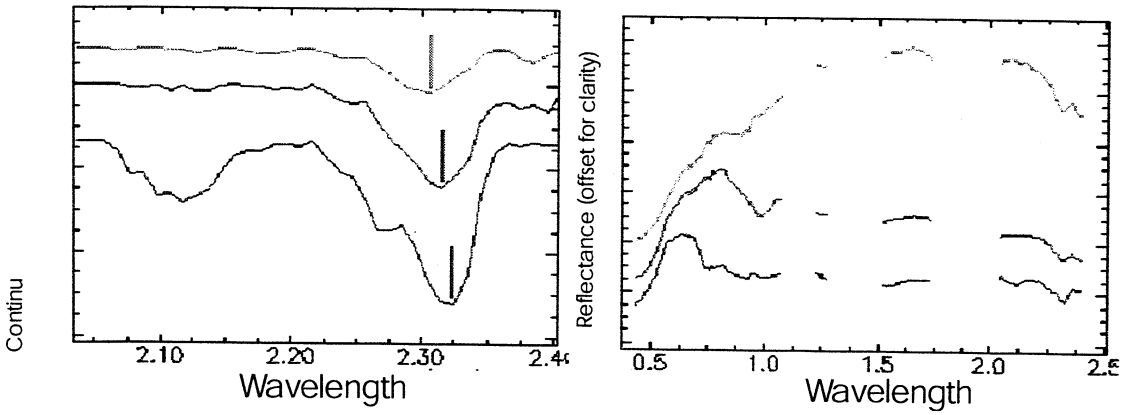

Figure 7 – Spectrum with Mg-OH bands: pimelite-saponite (green), saponite (blue) and antigorite (red)

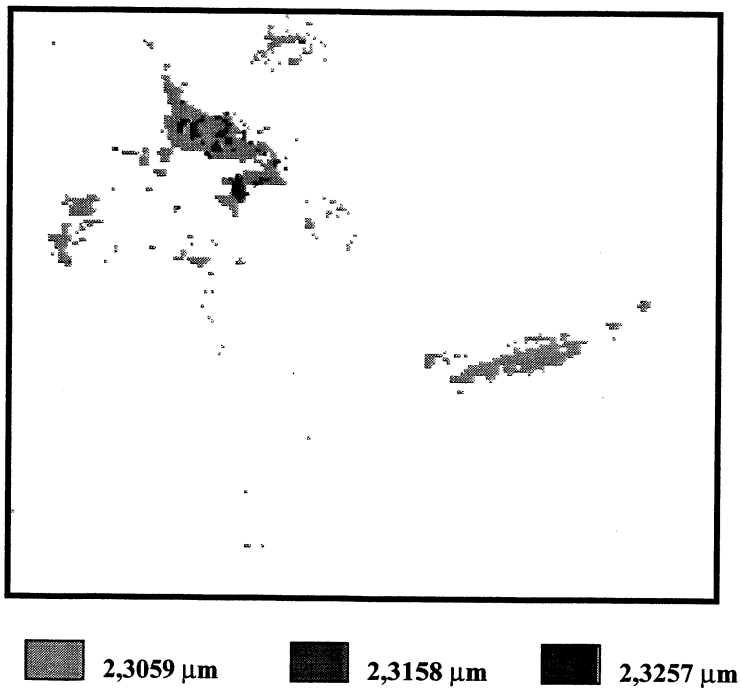

Figure 8 – AAPB image relative to the Mg-OH band.

References

Brindley, G. W., Pham T.H, 1973, The nature of garnierites: I. Structure, chemical composition and color characteristics. *Clay and Clay Minerals.* 21:17-40.

Carvalho Jr., O. A. & Menezes, P. R., 2000, Spectral Correlation Mapper (SCM): An Improving Spectral Angle Mapper. In: *Ninth JPL Airborne Earth Science Workshop.* JPL Publication 00-18, pp. 65-74.

Clark, R. N. & Swayze, G. A., 1995. Mapping Minerals, Amorphous Materials, Environmental Materials, Vegetation, Water, Ice and Snow, and Other Materials: The USGS Ticorder Algorithm. In: *Summaries of the Fifth JPL Airborne Earth Science Workshop*, JPL Publication 95-1 v.1, p. 39-40.

Clark, R. N; Swayze, G. A., King, T. V. V., Gallagher, A. J. & Calvin, W. M., 1993, The U.S. Geological Survey, Digital Spectral Reflectance Library: Version 1:0.2 to 3.0 µm *Summaries of the Fourth Annual JPL Airborne Geoscience Workshop*, JPL Publication 93-96, Vol.1, pp. 37-38.

Kruse, F. A., Lefkoff, A. B., Boardman, J. W., Heiedbrecht, K. B., Shapiro, A. T. Barloon, P. J. & Goetz, A. F. H., 1992. The Spectral Image Processing System (SIPS) - Software for Integrated Analysis of AVIRIS Data. *Summaries of the 4th Annual JPL Airborne Geoscience Workshop*, JPL Pub-92-14, pp. 23-25.

Kruse, F. A., Lefkoff, B. & Dietz, J. B., 1993a, Expert System-Based Mineral Mapping in Northern Death Valley, California/Nevada, Using the Airborne Visible/Infrared Imaging Spectrometer (AVIRIS), *Remote Sens. Environ.*, Vol. 44, No. 2, pp. 309-336.

Kruse, FA, Lefkoff, A. B; Boardman, J. W., Heiedbrecht, K. B., Shapiro, A. T., Barloon, P. J. & Goetz, A. F. H., 1993b, The Spectral Image Processing System (SIPS) – Interactive Visualization and Analysis of Imaging Spectrometer Data. *Remote Sens. Environ*. 44:145-163.

Trescasses, J. J. Melfi, A. J. & Oliveira, S. M. B., 1980, Nickeliferous Laterites of Brazil. *Proceeding of the International Seminar on Laterisation Process. Trivandrum*, India. pp. 170-184.

SPECTRAL IDENTIFICATION METHOD (SIM): A NEW CLASSIFIER BASED ON THE ANOVA AND SPECTRAL CORRELATION MAPPER (SCM) METHODS

OSMAR ABÍLIO DE CARVALHO JÚNIOR.[1]
ANA PAULA FERREIRA DE CARVALHO[2, 3]
PAULO ROBERTO MENESES[4]
RENATO FONTES GUIMARÃES[1]

[1]Departamento de Geografia - Universidade de Brasília (UnB)- Campus Universitário Darcy Ribeiro, Asa Norte, 70910-900, Brasília, DF, Brazil osmana@tba.com.br

[2]Departamento de Ecologia - Universidade de Brasília (UnB)- Campus Universitário Darcy Ribeiro, Asa Norte, 70910-900, Brasília, DF, Brazil

[3]INCRA – SBN Ed. Palácio do desenvolvimento, sala 1205, 70057-900, Brasília, DF, Brasil

[4]Instituto de Geociências - Universidade de Brasília (UnB)- Campus Universitário Darcy Ribeiro, Asa Norte, 70910-900, Brasília, DF, Brazil

Abstract: Spectral classifiers generate images that express the probability of the material sought according to a similarity parameter. The value of the similarity parameter that attests to the existence of the material varies for each spectral curve sought; this is done manually by the user. This work demonstrates the development of a new spectral classifier called the Spectral Identification Method (SIM). It supplies estimates according to confidence levels of the existence or not of the curve sought. The proposed method is based on two procedures: the algorithm of similarity of the SIM spectral classifier and the ANOVA statistical method. This method generates an image of the similarity parameter as much from the SIM as from three relative binary images of the existence of the material according to confidence levels.

Keywords: Spectral mixture, ANOVA, Spectral Correlation Mapper and imaging spectroscopy.

1 Introduction

Spectral classifiers allow good mapping of the materials based on spectral signatures: the *Spectral Angle Mapper-SAM* (Kruse *et al.* 1992, Kruse *et al.* 1993a and b), the *Spectral Correlation Mapper* - SCM (Carvalho & Meneses, 2000), the *Spectral Feature Fitting* - SFF and the correlation coefficient R used by Tricorder (Clark & Swayze, 1995).

However, an issue is the determination of the similarity degree that allows the statistical validation of the existence of the sought element. In the mentioned methods, the user determines the values that attest to the existence of the material. Is it asked, therefore, which is the value of the similarity parameter that confirms the existence of the sought element? It is important to highlight that the detection limit is variable and dependent on the analyzed material and the existent correlation among the materials in analysis. That variability hinders an automated delimitation of the sought material.

In this paper, the Spectral Identification Method (SIM) is proposed to establish a new similarity index and three estimates according to the levels of significance of materials. The method is based on two statistical procedures: ANOVA (Davis, 1973; Steel & Torrie, 1980; Vieira, 1988; Souza, 1998) and the SCM coefficient (Carvalho & Meneses, 2000). This

information can be used to evaluate the degree of correlation among the materials in analysis.

2 The ANOVA Method

The variance analysis uses a hypothesis test in order to determine if the spectral image belongs to the spectral reference group. In this test two alternatives are appraised based on the slope coefficient of linear regression:

$$Ho: \beta = 0$$
$$H1: \beta \neq 0$$

If the slope coefficient is close to 0, it is possible to conclude that scatter in Yr (Estimate of Y about linear regression) is low, close to mediu n Y and with low fit regression. The determination of Ho hypothesis establishes that the spectral image doesn't belong to the same population as the pattern curve. The hypothesis analysis can have two types of errors:

- Error type I - consists of rejecting Ho, and Ho is true; and
- Error type II - consists of accepting Ho, and Ho is false.

The occurrence probability of error type I is denominated, in the hypothesis test, as level of significance (α). A level of significance of 10% means that there exists a probability that 10% of the data has $\beta = 0$ and they be considered as $\beta \neq 0$.

The F test is used to validate (or not) the hypothesis. The F index calculation is:

$$\mathbf{F = \frac{MSr}{MSd}} \qquad \text{eq. 1}$$

Where:

MSr – Sums of squares mean regression

MSd – Sum of squares mean deviation

The test rejects the hypothesis (Ho) for the whole F value equal to or greater than the value contained within an F table dependent on the degree of freedom and level of significance of the numerator and denominator (Vieira, 1988). The characteristics of the F test for a simple linear regression are shown in table 1.

The degree of freedom of the denominator is expressed by (N-2), where N is a band number. However, hyperspectral images have a redundancy of information. With the use of APC or MNF, an absorption feature can be represented by three components. Therefore, in the present method, the N value, instead of being expressed by the number of bands, is represented by the number of APC or MNF components with information. For more spectral features that occupy major numbers of bands, as the case of the double feature of kaolinite, four components can be considered. Thus, the conditions of the proposed method are the degrees of freedom of the denominator (1 or 2), numerator (1) and the level of significance (2.5%, 5% and 10%).

Table 1 – ANOVA for Simple Linear Regression (Davis, 1973)				
Source of Variation	Sum of Squares	Degrees of Freedom	Mean Squares	F Test
Linear Regression	SSr	1	MSr	MSr/MSd
Deviation	SSd	n –2	MSd	
Total Variation	SSt	n –1		

3 Formulation of the Spectral Identification Method (SIM) for the Integration of ANOVA with the Coefficient (SCM)

The variance analysis of a linear regression is not sensitive to the presence of a negative correlation. Therefore, as complement to the proposed method, the correlation coefficient SCM should be used (Carvalho & Meneses, 2000). The areas with negative correlation are detected and integrated in the data that were obtained with ANOVA (**Figure 1**).

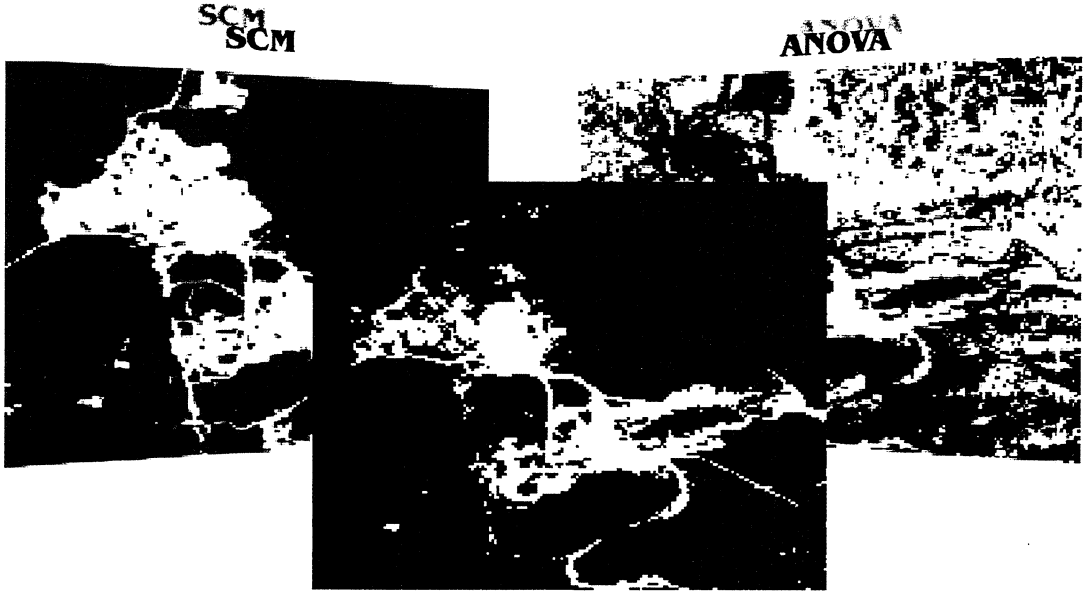

Figure 1. SIM method from SCM and ANOVA union.

4 Degrees of Significance Images

The present method generates binary images, relative to the existence (or not) of the information, inside a level of significance of 2.5%, 5% or 10%. This method was used for the features of pimelite/saponite (2.19μm - 2.36μm) and of vegetation (0.54μm - 0.75μm). These features used the value of degrees of freedom in the denominator equal to one.

Compared to the manual analysis, it is observed that the estimate of 2.5% was quite efficient to identify the areas for both features (Figure 2 and Figure 3). The other significance levels present an overestimated area. That characteristic is due to the high spectral correlation of the scene.

Figure 2. Comparison of the areas defined for pimelite presence, using the SIM method for the significance levels 2.5%, 5% and 10%.

Figure 3. Comparison of the areas defined for kaolinite presence, using the SIM method for the significance levels 2.5%, 5% and 10%.

5 Analysis of the Factor of Similarity SIM Image

The coefficient conjugate of the ANOVA and SCM methods varies between 0 and 1. The maximum value of that coefficient corresponds to the areas with levels equal to 2.5%, while the lower values are related to areas with SCM below 40% and F factor below 5%. The SIM images promote an intense expansion of the areas of greater SCM correlation, giving them an efficient and robust similarity index. Figure 4 presents the SIM images for the features of the pimelite-saponite and vegetation.

The SIM and SCM indexes are described by a function. Figure 5 presents the SCM x SIM scatter plot for the pimelite-saponite and vegetation features. The SIM promotes an expansion for SCM values with high correlation.

The generated curves are segmented in agreement with the differing degree of significance. The red area is relative to the significance of 2.5%, cyan 5%, blue 10% and yellow higher than 10%. The areas with pimelite and green vegetation are contained in the SIM value equal to one. Thus, this index establishes a great numeric difference between the intended data and the others. The author, in IDL language, inside of the ENVI program implemented the SIM.

6 Conclusion

SIM is a new method of spectral classification that provides estimates according to levels of significance of the most probable areas of the sought material, and an image related to the similarity parameter. The method demonstrated excellent estimates for study area.

The method has a similarity parameter that completely eliminates the false positives present in the algorithms of SAM, SFF and Tricorder and still maximizes the values of the areas where the sought material exists.

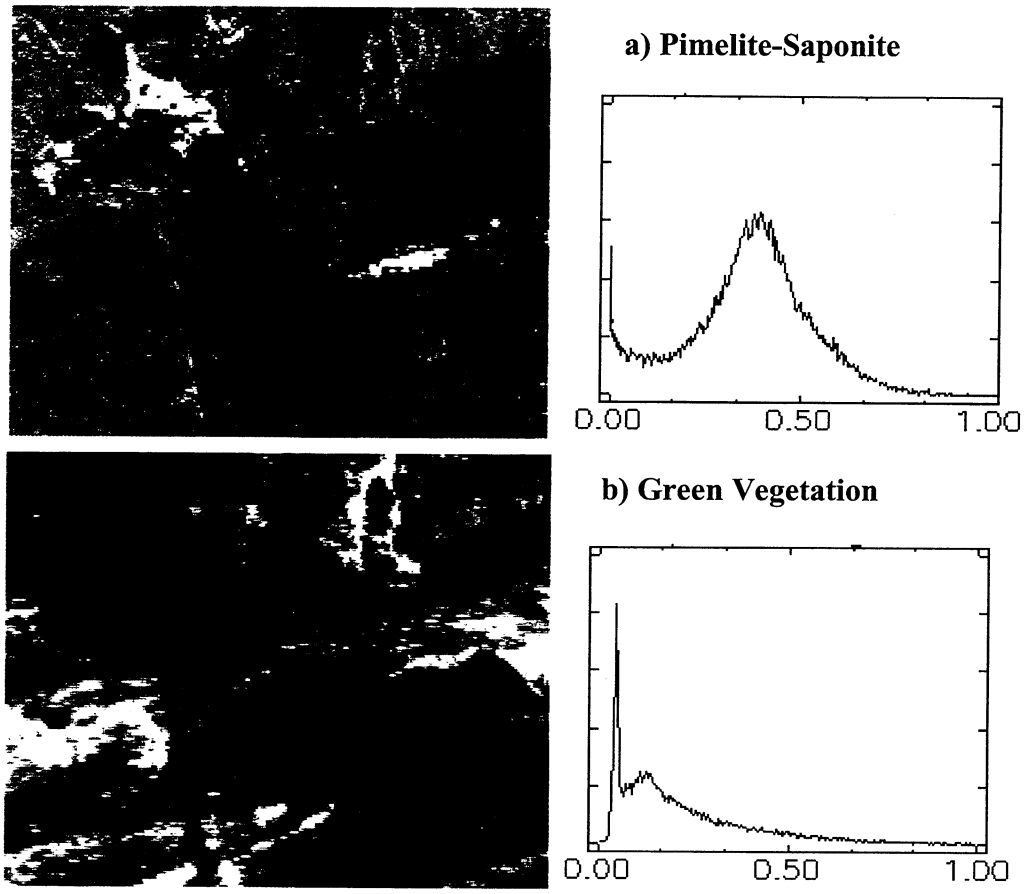

Figure 4. –SIM image for the area of the *Niquelândia* mine with its respective histogram of the features: a) pimelite, and b) vegetation.

References

Carvalho Jr., O. A. & Meneses, P. R., 2000, Spectral Correlation Mapper (SCM): An Improving Spectral Angle Mapper. In: *Ninth JPL Airborne Earth Science Workshop.* JPL Publication 00-18, pp. 65-74.

Clark, R. N. & Swayze, G. A., 1995. Mapping Minerals, Amorphous Materials, Environmental Materials, Vegetation, Water, Ice and Snow, and Other Materials: The USGS Tricorder Algorithm. In: *Summaries of the Fifth JPL Airborne Earth Science Workshop*, JPL Publication 95-1, v.1, p.39-40

Davis, 1973, *Statistics and analysis in geology.* New York, John Willey & Sons, Inc. 550 pp.

Kruse, F. A.; Lefkoff, A. B.; Boardman, J. W.; Heiedbrecht, K. B.; Shapiro, A. T.; Barloon, P. J. & Goetz, A. F. H., 1992. The Spectral Image Processing System (SIPS) - Software for Integrated Analysis of AVIRIS Data. *Summaries of the 4th Annual JPL Airborne Geoscience Workshop*, JPL Publication 92-14, pp. 23-25.

Kruse, F. A.; Lefkoff, B. & Dietz, J. B., 1993a, Expert System-Based Mineral Mapping in Northern Death Valley, California/Nevada, Using the Airborne Visible/Infrared Imaging Spectrometer (AVIRIS), *Remote Sens. Environ.*, Vol. 44, No. 2, pp. 309-336.

Kruse, FA; Lefkoff, A. B; Boardman, J. W.; Heiedbrecht, K. B.; Shapiro, A. T.; Barloon, P. J. & Goetz, A. F. H., 1993b, The Spectral Image Processing System (SIPS) – Interactive Visualization and Analysis of Imaging Spectrometer Data. *Remote Sens. Environ.* 44:145-163.

Souza, G. S., 1998, Introdução aos Modelos de Regressão Linear e Não-Linear, Brasília: EMBRAPA – SPI/EMBRAPA-SEA, 505 pp.

Steel, R. G. D.; Torrie, J. K., 1980, Principles and procedures of statistics. 2nd ed. New York: MacGraw-Hill.

Vieira, S., 1988, Indrodução à Bioestatística. 5th ed. Rio de Janeiro: Campus, 293 pp.

a) Pimelite-Saponite

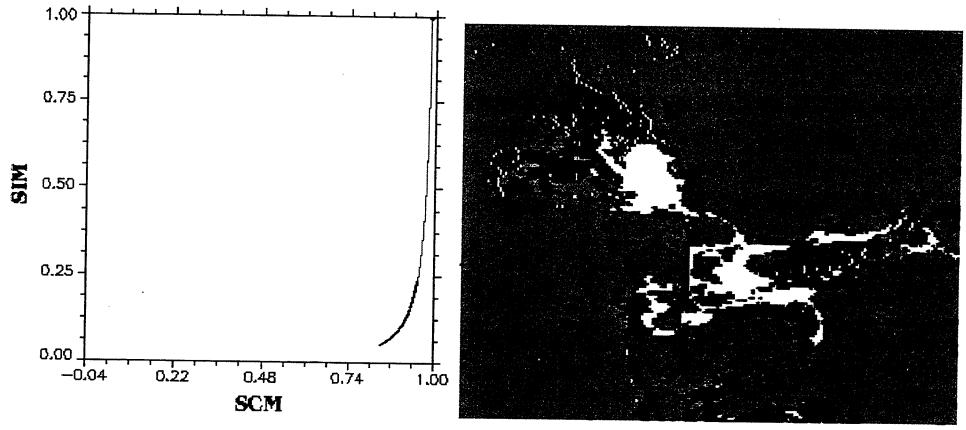

b) Green Vegetation

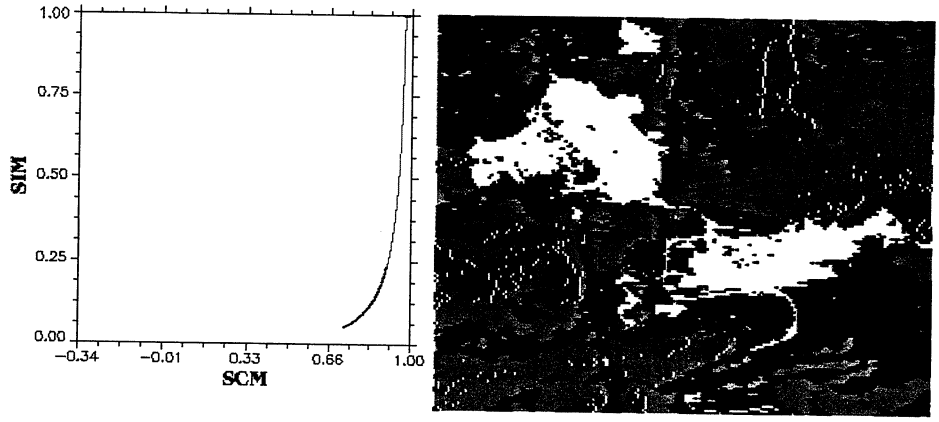

Figure 5 –Scatter plot among SCM x SIM for the features: a) pimelite and b) green vegetation. The curves are segmented in agreement with the degrees of significance: 2.5% (red), 5% (cyan) and 10%(blue). The areas in yellow have a relative value higher than 10%.

Employment of the Multiple Endmember Spectral Mixture Analysis (MESMA) Method in Mineral Analysis

OSMAR ABÍLIO DE CARVALHO JÚNIOR[1]
RENATO FONTES GUIMARÃES[1]

[1]Departamento de Geografia - Universidade de Brasília (UnB)- Campus Universitário Darcy Ribeiro, Asa Norte, 70910-900, Brasília, DF, Brazil
osmana@tba.com.br

Abstract: In the analysis of a spectral mixture, the Spectral Mixture Analysis (SMA) method presents many errors because it is hard to adjust the endmembers in the image with the elements really in each pixel. A method proposed to eliminate that source of mistakes is the Multiple Endmember Spectral Mixture Analysis (MESMA), which defines through the root mean square the best association of spectral mixture that describes each pixel. A routine was developed in IDL, which accomplishes that comparison of the models of mixtures defined for each pixel the most appropriate. This method was tested in the Niquelândia (Brazil) mine and showed excellent results being in agreement with the field.

Keywords: Spectral mixture, MESMA, imaging spectroscopy.

1 Introduction

Spectral Mixture Analysis (SMA) uses the multiple linear regression to define the endmembers abundance in the image (Smith & Adams, 1985). The main source of errors of SMA is that it considers all the pixels as a mixture of an unique initial group of endmembers. This way, the errors are (Sabol *et al.*, 1992):

a) Spectral variability of model components, and

b) Absence of modeled components.

The ideal condition of endmembers is difficult to obtain. Both insufficiency and excess of final members cause errors in SMA. To correct that kind of error it was proposed a new method that establishes for each pixel the best mixture model (Smith *et al.*, 1992; Sabol *et al.*, 1992; Roberts *et al.*, 1992). The evolution of this proposal was the development of the Multiple Endmember Spectral Mixture Analysis (MESMA) (Roberts *et al.*, 1998a). The MESMA differs from SMA because allows the number and the quantity of endmembers vary pixel by pixel in the image.

The MESMA adopts as the best model the one that has smaller root mean square (rms) error when compared to the spectral curve of the pixel (Okin *et al.*, 1998). The MESMA has been applied in the mapping of different areas (Painter *et al.*, 1996, 1998a, 1998b, Gardner, 1997; Roberts *et al.*, 1998a, 1998b, Okin *et al.*, 1998, 1999a). However, Roberts *et al.* (1998a) points to the necessity of additional research.

The computational effort is a problem to apply this method (Okin *et al.*, 1999b). The amount of endmembers increases as much as the possible combinations increasing the computational effort. To avoid the unnecessary use of models, it can be done a previous image segmentation for

the use of spectral classifiers, for instance, the Spectral Correlation Mapper (SCM) method (Carvalho & Meneses, 2000).

2. The employment of the MESMA for mineral analysis

The MESMA was applied to the AVIRIS subscene of Niquelândia, Brazil, that inclues a nickel lateritic mine. The main minerals present in the weathering profile are: pimelite/saponite, goethite, hematite and kaolinite.

To decrease the computational effort was applied the SCM that accomplishes a pre-classification of the mineral. A program in IDL language was developed to identify the best-fit models considering the minor rms error. The program disrespects model with negative values. The program presents as outputs: a) weighting coefficients images of each endmember, b) the rms image and c) an image with the most appropriate model to each pixel. The spectral range delineation of the minerals absorption features (0,43μm to 0,75 μm and 2,09 μm to 2,38 μm) allows a best-fit model. The MESMA algorithm was applied on spectra with and without the continuum removal.

a) Image

The weighting coefficient images related to the minerals from Niquelândia mine corresponds to the field observation (Figure 1). The clearest areas correspond to the major percentage of the mineral. A profile from the base to top mine is well characterized by the image. Pimelite-saponite and goethite constitute the base profile and, upward, is observed an increase of hematite and kaolinite. The RMS image shows the major errors in pimelite-saponite areas, probably due to the worse fit in the visible range (Figure 2).

Only six models were selected (Figure 3). The models ware coherent for most of the area. However some errors were observed, i.e. the model 2 on the mine top is wrong due to pimelite presence. Although, it doesn't compromise the method because of low values of pimelite.

b) Continuum-removed image

The weighting coefficient on the continuum-removed spectra corresponds to the normalized absorption band area. That index is equivalent to the scale coefficient (normalized absorption band depth) intensively used in the mineral abundance analysis. Figure 4 demonstrates the high correlation between those two factors considering the kaolinite feature.

A similarity exists among the images of the minerals with and without continuum removal (Figure 5). However, in that procedure only four mixture models are detected (Figure 6). The best-fit model is the one that contains all of them. That fact is due to two factors deriving from continuum removal: a) detection capacity of minerals in minor quantity, b) greater susceptibility to noise interference (Carvalho *et al.*, 2000). In spite of the best-fit model contain the four minerals, it was observed that the percentage of some of them is minimum. This way, the hematite detected in basal zone of the mine has the lowest values (Figure 7).

RMS image demonstrates that the models with worse fittings were concentrated in the limits of the mine where begins to appear the interference of the vegetation (Figure 7). The rms in the classification with the continuum removal is much smaller than the obtained without the continuum removal what demonstrates a better fit. It is observed that the error from the pimelite-saponite mineral decrease.

a) Pimelite - Saponite

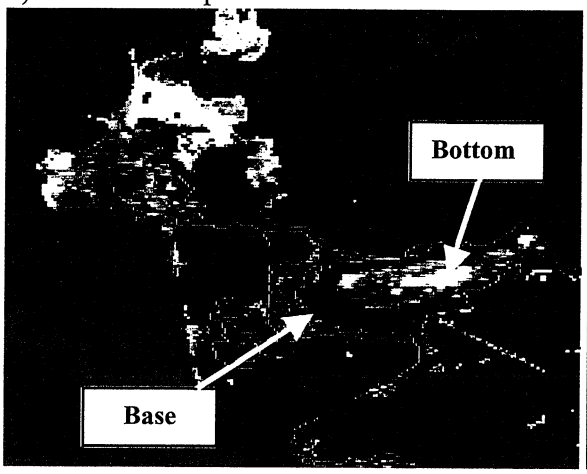

b) Goethite

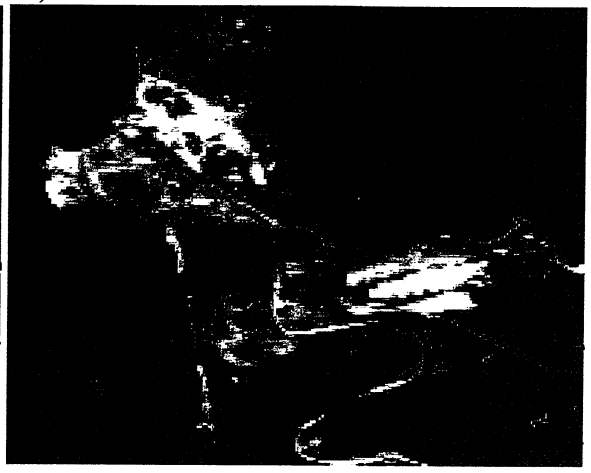

c) Hematite

d) Kaolinite

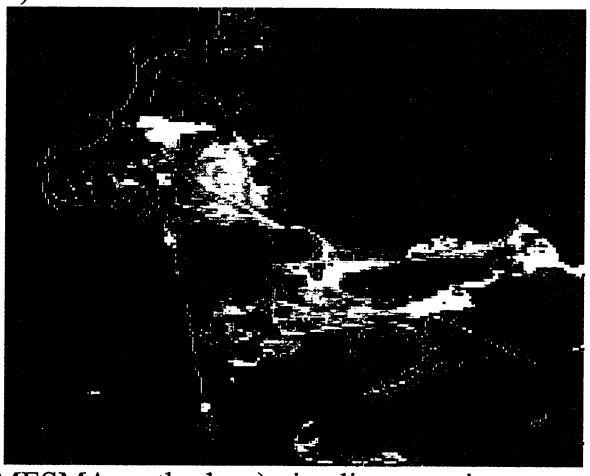

Figure 1 - Mineral images of the MESMA methods: a) pimelite-saponite, b) goethite, c) hematite, and d) kaolinite

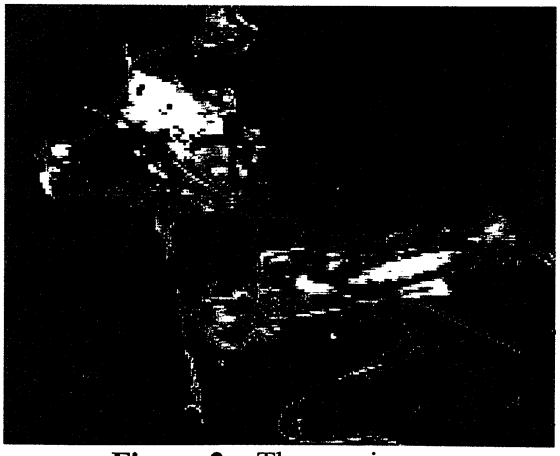

Figure 2 – The rms image

1 - pimelite-saponite and goethite

2 - pimelite-saponite, goethite and hematite

3 - pimelite-saponite, kaolinite, goethite and hematite.

4 - kaolinite, goethite and hematite

5 - pimelite-saponite, kaolinite and goethite

6 - kaolinite and goethite

Figure 3 – Mixture models image

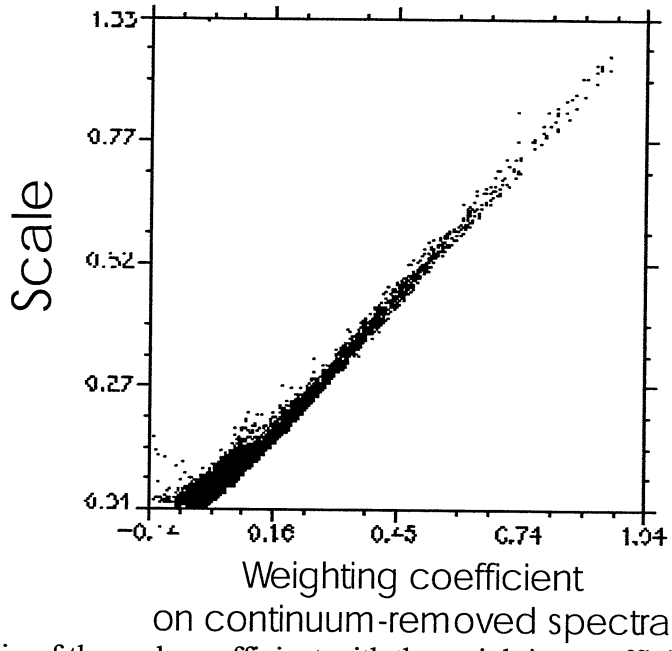

Figure 4 - Relationship of the scale coefficient with the weighting coefficient on continuum-removed spectra (normalized absorption band area).

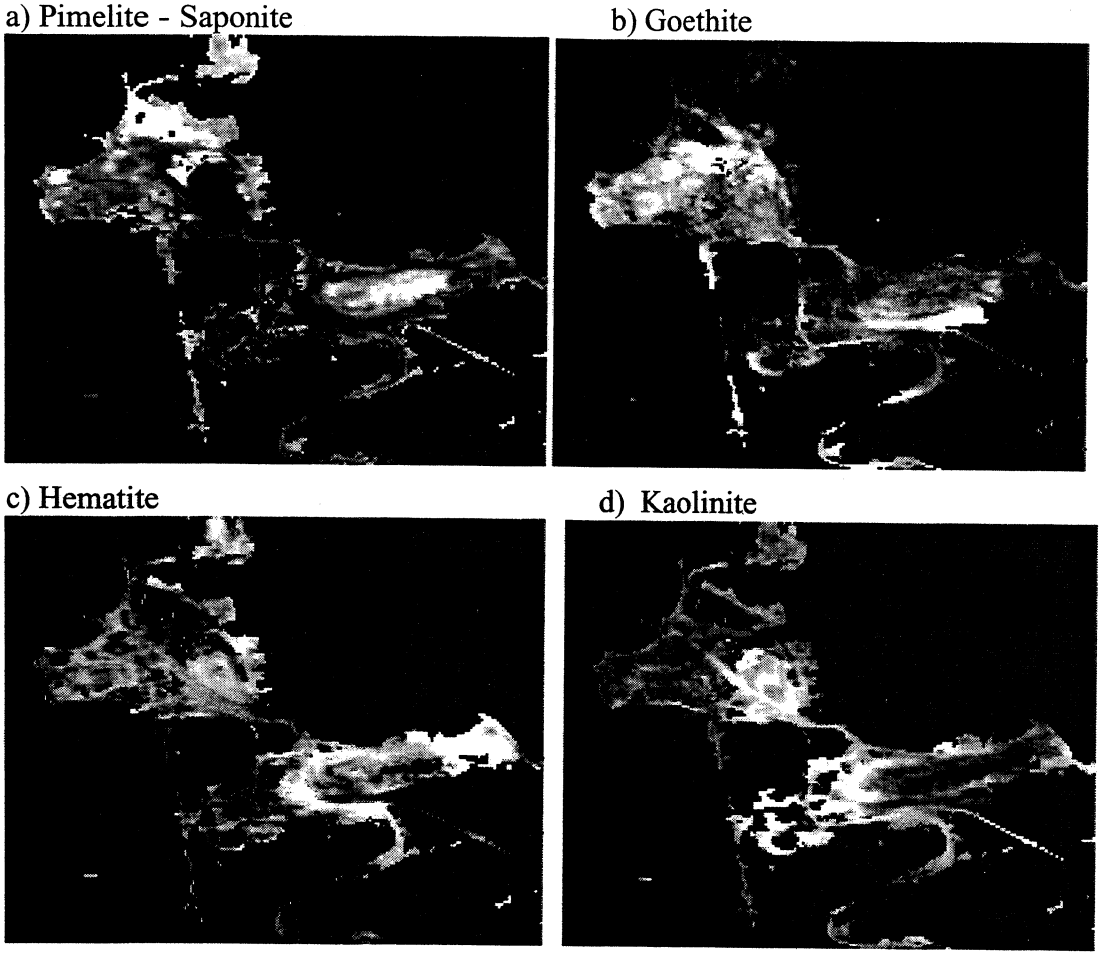

Figure 5 - Mineral images of the MESMA method considering continuum removal spectra: a) pimelite, b) kaolinite, c) goethite, and d) hematite

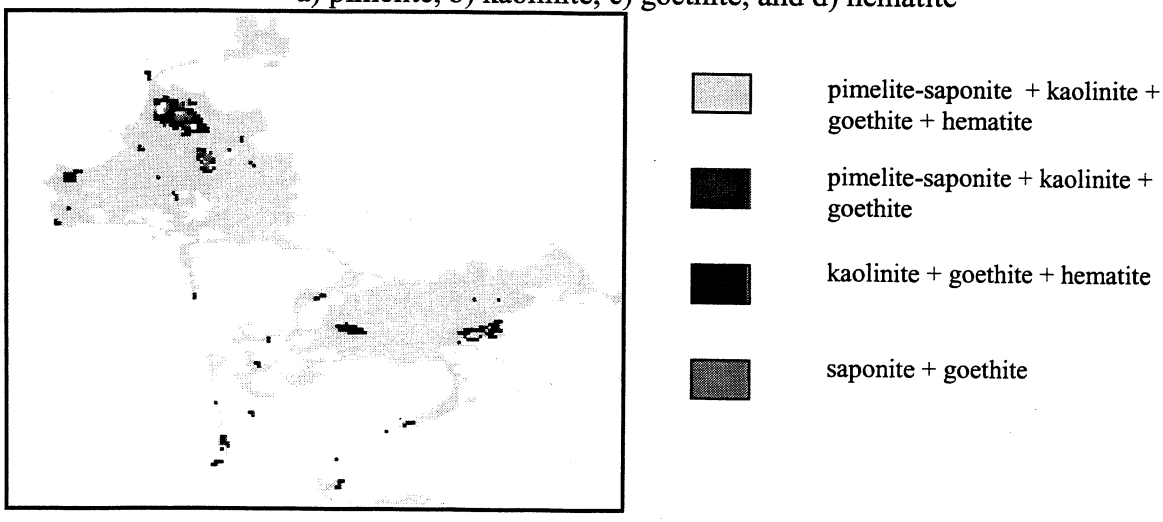

Figure 6 –Disposition of the models selected by the MESMA considering continuum-removed spectra.

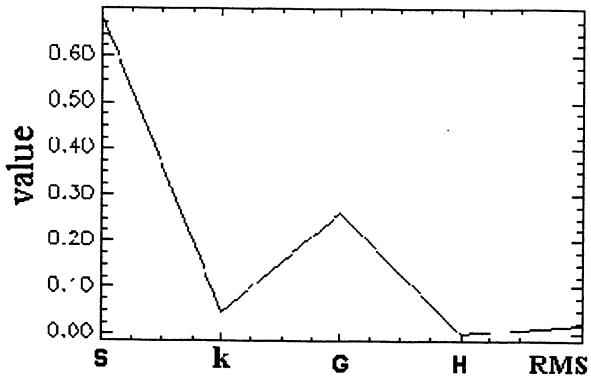

Figure 7 – Abundance distribution for a pixel placed in the zone garnieritic. S = saponite, C=kaolinite, G = goethite, H=hematite and RMS.

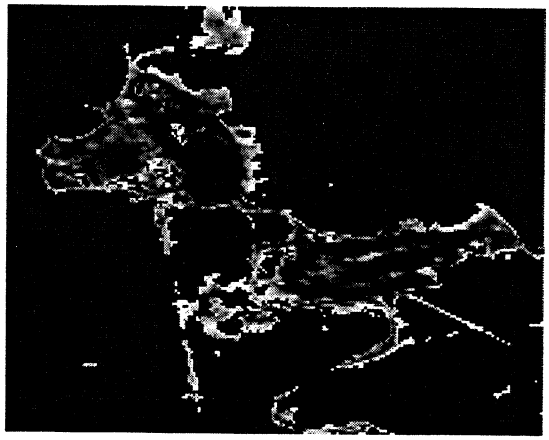

Figure 8 – RMS image of the MESMA from the continuum-removed spectra.

3 - Conclusion

The main conclusions are:

- MESMA method is an improvement of the SMA method because it allows identifying the best model for each pixel.
- The use of the spectral classifier SCM allows to select areas of interest decreasing the computational time. In the use of SCM the mineral occurrence can be overestimated because the MESMA define the best model.
- The delimitation of the spectrum for the absorption features of the existent minerals allows a better model adjustment. That procedure also allows decreasing the computational time.
- The use of the continuum removal spectra allows obtaining weights compatible to the scale coefficient, which is widely used in the mineral analysis.
- In the study area the continuum removal increased the number of models with the four minerals in the analysis due to: a) the larger detection capacity in a smaller abundance of minerals b) great susceptibility to noise interference. However, many minerals present very low concentrations.
- MESMA is a complete method because as allows identifying the areas of occurrence of the minerals as supplies indicators of its abundance.

References

Carvalho Jr., O. A. & Meneses, P. R., 2000, Spectral Correlation Mapper (SCM): An Improving Spectral Angle Mapper (SAM). *The Ninth JPL Airborne Earth Science Workshop.* http: //makalu.jpl.nasa.gov/docs/workshops/toc. htm

Carvalho Jr., O. A., Carvalho, A. P. F., & Meneses, P. R., 2000, An Approach to Hyperspectal Image Classification Based on Linear Regression. *The Ninth JPL Airborne Earth Science Workshop.* http: //makalu.jpl.nasa.gov/docs/workshops/toc. htm

Gardner, M., 1997, Mapping Chaparral with AVIRIS Using Advanced Remote Sensing Techniques, Master of Arts thesis: Department of Geography, University of California, Santa Barbara, CA.

Okin, G. S.; Okin, W. J.; Roberts, D. A.; Murray, B., 1998, Multiple Endmember Spectral Mixure Analysis: Application to an Arid/Semi-arid Landscape. *Summaries of the 7th JPL Airborne Earth Science Workshop*, JPL Publication 97-21 v.1, pp. 291-299.

Okin, G. S.; Siegel, H.; Collier, J.; Miller, G. D., Okin, W. J.; Roberts, D. A., Murray B., Curkendall, D. W.; Painter, T. H., 1999b, The Supercomputing Vizualization Workbench for Analysis and Classification of Imaging Spectrometer Data. *Summaries of the 8th JPL Airborne Earth Science Workshop*, JPL Publication 99-17 v.1, pp. 317-322.

Okin, W. J.; Okin, G. S.; Roberts, D. A; Murray B., 1999a, Multiple Endmember Spectral Mixture Analysis: Endmember Choice in an Arid Shrubland, *Summaries of the 8th JPL Airborne Earth Science Workshop*, JPL Publication 99-17 v.1, pp. 323-331.

Painter, T. H., Roberts, D. A.; Dozier J.; Green, R. O., 1998a, Automated Subpixel Snow Parameter Mapping with AVIRIS Data. *Summaries of the 7th JPL Airborne Earth Science Workshop*, JPL Publication 97-21 v.1, pp. 301-307.

Painter, T. H., Roberts, D. A.; Green, R. O. & Dozier J.; 1998b, The Effect of Grain Size on Spectral Mixture Analysis of Snow-Covered Areas from AVIRIS Data. *Remote Sens. Environ.* 65:320-332.

Painter, T. H., Roberts, D. A.; Green, R. O., Dozier J.; 1996, Subpixel Snow-Covered Area and Sow Grain Size from Mixture Analysis with AVIRIS Data. *Summaries of the 6th Annual JPL Airborne Earth Science Workshop*, JPL Publication 96-4 v.1.

Roberts, D. A., Smith, M. O., Sabol, D. E., Adams, J. B. & Ustin, S., 1992, Mapping the Spectral Variability in Photosynthetic and Non-photosynthetic Vegetation, Soils and Shade Using AVIRIS. *Summaries of the 3rd Annual JPL Airborne Geoscience Workshop*, JPL Publication 92-14, v.1, pp. 38-40.

Roberts, D. A.; Gardner, M.; Church R., Ustin, S. Scheer, G. & Green, R. O., 1998a, Mapping Chaparral in the Santa Monica Mountains using multiple endmember spectral mixture models. *Remote Sens. Environ.* 65:267-279.

Roberts, D. A.; Gardner, M.; Regelbrugge, J.; Pedreros, D.; Ustin, S. L., 1998b, Mapping the Distribution of Wildfire Fuels Using AVIRIS in the Santa Monica Mountains. *Summaries of the 7th JPL Airborne Visible/Infrared Imaging Spectrometer (AVIRIS) Workshop*, JPL Publication 97-21 v.1, pp. 345-352.

Sabol D. E. Jr., Adams J. B. & Smith M. O. 1992, Quantitative Subpixel Spectral of Targets in Multiespectral Images, *J. Geophys. Res.*, 97, 2.659-2.672.

Smith, M. O. & Adams, J. B. 1985, Interpretation of AIS images of Cuprite, Nevada, using constraints of spectral mixtures. In: Proc. Airborne Imaging Spectrometer Data Analysis Workshop, JPL Publication 85-41, pp. 62-68.

Smith, M. O., Adams J. B., Ustin S. L. & Roberts, D. A., 1992, Using endmembers in AVIRIS images to estimate changes in vegetative biomass. *Summaries of the 4th Annual JPL Airborne Geoscience Workshop*, JPL Publication 92-14, v.1, pp. 69-71.

INVESTIGATION OF IMAGING SPECTROSCOPY FOR DISCRIMINATING URBAN LAND COVERS AND SURFACE MATERIALS

Jeremy Chen[1]
George F. Hepner[2]

1. INTRODUCTION

Urban growth has been recognized by many globe change agendas as not only a regional phenomenon but also a continental, global scale phenomenon (Hepner et al., 1998). Many urban areas face environmental degradation, such as loss of open space, natural vegetation, agricultural lands, wetlands, and natural habitat at an increasing rate. The development of urban information systems, which contain baseline information and the urban growth models, is crucial for predicting regional patterns of urbanization. The implementation of the urban systems requires a variety of digital data sources, such as land covers and surface materials, as well as a temporal database.

Although urban analysis is one of the most common applications of remote sensing, the information derived from remotely sensed data is often insufficient for operational use. One of the main problems is that the spectral and spatial resolutions of sensors are too coarse to identify the desired information for urban analysis (Hepner et al., 1998). The urban landscape is extremely heterogeneous with a variety of land cover types and surface materials mixing together within a small area. If many materials are located within one sensor pixel, each material will contribute its unique spectral characteristic to the mixed pixel and make the pixel spectrally impure. In addition, many urban materials, such as soils and impervious surfaces, yield similar spectral signatures. Therefore, broadband data, such as Landsat, and pixel-based analysis, such as maximum likelihood classification, are inadequate for discriminating urban land covers and surface materials (Forster, 1985; Ridd, 1995).

Hyperspectral data such as AVIRIS which covers spectral range from 400 to 2500 nm and has 224 continuous channels with 10-nm bandwidth is capable of discriminating most of the terrestrial materials including urban surface materials (Goetz, 1992; Clark, 1999). Imaging spectroscopy has been successfully applied to geological, aquatic, ecological and atmospheric research (Curran, 1994). Surprisingly, it has been used sparsely for the study of urban areas (Ridd et al., 1992; Hepner et al., 1998). The objective of this study is to investigate the feasibility of using the field spectra as the reference to identify the urban land covers and surface materials in the low-altitude AVIRIS scene.

2. DATA COLLECTION

The urban area of Park City, Utah has a representative mixture of land covers and surface materials for western U.S. cities and other urban areas of the earth undergoing rapid urban growth. Although Park City area is not highly urbanized, it contains the diversity of land covers, surface materials, and vegetation associations. Park City also provides the typical example where urbanization spreads from lowlands to adjacent uplands. Therefore, the methodologies, spectral signatures and techniques investigated in this study should then be transferable to many western U.S. cities and other urban areas around the world with similar environments.

The low-altitude AVIRIS data with spatial resolution 2.9 m was obtained on 19 October 1999. There was no ground calibration site located in the low-altitude AVIRIS flight line and no field spectra were obtained during the low-altitude overflight. High-altitude AVIRIS data of Park City area was obtained from the Park City flight on 5 August 1998. The high-altitude AVIRIS data with spatial resolution 20 m was first corrected and then used to simulate the ground truth for calibrating the low-altitude AVIRIS data. A radiative transfer model (ATREM) provided by the University of Colorado was applied to the radiance data to remove the solar spectral response, atmospheric absorptions and atmospheric scattering. The path radiance scattering overcorrected by the ATREM was

[1] Department of Geography, University of Utah (CheMing.Chen@m.cc.utah.edu)
[2] Department of Geography, University of Utah (george.hepner@geog.utah.edu)

further corrected by the offset parameter provided by the USGS. Other artifacts of the spectra, which are small-scale spikes irresoluble by the ATREM, were also corrected by the multiplier parameter provided by the USGS derived from the ground calibration site (Rockwell, 2000). The spectrum of the bright rooftop of a supermarket in the high-altitude scene was selected and then edited to remove the residual atmospheric absorptions. Relatively, the ATREM calibration and path radiance correction were first applied to the low-altitude AVIRIS data. Then the same pixels, which cover approximately 6 by 6 pixels in the low-altitude scene over the supermarket roof, were sampled and averaged to provide the spectrum. This low-altitude spectrum was divided into the edited high-altitude spectrum to obtain the multiplier used to calibrate the low-altitude data.

Although existing spectral libraries provide many urban surface materials, their diversity is not enough for this study. The ability of the reference spectra to separate plant species as well as manmade materials might vary from one region to another and decrease as the geographic area covered increases. Thus, a regional spectral library of Park City was constructed to better match the AVIRIS data for the spectral analysis. During the summer and autumn of 2000, 80 urban surface materials including 20 roofing materials, 12 paving materials, 23 vegetation and other 25 materials, were measured in 9 field collection sites around the study area using an ASD field spectroradiometer.

3. ANALYSIS AND RESULTS

The selection of the optimal spectral analysis strategy to discriminate the urban surface materials is tied to spectral reflectance characteristics of the targets. Therefore, the spectral signatures of the urban field spectra were examined before determining the analysis strategy. In the broadband data, water and asphalt usually are confused due to low reflectance. However, the field spectra show that water has apparent fluctuation in the visible region due to the underwater materials, which are water plants in this case. Asphalt also has a broad weak absorption near 2.3 μm due to the hydrocarbons. Sand, concrete, and gravel are usually indistinguishable in the broadband data due to bright reflectance. In the field spectra, they could be discriminated by the magnitude in the visible region or by the weak absorption at 2.2 μm caused by the montmorillonite, which is narrower and stronger in the sand and gravel spectra than in the concrete spectrum. In addition, the spectral curve of concrete from red to near infrared region (0.6 –1.3 μm) is a concave, which is different from the convex of sand and gravel in the same spectral region. However, the strong absorption features of their individual chemical compositions might be flattened and broadened. Also, if dirt covered the targets during the measurement, weak absorption features at 0.95, 1.15, and/or 2.2 μm can be found.

Lacking of consistent, strong, and well-defined absorption features, most urban surface materials are not differentiable by matching the absorption bands. The full spectral mapping methods such as Spectral Angle Mapper (Yuhas et al., 1992; Kruse et al., 1993), which compare the spectra using full wavelength range, might be feasible for mapping urban materials with continuum shapes and/or very broad absorptions. Imaging processing was undertaken using ENVI 3.2 software. Low-altitude AVIRIS data with fewer materials mixed in one pixel were analyzed by the pixel-based method, spectral angle mapper (SAM). Field spectra of the most common land cover types and surface materials in Park City were chosen as the reference to compare the spectral similarity with the image spectra. The results of the SAM analysis show that many urban surface materials were discriminated including lawn grass, dry grass, conifer, deciduous, turbid water, clear water, concrete, asphalt, paint, and membrane, etc.

4. SUMMARY

This preliminary study demonstrated that the imaging spectroscopy approach with low-altitude AVIRIS data and field spectra makes it possible to discriminate the urban land covers and surface materials. The low-altitude AVIRIS data with 2.9 m spatial resolution successfully differentiates many surface materials in the urban scene.

REFERENCES

Clark, R. N. (1999). Chapter 1: Spectroscopy of rocks and minerals, and principles of spectroscopy, *Manual of Remote Sensing*, 3rd ed., John Wiley and Sons, Inc., New York.

Curran, P. J. (1994). Imaging spectrometry: Its present and future role in environmental research, *Imaging Spectrometry: A Tool for Environmental Observations*, ECSC, EEC, EAEC, Brussels, Luxembourg, and The Netherlands.

Forster, B. C. (1985). An examination of some problems and solutions in monitoring urban areas from satellite platforms, *International Journal of Remote Sensing*, 6(1): 139-151.

Goetz, A. F. H. (1992). Imaging spectrometry for earth remote sensing, Imaging Spectroscopy: Fundamentals and Prospective Applications, ECSC, EEC, EAEC, Brussels and Luxembourg, Netherlands, pp. 1-19.

Hepner, G. F., Houshmand, B., Kulikov, I., and Bryant, N. (1998). Investigation of the integration of AVIRIS and IFSAR for urban analysis, *Photogrammetric Engineering and Remote Sensing*, 64, pp. 813-820.

Kruse, F. A., Lefkoff, A. B., Boardman, J. W., Heidebrecht, K. B., Shapiro, A. T., Barloon, P. J., and Goetz, A. F. H. (1993). The spectral imaging processing system (SIPS) – Interactive Visualization and Analysis of Imaging Spectrometer Data, *Remote Sensing of Environment*, 44:145-163.

Ridd, M. K., Ritter, N. D., Bryant, N. A. and Green, R. O. (1992). AVIRIS data and neural networks applied to an urban ecosystem, *Third Airborne Geoscience Workshop, National Aeronautics and Space Administration*, Jet Propulsion Laboratory, Pasadena, Ca., 1, pp. 129-131.

Ridd, M.K. (1995). Exploring the VIS Model for Urban Ecosystems Analysis Through Remote Sensing, *Int. J. of Remote Sensing*, 16(12):2165-2186.

Rockwell, B. W. (2000). AVIRIS Data Calibration Information in Park City Region, USGS Spectroscopy Lab, http://speclab.cr.usgs.gov/earth.studies/Utah-1/park_city_calibration.html

Yuhas, R. H., Goetz, A. F. H., Boardman, J. W. (1992). Discrimination among semi-arid landscape endmembers using the spectral angle mapper (SAM) algorithm, *Third Annual JPL Airborne Geoscience Workshop*, Jet Propulsion Laboratory, Pasadena, pp.147-149.

ATMOSPHERIC INFLUENCE ON NDVI DETERMINATIONS FROM VARIABLE RED AND NEAR INFRARED AVIRIS BAND POSITIONING

Romero da Costa Moreira[1] and Lênio Soares Galvão[2]
[1]Instituto de Estudos Avançados - IEAv
Caixa Postal 6044, 12231-970, São José dos Campos, SP, Brazil.
[2]Instituto Nacional de Pesquisas Espaciais - INPE
Caixa Postal 515, 12231-970, São José dos Campos, SP, Brazil.

1. INTRODUCTION

Spectral vegetation indices are combinations of spectral values obtained from two or more remote sensor bands, generally the Red (R) and the Near InfraRed (NIR) spectral regions. The determination of these indices is important not only for the monitoring of the vegetation at a global scale, but also to allow the prediction of some vegetation parameters. A vegetation index frequently used in global vegetation studies is the Normalized Difference Vegetation Index - NDVI (Rouse et al., 1973) that relates spectral data according to the equation $NDVI=(\rho_{NIR}-\rho_R) / (\rho_{NIR}+\rho_R)$, where ρ_{NIR} is the reflectance value in the NIR band and ρ_R is the reflectance value in the R band.

Several works have shown the correlation of these indices, in particular the NDVI, with vegetation parameters such as biomass (Holben et al., 1980), Leaf Area Index - LAI (Asrar et al., 1985), and Absorbed Photosynthetically Active Radiation by vegetation canopy - APAR (Epiphanio and Huete, 1994). For instance, Elmore et al. (2000) obtained a coefficient of determination (r^2) of 0.83 from field measures of Percent Live Vegetation Cover and NDVI values obtained from a temporal image series (from 1984 to 1997) of the Thematic Mapper (TM) sensor. However, besides the vegetation itself, several factors influence correlations between vegetation indices and vegetation parameters. These factors include the soil (Huete, 1989) and the atmosphere (Carlson and Ripley, 1997) influences, the topographic effects (Slater, 1980), the illumination and viewing geometry (Epiphanio and Huete, 1995), and sensor characteristics such as band positioning and bandwidth (Galvão et al., 1999).

In relation to the atmosphere influence, Teillet et al. (1997) concluded that atmospheric effects could cause variations in vegetation index values depending on band positioning and bandwidth. In fact, the atmosphere modifies the radiation reflected by the surface in two ways. First, it introduces an additive component that increases the spectral values obtained by remote sensors. This effect is known as scattering, which happens more strongly in shorter wavelengths (ultraviolet and visible), being reduced progressively towards longer wavelengths (near infrared). Second, some atmospheric components such as oxygen and water vapor absorb selectively the radiation. Because of the spectral dependence of these effects, the spectral characteristics of the sensors are important to enhance or minimize the atmospheric influence. Thus, NDVI values obtained for the same area from different sensors having distinct spectral band positioning and bandwidth can show quite different values, depending on the target and on the relative positioning of the R-NIR bands face to the spectral location of the main atmospheric features.

The objective of this work is to discuss the basic problem of NDVI variations considering the atmospheric effects and the band positioning and bandwidth influences. For this purpose, the position and width of narrow and broad R and NIR bands, including those from some multispectral sensors, were simulated from AVIRIS (Airborne Visible/InfraRed Image Spectrometer) data collected in central Brazil, and NDVI values were calculated and compared from apparent and surface reflectance images.

2. METHODOLOGY

The AVIRIS radiance image was collected on August 20, 1995, in central Brazil. The study area is 90 km from Campo Grande city (State of Mato Grosso do Sul) and is centered in the coordinates 19°53'S/53°45'W. The data were acquired in 224 contiguous bands of less than 10 nm of width, in the 400-2500 nm spectral region, from 20 km of altitude and with a spatial resolution of 20 m.

The radiance data were converted into surface reflectance images (ρs) by using a MODTRAN-based method that minimized the effects of atmospheric absorption and scattering due to several constituents (e.g., water vapor, carbon dioxide, oxygen) (Green et al., 1991). For the conversion of radiance data into apparent reflectance images (ρa), that is, not corrected for the atmospheric influence, the following simple equation was used (Latorre et al., 1998):

$$\rho_\lambda = \pi L_\lambda / E_\lambda \cos \theta_s$$

where ρ_λ is the spectral reflectance, L_λ is the spectral radiance, E_λ is the spectral irradiance on the top of the atmosphere (complementary information accompanying the radiance-image) and θ_s is the solar zenith angle obtained to the central point of the scene, considering the date and time of image acquisition. In the present investigation, θ_s was of 31°.

By using these two datasets (ρs and ρa), narrow and broad R (10, 20, and 50 nm of width) and NIR (10, 100 and 200 nm of width) were simulated from endmember spectra of green vegetation (GV) and soil (S) selected from the ρs images through the sequential use of the Minimum Noise Fraction (MNF) and the Pixel Purity Index (PPI) techniques (Green et al., 1988; Boardman and Kruse, 1994; Boardman et al., 1995). Furthermore, the nominal intervals of the R and NIR bands of some multispectral sensors listed in Table 1 were also simulated.

NDVI values were then calculated from both datasets (ρs and ρa) and from the endmember spectra (GV and S), as a function of a variable band positioning and bandwidth, to assess the predominant influence of atmospheric scattering on the R interval and of atmospheric absorption on the NIR interval, and their effects on the vegetation index calculation.

3. RESULTS AND DISCUSSION

Figure 1 shows AVIRIS-derived apparent and surface reflectance spectra of green vegetation (riparian forest) and the positioning of R and NIR bands of some orbital multispectral sensors. The nominal intervals, center and width of the R-NIR bands usually used in the determination of the NDVI are listed in Table 1. As indicated in this figure and in this table, the sensors acquire data with bands placed at very different positioning and with variable width. Furthermore, the NIR bands of instruments such as AVHRR and MSS encompass spectral intervals of strong atmospheric absorption by water vapor (e.g., 940 nm absorption band). In the visible interval, the main effect of the atmosphere is related to scattering by gases and aerosols, whereas in the NIR interval oxygen and especially water vapor produce well-defined absorption bands, as visualized in the apparent reflectance spectrum.

Apparent and surface reflectance spectra of the selected endmembers are shown in Figure 2 in the full range of 450-2500 nm. The GV spectrum is from the riparian forest, the green vegetation that occurs along the drainage streams in the study area. Its surface reflectance spectrum presents the characteristic chlorophyll absorption bands in the blue and red intervals, the reflectance peak in the green, the absorption features due to leaf water in 960 and 1200 nm, and the lignin/cellulose features around 2100 and 2300 nm. The S spectrum is from *Latossolo Vermelho-Escuro* (oxisol). Its surface reflectance spectrum displays a broad absorption band at 900 nm,

due to hematite, and a well-defined narrow feature at 2200 nm due to kaolinite. These GV and S spectral characteristics are affected in the visible interval by atmospheric scattering and in the NIR interval by atmospheric absorption. The strongest water vapor absorption bands are located at 1400 and 1900 nm, spectral intervals not used in conventional remote sensing investigations.

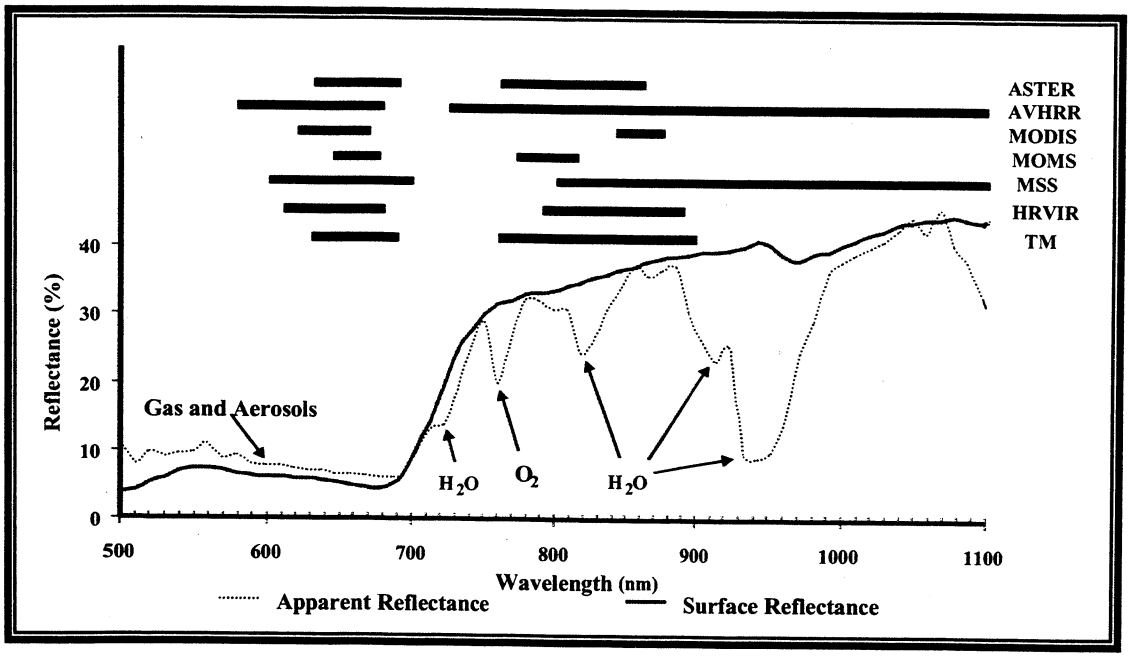

Figure 1 – AVIRIS-derived surface (continuous line) and apparent reflectance (dashed line) curves of green vegetation (riparian forest). The main atmosphere constituents responsible by well-defined absorption bands are indicated. The horizontal bars represent the nominal intervals of R and NIR bands of the sensors listed on the right side of the illustration.

Table 1. Spectral nominal intervals of the R and NIR bands of some orbital multispectral sensors

Sensor	*R Band (nm)*			*NIR Band (nm)*		
	Interval	*Width*	*Center*	*Interval*	*Width*	*Center*
ASTER/Terra	630-690	60	660	760-860	100	810
AVHRR/NOAA 14	580-680	100	630	725-1100	375	912
MODIS/Terra	620-670	50	645	841-876	35	858
MOMS-2	645-677	32	661	772-815	43	793
MSS/Landsat 5	600-700	100	650	800-1100	300	950
HRVIR/SPOT 4	610-680	70	645	790-890	100	840
TM/Landsat 5	630-690	60	660	760-900	140	830

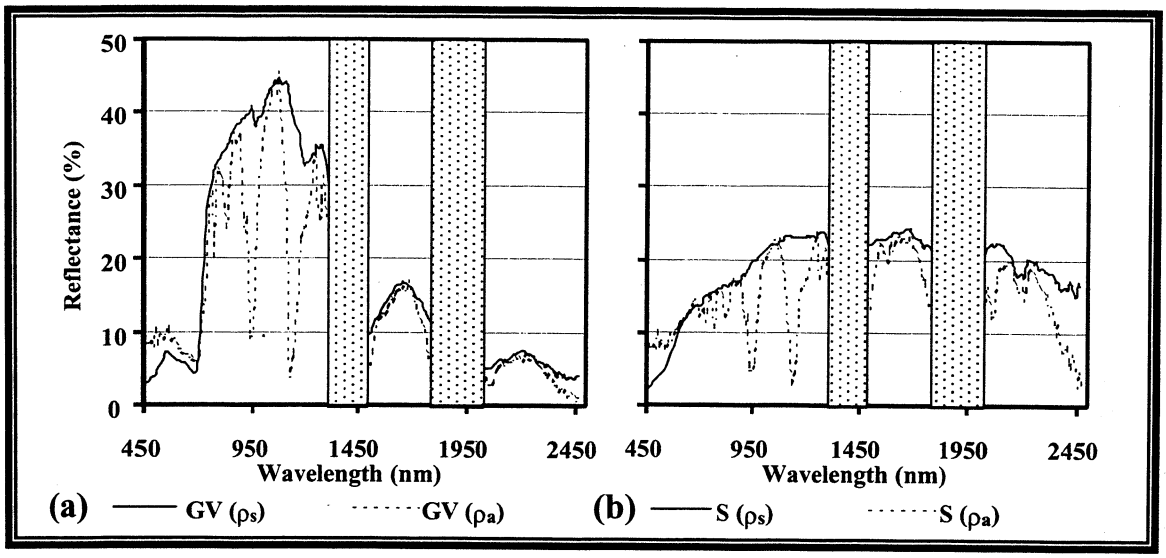

Figure 2 – AVIRIS-derived apparent (ρa) and surface (ρs) reflectance spectra of selected endmembers of green vegetation (GV) (a) and soil (S) (b). The vertical shaded columns around 1400 and 1900 nm indicate the two major intervals of atmospheric absorption.

To illustrate the impact of atmospheric scattering and absorption on the NDVI determinations from the use of narrow and broad R-NIR bands, Figure 3a shows the results obtained by using a fixed narrow NIR band at 923 nm and a variable placement for narrow and broad R bands. On the other hand, Figure 3b displays the NDVI variations for a fixed narrow R band at 677 nm and different positioning for narrow and broad NIR bands. In both figures, the results are shown only for calculations derived from the ρa and ρs spectra of GV. The results derived from ρa and ρs spectra of soil have been omitted in Figure 3 for a better graphic representation.

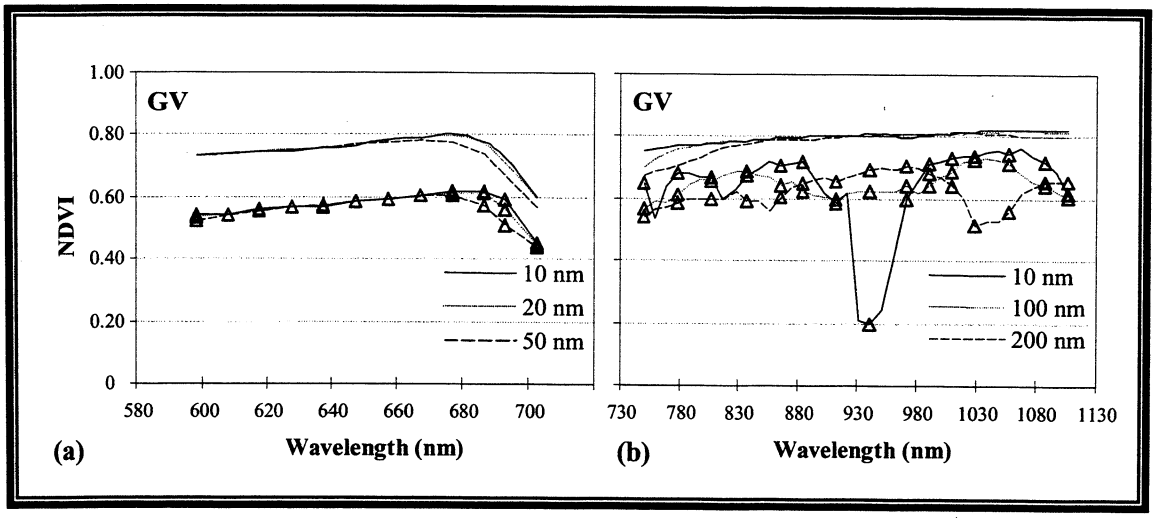

Figure 3 – NDVI variations, as a function of band positioning and bandwidth, derived from apparent (curves with triangles) and surface (curves without symbols) reflectance spectra of green vegetation (GV). In (a), the results were obtained with the NIR band fixed at 923 nm. In (b), the R band was fixed at 677 nm. The target is riparian forest.

As shown in Figure 3a, the NDVI values increase towards longer red wavelengths and reach a maximum around the center of the chlorophyll absorption band (677 nm) in both datasets (ρa and ρs). The effect of scattering, represented by the NDVI curve derived from the ρa spectrum of GV, is to decrease the vegetation index values because of the additive contribution of the atmosphere in the red interval. The width of the R bands is not an important factor for NDVI determination from ρa and ρs spectra if the R bands are not inserted into the red edge domain (690-750 nm range), which causes a decrease in the NDVI values. The contrary occurs in the NIR interval. The presence of well-defined absorption bands due to oxygen and especially water vapor in the ρa spectrum has a strong impact on the NDVI values derived from narrow NIR bands, especially those centered around the 940 nm water vapor absorption band.

Figure 4 shows the magnitude of the difference between the NDVI curves derived from the ρs and ρa spectra of GV, as a function of the positioning of R and NIR narrow AVIRIS bands. The results are also presented for the soil spectra. As illustrated in Figure 4a, the difference between the NDVI curves derived from corrected and non-corrected R bands for the atmospheric effects is almost constant and of the order of 0.2 for GV and slightly higher for S, considering a NIR band placement at 923 nm. The difference for the NIR bands increases substantially around the main intervals of atmospheric absorption and reaches values higher than 0.60 around the 940 nm water vapor absorption band for both targets. In Figure 4b, the main atmospheric windows, which comprises spectral intervals with small NDVI difference curves, are positioned in the 770-810 nm, 850-880 nm, and 1000-1070 nm ranges. The first two intervals are preferable to monitor vegetation from NDVI calculations because the shift of NIR bands towards shorter wavelengths tends to increase the NDVI contrast between GV and S and to produce also better fitted soil lines (Galvão and Vitorello, 1998; Galvão et al., 1999, 2000; Moreira, 2000).

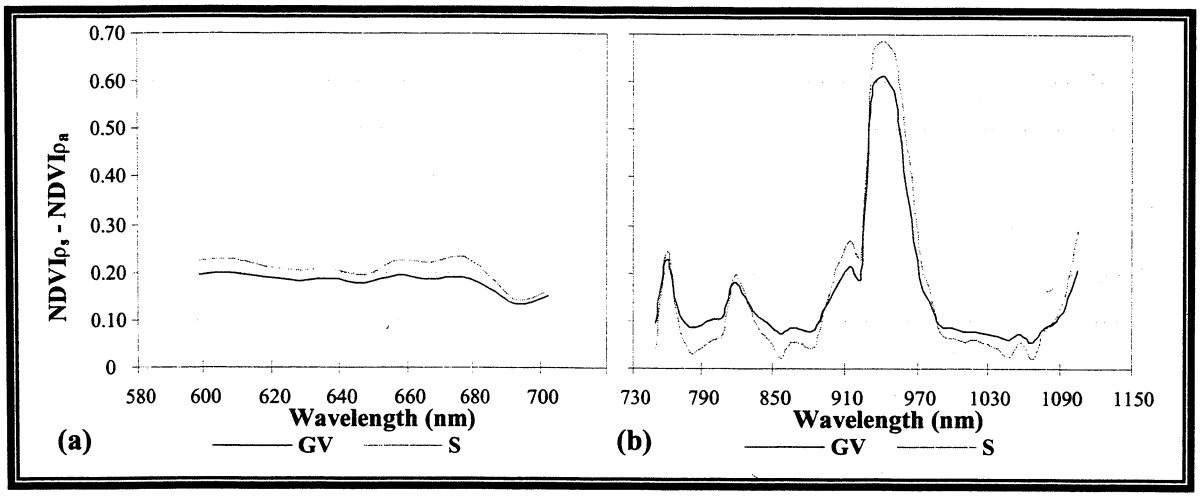

Figure 4 – NDVI difference curves derived from surface (ρs) and apparent (ρa) reflectance spectra of green vegetation (GV) and soil (S), as a function of the positioning of narrow R-NIR bands (10 nm of width). The results for GV are derived from Figure 3. In (a), the results were obtained with the NIR band fixed at 923 nm. In (b), the R band was fixed at 677 nm.

The sensors listed in Table 1 also produce NDVI differences introduced by atmospheric effects when compared to band positioning. As illustrated in Figure 5, the best results were obtained for MODIS with NDVI differences of 0.04 for S and of 0.07 for GV especially because of its NIR band placement in a very convenient atmospheric window. The worst results were obtained for AVHRR and MSS with NDVI differences higher than 0.10 for GV and S especially because their NIR bands encompass the strong 820 and 940 nm absorption bands due to water vapor.

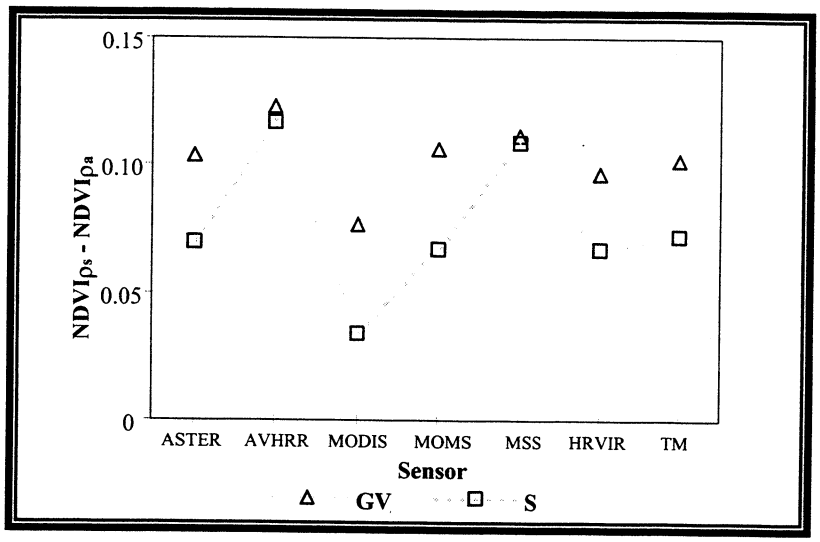

Figure 5 – NDVI difference curves derived from surface (ρs) and apparent (ρa) reflectance spectra of green vegetation (GV) and soil (S), as a function of the positioning of the R and NIR bands of the sensors listed in Table 1.

4. CONCLUSIONS

The results of this study indicate that the width of the R bands is not an important factor for NDVI determinations from ρa and ρs spectra if they are not inserted into the red edge domain (690-750 nm range). For the NIR interval, bandwidth is a very important factor because of the presence of well-defined absorption bands due to oxygen and especially water vapor in the ρa spectrum that have a strong impact on the NDVI values derived from narrow NIR bands. When the nominal intervals of the R and NIR bands of some orbital multispectral sensors were simulated, the best results were obtained for MODIS, which presented smaller NDVI difference values, derived from atmospherically corrected and non-corrected data, of 0.07 (GV) and 0.04 (S). On the other hand, the worst results were obtained for MSS/Landsat 5 and AVHRR/NOAA 14, which showed NDVI differences higher than 0.10 because their NIR bands encompass absorption bands due to atmosphere constituents, especially the 940 nm water vapor absorption feature. The present results emphasize the fact that NDVI values derived from different sensors are not directly comparable, and the importance of carefully selecting spectral intervals for band placement if one considers to use narrow bands in the design of a sensor.

REFERENCES

Asrar, G., Kanemasu, E.T. and M. Yoshida, 1985, Estimates of leaf area index from spectral reflectance of wheat under different cultural practices and solar angle. *Remote Sensing of Environment*, **17**, 1-11.

Boardman, J. W. and F.A. Kruse, 1994, Automated spectral analysis: a geological example using AVIRIS data, north Grapevine Mountains, Nevada. In *Proceedings of the Tenth Thematic Conference on Geologic Remote Sensing,* ERIM, Environmental Research Institute of Michigan, Ann Arbor, MI, p. I-407 - I-418.

Boardman, J. W.; Kruse, F.A. and R.O. Green, 1995, Mapping target signatures via partial unmixing of AVIRIS data. In *Summaries of the Fifth JPL Airborne Earth Science Workshop,* JPL Publication 95-1, v. 1, p. 23-26.

Carlson, T.N. and D.A. Ripley, 1997, On the relation between NDVI, fractional vegetation cover, and leaf area index. *Remote Sensing of Environment*, **62**, 241-252.

Elmore, A.J., Mustard, J.F., Manning, S.J. and D.B. Lobell, 2000, Quantifying vegetation change in semiarid environments: precision and accuracy of spectral mixture analysis and normalized difference vegetation index. *Remote Sensing of Environment*, **73**, 87-102.

Epiphanio, J.C.N and A.R. Huete, 1994, Influence of sun-view geometries on the relationships among vegetation indices, LAI, and absorbed PAR. In *Proceedings of International Geoscience and Remote Sensing Symposium '94* (IGARSS'94), Pasadena, California. Piscataway: IEEE, Vol. 3, pp.1455-1457.

Epiphanio, J.C.N. and A.R. Huete, 1995, Dependence of NDVI and SAVI on Sun/sensor geometry and its effect on *f*APAR relationships in alfalfa. *Remote Sensing of Environment*, **51**, 351-360.

Galvão, L.S. and I. Vitorello, 1998, Variability of laboratory measured soil lines of soils from southeastern Brazil. *Remote Sensing of Environment,* **63,** 166-181.

Galvão, L.S., Vitorello, I. and R.A. Filho, 1999, Effects of band positioning and bandwidth on NDVI measurements of tropical savannas. *Remote Sensing of Environment*, **67**, 181-193.

Galvão, L.S., Vitorello, I., and M.A. Pizarro, 2000, An adequate band positioning to enhance NDVI contrasts among green vegetation, senescent biomass, and tropical soils. *International Journal of Remote Sensing,* **21,** 1953-1960.

Green, A. A., Berman, M., Switzer, P, and Craig, M. D., 1988, A transformation for ordering multispectral data in terms of image quality with implications for noise removal. *IEEE Transactions on Geoscience and Remote Sensing*, **26**, 65-74.

Green, R.O., 1991, Retrieval of reflectance from AVIRIS measured radiance using a radiative tranfer code. In *Proceedings of the Third Airborne Visible/Infrared Imaging Spectrometer (AVIRIS) Workshop*, Pasadena, California (Pasadena: JPL publication 91-28), pp. 200-210.

Holben, B.N.; Tucker, C.J. and C.J. Fan, 1980, Spectral assessment of soybean leaf area and leaf biomass. *Photogrammetric Engineering and Remote Sensing*, **46**, 651-656.

Huete, A.R., 1989, Soil influences in remotely sensed vegetation-canopy spectra. In *Theory and applications of optical remote sensing* edited by G. Asrar (New York: J. Wiley & Sons), pp. 107-141.

Latorre, M.L., Shimabukuro, Y.E., and L.A. Vieira Dias, 1998, Methods of atmospheric correction applied to AVIRIS data collected in tropical regions. In *Proceedings of the Ninth Brazilian Remote Sensing Symposium,* Santos - SP, September 11-18, CD-ROM, 10 pp. (in Portuguese).

Moreira, R. C., 2000, Influence of band positioning and bandwidth of remote sensors and of atmospheric effects on the vegetation index determination. Master thesis in Remote Sensing. Instituto Nacional de Pesquisas Espaciais (INPE) (INPE-7528-TDI/735) (in Portuguese).

Rouse, J.W., Haas, R.H., Schell, J.A. and D.W. Deering, 1973, Monitoring vegetation systems in the Great Plains with ERTS. In *Proceedings of Third Earth Resources Technology Satellite Symposium*, Washington, D. C.: NASA. Goddart Space Flight Center, Vol. 1, pp. 309-317. (NASA SP-351).

Slater, P.N., 1980, *Remote sensing: optics and optical systems*. Reading: Addison Wesley,. 575 pp.

Teillet, P.M., Staenz, K.and D.J. Williams, 1997, Effects of spectral, spatial, and radiometric characteristics on sensing vegetation indices of forested regions. *Remote Sensing of Environment*, **61**, 139-149.

SPECTRAL CLASSIFICATION OF SIMILAR MATERIALS USING THE TETRACORDER ALGORITHM: THE CALCITE-EPIDOTE-CHLORITE PROBLEM

J. Brad Dalton,[1] Dana Bove,[2] Carol Mladinich,[2] Roger Clark,[2] Barnaby Rockwell,[2] Gregg Swayze,[2] Trude King,[2] and Stanley Church[2]

1. INTRODUCTION

Recent work on automated spectral classification algorithms has sought to distinguish ever-more similar materials. From modest beginnings separating shade, soil, rock and vegetation (Soha *et al.*, 1976) to ambitious attempts to discriminate mineral types (Kruse *et al.*, 1993; Boardman, 1993; Clark and Swayze, 1995) and specific plant species (Kokaly *et al.*, 1997), the trend seems to be toward using increasingly subtle spectral differences to perform the classification. Rule-based expert systems exploiting the underlying physics of spectroscopy such as the USGS Tetracorder system (Clark *et al.*, 2001) are now taking advantage of the high spectral resolution and dimensionality of current imaging spectrometer designs (*cf.* Eastwood *et al.*, 2000) to discriminate spectrally similar materials. The current paper details recent efforts to discriminate three minerals having absorptions centered at the same wavelength, with encouraging results.

2. THE CALCITE-EPIDOTE-CHLORITE PROBLEM

2.1 Relevance

One of the applications of remote hyperspectral analysis is the examination of mineralogy in mining districts. The current study was undertaken as part of the Animas River Watershed study (Nimick and von Guerard, 1998) of the U.S. Geological Survey Abandoned Mine Lands (AML) Project. A key goal of this project is the determination of levels of acidic mine drainage in the watershed, which includes several hydrothermal alteration zones (Bove *et al.*, 2000) associated with the Silverton Caldera in the San Juan Mountains of southwestern Colorado. Weathering of pyrite (FeS_2) results in an assemblage of minerals, which includes goethite, hematite and jarosite (Bigham *et al.*, 1996), as well as production of sulfuric acid (H_2SO_4) which then contaminates runoff, usually acquiring a load of dissolved metals along the way (Mast *et al.*, 2000) and eventually enters the river. In the Silverton Caldera, large areas of naturally-occurring exposed hydrothermal alteration zones (*ibid.*) contribute significant quantities of acid to the watershed, complicating efforts to ascertain the level of anthropogenic impact.

The Silverton Caldera overlies preexisting sedimentary rock containing large quantities of calcite as limestone (Lipman *et al.*, 1973). Where the acidic waters combine with waters that have passed through these limestone beds, the buffering action of the carbonates reduces the acidity of the water. This has strong effects on the water quality and concentrations of dissolved metals (Church *et al.*, 2000). Calcite also occurs within the igneous rock, at much lower concentrations, as a result of propylitic alteration. In order to accurately assess and model effects of pyrite weathering from natural and artificial sources, land managers and aqueous geochemists need to determine the occurrence and distribution of calcite in the watershed.

Previous attempts to classify and map calcite through hyperspectral imagery (Dalton *et al.*, 1998, 2000) have been held up by the spectral similarity of calcite to both epidote and chlorite, which also result from propylitic alteration. In such alteration zones, these three minerals are typically found together as a fine-grained mixture that appears homogeneous at greater than centimeter scales, but may be readily distinguished by field geologists upon examination with a hand-lens or microscope. Chlorite may have weak buffering capabilities (DesBorough *et al.*, 1998), though these are an order of magnitude weaker than those of calcite. A determination of stream buffering

[1] NASA-Ames Research Center, Mountain View, California 94035 (dalton@mail.arc.nasa.gov)
[2] U.S. Geological Survey, Denver, Colorado 80225

capacity in the watershed therefore requires knowledge of the distribution and abundance of all three minerals. Thus, solving the Calcite-Epidote-Chlorite problem became a primary interest for the authors of this study.

2.2 Spectral Comparisons

Near-infrared spectra of calcite, epidote and chlorite in the 2.0- to 2.5-μm (micron) range are shown in Figure 1. The diagnostic infrared absorption band of calcite ($CaCO_3$) is centered at 2.34 μm, as are those of epidote ($Ca_2(Fe^{3+},Al)_3(SiO_4)_3(OH)$) and chlorite ($(Mg,Fe^{2+})_5Al(Si_3Al)O_{10}(OH)_8$). Although chlorite is actually a broad term referring to a large family of minerals (Klein and Hurlbut, 1993), in this study we refer to a specific chlorite, ripidolite, which is a ferroan clinochlore (Fleischer and Mandarino, 1995) and is the primary type found in the study area. The 2.3 μm chlorite band complex may vary its shape, intensity and position in response to changes in composition (Hunt and Salisbury, 1970; King and Clark, 1989), and so care is recommended in applying the results of this study to other locations. The secondary band at 2.26 μm in the chlorite spectrum, for example, may change in strength relative to the primary band at 2.34 μm. However, for pure samples of the chlorite used in this study, the band positions and relative strengths remained constant with respect to grain size, as they did for the epidote. There is no corresponding band in the calcite spectrum, although a small shoulder is seen in the primary absorption band at 2.3 μm. Calcite does feature a weak absorption at 2.15 μm, which is not seen in the other two minerals. Finally, an absorption occurs at 2.0 μm, which is strongest in the calcite spectrum and weakest in epidote.

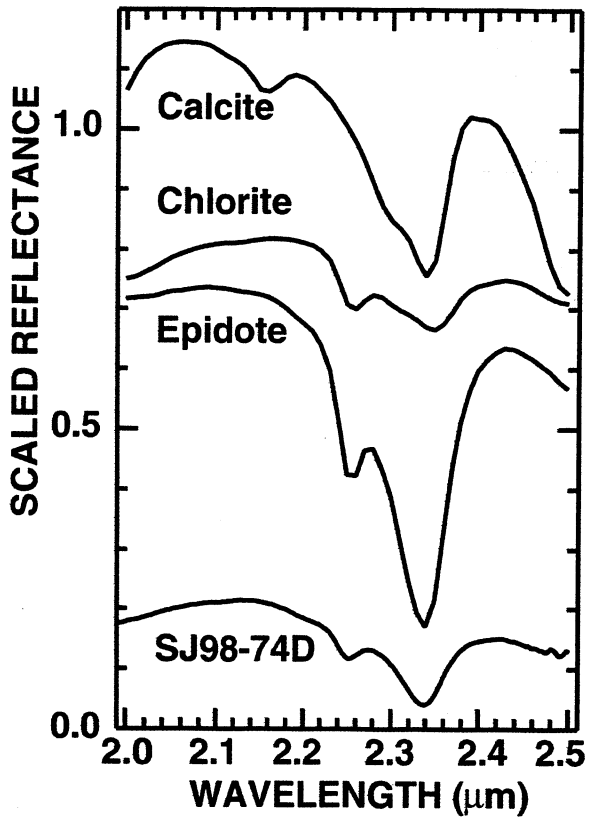

Figure 1. Infrared spectra of calcite, chlorite and epidote, along with spectrum of field sample SJ98-74D, a rock containing all three in a fine-grained matrix. The intimate mixture produces a spectrum exhibiting features of all three components.

This last absorption is not useful for terrestrial remote sensing studies because it conflicts with atmospheric water vapor. The 2.1- μm calcite absorption, in turn, cannot be used because it lies very close to a clay mineral feature centered at 2.2 μm. Since all of the remotely-sensed spectra in this study (and most AVIRIS studies) are of mixtures of a variety of materials, the discrimination method must be highly robust. While the 2.26-μm absorption seen in the chlorite and epidote spectra is sufficient to separate them from calcite when comparing pure samples in the laboratory, a further complication arises in the field. This is illustrated by the fourth spectrum in Figure 1, that of a rock sample acquired during preliminary field-checking of the classified AVIRIS data. Laboratory analysis shows sample SJ98-74D to be a fine-grained mixture of 44.58% epidote, 10.98% chlorite, and 6.73% calcite in a propylitic matrix containing other, infrared-inactive minerals. Normalized for weight, the spectral contributions of the three spectrally active minerals come to approximately 70% epidote, 20% chlorite, and 10% calcite. Since it is a fine-grained mixture, its spectrum is not a simple linear combination of its pure components. The infrared spectrum of this ground-truth sample has the same band center as calcite, despite its low calcite content. The overall band shape, width and position correlate strongly with all three of the pure endmember spectra. Given current signal-to-noise ratios, combined with other potential sources of error, a classification algorithm based only on the pure endmember information might easily misidentify the sample. Divulging the relative abundance of calcite, and thus acid-buffering potential, throughout the AVIRIS scenes is not therefore a matter of comparing single-channel intensity levels, ratios of band depths, nor even continuum-removed, area-weighted correlation coefficients of pure endmembers. Two main approaches may lend themselves to the solution of this problem: the first is the mathematically elegant, computationally expensive

quantitative unmixing approach based on optical constants (Hapke, 1993; Mustard and Sunshine, 1999); and the second is the less elegant empirical approach of comparing spectra of an assortment of fine-grained laboratory mixtures. Given the present limitations of modern microprocessors, this study utilizes the latter approach.

3. DETAILS OF EMPIRICAL APPROACH

3.1 Tetracorder Algorithm

The USGS Tetracorder Expert System (Clark *et al.* 2001, Clark and Swayze 1995, Clark *et al.* 1990) has been described fully elsewhere; such a description is beyond the scope of this paper and the reader is advised to consult the references given. The heart of the method is the comparison of continuum-removed absorption bands of spectra kept in a reference library, to those of an observed spectrum. The Tetracorder Algorithm can be trained to compare sets of diagnostic bands for a given material, and even exclude materials from consideration based on the presence or absence of certain bands . Each band under consideration is normalized against its continuum and then scaled by a multiplicative constant so that its depth matches that of the corresponding reference band. Least-squares correlation coefficients are calculated and weighted according to the area under the curve and optional user-defined weights. Sets of bands for specific materials are compared based on a prescribed set of rules. An identification is issued based on application of these rules to the calculated values. For imaging spectroscopy applications, an image is generated for each material under consideration, with the intensity of each pixel corresponding to the product of correlation coefficient and absorption band depth; this roughly scales with abundance (Clark *et al.*, 1990). The images of relevant materials are then assembled into a classified image.

3.2 Laboratory and field samples

For this study, the reference library (Tetracorder v3.6a2) of over 400 minerals, vegetation species, snow cover types and manmade materials was augmented with laboratory spectra of mixtures of calcite, epidote and chlorite. Figure 2 is a ternary diagram indicating the pure endmembers, mixture proportions, and a number of rock samples acquired in the field and used for testing. A set of field samples collected under a different portion of the watershed study was analyzed for composition using point counts of mineral grains to determine relative weight percents of calcite, epidote and chlorite. Due to expense, only two samples collected from known regions previously misidentified as calcite but actually containing little to no calcite could be analyzed in this manner. Most of the samples cluster in one region of the diagram, indicating a tendency toward such mixtures. Whether this is caused by selection effects during field sampling or, as is quite likely, accurately reflects the composition of the study region, is of little consequence to this study, because in any case a robust discrimination algorithm requires a consistent spread of compositions throughout the ternary diagram. For this reason as well as the presence of other mineral phases in the samples, the use of laboratory mixtures was deemed to give a more accurate reference set. Pure samples of each mineral were ground and wet-sieved using methanol. The 75–150-μm size fraction was found to closely match the band depths of pure inclusions of calcite, epidote and chlorite in the field samples. This fact conveniently eliminated sources of error due to differences in grain size between minerals in the mixtures. A set of powdered mixtures was prepared from the pure endmembers, in ratios allowing each of the three minerals commensurate representation in relation to the other two, as either major, equal, or minor proportions. These proportions are indicated on the ternary diagram by the letters B through N, and given numerically in Table I. Sample F (80% epidote, 10% each of calcite and chlorite) was omitted because the strong epidote signal rapidly overwhelms the other two minerals as epidote concentration increases. This is borne out by examination of continuum-removed spectra of mixture CEC-G and samples SJ98-74D and IDB6597. For realistic instrument noise levels, these mixtures will inevitably be classified as high in epidote and low in calcite.

Although it would seem that the 2.26 μm band in the spectrum of sample SJ98-74D could be used to rule out a pure calcite identification, in practice the quality of remotely sensed spectra are presently too noisy for this band to be reliable in automated applications. If all spectra in the scene were of similar quality to the laboratory data shown above, the solution would be trivial. However, due to their differing shapes, the quality of a least-squares match between SJ98-74D and each of the three endmembers is roughly the same for each, with typical noise levels sufficient to skew the results in favor of the wrong endmember. Furthermore, this study aims to determine the

distribution of calcite in mixtures as well. With the full suite of mixtures B through N listed in Table I, such a misidentification becomes much less likely.

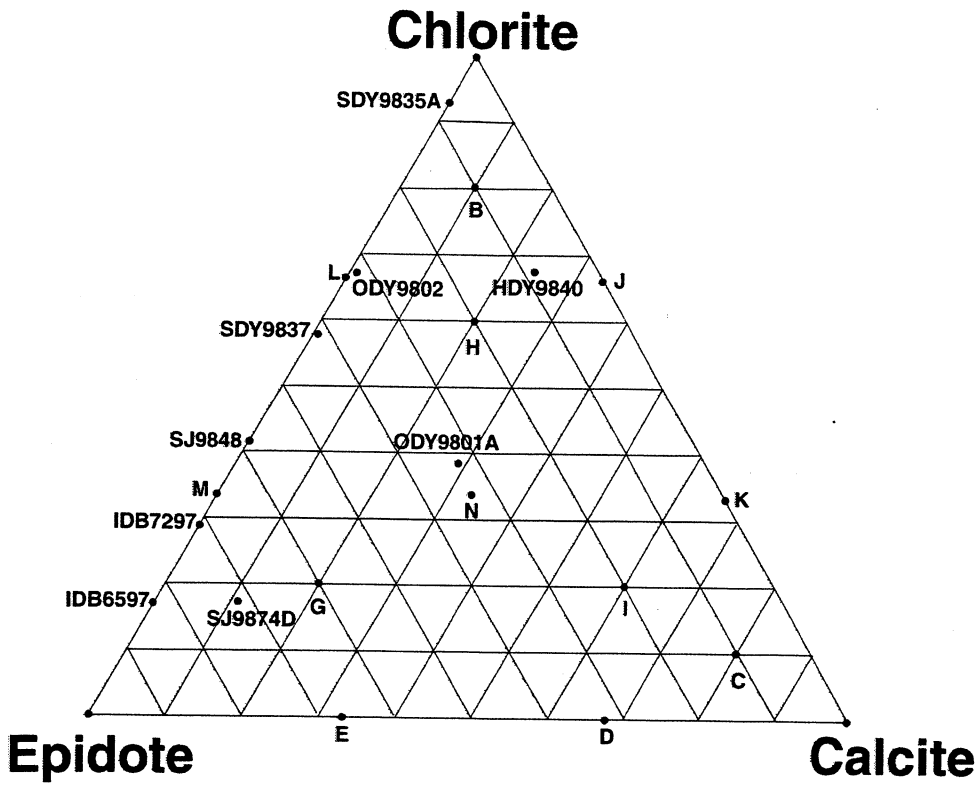

Figure 2. Ternary diagram indicating proportions of calcite, epidote and chlorite in each of the laboratory mixtures and several rock samples collected in the field. Vertices are 100% endmember; each line denotes a ten percent change in concentration.

Table I. Numeric values of proportions of calcite, epidote and chlorite used in mixtures.

Sample ID	% Calcite	% Epidote	% Chlorite
Calcite (GDS-304)	100		
Epidote (GDS-301)		100	
Chlorite (GDS-307)			100
CEC-B (GDS-308)	10	10	80
CEC-C (GDS-309)	80	10	10
CEC-D (GDS-310)	67	33	
CEC-E (GDS-311)	33	67	
CEC-G (GDS-312)	20	60	20
CEC-H (GDS-313)	20	20	60
CEC-I (GDS-314)	60	20	20
CEC-J (GDS-315)	67		33
CEC-K (GDS-316)	33		67
CEC-L (GDS-317)		33	67
CEC-M (GDS-318)		67	33
CEC-N (GDS-319)	34	33	33

All laboratory spectra were acquired using an Analytical Spectral Devices ASD-6015-7 Field Spectrometer with a quartz halogen light source and Spectralon reference standard. The spectral sampling of this instrument is 2 nm while the resolution is 11 nm (Goetz *et al.*, 1998). Wavelength calibration was performed using praseodymium-doped Corning Glass along with mylar plastic sheeting as transmission standards. The spectrometer was programmed to average 60 measurements, each having a one second integration time, together per spectrum; 25 such spectra were averaged to produce each reference spectrum, for a total integration time of 1800 seconds apiece. All spectra were corrected to absolute reflectance.

The reference spectra for the three endmembers and the twelve mixtures are shown in Figure 3. The depth of the primary band at 2.34 μm scales nonlinearly with composition; the resultant spectra are most sensitive to epidote. Note that the 2.26-μm secondary band is evident in all of the mixture spectra, including those (C, D, and K) dominated by calcite. The effects of small amounts of calcite on the overall band shape are more subtle, yet with 21 separate channels in the AVIRIS spectra of this band complex, the least-squares correlation coefficients differ sufficiently for the Tetracorder algorithm to distinguish between them.

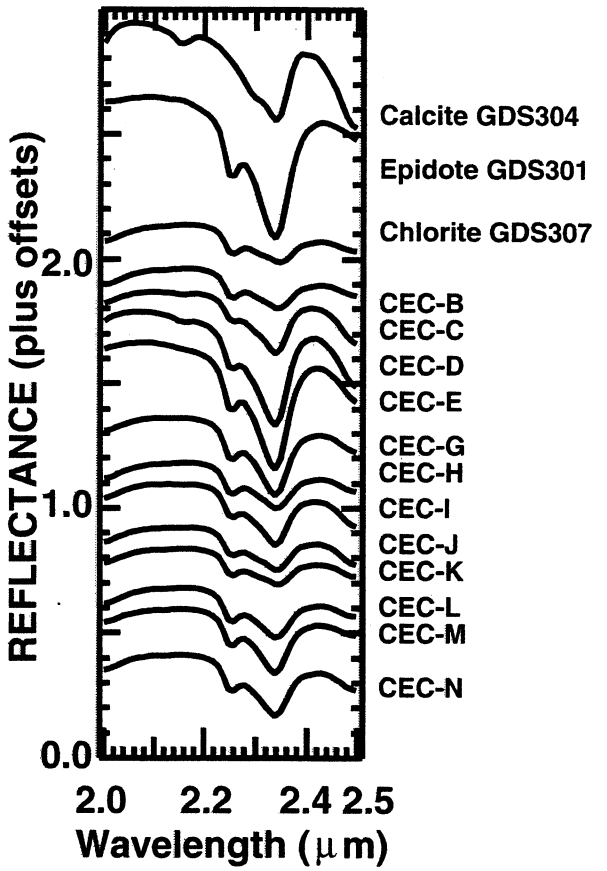

Figure 3. The 2.3-μm feature complex of calcite, epidote, chlorite and the twelve mixtures used to train the Tetracorder algorithm.

3.3 Tetracorder Processing

Each of the mixture spectra were added to the USGS Denver Spectroscopy Laboratory Tetracorder 3.6a2 reference library. The default continuum-removal approach was to fit a straight line to the reflectance continuum using the two continuum points on either side of the absorption band (Clark and Roush, 1984) and divide the spectrum by this fitted continuum line. In order to compare continuum-removed features, tie points were established at the edges of the primary band (at 2.18 and 2.42 μm) and also, separately, for the secondary band (2.21 and 2.28 μm) for each of the mixtures. The tie points for continuum removal were slightly different for each of the pure endmembers, leading to a better continuum-removed correlation coefficient for the pure cases.

The algorithm was tested first using the laboratory mixtures as the "observed" test spectra. All mixtures were properly categorized. The 2.15-μm calcite feature was not used in either the testing or analysis phases. The method was then tested on the field samples. There were problems classifying certain of the field samples due to the presence of a fourth spectrally active component, sericite, in several specimens. Sericite is a fine-grained form of muscovite which has a strong diagnostic feature at 2.2 μm and two weaker features at 2.35 and 2.45 μm which overlap the 2.3-μm wings of calcite, epidote and chlorite, complicating their identification. This is addressed in section 4.3. The two specimens collected during AVIRIS field-checking (SJ98-74D and SJ98-48) had previously been identified as calcite but were correctly identified as mixtures using the improved reference library. These samples contained no sericite. Extracted pixels from AVIRIS scenes corresponding to calcite-epidote-chlorite mixtures were the used as test spectra, and correctly identified as mixtures dominated in turn by each of the three. Pure samples of the endmembers, and library specimens of other epidote, calcite and chlorite samples were also correctly identified with the improved reference spectra. The new approach also correctly identified limestones.

The next step was application to the AVIRIS Animas Watershed flightlines. These two flight lines were acquired on June 18, 1996 at 9:30 AM and cover the region from Durango, Colorado to the headwaters of the Animas River at Animas Forks, Colorado. The study area is bounded by national forest on the east and west sides, and includes the town of Silverton and all of the Silverton Caldera. The full dataset and its analysis are described elsewhere (Dalton *et al.*, 2000, 2001); this paper is concerned specifically with the calcite-epidote-chlorite results, which are discussed below.

4. Results

4.1 Regional Context

The USGS Tetracorder Algorithm was able to successfully utilize the updated reference library to distinguish between the calcite, epidote and chlorite endmembers. Most importantly, nearly pure calcites such as limestone were easily differentiated from mixtures of calcite, epidote and chlorite. While AVIRIS pixels were separated into bins corresponding to each of the mixtures, it must be recognized that such fine division is in fact splitting hairs, due to inherent noise and the contributions of other materials in the scene.

The final images produced by the algorithm were grouped together into images reflecting the surface composition in a more general fashion. Referring to the ternary diagram of Figure 2, it is clear that many possible compositions would fall into the category of mixture CEC-N (equal parts calcite, epidote and chlorite) and many possible mixtures would fall into category CEC-D (mostly calcite, with epidote but no chlorite.) The georeferenced, orthorectified image in Figure 4 reflects an intuitive grouping of these materials. The color key shows each endmember having a certain primary color (yellow for calcite, blue for epidote, red for chlorite) and the mixtures represented by secondary colors. Thus, yellow-green represents a mixture of predominantly calcite but also containing epidote, similar to the region around sample mixture CEC-D in Figure 2; dark green is primarily calcite but contains both epidote and chlorite, as with mixtures CEC-I and CEC-C and the region surrounding them; blue-green is epidote with some calcite, as with CEC-E; and so forth.

Examining Figure 4, the regional context of the study becomes clearer. The town of Silverton is situated within the caldera and appears at the top center of the image. The confluence of the Animas River with Mineral Creek lies just below the town, and the river cuts through the center of the image. Sultan Mountain lies southwest of the confluence; Molas Lake, Little Molas Lake, and Andrews Lake are to the west of the river toward the middle of the image. As the river leaves the caldera just south of the town, it cuts through the sedimentary formations containing abundant limestones. The yellow outcrop of limestone in the lower left of the image is near the aptly-named Lime Creek, which flows into the Animas and contributes to the buffering of acidic waters introduced upstream by Mineral Creek. Limestones are also evident in road cuts paralleling the river just east of Sultan Mountain. The propylitic alteration zones in the upper right-hand corner of the image, however, exhibit a patterning which is due to the varying calcite, epidote and chlorite concentrations in the altered host rock. Preliminary analyses using Tetracorder v3.4a8 (Dalton *et al.*, 1998) classified much of this material as calcite.

4.2 Discrimination of Calcite-Epidote-Chlorite Mixtures

The propylitically altered zone from Figure 4 is enlarged in Figure 5 to show more details of the differentiated mixtures. The key is the same as for Figure 4. The astute reader will notice that there are no chlorite-dominated mixtures in the key other than chlorite with muscovite. During processing, it was found that few AVIRIS pixels gave a good match to a chlorite-dominated mixture. Pixels were generally dominated by either epidote or calcite. Referring to the ternary diagram in Figure 2, it is seen that few field samples from the Animas River Watershed and Silverton Caldera were dominated by chlorite. Laboratory analyses showed that most of these also contained sericite. The Tetracorder analysis found essentially the same thing: although there are some regions where chlorite does dominate the spectral signature, most areas lacking in epidote and calcite contained sericite as well. A more detailed discussion follows in section 4.3. The categories of mixtures CEC-B and CEC-C were found to be superfluous as well; along with CEC-F, the mixtures containing 80% of any one endmember gave similar correlations to the pure endmembers and were therefore not considered in the final analyses. As chlorite and

muscovite had already been encountered together in a different location (Swayze 1997), a chlorite-muscovite mixture was already in the USGS Tetracorder (v3.4a8) reference library (Dalton, 1998).

Four primarily northwest-southeast trending zones of exposed propylitic alteration are visible in Figure 5. The ridge of Hazelton Mountain in the upper right corner is highlighted in a profusion of light and dark blue, yellow-green and

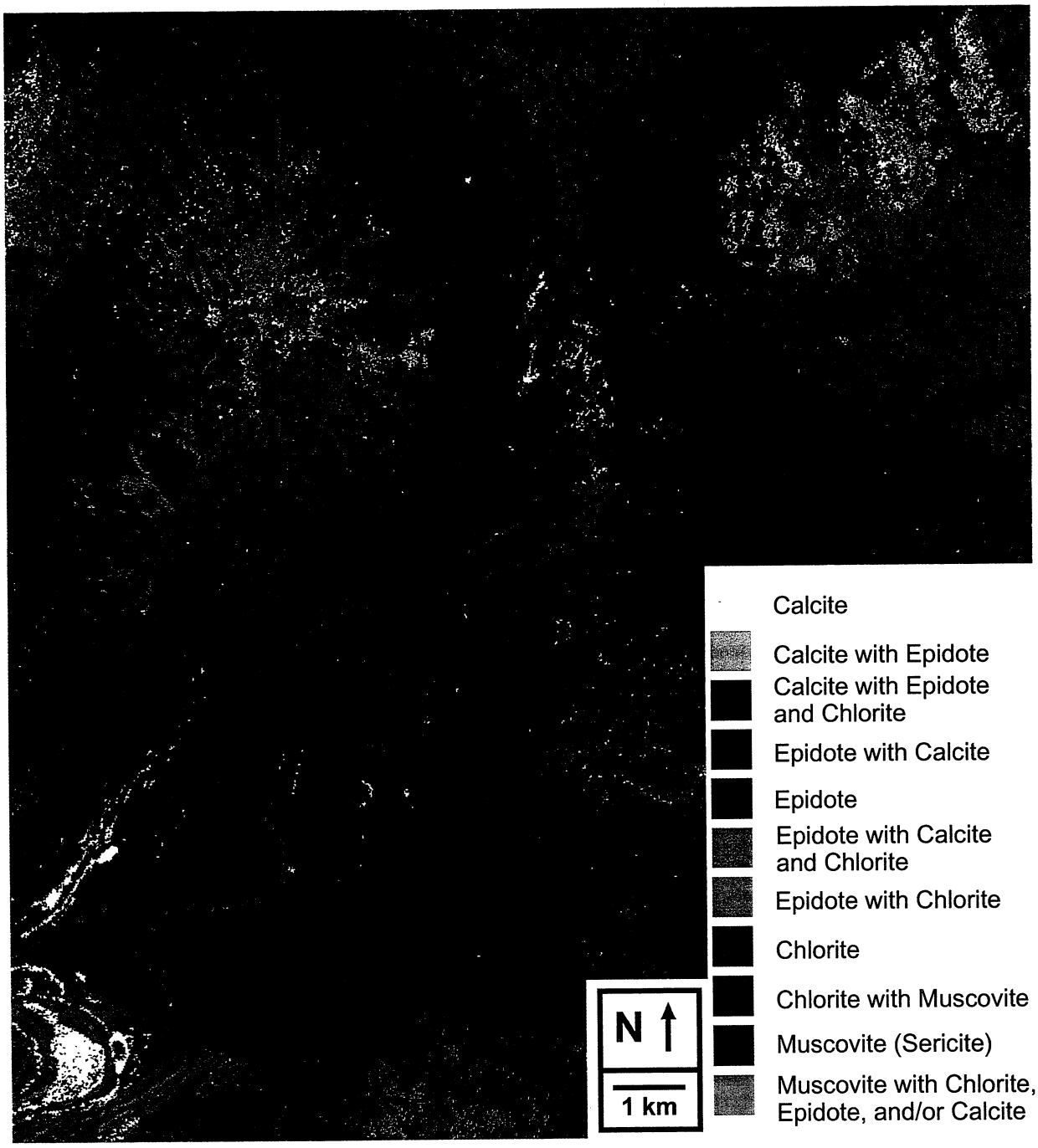

Figure 4. Georeferenced image of a portion of the Animas River Watershed study area. Tetracorder results are shown in color. The town of Silverton, Colorado is near the top center; the Animas River bisects the image vertically. This image has been engineering-corrected for roll, pitch, yaw, forward velocity, and smile, as well as orthorectified against a digital elevation model to remove topographic distortions.

yellow, evidence of mixtures of epidote and calcite. Although few pixels exactly matched the equal- parts mixture (CEC-N, 33% each), the dark green and light blue pixels illustrate areas containing all three minerals. An outcrop of predominantly chlorite (red) in the lower left corner lies on Kendall Mountain. The intermediate slopes contain a combination of all of these, along with orange pixels denoting the presence of all four minerals. In these orange pixels, no single mineral dominates the spectrum strongly enough to be realistically selected as the primary mineral. Within the limits of current technology, such pixels cannot yet be further constrained. An additional source of uncertainty arises from the presence of sericite around the edges of the zone. Regions identified as pure sericite (muscovite) are shown in purple while the chlorite-sericite mixture is shown in pink. These give some idea of how the sericite grades into the rest of the propylitic assemblages. Fortunately, there appears to be a steady and gradual shift from calcite-dominated to sericite-dominated spectra. Were the sericite randomly distributed throughout the zones, this would be cause for concern.

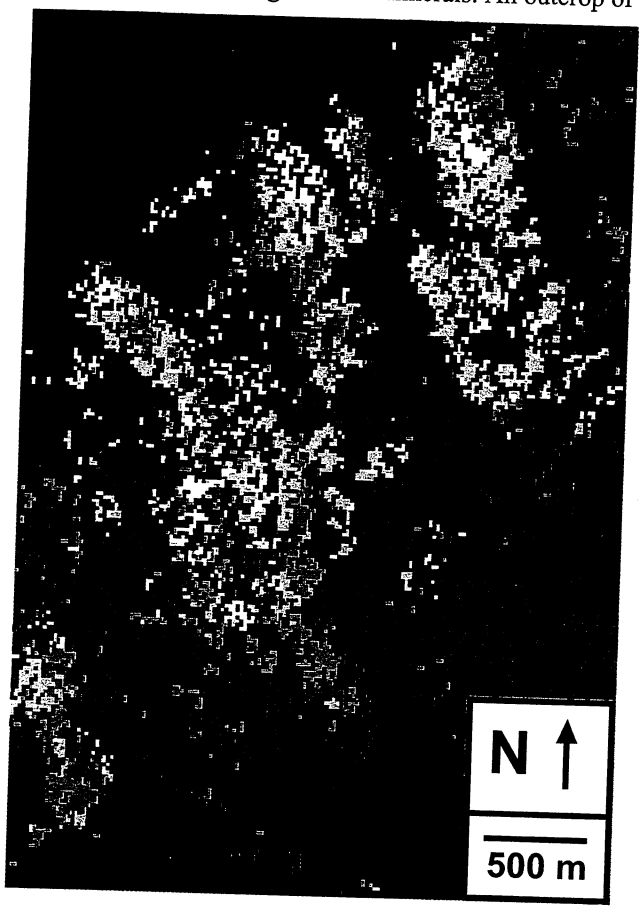

Figure 5. Enlargement of a portion of Figure 4 showing calcite, epidote, chlorite and muscovite mixtures in the Silverton Caldera. Woodchuck Basin lies right of center, between the ridges of Mount Hazelton (top right) and Mount Kendall (bottom center). Key is the same as in Figure 4.

The heterogeneous mix of pixels dominated by calcite, epidote and chlorite are indicative of the actual variations of concentration in the host rock. These variations result from the initial composition of the rock, variations in severity of propylitic alteration, and subsequent weathering. Although these specific slopes were not field-checked, earlier traverses of similar propylitic alteration zones in the watershed revealed exactly this pattern. The stronger spectral signal of epidote probably results in a slight overestimation of its abundance in these images. Likewise, the weaker signal of chlorite has probably caused its distribution to be slightly underestimated. However, these images represent a significant improvement over previous methods in deducing the distribution of calcite in the watershed, and will result in improved determination of stream buffering capacity from naturally occurring deposits.

4.3. The Muscovite Problem

Care should be applied when interpreting these results. As noted earlier, all chlorites in this region were well-represented by ripidolite. This is likely not the case at all sites outside of this study area. In addition, it must be stressed that the presence of sericite in propylitic alteration zones was not taken fully into account in this study. Because muscovites have a strong diagnostic absorption feature at 2.2 μm, and weaker absorptions at 2.35 and 2.45 μm, they interfere spectrally with the absorptions of calcite, epidote and chlorite. In the present study, this results in uncertainty in the absolute abundances of the minerals of interest. For locations evidencing the muscovite bands, relative concentrations of the three could not be established, and the Tetracorder algorithm was instructed to differentiate these into three categories. The easiest of course was muscovite only (purple in the key to Figure 4). Where the chlorite signature was seen together with muscovite, pixels were categorized as chlorite with muscovite (pink.) It is interesting to note that there was no apparent evidence for sericite alone with either calcite or epidote. In

the case of mixed pixels of epidote, calcite and/or chlorite, together with the muscovite signature at 2.2 μm, nothing further could be determined about the composition and these are the orange pixels in Figures 4 and 5.

A ready solution to this problem could be to conduct a similar study to this one, using laboratory mixtures of four endmembers instead of three. Due to financial and timing constraints, this was not possible within the current study. In planning for such work, the obvious question of whether a fifth, sixth and seventh such endmember could crop up was investigated. Examination of the AVIRIS spectra, laboratory spectra, field samples and laboratory mixtures indicates that there are no other spectrally active materials in the study area in this region of the spectrum which do not have other diagnostic features already being used by the Tetracorder system. Once appropriate mixtures of muscovites have been added to the reference library, the algorithm should be able to distinguish the remaining four-endmember (orange) pixels and further constrain the abundance of calcite and chlorite in the watershed.

5. Conclusion

The application of the USGS Tetracorder algorithm to the Animas River Watershed study demonstrates the ability of rule-based expert systems to differentiate between spectrally similar materials using comparisons of least-squares correlation coefficients derived from a reference library to those of the observed spectral data set. Including a set of spectra representing mixtures of the discrete endmembers calcite, epidote and chlorite was an essentially simple adjustment which enabled accurate discrimination between mineral mixtures in the host rock. The approach could be refined by the addition of muscovite-calcite-epidote-chlorite mixtures to the reference library. Researchers applying these results to other regions should first ensure that ripidolite is representative of the chlorites in their region of interest, or else adapt their reference library with local chlorites. This approach should prove useful in identifying other spectrally similar materials. These results will be useful to land managers wishing to constrain problems of acidic drainage in the Animas River Watershed, as well as to remote-sensing scientists with similar applications.

REFERENCES

Bigham, J.M., U. Schwertmann, S.J. Traina, R.L. Winland, and M. Wolf, Schwertmannite and the chemical modeling of iron in acid sulfate waters, *Geochimica et Cosmochimica Acta*, **60**:2111-2121, 1996.

Boardman, J.W., Automated spectral unmixing of AVIRIS data using convex geometry concepts, *Summaries of the 4th Annual JPL Airborne Geoscience Workshop*, JPL Publ. 93-26, **1**, Pasadena CA 1993.

Bove, D.J., M.A. Mast, W.G. Wright, P.L. Verplanck, G.P. Meeker, and D.B. Yager, Geologic control on acidic and metal-rich waters in the southeast Red Mountains area, near Silverton, Colorado, *Proceedings of the 5th International Conference on Acid Rock Drainage*, Denver CO 2000.

Church, S.E., D.L. Fey, and R. Blair, Pre-mining bed sediment geochemical baseline in the Animas River Watershed, southwestern Colorado, *Proceedings of the 5th International Conference on Acid Rock Drainage*, Denver CO 2000.

Clark, R.N. and T.L. Roush, Reflectance spectroscopy: Quantitative analysis techniques for remote sensing applications, *J. Geophys. Res.*, 89:6329-6340, 1984.

Clark, R.N., A.J. Gallagher, and G.A.S. Swayze, Material absorption band depth mapping of imaging spectrometer data using complete band shape least-squares fit with library reference spectra, *Proceedings of the 2nd annual JPL Airborne/Visible Imaging Spectrometer (AVIRIS) Workshop*, JPL Publ. 90-54, Pasadena, CA 1990.

Clark, R.N. and G.A.S. Swayze, Automated spectral analysis: mapping minerals, amorphous materials, environmental materials, vegetation, water, ice and snow, and other materials: The USGS Tricorder Algorithm, *Lunar and Planetary Science XXVI*, pp. 255-256, 1995.

Clark, R.N., G.A. Swayze, T.V.V. King, K.E. Livo, J.B. Dalton, and R.F. Kokaly, Expert system features identification rules for reflectance (and emittance) spectroscopy analysis I: Visible to near-infrared detection of minerals, organics, vegetation, water, amorphous and other materials, *J. Geophys. Res.*, 2001.

Dalton, J.B., T.V.V. King, D.J. Bove, R.F. Kokaly, R.N. Clark, J.S. Vance, and G.A.S. Swayze, Mapping of acid-generating and acid-buffering minerals in the Animas watershed by AVIRIS spectroscopy, *Summaries of the 7th Annual JPL Airborne Earth Science Workshop*, JPL Publ. 97-21, pp. 79-83, 1998.

Dalton, J.B., T.V.V. King, D.J. Bove, R.F. Kokaly, R.N. Clark, J.S. Vance, and G.A.S. Swayze, Distribution of acid-generating and acid-buffering minerals in the Animas River watershed by AVIRIS spectroscopy, *Proceedings of the 5th International Conference on Acid Rock Drainage*, Denver CO 2000.

Dalton, J.B., D.J. Bove, T.V.V. King, C.A. Mladinich, R.N. Clark, B. Rockwell, G.A.S. Swayze, R.F. Kokaly, K.E. Livo, J.S. Vance and S.E. Church, Remote Sensing Characterization of the Animas River Watershed by AVIRIS Imaging Spectroscopy,*to be published in U.S. Geological Survey Open File Report*, in technical review, 2001.

DesBorough, G.A., P.H. Briggs, and N. Mazza, Chemical and mineralogical characteristics and acid-neutralizing potential of fresh and altered rocks and soils of the Boulder River Headwaters in Basin and Cataract Creeks of northern Jefferson County, Montana, *U.S. Geological Survey Open File Report 98-40*, 1998.

Eastwood, M.L., R.O. Green, C.M. Sarture, B.J. Chippendale, C.J. Chovit, J.A. Faust, D.L. Johnson, S.P. Monacos, and J.J. Raney, Recent improvements to the AVIRIS Sensor: Flight Season 2000, *Proceedings of the 9th JPL Airborne Earth Science Workshop*, JPL Publ. 00-18 Pasadena, CA 2000.

Fleischer, M. and J.A. Mandarino, *Glossary of Mineral Species*, Mineralogical Record, Inc. Tucson AZ 1995.

Goetz, A.F., K.B. Heidebrecht, B. Kindel, and J.W. Boardman, Using ground spectral irradiance for model correction of AVIRIS data, *Summaries of the 7th Annual JPL Airborne Earth Science Workshop*, JPL Publ. 97-21, pp. 159-168, 1998.

Hapke, B., *Theory of reflectance and emittance spectroscopy*, Cambridge University Press, Cambridge, 1993.

Hunt, G.R. and J.W. Salisbury, Visible and near-infrared spectra of minerals and rocks: I. Silicate Minerals, *Modern Geology* **1**:283-300, 1970.

King, T.V.V. and R.N. Clark, Spectral characteristics of chlorites and Mg-serpentines using high-resolution reflectance spectroscopy, *J. Geophys. Res.* **13**:13997-14008, 1989.

Klein, C. and C.S. Hurlbut, *Manual of Mineralogy*, John Wiley and Sons, New York, 1993.

Kokaly, R.F., R.N. Clark, and K.E. Livo, Mapping the biology and mineralogy of Yellowstone National Park using imaging spectroscopy, *Summaries of the 3rd Annual JPL Airborne Geoscience Workshop*, JPL Publ. 97-21, **1**, Pasadena CA 1997

Kruse, F.A., A.B. Lekhoff, and J.B. Dietz, Expert system-based mineral mapping in northern Death Valley, California/Nevada, using the Airborne Visible/Infrared Imaging Spectrometer (AVIRIS), *Remote Sensing Environ.*, 44, pp. 309-335, 1993.

Lipman, P.W., T.A. Steven, R.G. Luedke, and W.S. Burbank, Revised volcanic history of the San Juan, Uncompahgre, Silverton, and Lake City calderas in the western San Juan Mountains, Colorado, *U.S. Geological Survey Journal of Research* **1**:627-642, 1973.

Mast, M.A., P.L. Verplanck, D.B. Yager, W.G. Wright, and D.J. Bove, Natural sources of metals to surface waters in the Upper Animas River Watershed, Colorado, *Proceedings of the 5th International Conference on Acid Rock Drainage*, Denver CO 2000.

Mustard, J.F. and J.M. Sunshine, Spectral Analysis for Earth Science: Investigations Using Remote Sensing Data, in *Remote Sensing for the Earth Sciences: Manual of Remote Sensing*, Ed. A.N. Rencz, John Wiley & Sons, New York, 1999.

Nimick, D.A. and P. von Guerard, Science for Watershed Decisions on Abandoned Mine Lands: Review of Preliminary Results, *U.S. Geological Survey Open File Report 98-297*, 1998.

Soha, J.M., A.R. Gillespie, M.J. Abrams, and D.P. Madura, Computer Techniques for Geological Applications, Caltech/JPL Conference on Image Processing Technology, Data Sources and Software for Commercial And Scientific Applications, JPL SP 43-30, pp. 4.1-4.21, Pasadena CA, 1976.

Swayze, G.A.S., The hydrothermal and structural history of the Cuprite Mining District, southwestern Nevada: an integrated geological and geophysical approach, Ph.D. dissertation, University of Colorado, Boulder, 1997.

ASSESSING THE SPATIAL DISTRIBUTION OF PLANT LITTER

C. S. T. Daughtry,[1] E. R. Hunt, Jr.,[1] C. L. Walthall,[1] T. J. Gish,[1] Shunlin Liang,[2] and E. J. Kramer[3]

1. INTRODUCTION

Quantifying crop residue cover on the soil surface is important for improving estimates of surface energy balance, net primary productivity, nutrient cycling, and carbon sequestration. Quantifying crop residue cover is also an important factor in controlling soil erosion and evaluating the effectiveness of conservation tillage practices. By reducing the movement of eroded soil into streams and rivers, the movement of nutrients and pesticides is reduced. The overall result is less soil erosion and improved water quality.

Current methods for quantifying crop residue cover are tedious and somewhat subjective. The standard technique for measuring crop residue cover used by the USDA Natural Resources Conservation Service (NRCS) is visual estimation along a line-transect (Morrison et al., 1993). Reviews of crop residue measurement techniques document recent modifications and illustrate the unresolved problems of current techniques (Corak et al., 1993; Morrison et al., 1995). Rapid, accurate, and objective methods to quantify residue cover are needed.

Attempts to replace the human visual judgment present in the line-transect method with a sensor designed to identify crop residue based on its reflectance characteristics have had only limited success. The reflectance of both soils and crop residue lack the unique spectral signature of green vegetation in the 400 to 1000 nm wavelength region (Aase and Tanaka, 1991; Daughtry et al., 1995). Crop residues and soils are often spectrally similar and differ only in amplitude at a given wavelength (Baird and Baret, 1997). This makes discrimination between crop residues and soil difficult or nearly impossible using reflectance techniques in the visible and near infrared wavelengths. Two promising approaches have been identified for discriminating crop residues from soil -- one based on blue fluorescence emissions and another based on shortwave infrared reflectance.

The fluorescence approach is based on research first reported by McMurtrey et al. (1993) that crop residues fluoresce more than soils when illuminated with ultraviolet radiation at 337 nm. The fluorescence of crop residues was a broad band phenomenon centered between 420 to 520 nm and was induced by a relatively broad range of excitation wavelengths centered between 350 and 400 nm (Daughtry et al., 1995). Soils had low intensity broad band emissions over the 400-690 nm region for excitations of 300-600 nm. Thus, fluorescence techniques may be less ambiguous than visible and near infrared reflectance techniques for discriminating crop residues from soils. Although considerable progress has been made in developing a portable agricultural residue sensor based on the fluorescence of soil and residues, several problems that must be addressed include (i) the excitation energy must be supplied to induce fluorescence and (ii) the fluorescence signal is small relative to normal, ambient sunlight.

The shortwave infrared approach utilizes a broad absorption band near 2100 nm that appears in all compounds possessing alcoholic -OH groups, such as sugars, starch, and cellulose (Murray and Williams, 1988). This strong absorption at 2100 nm was clearly evident in the reflectance spectra of the dry crop residues (Daughtry et al., 1996) and dry, intact plant materials (Elvidge, 1990). The cellulose absorption feature was absent in the spectra of the soils. Daughtry et al. (1996) defined a new spectral variable, cellulose absorption index (CAI) that quantifies the relative depth of this absorption feature and can discriminate between crop residues and soils. Additional work is needed to determine the effects of moisture, residue age, and mixed pixels (soil + residue) on discrimination of crop residues from soils. The CAI algorithm has yet to be tested with hyperspectral images for fields and watersheds for assessing crop residue cover.

---

[1]USDA-ARS Hydrology and Remote Sensing Laboratory, Bldg 007, Room 104, 10300 Baltimore Ave., Beltsville, Maryland 20705-2350 USA. email: cdaughtry@hydrolab.arsusda.gov

[2] Geography Department, University of Maryland, College Park, Maryland, USA

[3] USDA-ARS Facilities Maintenance and Operations Division, Farm Operations Branch, Beltsville, Maryland, USA

The objectives of this research were to (1) determine the spectral reflectance of green plants, plant litters, and soils as a function of water content, (2) assess the limits of discrimination that can be expected, and (3) evaluate hyperspectral imaging data for providing information on the spatial distribution of plant litter. This research provides the scientific foundation required for sensor development and field testing.

2. MATERIALS AND METHODS

2.1 Reflectance Spectra

Reflectance spectra were acquired with a spectroradiometer (FieldSpec Pro, Analytical Spectral Devices, Boulder, CO) over the 400-2500 nm wavelength region at 1 nm intervals. The samples were illuminated by two 300 W quartz-halogen lamps mounted on the arms of a camera copy stand at 50 cm over the sample at a 45° illumination zenith angle. The spectroradiometer was positioned 90 cm from the sample surface at a 0° view zenith angle. With the 18° optics on the spectroradiometer, the diameter of the field of view at the sample was 28 cm. The illumination and view angles were chosen to minimize shadowing and to emphasize the fundamental spectral properties of the soils and crop residues. Four spectra were acquired of each samples by rotating the sample tray 90° after each spectrum. A 76-cm square Spectralon reference panel (Labsphere, Inc., North Sutton, NH) was placed in the field of view, illuminated, and measured in the same manner as the samples.

Reflectance factors were calculated as described by Robinson and Biehl (1979). Mean reflectance spectra (n=4) were plotted as a function of wavelength and moisture condition. In addition, the reflectance spectra were integrated over wavelength to evaluate the relatively broad bands of the Landsat Thematic Mapper (TM): TM3 (630-690 nm); TM4 (760-900 nm); TM5 (1550-1750 nm); and TM7 (2080-2350 nm). The cellulose absorption index (CAI) was calculated as: $CAI = 0.5(R_{2.0} + R_{2.2}) - R_{2.1}$; where $R_{2.0}$, $R_{2.1}$, and $R_{2.2}$ are the reflectance factors in 10 nm bands centered at 2015, 2106, and 2195 nm, respectively. In previous work, 30 to 50-nm wide bands were used (e.g., Daughtry et al., 1996; Nagler et al., 2000).

Broad absorption features centered near 1730, 2100, and 2300 nm in the reflectance spectra of the dry crop residues were selected for continuum analysis (Kokaly and Clark, 1999). The continuum is an estimate of the reflectance spectrum without the absorption due to the compound of interest. Linear segments were used to approximate the continuum. The end points of each continuum segment used are given in Table 1. The continuum-removed spectra were calculated by dividing the original reflectance values by the corresponding values of the continuum line (Kokaly and Clark, 1999). Band depths within each absorption feature were normalized by dividing by the band depth at the center of the feature.

Table 1. Continuum end points and band centers for three absorption features in reflectance spectra of dried crop residues.

Spectroradiometer Data			**AVIRIS Data**		
Band Center, nm	Continuum Start, nm	Continuum End, nm	Band Center, nm	Continuum Start, nm	Continuum End, nm
1728	1652	1800	1733	1653	1802
2106	2010	2200	2111	2011	2201
2304	2238	2366	2300	2241	2370

2.2 Soil and Crop Residue Reflectance

Three topsoil samples were acquired for this study and provided a wide range of colors and textures (Table 2). Each soil was oven-dried at 105° C, crushed to pass a 2-mm screen, and placed to a depth of 0.5 cm in a 45-cm square sample tray that was painted flat black. After acquiring the spectral reflectance data from the oven-dried soils, the soils in the trays were saturated with water, allowed to drain freely for 2 h, and weighed before the spectral

reflectance was measured again. Relative water content (RWC) was calculated as the water content divided by the maximum water content of each samples (i.e., RWC = 0.0 is oven-dry and RWC = 1.0 is saturated).

Table 2. Soil names and sources of the top soils used in this study.

Soil Series	Location	Classification
Barnes	Morris, MN	coarse-loamy, mixed Udic Haploboroll
Codorus	Beltsville, MD	fine-loamy, mixed,mesic, Fluvaquentic Dystrochrept
Othello	Salisbury, MD	fine-silty, mixed mesic Typic Ochraqualt

Crop residues of corn (*Zea mays* L.) and soybean (*Glycine max* Merr.) were collected from agricultural fields near Beltsville, Maryland at 1 week and 8 months after harvest. The crop residues were dried at 70° C and then stored at room temperature. Spectral reflectance of intact dry crop residues were measured in 45-cm square sample trays filled to a depth of 3 cm. The samples and the trays then were placed in mesh bags, immersed in water for 2 h, allowed to drain freely for 2 h, and weighed before spectral reflectance was remeasured. Water content was expressed as relative water content (RWC).

In practice, reflectance spectra often represent mixed scenes with varying proportions of crops residues and soils. Reflectance factors of these mixed scenes ($R_{(M,\lambda)}$) were simulated using linear combinations of the reflectance factors for crop residues and soils: $R_{(M,\lambda)} = R_{(S,\lambda)}(1-f_R) + R_{(R,\lambda)}(f_R)$, where $R_{(S,\lambda)}$ and $R_{(R,\lambda)}$ are reflectance factors in waveband λ for soils and crop residues, respectively, and f_R is the fraction residue cover that ranged from 0 (100% soil) to 1.0 (100% crop residue). Scenarios for dry (RWC = 0) and wet (RWC =1.0) mixtures of each residue and soil were simulated.

2.3 AVIRIS Data

High-altitude AVIRIS radiance data (f000511t01p03_r02) were acquired by the Jet Propulsion Laboratory (JPL) on May 11, 2000 at 15:34 GMT (11:34 EDT) over the Beltsville Agricultural Research Center (BARC), Beltsville, Maryland. The flight line was south to north (38.13° to 38.65° latitude at -76.85° longitude). A cold-front went through the area without showers, so the visibility was excellent, with little haze, except for fog and clouds over the Goddard Space Flight Center in Greenbelt, MD. Five scenes were obtained over the flight line, scenes 2 and 3 were combined and the BARC area was subsetted for all analyses, the data were not georectified.

On May 11, spectral radiances of a number of surface features were acquired with spectroradiometers (FieldSpec Pro, Analytical Spectral Devices, Boulder, CO) over the 400-2500 nm wavelength region at 1 nm intervals. Apparent reflectance factors were calculated using Spectralon panels (Labsphere Inc., North Sutton, NH) without correction for the reflectance spectrum of the Spectralon. The primary calibration target was a large asphalt tarmac (approximately 100 m x 400 m) within the scene. The year 2000 wavelength calibration file provided by JPL was used to convert the ASD FieldSpec Pro data into the 224 AVIRIS bands by averaging the ASD reflectance factors from the center wavelength ± 0.5 of the Full Width at Half Maximum.

The Atmospheric Removal Program (ATREM 3.1) was obtained from the Center for the Study of Earth From Space (CSES), Cooperative Institute for Research in Environmental Studies (CIRES), University of Colorado. First, ATREM was used to estimate pixel reflectances from the radiance data. Second, the mean ATREM reflectance spectrum of the tarmac region of interest (ROI) and the mean ASD FieldSpec reflectance spectrum were used for a one-point empirical line calibration using Research Systems, Inc. Environment for Visualizing Images (ENVI) version 3.2. Finally, two major atmospheric water vapor absorption bands (108-118 and 155-172; 1364-1664 nm and 1832-1991 nm) were removed from the AVIRIS data.

End-members for linear spectral unmixing were selected from the corrected AVIRIS scene. The regions of interest (ROI) included: tarmac for asphalt, recently plowed fields with no residue for soil, several ponds for water, several roof tops, and fields of winter wheat and hairy vetch for bright green vegetation. Furthermore, we added the reflectance spectrum of a shaded Spectralon panel for the shade end-member, and the laboratory reflectance of corn residue for the residue end-member. The linear spectral unmixing routine in ENVI 3.2 was used with the seven end-

members without a unit sum constraint (i.e., the sum of the individual end-member fractions do not have to equal unity) to classify the AVIRIS image over BARC.

NDVI was calculated using bands 51 (827 nm) and 29 (646 nm). The Cellulose Absorption Index (CAI) was calculated using 176 (2031 nm), 183 (2101 nm) and 194 (2211nm). Mean spectra, NDVI, and CAI were obtained from ROI for various fields at BARC.

3. RESULTS AND DISCUSSION

3.1 Lab Spectra

Mean reflectance spectra of dry and wet corn and soybean residues are presented in Fig. 1. For each crop residue, the upper-most spectrum is the oven-dried residue and the lowest spectrum is for the water-saturated residue. The presence of water in the crop residue reduced reflectance across all wavelengths. Two major water absorption bands near 1450 and 1960 nm dominate the reflectance spectra at wavelengths >1300 nm. A broad absorption feature near 2100 nm is also evident in the reflectance spectra of all dry crop residues and is probably associated with lignin and cellulose in the crop residues (Murray and Williams, 1988). Similar absorption bands in the reflectance spectra of dry, intact plant materials have also been observed (Elvidge, 1990).

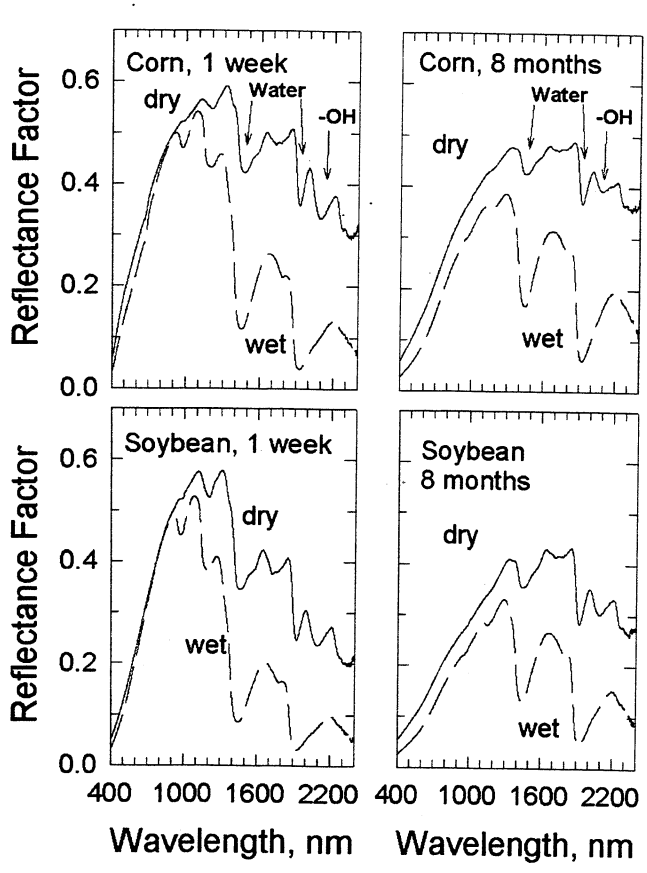

Figure 1. Reflectance spectra of dry and wet corn and soybean residues at 1 week and 8 months after harvest.

The effects of water absorption on the reflectance spectra gradually diminished as the water content of the crop residues decreased from water-saturated to oven-dry (Daughtry, 2001). Although the -OH absorption feature at 2100 nm was nearly obscured at high RWC, Gao and Goetz (1994) showed that cellulose and lignin absorption features can be identified in reflectance spectra dominated by water.

Mean reflectance spectra of the soils are shown in Fig. 2. As for the crop residue, water content reduced reflectance across all wavelengths. In addition to the two major water absorption features, a clay mineral absorption feature near 2200 nm (Baumgardner, et al., 1985) is evident in all three soils, but is especially strong in the Codorus spectra. The broad cellulose-lignin absorption feature near 2100 nm is not evident in the spectra of the soils.

The spectra of these crop residues and soils have similar shapes (Figs 1 and 2). Crop residues may be brighter or darker than a particular soil depending on moisture content. Thus, discrimination of crop residues from soils using reflectance in any single wavelength band in the 400-2400 nm wavelength region would be difficult and would require frequent adjustments of the discrimination thresholds for consistent results.

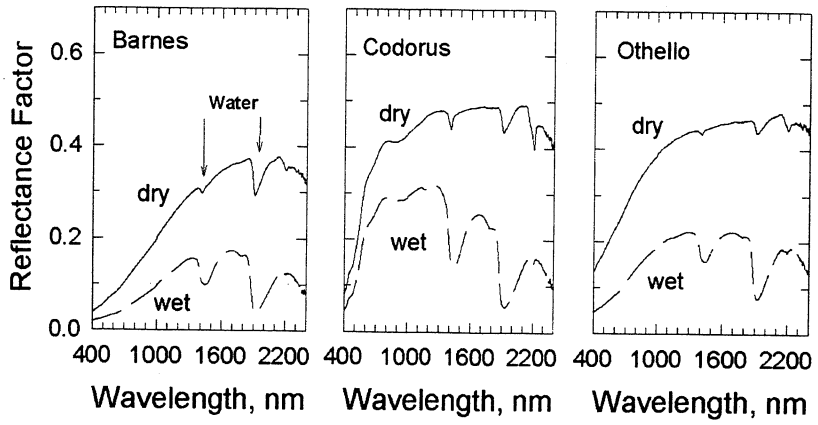

Figure 2. Reflectance spectra of dry and wet Barnes, Codorus, and Othello soils.

In the field, most reflectance spectra will represent scenes with mixtures of crop residues and soils. Changes in the fraction of crop residue cover produced differences in scene reflectance for the mixtures of dry (RWC = 0) crop residues and soils (Fig. 3). The wide range in reflectance factors for the spectra of mixtures of dry Barnes soil and dry corn residue made discrimination relatively easy at most wavelengths. However, for the Codorus and Othello soils, the addition of corn residue generally decreased reflectance across the spectrum. A closer examination of the 1600-2400 nm portion of the spectra (Fig. 4) shows the gradual shifts from the soil spectrum (f_R= 0) to the corn residue spectrum (f_R= 1.0) for each soil-residue mix. Although not shown, the narrow range of reflectance values for the mixtures of wet soil and wet residues (RWC = 1.0) increased the uncertainty of crop residue cover estimates (Daughtry, 2001). Clearly, moisture conditions are important for determining crop residue cover in mixed scenes.

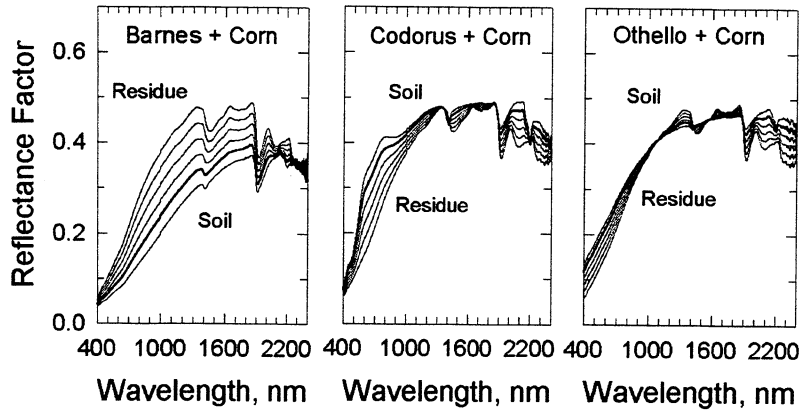

Figure 3. Reflectance specta of mixed scenes of dry corn residue (8 months) and three dry soils. The six spectra for each soil represent 0, 0.2, 0.4, 0.6, 0.8, and 1.0 fractions of corn residue in the scene.

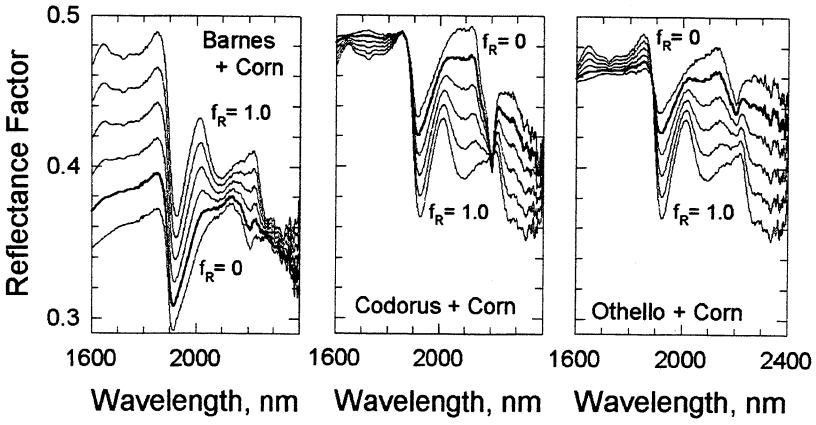

Figure 4. Expanded scale of mixed scenes of dry corn residue and dry soils. The six spectra for each soil represent 0, 0.2, 0.4, 0.6, 0.8, and 1.0 fractions of corn residue in the scene.

Many chemical bonds in plants have vibrational absorptions in the 1500 nm to 2500 nm wavelength region (Curran, 1989). Broad absorption features in the dry corn residue spectra centered near 1730 nm, 2100 nm, and 2300 nm were identified for continuum analysis. The end points of the continua of these three absorption features are given in Table 2 and are illustrated in Figure 5 for corn residues and two soils.

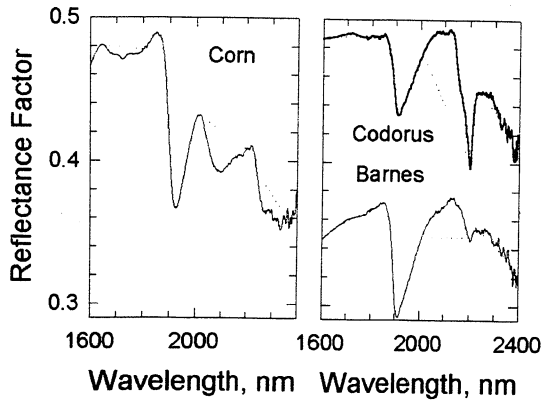

Figure 5 (Left). Linear continua for three major absorption features in corn residues. The same lines are also shown on the spectra of two soils.

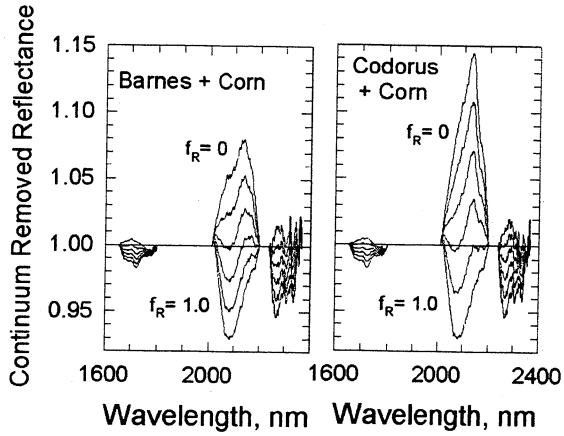

Figure 6 (Right). Continuum-removed reflectance spectra for Barnes and Codorus soils with 0, 0.2, 0.4, 0.6, 0.8, and 1.0 fractions of corn residue cover.

Once the continuum line was established, the continuum-removed spectra were calculated by dividing the original reflectance by the corresponding value from the continuum line (Kokaly and Clark, 1999). For the dry crop residues, the continuum line is greater than the original reflectance and the continuum-removed reflectance is less than 1.0 (Fig. 6). For the dry soils, the continuum-removed reflectance is greater than 1.0. The absorption feature near 2100 nm decreased rapidly as residue was added to the bare soils. The cellulose absorption index (CAI) is a adaptation of the continuum-removal method that uses reflectance in three bands -- two the shoulders and one in the center -- to estimate the depth of the absorption feature at 2100 nm. The continuum-removed reflectance (and CAI) provided better separation of crop residues from soils than reflectance factors because the crop residues could be darker or lighter than the soil.

3.2 AVIRIS Spectra

The AVIRIS scene (Fig. 7) covers most of the USDA Beltsville Agriculture Research Center, as well as portions of the Patuxent Wildlife Research Center (eastern 1/4 of image) and the commercial and residential corridor along US 1 (north western quarter of image). Mean reflectance spectra for six of the agricultural targets are shown in Figure 8. The conifer (Fig. 8A) and hairy vetch (Fig. 8B) targets have typical green vegetation spectra with low visible reflectance and high near infrared reflectance. The corn residue (Fig. 8D) and wheat residue (Fig. 8E) exhibit the absorption feature at 2100 nm that we observed in the reflectance spectra of dry corn and soybean residues (Fig 1). In Figure 8C, the cool season weeds (primarily wild mustards and cool season annual grasses), which had been recently sprayed with a contact herbicide, obscured much of the corn residue. Only a slight absorption at 2100 nm due the corn residue is evident in the mean reflectance spectrum. The bare soil field (Fig. 8F), which was rough from chiseled plowing several weeks earlier, showed a minor absorption (clay minerals) near 2200 nm.

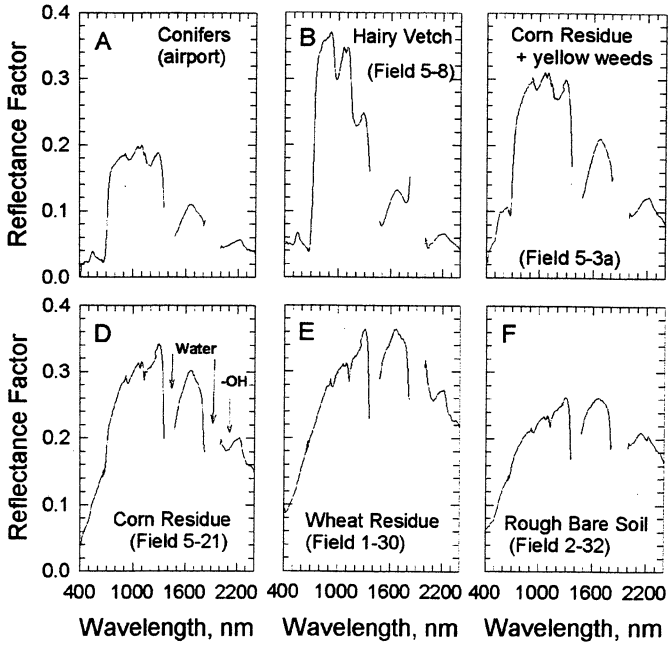

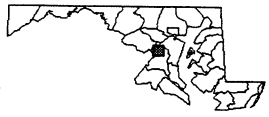

Figure 7 (Above). Composite image of AVIRIS over the Beltsville Agricultural Research Center(BARC) near Beltsville, Maryland on May 11, 2000. Bands 33, 54, and 174 (655 nm, 866 nm, and 2011 nm, respectively) were assigned as green, blue, and red.

Figure 8 (Left). Mean AVIRIS spectra for selected regions of interest

Table 3. Mean NDVI, CAI, and end-member relative weights from the linear spectral unmixing analysis for regions of interest.

Cover Type	n	NDVI	CAI	End Member Weights				
				Corn Residue	Hairy Vetch	Plowed Soil	Water	Error
Crop Residue	6	0.158	1.78	0.150	-0.071	1.111	0.033	0.013
Soil	4	0.192	-0.88	0.009	0.025	0.928	-0.117	0.009
Water	2	0.132	-0.08	0.002	0.013	-0.010	0.927	0.005
Green Vegetation	9	0.763	-0.31	-0.046	0.925	0.430	0.252	0.011
Yellow Vegetation	11	0.364	0.39	-0.033	0.387	0.948	0.475	0.014
Mowed Alfalfa	2	0.215	-0.68	0.060	0.114	0.813	-0.452	0.010

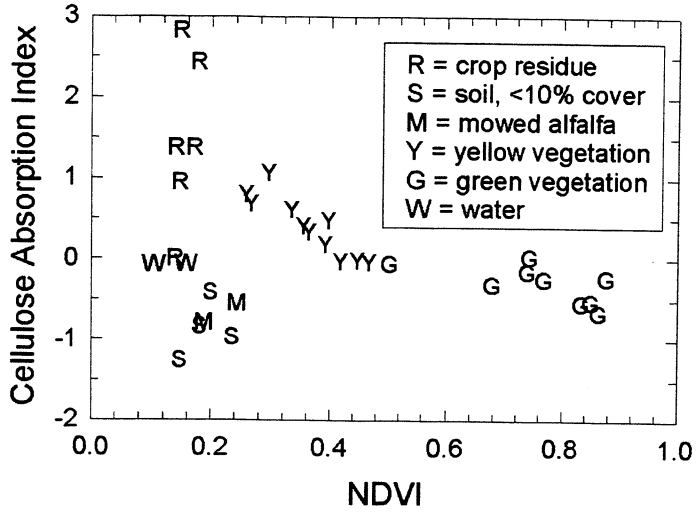

Figure 9. Scatter plot of the cellulose absorption index (CAI) as a function of NDVI.

For our initial analysis, we selected 34 regions of interest within the scene and grouped them into six cover types. The 'Crop residue' cover type consisted of fields with >80% cover of either corn or wheat residues. The 'Soil' class included fields that had been chiseled plowed or disked with <10% crop residue. The 'Water' class consisted of small lakes or ponds. The 'Green Vegetation' was broadly defined to include fields of hairy vetch, winter wheat, and orchardgrass and stands of conifers. The 'Yellow Vegetation' included fields that had been sprayed with foliar herbicides prior to no-till planting of summer crops and pastures with standing brown plant materials. The 'Mowed Alfalfa' fields had been harvested 1-2 days prior to the AVIRIS overflight and consisted of 5-10 cm alfalfa stems with very few leaves and bare soil.

The scatter plot of CAI and NDVI showed the clustering of cover types (Fig. 9). Green vegetation and water had similar CAI values, but significantly differed in NDVI. Likewise, the crop residues, water, soil, and mowed alfalfa had similar NDVI values, but differed significantly in CAI. Mow alfalfa and bare soil were confounded. One corn residue field that was wet was also confounded with water in this scatterplot (Fig. 9). Thus, pairs of vegetation indices may be useful in discriminating most, but not all, cover types.

The relative weights assigned to each end-member spectrum by the linear spectral unmixing analysis are shown in Table 3. The cover types were generally represented by the appropriate end-members. For example, the crop residue cover type was represented by the corn residue and the plowed soil end-members. The relative abundance of the soil, crop residue, and green vegetation end-members are shown in Figure 10. Fields with high relative abundance values of soil and crop residue have low values for green vegetation. High relative abundance of green vegetation also corresponds to high NDVI values.

4. CONCLUSIONS

Although reflectance spectra of crop residues and soils are similar in the 400-1000 nm wavelength region, three broad absorption features in the reflectance spectra of the crop residues are not evident in the soils spectra . Band-depth analysis of these absorption features using simulated mixed residue-soil scenes indicated that quantitative assessment of crop residue cover is possible. The CAI, which estimated the depth of the absorption at 2100 nm, separated crop residues from soils. In this preliminary study with early Spring AVIRIS data of the Beltsville Agriculture Research Center, NDVI and CAI provided better separation of fields with residue than the end-member analysis. A multiband radiometer with the two NDVI bands and the three CAI bands could be used as a replacement for the manual line-transect method of for measuring field crop residue cover. Regional surveys and maps of crop residue cover and conservation tillage practices may be feasible using hyperspectral imaging systems.

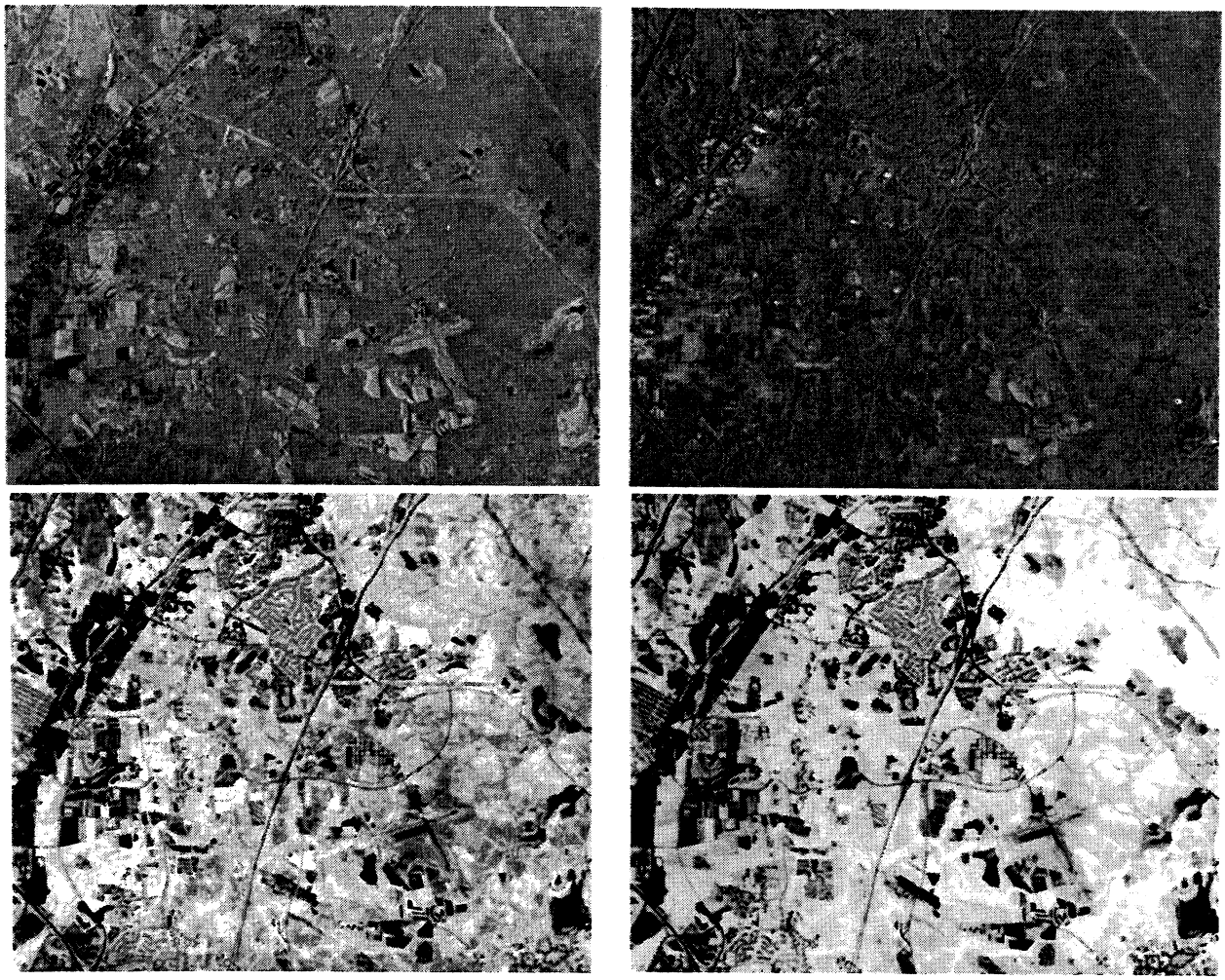

Figure 10. Relative abundance of soil (upper left), residue (upper right), and green vegetation (lower left) end-members. NDVI image (lower right). In each image, white represents high values and black represents low values.

5. REFERENCES

Aase, J. K. and D. L. Tanaka. 1991. Reflectance from four wheat residue cover densities as influenced by three soil backgrounds. Agronomy J. 83:753-757.

Baird, F. and Baret, F. 1997. Crop residue estimation using multiband reflectance. Remote Sens. Environ. 59:530-536.

Baumgardner, M. F., Silva, L. F., Biehl, L. L., and Stoner, E. R. 1985. Reflectance properties of soils. Advances in Agronomy 38:1-44.

Corak, S. J., Kaspar, T. C., and Meek, D. W. 1993. Evaluating methods for measuring residue cover. J. Soil Water Conservation 48:700-704.

Curran, P. J. 1989. Remote sensing of foliar chemistry. Remote Sens. Environ. 30:271-278.

Daughtry, C. S. T. 2001. Discriminating crop residues from soil by shortwave infrared reflectance. Agronomy J. 93:125-131.

Daughtry, C. S. T., J. E. McMurtrey III, E. W. Chappelle, W. P. Dulaney, J. R. Irons, and M. B. Satterwhite. 1995. Potential for discriminating crop residues from soil by reflectance and fluorescence. Agronomy J. 87:165-171.

Daughtry, C. S. T., P. L. Nagler, M. S. Kim, J. E. McMurtrey III, and E. W. Chappelle. 1996. Spectral reflectance of soils and crop residues. pp. 505-510. *In* A.M.C. Davies and Phil Williams (eds) Near Infrared Spectroscopy: The Future Waves. NIR Publications, Chichester, UK.

Elvidge, C. D. 1990. Visible and near infrared reflectance characteristics of dry plant materials. Int. J. Remote Sensing 10:1775-1795.

Gao, B. C. and Goetz, A. F. H. 1994. Extraction of dry leaf spectral features from reflectance spectra of green vegetation. Remote Sens. Environ. 47:369-374.

Kokaly, R. F. and Clark, R. N. 1999. Spectroscopic determination of leaf biochemistry using band-depth analysis of absorption features and stepwise multiple linear regression. Remote Sens. Environ. 67:267-287.

McMurtrey III, J. E., E. W. Chappelle, C. S. T. Daughtry, and M. S. Kim. 1993. Fluorescence and reflectance of crop residue and soil. J. Soil Water Conservation 48:207-213.

Morrison, J. E., Jr., C. Huang, D. T. Lightle, and C. S. T. Daughtry. 1993. Residue cover measurement techniques. J. Soil Water Conservation 48:479-483.

Morrison Jr., J. E., Lemunyon, J., and Bogusch Jr., H. C. 1995. Sources of variation and performance of nine devices when measuring crop residue cover. Trans. Amer. Soc. Agricultural Engineers 38:521-529.

Murray, I. and Williams, P. C. 1988. Chemical principles of near-infrared technology. pp.17-34. *In* Williams, Phil and Norris, Karl (eds) Near-Infrared Technology in the Agricultural and Food Industries. Amer. Assoc. Cereal Chemists, St. Paul, MN, USA.

Nagler, P. L., Daughtry, C. S. T. and Goward, S. N. 2000. Plant litter and soil reflectance. Remote Sens. Environ. 71:207-215.

Robinson, B. F. and Biehl, L. L. 1979. Calibration procedures for measurements of reflectance factor in remote sensing field research. Proc. Soc. Photo-Opt. Instrumentation Engineers. SPIE 196:16-26.

CALIBRATION AND VEGETATION FIELD SPECTRA COLLECTION FOR THE 2000 AVIRIS HAWAII DEPLOYMENT

Philip E. Dennison,[1] Margaret E. Gardner,[1] Dar A. Roberts,[1] and Robert O. Green[2]

[1] University of California, Santa Barbara, California
[2] Jet Propulsion Laboratory, Pasadena, California

Introduction

As part of the April 2000 AVIRIS Hawaii deployment, two researchers from the University of California, Santa Barbara, were sent to Hawaii to collect supporting field data. The primary goal of the fieldwork was to obtain spectra of bright targets to be used for retrieving surface reflectance from AVIRIS imagery. Secondary goals included recording the spectra of dominant vegetation, marking the position of homogeneous land cover for use as potential image endmembers (PIEs), and recording firsthand impressions of cover types. Primary and secondary goals were met. Spectra were recorded for 12 calibration targets on 5 islands and spectra were obtained for 61 vegetation species. Twenty PIEs were located, and video was used to document cover at 56 locations.

Background

An analytical spectral devices full range (FR) spectrometer was used to measure surface radiance. The FR spectrometer samples at an interval of 1.4 nm between 350 and 1000 nm and at an interval of 2.0 nm between 1000 and 2500 nm (Analytical Spectral Devices, Boulder, Colorado). A spectralon panel was used as a reference standard. Raw digital numbers (DNs) were recorded for both the material being measured and the standard. A differential global positioning system (GPS) was used to record the location of spectra, PIEs, and video recordings. The United States Coast Guard (USCG) differential signal was used to enhance positional accuracy. Coverage by the USCG signal was spotty and in many locations differential correction was not available. Estimated positional error, supplied by the GPS unit, was recorded for most locations.

Calibration Targets

Possible calibration targets were evaluated on the basis of their brightness, size, and probable Lambertian behavior. High reflectance, approximate Lambertian targets at least 40 meters by 40 meters in size were sought. Past experience from Southern California AVIRIS reflectance retrieval (Roberts et al., 1998) has shown that beaches provide excellent calibration spectra. Nine of the 12 documented targets are beaches (Table 1). One gravel and 2 bare soil targets were also acquired. Clouds restricted our ability to measure several of the calibration targets. Spectra were recorded in transects along each of the targets, except where noted.

Spectra of 5 calibration targets were recorded on Oahu. The highest-quality calibration site on Oahu was Waimea Bay Beach. Makaha Beach, on the west side of the island, was slightly smaller but was plagued by cloud cover. Waimea Bay Beach and Makaha Beach were the only beaches on Oahu to fit the target size criterion. A bright, flat field, recently cleared and graded for an industrial park, was found north of Kapolei. There was no activity at the site during two site visits on April 5th and April 7th, but the site likely saw activity soon afterward. Reflectance at this site appeared to be less homogeneous than at Waimea Bay or Makaha beaches. Spectra were also taken at Ala Moana Beach and at Kahe Point Beach; however, these beaches may not be wide enough to ensure a pure pixel within an AVIRIS image.

The Big Island (Hawaii) has few wide coral beaches. The best beach target on the island was Hapuna Beach, south of Kawaihae. The pier at Kawaihae, constructed of crushed rock, is also an adequate calibration target. The pier is a larger target but is probably less Lambertian than Hapuna beach. Cloud cover and a lack of wide, bright beaches prohibited obtaining a calibration target for the east side of the Big Island. Calibration targets were also difficult to find at high elevation. Spectra were taken along a transect of a sparsely vegetated hillslope at an elevation of 3000 meters on Mauna Kea. The slope of the target was measured at 14 deg, so it may be difficult to use for calibration.

Majors Bay Beach was the only calibration target on Kauai that fit the target criteria. The transect of Majors Bay Beach was interrupted by clouds, so the quality of the spectra is unknown. Cloud cover also interfered with obtaining spectra on Maui and Molokai. Sand samples from Oneloa Beach (Maui), the Kalaupapa Pennisula (Molokai), and Papohaku Beach (Molokai) were removed and sealed in plastic bags. The spectra of these samples were measured in Santa Barbara. A high-quality, cloudless transect of Papohaku Beach was done after the sample

was taken. Papohaku Beach was the widest beach encountered in the islands, and is considered the better of the two calibration targets for Molokai. Comparison of spectra from Kalaupapa and Papohaku Beach reveal differences in sand composition (Figure 1). The Papohaku beach spectrum indicates a deeper broad absorption feature between 800 and 1100 nm, possibly due to higher iron content. Carbonate absorption is evident in both beach spectra.

Vegetation species

Meetings with U.S. Fish and Wildlife, National Park Service, and National Tropical Botanical Garden scientists produced a list of important native and non-native vegetation species in the Hawaiian Islands. Dominance, prevalence, vegetation height, and likelihood of cloud cover were all considered in creating the list. Agricultural crops were given lowest priority, since their spectra can be collected from other sources or using PIEs. The variety of spectra is less than desirable for a few of the species. For example, *Metrosideros polymorpha*, although abundant, was only measured in a few locations within Volcanoes National Park, where stature is shorter and cloud cover was not a problem. Spectra were obtained for native rainforest dominants, including *Acacia koa* and *Metrosideros polymorpha*, lowland dominants including *Aleurites moluccana, Grevillea robusta, Hibiscus tiliaceus*, and *Syzygium cumini*, and dry montane dominants, including *Sophora chrysophylla* and *Styphelia tameiameiae*. Important invasive species sampled include *Lantana camera, Pennisetum setaceum, Schinus terebinthifolius*, and *Ulex europaeus*.

PIEs and Video Documentation

Large areas with homogeneous cover can be extracted from an AVIRIS image to obtain a relatively pure image endmember. Sites at least 40 meters by 40 meters, approximately four times the size of an AVIRIS pixel, can be selected as potential image endmember (PIE) sites. PIEs were also used when cloud cover or high canopies prevented direct spectral measurement. PIE locations were recorded and will be used to extract image endmembers from registered AVIRIS images. PIEs included agricultural crops (ex: coconut, sugar cane, pineapple, taro), homogeneous vegetation cover (ex: *Prosopis pallida, Bambusa vulgaris*) and non-vegetated areas (ex: basalt flows).

Video was used to document calibration targets and PIEs. Video was also recorded in locations that offered commanding views of surrounding terrain. This video footage will be used to assist image interpretation.

Results

Spectra were averaged and processed to reflectance. A total of 182 calibration reflectance spectra and 884 vegetation reflectance spectra were produced. Sixty species are represented in vegetation library. Calibration spectra are freely available for reflectance processing of AVIRIS data; contact the authors to receive a copy of the calibration library. The vegetation library and PIEs will be used to build regionally specific spectral libraries for the Hawaiian Islands. These libraries will be used to map vegetation cover in leeward areas of the islands. Vegetation maps will in turn be used to estimate fire hazard in these areas.

The utility of the calibration spectra and PIEs was demonstrated by mapping the extent of three introduced species on the Kalaupapa Peninsula and "topside" Molokai. The AVIRIS f000425t01p03_r02, scene 5 contains a calibration target on the tip of the Kalaupapa Peninsula and PIEs for *Lantana camera*, *Schinus terebinthefolius*, and *Casuarina spp. Lantana camera* dominates the north side of the peninsula, while *Schinus terebinthefolius* grows in the central portion of the peninsula. *Casuarina* has been planted as a timber tree on the cliffs above the peninsula. The AVIRIS scene was processed to reflectance, using the methods described in Green et al., 1993. Averaged reflectance from several calibration spectra was used to adjust the modeled reflectance.

PIEs were plotted on a map of the peninsula and image endmembers were extracted from single pixels in the AVIRIS scene. ENVI's matched filter routine was used to match image spectra to the three extracted image endmembers (Better Solutions Consulting, Lafayette, Colorado and Research Systems Inc., Boulder, Colorado). Matched filter sigmas greater than 0.4 are plotted in Figure 2. The matched filter results closely agree with field observations of extent for all three species.

Conclusions

Calibration spectra, vegetation spectra, and PIEs were acquired on five Hawaiian islands as part of the 2000 AVIRIS Hawaii deployment. Freely available calibration reflectance spectra can aid retrieving reflectance from AVIRIS imagery collected during the deployment. Vegetation reflectance spectra and image endmembers extracted from PIE sites will be used for mapping dominant vegetation cover. Matched filter mapping of three vegetation species on the Kalaupapa Peninsula and topside Molokai demonstrates the use of calibration spectra and PIEs for vegetation mapping.

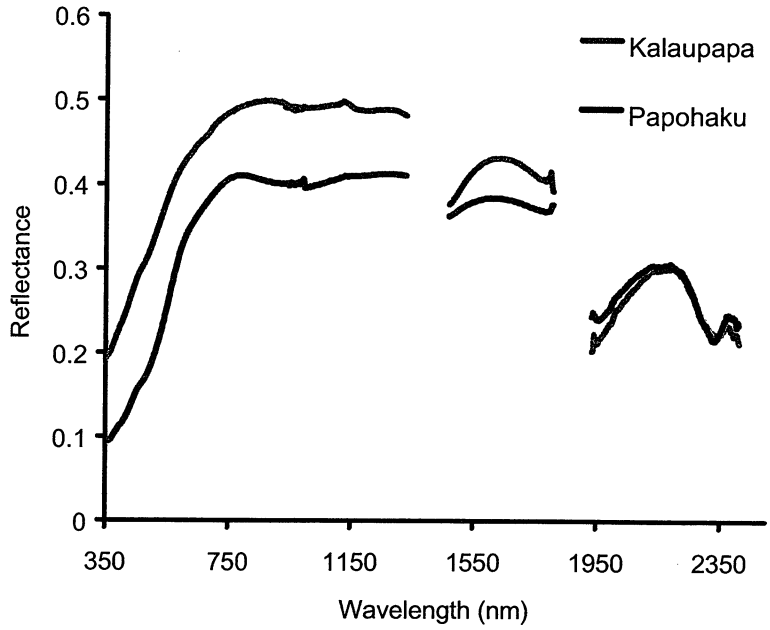

Figure 1. Spectra from Kalaupapa and Papohaku beaches.

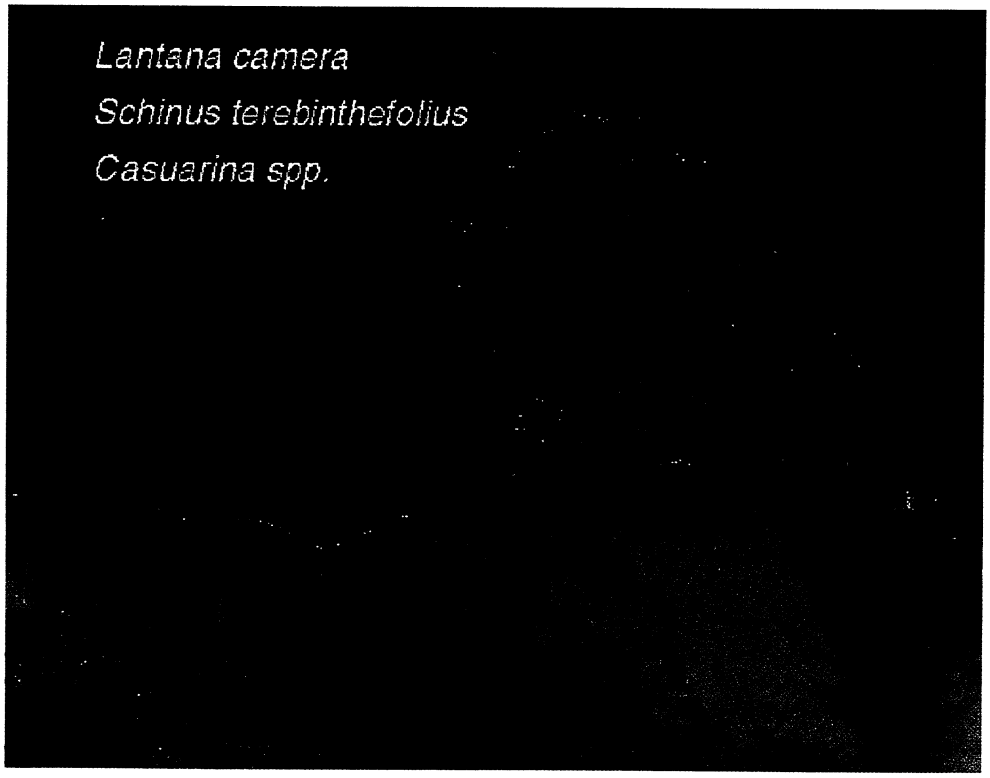

Figure 2. Matched filter results for three species found on the Kalaupapa Peninsula and topside Molokai.

Table 1. Calibration Targets

Date	Location	Island	#spectra	Latitude	Longitude	Elev. (m)	Surface	Comments
4/6/00	Ala Moana Beach	Oahu	7	21.288	-157.846	0	sand	clouds
4/7/00	Kapolei	Oahu	27	21.329	-158.088	0	compacted soil	clouds
4/7/00	Kahe Pt. Beach	Oahu	10	21.360	-158.132	0	sand	beach < 20 m wide
4/7/00	Waimea Bay Beach	Oahu	24	21.639	-158.064	0	sand	excellent
4/9/00	Makaha Beach	Oahu	4	21.476	-158.22	0	sand	clouds
4/11/00	Kawaihae	Hawaii	25	20.030	-155.83	0	gravel	excellent
4/11/00	Hapuna Beach	Hawaii	22	19.991	-155.826	0	sand	excellent
4/14/00	Mauna Kea	Hawaii	17	19.763	-155.619	3000	soil, rock and grass	east facing slope
4/18/00	Majors Bay Beach	Kauai	3	21.995	-159.767	0	sand	clouds
4/29/00	Papohaku Beach	Molokai	16	21.174	-157.254	0	sand	clouds
5/2/00	Oneloa Beach	Maui	10	20.633	-156.449	0	sand	measured in Santa Barbara
5/2/00	Kalaupapa	Molokai	8	21.209	-156.965	0	sand	measured in Santa Barbara
5/2/00	Papohaku Beach	Molokai	9	21.174	-157.254	0	sand	measured in Santa Barbara

Acknowledgements

The authors would like to thank the following people for their contributions:

Dr. Diane Ragone, Tim Flynn
Ron Nagata
Dean Alexander, Rick Potts
Darcy Hu
Pat Costales, Bob Hobdie, Jon Giffin, Ed Petteys
Ralston Nagata, Wayne Souza
Kevin Foster
Brian Farm, Jim Jacobi
Darryl Leer, Elizabeth Johnson
National Tropical Botanical Garden
NPS Haleakala NP
NPS Kalaupapa NHP
NPS Volcanoes NP
State of Hawaii Division of Forestry and Wildlife
State of Hawaii Division of State Parks
US Fish and Wildlife
USGS

Part of this research was carried out at the Jet Propulsion Laboratory, California Institute of Technology, under a contract with the National Aeronautics and Space Administration.

References

Green, R., J. Conel, and D. Roberts, 1993. Estimation of aerosol optical depth and additional atmospheric parameters for the calculation of apparent surface reflectance from radiance as measured by the Airborne Visible-Infrared Imaging Spectrometer (AVIRIS). *Fourth Annual JPL Airborne Sciences Workshop*, Jet Propulsion Laboratory, Pasadena, California, 73-76.

Roberts, D.A., M. Gardner, R. Church, S. Ustin, G. Scheer, and R.O. Green, 1998. Mapping chaparral in the Santa Monica Mountains using multiple endmember spectral mixture models, *Remote Sensing of the Environment*, 65 (3), 267-279.

NUTRIENT STRESS DETECTION IN CORN, USING NEURAL NETWORKS AND AVIRIS HYPERSPECTRAL IMAGERY

Lee Estep* and Bruce Davis**

1. INTRODUCTION AND BACKGROUND

The U.S. Department of Agriculture (USDA) Agricultural Research Service (ARS) Variable Rate (VRAT) Nitrogen Application site in Shelton, Nebraska, represents a well-documented, corn-growing quarter section. The USDA VRAT site is used to systematically study nutrient stress in corn by varying sub-plot application of fertilizer. The field has four replicates of five blocks that vary by nitrogen treatment from 0-kg/ha to 200-kg/ha in 50-kg/ha increments. The treatment blocks are set out in a randomized, complete block design.

Typically, the VRAT is planted in a ridge till, monoculture corn and is watered by a central pivot irrigation system on a three-day period. Since water stress can increase spectral reflectance from corn leaves (Wooley, 1971), it is important that the N-application plots be adequately watered so that only nutrient-related stress will predominate. Figure 1 shows imagery of the USDA VRAT site with the fertilizer amounts for each block shown.

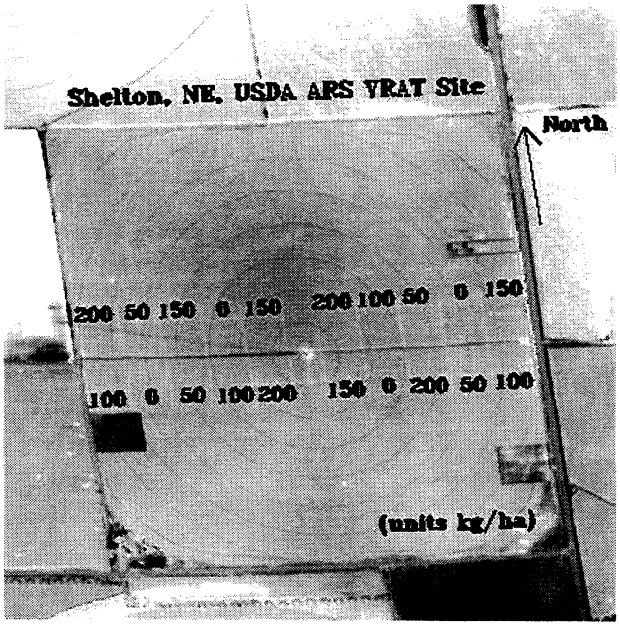

Figure 1. ATLAS NIR Image of USDA VRAT Study Site

* Lockheed Martin Space Operations – Stennis Programs, John C. Stennis Space Center (Leland.Estep@ssc.nasa.gov)
** NASA Geospace Applications and Development Directorate, John C. Stennis Space Center (Bruce.Davis@ssc.nasa.gov)

Portions of these data were kindly supplied by USDA ARS, the Boeing Company, Batelle Pacific Northwest Research Laboratory, and University of California, Santa Barbara, as part of a NASA-funded EOCAP project. This work was supported by the NASA Earth Science Applications Directorate under contract NAS 13-650 at the John C. Stennis Space Center, Mississippi.

Low-altitude AVIRIS hyperspectral imagery was acquired over the Shelton, Nebraska, VRAT site on July 22, 1999. The overflight produced 3-meter pixels with 224 spectral bands. Ground personnel supported the mission with measurements at the time of the overflight. The image data was pre-processed at JPL before being sent out to an investigator. The data arrived radiometrically corrected, allowing ready application of an atmospheric correction procedure. The Atmosphere Removal Program (ATREM) (Gao et al., 1993) was used to perform an atmospheric correction. The AVIRIS imagery after ATREM correction was output as relative reflectance. This relative reflectance file was scaled by an empirical line procedure to provide reflectances that matched closely those measured in the field.

2. APPROACH

The objective of this study was to compare the results of Artificial Neural Network (ANN) processing of hyperspectral image data for stress detection to the results of standard processing techniques and algorithms that have been exercised in the literature for the detection of crop, or plant, stress. A stress detection method or technique was evaluated by whether the imagery associated with the method or technique was capable of separating the different N-treatment blocks in the VRAT field from a set of controls – with the best nourished, 200-kg/ha plots as the controls.

The ANN program used in this study applies a standard back propagation method (Rumelhart and McClelland, 1986) to adjust the nodal weights and biases using an iterative, gradient descent technique so that the network "learns," or trains, given input data and output target values (Haykin, 1994). The neural network program used in this study was implemented in the following manner. First, reflectance values associated with regions of interest (ROI's) were extracted from each of the five plots, within the two replicates on the western side of the VRAT field. The pixel data were collated row-wise for each type treatment block and the amount of fertilizer provided to the plot (e.g., 50-kg/ha, 100-kg/ha) was appended to the end of the row of pixel spectral data. Once completed for each treatment plot, the merged data set for all the test blocks formed the input file used by the back-propagation, neural network for training.

When training was completed, the resulting weights and biases for the relevant network topology were saved and used to compute, on a pixel-by-pixel basis, an apparent fertilizer application over the two replicates on the eastern side of the VRAT field. The apparent fertilizer amounts for this region were then displayed as an image, which, in turn, could be interpreted as a nutrient stress index over the VRAT field.

3. DISCUSSION

Relevant algorithm results that were compared included the following:
1) Normalized Difference Vegetation Index (NDVI) (Rouse et al., 1974)
2) Rededge (Horler et al., 1983)
3) Weighted Difference Vegetation Index (WDVI) (Clevers, 1988)
4) Transformed Soil Adjusted Vegetation Index (TSAVI) (Baret and Guyot, 1991)
5) Three Channel Vegetation Index (TCHVI) (Efremenko et al., 2000)
6) Gitelson and Merzlyak (1996)
7) Red-edge Stress Vegetation Index (RSVI) (Merton, 1998)
8) Estep (2000)

The ANN results were also compared to results generated by two supervised classification procedures. Comparative imagery between the above algorithms and trained neural network imagery are displayed for the venerable NDVI algorithm only. Refer to Table 1 for a complete comparison summary of results.

3.1 Comparison of NDVI Neural Network and Plant Stress Algorithm Results

AVIRIS Bands 36 and 52 provide the requisite red and near-infrared (NIR) bands required for the NDVI computation. Figure 2 shows the NDVI results over the VRAT site. Note that the untreated blocks (0-kg/ha) are readily distinguishable. To a lesser extent, the 50-kg/ha treatment blocks exhibit some stress as well. Moreover, the 100-kg/ha block on the eastern margin of the field visually shows stress. This stress, however, can be somewhat ascribed to a misapplication of the fertilizer – but not all.

The AVIRIS NDVI image also picks up a stressed area of vegetation, seen as a darker-toned band on the north-central periphery of the field. The irrigator is turned off over this area to create water stress effects in the corn. This deliberately stressed region is used in this study to assess whether a given algorithm, or neural network result, can distinguish nutrient stress from water stress effects in corn.

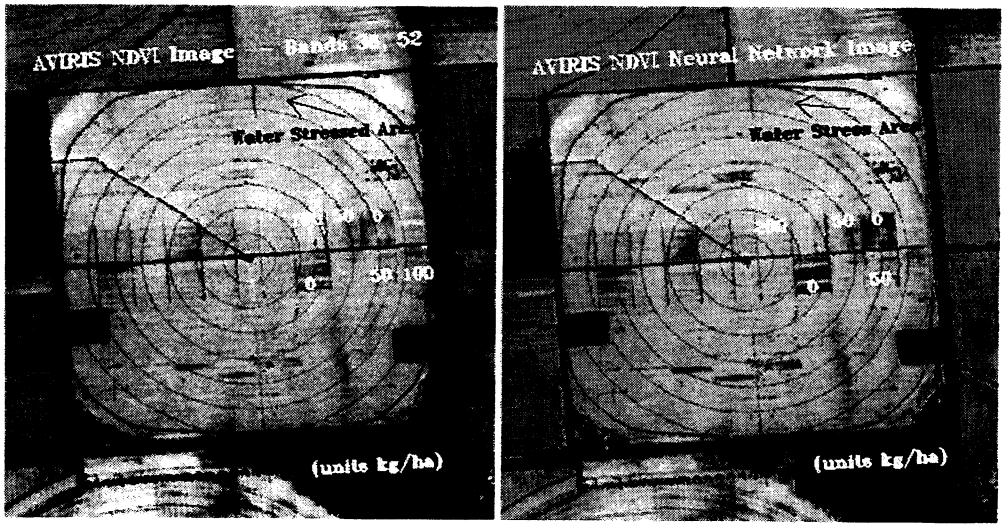

Figure 2. NDVI Comparison Images, Bands 37 and 51 (both images similarly stretched)

In comparison, Figure 2 also provides the neural network equivalent of the NDVI. Both images were stretched by the same default values. Here, "equivalent" means that the same bands that are used to compute the NDVI are used as input data to train the neural network. In this way, one can assess whether a neural network that has learned to distinguish the different levels of nutrient stress present over the VRAT can perform as well as the standard NDVI algorithm at displaying extant crop stress, given the selected spectral data input. As seen, the neural network version of a hyperspectral NDVI provides comparable nutrient stress information for the relevant treatment blocks. Note that both the neural network result and the NDVI algorithm detect the water stress area.

It is interesting to compare these two single-band images by plotting their average NDVI value side by side as a function of nitrogen treatment. Using ROI's, plot data were extracted from the images in Figure 2 and compiled. Figure 3 shows curves of the respective plot data.

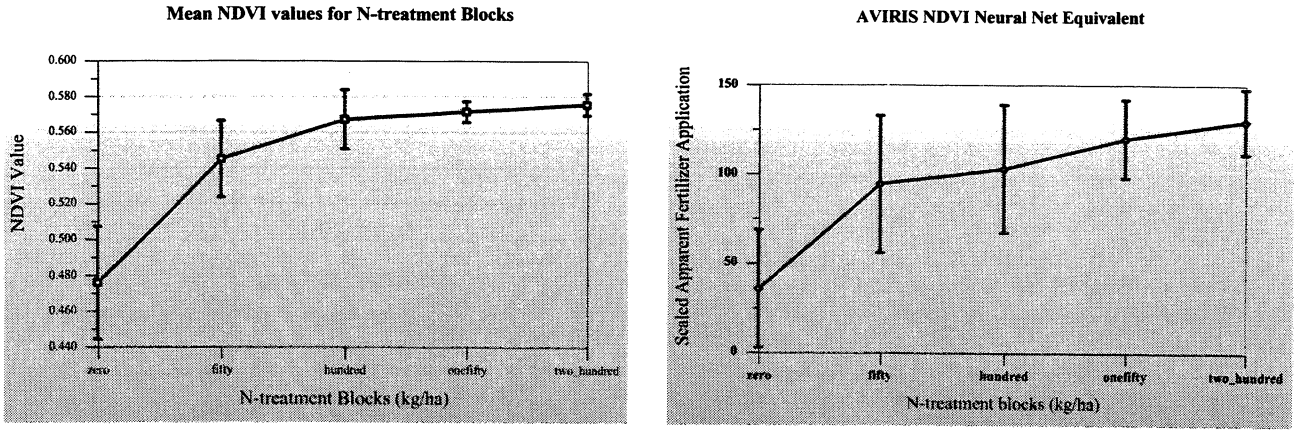

Figure 3. NDVI Algorithm and ANN Data Plot

The graph on the left in Figure 3 shows the mean NDVI values plotted against the N-treatment blocks from which the NDVI values were extracted. Error bars are also plotted and represent an excursion of one standard deviation above and below the mean value. In image terms, a given mean NDVI value is really a mean brightness associated with an N-treatment plot. The error bars, then, express the dominant range of brightness values that is associated with an N-treatment plot.

In both plots shown in Figure 3, a falling off of the NDVI-type values is seen at the higher levels of fertilizer application. This appears to be something of a saturation effect. This roll-off signals a loss of sensitivity in the detection of the N-treatment plots at the higher nitrogen applications. This loss can make it difficult to distinguish the higher N-treatment applications from the controls. Note that the roll-off seen in the ANN graph in Figure 3 is somewhat mitigated. The general trend of the plot stays the same – moving from lower to higher values of effective N-application.

Given the data used to construct Figure 3, an ANOVA was run. The results for both data sets provided for the rejection of the null hypothesis at the $p < 0.0001$ level. The follow-on Dunnett multiple comparison tests (Siegel, 1956), which compare the mean 0-, 50-, 100-, and 150-kg/ha plots to the controls, determined that the standard NDVI algorithm could separate all N-treatment plots from the controls. The mean 0-, 50-, and 100-kg/ha plots were separable from the controls at a $p < 0.01$ level. The mean 150-kg/ha plot was separable from the controls at the $p < 0.05$ level.

The Tukey-Kramer multiple comparison tests (Siegel, 1956), which intercompare all plots with one another, showed that the standard NDVI algorithm could not separate statistically the 100-kg/ha mean plot from the 150-kg/ha mean plot. This result is not surprising, given the fact that the NDVI saturates somewhat at higher fertilizer applications. In contradistinction, the neural network NDVI equivalent results allowed complete separation between all mean N-treatment plots and the controls at a $p < 0.01$ level of significance. Moreover, the Tukey-Kramer multiple comparison tests for the neural network results showed all mean blocks separable from one another at the $p < 0.01$ level.

3.2 Compilation of Comparison Results

Table 1 provides a head-to-head comparison between ANN outcomes and the associated standard algorithm results. Column 1 names the algorithm used. Columns 2 and 4 provide the mean N-treatment blocks that can be separated from the controls by the standard algorithm and the neural network, respectively. SAM and MLC refer to Spectral Angle Mapper and Maximum Likelihood Classifier respectively. The last column states whether the band of deliberately water-stressed corn was visible in either the imagery associated with the standard algorithms or the imagery associated with the neural network outcome, respectively. As can be seen, the neural network results are consistently better at statistically separating the N-treatment blocks from the controls.

Table 1. Comparison Summary of Standard Algorithms and Neural Network Results

Standard Algorithm Name/Clevers' Bandset	Block/Control Separation – Algorithm	Neural Network Bands Used	Block/Control Separation – Neural Net	Sensitive to Water Stress – Algorithm/ Neural Net (y/n)
NDVI	0,50,100,150	Bands 36,52	0,50,100,150	Y/Y
Red Edge	0,50,100,150	Bands 36-40	0,50,100,150	Y/Y
Gitelson-Merzlyak	0,50,100	Bands 19,43	0,50,100,150	N/Y
RVSI (Merton)	0,50,100	Bands 39,41,43	0,50,100	Y/Y
WDVI	0,50,100,150	Bands 36,53	0,50,100,150	Y/Y
TSAVI	0,50,150	Bands 36,53	0,50,100,150	Y/Y
TCHVI	0,50,100	Bands 20,36,53	0,50,100,150	Y/N
Estep	0,50,100,150	Bands 12,20	0,50,100,150	N/Y
Clevers VIS SAM/Nnet	0,50,100	Bands 15-38	0,50,100	Y/Y
Clevers NIR SAM/Nnet	0,50	Bands 41-107	0,50,100,150	Y/Y
Clevers SWIR SAM/Nnet	0	Bands 122-206	0,50,100	Y/Y
Clevers VIS MLC/Nnet	0,50	Bands 15-38	0,50,100	Y/Y
Clevers NIR MLC/Nnet	0,50,100	Bands 41-107	0,50,100	Y/Y
Clevers SWIR MLC/Nnet	0	Bands 122-206	0,50,100	Y/Y

4. SUMMARY

AVIRIS image cube data were processed for the detection of pre-visual stress in corn by both standard algorithmic forms and by trained artificial neural networks. The ANN results, compared to analogous forms of known stress algorithms, appear to provide a better overall capability to separate stressed crops from in-field controls.

The stress present over the VRAT arose from two predominant sources: nutrient stress and water stress. The deliberately water-stressed area on the northern boundary of the VRAT provided an important reference region. This water-stressed region allowed an assessment of the sensitivity of the tested stress detection techniques – both algorithmic and ANN – to discriminate between these two important types of crop stress. As shown in Table 1, in only three cases were the two sources of stress separated. However, this finding could possibly provide a benefit to the grower community, if further corroborated, by yielding a technique to distinguish between these important crop stressors.

5. REFERENCES

Baret, F., and G. Guyot, 1991, "Potentials and Limits of Vegetation Indices for LAI and APAR Assessment," Rem Sens. Env., vol. 35, pp. 161-173.

Clevers, J., 1988, "Application of a Vegetation Index in Correcting the Infrared Reflectance for Soil Background," International Archives of Photogrammetry and Remote Sensing, vol. 16, pp. 221-226.

Efremenko, V., A. Moshkov, A. Semenov, and T. Chimitdorzhiev, 2000, "Methods for Identifying Oppressed Vegetation from Spectral Scanner Data," Earth Obs. Rem. Sens., vol. 15, pp. 853-862.

Estep, L., 2000, Thermal and VNIR Remote Sensing of Nutrient Stress in Corn, NASA/Lockheed Martin Technical Report.

Gao, B., K. Heidebrecht, and A. Goetz, 1993, "Derivation of Scale Surface Reflectances from AVIRIS Data," Rem. Sens. Env., vol. 44, pp. 165-178.

Gitelson, A. and M. Merzlyak, 1996, "Signature Analysis of Leaf Reflectance Spectra: Algorithm Development for Remote Sensing of Chlorophyll," J. Plant. Phys., vol. 148, pp. 494-500.

Haykin, S., 1994, Neural Networks: A Comprehensive Foundation, New York, NY: MacMillan.

Horler, D., M. Dockray, and J. Barber, 1983, "The Red Edge of Plant Leaf Reflectance," Int. Journ. Rem. Sens., vol. 4, pp. 273-288.

Merton, R., 1998, "Monitoring Community Hysteresis Using Spectral Shift Analysis and the Red-edge Vegetation Stress Index," JPL, AVIRIS Workshop.

Rouse, J., R. Hass, J. Schell, D. Deering, and J. Harlan, 1974, Monitoring the Vernal Advancement and Retrogradation of Natural Vegetation, NASA Report, Greenbelt, MD.

Rumelhart, D., and J. McClelland, 1986, Parallel Distributive Processing, Vols. 1 and 2, Cambridge, MA: MIT Press.

Siegel, S., 1956, Non-parametric Statistics, New York: McGraw-Hill.

Wooley, J., 1971, Reflectance and Transmittance of Light by Leaves," J. Plant Phys., vol. 47, pp. 656-662.

ANALYSIS OF AVIRIS DATA: A COMPARISON OF THE PERFORMANCE OF COMMERCIAL SOFTWARE WITH PUBLISHED ALGORITHMS

William H. Farrand[1]

1. Introduction

An early handicap to the effective use of AVIRIS data was a lack of appropriate software (Vane and Goetz, 1993). With improvements to the AVIRIS sensor have also come improvements in the available software. While there are a variety of software packages currently in use, a review of the recent literature indicates that most users of AVIRIS data are using the commercial ENVI software. The documentation provided with the ENVI software (RSI, 2000) is generally quite adequate; however, specifics on how most processing routines are implemented are not provided. Moreover, the source code for ENVI routines are not readily available, thus the user who is curious about how certain algorithms are implemented is left with few options. The objective of this paper is to provide a comparison of how ENVI implementations of several mapping algorithms perform against implementations of those routines coded by the author from the original published algorithms. The mapping algorithms examined in this work are: linear spectral mixture analysis, constrained energy minimization/matched filtering, and band mapping. The ENVI routines used were from ENVI version 3.4 software release.

2. Spectral Mixture Analysis

While the ENVI User's Guide provides several references for linear spectral mixture analysis, the author compared results obtained from the ENVI "Linear Spectral Unmixing" module with those obtained from the algorithm developed at the University of Washington and described by Adams et al. (1993) and in earlier papers such as Smith et al. (1990), Possollo et al. (unpublished manuscript), and Gillespie et al. (1990). This algorithm will henceforth be referred to as the "UW algorithm."

The basis of linear spectral unmixing is to model the response of each spatial element as a linear combination of endmember spectra. The basis equation for linear spectral mixture analysis (SMA) is:

$$r(x,y) = \alpha\mathbf{M} + n$$

where: $r(x,y)$ = the relative reflectance spectrum for the pixel at position (x,y)
α = the vector of endmember abundances
$\mathbf{M}$ = the matrix of endmember spectra
n = the vector of residuals between the modeled and the measured reflectances

The result of Spectral Mixture Analysis (SMA) is a series of "fraction images" for each endmember wherein the data numbers range, ideally, between 0 and 1. Fraction image pixels with a DN of 0 are taken to be devoid of the endmember material. Fraction image pixels with a DN of 1.0 are taken to be completely covered with the endmember material.

The implementation of SMA in ENVI appears to be a relatively straightforward implementation that uses Singular Value Decompositon (SVD) to determine endmember abundances as detailed in Boardman (1989). The implementation of SMA described in the earlier references is slightly different in the way that it treats a "shade" endmember. The shade endmember is not a physical material but rather represents the "dark point" in the image scene; i.e., an ideal shade endmember would be a shadowed surface with zero reflectance at all wavelengths. While shade is not necessary for all analyses in which SMA can be used, it can be quite helpful for use in areas with substantial topographic relief, for use with forested scenes (to help determine canopy shade), or as a measure of surface roughness. Also, the procedure described in the ENVI User's Guide (RSI, 2000) for determining image endmembers almost always leads to the selection of a dark point image endmember. This ENVI method for

[1] Farr View Consulting/Space Science Institute, Boulder, Colorado (farrand@colorado.edu)

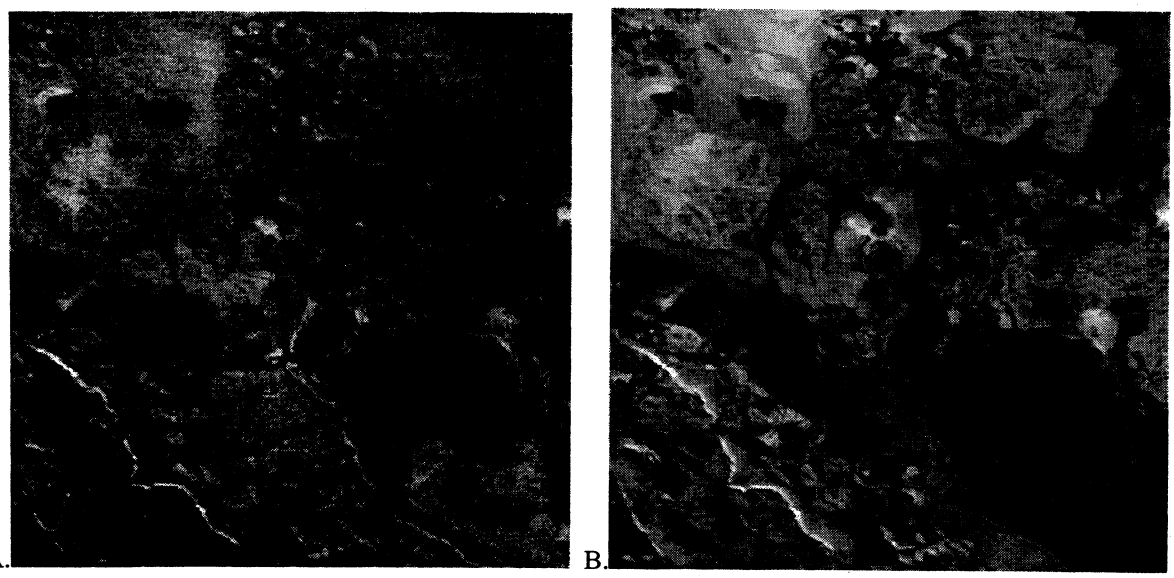

Figure 1. Comparison of shade images for AVIRIS scene over Lunar Crater Volcanic Field, Nevada, derived from applying SMA as implemented in A. ENVI and B. UW algorithm. Fraction images have been stretched between 0 and 1. The prominent diagonal cutting across the lower left corner represents shadows cast by a major cliff face.

determining image endmembers (eg., Boardman and Kruse, 1994) starts with the use of a Minimum Noise Fraction (MNF) transform to reduce spectral dimensionality. This is followed by the Pixel Purity Index reduction to find "spectrally pure" pixels. Finally, the ENVI n-dimensional visualization tool is used to find extreme "vertex" pixels at the edges of the n-dimensional data cloud. As mentioned above, in this author's experience if there is any significant shadowing in the scene, these "dark point" pixels will cluster together and generally constitute one of the more prominent clusters in the n-D data cloud. The user who selects these "shade" pixels might want to use them as an endmember in SMA. Thus, it is appropriate to determine how well the ENVI implementation of SMA treats shade.

The way that shade is handled in the UW algorithm is that:

1. the shade endmember spectrum is first subtracted from all other endmember spectra (eg., the "material" endmembers),
2. the endmember matrix is inverted to derive endmember fractions[2],
3. the sum of the material fraction images is subtracted from 1.0 and this difference is taken to be the shade fraction image.

The analyst who includes shade as an endmember with the ENVI "Linear Spectral Unmixing" module is including shade as a material endmember. Given the low data values in the shade endmember spectrum, erroneous fraction images can potentially result. Figure 1 shows shade fraction images derived from a 1994 AVIRIS scene of the Lunar Crater Volcanic Field in Nye County, Nevada. There are few if any substantive differences between the two fraction images. Shadowed to dark areas are bright as is expected. DN values of both fraction images are generally between 0 and 1.0 for both. This result ran counter to expectations since the author has observed flaws in shade fraction images derived from using the ENVI SMA implementation in past work. Specifically, when applied to lower dimensionality, multispectral data erroneous shade fraction images can result. An example is provide in Figure 2 wherein the same AVIRIS scene has been spectrally resampled to match the spectral bandpasses of the nine visible through SWIR channels of the ASTER sensor (Abrams, 2000). In this case, there is a marked difference between the two shade fraction images with the one derived from ENVI having erroneous shade fractions. The actual data values for the ENVI derived shade fraction image shown in Fig. 2a are all negative while those for the

[2] Possollo et al. (unpublished manuscript) describe the matrix inversion algorithm used in the UW implementation as being the QR factorization rather than SVD.

A. 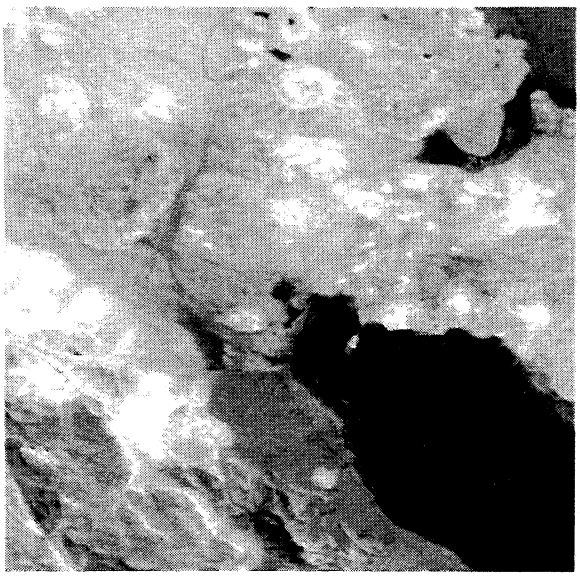 B. 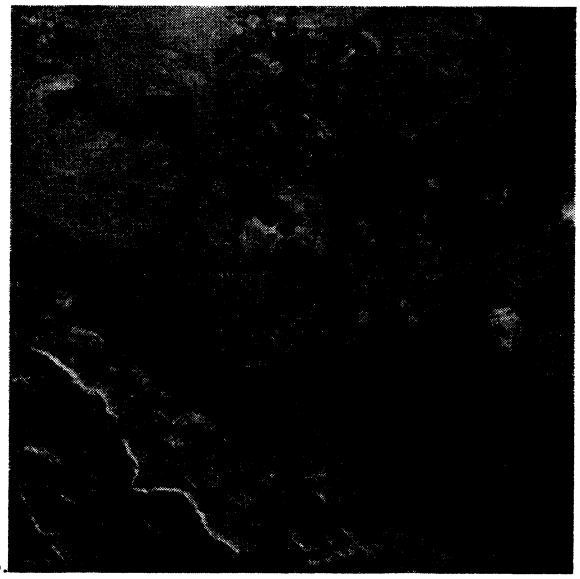

Figure 2. AVIRIS scene from Fig. 1 was resampled to ASTER Visible-SWIR bandpasses and SMA was applied. A. ENVI derived shade fraction image B. Shade fraction image derived from application of UW algorithm.

shade fraction image derived from the UW algorithm are predominantly between 0 and 1.0 as is desired for a fraction image.

While the straightforward linear spectral unmixing algorithm of ENVI does not handle shade in the same manner as the UW algorithm, the procedures implemented in the latter algorithm can be carried out entirely in ENVI. The ENVI "spectral math" routine can be used to subtract the shade endmember from the material endmembers. The ENVI linear spectral unmixing routine can be run using just the material endmembers. Then, using ENVI's "band math" routine, the sum of the material endmembers can be subtracted from 1.0 to produce a shade fraction image.

3. Constrained Energy Minimization/Matched Filter

ENVI has an implementation of a routine under the name of "Matched Filter" (MF) which is essentially the same algorithm described by Harsanyi (1993) and Farrand and Harsanyi (1997) as "Constrained Energy Minimization" (CEM). The CEM method is based on the linearly constrained adaptive beam-forming problem from the signal processing community. The solution to this problem is to minimize the average power received by a multielement antenna array subject to the constraint that a constant, unity response in the presumed direction of the target signal is maintained. In the instance of CEM/MF, a vector operator $\boldsymbol{w}$ is determined that suppresses the unknown and undesired background spectra while enhancing that of the known target spectrum, $\boldsymbol{d}$. The operator, $\boldsymbol{w}$, is defined by constraints to minimize the total output energy of all pixels and to require that when the operator is applied to the target signature, the output is 1.0. A solution that meets these constraints is provided by:

$$\boldsymbol{w} = \frac{\mathbf{R}_r^{-1}\boldsymbol{d}}{\boldsymbol{d}^T\mathbf{R}_r^{-1}\boldsymbol{d}}$$

where: $\mathbf{R}_r^{-1}$ = the inverse of the sample correlation matrix of the hyperspectral scene. Since $\mathbf{R}$ is ill-conditioned for hyperspectral images, it is difficult to calculate $\mathbf{R}^{-1}$. To circumvent this difficulty, the sample correlation matrix can be approximated by:

$$\mathbf{R} = \mathbf{V}\Lambda\mathbf{V}^T$$

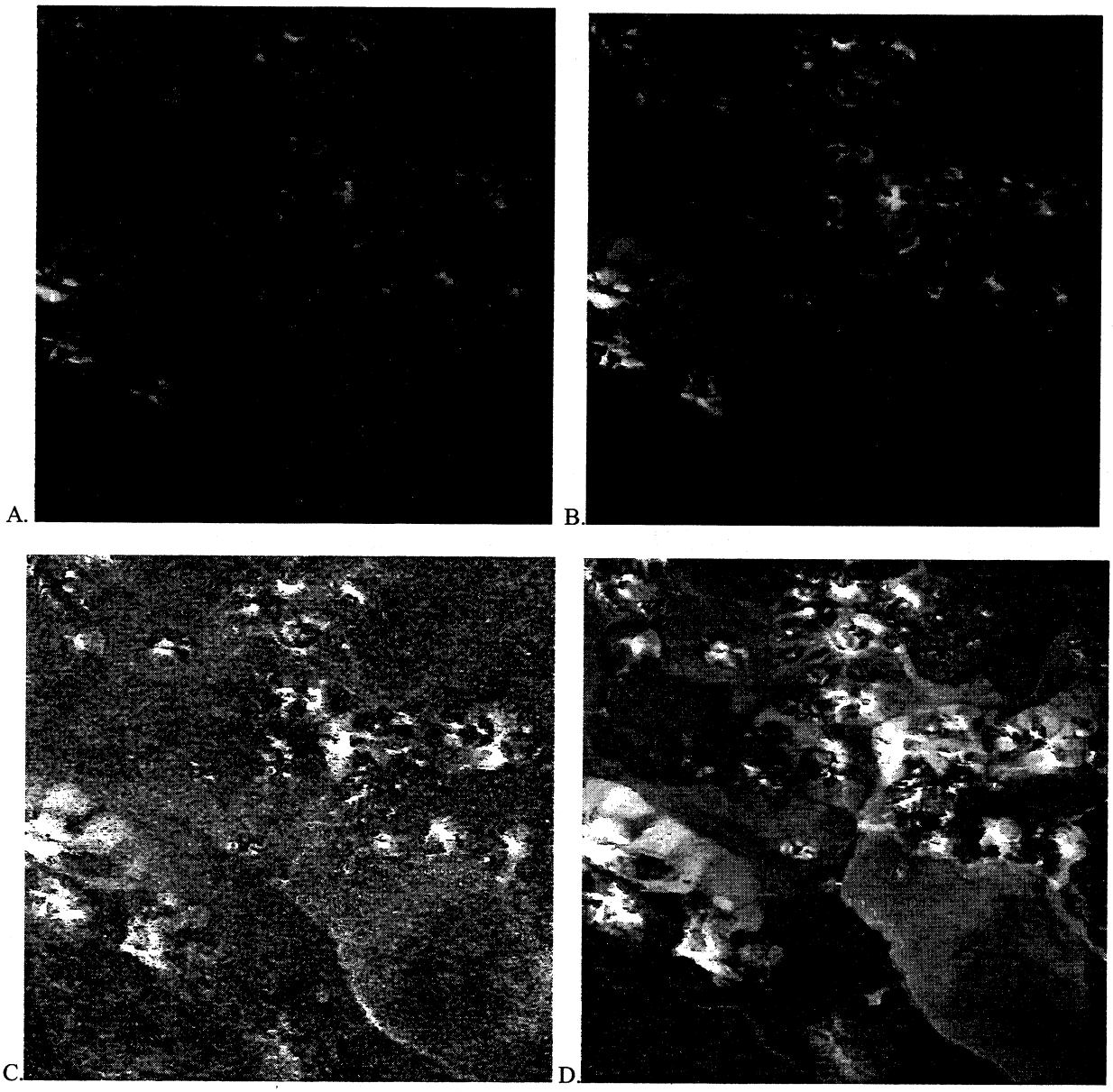

Figure 3: A. ENVI Matched Filter fraction image of red cinders for Lunar Crater Volcanic Field AVIRIS scene. Contrast stretch 0 to 1.0. B. CEM fraction image of red cinders for same scene with contrast stretch from 0 to 1.0. C. Same image as A. with no stretch. D. Same image as B. with no stretch.

where: **V** is a matrix populated by the eigenvectors of the sample correlation matrix, and Λ is a diagonal matrix with the eigenvalues of the sample correlation matrix. **V** can be approximated by a smaller matrix populated just with the first p significant eigenvectors. How to determine the value of p (i.e., how many significant eigenvectors are there?) can be somewhat subjective and in the author's experience the best results have been achieved by sometimes running CEM several times using a different number of significant eigenvectors each time. Unfortunately, the ENVI implementation of Matched Filter does not allow the user to specify the number of principal eigenvectors that will be used. Boardman (personal communication) suggests that this becomes a non-issue if MF is run not against the original AVIRIS data (or AVIRIS data converted to reflectance as was done in this study), but against the MNF-transformed data. However, this approach is not mentioned in the ENVI User's Guide; thus, the author compared results obtained from CEM, using a personally determined optimum number of principal eigenvectors, with those obtained running the ENVI MF routine against a non-MNF transformed AVIRIS scene. Figure 3 shows fraction images obtained from ENVI MF and from CEM for a red cinder target signature on the

same LCVF AVIRIS scene used above. Although the results are different, both are acceptable fraction images of the cinders; however, the unstretched versions of the images show a higher response from background materials in the MF image than in the CEM image- indicating a sub-optimal suppression of those background signatures.

Given that routines such as MF are often used for mineral exploration, a trial was also conducted using 1998 AVIRIS data collected over the Tushar Mountains/Marysvale mining district in central Utah (Farrand, 2000; Rockwell et al., 2000). In the author's experience, when mapping minerals whose diagnostic spectral features are in the SWIR (eg., alunite, kaolinite, etc.), the best results are obtained using a subset of SWIR channels. Likewise, when mapping Fe^{3+} - bearing minerals such as hematite and goethite, the best results are obtained using a VNIR only subset. This approach was pursued in this trial. Also, in this instance since the AVIRIS data were of high quality and there were excellent exposures of the target minerals, library spectra (from the USGS spectral library, Clark et al., 1993) were convolved to AVIRIS bandpasses and used as the target spectra. The results are shown in Figure 4 for a trial with kaolinite and in Figure 5 for a trial with hematite. It can be seen that the CEM and MF results for kaolinite are nearly identical while those for hematite show, as in the LCVF example above, a relatively high response from background materials for the MF versus the CEM image. The better performance of MF in the SWIR is attributed to a better ability to detect the proper cut-off point for the number of principal eigenvectors used in the suppression of the undesired background. There are more complicating background materials (primarily vegetation) with responses in the VNIR which make the selection of a proper number of principle eigenvectors more of a challenge for that spectral range.

4. Spectral Feature Fitting

Clark et al. (1990) described the algorithm that was the basis of what would evolve into the current USGS Tetracorder algorithm (Clark, 2001). While the current version of Tetracorder is a complex expert system, the basis algorithm is relatively simple. The "band mapping algorithm" described by Clark et al. (1990) is briefly recapitulated below. To map a given mineral with a specific absorption feature, for example, the 2.21 μm kaolinite doublet, a high resolution laboratory spectrum is re-sampled to the spectral resolution of AVIRIS. The spectrum is sub-sampled to match the specific absorption feature (i.e., only bands from the short wavelength shoulder of the absorption to the long wavelength shoulder are included). A straight line continuum (calculated based on a line between the two band shoulders) is divided out from both the laboratory and the AVIRIS spectra. The contrast between the library and the AVIRIS spectra are mitigated through the use of an additive constant, *k*. This constant is incorporated into a set of equations which are solved through the use of standard least squares.

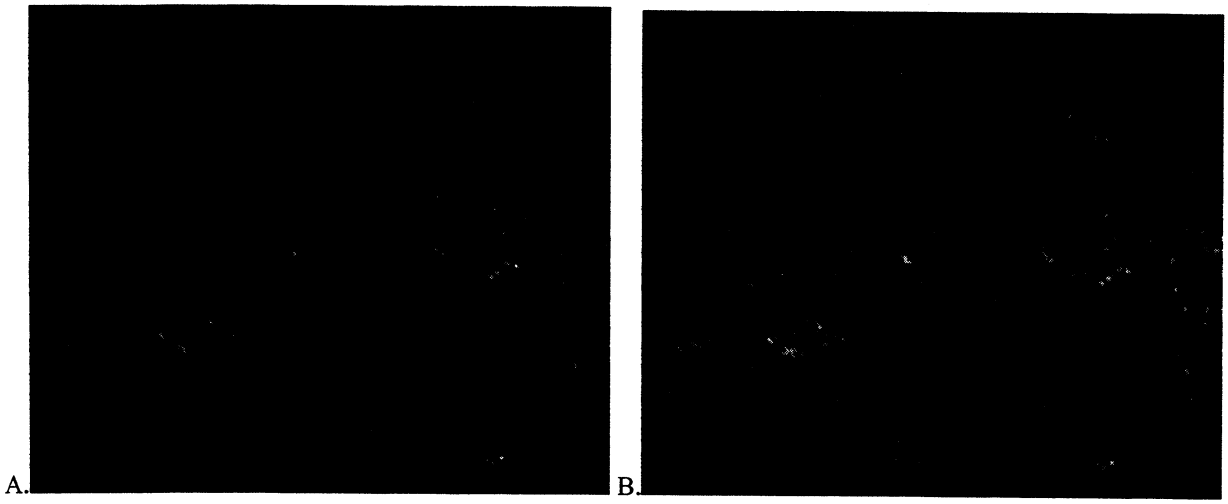

Figure 4. Comparison of fraction images derived for a library kaolinite target signature over the eastern Tushar Mountains/Marysvale mining district using A. ENVI Matched Filter (MF), and B. Constrained Energy Minimization (CEM). Images have been stretched between 0 and 1.

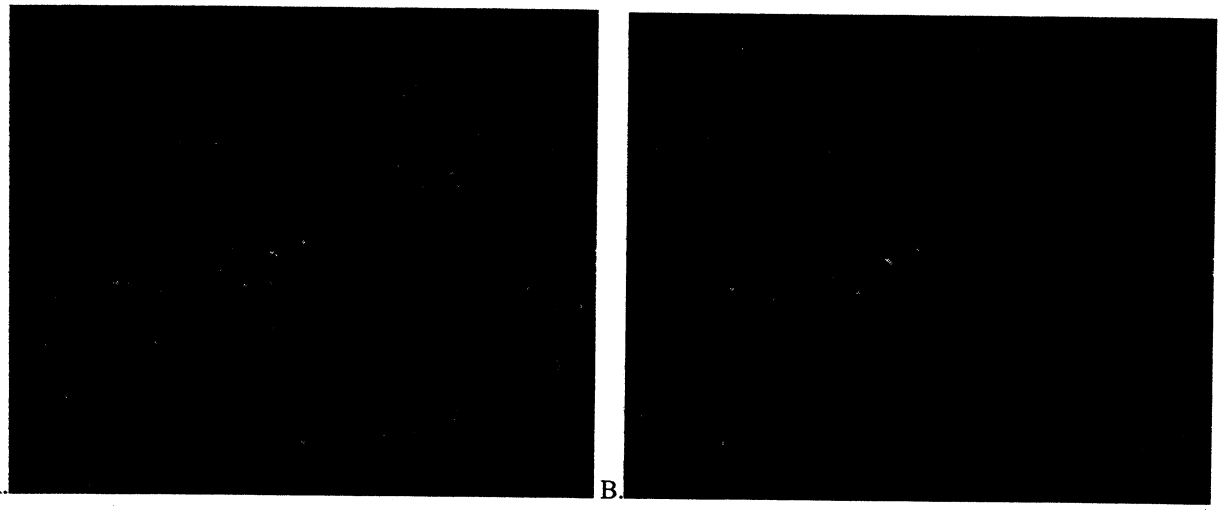

Figure 5. Comparison of fraction images derived for a library hematite target signature over the eastern Tushar Mountains/Marysvale mining district using A. ENVI Matched Filter (MF), and B. Constrained Energy Minimization (CEM). Images have been stretched between 0 and 1.

The result of the Clark et al. (1990) band mapping algorithm are two data numbers per spatial sample of the AVIRIS scene. First the band depth of the feature is calculated, and second a goodness-of-fit parameter is calculated. These two parameters are most often combined in a band depth times goodness-of-fit image.

The "Spectral Feature Fitting" routine incorporated in ENVI presumably uses similar equations to those recounted by Clark et al. (1990), but the basis equations for the ENVI algorithm are not provided in the ENVI User's Guide. Indeed, the output from the ENVI algorithm is rather different from that of the USGS band mapping algorithm. The output consists of a "scale" image, which appears comparable to the band depth image output by the band mapping algorithm, and a root mean square (rms) error image is also output. Presumably, the latter is the actual rms error of the fit between the library and the AVIRIS spectrum. The two images can be combined by dividing the scale image by the rms error image.

The author coded the band mapping algorithm described by the Clark et al. (1990) paper and compared results with those obtained by ENVI for the AVIRIS scene covering the eastern Tushar Mountains and Marysvale mining district in central Utah. Maps were produced of kaolinite, illite, and alunite. There were no substantive differences between the band depth times goodness-of-fit images derived from the band mapping algorithm and the scale/rms error images derived from the ENVI "spectral feature fitting" routine.

5. Conclusions

This study presented a comparison of the results obtained from implementations of published algorithms coded by the author and ENVI implementations of the corresponding algorithms. The linear spectral unmixing algorithm implemented in ENVI handles a "dark point" or "shade" endmember differently than the published Adams et al. (1993) spectral mixture analysis algorithm (SMA). It was found that using high dimensionality AVIRIS data, the dark point endmember could still be used to produce a reasonable fraction image; however, using lower dimensionality simulated multispectral data, the ENVI implementation of SMA produced an unreasonable "shade" fraction image.

In a comparison of Constrained Energy Minimization (Harsanyi, 1993; Farrand and Harsanyi, 1997) versus the ENVI implementation of the equivalent Matched Filter algorithm, it was found that results were generally similar; however, for materials whose primary spectral expression lie in the VNIR, the ENVI MF routine provided a sub-optimal suppression of the background. However, the performance of the MF routine can supposedly be enhanced by using it against MNF-transformed data (Boardman, personal communication).

It was found that results from the ENVI "spectral feature fitting" routine were essentially the same as those obtained from the Clark et al. (1990) band mapping algorithm. In using either approach, the analyst must exercise

care to use only those channels covering the absorption band of interest. In an early trial, the author used most of the AVIRIS spectrometer D channels with the ENVI "spectral feature fitting" algorithm and the results were inaccurate compared to those obtained in later trials using more precise spectral subsections covering just the absorption features of interest.

6. References

Abrams, M., 2000, "The Advanced Spaceborne Thermal Emission and Reflection Radiometer (ASTER): Data products for the high spatial resolution imager on NASA's Terra platform". *Int. J. Remote Sensing*, vol. 43, no. 5, pp. 847-859.

Adams, J.B., M.O. Smith, and A.R. Gillespie, 1993, "Imaging spectroscopy: Interpretation based on spectral mixture analysis". In *Remote Geochemical Analysis: Elemental and Mineralogical Composition*, edited by C.M. Pieters and P.A.J. Englert (New York: Cambridge University Press), pp. 145-166.

Boardman, J.W., 1989, "Inversion of imaging spectrometry data using singular value decomposition", in *Proc. IGARSS '89, 12th Canadian Symposium on Remote Sensing*, vol. 4, pp. 2069-2072.

Boardman, J.W., and F.A. Kruse, 1994, "Automated spectral analysis: A geological example using AVIRIS data, north Grapevine Mountains, Nevada", in *Proc. ERIM Tenth Thematic Conf. on Geologic Remote Sensing*, pp. I-407 – I-418.

Clark, R.N., 2001, "Tetracorder description and demonstration", Proc. 9th JPL Airborne Earth Science Workshop, (in press).

Clark, R.N., G.A. Swayze, A.J. Gallagher, T.V.V. King, and W.M. Calvin, 1993, "The U.S.G.S. Digital Spectral Library: Version 1: 0.2 to 3.0 μm". U.S. Geol. Surv. Open File Report 93-592.

Clark, R.N., A.J. Gallagher, and G.A. Swayze, 1990, "Material absorption band depth mapping of imaging spectrometer data using a complete band shape least-squares fit with library reference spectra," in *Proc. 2nd AVIRIS Workshop*, (R.O. Green, Ed.), JPL Publication 90-54, Pasadena, CA, pp. 176-186.

Farrand, W.H., 2000, "Mapping alteration mineralogy in the Tushar Mountains and Marysvale mining district, Utah using AVIRIS data". *Proceedings of the Fourteenth International Conference on Applied Geologic Remote Sensing*, pp. 62-69.

Farrand, W.H. and J.C. Harsanyi, 1997, "Mapping the distribution of mine tailings in the Coeur d'Alene River Valley, Idaho through the use of a Constrained Energy Minimization technique." *Remote Sens. Env.* vol. 59, pp. 64-76.

Gillespie, A.R., M.O. Smith, J.B. Adams, S.C. Willis, A.F. Fischer III, and D.E. Sabol, 1990, "Interpretation of residual images: Spectral mixture analysis of AVIRIS images, Owens Valley, California," in *Proc. 2nd AVIRIS Workshop*, (R.O. Green, Ed.), JPL Publication 90-54, Pasadena, CA, pp. 243-270.

Harsanyi, J.C., 1993, "Detection and classification of subpixel spectral signatures in hyperspectral image sequences", PhD thesis, Univ. of Maryland Baltimore County, 116 pp.

Rockwell, B.W., et al., 2000, "Mineral mapping in the Marysvale Volcanic Field, Utah, using AVIRIS data", in Proc. 9th JPL Airborne Earth Science Workshop, (R.O. Green, Ed.), JPL Publication 00-18, Pasadena, CA, pp. 407-417.

Research Systems, Inc., 2000, ENVI 3.4 User's Guide.

Smith, M.O., S.L. Ustin, J.B. Adams, and A.R. Gillespie, 1990, "Vegetation in deserts: 1. A regional measure of abundance from multispectral images". *Remote Sens. Env.* vol. 31, pp. 1-26.

Vane, G. and A.F.H. Goetz, 1993, "Terrestrial imaging spectrometry: Current status, future trends", *Remote Sens. Env.*, vol. 44, pp. 117-126.

MEASUREMENT OF COLOR IN HYPERSPECTRAL IMAGES (AVIRIS) USING THE CIE (COMMISSION INTERNATIONALE D'ÉCLAIRAGE) SYSTEM

Ana Paula Ferreira de Carvalho[1,2]
Osmar Abílio de Carvalho Júnior[3]
Renato Fontes Guimarães[3]
José da Silva Madeira Netto[4]
Mercedes Maria da Cunha Bustamante[1]

[1]Departamento de Ecologia - Universidade de Brasília (UnB)- Campus Universitário Darcy Ribeiro, Asa Norte, 70910-900, Brasília, DF, Brazil
[2]INCRA – SBN Ed. Palácio do desenvolvimento, sala 1205, 70057-900, Brasília, DF, Brazil
[3]Departamento de Geografia - Universidade de Brasília (UnB)- Campus Universitário Darcy Ribeiro, Asa Norte, 70910-900, Brasília, DF, Brazil osmana@tba.com.br
[4]Embrapa/CPAC-Centro de Pesquisa Agropecuária dos Cerrados - Caixa Postal 08223, BR 020, km 18, Rodovia Brasília/Fortaleza, 73301-970, Planaltina, DF, Brazil madeira@cpac.embrapa.br

Introduction

A new concept in the digital processing of images is appearing due to the spectroscopy image. The AVIRIS sensor (Airborne Visible/Infrared Imaging Spectrometer) developed by NASA in 1983 (Vane *et al.*, 1984) was the first imaging system capable of continually acquiring bands. This sensor captures along the portion of the reflected solar spectrum from 0.4 μm to 2.5 μm. The system was developed to obtain data that could be used in the several areas of geosciences. AVIRIS became operational in 1988 after some fittings and corrections accomplished by researchers at JPL (the Jet Propulsion Laboratory), NASA.

AVIRIS was brought to Brazil in 1995 for the SCAR-B (Smoke, Clouds and Radiation - Brazil), mission with the purpose of evaluating atmospheric effects. This activity was accomplished by NASA, INPE (National Institute of Space Researches) and AEB (Brazilian Space Agency) (Kaufman *et al.*, 1998).

Hyperspectral remote sensing is a recent technology that has been growing fast and provides a constant proliferation of new methods and algorithms for analysis. In those images, the large quantity of information allows for a wide propagation of methods in order to improve the detection and quantification of the materials that compose the scene.

During the SCAR-B mission, the AVIRIS sensor over-flew the Niquelândia area on August, 16th 1995, generating images of areas with supergenic mineral concentration (nickel lateritic). This high concentration of nickel has marked effects on the distribution of vegetation types. The flight line was accomplished longitudinally to the Niquelândia complex, crossing the geological units.

The aim of this work was to adapt and test the employment of the CIE color system in AVIRIS hyperspectral images to differentiate vegetation patterns. The employment of the color concept provides a reduction of the spectral space, concentrating the information, and it allows for better interactivity with the analyst because of the visual approach.

Characterization of the Study Area

The distribution and physiognomy of vegetation in the Niquelândia Massif represent a strong geological control, described by Brooks *et al.* (1990). At this site, extensive areas of ultramafic rocks are covered by herbaceous vegetation dominated by grasses (*campo rupestre*: Photo 1). The fires that occur during the driest months (June - August), might influence the

physiognomy of the vegetation. However, fires alone do not explain the abrupt limit among the gabroic rocks (mafic) and the ultramafic substrate.

Photo 1 – Vegetation on ultramafic rocks.

Different types of forests can be found along the streams and valleys. The existence of these areas demonstrates the ability of many species to tolerate soils originated from ultramafic rocks if soil depth and humidity are appropriate and some fire protection exists (Photo 2).

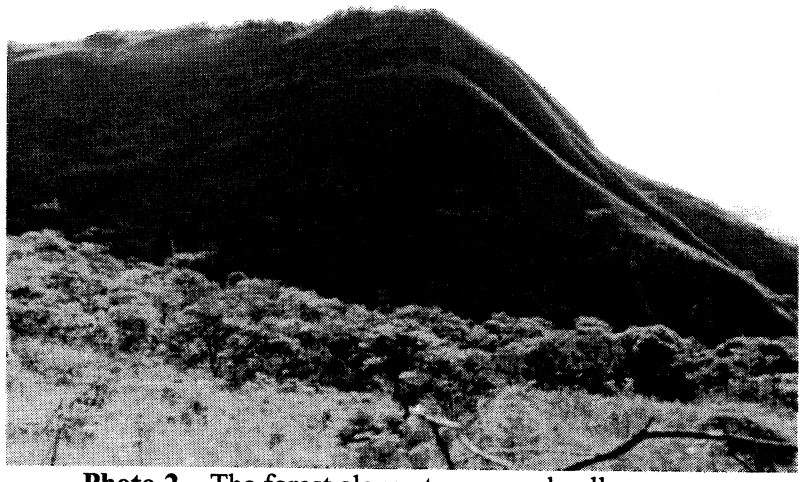

Photo 2 – The forest along streams and valleys.

In this environment/community the first hyper-accumulator of nickel in South America was identified. This species of *Cnidosculus*, described as *C. bahianus*, is a scrub from 1.5 to 2 m height, with thorny leaves and fruits. It produces large amounts of white latex, in which was later found 1.35% of nickel (dry matter basis). The leaves of *Cnidosculus* are much less rich in nickel than in latex, with 0.01-0.11% of Ni. Similar accumulation pattern was found in *Sebertia acuminata (Sapotaceae)* that occurs on serpentine soils, in New Caledonia. *S. acuminata* has a blue-green latex with more than 25% of nickel in the dry matter and 1.17% in the leaves. These

species are similar to *C vitifolius* widely distributed in *Americano do Brasil* and *Barro Alto* (central Brazil) where there are large deposits of nickel.

The canopy does not surpass 1 m height in the highest areas of the ultramafic massif. Among the most frequently occurring plants are the species of *Paepalanthus (Eriocaulaceae), Heteropteris (Malpighiaceae)* and *Vellozia (Velloziaceae)*. Several species of *Vellozia (canela-de-ema)* occupy varied substrates in the highest altitudes of central Brazil.

The CIE System

The CIE (*Commission Internationale d' Éclairage*) color system represents an international consensus. This system of colors has been used in radiometric studies in order to characterize soils (Madeira Netto, 1991). With this new technique for the spectroscopic image, the spatial distribution of CIE values can be obtained with greater accuracy.

The color equation to radiometric data in terms of red, green and blue, for human vision involves negative values, which hinders its use. With the adoption of the CIE system, the occurrence of negative values is eliminated (Evans, 1948). However, it generates a virtual system that doesn't clearly translate to the behavior of the human eye. Presence of negative values can be a source of occasional errors (Wright, 1944), i.e.:

- the negative signs not only occur in the chromaticity coordinates but also in the distribution coefficients;
- the calculation for specification of the values tri-incentives involves the product of the sum of positive and negative amounts; and
- the negative values hinder the development of colorimeters.

That system adopts as pattern for the international use:

- a curve of relative brightness,
- curves of color mixtures for three normalized imaginary lights; and
- a specific distribution of energy for a source of basic light.

Figure 1 gives the brightness curve for the reference observer.

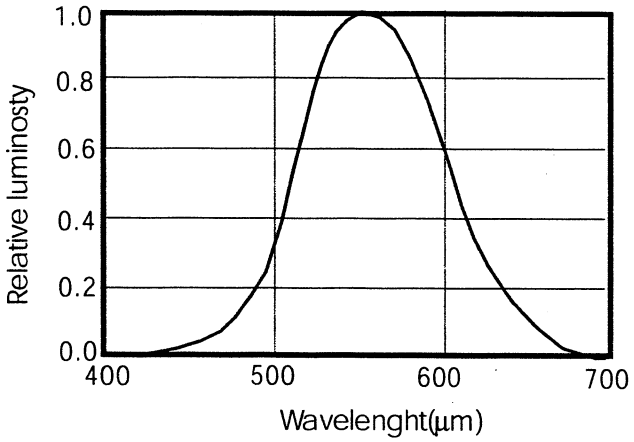

Figure 1 – Brightness curve (source: Evans, 1948)

The curves of the tri-stimulus of primary CIE in relation to wavelength are presented in **Figure 2**.

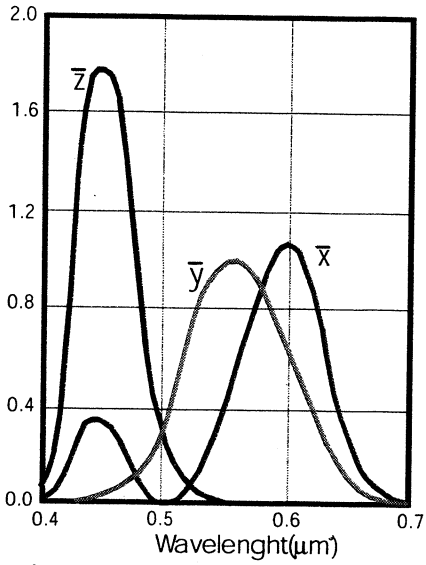

Figure 2 – CIE tri-stimulus values, x, y, and z for the spectral colors. (Source: Evans, 1948)

The procedure to derive a color specifies the tri-incentive (X, Y and Z) starting from a spectral composition E(λ). It can be algebraically expressed in the following way:

$$\mathbf{X} = \sum \mathbf{E}\lambda * \bar{\mathbf{X}}\lambda$$

$$Z = \sum E\lambda * \bar{Z}\lambda$$

$$Y = \sum E\lambda * \bar{Y}\lambda$$

And the chromaticity coordinate x, y e z is expressed by:

$$x = \frac{X}{X+Y+Z}$$

$$y = \frac{Y}{X+Y+Z}$$

$$z = \frac{Z}{X+Y+Z}$$

To calculate the values of X, Y, Z, x, y and z in the ambit of this work, an algorithm in IDL language from the ENVI program was developed. This program was tested to distinguish vegetation patterns in the Niquelândia area (GO), in Central Brazil.

The z value can be discarded, once it can be obtained from x and y.

$$\mathbf{1 = x + y + z}$$

$$\mathbf{1 - z = x + y}$$

Analysis of the Vegetation in the Niquelândia Area

In the image used, the atmospheric effect was corrected by the Green method. That method proposed by Green (1990) was specifically developed for AVIRIS hyperspectral images.

The Green method provides an estimate of the atmospheric parameters and a calculation of the apparent reflectance of the surface using the code of radioactive transfer together with a model of non-linear adjustment for the square mean (Green, 1991, Green *et al.*, 1993a,b).

After the atmospheric correction, an estimate was made of the CIE chromatic coordinate (x, y, z and Y). The images x, y and z and Y are presented in **Figure 3**. The x image presents larger values for red colors and points out the areas with exposed soil that are visually associated with that color. The larger value of the y image corresponds to the green objects and points out the presence of green vegetation that occurs along the waterways. It also occurs in areas of more fertile soils that are correlated to the basic rocks. The z and Y components point out the areas with vegetation of *campo rupestre* that are dry during this time of the year.

In **Figure 4**, the RGB color compositions are presented starting from the CIE images. It can be observed that the two-composition xyY allowed the identification of vegetation patterns that occur in different substrata. The composition that uses the brightness (xyY) allows a better differentiation of the vegetation that occurs on the ultrabasic rocks and appears as a purple color.

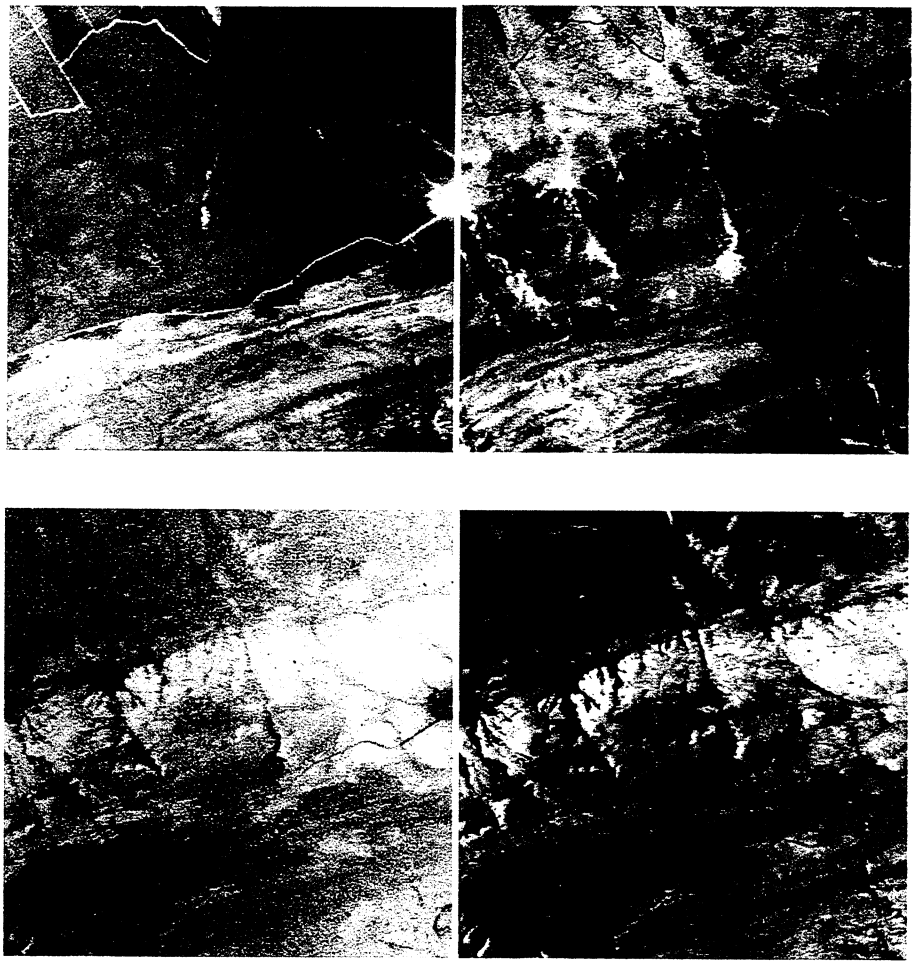

Figure 4– Niquelândia area CIE Image: a) x, b) y, c) z e d) Y.

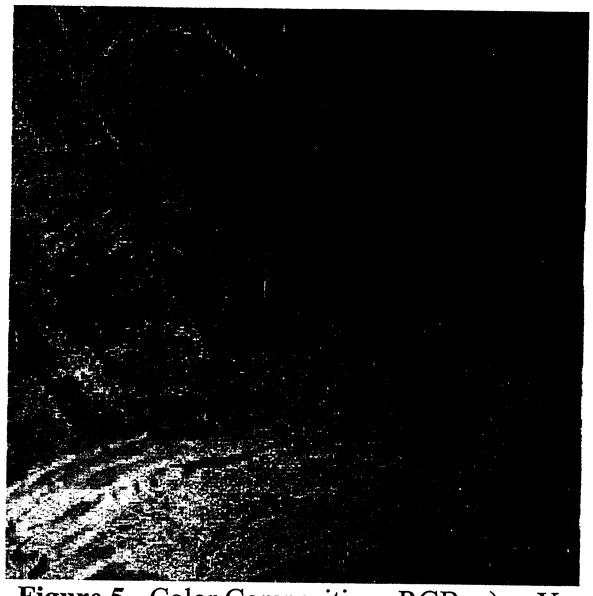

Figure 5 - Color Compositions RGB: a) xyY.

Conclusions

The main advantages of the employment of the CIE color system are:

1. Spectral dimensionality reduction;
2. Determination of chromatic values, which are easily understood by the human eye, allowing a cognitive interpretation; and
3. Establishment of values according to the international pattern that allows for comparisons among different areas. This characteristic is not obtained by other methods of dimensionality reduction such as the analysis of principal components and MNF (Minimum Noise Fraction - Green *et al.*, 1988).

For the Niquelândia area it was possible to separate for the parameters of CIE vegetation patterns in soils originated from ultramafic or mafic rocks.

References

Brooks, R. R., Reeves, R. D., Baker, A. J. M., Rizzo, J. A., Diaz Ferreira, H., 1990, The Brazilian Serpentine Plant Expedition (BRASPEX), 1988. National Geographic Research 6, 205-219.

Evans, 1948, R. M., An Introduction to Color, New York, Jown Wiley & Sons, 329 pp.

Green, A. A.; Berman, M.; Switzer, P. & Craig, M. D., 1988, A transformation for ordering multispectral data in terms of imagens quality with implications for noise removal: *IEEE Trans. Geosci. Remote Sensing*, Vol. 26, No.1, pp. 65-74.

Green, R. O., 1990, Retrieval of Reflectance from Calibrated Radiance Imagery Measured by the Airborne Visible/Infrared Imaging Spectrometer (AVIRIS) for Lithological Mapping of Clark Mountains, California, In: *Proceedings of the Second Airborne Visible/Infrared Imaging Spectrometer (AVIRIS) Workshop*, JPL Pub. 90-54, pp. 167-175.

Green, R. O., 1991, Retrieval of reflectance from AVIRIS – Measured Radiance Using a Radioative Transfer Code In: *Proceedings of the Third Airborne Visible/Infrared Imaging Spectrometer (AVIRIS) Workshop*, JPL Pub. 91-28, pp. 200-210.

Green, R. O., Conel, J. E.; Helmlinger, M.; Bosch, J.; Chovit, C. & Chrien, T., 1993a, Inflight Calibration of AVIRIS in 1992 and 1993. In: *Proc. Fourth Annual Airborne GeoScience Workshop*, JPL Public 93-26 pp.69-72.

Green, R. O.; Conel, J. E. & Roberts, D. A., 1993b, Estimation of Aerosol Optical Depth, Pressure Elevation, Water vapor and Calculation of Apparent Surface Reflectance from Radiance measured by the Airborne Visible/Infrared Imaging Spectrometer (AVIRIS) Using a Radiative Transfer Code", SPIE vol. 1937, Imaging Spectrometry in the Terrestrial Environment, G. Vane Editor, 2.11.

Kaufman, Y. J.; Hobbs, P. V.; Kirchhoff, V. W. J. H.; Artaxo, P.; Remer, L. A.; Holben, B. N.; King, M. D.; Ward, D. E.; Prins, E. M.; Longo, K. M.; Mattos, L. F.; Nobre, C. A.; Spinhirne, J. D.; Thompson, A. M.; Gleason, J. F.; Christopher, S. A. & Tsay S.-C., 1998, Smoke, clouds, and Radiation-Brazil (SCAR-B) experiment. *J. Geophys. Res.*, Vol. 103, No. D24. pp. 31.783-31.808.

Madeira Netto, J. S. 1991. Étude quantitative des relations constituants mineralogiques-réflectance difuse des latosols brésiliens/application a l'utilisation pedologique des données satellitaires TM (region de Brasília). Thèse de Doctorat, Université Pierre et Marie Curie. Paris. 224 p.

Wright, W. D., 1944, The Measurement of Color, London: Adam Hilger & Watts, Ltd. 259pp.

Vane, G.; Chrisp, M.; Enmark, H.; Macenka, S. & Solomon, J., 1984, Airborne Visible/Infrared Imaging Spectrometer (AVIRIS): An advanced tool for earth remote sensing, Proc. 1984 *IEEE Int. Geosci. Remote Sensing Symp.*, SP215, IEEE, New York, pp. 751-757.

Rejection Basin Detection Using the Integral Spectral Analysis (ISA) Method, Niquelândia, Brazil

Renato Fontes Guimarães[1]
Osmar Abílio de Carvalho Júnior[1]
Ana Paula Martins Ferreira[2,3]
Múcio Nobre da Costa Ribeiro[1]

[1]Departamento de Geografia - Universidade de Brasília (UnB)- Campus Universitário Darcy Ribeiro, Asa Norte, 70910-900, Brasília, DF, Brazil
[2]INCRA – SBN Ed. Palácio do desenvolvimento, sala 1205, 70057-900, Brasília, DF, Brazil
[3]Departamento de Ecologia - Universidade de Brasília (UnB)- Campus Universitário Darcy Ribeiro, Asa Norte, 70910-900, Brasília, DF, Brazil

Introduction

Niquelândia lateritic nickel deposits lie in the central portion of Brazil's Goias State-, about 23 km north of Niquelândia city. The Niquelândia Complex is a well-exposed, large, layered intrusion in central Brazil that comprises an area of about 1,800 square km and is approximately 15 km thick. Geology (Ferreira Filho *et al.*, 1992) and petrology (Girardi *et al.* 1986) studies showed many similarities between the Niquelândia Complex and well-known Precambrian layered intrusions such as Bushveld and Stillwater. Nevertheless, these layered intrusions (the Niquelândia Complex) show widespread tectonism and associated amphibolite to granulite facies metamorphism (Ferreira Filho *et al.*, 1992 and Ferreira Filho & Fawcett, 1992). Deposits are located in the ultrabasic zone of the Niquelândia Basic-Ultrabasic Complex as a result of the residual concentration developed by rocks weathering in this zone. There are two types of ore: garnerite and oxidated ore (Pedroso & Schmatz, 1986).

In 1973 the Níquel Tocantins Company built a metallurgic complex to produce nickel carbonate from lateritic ore. Nickel carbonate is transported to São Paulo, where metallic nickel is produced. The wastes are stockpiled in sedimentation basins around the company. Mainly opaque minerals (maghemite and magnetite) constitute the wastes.

The AVIRIS image shows the mill, rejection basins and the dam (Figure 1). The present work uses AVIRIS images in order to characterize the rejection basins formed by opaque minerals (Photo 1).

Methodology

Due to the lack of a specific absorption features in the ore rejection, spectral classification methods such as Tricorder (Clark *et al.*, 1990 and Clark & Swayze, 1995) and Spectral Feature Fitting (ENVI, 1997) are not effective. Diagnostic characteristics of the rejection minerals are the low reflectance throughout the spectral range.

A new procedure was proposed by Ribeiro *et al.* (2000) in order to detect opaque minerals. The method is based on two steps:

a) Discrimination of low albedo areas through the ISA algorithm, and
b) Segmentation of the low albedo materials by using MNF and scatterplot analysis.

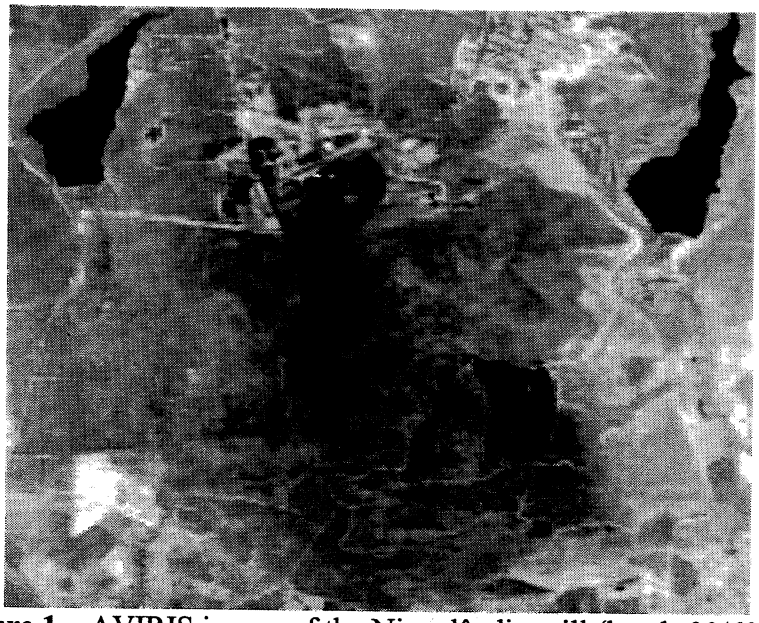

Figure 1 – AVIRIS image of the Niquelândia mill (bands 30/60/90)

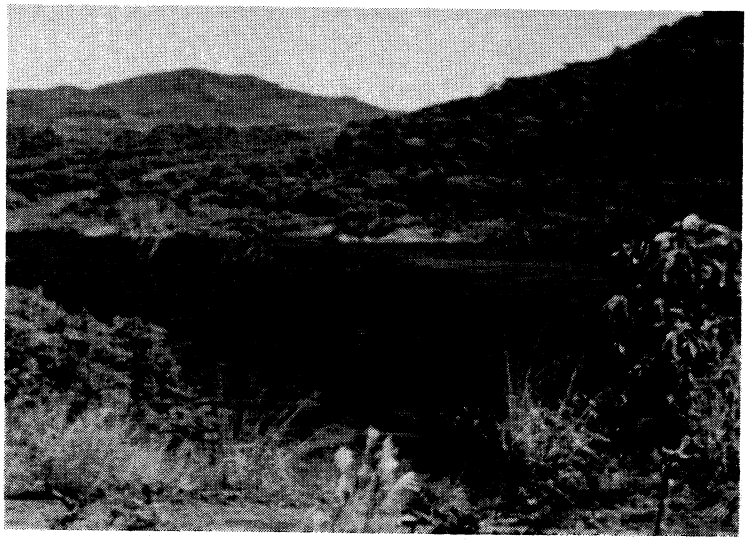

Photo 1 – Rejection basin

The ISA accomplishes a sum of reflectance intensity on bands multiplied by their respective FWHM:

$$\textbf{Spectral Integral} = \Sigma(R_b * FWHM_b)$$

Low-reflectance areas were separated, in order to make a mask, and applied in the MNF transformation. The MNF procedure is derived from the PCA (Principal Component Analysis). The main difference between them is that MNF considers the noise and PCA the data variation. MNF transformation is considered a method to order hyperspectral data in terms of image quality (Green *et al.,* 1988.).

Results and Conclusion

The rejection is mainly formed by the opaque maghemite and magnetite minerals characterized by low albedo. From ISA a mask was made isolating the water in the rejection basins. MNF was applied in the image using the mask (Figure 2).

A color composite of MNF images enhanced the two targets (Figure 3). In the rejection basin a variation of behavior can be observed due to opaque concentration. The use of the MNF scatterplot allows separating the rejection basins in the areas with major (black) and minor (red) opaque concentration (Figure 4). The dam is represented by the blue area where the dark blue corresponds to the edge with the highiest data dispersion.

The methodology presented here is an efficient method for mapping an opaque body.

Figure 2 – Mask image built from ISA Method

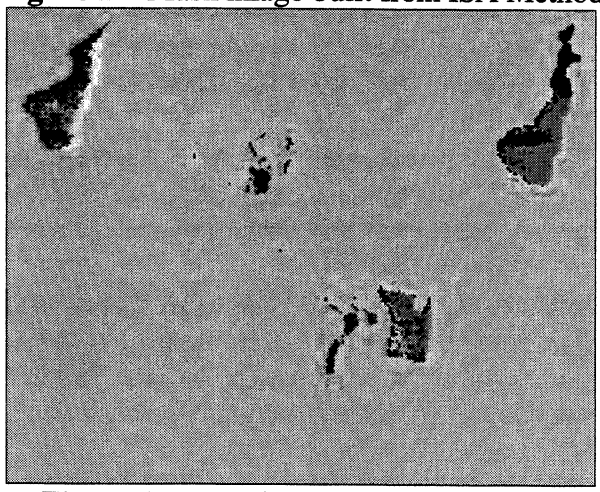

Figure 3 - MNF image to the study area.

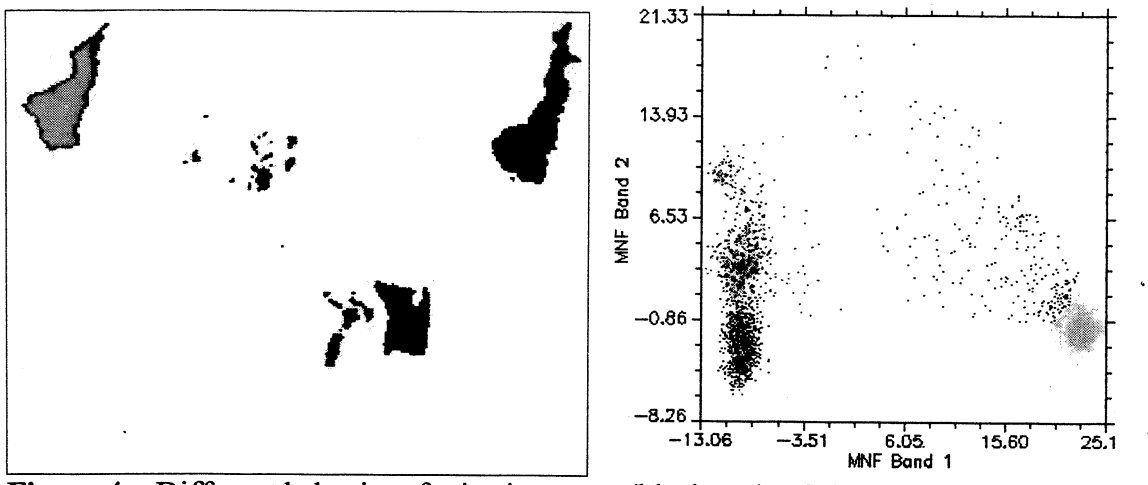

Figure 4 – Different behavior of rejection areas (black and red) in relation to the dam (blue)

References

Clark, R. N. & Swayze, G. A., 1995, Mapping Minerals, Amorphous Materials, Environmental Materials, Vegetation, Water, Ice and Snow, and Other Materials: The USGS Ticorder Algorithm. In: *Summaries of the Fifth JPL Airborne Earth Science Workshop*, JPL Publication 95-1 v.1, pp. 39-40.

Clark, R. N., Gallagher, A. J. & Swayze, G. A., 1990, Material Absorption Band Depth Mapping of Imaging Spectrometer Data Using a Complete Band Shape Least-Squares Fit With Library Reference Spectra. *Summaries of the 2nd Annual JPL Airborne Geoscience Workshop*, JPL Publication 90-54, pp. 176-186.

ENVI ®, 1997, Tutorials, Better Solutions Consulting Limited Liability Company Lafayette, Colorado, USA, 370 p.

Ferreira Filho, C. & Fawcett, J.J., 1992, Prograde metamorphism in the Niquelândia layered complex Brazil: evidence for an oblique cross-section through the continental crust. *Geol. Soc. Am. Abstr.* Program 24. A179.

Ferreira Filho, C. F., Nilson, A. A. & Naldrett, A. J., 1992, The Niquelândia mafic-ultramafic complex. Goiás, Brazil: a contribution to the ophiolite x stratiform controversy based on new geological and structural data. *Precambrian Res.* 59. 125-143.

Girardi, V. A. V., Rivalenti, G. & Sinigoi, S.,1986, The petrogeneses of the Niquelândia layered basic-ultra-basic complex, Central Goiás, Brasil. *J. Petrol.*, 27:715-744.

Green, A. A., Berman, M., Switzer, P. and Craig, M. D., 1988, A Transformation for Ordering Multispectral Data in Terms of Images Quality with Implications for Noise Removal, *IEEE Transactions on Geoscience and Remote Sensing*, v.26, no.1, pp. 65-74.

Pedroso, A. C. & Schmaltz, W. H., 1986, Jazimentos de Níquel laterítico de Niquelândia, Goiás. **IN**: Principais Depósitos Minerais do Brasil. C. Schobbenhaus & C. E. S. Coelho (eds.). DNPM. pp. 307-314.

Ribeiro, M. N. C., Carvalho Jr., O. A., Guimarães, E. M. & Meneses, P. R., 2000, Integral Spectral Analysis (ISA) applied to AVIRIS data for manganese mineralized laterites in São João da Aliança /GO, Brazil, *Ninth JPL Airborne Visible/Infrared Imaging Spectrometer (AVIRIS) Workshop* , JPL Publication 00-18.

ROAD EXTRACTION FROM AVIRIS USING SPECTRAL MIXTURE AND Q-TREE FILTER TECHNIQUES

Margaret E. Gardner, Dar A. Roberts, Chris Funk, and Val Noronha[1]

1.0 INTRODUCTION

Accurate road location and condition information are of primary importance in road infrastructure management. Additionally, spatially accurate and up-to-date road networks are essential in ambulance and rescue dispatch in emergency situations. However, accurate road infrastructure databases do not exist for vast areas, particularly in areas with rapid expansion. Currently, the U.S. Department of Transportation (USDOT) extends great effort in field GPS mapping and condition assessment to meet these informational needs. This methodology, though effective, is both time-consuming and costly, because every road within a DOT's jurisdiction must be field-visited to obtain accurate information. Therefore, the USDOT is interested in identifying new technologies that could help meet road infrastructure informational needs more effectively.

Remote sensing provides one means by which large areas may be mapped with a high standard of accuracy and is a technology with great potential in infrastructure mapping. The goal of our research is to develop accurate road extraction techniques using high spatial resolution, fine spectral resolution imagery. Additionally, our research will explore the use of hyperspectral data in assessing road quality. Finally, this research aims to define the spatial and spectral requirements for remote sensing data to be used successfully for road feature extraction and road quality mapping. Our findings will facilitate the USDOT in assessing remote sensing as a new resource in infrastructure studies.

2.0 DATA AND METHODS

Our research to date has focused on two primary objectives: development of a regionally specific spectral library for urban areas, and using advanced techniques to map urban materials from hyperspectral AVIRIS data.

2.1 AVIRIS Data

High resolution Airborne Visible/Infrared Imaging Spectrometer (AVIRIS) data acquired over Santa Barbara, California, in October 1999 were initially used in this research. AVIRIS samples between 0.37 and 2.5 μm in 224 spectral bands, providing detailed and continuous radiance information in this region. To retrieve surface reflectance from AVIRIS, we used an algorithm developed by Green et al. (1993; 1996) that fits radiance modeled using MODTRAN radiative transfer code to radiance measured from AVIRIS. A field target was used to remove artifacts from AVIRIS reflectance due to a variety of sources, including AVIRIS wavelength calibration and errors in MODTRAN.

The spatial resolution for these data is approximately 3.9 meters. This data set was selected because it covers a wide range of surface materials (industrial, residential, agricultural, barren, and natural areas and a wide assortment of road types) at a fine enough spatial resolution to be used in urban areas. The large number of bands and fine spatial resolution also make it possible to synthesize most major broad-band systems, including sensors such as SPOT, Landsat TM, and IKONOS.

2.2 Development of the Urban Spectral Library

A regionally specific urban spectral library was developed by extracting and averaging 3.9 meter resolution spectra from the 1999 AVIRIS flight over Santa Barbara (Roberts et al., 1999). Our initial objective was to develop a spectral library that included high quality spectra of many urban materials. To accomplish this, distinct cover types were first identified in the field then spectra were extracted from the image (Figure 1). Spectra were averaged over a

[1] University of California, Santa Barbara, Geography Department, 3611 Ellison Hall, Santa Barbara, California 93106
meg@geog.ucsb.edu, dar@geog.ucsb.edu, chris@geog.ucsb.edu, noronha@geog.ucsb.edu

range of pixels depending on the size of the target. Once extracted from the image each spectrum was given a unique identifier in the spectral library.

2.3 Mapping Urban Materials

Urban areas are spectrally complex and vary greatly across fine spatial scales. Therefore, it was imperative that a technique be used that accounts for the complexity and mixtures present in urban areas. Urban materials were mapped using Multiple Endmember Spectral Mixture Analysis (MESMA, Roberts et al., 1998). Traditional Spectral Mixture Analysis (SMA) is a technique designed to decompose spectra, acquired from "mixed" targets (more than one material within the Instantaneous Field of View of the instrument) into "fractions" of pure spectra, called endmembers. This technique, while well suited for natural areas, is inappropriate for urban areas where the number of unique spectra greatly exceeds the 3 to 4 endmembers typically used in SMA.

MESMA departs from the simple model in that it allows the number and type of endmembers to vary on a per pixel basis, and thus has the potential of mapping hundreds of unique materials. For this analysis, endmembers derived from the urban spectral library were coupled with shade and used to unmix the 1999 Santa Barbara AVIRIS data. The final product is a set of maps, one showing the model selected per pixel (essentially a land-cover map), two or more fraction images showing abundance of each endmember and a final image showing model error.

Utilizing MESMA is an iterative process—once the procedure is run for a scene the user is able to identify which models are working best and to adjust the library for a subsequent run. The goal is to determine the optimal set of models that extract the road features with least error. However, not all materials are spectrally distinct, and the potential exists for map errors due to spectral confusion between materials. Urban examples of spectral confusion include some types of road surfaces, which can appear spectrally similar to dark composite shingles. To alleviate this confusion, a spatial pattern recognition technique--termed a Q-tree filter--was applied that identifies linear, continuous pixels within the classified map as roads (Figure 2). Therefore, the technique developed in this research exploits both spectral *and* spatial information, creating a cleaner road map than traditional methods that incorporate only one of these components.

MESMA will also be the technique used in road condition assessment, although our initial emphasis in this project is on road extraction. Once the road extraction technique is completed, a spectral library including roads of various conditions will be utilized within MESMA to map road quality.

3.0 RESULTS AND DISCUSSION

A ten-scene AVIRIS flight line over Santa Barbara, California was processed to reflectance for this research. From this, a total of over 140 image spectra were extracted for the urban spectral library. For each spectrum, metadata describing the location and type of material were recorded in an Excel spreadsheet. Sample spectra from this library are plotted in Figure 3. As indicated, many urban features are spectrally distinct from one another, and similar surface materials such as roof and road cover types have unique, though subtle, differences in their spectral signatures.

Initial results from MESMA were promising, showing that the technique is capable of mapping a large number of urban surfaces, including roads, given a high quality spectral library of endmembers (Figure 4, center frame). However, the results also showed areas where MESMA was incapable of separating road surfaces from composite shingle roofs. In these cases, either the spectral contrast between these materials was low or the spectral library lacked sufficient spectra for separation. This confusion occurs because many roofs and roads are composed of the same basic materials. Although most road surfaces can be extracted utilizing MESMA alone, many roof materials become misclassified as road due to their spectral similarity to the road signatures. When combined with the Q-tree filter technique, confusion between roads and roofs was reduced (Figure 4, right frame). For example, while road surfaces and composite roofs may appear spectrally similar, their spatial patterns should be unique--roads are likely to form linear features, while roofs are likely to be more rectangular. Therefore, in a classified map of "road materials" in which many roofs are misclassified as roads due to spectral confusion, the Q-tree filter can be used to extract the true roads from the map.

An alternate approach towards improved map accuracy is to further refine the spectral library. The current spectral library is limited in that endmembers were image derived--homogeneous pixels within the image were averaged to build the endmember library. Due to the 3.9-meter spatial resolution of the imagery, these endmembers inherently

contain mixtures of different surface materials. Purer endmembers may be obtained by using a field spectrometer to collect known surface types. Therefore, the next major step in this project will be to develop a reference spectral library from field-collected spectra. A reference endmember library will provide a better "start point" for MESMA because the user has more control over the specific material included in the endmembers.

A second significant challenge in road feature mapping is tree covered and shadowed roads. This leads to discontinuous road maps. For instance, a tree canopy over a road is spectrally represented as vegetation. To overcome this, one approach would be to apply a secondary level of Q-tree spatial filter. After the initial application of the Q-tree filter--which basically "cleans" the roads--a second type of Q-tree filter will be used to reclassify some vegetation pixels that occur along classified road pixels as road (Figure 5). A threshold will specify the maximum number of pixels that can be reclassified in this manner to achieve optimum results.

4.0 CONCLUSIONS AND FUTURE WORK

As indicated, road feature extraction from remote sensing is a complex problem. However, the solutions that are being explored in this research have potential to bring hyperspectral remote sensing into a new and large application area. Once the road extraction technique is further developed with high resolution AVIRIS, we will explore the use of hyperspectral imagery in condition assessment. Next, we will begin determining the minimum spectral and spatial requirements for mapping urban materials. AVIRIS will be spatially degraded to test the resolution required to be successful in urban areas. To evaluate broad-band systems such as Landsat TM or SPOT, we will convolve AVIRIS wavelengths to the equivalent broad-band spectra. This will allow us to better define the imagery requirements—and therefore cost—for the technique to be used on the large scale.

5.0 REFERENCES

Green, R.O., Conel, J.E., and Roberts, D.A., 1993, Estimation of Aerosol Optical Depth and Additional Atmospheric Parameters for the Calculation of Apparent Surface Reflectance from Radiance Measured by the Airborne Visible-Infrared Imaging Spectrometer (AVIRIS), *Summaries of the Fourth Annual JPL Airborne Geoscience Workshop*, Oct 25-29, 73-76.

Green, R.O., Roberts, D.A., and Conel, J.E., 1996, Characterization and Compensation of the Atmosphere for the Inversion of AVIRIS Calibrated Radiance to Apparent Surface Reflectance, *Summaries of the Sixth Annual JPL Airborne Earth Science Workshop*, March 4-8, 135-146.

Roberts, D.A., Gardner, M., Church, R., Ustin, S., Scheer, G.,and Green, R.O., 1998, Mapping Chaparral in the Santa Monica Mountains using Multiple Endmember Spectral Mixture Models, *Rem. Sens. Environ.* 65: 267-279.

Roberts, D.A., Dennison, P., Ustin, S.L., Reith, E., and Morais, M., 1999, Development of a Regionally Specific Library for the Santa Monica Mountains using High Resolution AVIRIS Data, Proc. 8th AVIRIS Earth Science Workshop, JPL, Pasadena, CA 349-354, Feb 8-11, 1999.

6.0 ACKNOWLEDGEMENTS

This research is supported under the UCSB National Consortia on Remote Sensing in Transportation-Infrastructure (NCRST-I) program, funding provided by the Department of Transportation and NASA. We would also like to thank the AVIRIS team and Rob Green for providing great data to work with and the necessary code for reflectance retrieval.

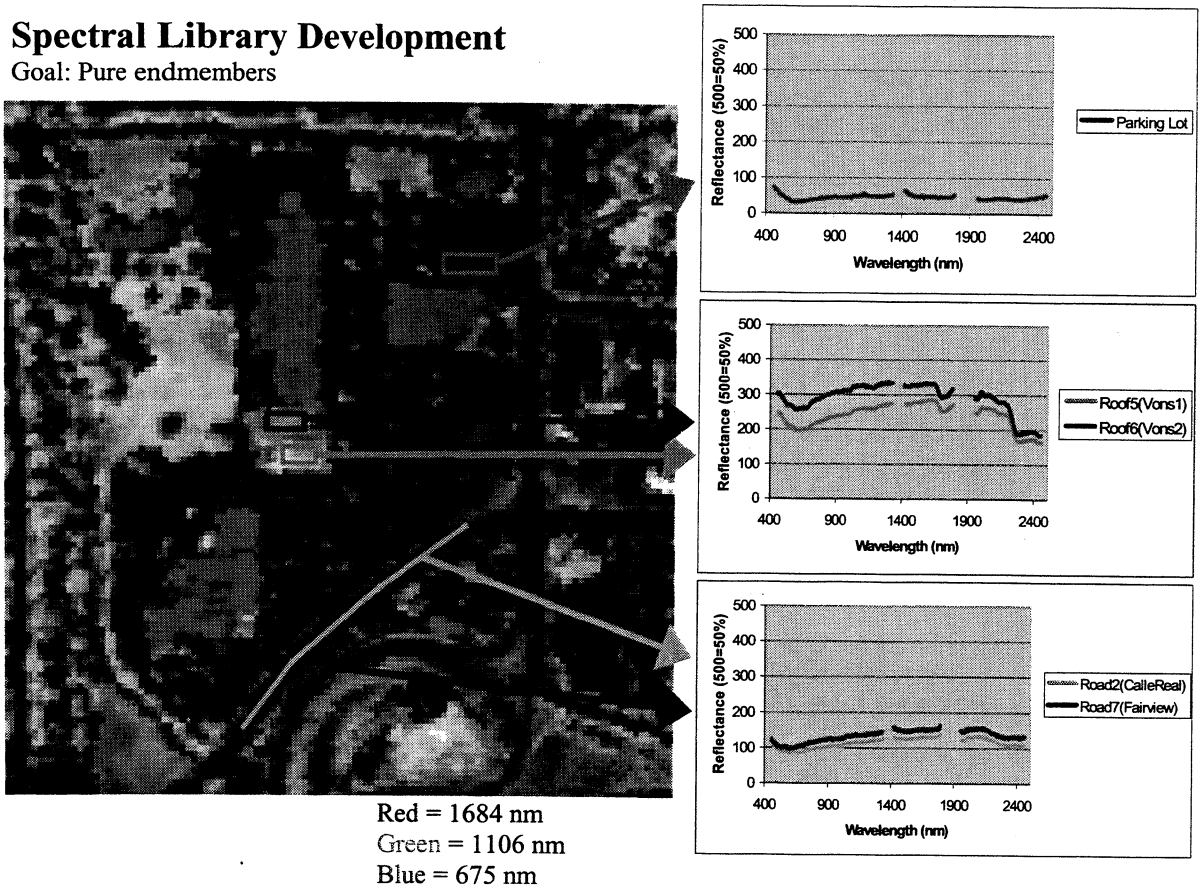

Figure 1. Methodology for creating the urban spectral library. Homogeneous areas were first identified in the field and then identified in the AVIRIS image to be included in the library.

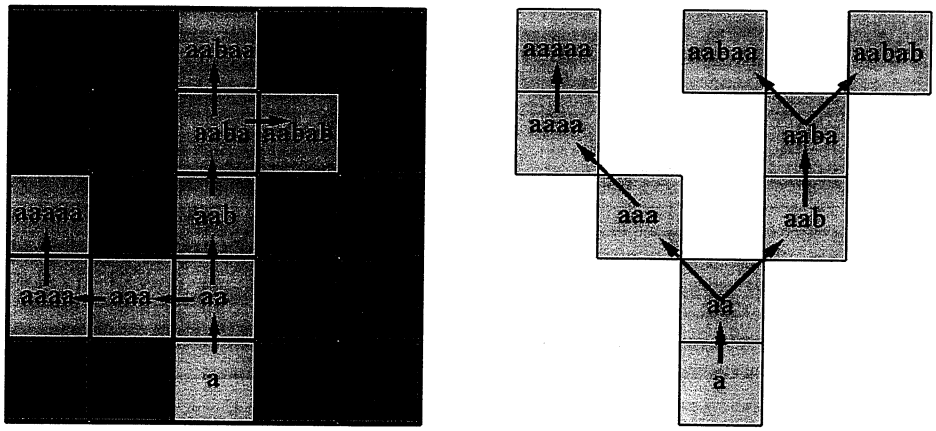

Image with neighborhood assignments beginning with pixel 'a'.

Corresponding Q-Tree with nodes linked to 'a'. Total length = 9.

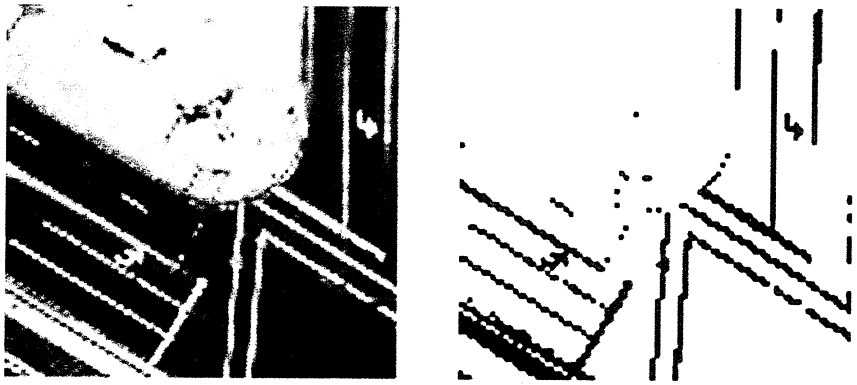

Pan-chromatic image of urban intersection.

Q-Tree filtered white lines.

Figure 2. Q-tree filter concept. This approach incorporates spatial information into the procedure to alleviate spectral confusion, particularly between composite shingles and roads.

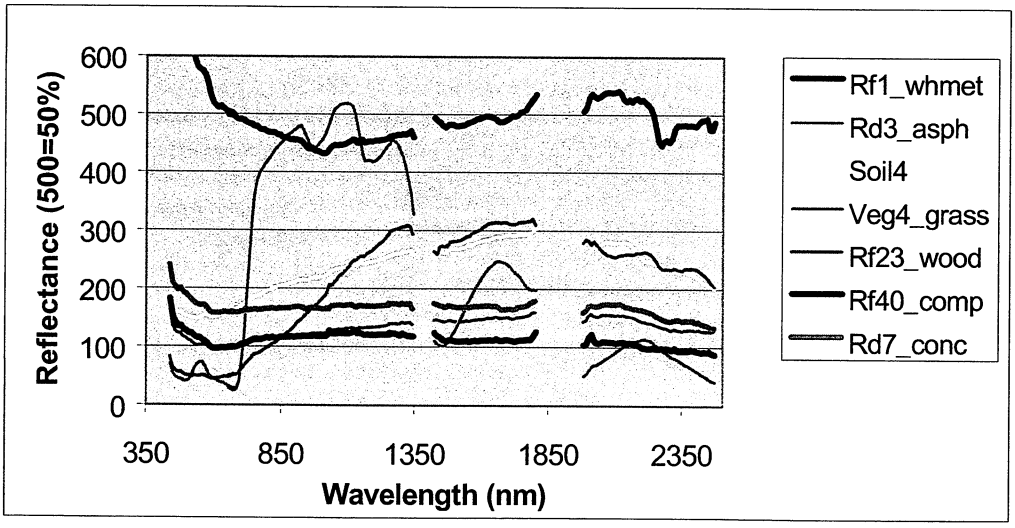

Figure 3. Example Library Spectra. Rf1_whmet=white metal roof; Rd3_asph=asphalt-concrete road; Soil4=bare soil; Veg4_grass=irrigated grass; Rf23_wood=wood roof; Rf40_comp=composite shingle roof; Rd7_conc=concrete road

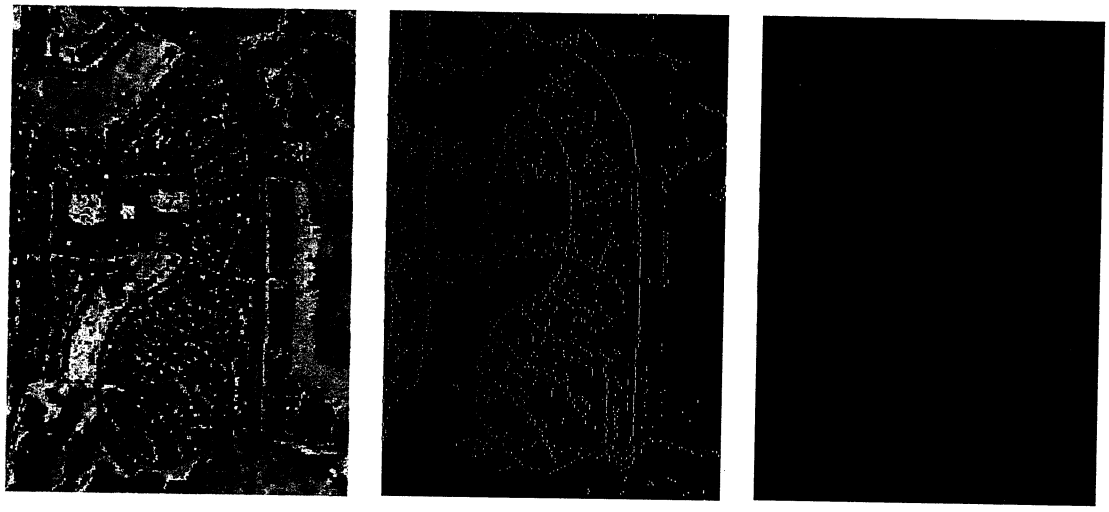

Figure 4. Road extraction procedure. Left image is a color composite of the original image; middle image contains the MESMA results for classified road pixels; right image is the final road map from the Q-tree spatial filter.

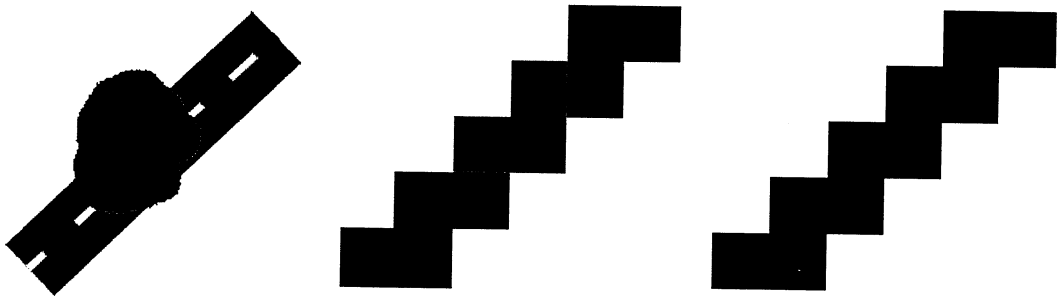

Tree canopy over road → classified pixels → Q-tree filter "removes" the tree

Figure 5. Q-tree road "gap" filling. Gap filling is a second application of the Q-tree filter that enables a cleaner and more accurate final road map.

OCEANOGRAPHIC AND ATMOSPHERIC RETRIEVALS FROM AVIRIS HYPERSPECTRAL DATA

Craig Gelpi, Benjamin C. Schuraytz, and Matthew E. Husman[1]

1. INTRODUCTION

The ocean and coastal zone are particularly challenging environments for using high-altitude, hyperspectral data. To discern ocean characteristics, atmospheric effects must be compensated for; not only does absorption by atmospheric gases affect a large portion of the reflective spectrum, but atmospheric path scattering contributes a much greater percentage of the measured radiance than that which emanates from the surface and water column. Additionally, the water surface has a strong bi-reflectance distribution function (BRDF) that changes as a function of wind and wave conditions. These effects, too, must be compensated for to make full use of hyperspectral signatures of water column and surface phenomena, an area rich in potential for hyperspectral applications.

We are developing hyperspectral techniques to perform these compensations for over-ocean analysis. One method, the Modulated Surface Reflectance (MSR) algorithm (Gelpi, 2000; Gelpi and Nguyen, 2000), employs scale-size differences between atmospheric variations and the modulated radiance produced by surface waves to remove atmospheric path-scattered radiance. The modulated-radiance spectrum is used directly to compute water-vapor column density, which is required to compensate for water-vapor absorption. In the present work, we continue to exploit the modulated radiance by developing techniques that relate its amplitude to the surface waveheight by accounting for atmospheric and surface effects. Although waveheight is a desired quantity in its own right, these techniques promise to be especially useful for the analysis of hyperspectral data gathered from satellites, where sea and atmospheric conditions are expected to be inhomogeneous across the image.

In the following sections we give the modulation transfer function relating waveheight to at-sensor radiance modulations and sketch its derivation. Then we retrieve atmospheric and oceanic parameters required to compute the waveheight spectrum, perform the calculation and compare the resulting spectrum to measurements made by nearby NOAA (National Oceanic and Atmospheric Administration) buoys. Retrieved atmospheric parameters are compared to radiative transfer calculations executed with MODTRAN to estimate aerosol characteristics. Finally we remove atmospheric and ocean surface reflectance effects from the at-sensor radiance to derive upwelling, water-column radiance.

[1] XonTech, Inc., 6862 Hayvenhurst Ave., Van Nuys, California 91406, USA
craig_gelpi@xontech.com

2. MODULATION TRANSFER FUNCTION

We develop a modulation transfer function applicable to geometries where sun glint is the most significant factor in the surface reflectance. Cox and Munk (1954) derived the relationship between the received radiance and the ocean wave statistics. Using a Gaussian distribution for the wave slopes, they computed the expected radiance reflected into the sensor. We modify their model to include waves resolved by the sensor's spatial sampling. In our model the large-scale, resolved waves are deterministic while the small-scale waves are described by Gaussian statistics. The at-sensor radiance, spatial power spectral density, P_L, is related to the large-scale waveheight spectrum, P, via the modulation transfer function, M, *i.e.*,

$$P_L(\vec{k}) = M(\vec{k})P(\vec{k}). \tag{1}$$

To second order in the large-scale to small-scale wave slope ratio, and for observations that do not include the "hot spot", the transfer function is given by

$$M(\vec{k}) = \left[\frac{E_0(\lambda)\left(1+|\nabla\zeta|^2\right)^2}{2\pi\cos\theta} \frac{T\rho_{sp}(\chi)}{\sigma^4} e^{-\frac{(\nabla\zeta)^2}{\sigma^2}} \nabla\zeta\cdot\vec{k} \right]^2 \tag{2}$$

where

E_0 solar irradiance at top of the atmosphere.

λ electromagnetic wavelength.

$\nabla\zeta$ surface slope required for specular reflection.

T two-way atmospheric transmittance.

ρ_{sp} Fresnel reflectivity of water surface.

σ^2 small-scale wave slope variance.

$\vec{k}$ spatial wavevector.

θ view angle from nadir.

χ incidence angle.

In addition to the observation geometry, the transfer function depends on the environmental parameters T, σ^2, and ρ_{sp}. Note that M vanishes for waves that propagate perpendicularly to the required slope. These waves are invisible to the sensor. M also is zero where the required slope is zero, *i.e.*, at the "hot spot". This condition is not present in the data analyzed below.

3. DATA SETS AND ATMOSPHERIC AND OCEANIC PARAMETERS

Computing the waveheight from the radiance requires the atmospheric transmittance, small-scale wave slope variance, and the Fresnel reflectivity. In the absence of surfactants we assume the surface reflectivity is that corresponding to the air-seawater interface. When environmental

conditions are homogeneous, we can take advantage of AVIRIS's large field of view (>30°) to derive the other environmental parameters by using the BRDF of the ocean to relate the change in at-sensor radiance to view angle.

We searched the AVIRIS archives for recent over-ocean campaigns where apparent homogeneous atmospheric conditions were encountered and the flight trajectory was linear. We found 2 flights: f970410t01p02r02 and f970414t01p02r02, executed on April 10 and 14, 1997, respectively, over the Santa Barbara Channel of California. Conditions in the Channel are measured with NOAA buoys; the significant wave height (SWH) was 2.9 m and 2.2 m at the westernmost buoy for April 10th and 14th, respectively. An example of the April 10th data is shown in Figure 1. Waves are clearly visible and there are apparent white caps, consistent with the large SWH.

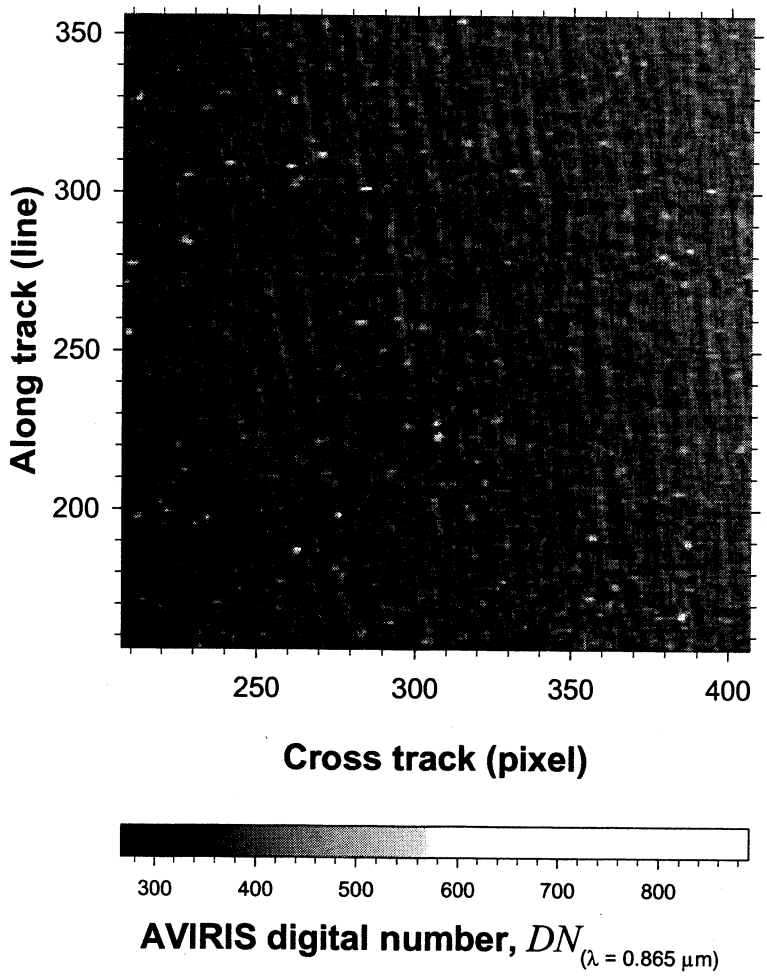

Figure 1. Raw data image of band 54 excised from scene 4 of AVIRIS flight f970410t01p02r02.

For infrared bands (those that exhibit no upwelling, water-column radiance) the line (along-track) ensemble radiance, L^s, should satisfy

$$\left\langle L^s(\lambda,\theta)\right\rangle = \frac{E_0(\lambda)\left(1+\left|\nabla\zeta(\theta)\right|^2\right)^2}{4\pi\cos\theta}\frac{T\rho_{sp}(\chi)}{\sigma_t^2}e^{\frac{(\nabla\zeta)^2}{\sigma^2}} + \frac{L^P(\lambda)}{\cos\theta}. \tag{3}$$

We have included contributions from the path radiance, L^P but have ignored the scattering phase function. Equation 3 also uses the total slope variance, σ_t^2. The ensemble removes the effects of small-scale waves.

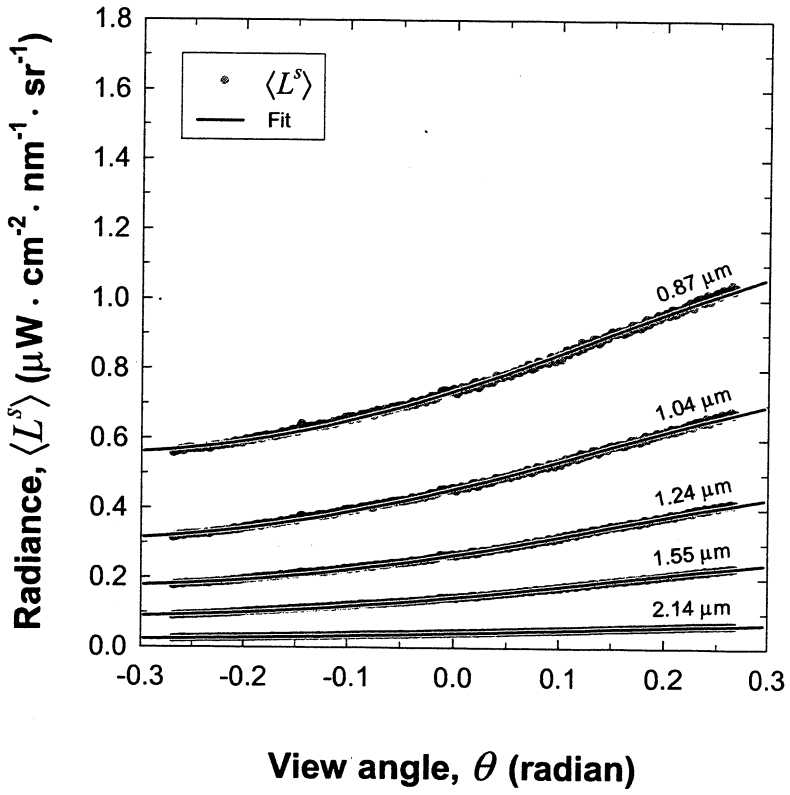

Figure 2. Line ensembles and fits for data from scene 4 of AVIRIS flight f970410t01p02r02.

We fit the total-slope variance, transmittance, and path radiance in the above equation to the ensemble. The data and the goodness of the fit for the April 10th case at several wavelengths are shown in Figure 2. The fitted values for the transmittance and wave slope variance are shown as a function of wavelength in Figure 3. In this case the total wave slope variance is 0.06. Using

buoy data to estimate that portion of the total wave-slope variance produced by the large waves, we can estimate the variance of the small-scale wave slopes.

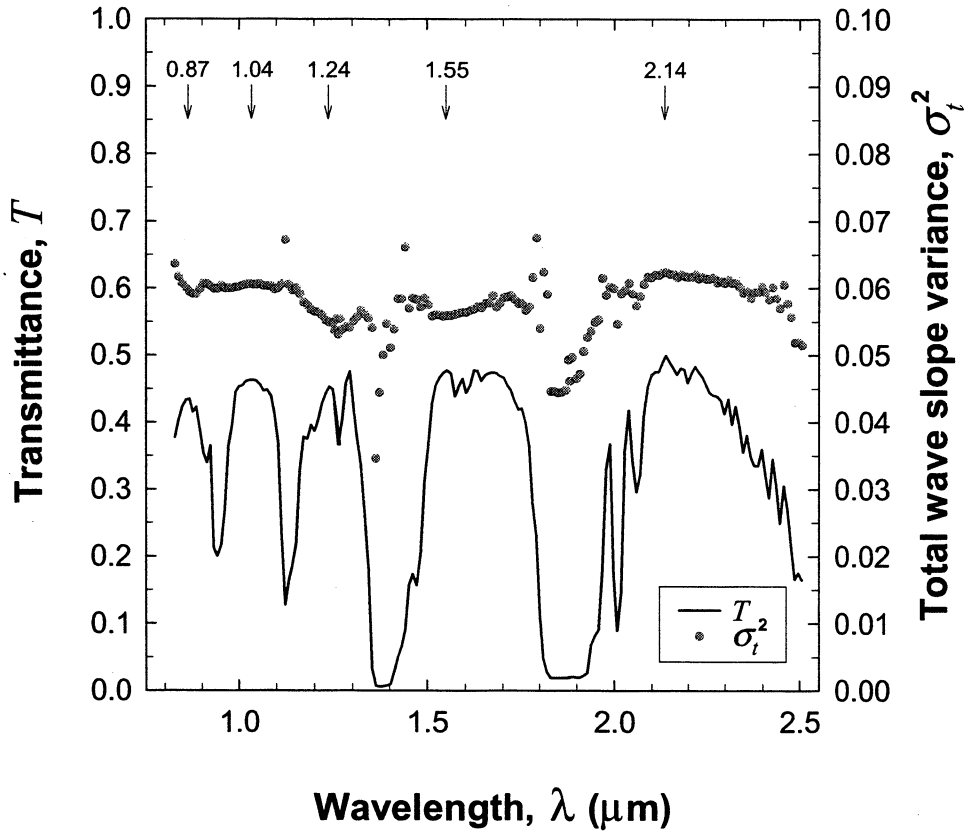

Figure 3. Fitted transmittance and total wave slope variance retrievals from scene 4 of AVIRIS flight f970410t01p02r02.

The fitted transmittance was unexpectedly low for the April 10th data. However, we were able to construct a reasonable aerosol model that closely reproduced both the fitted transmittance and path radiance when employed in the radiative transfer calculations embodied in MODTRAN. We used a 70% standard maritime component that is used in ATREM and a 30% custom urban model. Our custom model employed the standard dust-like and water-soluble parts supplied by ATREM, but we added a soot component that is lognormal with a mean radius of 0.1 μm and with a standard deviation of 2.50 μm. Loading was chosen to give a visibility of 18 km. Water vapor amounts were chosen to be consistent those found with our MSR algorithm. The fitted and modeled spectra for the transmittance and path radiance are compared in Figure 4.

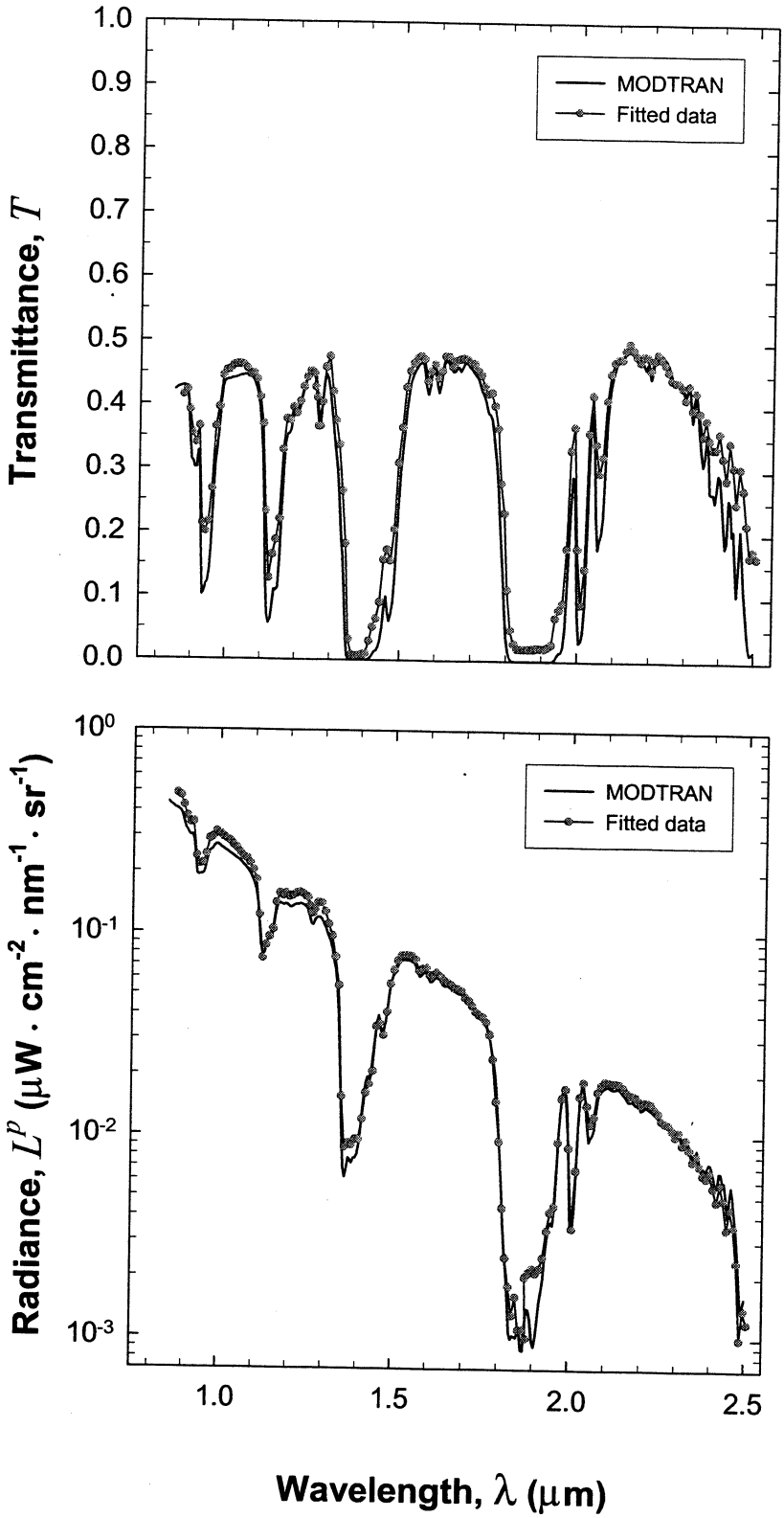

Figure 4. Transmittance and path-scattered radiance derived from fits compared to results from MODTRAN4 with custom aerosol model.

Using these retrieved values, we compute the large-scale wave spectra using Equations 1 and 2 from the data corresponding to Figure 1. We georectify the radiance data, Fourier transform it, and apply a gain factor to compensate for the georectification. The MTF is computed from the retrieved environmental values and divided into the radiance spatial spectra to compute the waveheight spectra. These spectra are integrated to provide a buoy-equivalent (1-dimensional) measurement. These values, computed at 5 wavelengths situated in atmospheric transmission windows, are compared to the western channel buoy measurements in Figure 5. The buoy and image are not collocated, being separated by about 50 km and with a relation that would yield higher waves at the buoy location. Using historical data from both the eastern and western buoys we adjusted the buoy SWH measurement for the location of the images. The adjusted data and the optically derived SWH measurements are shown in Figure 6. The agreement is excellent.

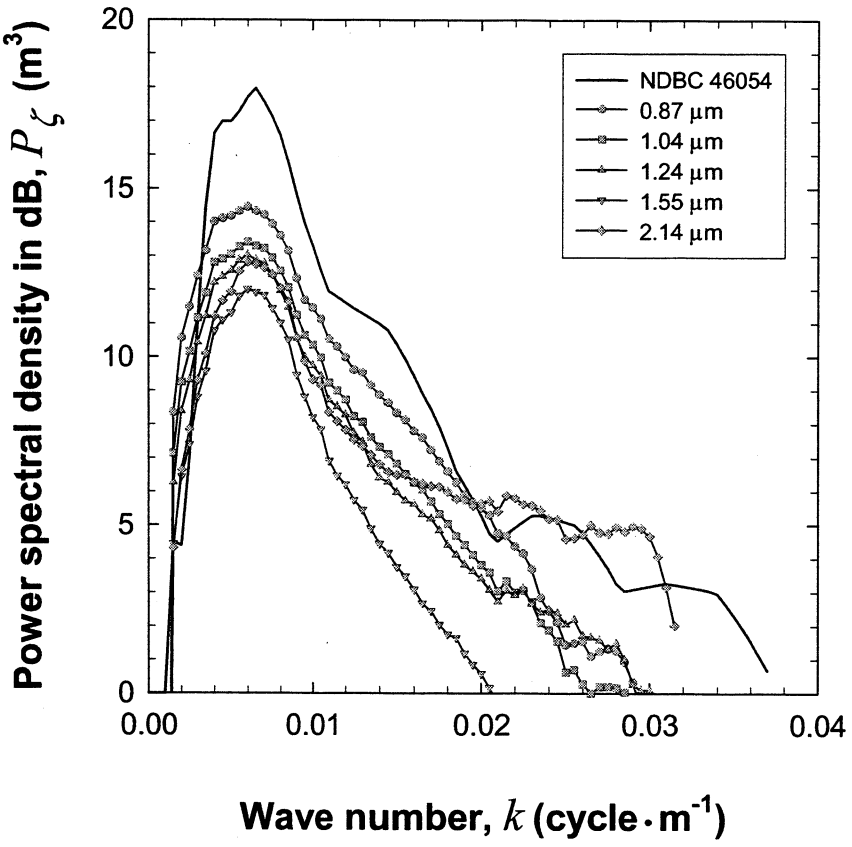

Figure 5. Buoy and optically-derived wave spectra from AVIRIS data acquired on April 10th.

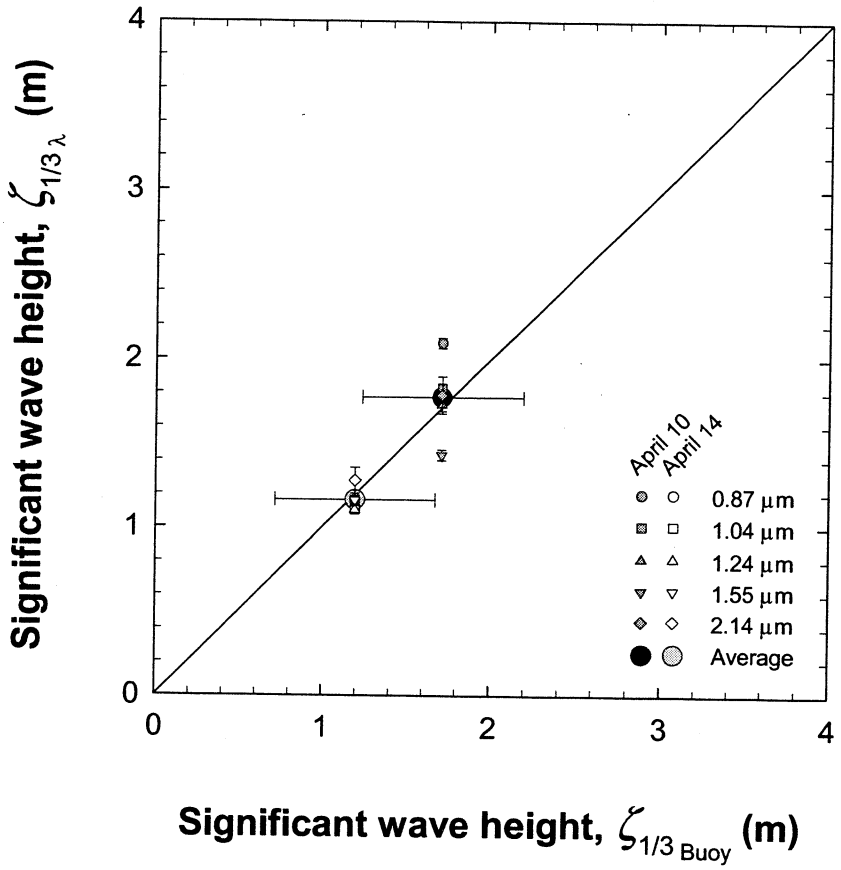

Figure 6. Comparison between optically-derived SWH and buoy measured SWH.

4. INTRINSIC SURFACE REFLECTANCE AND UPWELLING RADIANCE

The most intriguing use of over-ocean hyperspectral data is for the analysis of the water column using the upwelling radiance. To do so, both the atmospheric effects and the surface reflectance must be removed. The atmospheric parameters derived from the fits can be used to remove the effects of the atmosphere in the infrared regime. The aerosol parameters derived from comparisons to MODTRAN simulations provide a means to extrapolate the compensations into the visible regime, though, of course, small aerosol particles that do not influence the infrared wavelengths cannot be accounted for in this manner.

Surface reflectance of direct solar radiation also has been computed using the infrared bands. The physical parameters such as wave slope computed for these data are, of course, electromagnetic wavelength independent. They can be used to remove the effects of glint in the visible regime with the Fresnel reflectivity appropriate for the wavelength.

We have removed atmospheric and solar glinting effects to estimate the upwelling water-column radiance or the remote sensing reflectance. This reflectance can be used to to calculate standard oceanographic products, such as the chlorophyll concentration. Applying standard chlorophyll retrieval algorithms (O'Reilly et al., 1998) to the remote sensing reflectance has produced plausible results. We are refining this technique by including aerosol phase functions and multiple scattering in the computation of the remote sensing reflectance cube.

5. Conclusions and Summary

Using several techniques, we have retrieved oceanographic, atmospheric, and water column properties from AVIRIS coastal observations. The oceanographic properties include waveheight spectra and the small-scale wave slope statistics used to infer surface wind speed. Atmospheric properties include atmospheric transmittance, path-scattered radiance and water-vapor column density. The former values are used to infer aerosol loading and extinction characteristics. These parameters are used to compute an intrinsic surface reflectance cube. The glint component can also be removed to provide information on the upwelling water column radiance.

The environmental parameters were obtained using the large field of view of AVIRIS for homogenous atmospheric and oceanic conditions. If the surface-slope parameters are obtained from other sources (e.g., buoy measurements or models), then the atmospheric parameters can be retrieved from Equations 1 and 2. This technique enables a local measurement of atmospheric parameters that may be generally more applicable, especially for spaceborne observations.

6. Acknowledgements

This work was funded by the Internal Research and Development Program of XonTech's Special Studies Division. Buoy data were obtained from the National Data Buoy Center's web site and the AVIRIS data were provided by JPL.

7. References

Cox, C. and W. Munk, Measurement of the roughness of the sea surface from photographs of the sun's glitter, *J. Opt. Soc. Am., 44*, 838-850, 1954.

Gelpi, C.G., Removing path-scattered radiance from over-ocean spectrometer images for water-vapor estimation, *Remote Sens. Environ., 74*, 414-421, 2000.

Gelpi, C.G., and B. Nguyen, Water-vapor estimation for ocean scenes using modulated surface reflectance, in *Summaries of the Ninth JPL Earth Science Workshop*, edited by R. O. Green, Jet Propulsion Laboratory, Pasadena, California, in press, 2000.

O'Reilly, J.E., S. Maritorena, B.G. Mitchell, D. A. Siegel, K.L. Carder, S.A. Garver, M. Kahru, and C. McClain, Ocean color chlorophyll algorithms for SeaWiFS, *J. Geophys. Res., 103*, No. C11, 24937-24953, 1998.

HYPERSPECTRAL IMAGE ANALYSIS OF CORAL REEFS IN THE HAWAIIAN ISLANDS

James A. Goodman and Susan L. Ustin[1]

1. INTRODUCTION

Concern over the health of coral reef communities has greatly intensified in recent years, particularly with regard to the complex dynamics of global change. The synoptic spatial and temporal monitoring capabilities of remote sensing provide a valuable avenue for evaluating the impacts of local, regional and global change on this important natural resource. Hyperspectral imagery acquired over the Hawaiian Islands in the spring of 2000 by NASA's Airborne Visible InfraRed Imaging Spectrometer (AVIRIS) will be used to develop, apply and evaluate algorithms for analyzing coral reefs using remote sensing data. In order to truly leverage the synoptic capabilities of remote sensing, algorithms developed in this research will be based on fundamental scientific principals that will allow methods to be used in diverse geographic locations. Primary algorithm development will be conducted in Kaneohe Bay, Oahu due to the extensive supporting resources available for evaluating algorithm accuracy. Subsequent to the Kaneohe Bay phase of the research, the resulting analysis tools will be applied to portions of the recently established Northwestern Hawaiian Islands Coral Reef Ecosystem Reserve. Work for this project is being conducted at the Center for Spatial Technologies and Remote Sensing at the University of California, Davis in collaboration with the Hawaii Institute of Marine Biology at the University of Hawaii.

An essential element of any program to preserve, protect and manage coral reefs is to identify a reliable means for quantitatively mapping and assessing the dynamics of community distribution, identifying stressor-response relationships, incorporating multiple levels of spatial analysis and efficiently monitoring the current and future health of the ecosystem. The ability to address such issues using remote sensing is made possible by recent advances in detector technologies, the acquisition of coral-specific spectral information, increases in the spatial and spectral resolution of sensors, as well as by improved computer capabilities and analysis methods. This research project will develop a set of analysis tools using the latest advances in hyperspectral remote sensing. Hyperspectral technology provides improved spectral resolution over more traditional remote sensing methods, and thus translates to greater usefulness in being able to distinguish between the varying spectral characteristics of different benthic habitat types. Specific objectives of the overall research project are 1) to develop algorithms for bathymetry and benthic habitat mapping, 2) create tools for the identification of large-scale coral community composition and 3) to examine causal relationships associated with environmental stress and global change. Presented here are results from the first phase of this analysis examining spectral separability of different species and different habitat types in Kaneohe Bay using both field spectra and imagery.

2. BACKGROUND

2.1 Corals

The overall interest of this research is to develop generalized algorithms for analyzing coral ecosystems that are readily observable from airborne and spaceborne remote sensing platforms. Hence, this research focuses on shallow-water, tropical, reef-building corals. Many factors affect the distribution, diversity and relative health of coral reef ecosystems. These factors exhibit temporal and spatial variations that fluctuate as a result of both natural processes and anthropogenic influences. Coral reefs have naturally adapted to a certain level of environmental stress, such as the seasonal rise and fall in water temperatures, climatic variations like El Niño and La Niña, and the occurrence of hurricanes and other destructive storms. Unfortunately, as with most other ecosystems, the addition of human influences to this system is rarely positive. This tends to result in an unstable equilibrium where the coral reefs become very sensitive to any additional stress.

[1] Center for Spatial Technologies and Remote Sensing (CSTARS), Department of Land, Air and Water Resources, University of California, Davis (jagoodman@ucdavis.edu).

Coral bleaching is perhaps the most obvious visual indication of decline and has been attributed to a variety of stressors. Coral bleaching describes a situation whereby unfavorable conditions cause the corals to expel their symbiotic zooxanthellae, which contain the pigments producing the colorful coral exterior. The loss of these organisms results in exposure of the underlying, almost colorless, coral skeleton (hence the term "bleaching"). Corals can recover from a bleaching event, but are very vulnerable during the recovery process and additional disturbances can be fatal. Furthermore, the overall decline in health of coral communities is not always spatially contiguous. Not only are the affected areas patchy, but in many cases there is a transitory temporal dynamic, with some reef areas being unaffected, some areas recovering, some areas exhibiting lingering affects, and other areas dying. The exact mechanisms for these processes are not entirely clear, and although some corals do recover, the end result is greater stress and a less healthy coral environment.

2.2 Project Rationale

It is becoming increasingly apparent that without adequate protection and preservation, coral reef ecosystems face an uncertain future (Dight and Scherl, 1997; Hoegh-Guldberg, 1999; Wilkinson, 2000). The global implications of this decline are significant because of the crucial role coral reefs play in overall marine ecosystem health and biodiversity. They also contribute numerous other economic and social benefits, as well as an inherent aesthetic appeal. Fortunately, the ecosystems themselves are incredibly resilient and have the ability to recover and thrive if adequate management and conservation measures are implemented. However, the complexity of both the natural system and the many factors involved does not lend itself to simple solutions, particularly when human factors are included in the equation (Hodgson, 1999).

This research is based on an understanding that establishing effective quantitative methods for rapidly monitoring and assessing coral reef ecosystems forms an essential component of resource management decisions and risk management evaluations. Such research has become more relevant recently because of the alarming rate of decline that has been observed in these communities (Hoegh-Guldberg, 1999; Sammarco, 1996; Wilkinson, 2000). The efforts to conserve and protect this valuable natural resource require quantitative information on characteristics of the stressors contributing to this decline, which exhibit local, regional and global variations (Hodgson, 1999; Hughes and Connell, 1999). Further requirements include consideration for the inherent spatial complexities of these ecosystems as well as their varying response to the associated environmental perturbations. A viable avenue for monitoring and assessing the complex dynamics of coral ecosystems is the synoptic spatial and temporal capabilities of remote sensing. Furthermore, advancements in the field of hyperspectral image acquisition and analysis are allowing a progression in the level of questions that can be addressed using remote sensing and an increase in the effectiveness of the resultant management tools. Imagery acquired in the spring of 2000 by AVIRIS affords a valuable opportunity for evaluating the applications of hyperspectral remote sensing to coral reefs. By linking this imagery with traditional methods of analysis, field data, and local knowledge of site conditions, a more robust management and analysis tool is created, one that encompasses site-specific information within a spatial and temporal monitoring context.

2.3 Coral Remote Sensing

Much of the past work on remote sensing of coral reefs has focused on the use of more traditional multispectral sensors (e.g., LANDSAT and SPOT) and reported results have been mixed (Dustan et al., 2000; Holden and LeDrew, 1998b; Mumby et al., 1998). Essentially, the limited spectral resolution of these sensors has restricted their applicability in such an environment. Nevertheless, remote sensing techniques have been identified as a valuable tool for scientists and resource managers working with these ecosystems. Recent investigations using hyperspectral imagery and field spectral data provide very promising indications of the utility of using this technology for coral reef investigations (Lubin et al., 2001; Mumby et al., 1998; Myers et al., 1999; Richardson and Kruse, 2000). Of particular interest are recent studies demonstrating that significant spectral resolution is required to differentiate among the varying coral species, between healthy and unhealthy coral colonies and between other associated benthic species (Hochberg and Atkinson, 2000a, 2000b; Holden and LeDrew, 1999, 1998a; Myers et al., 1999; Schalles et al., 2000). Hence, these analyses have indicated the utility of using hyperspectral instruments as tools for remotely analyzing coral communities.

3. STUDY AREA

3.1 Kaneohe Bay

The primary study area for this project is the coral reef ecosystem of Kaneohe Bay, located on the windward shore of Oahu, Hawaii (Figure 1). There are many benefits associated with working in this particular study area, most importantly because of the extensive amounts of field information and research that are available for evaluating and validating the calibration and classification results. Additionally, because the Hawaii Institute of Marine Biology (HIMB) is located within Kaneohe Bay, this study area also has the advantage of easy accessibility for fieldwork.

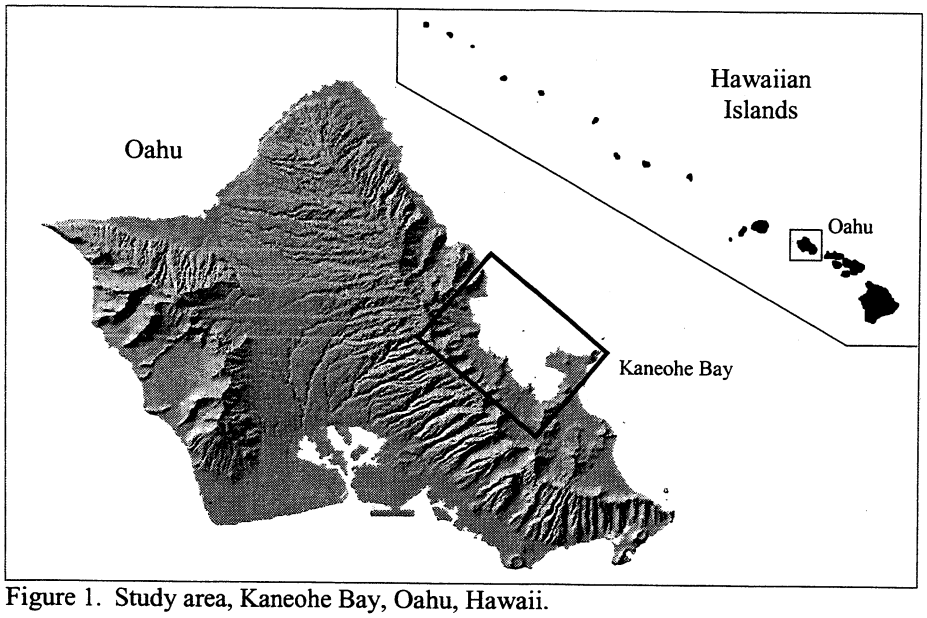

Figure 1. Study area, Kaneohe Bay, Oahu, Hawaii.

Kaneohe Bay is an extensive embayment, extending nearly 13-km along its northwest-to-southeast axis and 4-km in width. The hydrologic conditions within the bay are predominantly controlled by the exchange of seawater with the open ocean and by internal circulation patterns, which are in turn affected by tides, waves and wind. In addition to the oceanic influence, the hydrology of Kaneohe Bay is also affected by inflows from streams and directly through overland runoff. These inflows not only impart an influx of freshwater into the marine environment, but also sediments, nutrients and pollutants. The southeastern end of the bay is the most developed, containing both the town of Kaneohe and the Kaneohe Marine Corps Air Station. It is also mostly enclosed, resulting in limited circulation and poor water quality conditions. In contrast, the northwest portion of the bay experiences significant water exchange with the surrounding ocean and thus exhibits conditions resembling the oceanic environment. These differences have important implications with respect to the chemical and biological constituents in the water column, and ultimately to coral health.

3.2 Corals

Kaneohe Bay contains patch reefs, fringing reefs, and an extensive protecting barrier reef. Spatially, the corals tend to occur along the crests and slopes of these reef formations and are mostly absent from the lagoon bottom and reef flats. There are greater than 60 individual patch reefs within the bay, at locations that tend to be clustered near the two natural channels (Jokiel, 1991). These reefs have diameters ranging from 21 to 850-m and typically extend almost to the water surface. Fringing reefs are found along much of the shoreline, with natural breaks at stream outlets and artificial breaks where boat channels have been dredged. The barrier reef bounds the ocean side of the bay. It is more than 5-km long and has a width of approximately 2-km (Jokiel, 1991). The lagoon side of the barrier reef has an extensive reef flat, while the offshore side transitions into spur and groove formations.

Overall, the Hawaiian Islands tend to have a low coral diversity as a result of their isolated geographic location, and accordingly so too does Kaneohe Bay. Although less diverse than many other tropical reef systems, this simplicity is advantageous for developing the foundations of coral remote sensing. The most abundant coral in Kaneohe Bay is *Porites compressa*, which occurs mostly in low energy areas and comprises as much as 85% of the total coral in the bay (Jokiel, 1991). Other common coral species include *Montipora verrucosa*, *Montipora capitata*, *Pocillopora damicornis*, *Cyphastrea ocellina*, *Pavona varians*, *Fungia scutaria*, *Porites lobata* and *Pocillopora meandrina*. Figure 2 illustrates some of these species as well as a common algae species in Kaneohe Bay. What is important to note from a remote sensing perspective is the complexity of this environment, in terms of species composition, structural organization and variations in water depth.

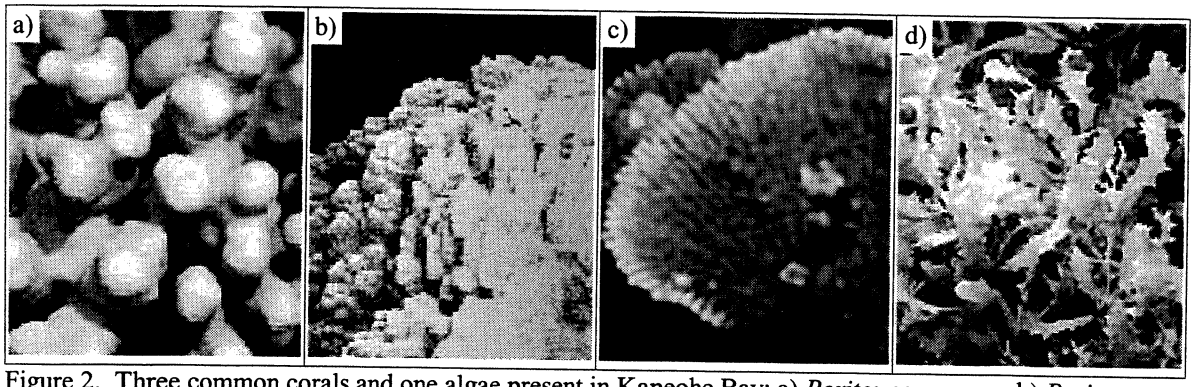

Figure 2. Three common corals and one algae present in Kaneohe Bay: a) *Porites compressa*; b) *Porites lobata*; c) *Montipora capitata*; d) algae, *Sargassum echniocarpum*.

3.3 Human Impacts

Kaneohe Bay has been the subject of numerous studies examining the characteristics and dynamics of its coral reef ecosystem over the last 30-years (Hunter and Evans, 1993; Jokiel, 1991). This is primarily attributed to scientific interest in the bay's ability to return to a coral-dominated system after excessive nutrient inputs caused a shift to an algae-dominated system in the 1970s (Hunter and Evans, 1993; Jokiel et al., 1993). The Kaneohe Marine Corps Air Station, located on the peninsula at the southeast end of the bay, began discharging untreated sewage directly into the bay starting in 1952. The city of Kaneohe further contributed to these sewage inputs when it began releasing secondarily treated sewage into the bay during 1963 (Jokiel, 1991). At the same time, other nutrient sources were also increasing due to changing land use and agricultural practices within the surrounding watershed. As a result, eutrophication in the southeast end of the bay began to produce a shift in species composition and a decrease in diversity. The effect on coral reefs was that large growths of algae began to smother and displace the corals as the dominant species. Eventually, in an effort to halt and reverse the effects of this phase-shift, both of the sewage outfalls were shifted to the deep ocean in 1978. The Kaneohe Bay ecosystem initially responded well to this change, but recovery has slowed in recent years and is still considered incomplete (Hunter and Evans, 1993). Other detrimental human influences on the Kaneohe Bay ecosystem include: increased pollutant loading due to urbanization; modification of much of the shoreline (e.g., native fishponds, seawalls, landfills, boat channels and the introduction of mangroves); overfishing; increased sediment influx due to changing land use and agricultural practices; and dredging and filling to accommodate larger ships within the main channels.

4. METHODS AND RESULTS

4.1 AVIRIS in Hawaii

One of the major AVIRIS missions during the 2000 flight season was a month-long assignment in April to the Hawaiian Islands. Over this time, AVIRIS was used to collect nearly 100 flightlines of data covering both the main Hawaiian Islands (Hawaii, Kahoolawe, Kauai, Maui, Molokai, Oahu and Niihau), as well as four regions of the remote Northwestern Hawaiian Islands (French Frigate Shoals, Gardner Pinnacles, Necker Island and Nihoa Island) (Figure 3). All of the data collected during this campaign utilized the high-altitude ER-2 platform, resulting in a pixel resolution of 20 by 20-m. Although many of these flightlines were acquired for a variety of research purposes, a significant number of the flightlines included imagery over coral reef habitats. Considering the amount of data

that this campaign has made available for coral reef analysis, which includes both significantly human impacted ecosystems in the main Hawaiian Islands and the relatively pristine environments of the Northwestern Hawaiian Islands, this imagery represents a valuable resource for developing and validating coral reef specific hyperspectral analysis tools. Furthermore, the currently scheduled additional AVIRIS flightlines to be acquired in fall of 2001 will only serve to improve on the spatial extent of available data as well as providing repeat coverage for temporal change analysis.

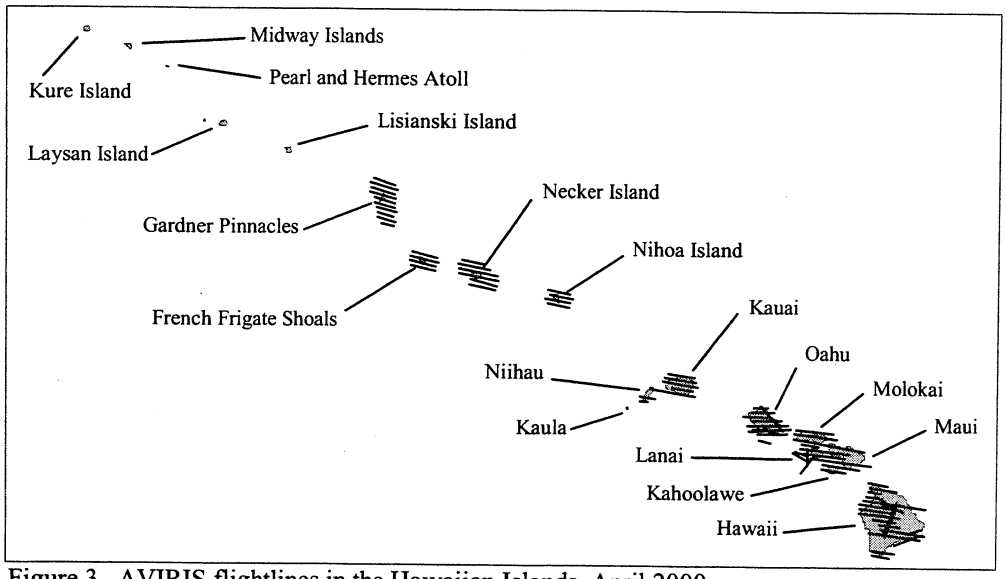

Figure 3. AVIRIS flightlines in the Hawaiian Islands, April 2000.

4.2 Kaneohe AVIRIS data

The flightline used for this project covers the coastal area of the windward shore of Oahu, including the entirety of Kaneohe Bay (AVIRIS flightline: f000412t01 p03_r08). Note that this flightline is predominantly cloud-free over the bay (Figure 4).


Figure 4. AVIRIS flightline, windward shore of Oahu, covering Kaneohe Bay.

4.3 Energy Interactions

In addition to the atmosphere interactions considered in terrestrial investigations, remote sensing of benthic habitats requires additional consideration for the water column and the air-water interface. At this interface, the majority of the energy is transmitted downward into the water column and a small portion is reflected back to the atmosphere (except at low sun angles, when significant amounts of energy can be reflected). Also at this interface, refraction alters the direction of incoming energy such that it is closer to vertical in the water column. Absorption and scattering in the water column then significantly attenuate the downwelling radiation. Absorption in the water column is similar to that in the atmosphere and is controlled by four main components (Kirk, 1996): the water itself, dissolved yellow pigments, photosynthetic biotic components, and abiotic particulate matter. Scattering in the water column is a function of both density fluctuation scattering (causing similar effects to Raleigh scattering at shorter wavelengths) and particle scattering. If it has not already been absorbed, the energy interacts with benthic features where it can be reflected, absorbed, or transmitted. Reflected energy, however, must pass back through the water column, the water-air interface, and the atmosphere before finally reaching the sensor. Ultimately, because the

shorter wavelengths are strongly affected by Raleigh scattering and wavelengths in the near-infrared and longer are significantly absorbed in the water column, the remaining window for analyzing benthic reflectance is limited to approximately 400 to 800-nm.

4.4 Field Spectra

As with most terrestrial-based hyperspectral image analysis, field spectral measurements also constitute a valuable aspect of analyses in marine ecosystems. The measurements are used to identify characteristic spectra of the various habitat types, as well as providing an indication of the potential for distinguishing these different habitats in the hyperspectral imagery. Figure 5 illustrates average reflectance spectra of three major coral species, one algae species, rubble and sand in Kaneohe Bay. Each of the spectra in Figure 5 represents an average of numerous measurements made throughout Kaneohe Bay and thus does not depict the variability present within each species or habitat type. Instead, these spectra are used to illustrate that significant differences do exist between species and particularly between coral and algae (note the differences in inflection points at around 570-nm). Additionally, note the considerable variation in magnitude evident by the spectra of sand and rubble. Thus, these spectra provide a promising indication of the potential for classifying independent habitat types in the AVIRIS data.

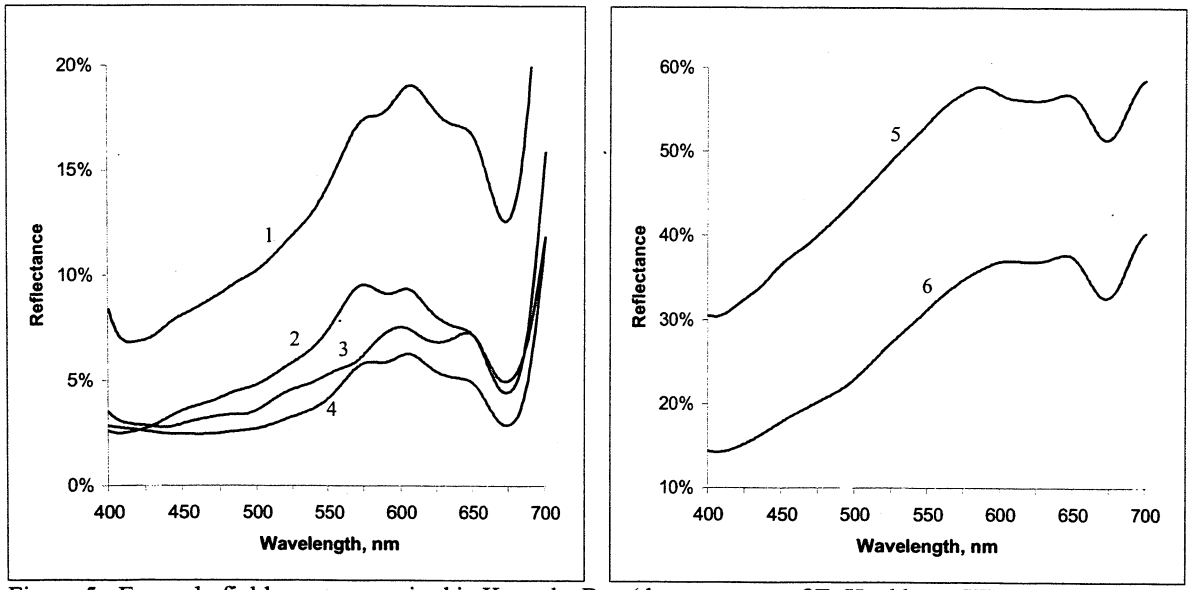

Figure 5. Example field spectra acquired in Kaneohe Bay (data courtesy of E. Hochberg, HIMB): 1) *Porites lobata*; 2) *Porites compressa*; 3) algae, *Sargassum echniocarpum*; 4) *Montipora capitata*; 5) sand; 6) rubble.

4.5 Image Analysis

Spectral separability refers to an ability to distinguish quantifiable differences in the reflectance characteristics between the categories selected for classification. Analysis conducted for this phase of the project was used to investigate spectral separability in the AVIRIS flightline covering Kaneohe Bay. This was accomplished using an unsupervised classification (Isodata clustering with 10 classes and 50 iterations applied to bands between 400 and 800-nm) to examine the potential for distinguishing different benthic habitat types in this flightline (Figure 6). It is important to note that this analysis was conducted directly on the radiance values, not reflectance, and did not incorporate atmospheric or water column corrections. Although no attempt was made to explicitly identify each of the resulting classes, observed patterns match those known to be present in the bay and illustrate clear spectral differences between habitat types. These results strongly support the validity of this approach and show promise for improved separability following atmospheric and water column corrections.

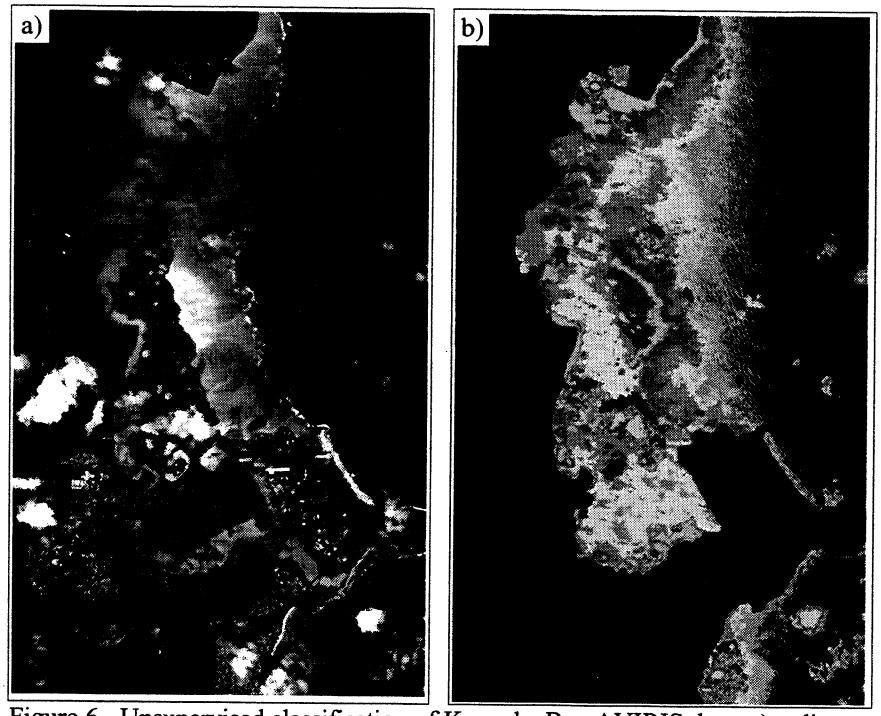

Figure 6. Unsupervised classification of Kaneohe Bay AVIRIS data: a) radiance image; b) classification output.

5. CONCLUSION

By taking advantage of the synoptic spatial and temporal monitoring capabilities of remote sensing as well as the spectral detail available from AVIRIS, the end product of this research will be an efficient tool for monitoring and assessing coral reefs. Adding this tool to the existing resources available to scientists and ecosystem managers will result in better preservation and protection strategies. Results from the first phase of this analysis have provided promising indications of the utility of the hyperspectral approach. Continued phases will address atmospheric and water column image corrections and identification of appropriate classification tools. Ultimately, a complete set of analysis tools will be developed that utilize the spectral resolution provided by AVIRIS and provide valuable products for coral management.

6. ACKOWLEDGEMENTS

This project is funded by the Department of Land, Air and Water Resources at the University of California, Davis with support from the Center for Spatial Technologies and Remote Sensing (CSTARS). The authors would also like to thank the Jet Propulsion Laboratory (JPL) for providing the AVIRIS data and Eric Hochberg at the Hawaii Institute of Marine Biology for use of the Kaneohe Bay field spectra.

7. REFERENCES

Dight, I.J. and L.M. Scherl, 1997, "The International Coral Reef Initiative (ICRI): Global Priorities for the Conservation and Management of Coral Reefs and the Need for Partnerships," Coral Reefs, vol. 16, no. S, pp. 139-147.

Dustan, P., S. Chakrabarti, and A. Alling, 2000, "Mapping and Monitoring the Health and Vitality of Coral Reefs from Satellite: A Biospheric Approach," Life Support & Biosphere Science, vol. 7, pp. 149-159.

Hochberg, E.J. and M.J. Atkinson, 2000a, "Spectral Discrimination of Coral Reef Benthic Communities," Coral Reefs, vol. 19, pp. 164-171.

Hochberg, E.J. and M.J. Atkinson, 2000b, "Spectral Reflectance Characteristics of Coral Reef Benthic Communities," Ninth International Coral Reef Symposium, Bali, Indonesia, 23-27 October.

Hodgson, G., 1999, "A Global Assessment of Human Effects on Coral Reefs," Marine Pollution Bulletin, vol. 38, no. 5, pp.:345-355.

Hoegh-Guldberg, O., 1999, "Climate Change, Coral Bleaching and the Future of the World's Coral Reefs," Marine & Freshwater Research, vol. 50, pp. 839-866.

Holden, H. and E. LeDrew, 1998a, "Spectral Discrimination of Healthy and Non-Healthy Corals Based on Cluster Analysis, Principal Components Analysis, and Derivative Spectroscopy," Remote Sensing of the Environment, vol. 65, pp. 217-224.

Holden, H. and E. LeDrew, 1998b, "A Critical Literature Review of the Scientific Issues Surrounding the Remote Detection of Coral Health," Progress in Physical Geography, vol. 22, no. 2, pp. 190-221.

Holden, H. and E. LeDrew, 1999, "Hyperspectral Identification of Coral Reef Features," International Journal of Remote Sensing, vol. 20, no. 13, pp. 2545-2563.

Hughes, T.P. and J.H. Connell, 1999, "Multiple Stressors on Coral Reefs: A Long-Term Perspective," Limnology and Oceanography, vol. 44, no. 3, pp. 932-940.

Hunter, C.L. and C.W. Evans, 1993, "Reefs in Kaneohe Bay, Hawaii: Two Centuries of Western Influence and Two Decades of Data," In Global Aspects of Coral Reefs: Health, Hazards, and History, R.N. Ginsburg compiler, Rosenstiel School of Marine and Atmospheric Sciences, University of Miami, 420 pp.

Jokiel, P.L., 1991, "Jokiel's illustrated scientific guide to Kaneohe Bay, Oahu," Hawaiian Coral Reef Assessment and Monitoring Program.

Jokiel, P.L., C.L. Hunter, S. Taguchi, and L. Wotari, 1993, "Ecological Impact of a Fresh-Water "reef kill" in Kaneohe Bay, Oahu, Hawaii," Coral Reefs, vol. 12, pp. 177-184.

Kirk, J., 1996, "Light & photosynthesis in aquatic ecosystems, second edition," Cambridge University Press, 509 pp.

Lubin, D., W. Li, P. Dustan, C.H. Mazel, and K. Stamnes, 2001, "Spectral Signatures of Coral Reefs Features From Space," Remote Sensing of Environment, vol. 75, no. 1, pp. 127-137.

Mumby, P.J., E.P. Green, C.D. Clark, and A.J. Edwards, 1998, "Digital Analysis of Multispectral Airborne Imagery of Coral Reefs," Coral Reefs, vol. 17, pp. 59-69.

Myers, M.R., J.T. Hardy, C.H. Mazel, and P. Dustan, 1999, "Optical Spectra and Pigmentation of Carribean Reef Corals and Macroalgae," Coral Reefs, vol. 18, pp. 179-186.

Richardson, L. and F.A. Kruse, 2000, "Hyperspectral Imaging Sensors and Assessment of Coral Health in the Florida Keys," Ninth International Coral Reef Symposium, Bali, Indonesia, 23-27 October.

Sammarco, P.W., 1996, "Comments on Coral Reef Regeneration, Bioerosion, Biogeography, and Chemical Ecology: Future Directions," J. Exp. Marine Biology and Ecology, vol. 200, pp. 135-168.

Schalles, J., J. Maeder, D. Rundquist, J. Keck, and S. Narumalami, 2000, "Spectral Reflectance Measurements of Corals and Other Reef Substrates at Close Range and Near the Surface," Ninth International Coral Reef Symposium, Bali, Indonesia, 23-27 October.

Wilkinson, C. ed., 2000, "Status of coral reefs of the world: 2000," Australian Institute of Marine Science, 363 pp.

Estimating the Expressed Temperature and Fractional Area of Hot Lava at the Kilauea Vent with AVIRIS Spectral Measurements

Robert O. Green
Jet Propulsion Laboratory, California Institute of Technology, Pasadena, California 91109

INTRODUCTION

Imaging spectroscopy offers a framework based in physics and chemistry for scientific investigation of a wide range of phenomena of interest in the Earth environment. In the scientific discipline of volcanology knowledge of lava temperature and distribution at the surface provides insight into the volcano status and subsurface processes. A remote sensing strategy to measure surface lava temperatures and distribution would support volcanology research. Hot targets such as molten lava emit spectral radiance as a function of temperature. Figure 1 shows a series of Planck functions (Liou, 1980) calculated radiance spectra for hot targets at different temperatures. A maximum Lambertian solar reflected radiance spectrum is shown as well. While similar in form, each hot target spectrum has a unique spectral shape and is distinct from the solar reflected radiance spectrum. Based on this temperature-dependant signature, imaging spectroscopy provides an innovative approach for the remote-sensing-based measurement of lava temperature. A natural site for investigation of the measurement of lava temperature is the Big Island of Hawaii where molten lava from the Kilauea vent is present at the surface. Figure 2 shows a satellite image of Hawaii with the vent location identified.

On April 26, 2000 the Airborne Visible/Infrared Imaging Spectrometer (AVIRIS) (Green et al., 1998) measured the active volcanic vent on the Big Island of Hawaii. Figure 3 shows the AVIRIS image of the vent. AVIRIS measures spectra from 400 to 2500 nm with nominally 10-nm sampling and response function full-width-at-half maximum. These spectra are acquired as images with a width of 11 km and length of up to 800 km from the Q-bay of the ER-2 aircraft platform flying at 20 km altitude. AVIRIS spectral images are spectrally, radiometrically, and spatially calibrated (Chrien et al., 1990, 1995, 1996, 2000).

In the past, AVIRIS data sets have been used for the analysis of hot volcanic targets (Oppenheimer et al., 1993) and hot burning fires (Green, 1996). The research presented here builds upon and extends this earlier work. The year 2000 Hawaii AVIRIS data set has been analyzed to derive lava temperatures taking into account factors of fractional fill, solar reflected radiance, and atmospheric attenuation of the surface emitted radiance. The measurements, analyses, and current results for this research are presented here.

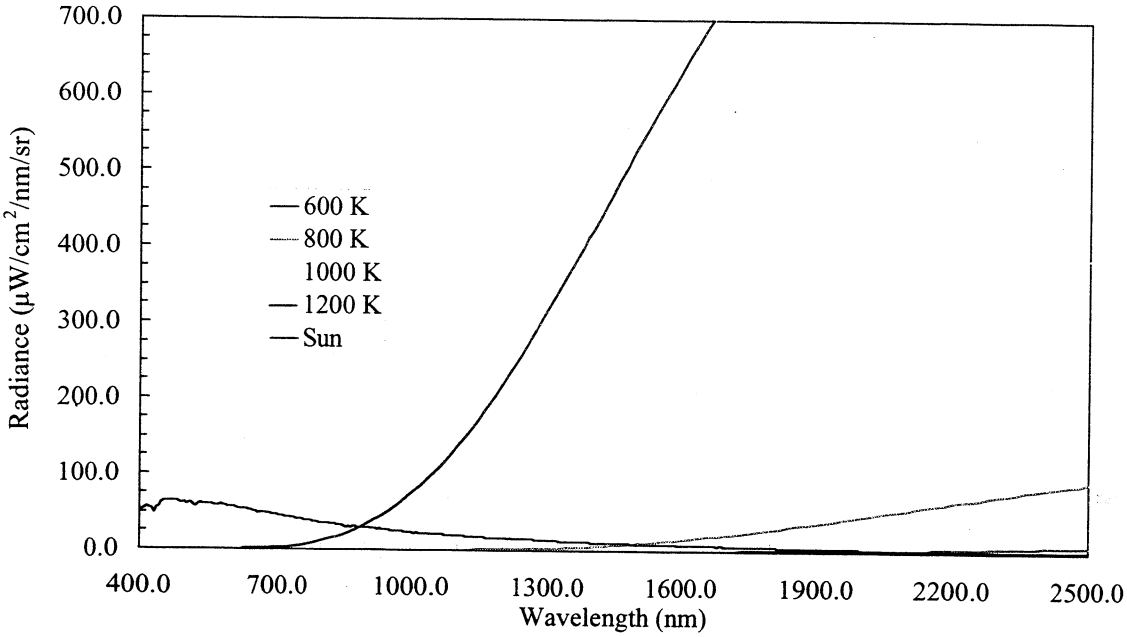

Figure 1. Maximum Lambertian reflected solar radiance spectrum as well as the emitted radiance spectra from the Planck function at temperatures of 600, 800, 1000, and 1200 K.

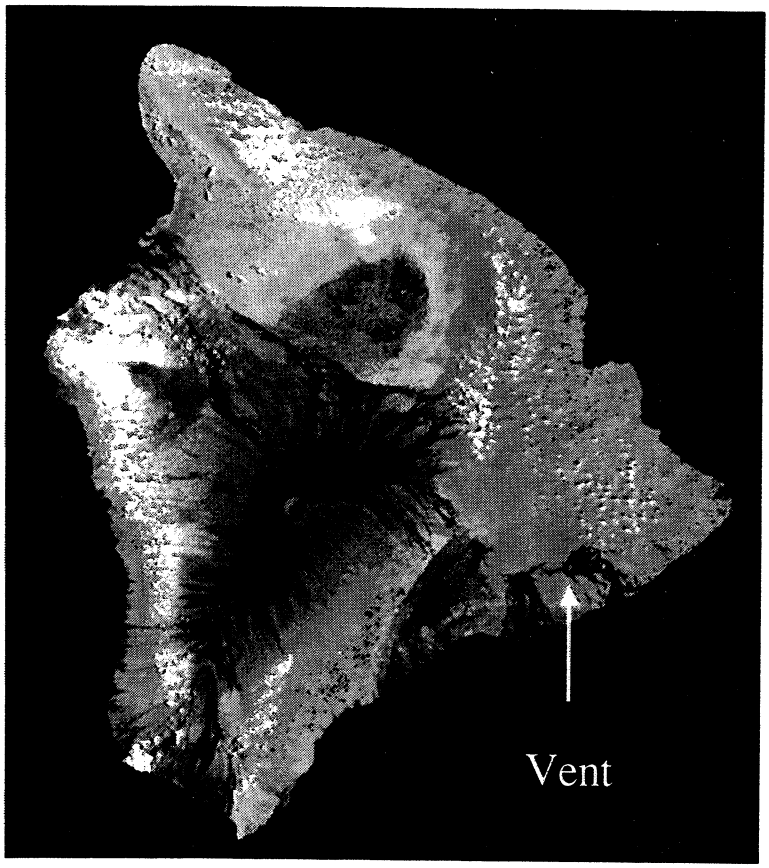

Figure 2. Image of Hawaii acquired by 1-km multispectral satellite sensor showing the location of the active volcanic vent on the Big Island of Hawaii.

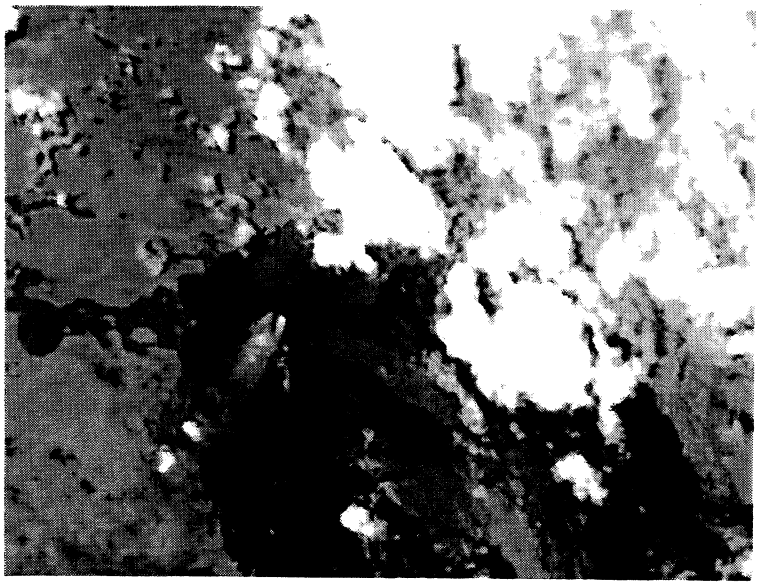

Figure 3. AVIRIS image of the active volcanic vent on Hawaii acquired on April 26, 2000.

AVIRIS MEASUREMENTS

The AVIRIS instrument imaged the active vent on the Big Island of Hawaii April 26, 2000. The complexity of the spectral signatures of a hot lava target and other Earth environment components is revealed through the different wavelength images of the AVIRIS data set. Figure 4 shows the AVIRIS image measured at 500.4 nm in the solar reflected spectrum. This image shows the volcanic plume exiting from the vent, surface rock, and dark vegetation features, as well as an extensive field of bright water vapor clouds. Figure 5 shows an image at 1503.4 nm wavelength. At this wavelength the plume is less opaque and bright spots at the surface are apparent. These high intensity spots near the source of the plume are an indication that radiance emitted by the lava is being measured by AVIRIS. Vegetation is consistently brighter than the rock cover surface near the active vent. The water vapor clouds are bright and dominate the image. In Figure 6 the AVIRIS image measured at 2500.9 nm is shown. At this wavelength the plume is largely transparent, and seven high intensity hot spots are evident near the source of the plume. These hot spots are sources of emitted radiance and are the highest intensity components of the image at this wavelength. The signal levels for the solar reflected radiance from the surface and clouds components are low due to the strong attenuation by atmospheric water vapor.

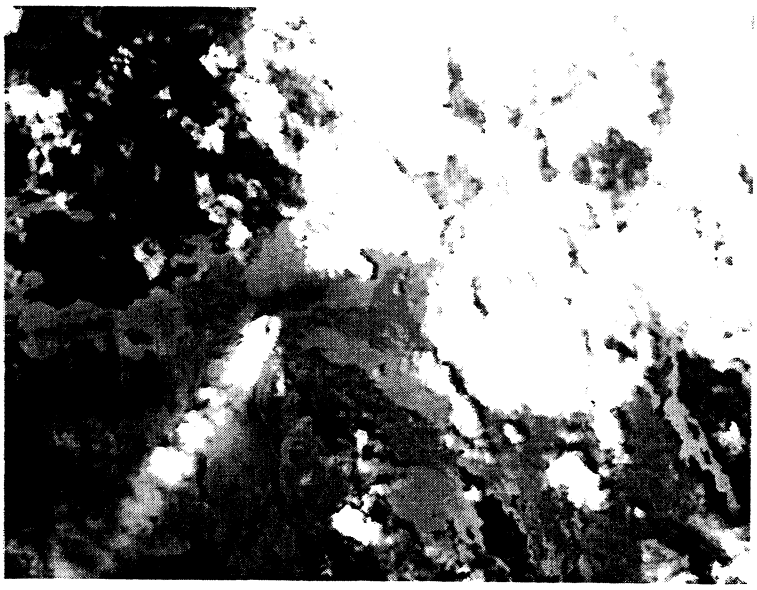

Figure 4. AVIRIS image from 500.4 nm showing solar reflected radiance from the region including the active volcanic vent.

Figure 5. AVIRIS image at 1503.4˚nm showing mixture of solar reflected radiance and hot target radiance from the active volcanic vent.

Figure 6. AVIRIS image at 2500.9 nm showing the emitted radiance of the hot lava.

In addition to the image perspective, the AVIRIS data set allows examination of the contiguous spectral signature of each measured spatial element in the image. Figure 7 shows selected spectra from the data set. Absorption and scattering effects due to the atmosphere are present in each spectrum. The dominant atmospheric absorber is water vapor with significant absorption bands at 940, 1150, 1400, 1900, and 2600 nm. The vegetation spectrum shows the chlorophyll absorption in the range 400 to 700 nm, high radiance levels from 750 to 1350 nm, and low intensity from 1350 to 2500 nm. The rock surface shows a comparatively uniform low radiance signal across the spectral range. In contrast, the cloud is bright across the spectral range. The hot lava spectrum has a form similar in shape to the cloud from 400 to 1000 nm. Beyond 1000 nm, the spectral radiance signature increases until the AVIRIS dynamic range saturates near 2000 nm. In the 1450 to 2500 nm portion of the spectrum, the emitted radiance from the hot lava target dominates the spectral signature. The distinct intensity and shape of this emitted spectral radiance provides the basis for lava temperature and fractional area estimation.

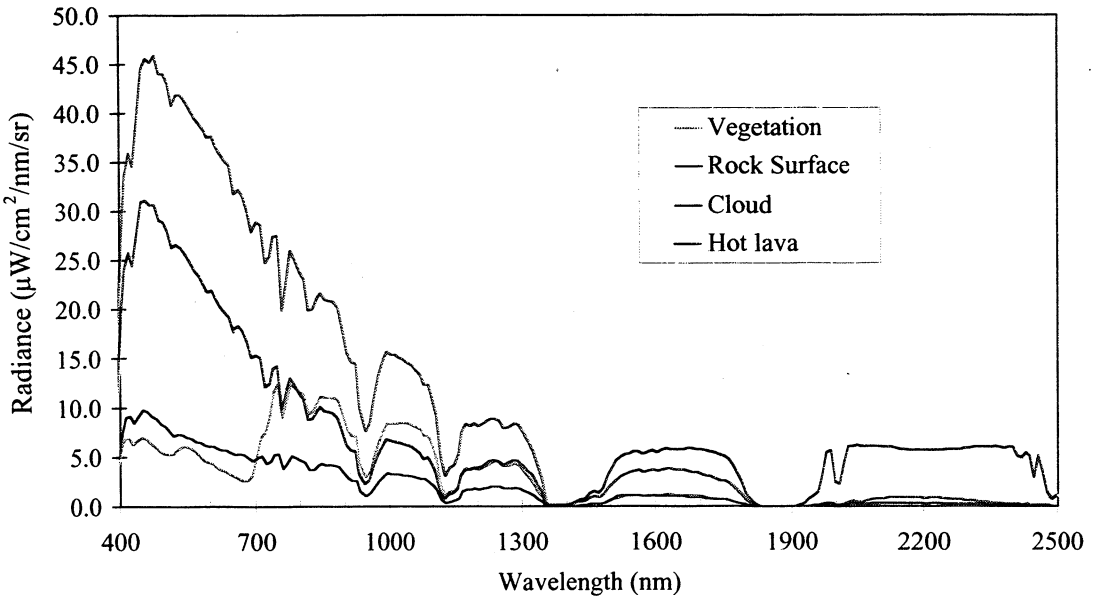

Figure 7. AVIRIS spectra spanning the range of major spectral signatures in the April 26, 2000 volcanic vent data set. At 2000 nm AVIRIS is saturated by emitted radiance over the hot lava target.

TEMPERATURE ANALYSIS

For the AVIRIS Hawaii data set, seven hot spots were analyzed to determine the expressed lava temperature and fractional area. Figure 8 shows an image with these seven targets labeled A through G. From each hot spot, the spectrum with the highest radiance from 1200 to 2500 was extracted for analysis. These extracted radiance spectra include effects from the solar source, the atmosphere, the surface, and the exposed hot lava. Equation 1 gives a simplified expression for the total radiance measured by AVIRIS over a hot target. In this equation L_t is the radiance measured by AVIRIS, I_0 is the exoatmospheric solar irradiance, ρ_a is the atmospheric reflectance, T_d is the downward transmittance, ρ_s is the surface reflectance, T_u is the upward transmittance, F_1 is the fractional area of the hot target, and B_{t1} is the Planck function radiance emitted for a given temperature. All quantities are for the illumination and observation geometry of the measurement at each wavelength across the AVIRIS spectral range.

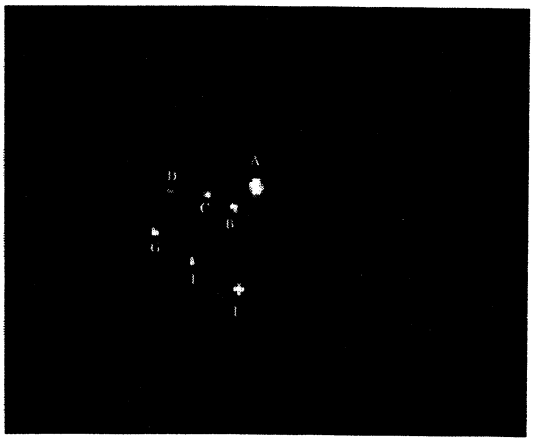

Figure 8. Location of hot spots near volcanic vent on April 26, 2000.

The approach for temperature estimation with the extracted AVIRIS spectra is based upon the Planck function. The Planck function allows direct calculation of the spectral distribution of radiance for a target of a given temperature and unity emissivity. For each AVIRIS hot target spectrum, an adjacent cool surface spectrum was identified that best matched the hot spectrum in the range from 400 to 1000 nm. This cool spectrum was used to assess and suppress the atmospheric radiance and surface reflected radiance in the hot target spectrum. Figure 9 shows the hot spectrum, adjacent cool spectrum, and difference spectrum for hot spot A. The resulting difference spectrum is dominated by the hot lava emitted radiance. Effects of atmospheric transmittance from the surface to AVIRIS are still present as well as saturation of the AVIRIS dynamic range beyond 1500 nm. For this initial analysis, a Planck function model with parameters temperature and fractional area fill was fit to the AVIRIS difference spectrum only in the spectral regions of high atmospheric transmittance and unsaturated data. Figure 10 shows a temperature and area estimation result from this analysis for hot spot A with a temperature of 908 K and fractional area fill of 0.068. The analysis was repeated for the seven extracted hot spot spectra. Figures 11 and 12 give the temperature and fractional area fill results for hot spots C and E, respectively. A temperature of 1239 K and 0.0016 fractional fill was derived for hot spot C and 1067 K and 0.025 fractional fill for hot spot E. Hot spot C had the highest derived temperature and yet due to a low fractional fill did not saturate in any portion of the AVIRIS spectral range. Hot spot E saturated the AVIRIS dynamic range in portions of the spectrum beyond 2000 nm. A summary of the temperatures and area fraction derived for each of the hot spots analyzed is given in Table 1. The temperatures range from 908 K to 1204 K and fractional areas from 0.0016 to 0.24. This simple algorithm of Equation 1 demonstrates the leverage of imaging spectrometer measurements for derivation temperature and fractional fill areas estimates for hot targets on the surface of the Earth.

$$L_t = I_0\rho_a/\pi + I_0T_d\rho_sT_u/\pi + F_1B_{t1} \qquad \text{Equation 1}$$

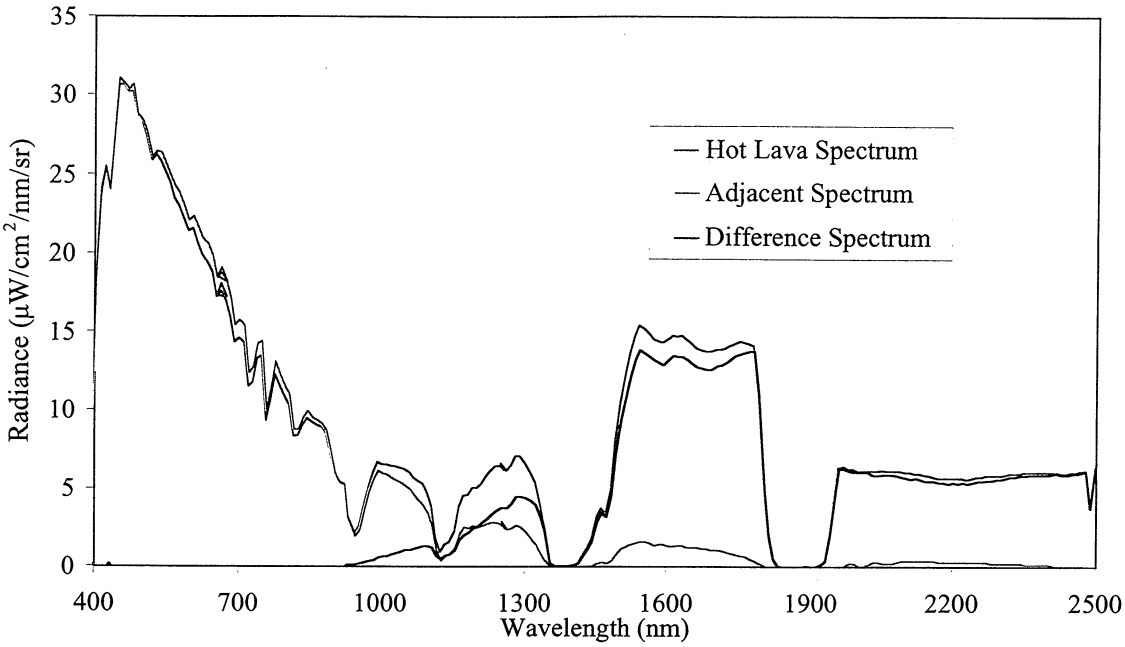

Figure 9. Spectra from hot lava target A, adjacent spectrum, and difference spectrum.

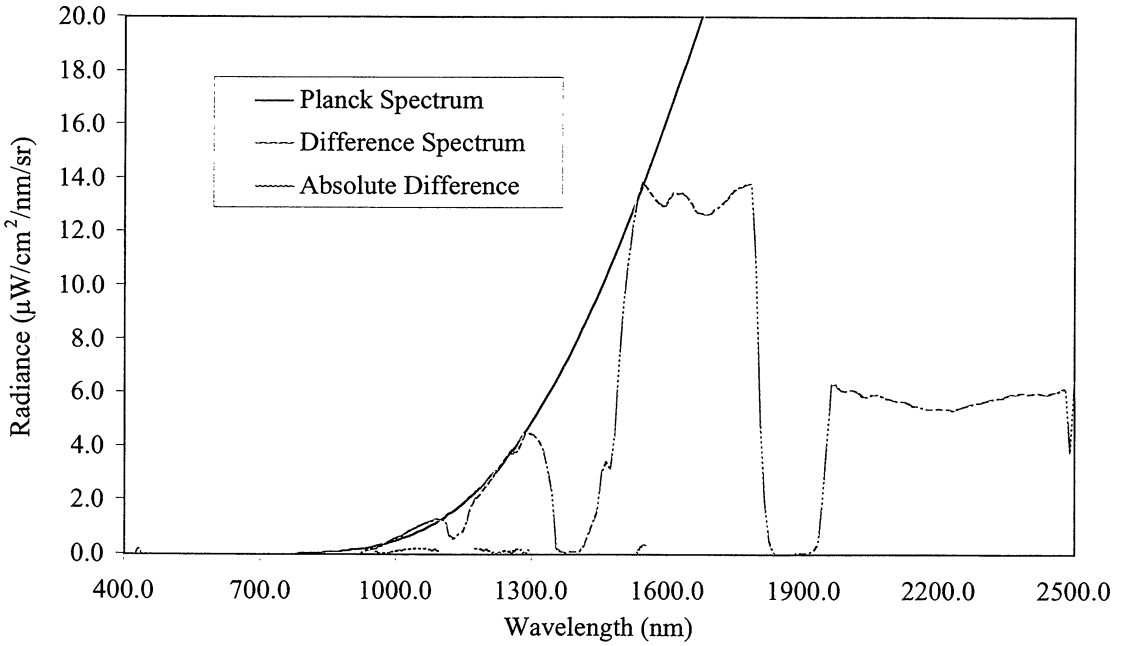

Figure 10. Fit of Planck function to AVIRIS spectrum for hot spot A with correction for solar reflected radiance. A temperature of 923°K and area fraction of 0.24 was derived. The AVIRIS dynamic range is saturated in portions of the spectrum beyond 1500 nm.

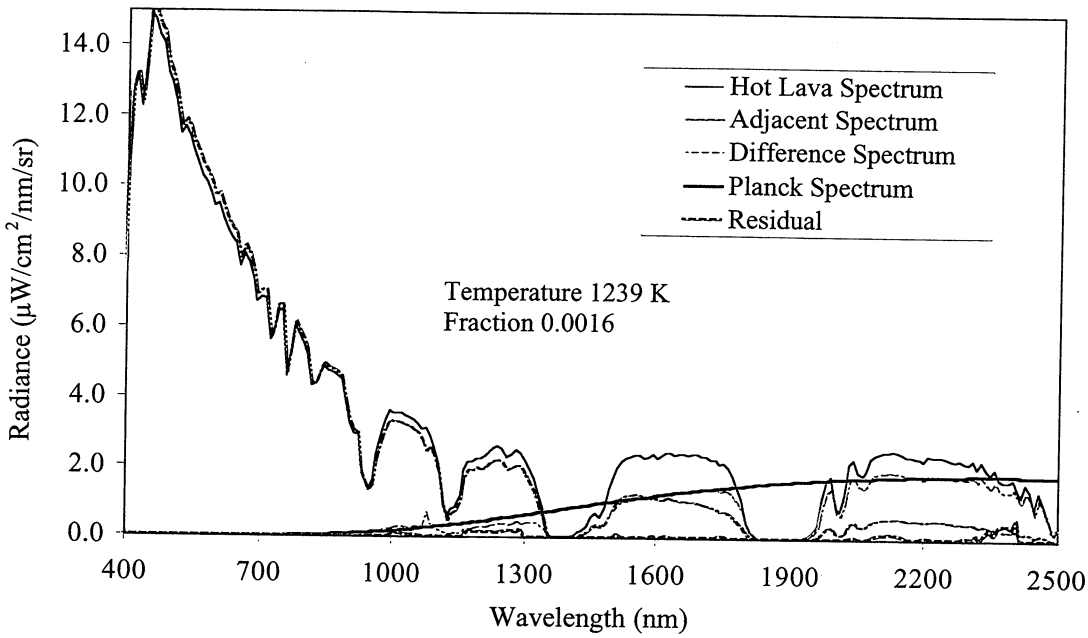

Figure 11. Spectral temperature and fractional area determination for hot spot C.

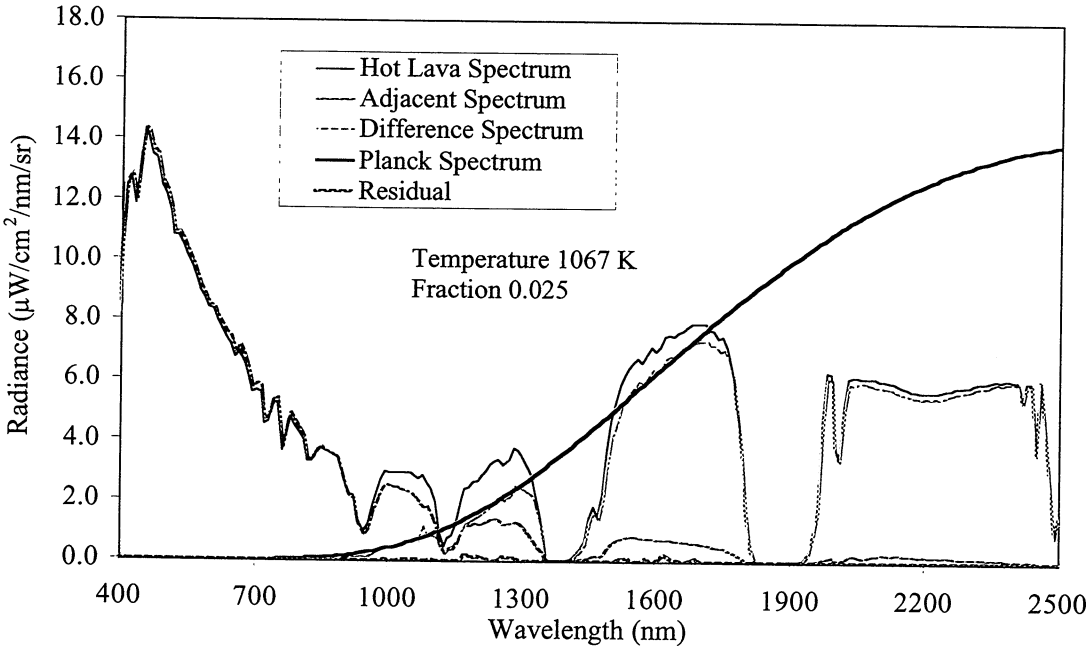

Figure 12. Spectral temperature and fractional area determination for hot spot E.

Table 1. Hawaii hot spot temperature and fractional fill determinations.

Site	Temperature (K)	Fractional Area
A	923	0.24
B	908	0.068
C	1239	0.0016
D	973	0.027
E	1067	0.025
F	1052	0.034
G	1168	0.0023

To further explore temperature and fractional area determinations with these AVIRIS measurements, a second form of spectral fitting algorithm was developed. Equation 2 gives the expression of the total radiance measured by AVIRIS used for this more sophisticated model based algorithm. In addition to the components given in Equation 1, the factor T_u is used to account for the upward attenuation of the lava emitted radiance and the factors F_2 and B_{t2} provide a second temperature target at the surface. This algorithm used the MODTRAN (Berk et al., 1989; Anderson et al., 1995, 2000) radiative transfer code to calculate the atmosphere and surface reflected radiance components as well as the one way transmittance for the emitted radiance from the surface to AVIRIS. To estimate the atmospheric radiance and surface reflected radiance, a MODTRAN spectrum was generated to fit the measured spectrum over the range 400 to 950 nm. For this fit the surface reflectance and visibility parameters were allowed to vary for the 5-km-visibility tropical atmospheric model until an optimal fit was achieved. MODTRAN was also used to calculate the transmittance from the surface to AVIRIS to account for attenuation of the surface emitted radiance. Figure 13 shows the extracted spectrum for hot spot C as well as the MODTRAN modeled spectrum calculated to match over the 400 to 950 nm range and the upward transmittance spectrum.

$$L_t = I_0\rho_a/\pi + I_0T_d\rho_sT_u/\pi + T_u(F_1B_{t1}+F_2B_{t2}) \qquad \text{Equation 2}$$

For temperature and fractional area analysis, the calculated MODTRAN spectrum was subtracted from the measured spectrum and the upward transmittance divided to generate a spectrum dominated by the hot target emitted radiance. The resulting corrected spectrum was fit with two Planck functions at two independent temperatures and fractional areas. Regions of near total atmospheric absorption were excluded from the fit. Figure 14 shows the fit for temperature and fractional area determination of hot spot C. The temperatures derived were 1283 K and 600 K at fractions fill areas of 0.0018 and 0.0033 respectively. The quality of the spectral fit is good with some residual disagreement near regions of atmospheric absorption. This more sophisticated algorithm more accurately models and compensates for the solar reflected and atmospheric attenuation factors in the estimation of surface lava temperature from the calibrated AVIRIS measurements. Future work is planned to refine the algorithm and model and further understand and minimize the effects of uncertainties in AVIRIS calibration and the MODTRAN radiative transfer calculations.

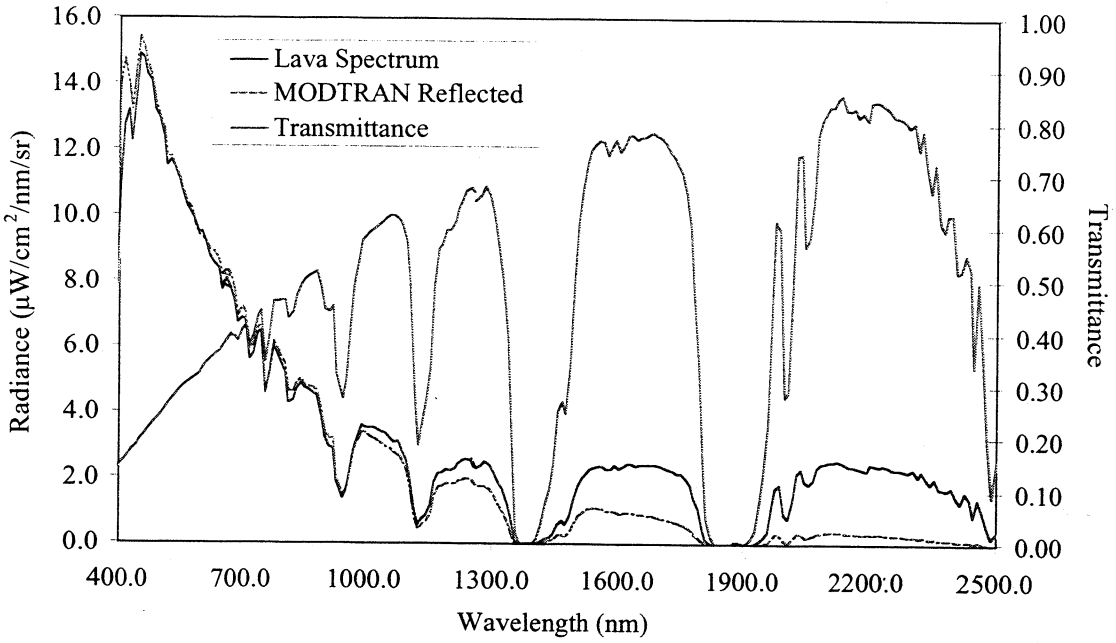

Figure 13. AVIRIS measured spectrum, MODTRAN modeled solar reflected spectrum and MODTRAN modeled upwards transmittance spectrum for hot lava target C.

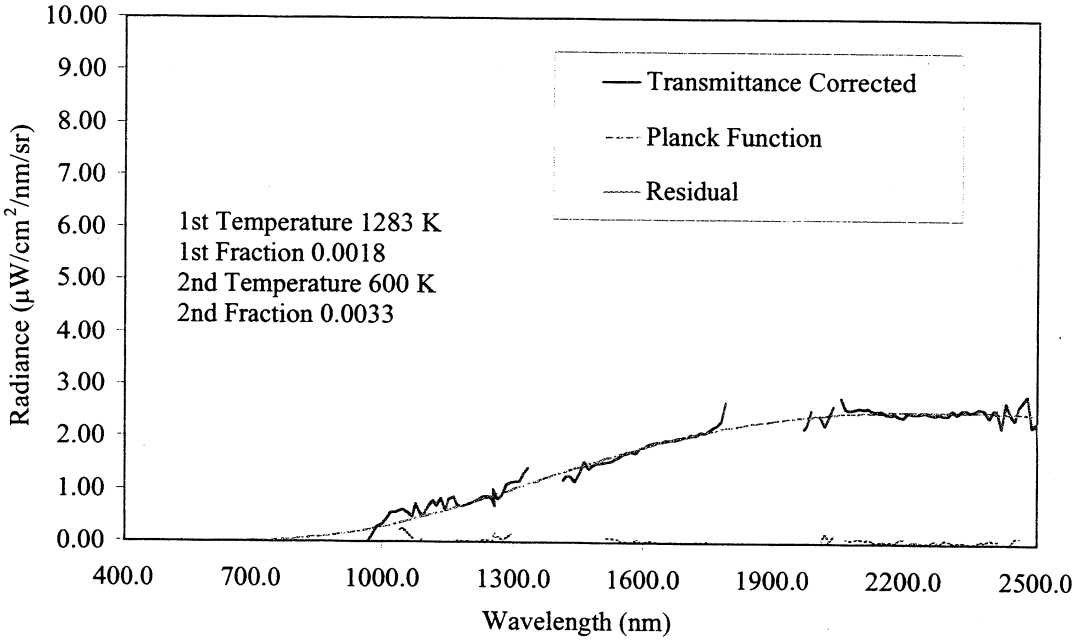

Figure 14. Spectral fit between two-Planck-function model and AVIRIS measured spectrum from hot lava target C with reflected solar radiance and atmospheric correction. Regions of strong atmospheric attenuation are excluded.

CONCLUSION

The AVIRIS imaging spectrometer measured the active volcanic vent region on the Big Island of Hawaii on April 26, 2000. Examination of the spectral image data set showed distinct expression of seven lava

hot spots. These hot spots show enhanced radiance signatures in the spectral region beyond 1000 nm with respect to all other Earth environment components in the AVIRIS data set. The full spectral shape measured by AVIRIS provided a basis for temperature and fractional area estimation from these hot spot spectra. An initial simple algorithm was used to estimate temperature and fractional area. This algorithm suppressed the solar reflected radiance in the hot lava spectrum by subtraction of an adjacent cool target spectrum. Following this correction, a spectral Planck-function model with both temperature and fractional area parameters was fitted to the corrected spectrum. The fit was restricted to spectral regions of high atmospheric transmittance and regions where the AVIRIS dynamic range was not saturated. Good spectral fits were achieved for the analyzed spectra from each of the seven lava hot spots. Derived temperatures ranged from 923 K to 1239 K and fractional areas from 0.0016 to 0.24.

A second temperature estimation algorithm was implemented that used the calculations by the MODTRAN radiative transfer code. This algorithm used MODTRAN to estimate the solar reflected component in the measured spectrum as well as the atmospheric transmittance from the surface to AVIRIS. With these MODTRAN-based corrections more of the spectral range of the measured spectrum was usable for fitting. In conjunction with these more advanced corrections, a two-Planck-function model with independent temperatures and fractional area was used. When applied to lava hot spot C, temperatures of 1283 K and 600 K (and respective fractional areas of 0.0018 and 0.0033) were derived. This more sophisticated temperature and fractional-area estimation algorithm more fully accounts for the complexity of the surface and atmospheric components expressed in the measured hot lava spectrum.

These analyses and results demonstrate the use of full solar reflected spectrum imaging spectrometer measurements for hot target temperature and fractional area estimation. The results are tied to the spectral shape of the measured radiance as well as the intensity. Accounting for both spectral shape and intensity is required to avoid the ambiguity between intensity and fractional-area fill. Imaging spectrometer measurements enable a direct approach, based in fundamental physics rather than data statistics, to derive these important properties of hot targets from the remote sensing perspective.

REFERENCES

Anderson, G. P., J. Wang, and J. Chetwynd, "An Update and Recent Validations Against Airborne High Resolution Interferometer Measurements," *Summaries of the Fifth Annual JPL Airborne Earth Science Workshop*, JPL Pub. 95-1, Vol. 1, *AVIRIS Workshop*, Jet Propulsion Laboratory, Pasadena, California, pp. 5–8, January 23, 1995.

Anderson, G. P., A. Berk, P. K Acharya, M. W. Mathew, L. S. Bernstein, J. H. Chetwynd, H. Dothe, S. M. Adler-Golden, A. Ratkowski, G. W. Felde, J. A. Gardner, M. L. Hoke, S. C. Richtsmeir, B. Pukall, J. Mello, and L. S. Jeong, "MODTRAN4: Radiative transfer modeling for remote sensing," in *Proceedings SPIE, Algorithms for Multispectral, Hyperspectral, and Ultraspectral Imagery VI*, Vol. 4049, S. S. Shen and M. R. Descour, eds., pp. 176–183, 2000.

Berk, A., L. S. Bernstein, and D. C. Robertson, *MODTRAN: A Moderate Resolution Model for LOWTRAN 7*, Final report, GL-TR-0122, AFGL, Hanscomb AFB, Massachusetts, 42 pp., 1989.

Chrien, T. G., R. O. Green, and M. L. Eastwood, "Accuracy of the spectral and radiometric laboratory calibration of the Airborne Visible/Infrared Imaging Spectrometer (AVIRIS)," *SPIE Vol. 1298, Imaging spectroscopy of the terrestrial environment*, G. Vane, ed., pp. 37–49, 1990.

Chrien, T. G., R. O. Green, C. Chovit, M. Eastwood, J. Faust, P. Hajek, H. Johnson, H. I. Novack, and C. Sarture, "New Calibration Techniques for the Airborne Visible/Infrared Imaging Spectrometer

(AVIRIS), 1995," *Proc. Fifth Annual Airborne Earth Science Workshop*, JPL Pub. 95-1, Jet Propulsion Laboratory, Pasadena, California, pp. 33–34, 1995.

Chrien, T. G., R. O. Green, C. J. Chovit, M. L. Eastwood, and C. M. Sarture, "Calibration of the Airborne Visible/Infrared Imaging Spectrometer in the Laboratory," *Proc. Sixth Annual Airborne Earth Science Workshop*, JPL Pub. 96-4, Vol. 1, Jet Propulsion Laboratory, Pasadena, California, pp. 39–48, March 3–5, 1996.

Chrien, T. G., R. O. Green, B. Pavri, and J. Wall, "Calibration Validation of the AVIRIS Portable Radiance Standard," *Proc. Ninth Airborne Earth Science Workshop*, JPL Pub. 00-18, Jet Propulsion Laboratory, Pasadena, California, pp. 101–110, 2000.

Green, R. O., "Estimation of Biomass Fire Temperature and Areal Extent from Calibrated AVIRIS Spectra," Proc. Sixth Annual Airborne Earth Science Workshop, Jet Propulsion Laboratory, JPL Pub. 96-4, Vol. 1, pp. 105–113, March 3-5, 1996.

Green, R. O., M. L. Eastwood, C. M. Sarture, T. G. Chrien, M. Aronsson, B. J. Chippendale, J. A. Faust, B. E. Pavri. C. J. Chovit, M. Solis, M. R. Olah, and Q. Williams, "Imaging spectroscopy and the Airborne Visible/Infrared Imaging Spectrometer (AVIRIS)," *Remote Sens Environ* 65: (3) 227–248, Sept. 1998.

Liou, K. N., *An Introduction to Atmospheric Radiation*, Academic Press, Inc., New York, pp. 392, 1980.

Oppenheimer, C., D. A. Rothery, D. C. Pieri, M. J. Abrams, V. Carrere, "Analysis of Airborne Visible/Infrared Imaging Spectrometer (AVIRIS) Data of Volcanic Hot-Spots," Open Univ., Dept. Earth Sci./Milton Keynes/MK7 6AA/Bucks./ENGLAND/*International Journal of Remote Sensing*, 14, (16), 2919–2934, 1993.

ACKNOWLEDGEMENTS

The research described herein was carried out at the Jet Propulsion Laboratory, California Institute of Technology, under a contract with the National Aeronautics and Space Administration.

Reference herein to any specific commercial product, process, or service by trade name, trademark, manufacturer, or otherwise, does not constitute or imply its endorsement by the United States Government or the Jet Propulsion Laboratory, California Institute of Technology.

Measuring the Spectral Expression of Carbon Dioxide in the Solar Reflected Spectrum with AVIRIS

Robert O. Green
Jet Propulsion Laboratory, California Institute of Technology, Pasadena, California 91109

INTRODUCTION

Carbon dioxide is a low-concentration, but important, component of the Earth's atmosphere. This gas absorbs electromagnetic radiation (EMR) in several regions of the spectrum. Absorption of energy by carbon dioxide adds heat to the atmosphere. In the world today, the burning of fossil fuels and other anthropogenic processes adds carbon dioxide to the atmosphere. Other natural processes in the Earth's system both add and remove carbon dioxide. Overall, measurements of atmospheric carbon dioxide at selected sites around the globe show an increased carbon dioxide concentration in the atmosphere. Figure 1 shows the measured carbon dioxide from Mauna Loa, Hawaii, from 1958 to 2000. Overall, the concentration has increased from 315 to 365 ppm at this site over this period. (There is also a yearly cycle to the concentration that is timed with and hypothesized to be related to the vegetation growing season in the Northern Hemisphere.) The overall expected effect of this increase of atmospheric carbon dioxide is trapping of heat in the atmosphere and global warming. While this overall relationship between carbon dioxide and global warming seems straightforward (IPCC, 1996), many of the specific details relating to regional and local sources and sinks and gradients of carbon dioxide are not well understood. A remote sensing capability to measure carbon dioxide could provide important inputs for scientific research to better understand the distribution and change in atmospheric carbon dioxide at detailed spatial and temporal levels.

In pursuit of this remote sensing of carbon dioxide objective, this paper analyzes the expression of carbon dioxide in the spectral range measured by the Airborne Visible/Infrared Imagery Spectrometer (AVIRIS) (Green et al., 1998). Based on these analyses, a spectral-fitting algorithm that uses AVIRIS measured spectra and MODTRAN radiative-transfer code (Berk et al., 1989; Anderson et al., 1995, 2000) modeled spectra to derive total column carbon dioxide abundance has been developed. This algorithm has been applied to an AVIRIS data set acquired over Pasadena, California, in 1999 and a data set acquired over the Pacific Ocean near Hawaii in 2000 with promising results. This is ongoing research; the current initial analyses, measurements, and results are reported in this paper.

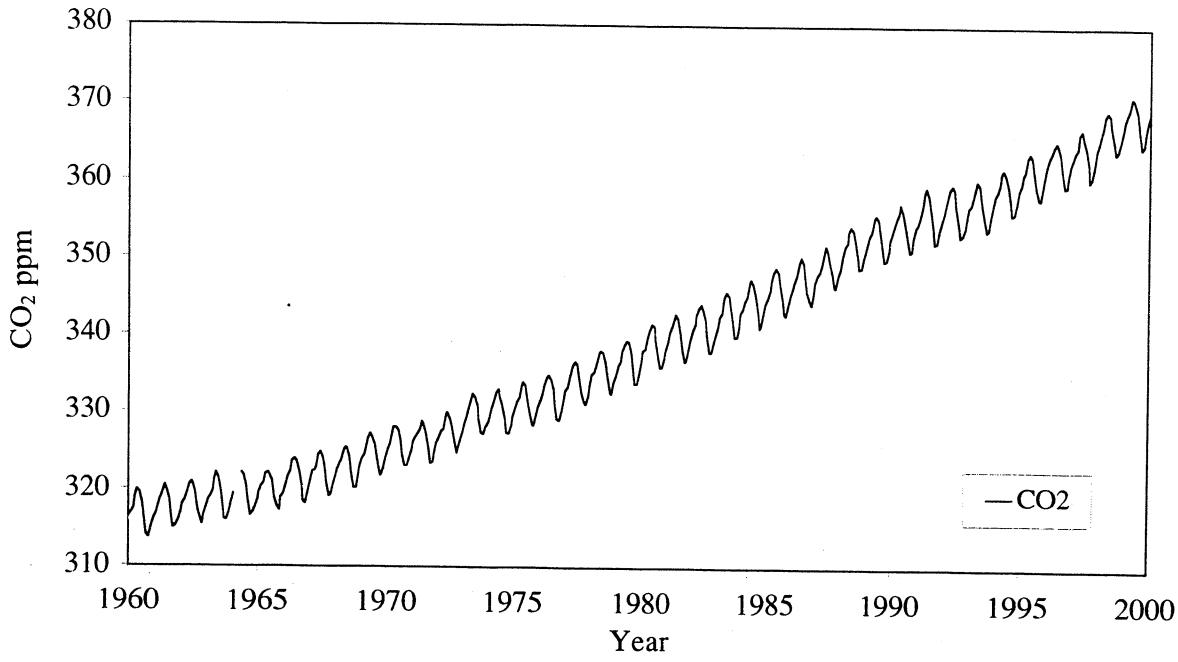

Figure 1. Plot of measured carbon dioxide concentration over time from Mauna Loa (Keeling and Whorf, 2001).

EXPRESSION OF CARBON DIOXIDE IN THE AVIRIS SPECTRUM

AVIRIS measures the upwelling spectral radiance from 370 to 2500 nm at nominally 10 nm sampling. From the ER-2 aircraft platform at 20 km altitude, an AVIRIS spectrum is measured for each 20-by-20 m area across an image approximately 11 km wide and up to 800 km in length. The spectra are spectral, radiometrically and spatially calibrated (Chrien et al., 1990, 1995, 1996, 2000). Figure 2 shows the AVIRIS spectral range and a transmittance spectrum of the terrestrial atmosphere. The effects of aerosols and molecular scattering (as well as the absorption of water vapor, oxygen, methane, ozone, and carbon dioxide) are present in each AVIRIS spectrum. In this portion of the spectrum, water vapor is the dominant absorber, as indicated in Figure 3 that shows a transmittance spectrum of the atmosphere with and without water vapor in the atmosphere. In the AVIRIS spectral range, the principal carbon dioxide absorption bands occur in the 1600 nm and 2000 nm spectral regions. Figure 4 shows the expression of these carbon dioxide absorption bands in an AVIRIS spectrum measured over an area of Pasadena, California on June 22, 1999. In addition to the carbon dioxide features, the AVIRIS spectrum contains the integrated effects of the solar irradiance source, two-way transmittance, and scattering of the complete atmosphere, as well as the reflectance of the surface. To model these effects in measured AVIRIS spectra, a radiative-transfer code is used. The MODTRAN radiative transfer code is one such model. Figure 5 shows a MODTRAN predicted spectrum at high spectral resolution and convolved to AVIRIS spectral resolution. This modeled spectrum accounts for the source, atmosphere, surface, and geometry of the modeled observation.

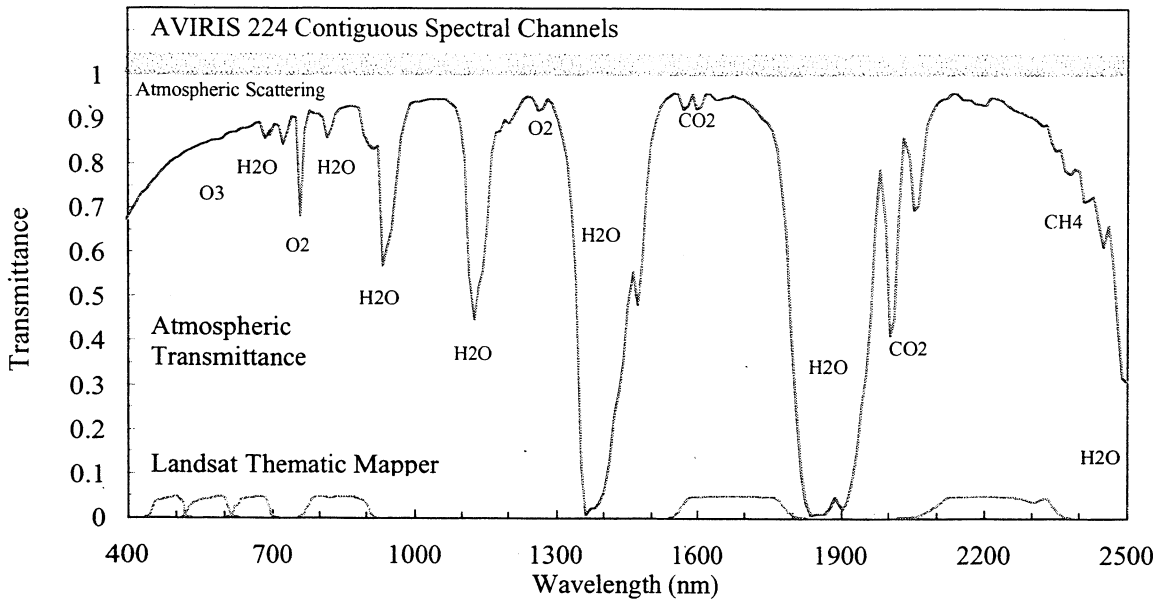

Figure 2. AVIRIS spectral coverage and a transmittance spectrum of the atmosphere. Also shown are the Landsat Thematic Mapper multi-spectral bands.

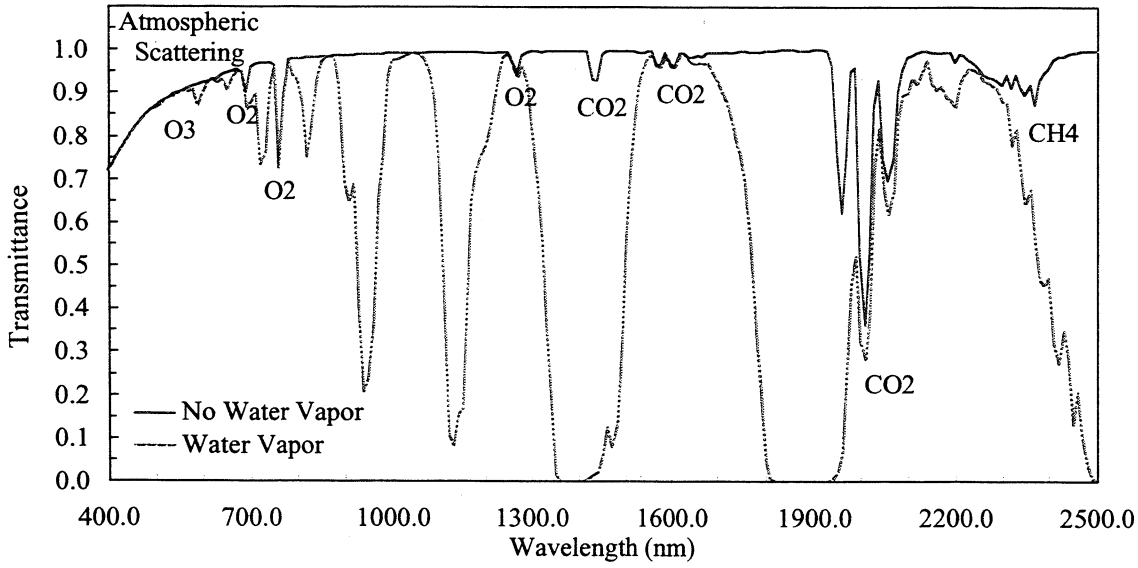

Figure 3. A transmittance spectrum of the atmosphere with and without water vapor convolved to AVIRIS spectral resolution.

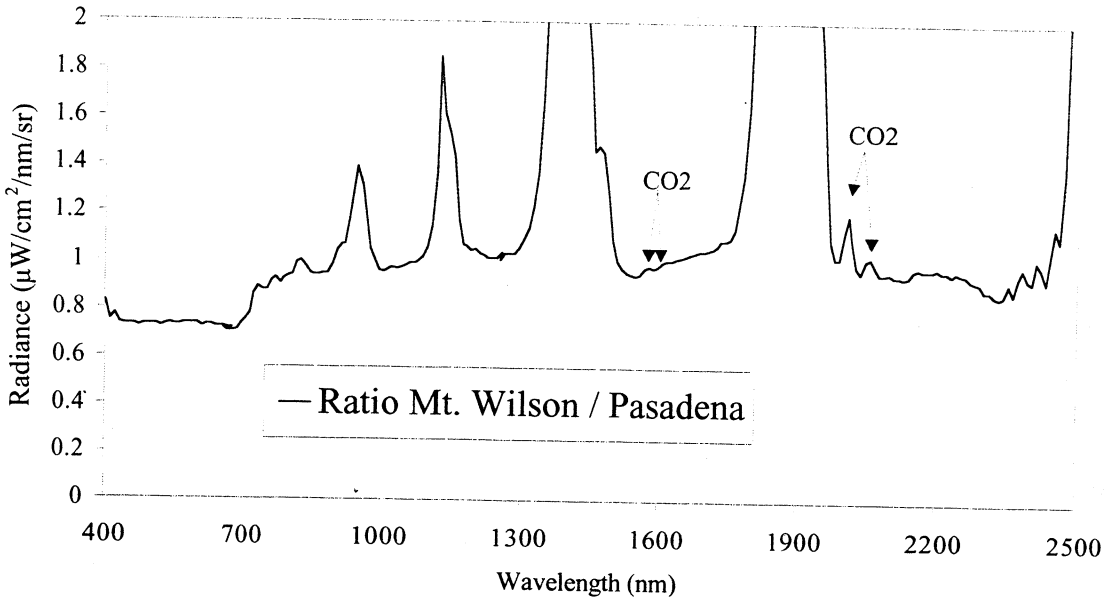

Figure 4. AVIRIS calibrated radiance spectrum showing the expression of the absorption of carbon dioxide.

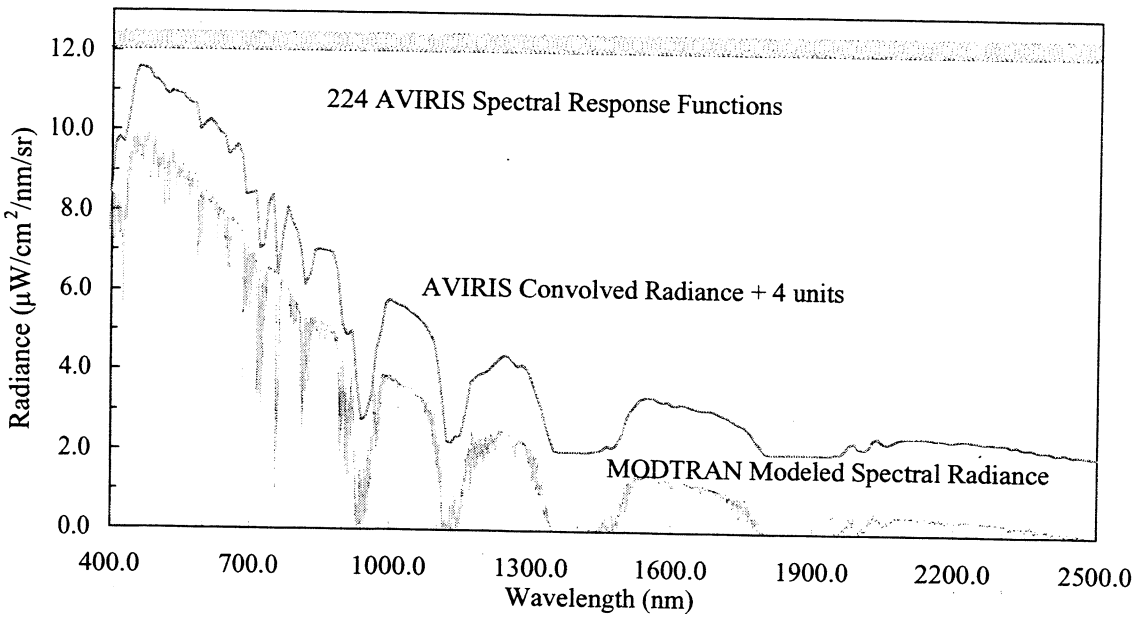

Figure 5. A radiative transfer code modeled spectrum at nominal MODTRAN resolution and convolved to AVIRIS spectral resolution.

CARBON DIOXIDE OVER LAND

To explore the potential for AVIRIS to measure changes in carbon dioxide, an AVIRIS data set acquired over Pasadena, California was identified for analysis. This data set contains the lower elevation areas of Pasadena and the higher elevation areas of the San Gabriel Mountains. Figure 6 show a single-band image of this data set with Pasadena in the center and the San Gabriel Mountains to the left. The 20-by-

20 m AVIRIS data were averaged to 80-by-80 m spatial resolution to improve the data signal-to-noise ratio. From the spatially averaged data set, spectra from the Pasadena city area at an elevation of 350 meters as well as from the Mt. Wilson summit area at an elevation of 1742 meters were extracted. Both spectra were extracted from bright areas with low amounts of vegetation. These spectra are shown in Figure 7. From a path-length perspective, the expressed absorption of carbon dioxide should be greater for the lower-elevation Pasadena spectrum than for the higher elevation Mt. Wilson spectrum. The path downward from the top of the atmosphere to the reflecting surface in Pasadena and upward to the AVIRIS sensor is longer than the corresponding path for the Mount Wilson radiance spectrum. There should be less absorption by carbon dioxide in the shorter Mount Wilson path spectrum. A simple ratio of the Mt. Wilson spectrum over the Pasadena spectrum should show enhanced values in the carbon dioxide portions of the spectrum. Figure 8 shows the ratio of the Mt. Wilson spectrum over the Pasadena spectrum. The enhanced ratio values are evident in the carbon dioxide absorption regions of the spectrum. This simple analysis shows that calibrated AVIRIS spectra are sensitive to the differences in atmospheric carbon dioxide. The differences in this case were caused principally by the difference in path length through the atmosphere for the spectra analyzed. For this case, the AVIRIS spectral region of greatest sensitivity is indicated by the larger ratio values for the carbon dioxide band centered near 2010 nm.

Based on this demonstrated sensitivity, a simple spectral fitting algorithm was developed to attempt to quantify the carbon dioxide abundance in each AVIRIS spectrum. The MODTRAN radiative transfer code was used to calculate a series of high-spectral-resolution spectra for the Pasadena AVIRIS data set with varying amounts of carbon dioxide in the atmosphere. The AVIRIS observation geometry and a 0.25 reflectance surface were used for these calculations. The spectra were convolved to the AVIRIS spectral calibration characteristics, and several are show in Figure 9. To match the MODTRAN spectra to the AVIRIS measured spectra, normalization factors were calculated near 1985 and 2095 nm, respectively, on either side of the carbon dioxide absorption features. These normalization factors were then linearly interpolated for the intervening AVIRIS spectral values. The absolute value of the difference between the AVIRIS measured spectrum and each MODTRAN modeled spectrum was calculated. The carbon dioxide value of the MODTRAN spectrum giving the best fit was reported as the derived value for each AVIRIS spectrum in the Pasadena data set.

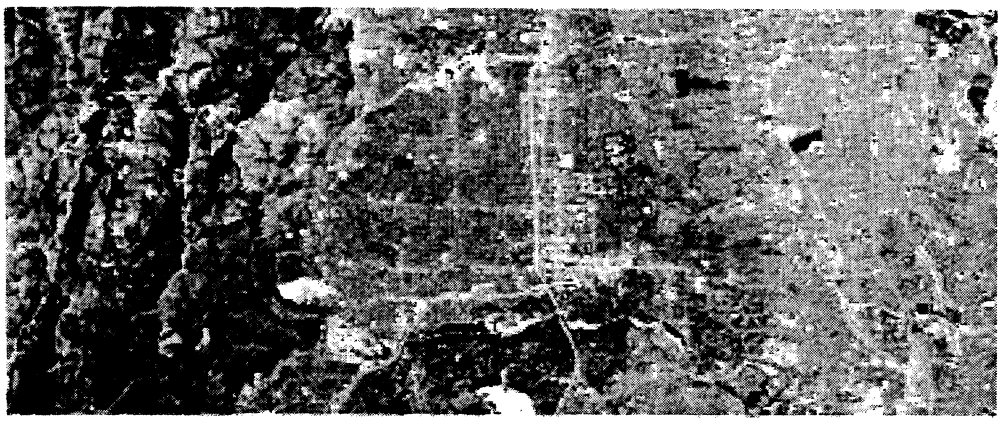

Figure 6. Single AVIRIS spectral image from Pasadena, California, region acquired on June 22, 1999. The San Gabriel Mountains are to the left and Pasadena to the right. The data have been spatially average to 80-by-80 m equivalent to enhance the data signal-to-noise ratio.

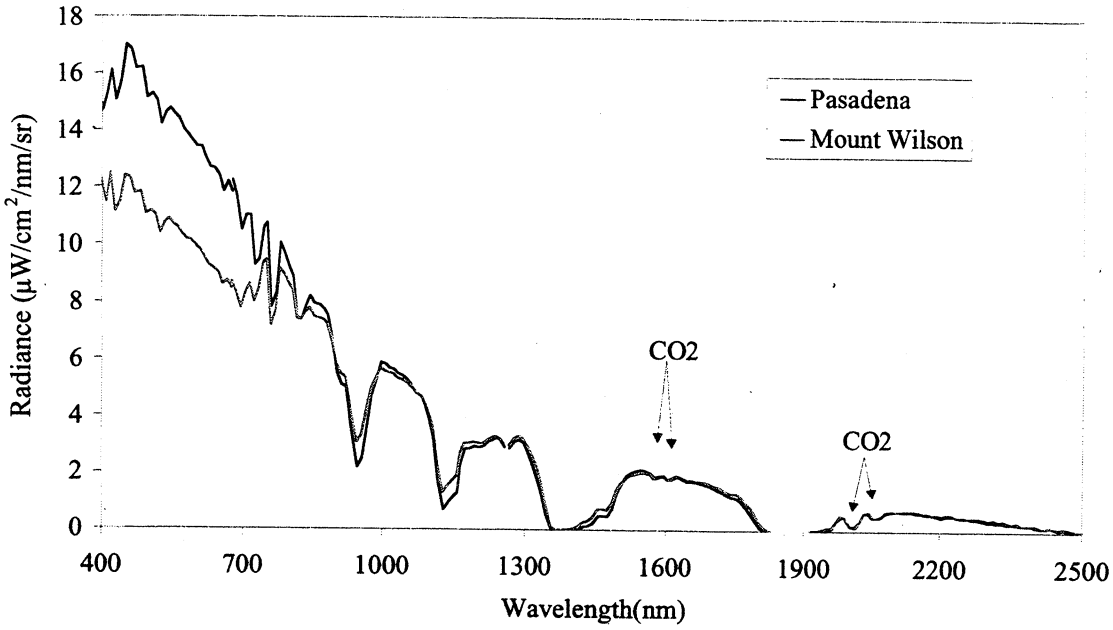

Figure 7. Spectra extracted from Pasadena and Mt. Wilson regions of the AVIRIS data set acquired on June 22, 1999.

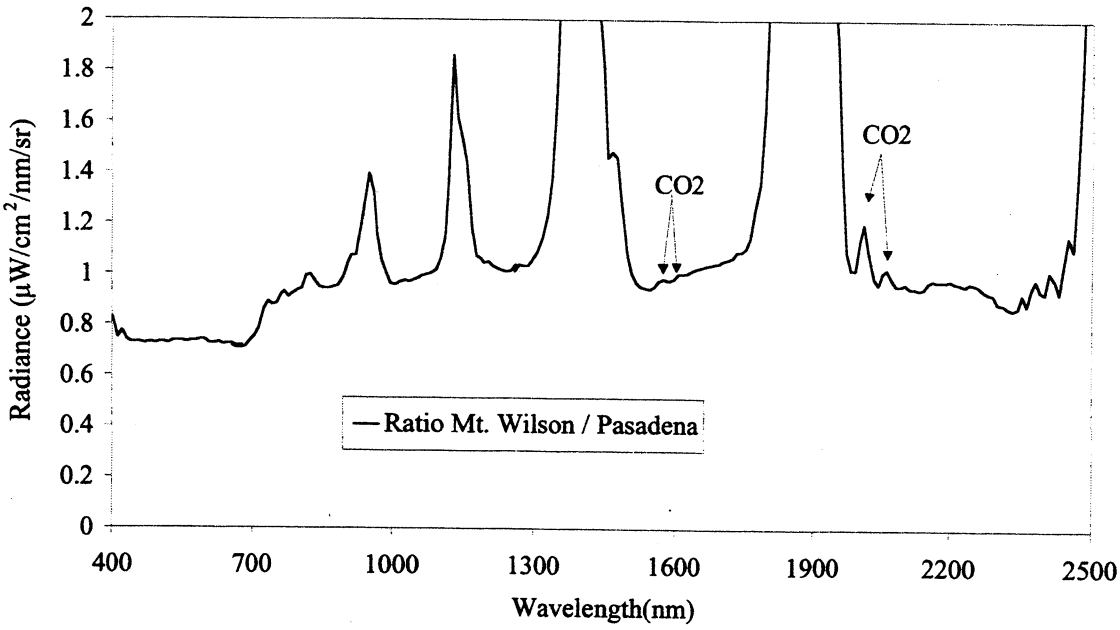

Figure 8. Ratio of AVIRIS Mt. Wilson spectrum to Pasadena spectrum. The enhanced ratio values in the carbon dioxide absorption band show the AVIRIS sensitivity to carbon dioxide abundance. The sensitivity of AVIRIS to water vapor is also clearly shown.

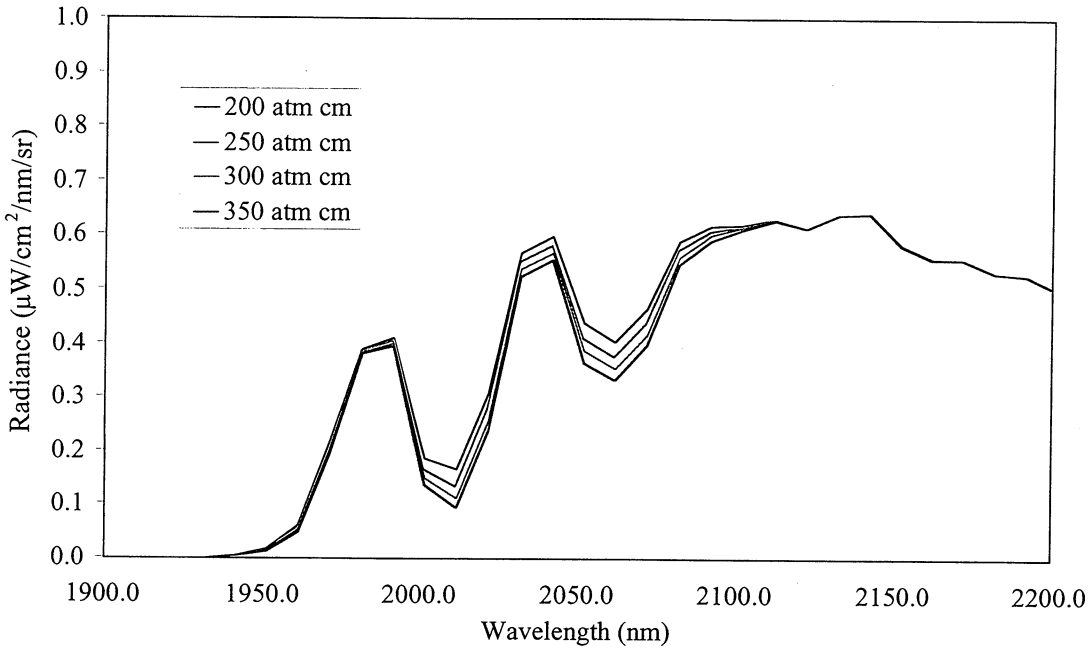

Figure 9. MODTRAN calculated spectra convolved to AVIRIS spectral characteristics for the Pasadena data set observation conditions with differing amounts of carbon dioxide.

An example spectral fit from a Pasadena data set spectrum is shown in Figure 10. The derived carbon dioxide value was 256 atmospheric centimeters (atm cm) for this spectrum. A value of 256 atmospheric centimeters (atm cm) in conjunction with the surface elevation of Pasadena corresponds to an estimated atmospheric mixing ratio of 363 ppm. The full carbon dioxide image for Pasadena is shown in Figure 11. Across the AVIRIS data set, carbon dioxide varied from 160 to 270 atm cm. Lower values were derived in the higher elevation areas of the Mt. Wilson region and San Gabriel Mountains, while higher values were derived in the lower elevation areas of Pasadena and Glendale. This first order variation in carbon dioxide over the data set is attributed primarily to path length variation modulated by surface elevation. The variation in derived carbon dioxide values for adjacent spectra is moderately high. To access this variability, the average and standard deviation of 100 carbon dioxide values in the lower elevation Pasadena portion of the image were calculated. An average of 256 and a standard deviation of 3.41 were found. This corresponds to a nominal 1.3 percent precision for the carbon dioxide retrieval. This variability or noise in the derived carbon dioxide is attributed to a number of factors. These include: the signal-to-noise ratio performance of AVIRIS; the comparatively small change in the spectrum compared to the large background of carbon dioxide in the atmosphere; and residual uncompensated surface reflectance effects. Factors that affect the accuracy of the derivation include: the MODTRAN model and calculations; the simplicity of the fitting algorithm; uncompensated atmospheric aerosols affects; surface reflectance effects; and limitation in AVIRIS spectral and radiometric calibration accuracy. The modification of the spectrum by water vapor also potentially affects the accuracy of the derived carbon dioxide values. These factors and others are planned to be investigated to validate and improve the precision and accuracy of this carbon dioxide derivation approach from AVIRIS measured spectra. However, even with the current implementation, this research has demonstrated the derivation of atmospheric carbon dioxide abundance using AVIRIS measured spectra over a land surface.

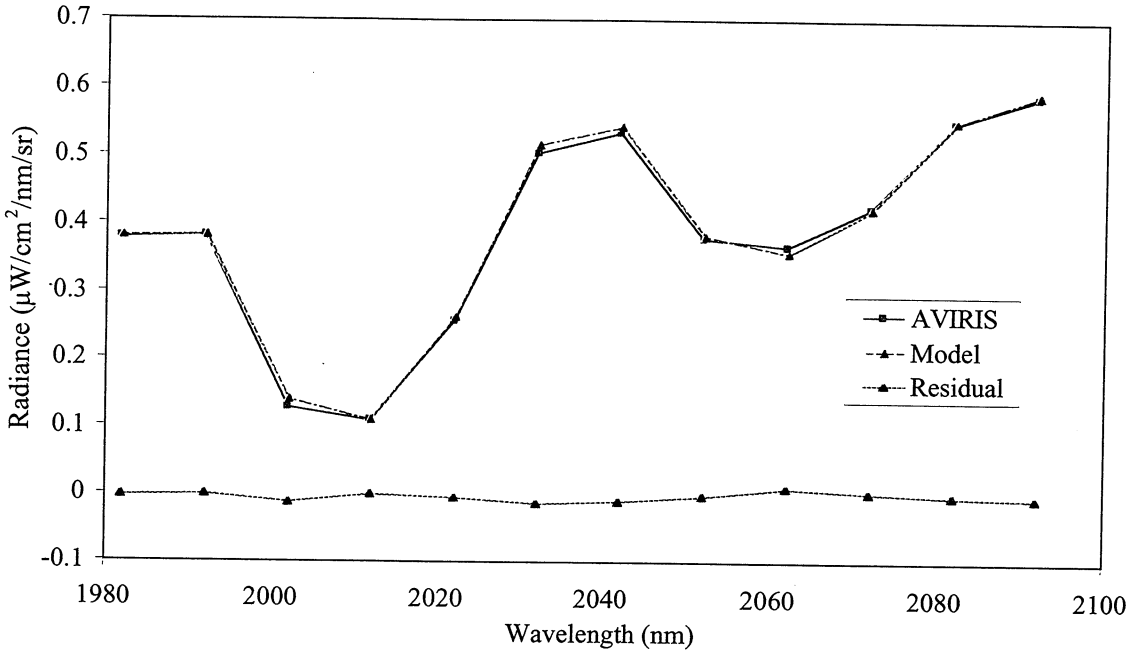

Figure 10. Spectral fit between AVIRIS measured spectrum with MODTRAN-modeled spectrum.

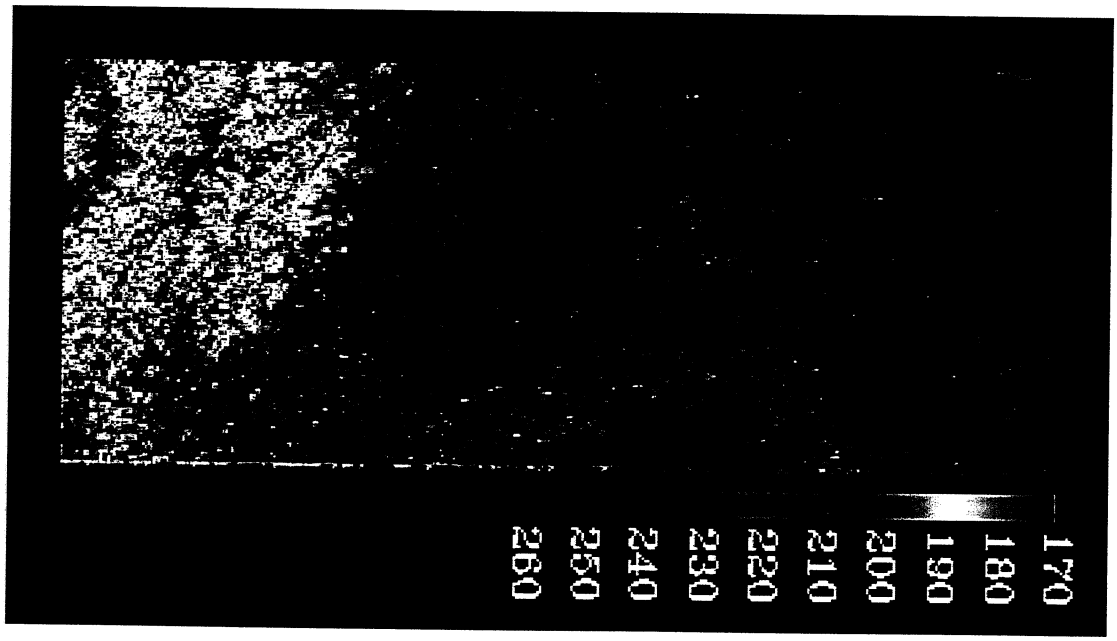

Figure 11. AVIRIS carbon dioxide image in atm cm. Lower carbon dioxide values are derived for the higher elevation regions to the left. Higher values of carbon dioxide are derived at lower elevation in the center and right of the image.

CARBON DIOXIDE OVER WATER

Two thirds of the Earth's surface is covered with water. For any remote sensing strategy for carbon dioxide, it is important to have an approach for water surfaces. Liquid water is a strong absorber at wavelengths longer than 700 nm and effectively absorbs all energy at 1600 and 2000 nm. However, under certain observations sunlight is almost totally reflected from the surface causing sun glint. Sun glint is observed when the angle of observation to the surface is equal and opposite to the angle of solar illumination incidence. The sun glint signal provides a basis for derivation of carbon dioxide over water surface with AVIRIS spectra. On April 12, 2000 AVIRIS acquired an ocean sun glint data set near Hawaii. The data were acquired as AVIRIS turned in a circle to match observation geometry with the SeaWiFS satellite sensor for on-orbit calibration research (Pavri et al., 2000). In a portion of this circular data set, AVIRIS measured the zone of peak sun glint from the ocean surface. Figure 12 shows the sun glint portion of the AVIRIS Hawaii image as well as the dark ocean signal away from the sun glint. The image also contains a number of small clouds. AVIRIS spectra from portions of this image are shown in Figure 13. There is significant signal at the 2000 nm spectral region, and the carbon dioxide absorption features are evident in the sun glint spectrum. The converse is true for the dark ocean spectrum with effectively no expressed signal in the 2000 nm spectral region. The spectral-fitting carbon dioxide algorithm was applied to this data set based upon the good signal available in the sun glint region. The derived carbon dioxide abundance is shown in Figure 14. Nearly uniform values are derived across the image in the sun glint zones. Somewhat lower and more variable values are derived in the dark ocean zones where the signal to AVIRIS is weighted more towards the atmospheric scattered radiation. For the central portion of the sun glint area, an average carbon dioxide abundance of 302 atm cm with a standard deviation of 2.91 atm cm was determined. This yields a precision estimate of 0.96 percent for this AVIRIS data set. The result demonstrates a viable remote sensing strategy for derivation of carbon dioxide abundance in the AVIRIS spectral range of water targets. For a satellite mission, continuous tracking of the sun glint can be achieved with modern pointable satellites.

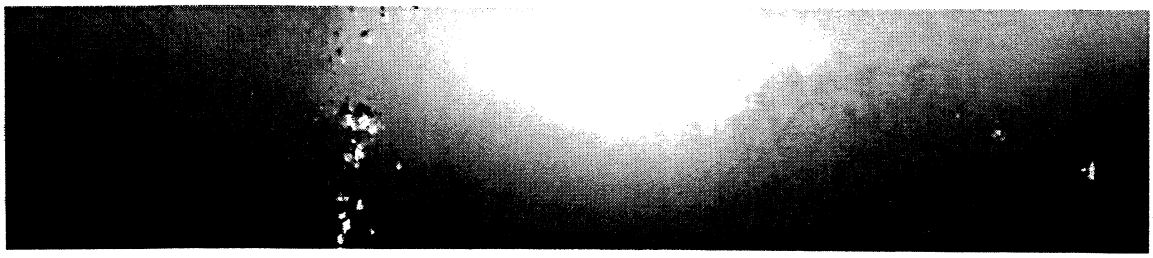

Figure 12. Portion of an AVIRIS image capturing the sun glint zone acquired on April 12, 2000 near Hawaii.

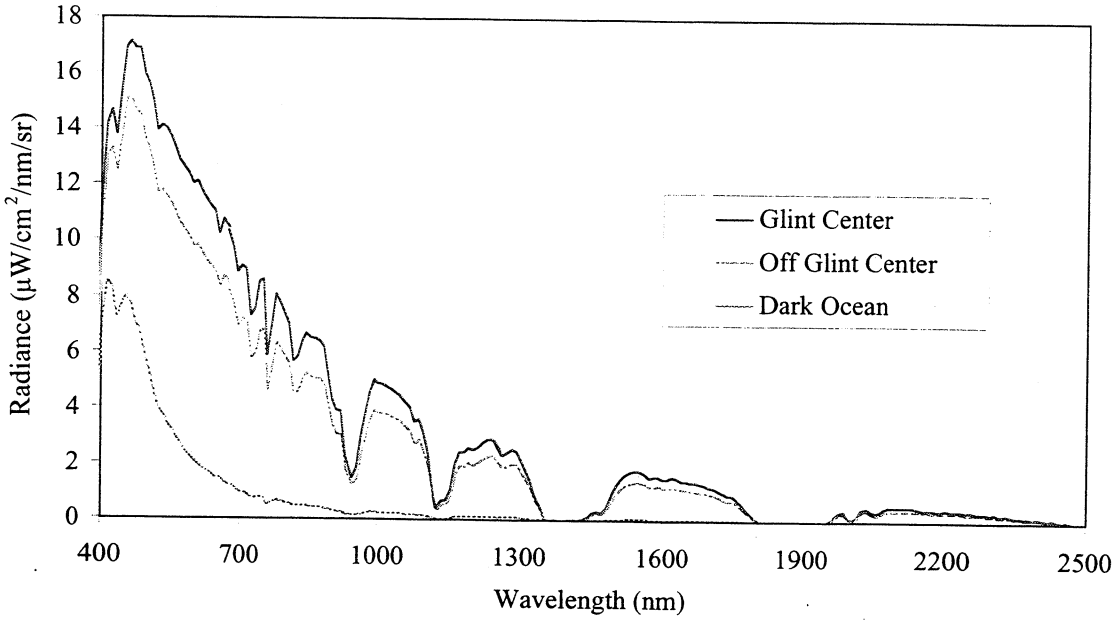

Figure 13. AVIRIS spectra of sun glint off the ocean and adjacent dark ocean.

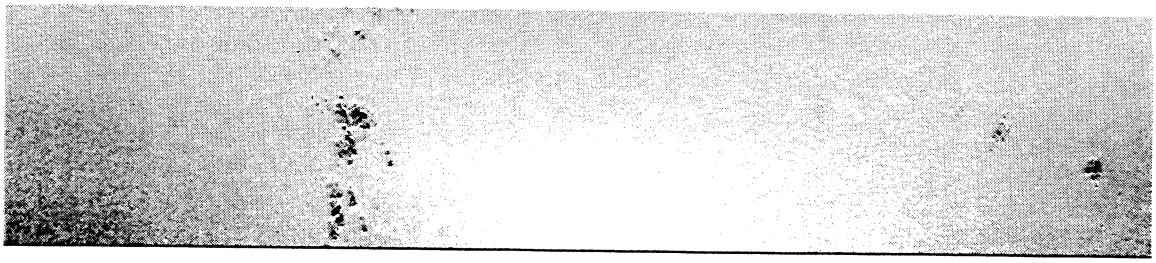

Figure 14. Spectral fitting derived carbon dioxide image from 2000 AVIRIS ocean sun glint data set. A carbon dioxide value of 302 atm cm was obtained with a standard deviation of 2.91 atm cm in the central sun glint region. Clouds high in the atmosphere yield low carbon dioxide values.

CONCLUSION

The spectroscopic expression of carbon dioxide in the AVIRIS spectral range has been shown. Specific carbon dioxide absorption bands are expressed near 1600 and 2000 nm. The MODTRAN radiative transfer code was used to calculate spectra that closely model the spectra measured by AVIRIS. A simple analysis with AVIRIS spectra from two different elevations in a Pasadena, California data set was performed to show that AVIRIS spectra are sensitive to different amounts of carbon dioxide in spectra passing through different paths of the atmosphere. This analysis also showed that the carbon dioxide bands near 2000 nm are more sensitive than the 1600 nm features given the AVIRIS spectral, radiometric, and spatial characteristics. With this demonstrated sensitivity and the MODTRAN radiative transfer code, a spectral-fitting algorithm was developed to derive carbon dioxide from AVIRIS spectra. This algorithm fit MODTRAN spectra calculated with different amounts of carbon dioxide to the AVIRIS measured spectrum. The best-fit result yields a carbon dioxide estimate for each spectrum. The resulting carbon dioxide image of Pasadena shows a consistent result with low values in areas of high surface elevation and high values in areas of low surface elevation. In a homogeneous zone of the Pasadena data

set, an average carbon dioxide abundance of 256 atm cm with a standard deviation of 3.41 was calculated. This leads to an estimated precision of 1.3 for the derivation. Critical factors effecting the precision were identified as the signal-to-noise ratio characteristics of the AVIRIS spectra as well as the uncompensated spectral variation in the surface reflectance. Factors affecting the accuracy were tied to the MODTRAN model, AVIRIS calibration, and simplicity of the algorithm. Research is planned to assess these factors and work to improve the precision and accuracy of the algorithm and derived results. As presented, this research demonstrates the retrieval of carbon dioxide abundance over land surfaces with AVIRIS spectra.

This research was extended to water targets with a data set acquired in Hawaii in the year 2000 containing a strong sun glint signal. Application of the spectral fitting algorithm to this data set derived carbon dioxide values of 302 atm cm with a standard deviation of 2.91. The corresponding estimated precision is 0.96 percent. Many issues remain for research and analysis with this approach to the derivation of carbon dioxide from AVIRIS measured spectra. However, the preliminary results presented here show potential for precise and accurate derivation of carbon dioxide from AVIRIS and AVIRIS like spectral measurement. This class of measurement can, therefore, contribute to the broad scientific research objectives related to carbon dioxide abundance, distribution, sources, and sinks.

REFERENCES

Anderson, G. P., J. Wang, and J. Chetwynd, "An Update and Recent Validations Against Airborne High Resolution Interferometer Measurements," *Summaries of the Fifth Annual JPL Airborne Earth Science Workshop*, JPL 95-1, Vol. 1, *AVIRIS Workshop*, Jet Propulsion Laboratory, Pasadena, California, pp. 5–8, January 23, 1995.

Anderson, G. P., A. Berk, P. K Acharya, M. W. Mathew, L. S. Bernstein, J. H. Chetwynd, H. Dothe, S. M. Adler-Golden, A. Ratkowski, G. W. Felde, J. A. Gardner, M. L. Hoke, S. C. Richtsmeir, B. Pukall, J. Mello, and L. S. Jeong, "MODTRAN4: Radiative transfer modeling for remote sensing," in *Proceedings SPIE, Algorithms for Multispectral, Hyperspectral, and Ultraspectral Imagery VI*, Vol. 4049, S. S. Shen and M. R. Descour, eds., pp. 176–183, 2000.

Berk, A., L. S. Bernstein, and D. C. Robertson, *MODTRAN: A Moderate Resolution Model for LOWTRAN 7*, Final report, GL-TR-0122, AFGL, Hanscomb AFB, Massachusetts, 42 pp., 1989.

Chrien, T. G., R. O. Green, and M. L. Eastwood, "Accuracy of the spectral and radiometric laboratory calibration of the Airborne Visible/Infrared Imaging Spectrometer (AVIRIS)," *SPIE Vol. 1298, Imaging spectroscopy of the terrestrial environment*, G. Vane, ed., pp. 37–49, 1990.

Chrien, T. G., R. O. Green, C. Chovit, M. Eastwood, J. Faust, P. Hajek, H. Johnson, H. I. Novack, and C. Sarture, "New Calibration Techniques for the Airborne Visible/Infrared Imaging Spectrometer (AVIRIS), 1995," *Proc. Fifth Annual Airborne Earth Science Workshop*, JPL Pub. 95-1, Jet Propulsion Laboratory, Pasadena, California, pp. 33–34, 1995.

Chrien, T. G., R. O. Green, C. J. Chovit, M. L. Eastwood, and C. M. Sarture, "Calibration of the Airborne Visible/Infrared Imaging Spectrometer in the Laboratory," *Proc. Sixth Annual Airborne Earth Science Workshop*, JPL Pub. 96-4, Vol. 1, Jet Propulsion Laboratory, Pasadena, California, pp. 39–48, March 3–5, 1996.

Chrien, T. G., R. O. Green, B. Pavri, and J. Wall, "Calibration Validation of the AVIRIS Portable Radiance Standard," *Proc. Ninth Airborne Earth Science Workshop*, JPL Pub. 00-18, Jet Propulsion Laboratory, Pasadena, California, pp. 101–110, 2000.

Green, R. O., M. L. Eastwood, C. M. Sarture, T. G. Chrien, M. Aronsson, B. J. Chippendale, J. A. Faust, B. E. Pavri. C. J. Chovit, M. Solis, M. R. Olah, and Q. Williams, "Imaging spectroscopy and the Airborne Visible/Infrared Imaging Spectrometer (AVIRIS)," *Remote Sens Environ* 65: (3) 227–248, Sept. 1998.

IPCC Second Assessment: Climate Change 1995, Intergovernmental Panel on Climate Change, p. 73, 1996.

Keeling, C. D. and T. P. Whorf, Atmospheric CO_2 concentrations (ppmv) derived from in-situ air samples collected at Mauna Loa Observatory, Hawaii, Scripps Institution of Oceanography (SIO), University of California, La Jolla, California USA 92093-0244, Aug. 13, 2001, URL: http://cdiac.esd.ornl.gov/ftp/maunaloa-co2/maunaloa.co2 (URL accessed Jan. 25, 2002).

Pavri, B. and R. O. Green, "AVIRIS/SeaWIFS Cross-Calibration for 1999," *Proc. Ninth Airborne Earth Science Workshop*, JPL Pub 00-18, Jet Propulsion Laboratory, Pasadena, California, pp. 359–364, 2000.

ACKNOWLEDGMENT

The research described in this paper was carried out at the Jet Propulsion Laboratory, California Institute of Technology, under a contract with the National Aeronautics and Space Administration.

Reference herein to any specific commercial product, process, or service by trade name, trademark, manufacturer, or otherwise, does not constitute or imply its endorsement by the United States Government or the Jet Propulsion Laboratory, California Institute of Technology.

Exploring a Black Body Source as an Absolute Radiometric Calibration Standard and Comparison with a NIST Traced Lamp Standard

Robert O. Green, Thomas Chrien, and Chuck Sarture
Jet Propulsion Laboratory, California Institute of Technology, Pasadena, California 91109

INTRODUCTION

Radiometric calibration of the Airborne Visible/Infrared Imaging Spectrometer (AVIRIS) is required for the scientific research and application objectives pursued with the spectroscopic measurements (Green et al., 1998). Specifically calibration is required for: inter-comparison of AVIRIS data measured at different locations and at different times; analysis of AVIRIS data with data measured by other instruments; and analysis of AVIRIS data in conjunction with computer models. The primary effect of radiometric calibration is conversion of AVIRIS instrument response values (digitized numbers, or DN) to units of absolute radiance (Green et al., 1991). For example, Figure 1 shows the instrument response spectrum measured by AVIRIS over a portion of Rogers Dry Lake, California, and Figure 2 shows the same spectrum calibrated to radiance. Only the calibrated spectrum may be quantitatively analyzed for science research and application objectives.

Since the initial development of the AVIRIS instrument-radiometric calibration has been based upon a 1000-W irradiance lamp with a calibration traced to the National Institute of Standards and Technology (NIST) (Chrien et al., 1990, 1995, 1996, 2000). There are several advantages to this irradiance-lamp calibration approach. First, the considerable effort of NIST backs up the calibration. Second, by changing the distance to the lamp, the output can closely span the radiance levels measured by AVIRIS. Third, this type of standard is widely used. Fourth, these calibrated lamps are comparatively inexpensive. Conversely, there are several disadvantages to this approach as well. First, the lamp is not a primary standard. Second, the lamp output characteristics may change in an unknown manner through time. Third, it is difficult to assess, constrain, or improve the calibration uncertainty delivered with the lamp. In an attempt to explore the effect and potentially address some of these disadvantages a set of analyses and measurements comparing an irradiance lamp with a black-body source have been completed. This research is ongoing, and the current set of measurements, analyses, and results are presented in this paper.

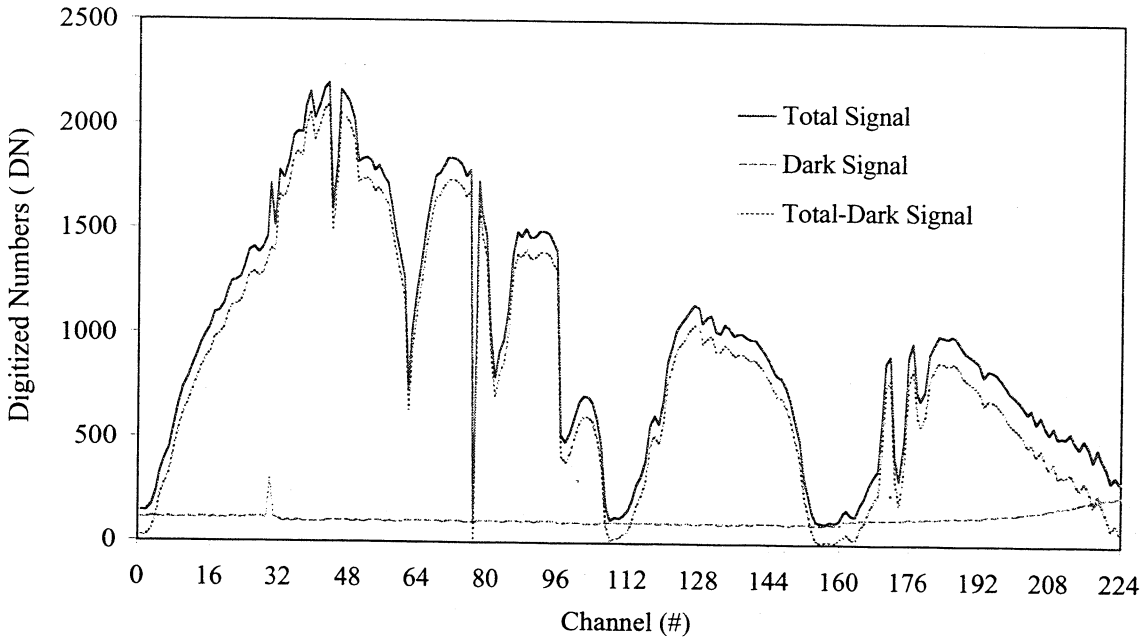

Figure 1. AVIRIS uncalibrated instrument response for a spectrum acquired over Rogers Dry Lake, California. The dark signal and instrument response with dark signal subtracted are shown as well.

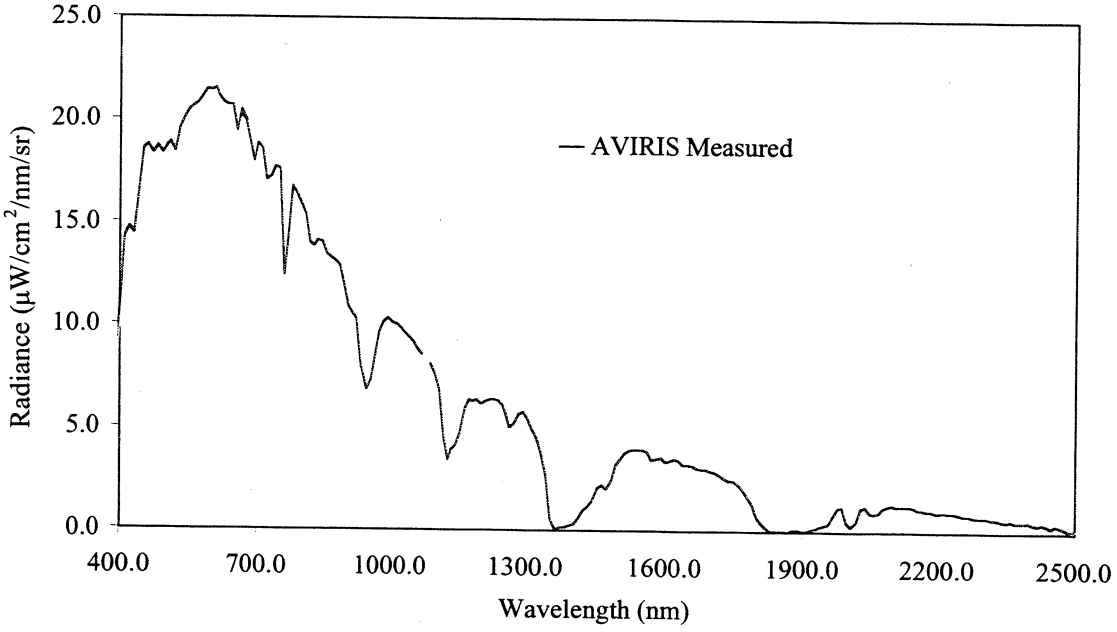

Figure 2. AVIRIS calibrated radiance from a spectrum acquired over Rogers Dry Lake, California.

LAMP RADIOMETRIC STANDARD

AVIRIS radiometric calibration is based on an irradiance standard lamp and a calibrated reflectance panel. The lamp is a 1000-W quartz-halogen tungsten coiled-coil filament lamp purchased from Optronics Laboratories, Inc. The irradiance lamp is held a known distance (nominally 500 mm) from the panel in a fixture with baffles to reject scattered light. For radiometric calibration this fixture is positioned such that AVIRIS views the panel at 45 degrees inclination. The AVIRIS instrument response

output is calibrated with respect to the NIST traced radiance of the illuminated panel. Factors of the panel bidirectional reflectance distribution function (BRDF), as well as variation of lamp distance and angle from the panel, are calculated for the projected AVIRIS aperture. These factors are applied as part of the absolute radiometric calibration calculation. This approach eliminates the need for an integrating sphere and the transfer of a radiometric calibration to the integrating sphere. Figure 3 shows a diagram of the AVIRIS radiometric calibration fixture with standard lamp and reflectance panel. The primary factor in the absolute accuracy of the AVIRIS laboratory calibration is the accuracy of the irradiance standard lamp. A spectrum of the irradiance and uncertainty for the standard lamp (S-912) used in the year 1999 calibration of AVIRIS is given in Figure 4. The uncertainty varies from near 1 percent to greater than 6 percent in the AVIRIS spectral range from 400 to 2500 nm. Both the irradiance values and interpolated irradiance values are those provided with the lamp. The uncertainty values are those provided with the lamp. The interpolated uncertainty values have been calculated with a cubic spline algorithm (Press et al., 1988). To first order the spectral form of the irradiance lamp output appears to follow that of a Planck function (Liou, 1980). To explore aspects of this lamp calibration standard, the lamp was compared and analyzed with respect to Planck function calculations as well as a black body radiometric source.

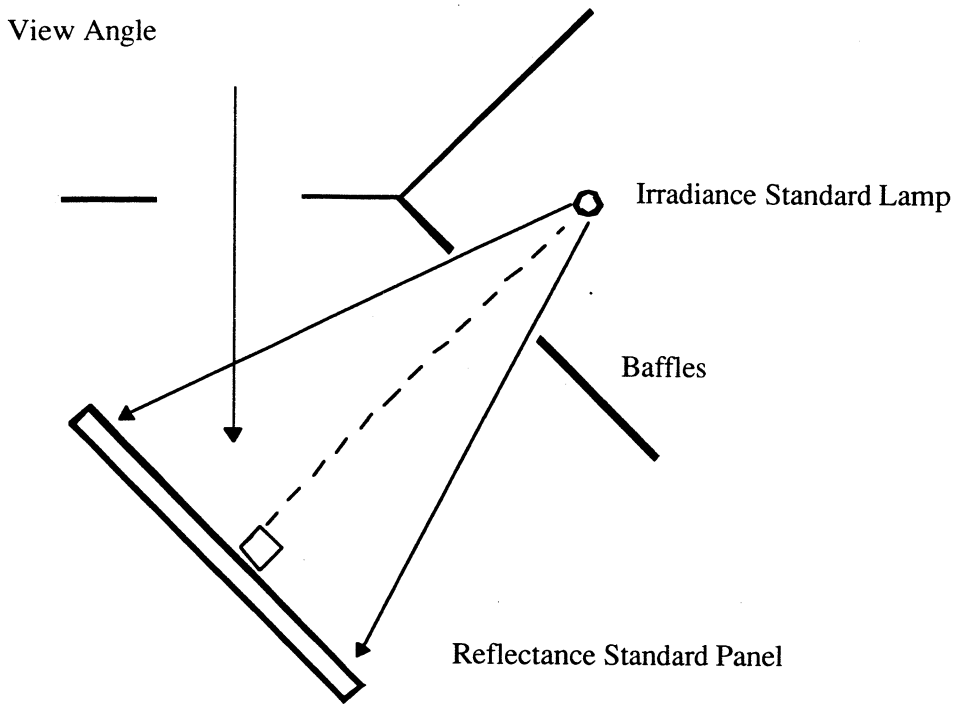

Figure 3. AVIRIS radiometric calibration fixture with irradiance lamp standard and reflectance standard panel.

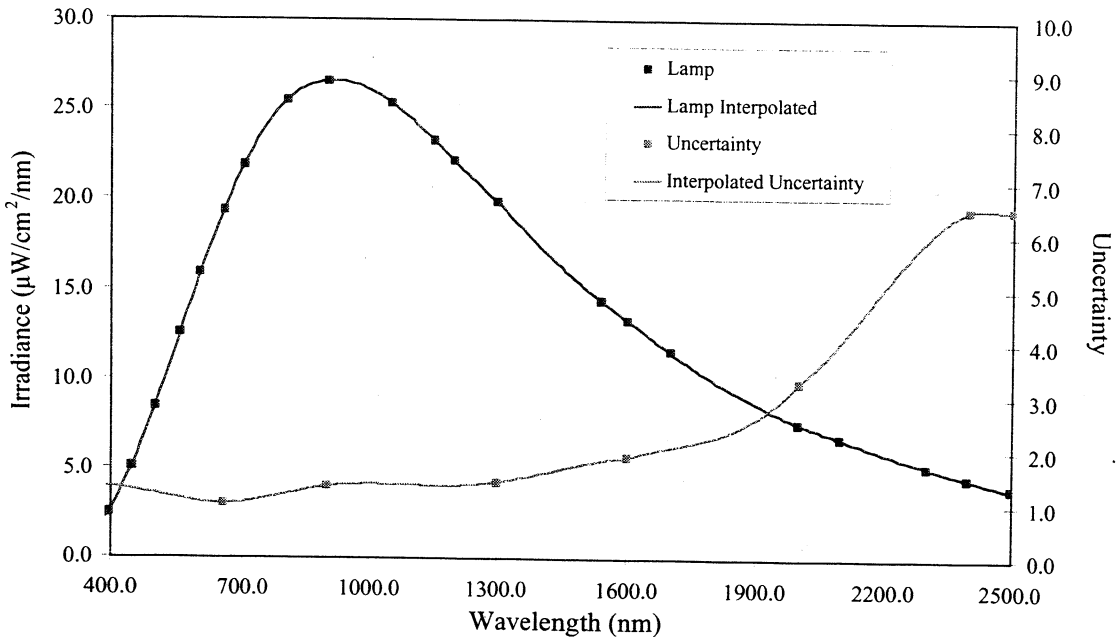

Figure 4. Calibration lamp irradiance at 500 mm distance with uncertainty traced to NIST. The lamp, lamp interpolated, and uncertainty values are given as delivered with the lamp. The interpolated uncertainty values were calculated with a cubic spline function.

CAVITY BLACK BODY SOURCES

The radiance from a cavity black body may be calculated with the temperature, the emissivity, and the Planck function. A high temperature cavity black body offers potential as a primary absolute radiometric calibration standard that may be used for the calibration of AVIRIS as well as to explore the lamp irradiance uncertainty. Figure 5 shows the spectral distribution of radiance from a cavity black body at temperatures of 3000, 2000, and 1000 K. The radiance magnitude has been scaled to a value of 100 at the peak. To calculate the radiance output of any cavity black body, accurate knowledge of the temperature is required. For a high temperature black body, there is feedback on the accuracy of the temperature based on the peak of the black body curve. The relationship between temperature and radiance peak is given by Wien's displacement law (Liou, 1980). With a good relative spectral measurement of the black body output the temperature may be validated and potentially determined directly. With knowledge of the temperature and emissivity, the radiance of the cavity black body may be calculated directly with the Planck function. The cavity black body may then be used as a primary absolute radiometric calibration standard. AVIRIS has access to a high temperature cavity black body with a range from 1000 to 3000 K built by Electro Optical Industries, Inc. The emissivity of the cavity is better than 0.99. For practical use, precision apertures are required to bring the output of the high temperature source into the range of AVIRIS measurements. Research is ongoing for the use of the high temperature cavity black body for the calibration of AVIRIS.

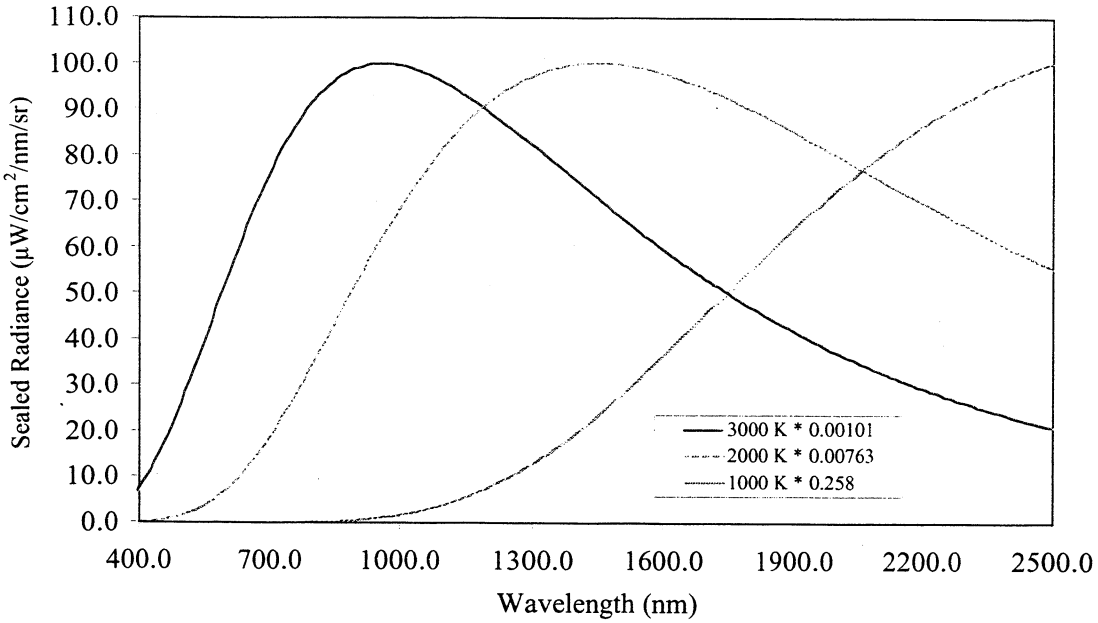

Figure 5. Planck functions for a cavity black body at different temperatures. The data are scaled to a peak value of 100. The scaling factors are 0.00101, 0.00763, and 0.258 for the 3000, 2000, and 1000-K spectra, respectively.

COMPARISON OF THE IRRADIANCE LAMP TO A PLANCK FUNCTION

To a first order the calculated Planck function for a 3000-K cavity black body resembles the form of the calibration curve for the irradiance lamp standard. A simple analysis was performed to explore how well the irradiance lamp output could be modeled by a Planck Function. Initially a spectral fitting approach was used to match a single temperature Planck function with fractional fill parameter to the irradiance calibration of the lamp. The fractional fill parameter accounts for geometric and distance factors as well as spectrally uniform variations in the emissivity of tungsten and the lamp quartz envelope. A model with two temperatures and fractional fill parameters provided a better fit, though only over the spectral range from 1000 to 2500 nm. Figure 6 shows the achieved fit between the irradiance lamp calibration and a two-temperature Planck function model. Temperatures of 3425 K and 511 K were required in the model with a fractional fill of 0.000148 and 0.0054 respectively. The percent difference between the irradiance lamp calibration and the two-temperature Planck function model shows spectral variation ranging from +2 to –4 percent in the range from 1000 to 2500 nm. This spectral variation could be due to tungsten emissivity, interpolation errors, or other factors. This variation may also be an indication of the spectral form of the uncertainty in the lamp calibration. Insight into the spectral form of the uncertainty in the irradiance lamp output is the objective of this research and is critical to improving the absolute radiometric calibration of AVIRIS.

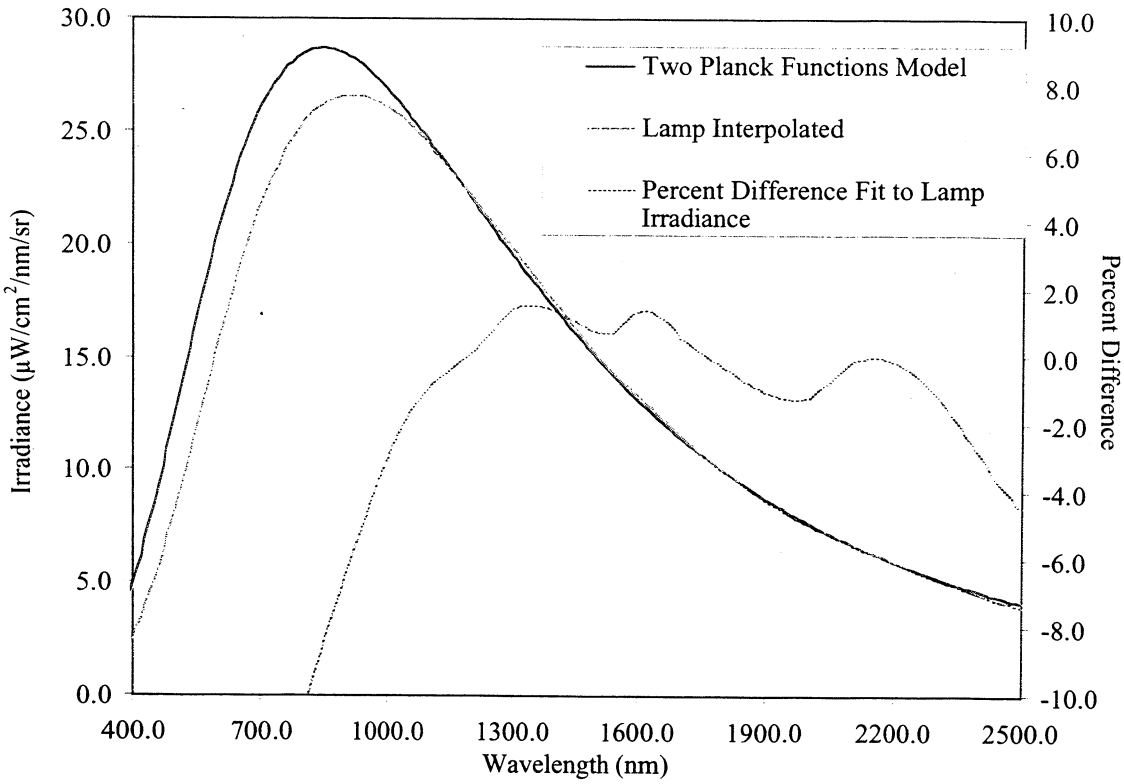

Figure 6. Results of fit between lamp irradiance and two-temperature Plank function calculations plus a fractional fill factor over the range from 1000 to 2500 nm.

MEASURED BLACK BODY AND THE IRRADIANCE LAMP

In addition to exploring a simple Planck function model for the irradiance lamp spectral output, spectral measurements were made comparing the output of a moderate-temperature cavity black body with the output of the irradiance lamp standard. Figure 7 shows the calculated output of an 820-K cavity black body source in the AVIRIS calibration laboratory. This source was measured by a portable spectrometer that covers the spectral range from 350 to 2500 nm at nominally 10 nm intervals with 1 nm output sampling. Figure 8 show the spectrometer output from the 820-K black body source as well as the measured output for AVIRIS calibration fixture with the NIST traced irradiance lamp and calibrated panel. From these measurements, usable signal levels were obtained for both sources over the spectral range from 1000 to 2500 nm. The radiance from AVIRIS calibration fixture and these portable spectrometer measurements were used to predict the radiance output of the 820-K black body source. The predicted radiance is shown in Figure 9. The shape of the predicted radiance spectrum conforms to that expected for a cavity black body. The low measured signal level for the lamp source at the long wavelength end of the spectrum induces increased noise and uncertainty near 2500 nm. A comparison of the AVIRIS calibration-fixture derived radiance and the Planck function calculated radiance is given in Figure 10. Over the spectral range from 1000 to 2500 nm the agreement is good. The percent difference curve shows the areas of disagreement. In the 1400 and 1900 nm spectral regions there are some disagreements because there was a longer path and more water vapor in the calibration fixture measurement than the black body measurement. The low signal level effects of the lamp measurement at 2500 nm are also apparent. In the spectral range from 1200 to 2400 nm, the spectral variation of the percent difference ranges from +2 to –4 percent. This is similar to the range of expected uncertainty values delivered with the NIST traced lamp is from 2 to 6 percent in this spectral region. It is reassuring

the NIST traced AVIRIS calibration fixture can predict the radiance of the 820-K cavity black body to this level of accuracy.

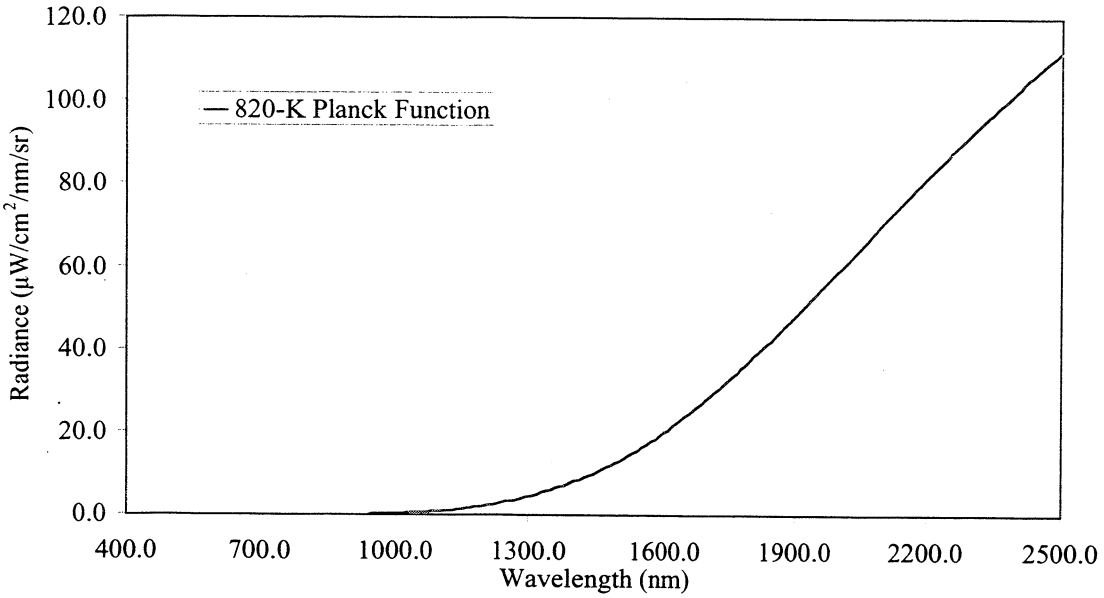

Figure 7. Planck function calculation for 820-K black body source in the AVIRIS calibration laboratory.

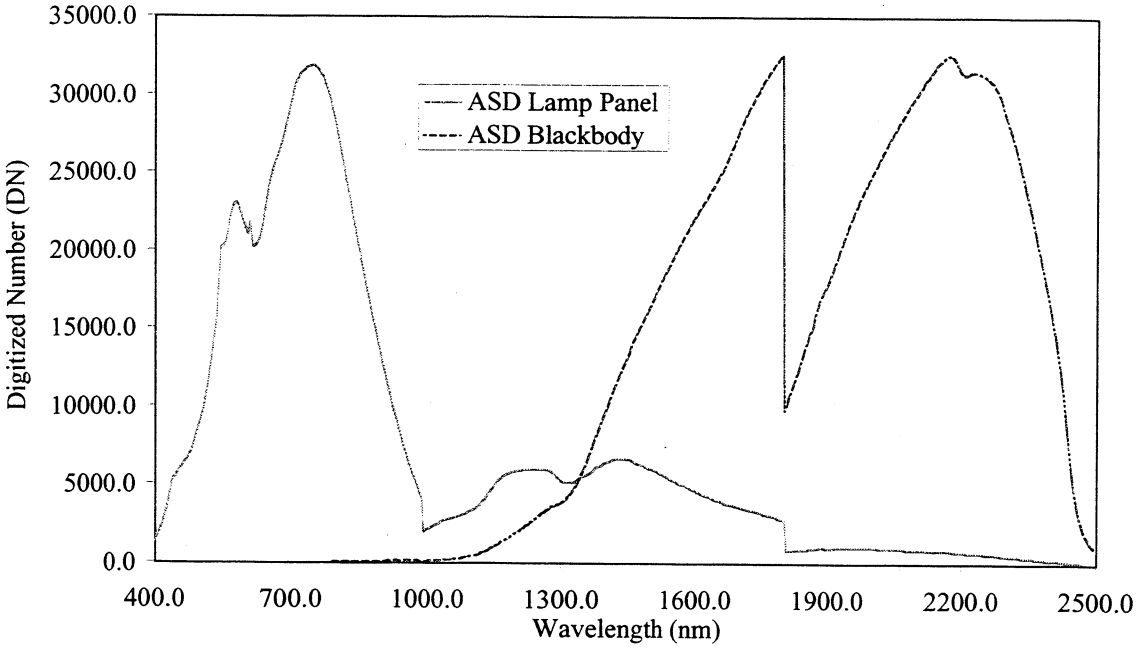

Figure 8. Spectrometer measurement of lamp panel source and 820-K black body source.

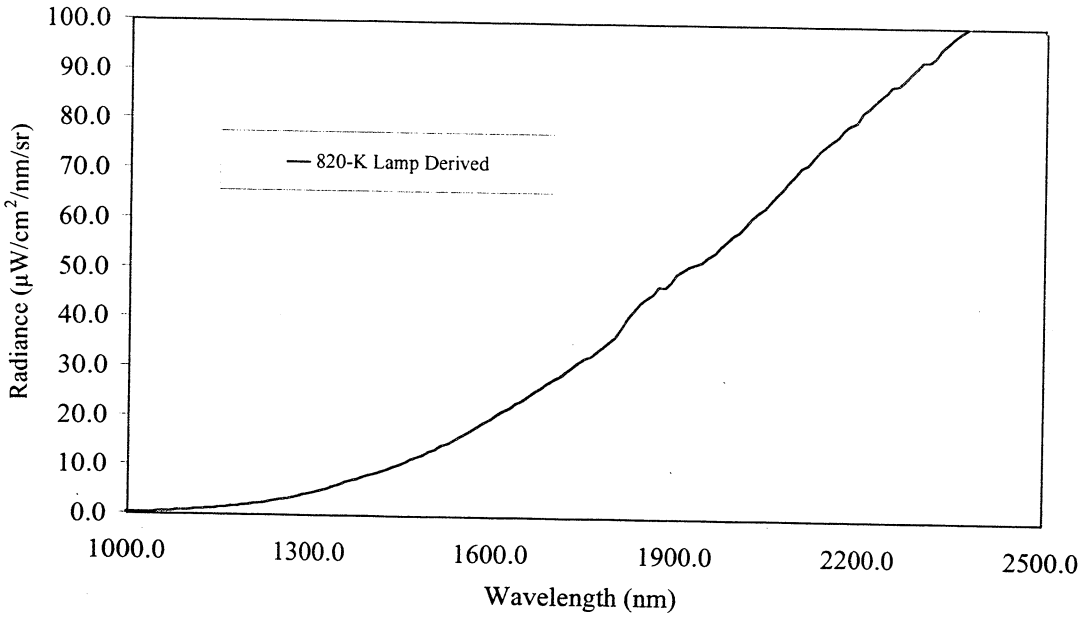

Figure 9. Predicted radiance from 820-K black body based on lamp panel calibration.

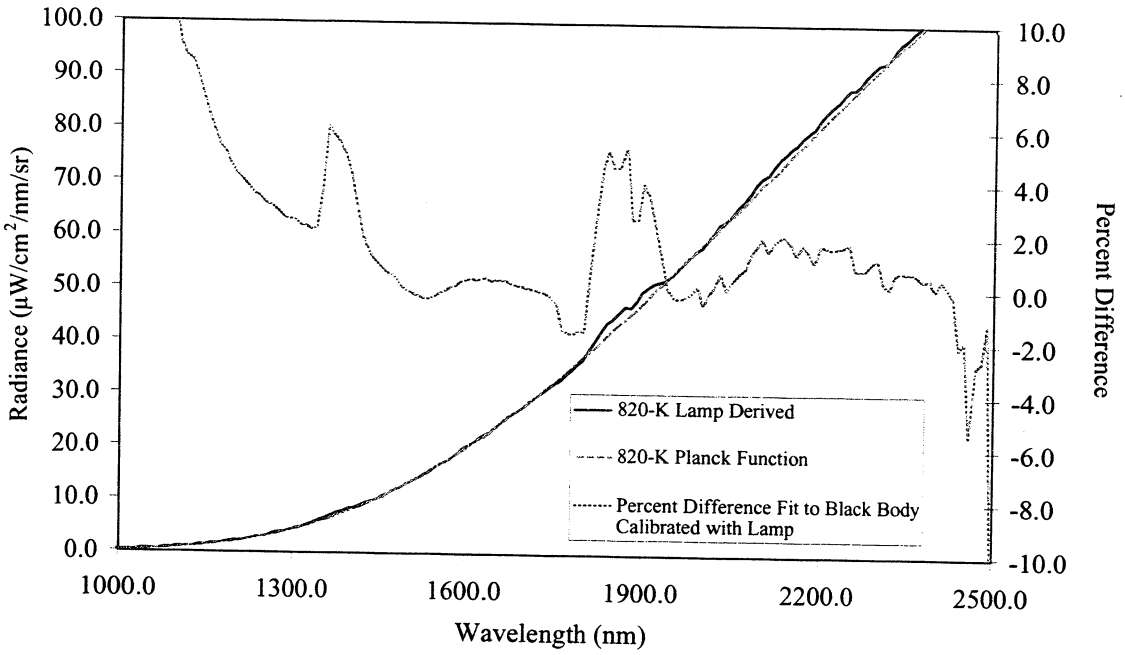

Figure 10. Comparison of 820-K Planck function calculation and lamp based predicted irradiance from 820 K black body source. The percent difference is shown as well.

In the range from 1200 to 2500 nm, the cavity black body measurement based percent difference is of a similar form and magnitude to that found in the comparison of the two-temperature Planck function model and the irradiance lamp calibration. Figure 11 shows these two spectral percent difference results. The similarity suggests this spectral form may represent the uncertainty in the irradiance lamp calibration.

The source of this spectral variation is likely a combination of irradiance lamp calibration uncertainty and uncertainty introduced in the interpolation to a continuous spectrum. The interpolated data analyzed here are those provided with the NIST traced lamp. Interpolation is a required step for calibration of any instrument operating in this spectral range. Only the interpolated spectral radiometric source can be convolved to the spectral response functions of the remote sensing instrument. This uncertainty is relevant for AVIRIS and other instruments measuring in this spectral range and using irradiance lamp based calibration. Improved understanding the uncertainty of the radiometric calibration of the NIST traced lamp was a primary objective of this effort. This understanding in conjunction with cavity black body source will support development of a strategy for an improved radiometric calibration of AVIRIS.

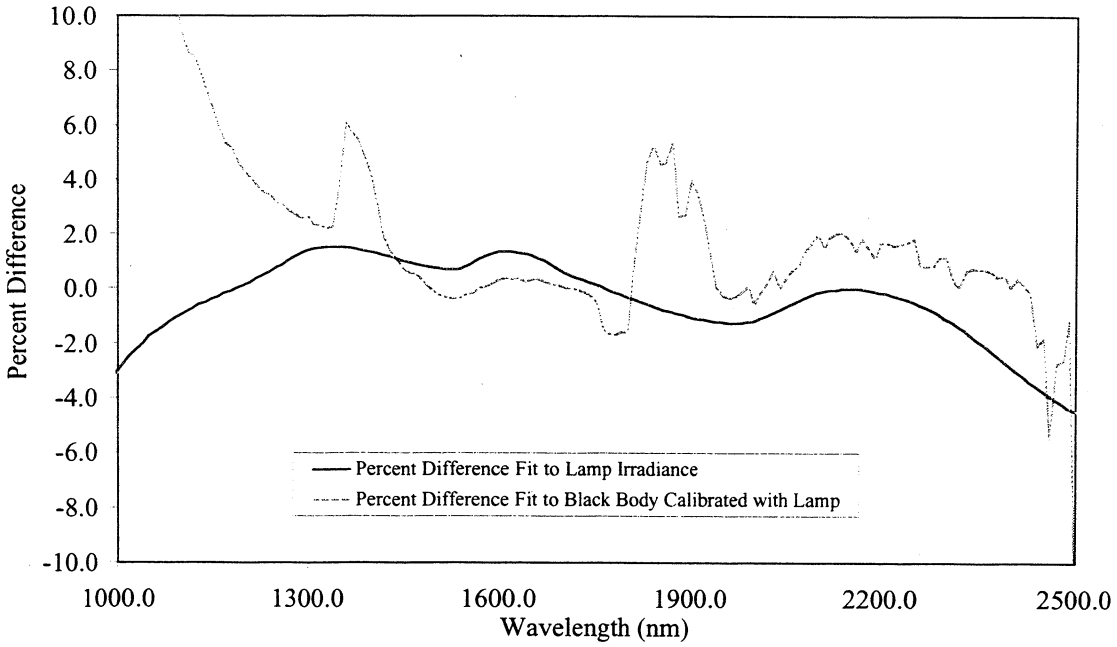

Figure 11. Comparison of percent difference from Planck function fit to lamp irradiance with percent difference from 820-K Planck function and 820-K black body source calibrated with lamp panel standard.

CONCLUSION

Radiometric calibration of AVIRIS data is required for quantitative use of the AVIRIS spectral measurements for Earth science research and application objectives. From the time of the first AVIRIS flights the instrument as been calibrated based on irradiance lamp standards. The standard lamp approach has both advantages and disadvantages. Important disadvantages are the user does not control the primary radiometric standard and the user is limited to the calibration uncertainty of the lamp. The research presented here explores the properties of the AVIRIS irradiance lamp based calibration standard with respect to a Planck function model and cavity black body measurements over the range from 1000 to 2500 nm.

A simple two-temperature Planck function model with fractional fills provides a good fit in the spectral range from 1000 to 2500 nm using the interpolated calibration irradiance values delivered with the standard lamp. In detail the percent difference between the model and lamp show some spectral variation in the range from +2 to –4 percent. This percent difference is consistent with the calibration uncertainty delivered with the standards lamp. With the goal to continue to improve AVIRIS absolute radiometric

calibration it is necessary to understand and improve upon the radiometric calibration uncertainty of the NIST traced irradiance lamps.

The measurements and analysis of the 820-K laboratory cavity black body suggests that this source may be a viable absolute radiometric calibration standard over the range from 1000 to 2500 nm. Even if not used as a source, the black body measurements provide a check of the calibration delivered with the NIST traced irradiance lamp. A higher temperature source will be required to calibrate the spectral range from 400 to 1000 nm. Work has begun experimenting with a 3000-K black body source for this objective. An advantage of a high temperature black body is that the temperature may be determined by the spectral location of the peak radiance output. This temperature may in turn be used to validate and improve the calibrated output of the cavity black body source. The AVIRIS calibration laboratory currently has access to a high temperature black body source. This offers the potential to have a new primary radiometric calibration standard in the AVIRIS laboratory and to improve upon the uncertainty of the irradiance lamp calibration approach. The overall objective of this work is to move AVIRIS radiometric calibration toward the 1 percent absolute accuracy.

REFERENCES

Chrien, T. G., R. O. Green, and M. L. Eastwood, "Accuracy of the spectral and radiometric laboratory calibration of the Airborne Visible/Infrared Imaging Spectrometer (AVIRIS)," *SPIE Vol. 1298, Imaging spectroscopy of the terrestrial environment*, G. Vane, ed., pp. 37–49, 1990.

Chrien, T. G., R. O. Green, C. Chovit, M. Eastwood, J. Faust, P. Hajek, H. Johnson, H. I. Novack, and C. Sarture, "New Calibration Techniques for the Airborne Visible/Infrared Imaging Spectrometer (AVIRIS), 1995," *Proc. Fifth Annual Airborne Earth Science Workshop*, JPL Pub. 95-1, Jet Propulsion Laboratory, Pasadena, California, pp. 33–34, 1995.

Chrien, T. G., R. O. Green, C. J. Chovit, M. L. Eastwood, and C. M. Sarture, "Calibration of the Airborne Visible/Infrared Imaging Spectrometer in the Laboratory," *Proc. Sixth Annual Airborne Earth Science Workshop*, JPL Pub. 96-4, Vol. 1, Jet Propulsion Laboratory, Pasadena, California, pp. 39–48, March 3–5, 1996.

Chrien, T. G., R. O. Green, B. Pavri, and J. Wall, "Calibration Validation of the AVIRIS Portable Radiance Standard," *Proc. Ninth Airborne Earth Science Workshop*, JPL Pub. 00-18, Jet Propulsion Laboratory, Pasadena, California, pp. 101–110, 2000.

Green, R. O., S. A. Larson, I. Novack, "Calibration of AVIRIS Digitized Data," *Proceedings of the Third AVIRIS Workshop*, JPL-Pub 91-28, Jet Propulsion Laboratory, Pasadena, California, pp. 109–118, 1991.

Green, R. O., M. L. Eastwood, C. M. Sarture, T. G. Chrien, M. Aronsson, B. J. Chippendale, J. A. Faust, B. E. Pavri. C. J. Chovit, M. Solis, M. R. Olah, and Q. Williams, "Imaging spectroscopy and the Airborne Visible/Infrared Imaging Spectrometer (AVIRIS)," *Remote Sens Environ* 65: (3) 227–248, Sept. 1998.

Liou, K. N., *An Introduction to Atmospheric Radiation*, Academic Press, Inc., New York, pp. 392, 1980.

Press, W. H., S. A. Teukolsky, W. T. Vetterling, and B. P. Flannery, *Numerical Recipes in C*, Cambridge University Press, pp. 994, 1988.

ACKNOWLEDGMENT

The research described in this paper was carried out at the Jet Propulsion Laboratory, California Institute of Technology, under a contract with the National Aeronautics and Space Administration.

Reference herein to any specific commercial product, process, or service by trade name, trademark, manufacturer, or otherwise, does not constitute or imply its endorsement by the United States Government or the Jet Propulsion Laboratory, California Institute of Technology.

AVIRIS Inflight Calibration Experiment Measurements, Analyses, and Results in 2000

Robert O. Green and Betina Pavri
Jet Propulsion Laboratory, California Institute of Technology, Pasadena, California 91109

INTRODUCTION

The NASA Airborne Visible/Infrared Imaging Spectrometer (AVIRIS) (Green et al., 1998a) measures spectra from 370 to 2500 nm with nominally 10-nm sampling and resolution. The spectra are acquired as images with an 11 km width and up to 800 km length from the ER-2 platform or 2.1 km width and 160 km length from the Twin Otter platform. AVIRIS measurements are used for a range of Earth science research and application objectives. The molecular absorption and particle scattering properties expressed in the calibrated AVIRIS measurements are used. For both science research and application objectives, calibration of the AVIRIS spectra is required to produce useful results. Each year prior to the flight season AVIRIS is calibrated in the laboratory (Chrien et al., 1990, 1995, 1996, 2000). However, the temperature, pressure, vibration, and observational geometry, as well as mechanical, electrical and operational interfaces of the laboratory are different than the environment on board the airborne platform. To validate the calibration of AVIRIS in the flight environment, an inflight calibration experiment is orchestrated at the beginning of each flight season (Conel et al., 1988; Green et al., 1990, 1992, 1993, 1995, 1996, 1998b, 1999). In most years additional inflight calibration experiments occur towards the middle and end of the flight season as well. For an inflight calibration experiment, AVIRIS acquires airborne data over a designated calibration target. In concert with the airborne data acquisition, surface and atmospheric properties at the calibration target are measured in situ. These in situ measurements are used to constrain a radiative transfer code and predict the radiance incident at the AVIRIS instrument from the calibration target. This prediction is compared with the AVIRIS-measured radiance to validate the calibration of AVIRIS in the flight environment. Additional properties (such as the AVIRIS inflight measurement precision) are determined as well. This paper presents measurements, analyses, and results from the inflight calibration experiment held on the dry lake bed surface of Rogers Dry Lake, California, on June 5, 2000.

IN SITU MEASUREMENTS

In order to predict the radiance at AVIRIS, in situ measurements of surface and atmospheric properties at the time of the overflight are required. For the experiment of June 5, 2000, a calibration target was designated on the surface of Rogers Dry Lake, California. Rogers Dry Lake is located on Edwards Airforce Base about 120 km north of Los Angeles, California. The target was located near north latitude 34.985 and west longitude 117.833 and was selected as a visually homogeneous portion of dry lake bed surface measuring 40 by 120 m. At each end of the calibration target, blue demarcation tarps were position and staked to the surface. In the period from 30 minutes before to 30 minutes after the AVIRIS over flight, surface reflectance measurements were acquired between the demarcation tarps. A portable field spectrometer that covers the range from 350 nm to 2500 nm with approximately 10 nm resolution and 1 nm sampling was used. The field of view of the spectrometer was 8 degrees or 14 cm diameter for a 1-m observation distance. Sets of spectra were acquired along transects at 0, ±10, and ±20 m of the central line between the demarcation tarps. At the beginning, middle, and end of each transect, a reflectance standard was measured.

Following acquisition, the surface measurements were converted to surface reflectance using the interspersed reflectance standard measurements. The absolute reflectance of the reflectance standard and the corresponding bidirectional reflectance distribution function (BRDF) for the average 20-degree solar

zenith angle were used for this reflectance calculation. Figure 1 shows the calculated average reflectance of the calibration target from the 890 surface measurements. Also shown is the standard deviation of the measurements that is roughly ±1 percent reflectance across the spectrum. The standard deviation of the mean (Taylor, 1982) calculated as the standard deviation divided by the square root of the number of samples is less than 0.1 percent across the spectrum. The statistical uncertainty in knowledge of the average reflectance of the reflectance measurements of this calibration target is best characterized by the standard deviation of the mean and is excellent based on the 890 measurements. This average surface reflectance provides the basis for constraining the surface reflectance used in the radiative transfer code prediction of the radiance incident at AVIRIS.

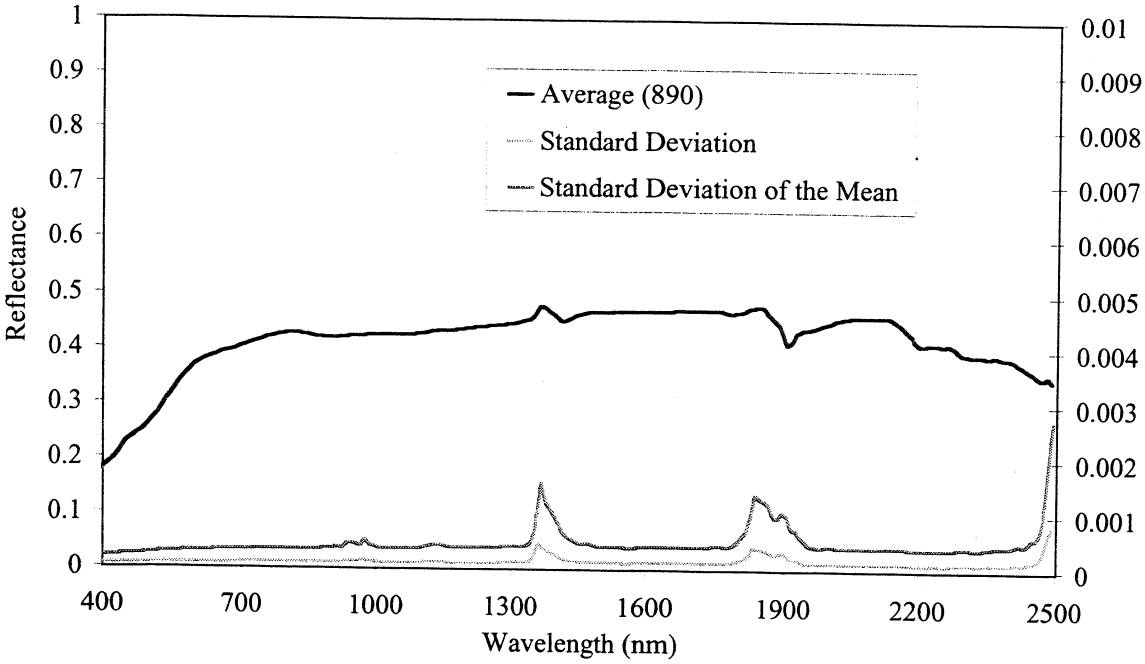

Figure 1. Average, standard deviation, and standard deviation of the mean, for measured surface reflectance at the time of the AVIRIS over flight of Rogers Dry Lake, California, on June 5, 2000.

In addition to surface reflectance, the atmospheric properties were measured at a site adjacent to the surface calibration target. These atmospheric measurements were acquired by a sun-tracking solar radiometer. The radiometer has 10 spectral channels located at 370, 400, 440, 520, 620, 670, 780, 870, 940, and 1030 nm in the solar reflected spectrum. This instrument records voltage output as a function of time. On June 5, 2000 the solar radiometer was operated from 7:53 to 13:18 local time with measurements every 5 minutes. Figure 2 shows the voltage output of the solar radiometer over this period. The measurements are used to calculate the average optical depth of the atmosphere in each channel (Liou, 1980). Also, with an absolute calibration estimate for the spectral channels, the attenuation of the atmosphere for each measurement may be calculated. The calculated instantaneous optical depths for this experiment are plotted in Figure 3. The optical depths at the time of the over flight are required to constrain the radiative transfer code to predict radiance at AVIRIS.

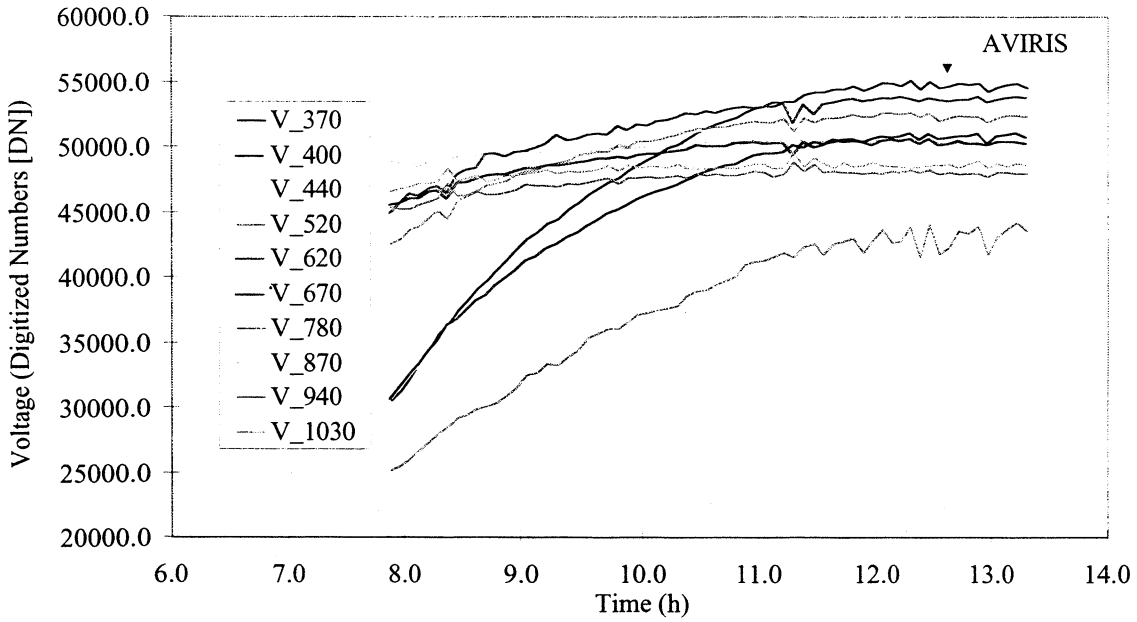

Figure 2. Measured voltages of the sun photometer for derivation of atmospheric optical depths at designated wavelengths at Rogers Dry Lake, California, June 5, 2000.

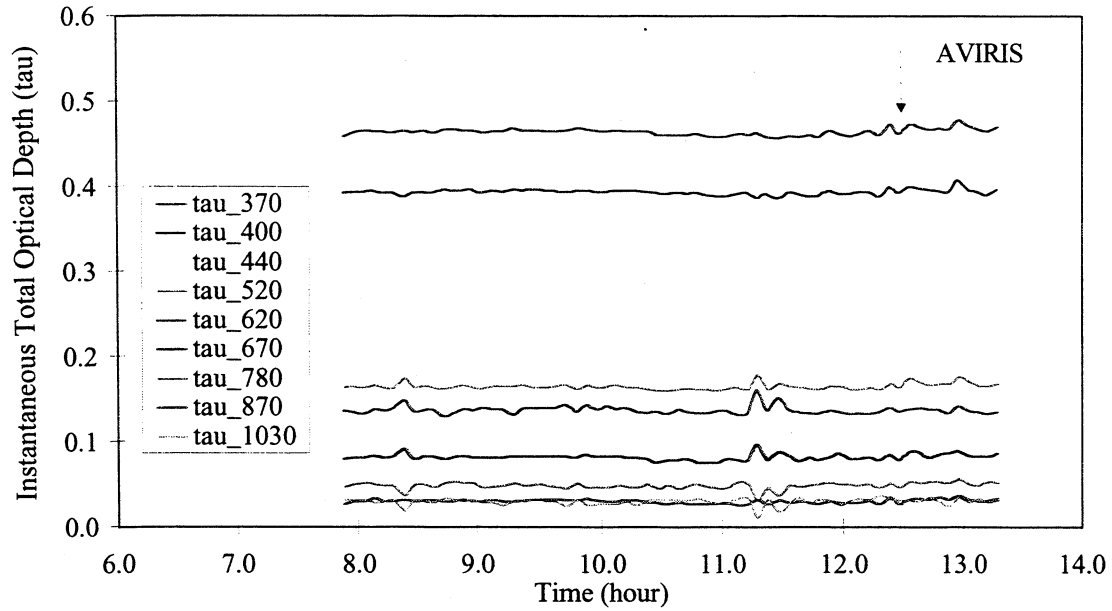

Figure 3. Derived instantaneous optical depths for the calibration experiment on June 5, 2000, at Rogers Dry Lake, California.

In addition to determination of atmospheric optical depth, the sun tracking solar radiometer has a spectral channel at 940 nm. This channel is centered in a moderately strong atmospheric water vapor absorption band. With the voltage measurements over the range of air mass observations the water vapor abundance may be calculated (Reagan et al., 1987; Bruegge et al., 1992). With an absolute calibration estimate for the solar radiometer water vapor channel, the water vapor abundance may be calculated for each measurement. Figure 4 shows the water vapor calculated over the period of measurements with a range

from 4.1 to 3.8 precipitable mm. A value of 3.9 mm is estimated for the time of the AVIRIS over flight. This value, in conjunction with the surface reflectance and atmospheric optical depths, is the in situ parameter required to constrain the radiative transfer code to predict the radiance at the AVIRIS instrument.

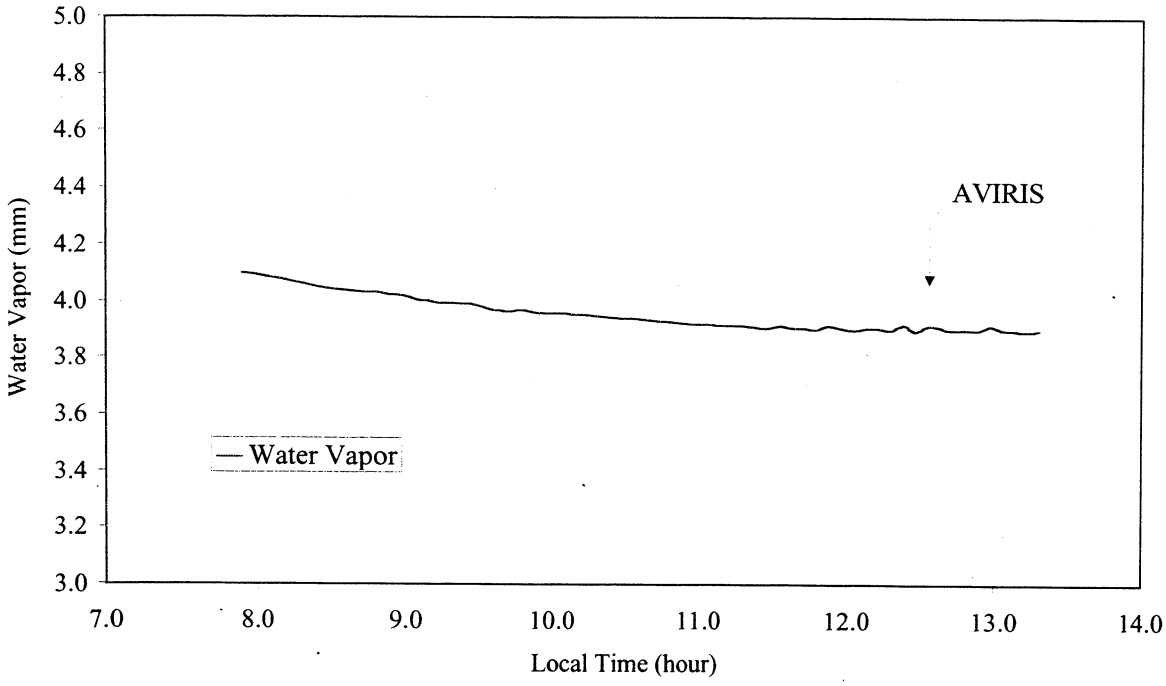

Figure 4. Derived instantaneous water vapor abundance from the 940-nm channel of the solar radiometer data set.

AVIRIS MEASURED RADIANCE

The essential measurements of the calibration target for the inflight calibration experiment are data acquired by AVIRIS onboard the ER-2 aircraft flying at 19.6 km altitude. The corresponding AVIRIS image of Rogers Dry Lake, California, for these measurements is shown in Figure 5. The area of the calibration target is towards the top center of the image. On the surface, blue demarcation tarps were placed at either end of the calibration target. The spectral reflectance contrast between these tarps and the surface allows unambiguous identification of the location of the calibration target. Figure 6 shows a spectrum of the blue tarps and of the lake bed surface. A ratio of the 600 nm over the 450 nm AVIRIS image generates low values for the tarp spectral signature in contrast to the lake bed reflectance. Figure 7 shows an extracted portion of this ratio image with the demarcation tarps clearly evident. The calibration target is the lake bed surface between the tarps. The time of acquisition of this calibration target was recorded in the AVIRIS ephemeris data stream as 18:39:43 UTC.

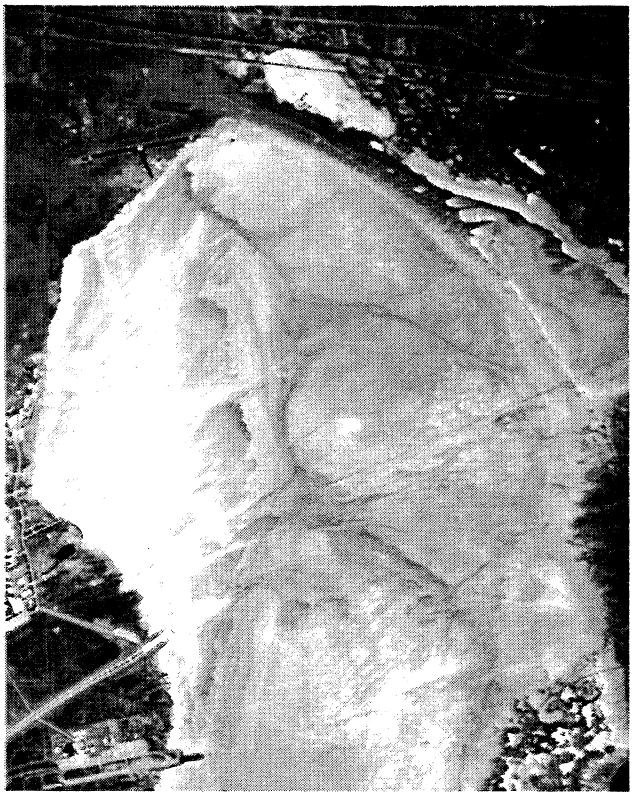

Figure 5. AVIRIS image of Rogers Dry Lake, California, acquired on June 5, 2000. (North is up.)

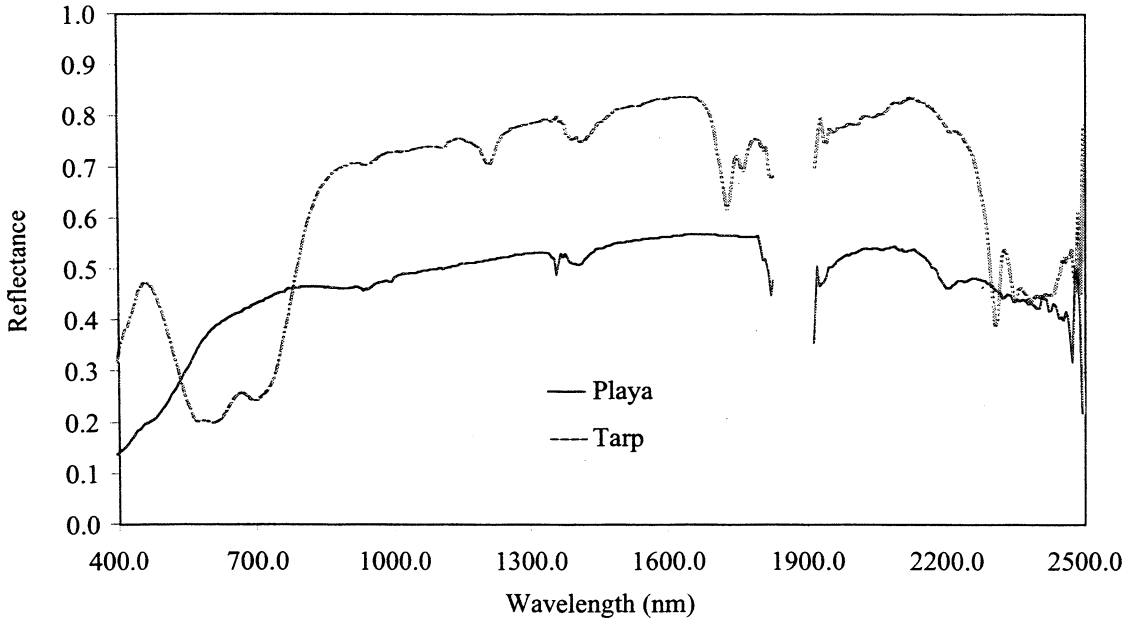

Figure 6. Spectra of blue demarcation tarps used to identify the calibration target surface.

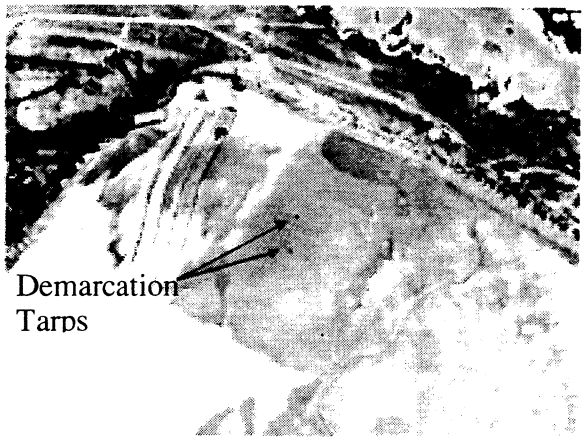

Figure 7. AVIRIS inflight calibration target on the surface of Rogers Dry Lake, California, on June 5, 2000.

With the identification of the calibration target in the AVIRIS data set, the average spectrum for the target is extracted. Figure 8 shows the extracted average uncalibrated data for calibration target. The total signal, dark signal, and total minus dark signal are plotted. The dark is measured as the average of 64 spectra at the end of each scan line with the AVIRIS primary shutter closed. These uncalibrated data are calibrated with the radiometric calibration coefficients and the spectral calibration file and data from the AVIRIS onboard calibrator (Green et al., 1991; Green, 1993). Figure 9 shows the average calibrated AVIRIS spectrum for the calibration target. This is the measured AVIRIS spectrum to be validated with respected to the radiative transfer code predicted radiance for the calibration target.

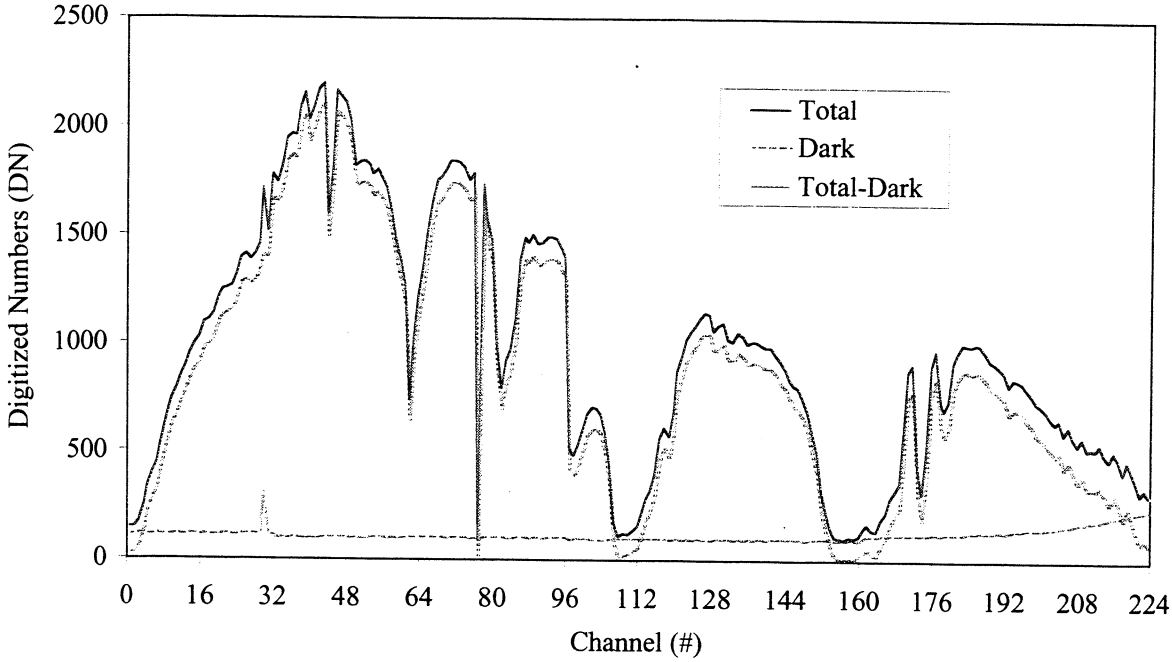

Figure 8. AVIRIS average measured data for the calibration surface.

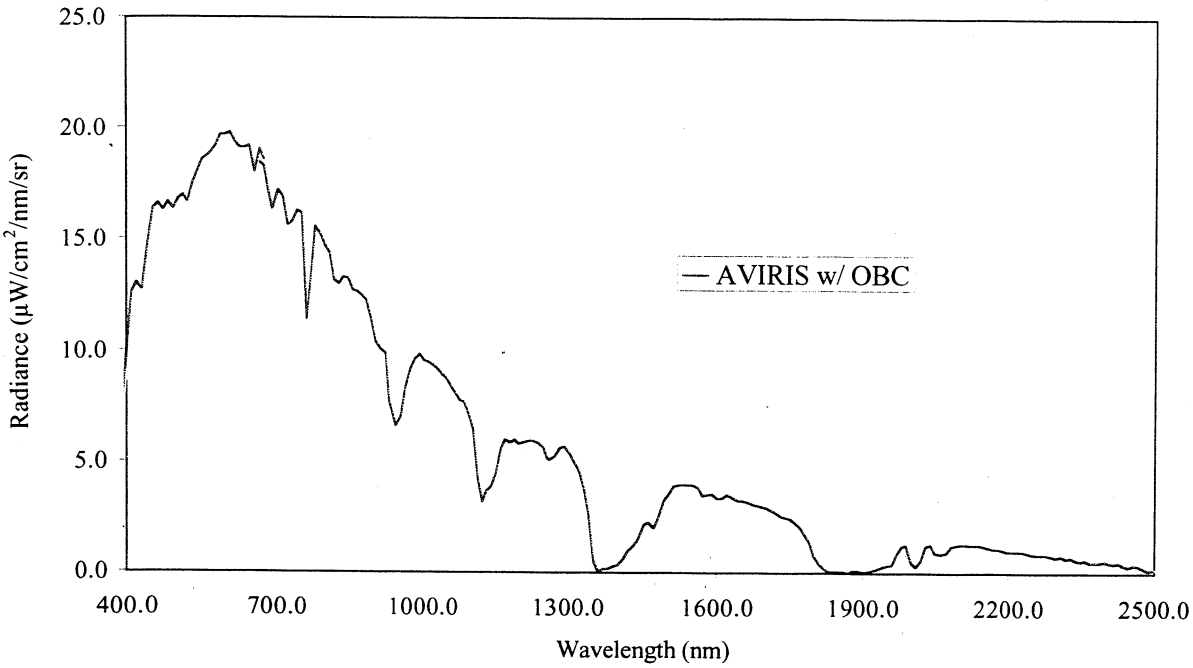

Figure 9. AVIRIS calibrated radiance for the calibration surface with corrections of the onboard calibrator (OBC).

MODTRAN PREDICTED RADIANCE

The radiance incident at the AVIRIS instrument is predicted with a radiative transfer code constrained by the in situ surface and atmospheric measurements acquired at the calibration target site. The MODTRAN radiative transfer code (Berk et al., 1989; Anderson et al., 1995, 2000) was used for the analysis. MODTRAN constraint parameters were set for the time, location, and observation geometry of the AVIRIS measurements based on ephemeris information. Through adjustment of the visibility parameter, the mid-latitude summer atmospheric model was constrained to closely match the measured atmospheric optical depths. A comparison between the measured optical depths and those of MODTRAN are shown in Figure 10. This level of agreement was achieved with an atmospheric visibility of 150 km. Both the in situ measured surface reflectance and water vapor abundance were included in the MODTRAN constraint parameter. The amount of carbon dioxide in the MODTRAN model was adjusted to a 370 ppm mixing ratio for the year 2000 (Keeling et al., 2001). Ozone was constrained by the total ozone mapping spectrometer (TOMS) (McPeters, 2001) derived value of 310 dobsin units for June 5, 2000. With this complete set of constraints, a predicted radiance spectrum was calculated at full MODTRAN spectral resolution. This spectrum with a 1 wavenumber sampling interval and 2 wavenumber resolution is shown in Figure 11. For comparison with AVIRIS, the high resolution output was convolved to the AVIRIS spectral response functions determined in the laboratory. Figure 12 shows the resulting MODTRAN predicted radiance for the calibration target on Rogers Dry Lake at 18:39:43 on June 5, 2000. This predicted radiance spectrum forms the basis for validating the inflight calibration of AVIRIS for the 2000 flight season.

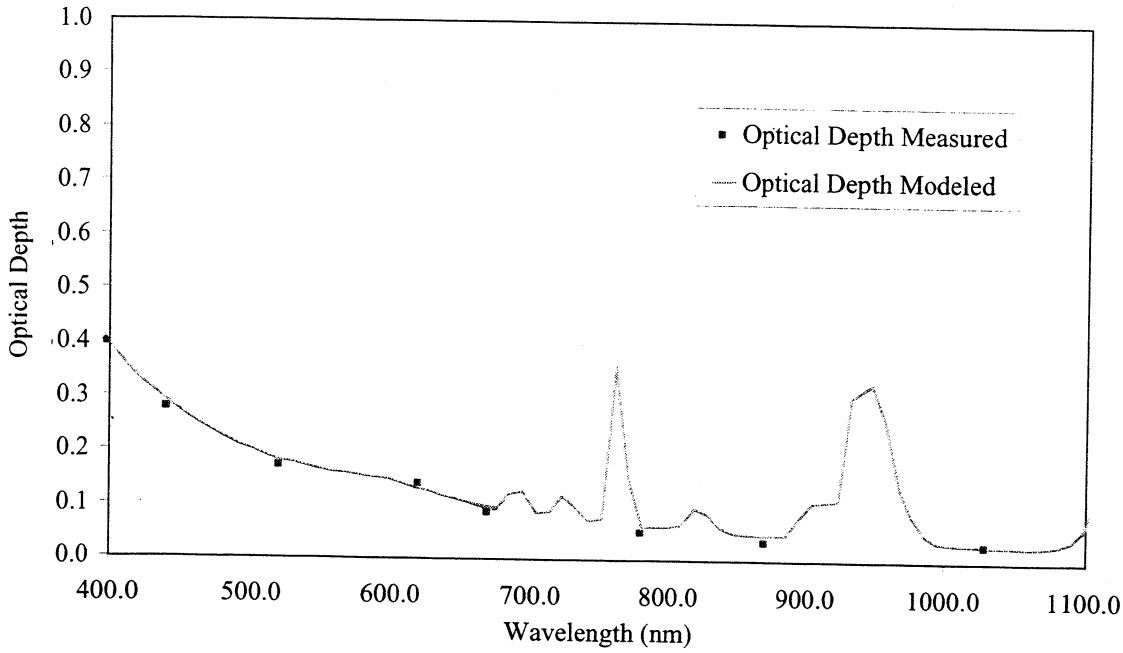

Figure 10. In situ measured optical depths for the time of the AVIRIS over flight and corresponding MODTRAN optical depths for a 150-km visibility mid-latitude summer atmosphere model.

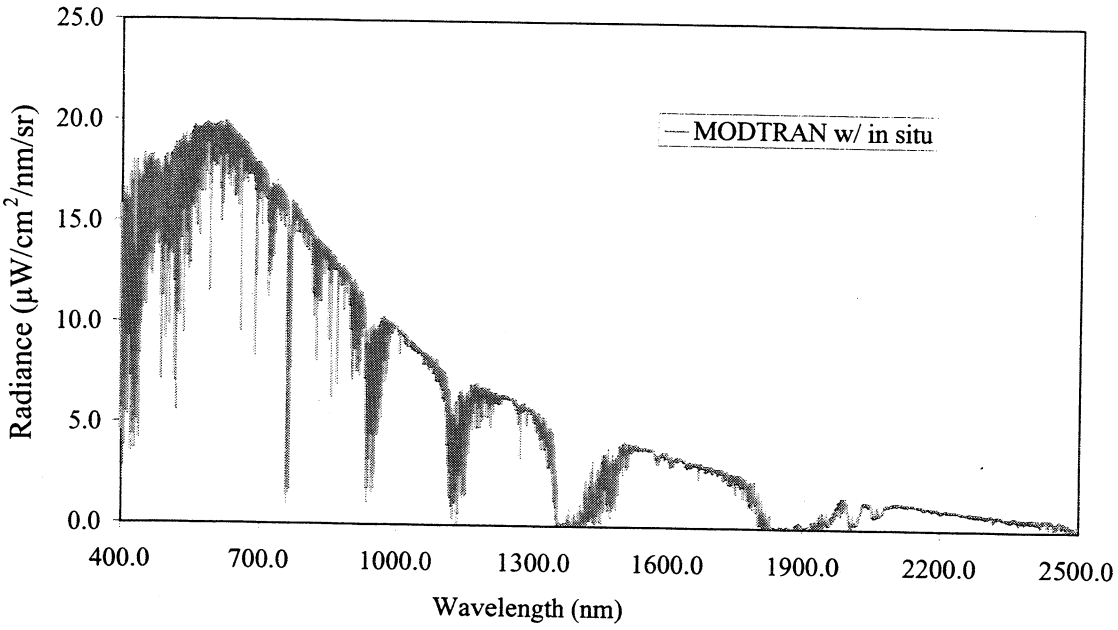

Figure 11. MODTRAN modeled radiance for the inflight calibration experiment calculated with in situ constraints.

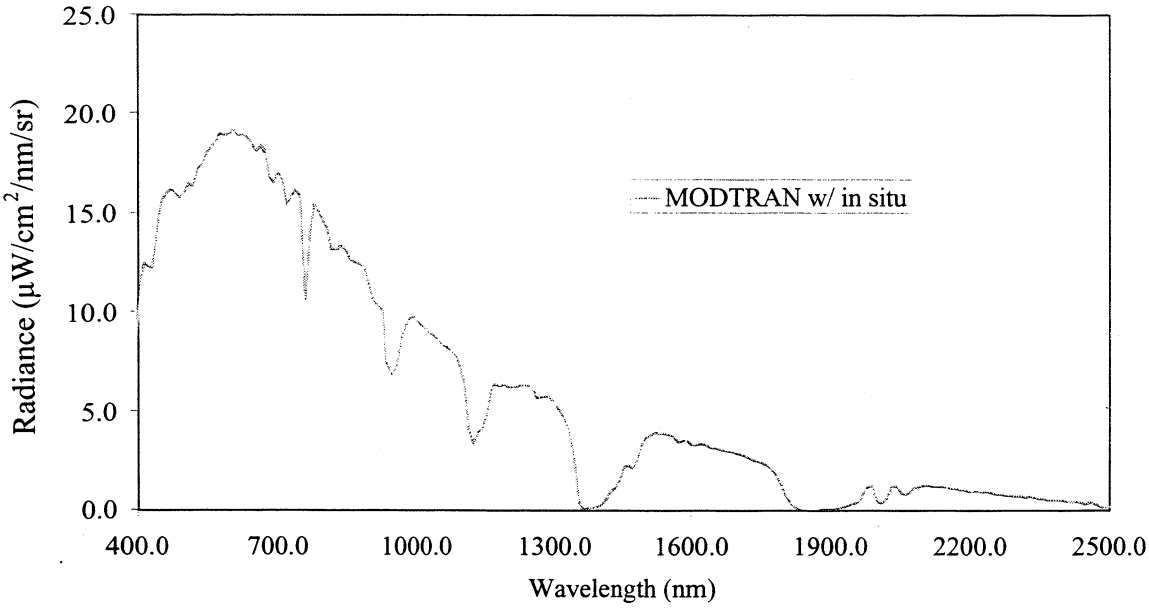

Figure 12. MODTRAN-predicted radiance convolved to the AVIRIS spectral characteristics calculated with in situ restraints.

COMPARISON ANALYSIS

With the AVIRIS measured spectrum and the MODTRAN predicted radiance spectrum, a simple comparison analysis was performed to validate the calibration of AVIRIS in the flight environment. Figure 13 shows a combined plot of the measured and predicted radiance spectra. The AVIRIS spectrum has been calibrated with the laboratory-generated radiometric calibration coefficients and onboard calibrator measurements. The MODTRAN spectrum was generated with the surface reflectance, atmospheric optical depths, and water vapor abundance measured at the calibration target site. The absolute average agreement between the AVIRIS and MODTRAN spectra is 96.2 percent. This agreement is calculated excluding the regions of strong atmospheric absorption where the radiance levels approach zero. A comparison ratio of these two spectra is shown in Figure 14. In several regions of the spectrum there are areas of disagreement. These disagreements may result from either or both AVIRIS and MODTRAN uncertainty factors. The slightly higher values of AVIRIS in the 400- to 700-nm region of the spectrum are likely do to changes in the throughput performance of the first AVIRIS instrument spectrometer. The sharp deviations near 760, 940, and 1150 nm probably relate to small shifts (on the order of 1 nm) in the in flight spectral calibration of AVIRIS with respect to the spectral calibration of AVIRIS in the laboratory. Other factors (such as the absolute calibration standards of AVIRIS and changes in AVIRIS performance through time) may contribute to these absolute uncertainties. For MODTRAN, factors (such as the solar irradiance and parameterization of the atmosphere) may contribute to uncertainties. In addition, uncertainties in the in situ measurements and derived parameters will contribute to uncertainty in the MODTRAN predicted radiance. However, the primary result of this inflight calibration experiment is a baseline validation of AVIRIS inflight calibration at the 96 percent level for the 2000 flight season.

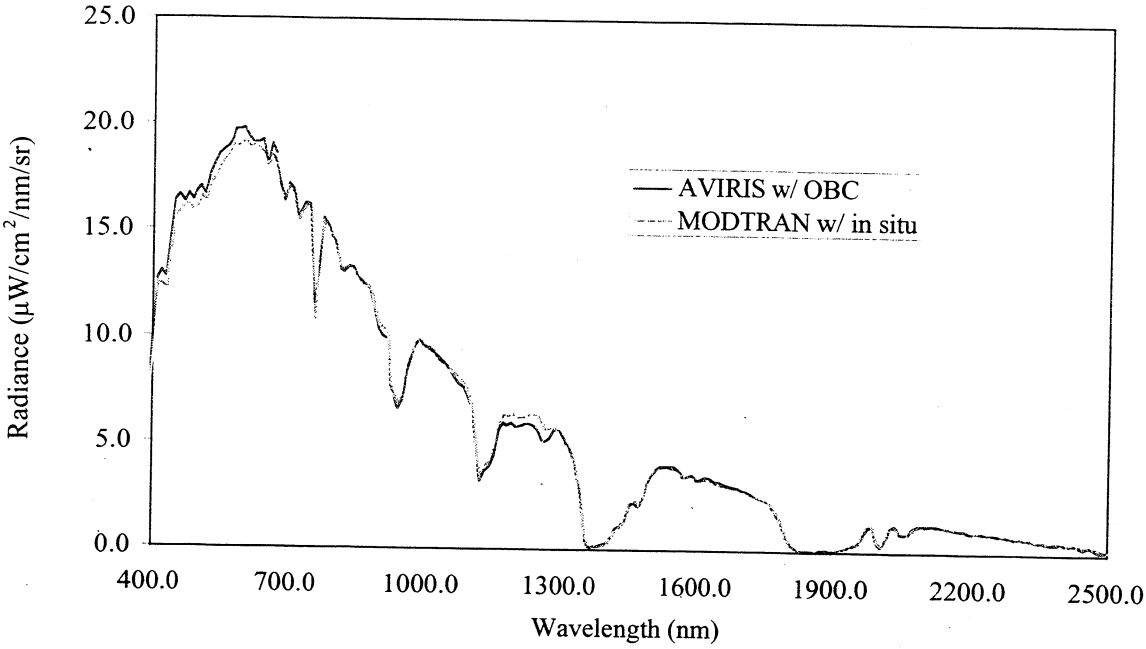

Figure 13. Comparison of the AVIRIS-measured radiance and the MODTRAN-predicted radiance from the inflight calibration experiment on June 5, 2000.

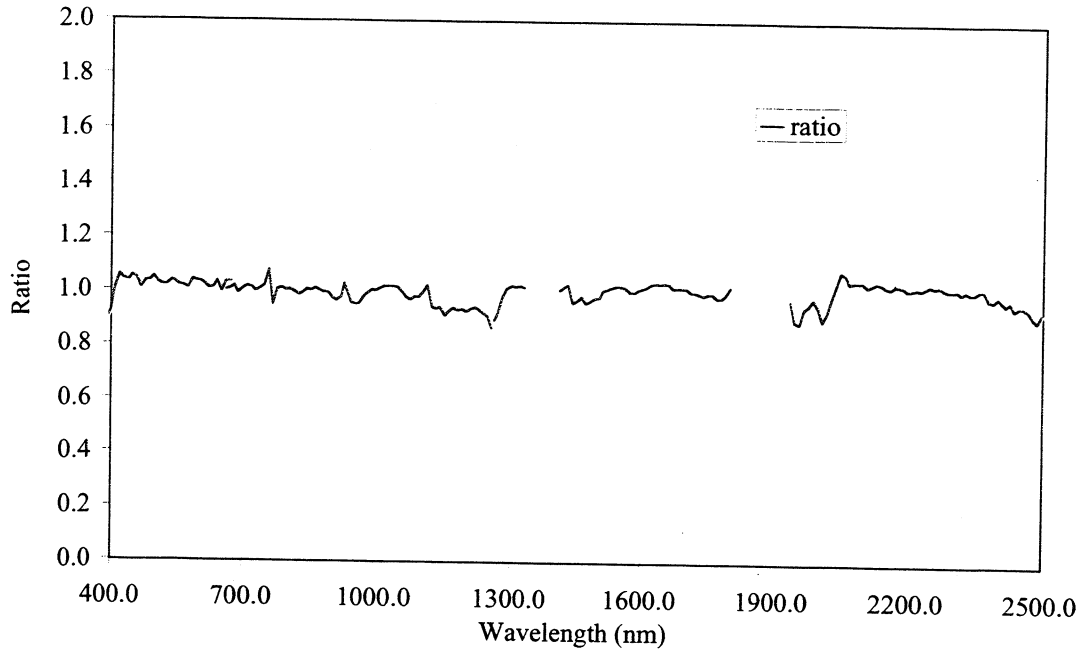

Figure 14. Ratio of AVIRIS-measured to MODTRAN-predicted radiance.

AVIRIS PRECISION

In addition to AVIRIS radiometric accuracy, knowledge of the inflight radiometric precision is often required for both science research and application objectives. A measure of AVIRIS inflight precision is provided by the dark signal data measured before and after acquisition of each spectral image data set. The standard deviation of these dark signal data provide an estimate of the instrument noise. Figure 15

shows a plot of the AVIRIS noise calculated for the inflight calibration experiment data set acquired on June 5, 2000. The AVIRIS channel at 655 nm was excessively noisy in 2000 and is not included in this analysis. Across the spectrum from 400 to 1900 nm, the AVIRIS noise is quite uniform at about 0.7 digitized number (DN). Beyond 1900 the noise rises steadily to 1.4 in DN at 2500 nm. This increase in noise due to the uncertainty in the radiance signal emitted by the AVIRIS spectrometer onto the detectors. At these wavelengths the spectrometer is as significant source of dark signal radiance. AVIRIS radiometric precision may be reported as the noise-equivalent-delta-radiance (NEdL). NEdL is calculated by multiplying the noise in DN by the radiometric calibration coefficients. Figure 16 shows the NEdL for the inflight calibration experiment on June 5, 2000, as well as inflight values from a 1999 data set. This is the dark signal precision of AVIRIS in units of radiance and may be thought of as the precision-related error bars for each spectrum for a dark target. Lower values of NEdL correspond to better precision and better AVIRIS performance. The improvement of AVIRIS from 1999 to 2000 in NEdL is related to a new detector array in the first spectrometer and general efforts towards signal-chain noise suppression across the AVIRIS spectral range. As target brightness increases, the NEdL increases due to the statistical uncertainty in the radiance signal incident at the AVIRIS instrument. The inflight NEdL for 2000 given here provides a basis for comparison of AVIRIS performance from year to year as well as an estimate of the radiance uncertainty in each AVIRIS spectrum due to noise.

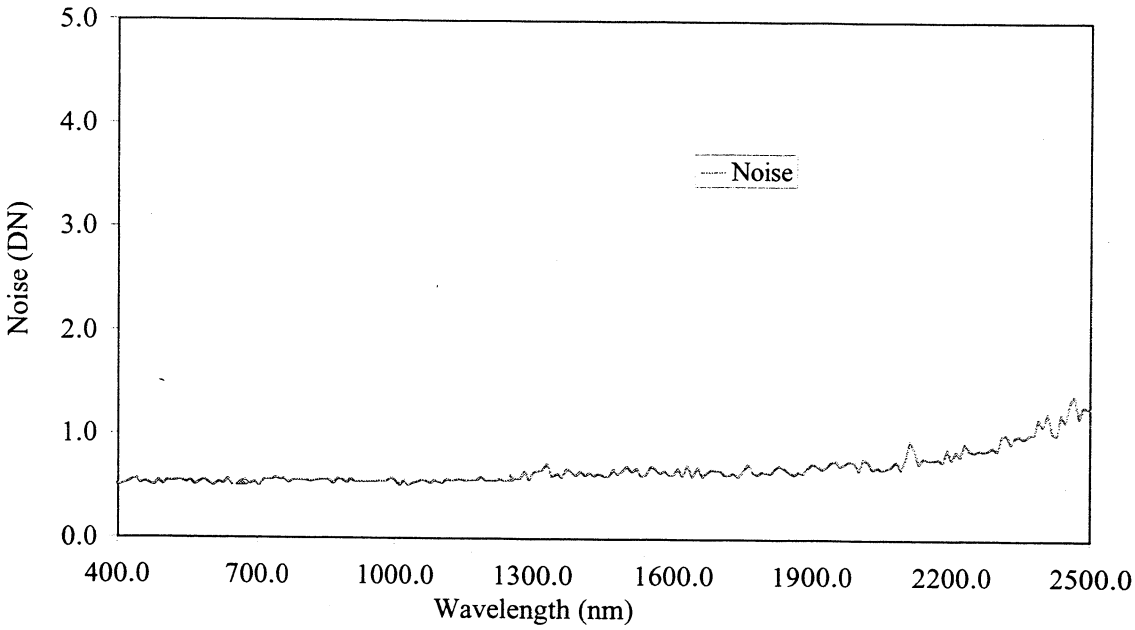

Figure 15. AVIRIS noise calculated from the dark signal for the inflight calibration experiment.

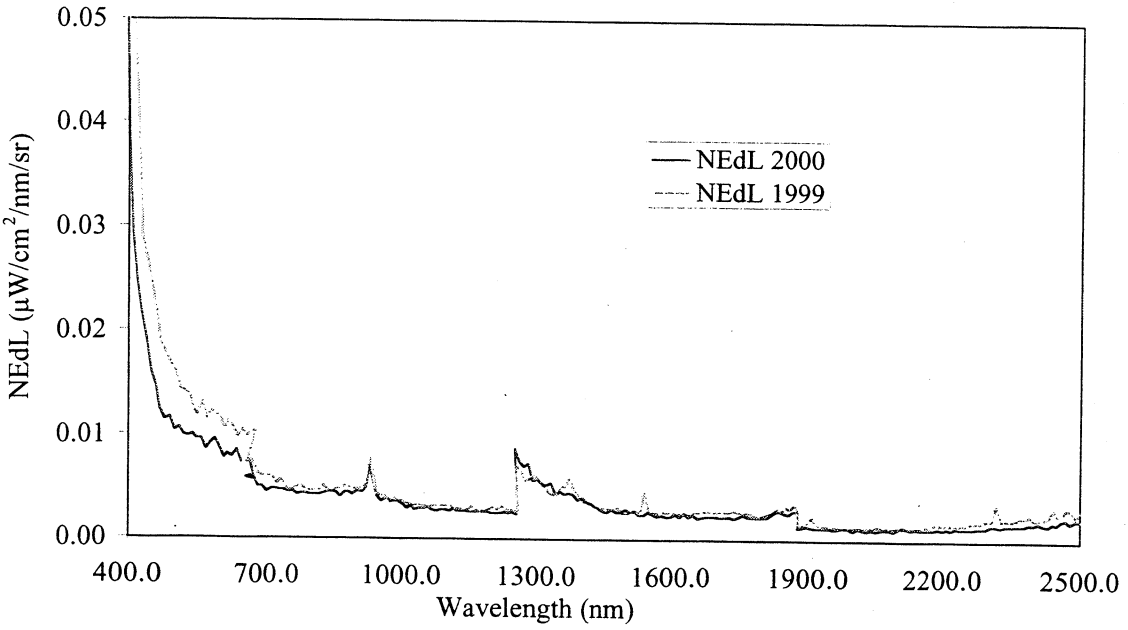

Figure 16. Noise equivalent delta radiance for the inflight calibration experiment on June 5, 2000. The corresponding values are given for 1999.

CONCLUSION

An AVIRIS inflight calibration experiment was orchestrated on June 5, 2000, at Rogers Dry Lake, California. For this experiment, a visually homogeneous calibration target was designate on the dry lakebed bed surface. Surface reflectance measurements were acquired by thoroughly sampling a 40- by 120-m area of the calibration target. The data were analyzed to produce an average reflectance spectrum for the calibration target with compensation for surface BRDF and for the reflectance standard spectral characteristics. Adjacent to the calibration target a solar radiometer was used to measure atmospheric attenuation in 10 spectral channels from 370 to 1030 nm. These measurements were analyzed to derive the atmospheric optical depth as well as the total column water vapor abundance at the time of the AVIRIS overflight of the calibration target. A ratio of the 600-nm and 4450-nm AVIRIS images was formed to locate the calibration target between the blue demarcation tarps in the AVIRIS data set. The average AVIRIS spectrum of the calibration target was extracted and calibrated to radiance using the laboratory-derived radiometric calibration coefficient and spectral calibration data. The measured in situ surface and atmospheric measurements were used to constrain the MODTRAN radiative transfer code and predict the radiance incident at the AVIRIS instrument. The AVIRIS-measured and MODTRAN-predicted radiance spectra were compared and found to have a 96.2 percent absolute average agreement exclusive of the strong atmospheric absorption regions. The regions of residual disagreement in the spectral comparison are related to a number of factors. These include uncertainties in the AVIRIS calibration standards, changes in AVIRIS performance, uncertainties in the underlying MODTRAN parameters and calculation, as well as uncertainties in the surface and atmospheric measurements and analyses. Research is ongoing to identify, assess, and improve the residual uncertainty in these factors that effect the inflight calibration experiment results. In addition to radiometric accuracy, the inflight radiometric precision was calculated and reported as the dark signal NEdL of AVIRIS in 2000. Comparison with the 1999 NEdL showed marked improvement in the range from 400 to 700 nm, as well as modest improvement across the spectrum. The measurements, analyses, and results reported here provide the core validation of AVIRIS inflight performance for the 2000 flight season. Assessment and

validation of AVIRIS performance in the flight environment is essential because data sets acquired for scientific research and application objectives are only acquired in the flight environment.

REFERENCES

Anderson, G. P., J. Wang, and J. Chetwynd, "An Update and Recent Validations Against Airborne High Resolution Interferometer Measurements," *Summaries of the Fifth Annual JPL Airborne Earth Science Workshop*, JPL 95-1, Vol. 1, *AVIRIS Workshop*, Jet Propulsion Laboratory, Pasadena, California, pp. 5–8, January 23, 1995.

Anderson, G. P., A. Berk, P. K Acharya, M. W. Mathew, L. S. Bernstein, J. H. Chetwynd, H. Dothe, S. M. Adler-Golden, A. Ratkowski, G. W. Felde, J. A. Gardner, M. L. Hoke, S. C. Richtsmeir, B. Pukall, J. Mello, and L. S. Jeong, "MODTRAN4: Radiative transfer modeling for remote sensing," in *Proceedings SPIE, Algorithms for Multispectral, Hyperspectral, and Ultraspectral Imagery VI*, Vol. 4049, S. S. Shen and M. R. Descour, eds., pp. 176–183, 2000.

Berk, A., L. S. Bernstein, and D. C. Robertson, *MODTRAN: A Moderate Resolution Model for LOWTRAN 7*, Final report, GL-TR-0122, AFGL, Hanscomb AFB, Massachusetts, 42 pp., 1989.

Bruegge, C. J., J. E. Conel, R. O. Green, J. S. Margolis, R. G. Holm et. al., "Water vapor column abundance retrievals during fire," *Journal of Geophysical Research Atmospheres*, 97(D17) 18759–18768, 1992.

Chrien, T. G., R. O. Green, and M. L. Eastwood, "Accuracy of the spectral and radiometric laboratory calibration of the Airborne Visible/Infrared Imaging Spectrometer (AVIRIS)," *SPIE Vol. 1298, Imaging spectroscopy of the terrestrial environment*, G. Vane, ed., pp. 37–49, 1990.

Chrien, T. G., R. O. Green, C. Chovit, M. Eastwood, J. Faust, P. Hajek, H. Johnson, H. I. Novack, and C. Sarture, "New Calibration Techniques for the Airborne Visible/Infrared Imaging Spectrometer (AVIRIS), 1995," *Proc. Fifth Annual Airborne Earth Science Workshop*, JPL Pub. 95-1, Jet Propulsion Laboratory, Pasadena, California, pp. 33–34, 1995.

Chrien, T. G., R. O. Green, C. J. Chovit, M. L. Eastwood, and C. M. Sarture, "Calibration of the Airborne Visible/Infrared Imaging Spectrometer in the Laboratory," *Proc. Sixth Annual Airborne Earth Science Workshop*, JPL Pub. 96-4, Vol. 1, Jet Propulsion Laboratory, Pasadena, California, pp. 39–48, March 3–5, 1996.

Chrien, T. G., R. O. Green, B. Pavri, and J. Wall, "Calibration Validation of the AVIRIS Portable Radiance Standard," *Proc. Ninth Airborne Earth Science Workshop*, JPL Pub. 00-18, Jet Propulsion Laboratory, Pasadena, California, pp. 101–110, 2000.

Conel, J. E., R. O. Green, R. E. Alley, C. J. Bruegge, V. Carrere, J. S. Margolis, G. Vane, T. G. Chrien, P. N. Slater, S. F. Biggar, P. M. Teillet, R. D. Jackson and M. S. Moran, "In-Flight Radiometric Calibration of the Airborne Visible/Infrared Imaging Spectrometer (AVIRIS)," *SPIE Vol. 924, Recent advances in sensors, radiometry and data processing for remote sensing*, pp. 197–214, 1988.

Green, R. O., J. E. Conel, V. Carrere, C. J. Bruegge, J. S. Margolis, M. Rast, and G. Hoover, "In-flight Validation and Calibration of the Spectral and Radiometric Characteristics of the Airborne Visible/Infrared Imaging Spectrometer (AVIRIS)," *SPIE Vol. 1298, Imaging spectroscopy of the terrestrial environment*, G. Vane, ed., pp. 18–36, 1990.

Green, R. O., S. A. Larson, I. Novack, "Calibration of AVIRIS Digitized Data," *Proceedings of the Third AVIRIS Workshop*, JPL-Pub 91-28, Jet Propulsion Laboratory, Pasadena, California, pp. 109–118, 1991.

Green, R. O., J. E. Conel, C. J. Bruegge, J. S. Margolis, V. Carrere, G. Vane, and G. Hoover, "In-flight Calibration of the Spectral and Radiometric Characteristics of AVIRIS in 1991," *Summaries of the Third*

Annual JPL Airborne Geoscience Workshop, JPL Pub. 92-14, Vol. 1, Jet Propulsion Laboratory, Pasadena, California, pp. 1–4, 1992.

Green, R. O., J. E. Conel, M. Helminger, J. van den Bosch, C. Chovit, and T. Chrien, "Inflight Calibration of AVIRIS in 1992 and 1993," *Summaries of the Fourth Annual JPL Airborne Geoscience Workshop*, JPL Pub. 93-26, Vol. 1, Jet Propulsion Laboratory, Pasadena, California, pp. 69–72, Oct. 25, 1993.

Green, R. O., "Use of Data from the AVIRIS Onboard Calibrator," *Summaries of the Fourth Annual JPL Airborne Geoscience Workshop*, JPL Pub. 93-26, Vol. 1, Jet Propulsion Laboratory, Pasadena, California, pp. 65–68, Oct. 25, 1993.

Green, R. O., J. E. Conel, M. Helmlinger, J. van den Bosch, P. Hajek, "In-Flight Radiometric Calibration of AVRIS in 1994," *Proc. of the Fifth Annual JPL Airborne Earth Science Workshop*, JPL Pub. 95-1, Jet Propulsion Laboratory, Pasadena, California, pp. 83–86, Jan. 23–26, 1995.

Green, R. O., Conel, J. E., Margolis, C. Chovit, and J. Faust, "In-Flight Calibration and Validation of the Airborne Visible/Infrared Imaging Spectrometer (AVIRIS)," *Proc. Sixth Annual Airborne Earth Science Workshop*, JPL Pub. 96-4, Vol. 1, Jet Propulsion Laboratory, Pasadena, California, pp. 115–126, March 3–5, 1996.

Green, R. O., M. L. Eastwood, C. M. Sarture, T. G. Chrien, M. Aronsson, B. J. Chippendale, J. A. Faust, B. E. Pavri. C. J. Chovit, M. Solis, M. R. Olah, and Q. Williams, "Imaging spectroscopy and the Airborne Visible/Infrared Imaging Spectrometer (AVIRIS)," *Remote Sens Environ* 65: (3) 227–248, Sept. 1998a.

Green R. O., B. Pavri, J. Faust, O. Williams, and C. Chovit, "Inflight Validation of AVIRIS Calibration in 1996 and 1997," *Proc. Seventh Airborne Earth Science Workshop*, JPL Pub. 97-21, Vol. 1, Jet Propulsion Laboratory, Pasadena, California, pp. 193–205, 1998b.

Green, R. O., B. Pavri, J. Faust, C. Chovit, and O. Williams, "AVIRIS Radiometric Laboratory Calibration In-Flight Validation and a Focused Sensitivity Analysis in 1998," *Proc. Eighth Airborne Earth Science Workshop*, JPL Pub. 99-17, Vol. 1, Jet Propulsion Laboratory, Pasadena, California, pp. 161–175, 1999.

Keeling, C. D and T. P. Whorf, Atmospheric CO2 concentrations (ppmv) derived from in-situ air samples collected at Mauna Loa Observatory, Hawaii, Scripps Institution of Oceanography (SIO), University of California, La Jolla, California, USA 92093-0244 http://cdiac.esd.ornl.gov/ftp/maunaloa-co2/maunaloa.co2 (accessed Nov. 15, 2001).

Liou, K. N., *An Introduction to Atmospheric Radiation*, Academic Press, Inc., New York, pp. 392, 1980.

McPeters, R. D., EarthProbe/TOMS data set, NASA/GSFC TOMS Ozone Processing Team (OPT), Code 916, NASA Goddard Space Flight Center, Greenbelt, MD 20771, ftp://toms.gsfc.nasa.gov/pub/eptoms/images/global/y2000/et000605.gif (accessed Nov. 15, 2001).

Reagan, J. A., K. Thome, B. Herman, and R. Gall, "Water Vapor Measurements in the 0.94 Micron Absorption Band: Calibration, Measurements and Data Applications," *Proc. IGARSS*, Ann Arbor, Michigan, 18–21 May 1987.

Taylor, J. R., *An Introduction to Error Analysis*, Oxford University Press, p. 270, 1982.

ACKNOWLEDGMENT

The research described in this paper was carried out at the Jet Propulsion Laboratory, California Institute of Technology, under a contract with the National Aeronautics and Space Administration.

Oleoresin Chemistry and Spectral Reflectance in "Stressed" Lodgepole and White Bark Pine, Mammoth Mountain, California

James C. Hickey,[1] Richard W. Birnie,[1] Meixun Zhao[1]

I. Introduction/Background

Development of methods to identify the physical and chemical character of materials on the earth's surface is one of the foci of hyperspectral remote sensing activities. Enhancing the ability to elucidate changes in foliar chemistry that relate to the health of a plant is a benefit to plant physiologists, foresters, and plant ecologists, as well as geologist and environmental scientists. Vegetation covers the landscape throughout the temperate and tropical regions of the earth. The existence of vegetation in these areas presents special problems to remote sensing systems since geologic bedrock and alteration zones are masked (Sabins, 1999). At times, however, alterations in the soil/sediment geochemical environment result in foliar chemical changes that are detectable via remote sensing. Examples include monitoring of chlorophyll reflectance/fluorescence and equivalent water thickness indices as indicators of drought-induced plant stress (Datts, 1999; Zarco-Tejada, et al. 2000). Another processing and interpretation approach used with hyperspectral data has been principal components analysis (PCA). Rowan, et al. (2000), used PCA to identify absorption feature patterns obtained from vegetated areas with discrete bedrock geology or mineralization as the substrate. Many researchers highlight the need to advance our ability for hyperspectral imaging in vegetated areas as a near-term priority (Vincent, 1997 and Sabins, 1999).

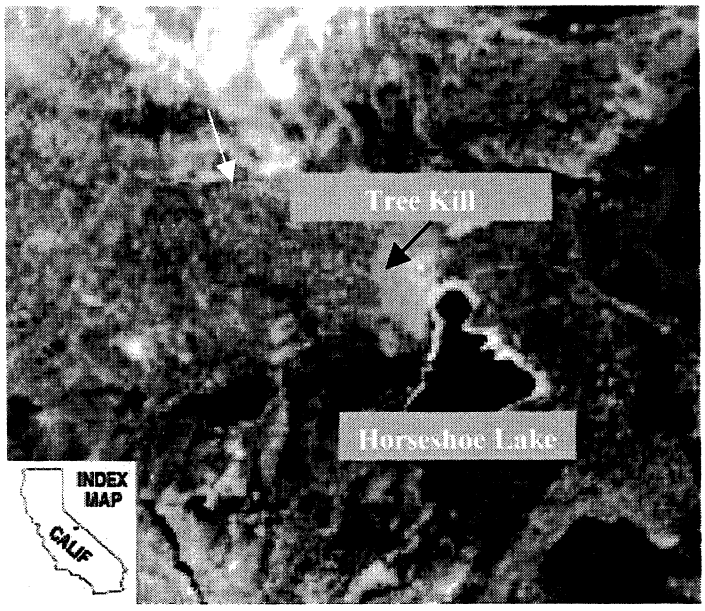

Figure 1. AVIRIS image of Horseshoe Lake and tree kill area. Bright area immediately southwest of the lake is the closed USFS campground and high CO_2/tree kill area. This scene was extracted from 1999 JPL AVIRIS Flight Line over Mammoth Mountain.

The premise of this investigation is to elucidate the connection between changing geochemical substrates (high [CO_2] in soil gas], resultant changes in conifer biochemistry (i.e., monoterpenes in oleoresin and other coincidentally responding constituents) and any associated alteration of the plant's reflectance curve. Predicting a change in monoterpene/oleoresin chemistry and in turn the geochemical substrate, using either field spectroscopy or hyperspectral imagery, is the ultimate goal of the research behind this project.

1 – Dartmouth College, Department of Earth Sciences; jhickey@dartmouth.edu

A preliminary sampling program was conducted in October 2000 at the Horseshoe Lake (HSL) tree kill area, Mammoth Mountain, California (Figure 1). The HSL tree kill is situated on the north and west sides of Horseshoe Lake. Conifers dominate the HSL area with lodgepole (*Pinus contorta)* and white bark (*Pinus albicaulis*) pines being the most common species identified and sampled during this study.

Mammoth Mountain is a cumulovolcano that was formed as a result of multiple eruptions from more than 10 different edifices 100,000 to 300,000 years ago (Sorey, et al. 1998). It is located in the eastern Sierra Mountains on the southwest corner of Long Valley Caldera. Increased magmatic activity occurred in the late 1980's across the western portion of the caldera (Sorey, et al. 1998). This magmatic activity was indicated by increases in seismicity, expansion of the caldera's resurgent dome and higher levels of fumarolic activity (Sorey, et al. 1998). Initiation of diffuse CO_2 discharge at several locations around the mountain occurred in late 1989 (Sorey, et al. 1998). The source of the CO_2 is interpreted to be a subsurface reservoir of magmatically derived CO_2 that was breached (Farrar, et al. 1995 and Sorey, et al. 1998) as a result of the deformation. It is theorized that the excessive concentrations of CO_2 (> 50%) in the soil gas may have decreased root function of the trees in these areas (Farrar, et al. 1995). A decline of tree health that eventually leading to tree kills in the area of highest CO_2 concentration (see Figure 2) then followed (Farrar, et al. 1995). Though the area of the HSL tree kill has remained relatively constant for the last three to four years, trees forming the periphery of the main kill area still display indications of health impact (e.g., needle loss or >35 % of dead/dying branches).

Figure 2. View of the Horseshoe Lake tree kill from the former campground parking lot.

The HSL tree kill area has been the target of multiple geochemical and remote sensing studies since its discovery in 1994. Members of the USGS Volcanic Hazard Monitoring team have been collecting CO_2 soil gas and flux data since 1994 (Farrar, et al. 1995). The status of tree health and detection of the CO_2 boundary temporal shifts were investigated by DeJong (1996), Hausback, et al. (1998) and Martini, et al. (2000) using a combination of field spectroscopy, AVIRIS and other hyperspectral imagery. Since conifers of varying health are still present around the boundary area, HSL was selected to test our premise. One objective of this ongoing investigation is to elucidate the connection between changing geochemical substrates, resultant changes in conifer biochemistry (i.e., monoterpenes in oleoresin or other coincidentally respondent constituents) and any associated alteration of the plant's reflectance spectrum. Predicting a change in monoterpene/oleoresin chemistry and in turn the nature of the geochemical substrate, using either field spectroscopy or hyperspectral imagery, is the ultimate goal of this research.

Soil vapor surveys conducted for resource exploration and environmental investigations first indicated the connection between alterations in monoterpene chemistry and changing geochemical substrates. The presence of sesquiterpenes (the C_{15} terpenoids) was found to indicate the presence of fault and fracture systems in several soil vapor surveys (Hickey, et al. 1983 and Hickey, 1986). Additionally, previous commercial soil vapor data also indicated that organic vapor samples collected from conifers growing on geochemically normal and anomalous substrates contained different ratios of monoterpenes

(Hickey, unpublished data). These observations support the premise that a discernable relationship exists between changes geochemical substrate and coincident changes in oleoresin/monoterpene chemistry.

Oleoresin is a secondary metabolic product in conifers that is used as a plant defense agent (Gijzen, et al. 1993 and Taiz, L. and Zeiger, C., 1998). It consists of approximately 50% monoterpenes and 50% diterpane resin acids and exists in resin ducts and specialized cells that are distributed throughout the trunk, branches, twigs and needles of conifers (Gijzen, et al. 1993 and Litvak and Monson, 1998). Since the monoterpenes are indicative of oleoresin chemistry, they were selected as the proxy to measure the oleoresin changes. Monoterpenes found in conifers are C_{10} olefinic hydrocarbons that are synthesized for plant defense purposes (Gijzen, et al. 1993 and Litvak and Monson, 1998). The monoterpenes consist of over 20 different compounds and optical isomers. Many plant physiologists report variations of monoterpene chemistry as a function of decreasing plant health and different types of impact (e.g., herbivory versus alleopathy or drought versus increasing [CO_2]) indicating that monoterpene chemistry is sensitive to environmental change (Gijzen, et al. 1993 and Litvak and Monson, 1998). Biotic impacts typically induce more drastic compositional changes than abiotic impacts (e.g., 10 fold increase of 3-carene during bark beetle infestation where only 0.5 fold increase of a-pinene when atmospheric CO_2 is increased) (Gijzen, et al. 1993).

Previous researchers have demonstrated that many organic chemicals found in the foliage and branches of trees and shrubs are active in the NIR portion of this spectral range (Elvidge, 1990, Bammel and Birnie, 1994, Kokaly and Clark, 1999). The spectral activity in this region is associated with a series of combination and overtone bands derived from organic compounds with fundamental vibrations around 3000 to 5000 nm (the mid infrared or MIR). The IR absorption features typically found in this region area associated with vibrational modes of C-H, O-H and C-O bonds in the molecules (Weyer, 1985 and Workman, 1996). It should be noted that each of the monoterpenes have slightly different absorption features in the MIR (Weyer, 1985 and Workman, 1996) and by inference, in the NIR.

Elvidge (1990) analyzed various plants and associated biochemical materials by VNIR reflectance spectroscopy to identify the primary absorption features. Of particular interest to this study was the series of spectra recorded from the bark, needles and cones of pinion pine at three levels of dehydration (Elvidge, 1990). A sample of oleoresin (sap) was also analyzed as part of the pinion pine analytical suite evaluated by Elvidge (1990). Elvidge (1990) identified a series of absorption features from the pinion sap. These features occurred at 860, 910, 990, 1140, 1190, 1450, 1670 and 1930 nm, the majority of which correspond to C-H bond types that are prevalent in monoterpenes.

Hyperspectral imaging systems collect EM energy in the range of 350 to 2500 nm (visible-near infrared or VNIR) with significantly narrower bandwidths than other remote sensing systems. In the case of the AVIRIS system, the spectral bandwidth is 10 nm resulting in the acquisition of high-resolution spectral signatures from 20 m^2 scene pixels (Green, et al. 1998). Another objective of this research is to apply prominent absorption features elucidated above to the AVIRIS imagery of Mammoth Mountain.

II. Field and Laboratory Methods

Twig and needle samples representing the last two to three growth seasons were collected from lodgepole (*Pinus contorta*) and white bark (*Pinus albicaulis*) pines throughout the HSL tree kill site in October 2000. Using a visual needle retention index, tree specimens were classified as healthy, one of three stages of declining health and dying/dead. The health classes were based on visual observations of needle retention and percent of dead branches throughout the crown. Though the five different classes are clearly separated in many of the samples, approximately 30% of the healthy/slight impact and moderate/heavy impact samples show significant overlap. This indicates that there are likely only three and a maximum of four classes that can be distinguished. Future sampling efforts will evaluate this observation.

Sample collection involved clipping twigs and needles from branches at the top of the lower third of the canopy to minimize shading differences. After clipping the samples, they were placed in Ziplock© freezer bag with a damp paper towel and stored on ice then transported back to a temporary field lab for spectral analysis. A sub-sample of the twigs and needles were also placed in 20 ml VOA vials with

Teflon©-lined caps, stored on ice and transported to the organic geochemistry laboratory at Dartmouth College for monoterpene analysis.

A temporary field laboratory was established using a table, light stands and tripod for analytical consistency. The samples were analyzed using an ASD© Field Spec VNIR spectrometer in a fixed position at a height of 0.75 meters above the table/light stand setup. The spectrometer collects EM energy at the fiber-optic detector in the spectral range of 350 to 2500 nm and spectral resolution of 10 nm (ASD). The spectrometer is controlled using an on-board PC notebook computer that collects, stores and allows initial data processing/reformatting. Replicate samples were collected in reflectance mode after calibrating the spectrometer to a white reference standard. Example VNIR reflectance spectra for each health class are provided in Figure 3.

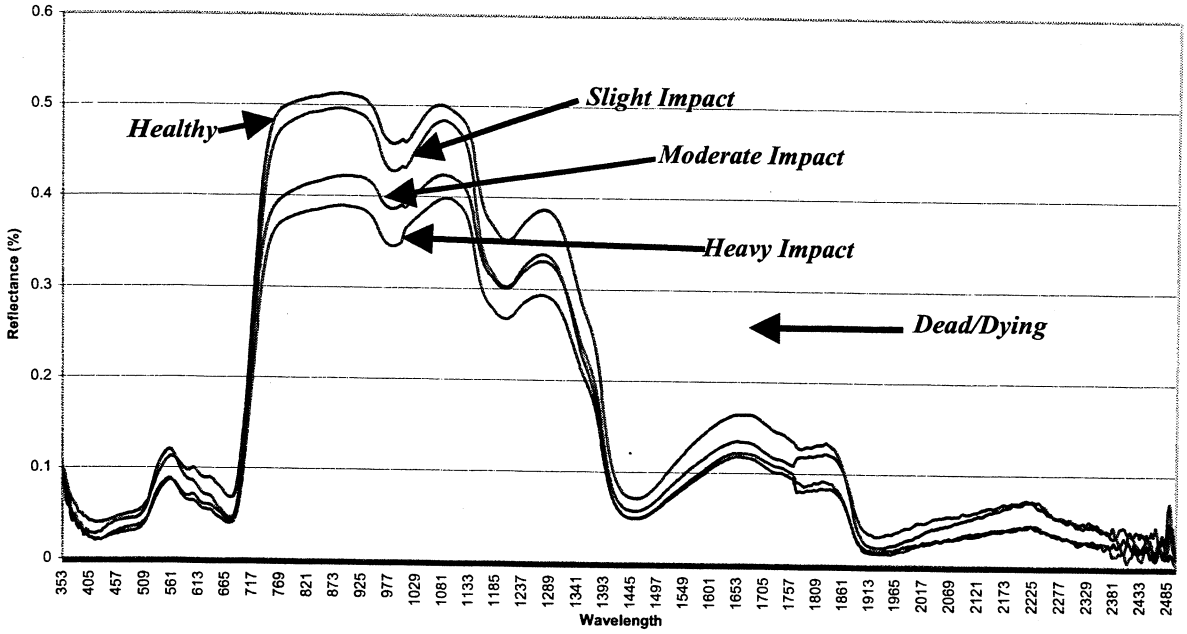

Figure 3. Reflectance spectra of lodgepole pine (*Pinus contorta*) from Horseshoe Lake tree kill area. Reflectance curves represent a series of samples showing declining health as determined by needle retention and percentage of dead branches across entire canopy.

Monoterpene compositions of the different specimens were measured by headspacing pine needles using Solid Phase Micro-extraction (SPME) field sampler manufactured by Supelco©. The SPME sampler consists of a retractable tippet comprised of 100 µms of PDMS absorbent coated on an inert substrate that was developed by Pawlisyn (1999). Preparation of the needles involved slicing the full needles into ~1cm lengths, transferring the particles into a pre-cleaned 40 ml VOA vial, adding 10 µls of a solution of 1,9 decadiene in $MeCl_2$ as an internal standard. After a one-minute exposure to the sample headspace, the SPME sampler was desorbed in the GC inlet directly onto the analytical column. The GC system included an HP© 6890 GC with a manual injector and SPME liner running isothermally at 250°C in a 100:1 split mode. The GC system also included a 50m HP-1 column operated with a programmed temperature mode of 40°C with an initial ramp of 4°C/minute to 220°C and a 2 minute hold time then 20°C/minute to a final temperature of 300°C and an FID running isothermally at 320°C. The data were acquired and preprocessed using HP© Chemstation© software. Identification of the compounds was performed using retention time database for the monoterpenes previously established in our lab. Monoterpene concentrations were calculated using the internal standard/compound peak areas, internal standard concentration and a single point calibration algorithm.

Each dataset was evaluated independently to facilitate feature selection and investigate any variance as a function of apparent plant health. An overview of the processing steps employed is shown in Figure 4. After the pertinent features were selected from each set, the covariance between the monoterpenes and spectral features was evaluated using ANOVA and regression techniques.

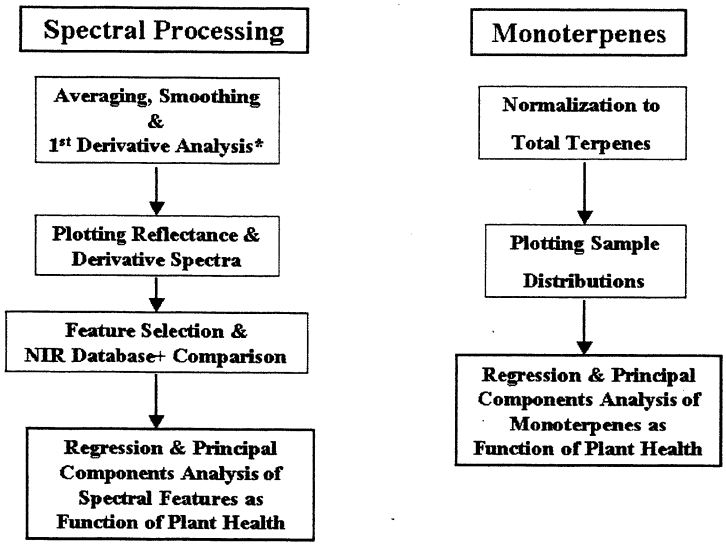

Figure 4. Flowcharts of processing steps used in evaluation of monoterpene (oleoresin) & spectral absorption features

III. Results and Discussion

The reflectance spectra depicted in Figure 3 shows there is an obvious decrease in NIR reflectance with decrease in tree health. Further data processing and interpretation was undertaken to identify prominent absorption features. Identification of absorption peak shifts involved interpretation of the 1st derivative transformation of the reflectance spectra (Tsai and Philpot, 1998). Examples of the 1st derivative curves are shown in Figure 5. Table 1 compares the key absorption peaks in our study with those of pinion oleoresin (Elvidge 1990). It is clear that, though the peaks do not coincide exactly, they fall in close proximity to each other. The differences are attributed to the variation in the plant biochemistry as a function of health.

Many of the characteristic absorption features found in the pure compounds are close to the features we identified. The oleoresin monoterpenes, however, are a mixture of eight or more compounds (Hirschfeld, T., & Hed, A. Z., (1981)). Any reflectance spectra derived from the oleoresin/monoterpenes, therefore, represent a combination of the individual constituent spectra. Since pines of different health levels have different monoterpene compositions, each mixture is expected to have different NIR signals and slight shifts in band position are expected. Additionally, the bond types associated with absorption features reported in Table 1 are derived from C-H bond variations prevalent in monoterpenes. It is important to note that other organics (e.g., sugars, waxes, etc.) also contain similar bonds. Further work is required to increase our understanding of the absorption feature source before a direct correlation between the absorption features and oleoresin/monoterpenes can be established.

TABLE 1: Pertinent Absorption Feature Comparison (nm)

ELVIDGE, 1990	-	860	910	990	1140	1190	-	1450	1670	-	1920
CURRENT	670	880	-	980	1075	1200	1270	1450	1650	1820	1920

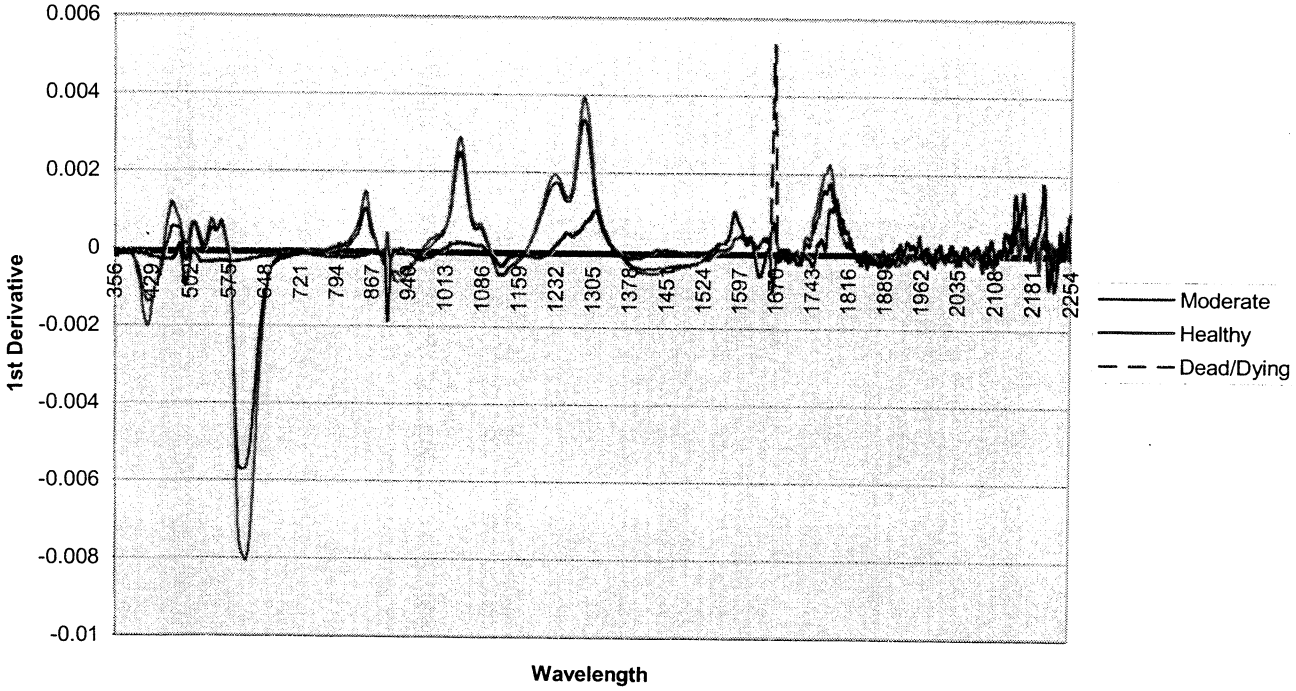

Figure 5. 1st derivative spectra from Horseshoe Lake lodgepole pine sample. Examples are the same samples used to create Figure 3 (reflectance spectra).

A combination of bivariate plot analysis, ANOVA and regression techniques was employed to assess the ability of the features listed in Table 1 for separating healthy from dying/dead pines. The features at 670, 880, 980, 1450, 1650, 1820 and 1920 nm separated the samples into two clusters. The intermediate health class samples (distinct signs of impact and with < 65% intact branches) tended to cluster around the healthy samples relative to the absorption features above 1450 nm. A greater level of dispersion, especially of the samples approaching greater than 35% intact branches, was observed in the shorter wavelength features. The features at the longer wavelengths are likely related to water loss. It is clear that some of the features (980, 1200, 1450 nm) fall in close proximity water absorption bonds, but the others do not. As a plant's health declines, many biochemicals, such as the monoterpenes, go through both a compositional change and quantitative reduction, as the plant re-allocates its energy and carbon resources.

Evaluation of the monoterpene chemistry was conducted to identify general trends in the composition relative to tree health. First, a few similarities and differences are observed when comparing the relative quantities of monoterpenes from the lodgepole and white bark pines. Where beta-pinene (50 to 75%), alpha-pinene (9 to 15%) and limonene (8 to 28%) are the most prominent terpenes in lodgepole pine, 3-carene (40 to 70%), alpha-pinene (12 to 25%) and myrcene (5 to 20%) dominate the composition of white bark pine. A graphical depiction of the composition for the lodgepole pine end-members is provided in Figure 6. Examples of monoterpene chemistry alteration related to possible biotic influences were also observed. In the case of lodgepole pine, the relative concentrations of alpha and beta pinene decreased where 3-carene and terpinolene increased in samples indicating biotic impacts. Nearly the opposite occurred in white bark pine. Alpha pinene and myrcene were all found to increase while phellandrene, terpinene and terpinolene decreased in relative concentration. Similar but subtler results were observed in the absolute monoterpene concentration data. The influence of both biotic and abiotic impact leads to a

higher level of complexity in the intermediate health classes. Identification and separation of the abiotic and biotic influences is, therefore important. Data processing and interpretation is continuing in this regard.

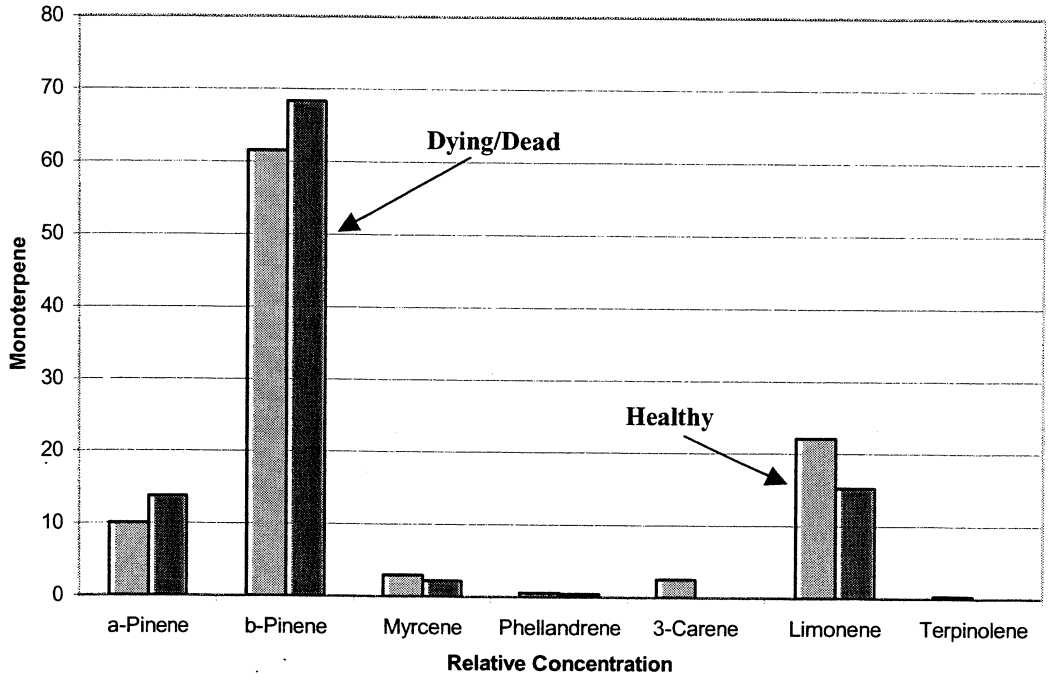

Figure 6. Example relative concentration change for the healthy (medium gray) and dying/dead (dark gray) lodgepole pine samples.

After evaluating each of the variables independently, we investigated the variables pair-wise to identify any significant co-varying sets that separate the end-member classes. Bivariate scattergrams for the reflectance value of each prominent absorption feature versus the relative concentration of each of monoterpenes were prepared. Table 2 summarizes all of the pairs that both discriminate the healthy from dying/dead clusters and indicate the presence of a statistically significant linear regression fit. A graphical example of the regression analyses depicting a positive correlation is provided in Figure 7. Superposition of the remaining "intermediate health" samples onto the regression models indicates there are multiple influences that lead to a high degree of variance in the data. An example of this is the biotic versus abiotic influences on monoterpene response. Attempts to mathematically resolve these complexities using techniques such as principal components and discriminant analyses are ongoing.

Table 2: Results of Covariance Analysis for Monoterpene-Absorption Feature Pairs of Lodgepole Pine End-members

SPECTRAL BAND	MONOTERPENE	R	R^2	F RATIO	PROB>F
670 nm	Alpha-pinene	0.67	0.45	9.1	0.012
880 nm	Alpha-pinene	0.75	0.57	14.5	0.003
1450 nm	Alpha-pinene	0.82	0.67	22.7	0.001
1820 nm	Alpha-pinene	0.83	0.70	25.1	0.0004
1920nm	Alpha-pinene	0.85	0.72	27.9	0.0003
1650 nm	Beta-pinene	0.81	0.66	23.3	0.0004
880 nm	Limonene	0.78	0.62	17.7	0.002
980 nm	Limonene	0.71	0.5	11.0	0.007
1075 nm	Limonene	0.66	0.44	8.5	0.013
1650 nm	Limonene	0.73	0.53	13.4	0.003

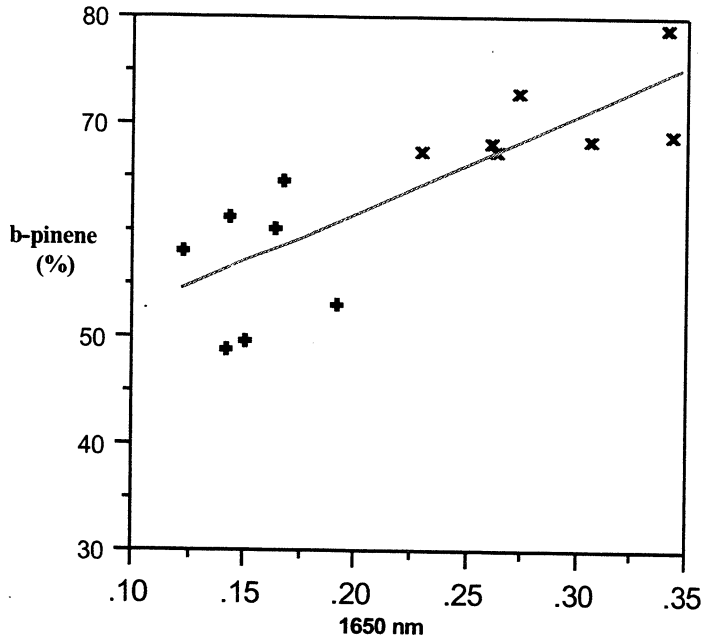

Figure 7. Regression results where the intensity of the absorption band at 1650 nm is plotted vs. the relative concentration of beta-pinene. The + markers correspond to the healthy samples and the x markers to the dying/dead samples of lodgepole pine.

Efforts to date have focused on elucidating the monoterpene-field spectroscopic relationship. Initial processing (atmospheric correction) of the AVIRIS 1999 Mammoth Mountain flight line data is currently underway. Once completed, use of the absorption features identified to assist in image interpretation will commence.

IV. Summary and Future Efforts

Sampling and analysis of lodgepole white bark pines to evaluate the relationship between oleoresin chemistry and spectral reflectance changes as a function of plant health were completed at the HSL tree kill area, Mammoth Mountain, California during the Fall of 2000. Both review of the literature and the analysis of our HSL dataset indicate that each variable undergoes a series of changes that relate not

only to the health state but also the nature of the impact (i.e., biotic vs. abiotic). Included are the identification of a series of absorption features and monoterpene composition that discriminate between the two end-member health states (healthy vs. dying/dead). Additionally, covariance and regression analysis between the absorption features and monoterpenes shows that a statistically significant model exists that also separates the healthy from dying/dead end-members of the conifers.

This paper is summarizes the preliminary results of an ongoing study. The first phase of field and analytical work lead to several exciting and promising results and additional rounds of field sampling and data analysis will occur throughout 2001. The products of this work will be used to enhance both our understanding of the underlying biogeochemical-spectral relationships and how it may be applied to processing and interpreting the hyperspectral imagery for the area.

V. Acknowledgements

We wish to extend our sincere appreciation to the Dartmouth College, Department of Earth Sciences and NASA NH Space Grant Consortium for their continuing financial support of this research, Dr. Bert Davis (USCOE-CRREL) for the use of their ASD Field Spectrometer, Dr. Barry Rock (UNH-Complex Systems) and Dr. David Pieri (NASA-JPL) for their insight of the field area, and lastly, Dr. Michael Sorey (USGS) and Larry Ford (USFS) for their help with obtaining access to the research area.

VI. References

Analytical Spectral Devices, Field Spectroradiometer Manual

Bammel, B. H. & Birnie, R. W. (1994), Spectral reflectance response of big sagebrush to hydrocarbon-induced stress in Bighorn Basin, Wyoming, Photo. Eng. & Remote Sen., 60 (1), 87-96

Datts, B. (1999), Remote sensing of water content in Eucalyptus leaves, Austral. J. of Bot., 47(6):909-923

DeJong, S. M. (1996), Surveying dead trees and CO_2-induced stressed trees using AVIRIS in the Long Valley Caldera, in Sum. of the Sixth Ann. JPL Airb. Earth Sci. Wkshp, JPL Pub. 96:67-74

Elvidge, C. D. (1990), Visible and near infrared reflectance characteristics of dry plant materials. Int. Jour. of Remote Sensing, 11:1775-1795

Farrar, C. D., et al. (1995), Forest-killing diffuse CO_2 emissions at Mammoth Mountain as a sign of magmatic unrest. Nature, 376:675-677

Gijzen, M., et al. (1993), Conifer Monoterpenes: Biochemistry and Bark Beetle Ecology in Bioactive Volatile Compounds from Plants, American Chemical Society, Washington, D.C., 309 p.

Green, R. O., et al. (1998), Imaging spectroscopy and the airborne visible infrared imaging spectrometer (AVIRIS), Remote Sens. Environ., 65:227-248

Hausback, B. P., et al. (1998), Monitoring of volcanogenic CO_2-induced tree kills with AVIRIS image data at Mammoth Mountain, California, in Sum. of the Seventh Ann. JPL Airb. Earth Sci. Wkshp, JPL Pub. 98

Hickey, J. C., Klusman, R. W., Voorhees, K. J. (1983), Fault leakage characterization by integrative gas geochemistry/mass spectrometry/pattern recognition procedures, AAPG Bulletin, 67 (8), p. 1342

Hickey, J. C. (1986), Colorado School of Mines – Unpublished Master's Thesis no. T-3080, 72 p.

Hirschfeld, T., and Hed, A. Z. (1981), The Atlas of Near Infrared Spectra. Sadtler Res. Labs: Phil. PA

Kokaly, R. F. and Clark, R. N. (1999), Spectroscopic determination of leaf biochemistry using bad-depth analysis of absorption features and stepwise multiple linear regression. Rem. Sens. Of Envir., 67:267-287

Litvak, M. E., and Monson, R. K. (1998), Patterns of induced and constitutive monoterpene production in conifer needles in response to herbivory, Oecologia, 114:531-540

Martini, B. A., et al. (2000), Geological and Geobotanical Studies of Long Valley Cladera, CA, USA, utilizing new 5mm hyperspectral imagery, *Proc. IEEE Int'l. Geosc./Remote Sensing Symp.* July 2000

Pawlisyn, J. (1997), Solid Phase Microextraction – Theory and Practice Wiley-VCH, NY, 246 p.

Rowan, et al. (2000), Mapping hydrothermally altered rocks by analyzing hyperspectral image (AVIRIS) data of forested areas in the southeastern United States, J. Geoch. Expl., 68(3):145-166

Sabins, F. F. (1999), Remote sensing for mineral exploration, Ore Geol. Rev., 14:157-183

Sorey, M. L., et al. (1998), Carbon dioxide and helium emissions from a reservoir of magmatic gas beneath Mammoth Mountain, California. Jour. of Geophys. Res., 103:15303-15323

Taiz, L. & Zeiger, C. (1998), Plant Physiology, Sinauer Assoc., Inc., Sunderland, MA, 792 p.

Tsai, F. and Philpot, W. (1998), Derivative analysis of hyperspectral data, Rem. Sens. Environ., 66:41-51

Vincent, R. K. (1997), Fundamentals of Geologic and Environmental Remote Sensing, Prentice Hall, Upper Saddle River, NJ 366 p.

Weyer, L.G., (1985), Near-Infrared Spectroscopy of Organic Substances, Appl. Spec. Rev. 21(1&2):1-43

Workman, J. J., (1996), Interpretative Spectroscopy for Near Infrared, Appl. Spec. Rev., 31(3):251-320

Zarco-Tejada, P. J., et al. (2000), Chlorophyll fluorescence effects on vegetation apparent reflectance: II. Laboratory and airborne canopy-level measurements with hyperspectral data, Remote Sens. Environ. 47:596-605

Adaptive HSI Data Processing for Near-Real-time Analysis and Spectral Recovery*

Su May Hsu,[1] Hsiao-hua Burke and Michael Griffin
MIT Lincoln Laboratory, Lexington, Massachusetts

1. INTRODUCTION

Hyperspectral imaging (HSI) sensors collect spatially resolved data in hundreds of spectral channels. While the technology matures and finds broad applications, data downlink from the collection platform and near real-time processing remain key challenges, especially for near-term spaceborne sensors. It is desirable to process the data on-board for near-real-time analysis and downlink compressed data allowing near full spectral recovery for post-mission analysis.

Principal component analysis (PCA) can be used to determine the reduced dimensionality and separate noise components in the data. While PCA is useful for image feature analysis such as smoke/cloud discrimination (Griffin et al., 2000), it can also be used as a data compression tool. With PCA, the majority of information in an HSI data cube is effectively compressed to a small number of principal components. The data volume is significantly reduced while the feature contrast is enhanced. Spectral information can be recovered from the compressed data with minimal loss. In this paper, the reconstructed data are compared to the original "truth" data with difference analysis using sample AVIRIS imagery.

This methodology also allows for the HSI data to be used adaptively for various multispectral band simulations without the constraint of data volume and processing burden. Based on AVIRIS data, emulation of MODIS sensor bands are carried out and compared with the PCA-reconstructed data. Two products are also derived and compared: Normalized Difference Vegetation Index (NDVI) and the integrated column water vapor (CWV) using the full set of AVIRIS data and the reconstructed spectral information.

2. PRINCIPAL COMPONENT ANALYSIS OF HSI DATA

Principal component analysis (PCA) is generally used to de-correlate data and maximize the information content in a reduced number of features [Richards, 1994; Geladi,1997]. It can be applied to HSI data to reduce the dimensionality, aid in anomaly detection and separate scene information from noise components. The covariance matrix is first estimated over the pixel spectra contained in the HSI data cube of interest. Eigenvalues and Eigenvectors are then obtained for the covariance matrix Σ as given below,

$$\Sigma = E\{(X - X_m)(X - X_m)^T\} = \Phi \Lambda \Phi^T,$$

where X represents the spectral vector data; X_m, the mean spectral vector over the data cube and **E**, the average operator over the entire data cube. Φ is a matrix consisting of columns of Eigenvectors and Λ is a diagonal matrix of Eigenvalues.

Using the Eigenvector matrix Φ, the HSI data cube is then transformed into principal components, also called Eigenimages. The components at an image location with a spectral vector X is obtained as below,

$$\mathbf{PC}(X) = \Phi^T X .$$

* This work was sponsored by the Department of Defense under Contract F19628-00-C-0002. Opinions, interpretations, conclusions and recommendations are those of the authors and not necessarily endorsed by the United States Air Force.
[1] Telephone (781) 981-2920; Fax (781) 981-7271; e-mail sumayhsu@ll.mit.edu, 244 Wood Street, Lexington, Massachusetts. 02420-9185

The components are ranked in descending order of the Eigenvalues (image variances). The Eigenimages associated with large Eigenvalues contain most of the image variations while the Eigenimages associated with small Eigenvalues are usually noise-dominated. The majority of variations in the scene are generally contained in the first few principal components although some anomalous image features may still be apparent in the 10^{th} or later Eigenimage. Thus principal component transform allows the determination of the inherent dimensionality and segregation of noise components in the HSI data. With the information compression property in the leading principal components, the full spectral image data can be recovered from truncated sets of the principal components. The information content that was lost is indicated by the sum of the Eigenvalues below the level of component truncation.

The PCA processing is demonstrated on an AVIRIS scene taken over Brazil during the Smoke, Clouds, Aerosols and Radiation - Brazil (SCAR-B) experiment in August of 1995. Figure 1 shows RGB and pseudo color images of the cumulus cloud scene from an AVIRIS image on 20 August 1995. Eigenvalues and sample Eigenvectors obtained from the data cube are plotted in Figures 2a and b, respectively. In Figure 2a, there are approximately four orders of magnitude separation between the 1^{st} and 10^{th} Eigenvalues, which indicate the relative information content of the related Eigenimages. The Eigenimages can be considered as a weighted sum of the spectral images. The component weights over the spectral bands are represented by the Eigenvectors. Sample Eigenimages are shown in Figure 3. Scene features are well contrasted in the images. Clouds, water and shadows are the most contrasted features shown in the first Eigenimage. In the second Eigenimage, vegetation features are enhanced. Detailed cloud structures are seen in the 3^{rd} Eigenimage. Burned areas are evident in the 4^{th} Eigenimage.

The most computation-intensive operation in PCA is projecting the spectral data into Eigenimages. It requires $2n$ FLOPs (floating point operations) per pixel per Eigenimage where n is the number of spectral bands. To obtain 10 Eigenimages from an AVIRIS-like image of 500x500-pixel, 200 spectral-band HSI, it takes approximately 10^9 FLOPs. This is the same order of computation required for pixel-level atmospheric compensation. The basic computation performed in ATREM (Gao et al, 1996) requires about 15 FLOPs per pixel per band. This amounts to 7.5×10^8 FLOPs to compensate the same spectral image.

In a multispectral image, the number of data points can be expressed as,

$$S L n,$$

where S, L and n are numbers of samples, lines and spectral bands, respectively in the image. The number of data points in the compressed image and the corresponding Eigenvectors are shown below,

$$(S L + n) p,$$

where p is the number of principal components used. The Eigenvectors are necessary for spectral data recovery. Notice that number of spectral bands, n is typically much less than the number of pixels in the image, $S L$. The compression ratio is,

$$S L n / (S L + n) p \sim n/p.$$

Considering there are approximately 200 spectral bands in the AVIRIS data, the compression ratio using 10 PCs is about 20 for a typical image frame of 500x500 pixels.

3. SPECTRAL COMPARISON

The spectral image data are recovered with inverse PCA using 5, 10, and 15 principal components. The recovered data are compared to the original data for performance evaluation. Different spectra from various features in the image are plotted in Figure 4. Good agreements are seen for all features between the reconstructed and original data, water being the exception. The reflected signal from a water surface is very low in the NIR/SWIR. Therefore, even small errors in the reconstruction of the spectral information are exaggerated for low reflecting surfaces. The reconstruction error is largest for 5 PCs and reduces considerably for 10 PCs and higher.

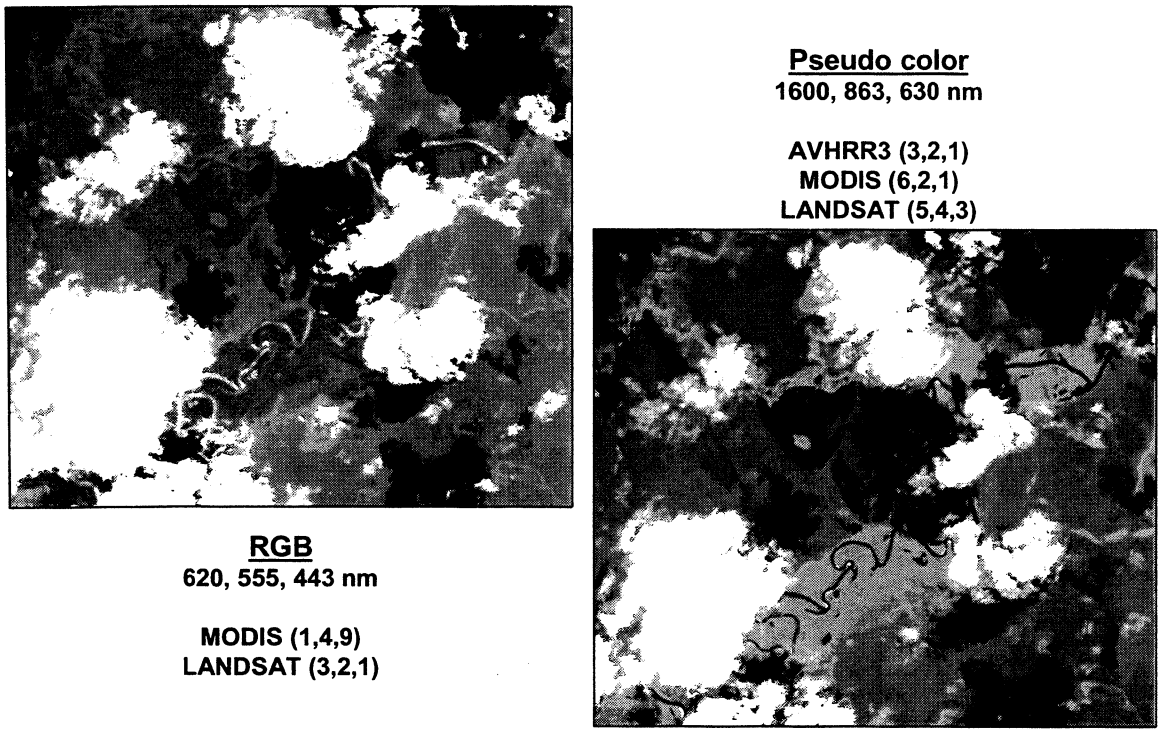

Figure 1. Color images of the AVIRIS SCAR-B data.

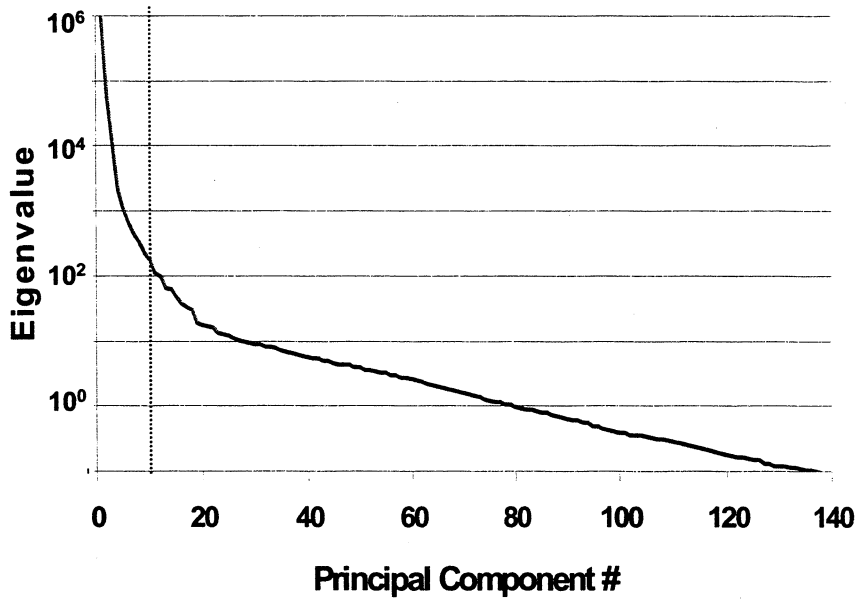

Figure 2(a). Eigenvalues of the SCAR-B HSI data.

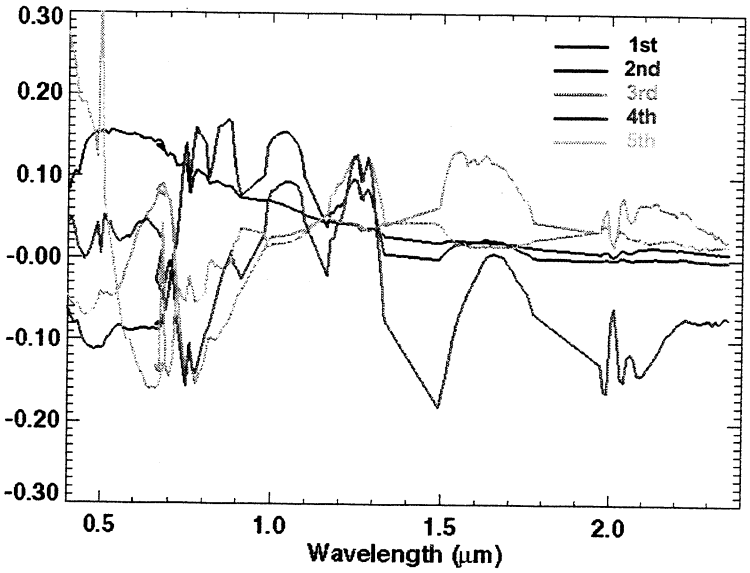

Figure 2(b). Eigenvectors of the SCAR-B HSI data.

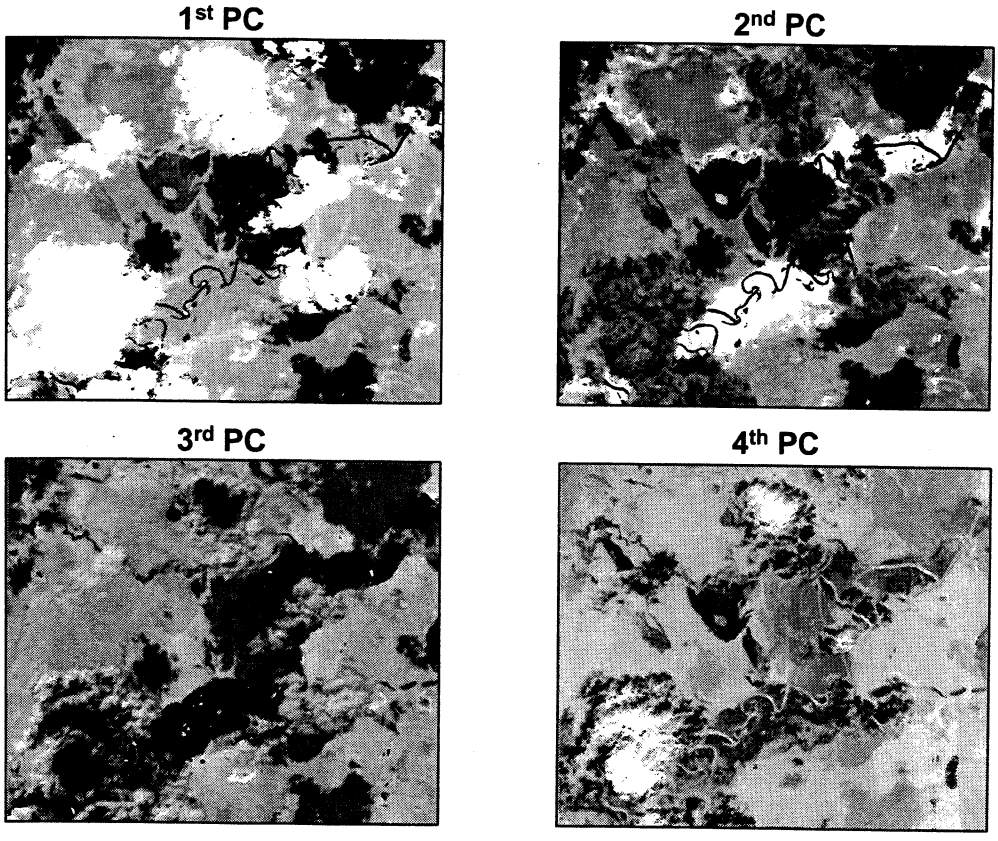

Figure 3. Sample principal components of SCAR-B HSI data.
Each component highlights various features in the scene,
1st PC: cloud, water, shadow; 2nd PC: vegetation;
3rd PC: cloud structure and 4th PC: burned area.

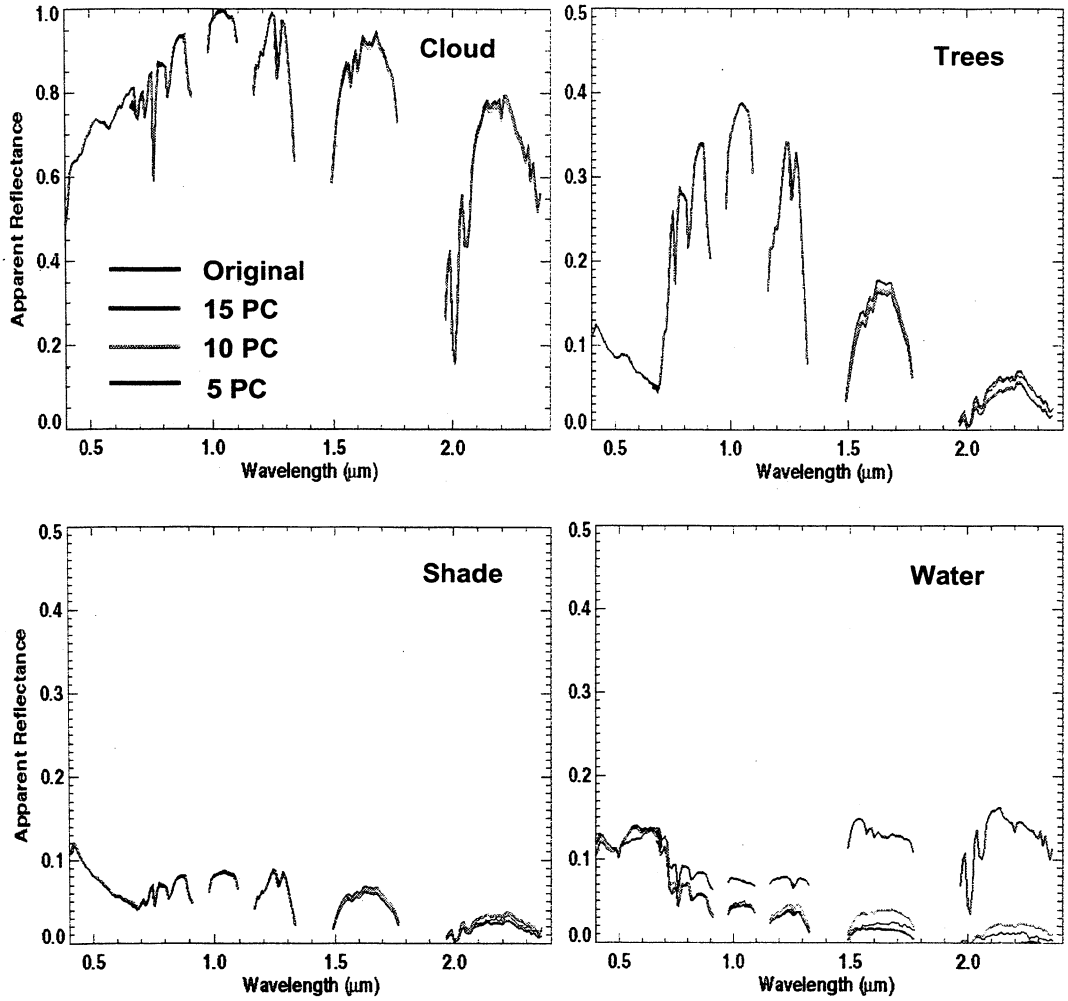

Figure 4. Comparison of reconstructed and original data for sample features in the SCAR-B scene.

Examples of reconstructed spectral images from 10 principal components are illustrated in Figure 5. The differences between the reconstructed and original images are also shown. The agreements are typically within a few percent. Quality of image reconstruction from overall spectral coverage can also be carried out. The original AVIRIS spectral data as well as the reconstructed data are band-integrated to simulate 16 MODIS spectral bands. Two measures, spectral angle and normalized spectral distance (Euclidean distance), are used to evaluate the reconstructed images. These are calculated from the formulas,

$$\text{Spectral Angle } (X,M) = \cos^{-1}(X \cdot M / |X|\,|M|),$$

$$\text{Normalized Spectral Distance } (X,M) = |X - M| / |M|,$$

where, M and X are the multispectral image spectra from the original and reconstructed AVIRIS data, respectively.

A zero angle and zero distance represent a perfect match of the two spectra. The images generated from the original AVIRIS data are considered the "truth" data here. The reconstructed images are compared to the truth data in terms of spectral angle and spectral distance. The spectral distance normalized by the pixel amplitude in the truth image is calculated for comparison. The frame-averaged differences are listed in Table 1. It shows that, as expected, the more principal components (PC) used, the closer is the reconstruction to the truth data. The 10-PC reconstruction appears to be a reasonable one in that it is much closer to the truth in spectral angle and distance compared to 5-PC, but only slightly worse than the 15-PC. As illustrated in the previous section, the 10-PC compression ratio in this case is about 20.

Table 1. Frame Average over the SCAR-B Scene.

p (No. of PCs)	15	10	5
(Variance Ratio)	(3.8e-5)	(1.4e-4)	(8.7e-4)
Compression Ratio	~ 13	~ 20	~ 40
Spectral Angle $\cos^{-1}(X \cdot M / \|X\|\,\|M\|)$			
Normalized Spectral Distance $\|X - M\| / \|M\|$			

M: Pixel spectrum in reference image

X: Pixel spectrum in reconstructed image

4. IMAGE PRODUCT COMPARISON

Accuracy of the reconstructed image can also be evaluated based on spectral products such as vegetation index and column water vapor (CWV). An AVIRIS scene over Moffett Field, CA was employed for the image product comparison. The color images of the AVIRIS data are depicted in Figure 6 and the comparison on derived NDVI is illustrated in Figure 7. Except for the lake region, the 20-PC derived NDVI agreed with the truth to within 0.01. The range of NDVI is ~0.8, the agreement is of the order of a few percent. The Eigenvalue ratio of the 20th and 1st components of this data set is 1.9×10^{-4} which is comparable to the ratio of 10th and 1st components of the Brazil cloud scene.

The CWV field was also computed for both sets of AVIRIS data as a by-product of the ATREM model application for the Moffett Field scene shown in Figure 6. The scene could be characterized as relatively dry (from nearby radiosonde observations) with approximately 1.27 cm of CWV. ATREM was applied to both the original AVIRIS image and the reconstructed image. The primary product of the model being the spectral surface-leaving

reflectance and a secondary product, the CWV, was used for this comparison. Figure 8 displays the retrieved CWV from the original AVIRIS data and from reconstructed data using 5, 10, 15, and 20 PCs. From the water vapor image and related RGB image, it is clear that topography plays a role in the distribution of water vapor across the scene. Water vapor is maximum over the urban area which is in close proximity to the San Francisco Bay, and decreases somewhat as the terrain elevation increases (upper part of the image). It is clear from the component difference images that accuracy of the water vapor retrieval (as compared with the original image) improves with increasing PC. Both of the product comparisons shown here suggest that to keep information loss errors below 1%, requires a minimum of 15 PCs to be saved.

5. SUMMARY

Future spaceborne HSI sensors will require onboard data volume reduction before transmission to surface receiving sites. Using principal component analysis (PCA) in a data compression mode, an end-to-end comparison was made on the accuracy of retrieving specific data products from compressed and reconstructed hyperspectral data. PCA was applied to HSI data to produce a set of component images. The original HSI data (at full spectral resolution) was reconstructed from selected sets of the component images. The reconstructed images were used in applications to derive the NDVI and CWV products as well as simulate multispectral channels on the MODIS sensor. Results of the product comparisons show that as few as 15 PCs could be used to obtain product values within 1% of those obtained using the full complement of HSI data.

Using adaptive channel processing, it was shown that multispectral channels could be simulated from reconstructed HSI data with minimal loss in image quality. The study does not deal with individual channel issues such as signal-to-noise which could be channel specific. In this case, the specifications of the HSI bands used in the simulation would determine the specific characteristics of the channel. The reconstruction of HSI data from a selected subset of PCs also has the effect of noise filtering, since much of the information lost due to the truncation of components was noise. On a similar note, the NDVI obtained from simulation of NOAA AVHRR channels using HSI could be improved by selectively excluding spectral bands which do not contribute to the vegetation signatures (i.e., water vapor absorption bands near 0.82 and 0.94 μm).

6. REFERENCES

Gao, B.C., K.B. Heiderbrecht, and A.F.H. Goetz, 1996, "Atmosphere Removal Program (ATREM) Version 2.0 Users Guide", *Center for the Study of Earth from Space/CIRES*, University of Colorado, Boulder, Colorado.

Geladi, P. and H. Grahn, 1997, Multivariate Image Analysis, John Wiley & Sons.

Griffin, M.K., S.M. Hsu, H.K. Burke and J.W. Snow, 2000, "Characterization and Delineation of Plumes, Clouds and Fires in an AVIRIS Image," *Proc. of the 2000 JPL Airborne Earth Science Workshop*, JPL, Pasadena, California.

Richards, J., 1994, Remote Sensing Digital Image Analysis, Springer-Verlag, p. 133.

ACKNOWLEDGEMENTS

The authors wish to thank CAPT Frank Garcia at DUSD (S&T), program manager for the Hyperspectral Technology Assessment Program (HTAP), and Dr. Edward Howard at NOAA, task manger for the GOES Program at Lincoln Laboratory, for their support and leadership.

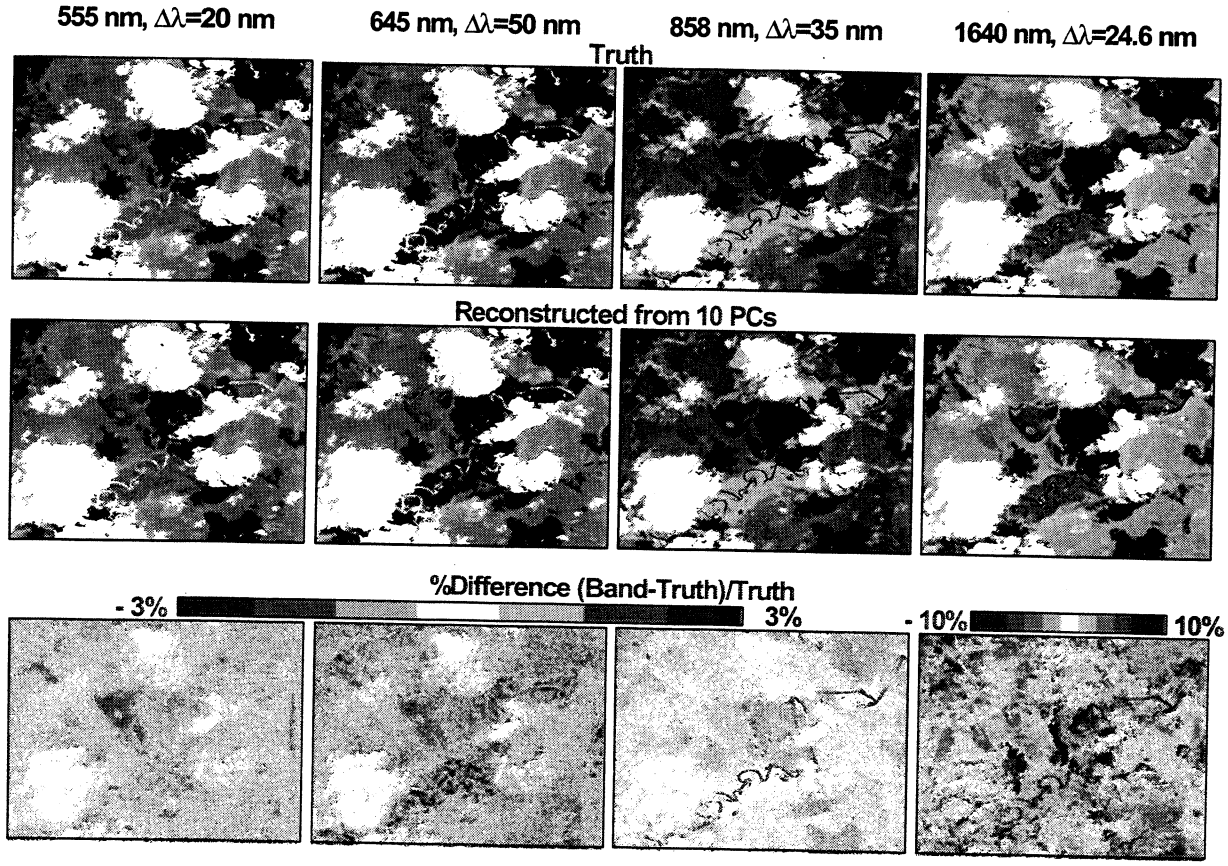

Figure 5. Comparison of reconstructed and original spectral data for simulated MODIS bands.

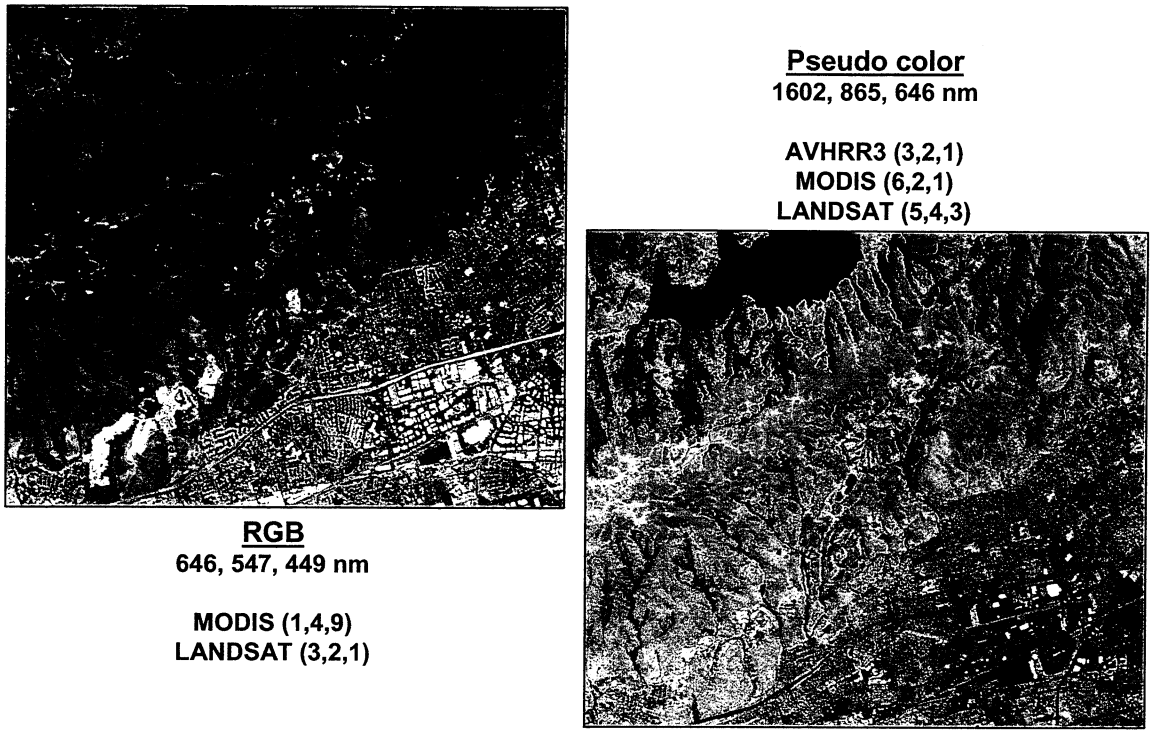

Figure 6. Color images of AVIRIS HSI data over Moffett Field.

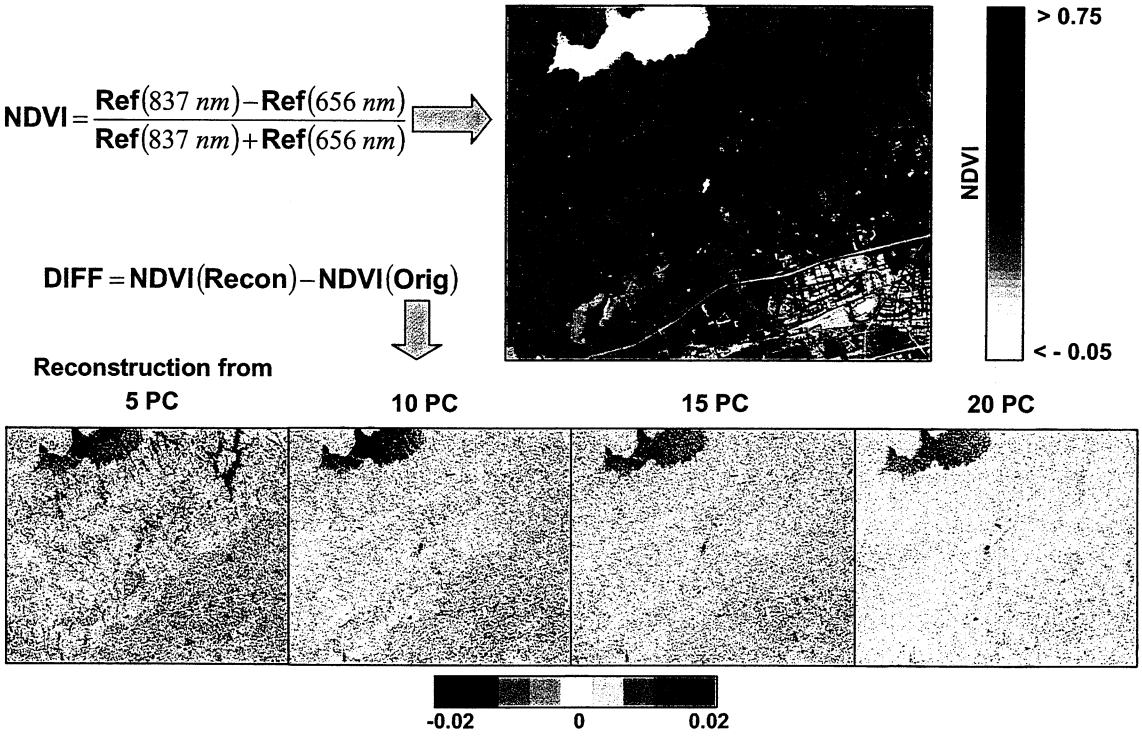

Figure 7. Comparison of NDVI derived from reconstructed and truth data over the Moffett Field scene.

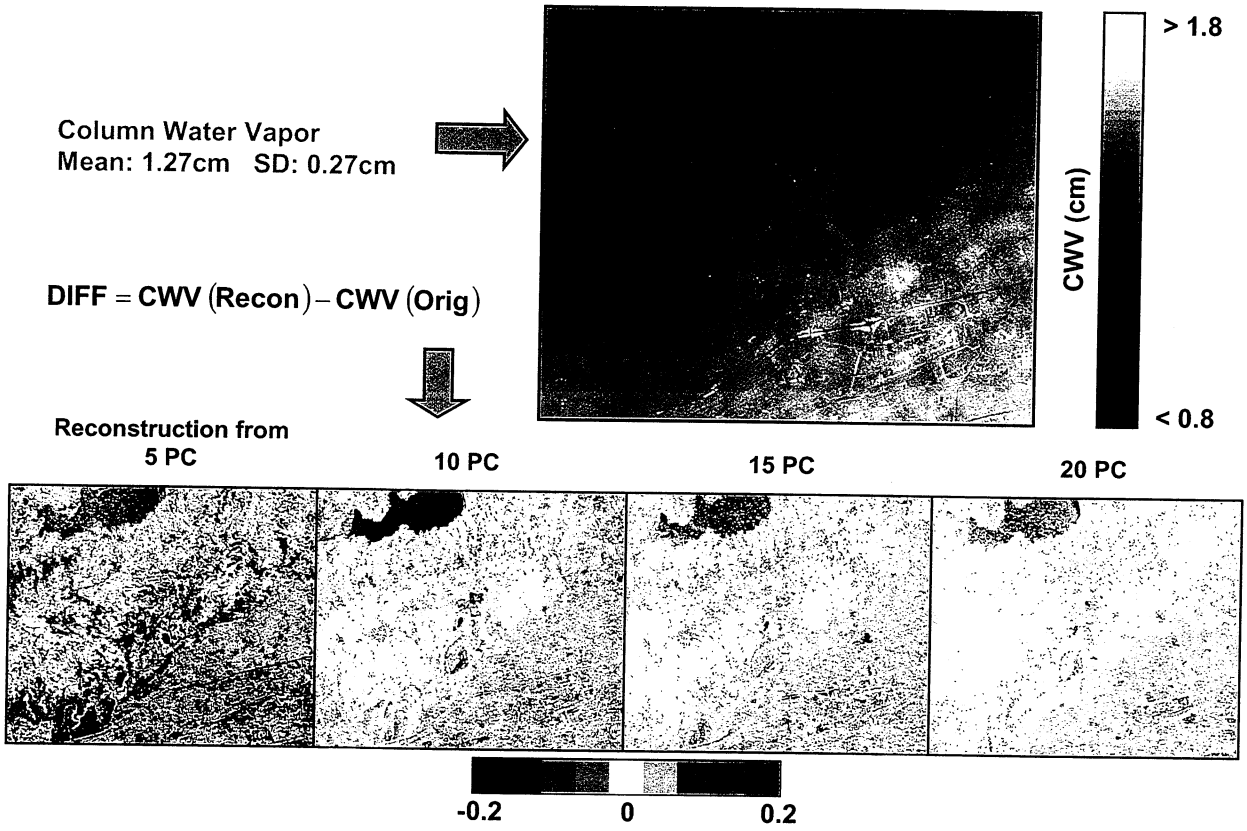

Figure 8. Comparison of CWV derived from reconstructed and truth data over the Moffett Field scene.

The Effects of Temporal Sampling and Changing Spatial Scales on the Mapping of Forest Cover in Yellowstone National Park Using Imaging Spectroscopy

Raymond F. Kokaly,* Roger N. Clark,* Don G. Despain,** and K. Eric Livo*

* U.S. Geological Survey, MS 973, Box 25046, Federal Center, Denver, Colorado 80225
** U.S. Geological Survey-Biologic Resources Division, Bozeman, Montana

1. INTRODUCTION

The U.S. Geological Survey (USGS), in cooperation with the National Park Service, is using imaging spectroscopy to advance the understanding of the geologic features and biologic systems in Yellowstone National Park. Kokaly et al. (1998 and 2001) presented the methods and results of applying imaging spectroscopy to the study of the biotic components of Yellowstone National Park. Knowledge of the distribution of vegetation such as whitebark pine is desired for understanding the habitat and movements of grizzly bears, bison and other large mammals. This paper addresses several questions regarding the mapping of forest cover in Yellowstone National Park (Yellowstone) using imaging spectroscopy, including:

1) How do the spectral signatures of conifer forest stands differ when changing the spatial scale and temporal sampling of Airborne Visible and Infrared Imaging Spectrometer (AVIRIS) data?
2) Can conifer forest cover types be robustly identified in high spatial resolution AVIRIS data using the USGS Tetracorder system and a vegetation spectral library derived from a lower spatial resolution data set?
3) How do maps of forest cover derived from low and high spatial resolution AVIRIS data compare?

2. BACKGROUND

2.1 Yellowstone Forest Cover

Most of Yellowstone is covered by forests which can be divided into four major conifer cover types: lodgepole pine (*Pinus contorta*), whitebark pine (*Pinus albicaulis*), Douglas-fir (*Pseudotsuga menziesii*), and mixed Engelmann Spruce/Subalpine Fir (*Picea engelmannii/Abies lasiocarpa*). As a result of fire history and soil conditions, the current dominant forest cover in Yellowstone is lodgepole pine. The temperate forests at high elevations in the park receive much moisture during the long, cold winter. According to Despain (1990), the mean duration of snow cover is about 271 days at 9,000 feet elevation. At lower elevations, in Yellowstone's relatively drier valleys, dry grasslands and sagebrush steppe communities dominate. The geology underlying the vegetation in Yellowstone has an influence on the distribution of plants within the park (Despain, 1990). In areas with andesitic rocks, the higher nutrient content supports climax forests of mixed Engelmann spruce/subalpine fir. Douglas-fir occurs in moisture rich areas of

the park such as north-facing slopes. Soils derived from rhyolite flows within the park have relatively low nutrient content; in these areas, the dominant forest type is lodgepole pine

2.2 Imaging Spectroscopy of Forests and Remote Sensing of Yellowstone

Airborne imaging spectroscopy has been shown to have the ability to discriminate different vegetation types from one another. Clark et al. (1995a) used AVIRIS data to accurately map the distributions of various agricultural crops in the San Luis Valley of Colorado. Natural forest types in an area of deciduous, mixed deciduous/conifer, and conifer cover have also been differentiated (Martin et al., 1998). Imaging spectroscopy has also been studied for the possibility of determining canopy nitrogen concentrations (Wessman et al., 1989; Martin and Aber, 1997; Kokaly and Clark, 1999). Ustin et al. (1999) reviewed the role of remote sensing in linking biologic observations to geologic studies in their discussion of geobotanical studies. Roberts et al. (1998) used airborne spectrometer data combined with spectral mixture modeling to map the distribution of different chaparral vegetation types in the Santa Monica Mountains.

In Yellowstone National Park (Yellowstone), Despain (1990) used aerial photography to make vegetation maps. These maps include the distribution of the four major forest types and various age classes of lodgepole pine. Jakubauskas (1996) used Landsat TM data in an attempt to map the distribution of forest cover types in Yellowstone. Kokaly et al. (1998 and 2001) used AVIRIS data over several areas of Yellowstone to map the distribution of forest cover types, nonforest cover types, and surface microbial mats. This study used the USGS Tetracorder system applied to AVIRIS data obtained on the high altitude platform (an ER-2 aircraft collecting data at approximately 17 meter pixel size). In particular, this study was effective at identifying the occurrence of whitebark pine using a comparison of the shapes of vegetation chlorophyll and water absorption features (Kokaly et al., 2001).

3. METHODS

3.1 AVIRIS Data Collection and Calibration

The AVIRIS instrument was flown over Yellowstone in 1996 and 1998. The 1996 AVIRIS data, hereafter referred to as the high altitude data, was acquired using the NASA ER-2 aircraft at 65,000 ft altitude. The 1998 AVIRIS data, hereafter referred to as the low altitude data, was acquired using a Twin Otter aircraft flying at approximately 12,000 ft altitude. For this paper, an area of lodgepole forest near Old Faithful Geyser was selected to compare reflectance spectra and mapping results between these two data sets. Table 1 summarizes the data collection parameters for this study site. In particular, note the low solar elevation for the low altitude data (34°).

In order to convert AVIRIS data from radiance to reflectance, the data had to be corrected for the influence of several variables, including solar irradiance, atmospheric gas absorptions, and path radiance. A two-step procedure for this conversion, as described by Clark et al. (1993a, 1995b, and 2001a), was employed, which includes: 1) primary atmospheric correction using the ATREM algorithm (Gao et al., 1993 and 1997), and 2) correction of residual features using ground calibration.

For both AVIRIS data acquisitions, a ground calibration site was selected by field survey as having the properties of being fairly large, homogenous, and not containing material with strong absorption features. A gravel staging area, located near Norris Geyser Basin, was utilized for

calibration of high altitude data. On the day of the AVIRIS flight, reflectance measurements of this site were made with a field spectrometer having the same spectral coverage as the AVIRIS instrument. Spectra of the calibration site, extracted from the ATREM-corrected AVIRIS data, were used with the field measurements to generate a multiplicative correction. An additive path radiance correction was derived using an area of vegetation in shadow. Following the initial correction using ATREM, these additive and multiplicative corrections were applied to each pixel of AVIRIS data to derive surface reflectance. For more specific information on the calibration of the high altitude data see Kokaly et al. (2001).

The low altitude data were calibrated using field reflectance spectra of the large parking lot near Old Faithful Geyser. The procedure for reflectance calibration of the data was similar to that of the high altitude data, including the use of the darkest, shaded vegetation pixels for path radiance correction. The low altitude data were sampled at 1.5 meters in the cross-track direction and 4.3 meters in the along track direction. The data were corrected for aircraft motions and resampled using nearest-neighbor methods to give a rectified image (Boardman, 1999).

3.2 Spectral Feature Analysis

In order to compare the shapes of the absorption features between samples, this study used a method of normalization called continuum removal. Continuum removal, or baseline normalization, is a method commonly used in laboratory infrared spectroscopy (Ingle, 1988). Clark and Roush (1984) discussed the application of this method to remotely-sensed reflectance spectra. Clark et al. (1990) first applied this method to terrestrial imaging spectrometer data to map the distribution of minerals and vegetation by comparing remotely sensed absorption band shapes to those in a reference spectral library. Continuum removal is a numerical method to estimate the absorptions not due to the band of interest and remove their effects and to eliminate reflectance level changes due to view and illumination geometry variations (Clark and Roush, 1984; Clark, 1999).

Figure 1 shows the continuum removed chlorophyll absorption feature of the Yellowstone forest cover types. The depth of the chlorophyll absorption feature is affected by the concentration of chlorophyll in the forest canopy, the percent cover of the forest canopy, the understory vegetation, and soil background. In addition, multiple scattering effects can also affect the apparent strength of the chlorophyll absorption feature. In Figure 1, the pines show weaker absorption strengths with lodgepole pine (LP) having the weakest chlorophyll absorption. Douglas-fir (DF) has the strongest absorption feature. Continuum removed absorption features of plants have been compared by scaling them to the same depth at the band center, thus, allowing a comparison of the shapes of absorption features (see Kokaly and Clark, 1999).

3.3 USGS Tetracorder Expert System

In this study, the USGS Tetracorder system was applied to AVIRIS data over Yellowstone to differentiate between vegetation cover types. The USGS Tetracorder system has been used to identify and map distributions of minerals and vegetation in AVIRIS data (Clark et al., 1990, 1991, 1993b, 1995c, and 2001b). Tetracorder is an expert system that can compare the characteristic absorption features of materials assembled in a spectral library to the absorption features present in the spectrum of each pixel of AVIRIS data. Tetracorder uses continuum removal to isolate specific absorptions and remove the effects of changing slopes and overall reflectance levels (Clark and Roush, 1984). Tetracorder compares the wavelength position and

shape of absorption features in the reference spectra of entries in the library with those in the AVIRIS data. A modified least-squares fitting algorithm is used to assess the closeness of the match (Clark et al., 1990). The Tetracorder expert system makes further refinements to select the closest match using threshold values, continuum slope constraints and other methods (Clark et al., 2001b).

The development of a spectral library of vegetation reflectance was an integral part of vegetation cover mapping in Yellowstone National Park (see Kokaly et al., 2001). The major cover types in Yellowstone NP were identified during a field survey. These cover types included all significant forest cover types, including lodgepole pine (LP), whitebark pine (WB), Douglas-fir (DF), and a mixed Engelmann spruce/subalpine fir category (SF). To define spectral signatures of these vegetation types, pixels in the AVIRIS data covering these vegetation types were averaged together to generate representative spectra. Nearly 40 such training sites were identified in the AVIRIS data. To illustrate the comparison of spectral features by Tetracorder, the reflectance spectrum of a single pixel of AVIRIS data was compared to the entries of this spectral library. Figure 2 shows how the continuum removed chlorophyll absorption features compare between the pixel and the closest match identified by the USGS Tetracorder system (lodgepole pine).

4. SPECTRAL COMPARISONS

4.1 Observations in Low Altitude AVIRIS Reflectance Data

The low altitude AVIRIS data with its small pixel size and lower sun angle showed variations in reflectance level based on local slope of the surface. For example, Figure 3 shows the change in reflectance level between the two pitched sides of the roof of a visitor's lodge in the Old Faithful area. The reflectance level at 1.7 μm for the south facing side is over 4.5 times higher than the dark north-facing slope of the roof. Thus, algorithms applied to this data set must be insensitive to these reflectance level variations. The continuum removal process used in the USGS Tetracorder system is an example of one type of normalization procedure that compensates for reflectance level. Algorithms such as linear unmixing will be sensitive to this change and increase the fraction of the compensatory "shade" endmember. Thus, linear unmixing of the sunlit vs. shaded side of the roof will yield different coverage fractions. As a result, this simple situation shows that the fraction values yielded by linear unmixing do not represent physical fractions of areal coverage.

This simple observation of reflectance level changes based on local slope of a surface led to an investigation of the more complex situation encountered in a forest stand. The low altitude data had a pixel size of 1.5 meters. In a forest, this allows resolution of a variety of surfaces, including: sunlit and shaded tree crowns and sunlit and shaded understory vegetation. The reflectance spectrum of a single pixel of the low altitude AVIRIS data results from one or more of these components. A simple example of these effects was examined in the parking lot of Old Faithful. The reflectance spectra of lodgepole trees in the parking lot, shaded trees, shaded asphalt and sunlit asphalt are shown in Figure 4. The reflectance variations show a complication in the shaded pixels. The reflectance of shaded parking lot pixels shows an artificial increase toward the short wavelengths. It is suggested that this effect is primarily due to an inaccurate calculation of true reflectance by an insufficient estimation of the diffuse sky irradiance of the surface. ATREM assumes a standard ratio of diffuse:direct irradiance for every pixel. Mustard

et al. (1999) observed ATREM's inability to give reflectance curves over the ocean surface. Mustard et al. (1999) used cloud shadows to estimate atmospheric path radiance correction and used the assumption of a constant multiplicative factor to compensate for diffuse sky irradiance. Gao et al. (1993) noted several limitations and possible error sources for ATREM, including: hazy conditions, assumption of a mean elevation and orientation for the entire scene, assumption of nadir view angle only, and atmospheric and topographic adjacency effects.

A more complicated method of estimating the diffuse:direct irradiance on a pixel by pixel basis is required to derive true surface reflectance for each pixel. The assumption of a constant sky irradiance correction factor used by Mustard et al. (1999) for correcting AVIRIS data over water is not applicable in this situation because terrestrial surfaces have variable slopes and land surface elements cast shadows. The use of a Digital Elevation Model (DEM) will allow the correction for topographic variation. However, local slope changes such as the roof slope in Figure 3, the shaded parking lot in Figure 4, or the orientation and illumination of tree crowns is a much more difficult problem to correct. Thus, if such corrections are not feasible, analysis algorithms must be able to deal with these complicated effects on reflectance spectra due to changing illumination conditions.

4.2 Reflectance from a Lodgepole Pine Stand in Low Altitude AVIRIS Data

The situation of shading caused by trees in the simple example in the Old Faithful parking lot becomes much more complicated in the midst of a stand of conifer trees. Figure 5 shows the variation in spectra of low altitude data for a stand of lodgepole pine located just north of the Old Faithful Geyser. The range in reflectance level and the spectral shapes are quite high. This pixel-to-pixel variation is attributed to the measurement of sunlit and shaded tree crowns and understory vegetation, as well as multiple scattering effects. In addition, shaded pixels show an increase in reflectance toward the short wavelengths similar to that observed for shaded pixels in the Old Faithful parking lot. Thus, the shaded forest pixels have not been converted to true reflectance. Therefore, care must be taken in interpreting the spectra from these pixels.

In order to assess the change in spectra from high spatial resolution (1.5 m) to low spatial resolution (~17.5 m), 12x12 pixel areas of the low altitude data were averaged to approximate the pixel size of the high altitude data. The resulting variations in reflectance between averaged areas (Figure 6) are less than the variations for single pixels (Figure 5). Note that the averaged pixels still contain the influence of shaded pixels that have not been corrected to true reflectance.

4.3 Comparisons of Lodgepole Reflectance between High and Low Altitude AVIRIS Data

To assess the changes in reflectance for conifer forests between high and low altitude AVIRIS data, the pixels covering an area of lodgepole pine forest north of Old Faithful were averaged for the high altitude and low altitude data sets. Figure 7a shows the comparison of low altitude and high altitude average reflectance spectra. The curves show similar spectral shape but an offset in overall reflectance level. There are several influences that may cause this change in the level, including: differences in illumination and viewing geometry and changes in overstory and understory vegetation state. The geometrical considerations act to lower the reflectance of the low altitude data as observed. The lower sun angle of the low altitude data contributes to a higher degree of shading which lowers the overall reflectance level of the forest stand. Changes in understory vegetation are another factor; a comparison of the reflectance from adjacent meadows shows that the grasses have senesced more in the October low altitude data set compared to the August high altitude data set. The influence of the change in understory would

be to increase the reflectance level due to decreased absorption by chlorophyll and water in the nonforest vegetation. However, as Figure 7a shows, the changing illumination has a stronger influence than the background vegetation in the lodgepole pine stand and the October data has a lower reflectance level than the August data.

A comparison of the chlorophyll absorption feature at 0.68 μm after continuum removal and normalization to the band depth showed a high level of comparison (Figure 8b). Using the modified least-squares approach of Clark et al. (1990), the correlation fit number (which ranges from 0, no correlation, to 1, an exact correlation) between the two spectra was 0.999. Thus, despite the changing reflectance level due to differing sun-surface-sensor geometry between the measurements and the change in vegetation state from the August 1996 to the October 1998 data collections, the average spectra of the lodgepole pine stand were remarkably similar in shape. In particular, continuum removal and normalization to the band center showed that the chlorophyll feature has changed very little between measurements (Figure 7b). There is a slight blue-shift of the red-edge in the high altitude spectrum as compared to the low altitude spectrum. The effects of changing illumination conditions and vegetation state influence the position of the red edge.

5. MAPPING RESULTS

In order to test the forest cover mapping method developed for the high altitude 1996 AVIRIS data by Kokaly et al. (2001), the same procedure used in that study was applied to the low altitude 1998 AVIRIS data for a scene covering the Old Faithful geyser area. Specifically, the USGS Tetracorder system was used to compare the reflectance spectrum of each pixel of the low altitude AVIRIS scene to the entries in the spectral library of vegetation cover types. This library of vegetation cover types was derived from the high altitude data set by extracting and averaging pixels over known vegetation cover types. Kokaly et al. (2001) used the USGS Tetracorder system applied to the 0.68 μm chlorophyll feature and the 0.98 μm and 1.20 μm water absorption features observed in vegetation canopy reflectance.

The results of the high altitude study for the Old Faithful area are presented in Figure 8. The vegetation in this area was identified as dominantly lodgepole pine. However, scattered pixels of the other conifers are found in a noisy pattern throughout the scene. While the majority of pixels in the high altitude data mapped as lodgepole pine, some mapped as whitebark pine. Fewer numbers of pixels are mapped as Douglas-fir. Finally the least number of pixels in the high altitude data are mapped as Engelmann spruce/Subalpine fir.

The results of the low altitude mapping of forest cover types are shown in Figure 9. Again, the dominant cover type mapped is lodgepole pine. The pixels that map as forest cover are mainly the brightly-lit tree crowns of the forest stand. Note that the shadow pixels in the lodgepole forest stand in Figure 9 are not identified as any of the forest cover types. The reasons for this are suggested as follows: 1) the shadow pixels are mainly shaded nonforest vegetation, 2) the reflectance levels of the shaded pixels are very low, and 3) the atmospheric correction procedure is inaccurate for the shaded pixels which have a high degree of diffuse illumination relative to direct solar illumination and, therefore, spectra of these pixels do not represent the true reflectance of the surface.

Figure 10 shows a subset of the high altitude forest cover map for comparison to the low altitude cover map in Figure 9. There is generally good agreement in mapping most of the area as lodgepole pine cover. The low altitude data with its smaller pixel size shows a slightly

different distribution of lodgepole. In particular, the low altitude data resolve individual trees within the lodgepole stand and show the gaps between trees. The low altitude data also show the occurrence of just a few trees in some areas (e.g., the parking lot of the Old Faithful area). In comparison, the high altitude data show the forest stands as being near contiguous pixels of conifer cover. In this study, the ability of the high altitude data to estimate the variability in density of trees was not explored. Also, small stands or single trees mapped in the low altitude data were not detected in the high altitude data (e.g., note the developed areas south of Old Faithful geyser). The fact that the tree crowns of lodgepole pine are mapped in the low altitude data using average reflectance signatures from the high altitude data suggests that the conifer reflectance at the 17.5 meter scale is dominated by the reflectance from the individual trees.

6. CONCLUSIONS

This study of the differences in mapping forest cover with high altitude August 1996 AVIRIS data and low altitude October 1998 AVIRIS data was conducted to understand reflectance changes between spectral data with different seasonal sampling and spatial resolution. Furthermore, the forest cover mapping method of Kokaly et al. (2001) was tested for robust application between the data sets. The results of the study showed that the low altitude data set, with its low sun angle and small pixel size, showed greater variation in reflectance level due to local slope and the orientation of surfaces such as tree crowns. In addition, for pixels in shadow true reflectance was not calculated by the atmospheric correction procedure because the correct proportion of diffuse:direct illumination was not specified on a pixel by pixel basis. The observed error in surface reflectance retrievals due to diffuse:direct irradiance is dependent on solar zenith angle, sky conditions (e.g., cloudiness), local slope of the surface, and the orientation of elements such as tree crowns. The high altitude data with 17.5 meter pixel size does not contain a single pixel that is fully shadowed. However, the reflectance of forests as measured from the high altitude data also had the influence of incorrect calculation of true reflectance due to inadequate specification of the diffuse:direct reflectance for shaded parts of the canopy and understory.

An examination of the reflectance changes through a stand of lodgepole pine in the Old Faithful area showed the pixel to pixel variations to be much greater at the 1.5 meter scale compared to 17.5 meter pixels. The variations are due to sunlit vs. shaded tree crowns and understory. It is also suggested that multiple scattering between canopy elements affects the shape of the spectra. Reflectance observed for forest pixels, from the high altitude data, are likely a combination of reflectance from individual surface elements that have not been compensated for nonlinear effects (e.g. multiple scattering, sunlit vs. shaded vegetation). These nonlinear effects were observed in low altitude data. It was observed that the reflectance of deeply shaded forest areas was affected by insufficient correction for illumination conditions, which altered the spectral shapes. Thus, in some shadowed pixels the identification of vegetation cover type was compromised.

A comparison of the average reflectance for a stand of lodgepole pine between the high altitude and low altitude AVIRIS data showed a higher reflectance level in the high altitude data. The reflectance level of the low altitude data is suggested to be lower due to the low sun angle and a greater proportion of shadowed vegetation in the forest stand. However, continuum removal and normalization to band depth of the 0.68 μm chlorophyll absorption feature show

very little variation between the two data sets. This suggests that, despite the limitations of the combined radiative transfer and ground calibration method of atmospheric correction employed here, the forests in Yellowstone have consistent spectral absorption features that may be used for consistent and repeatable mapping of forest cover types.

The possibility of developing a robust vegetation cover mapping method for the Yellowstone area was tested by mapping the distribution of forest cover types in the low altitude 1998 AVIRIS data using the USGS Tetracorder system and a spectral library of vegetation cover types derived from the high altitude 1996 AVIRIS data. The USGS Tetracorder system successfully handled the change in spatial scale and timing of AVIRIS data collection to reproduce maps of forest cover in the Old Faithful area of Yellowstone National Park. Indeed, the increased spatial resolution of the low altitude data enables improved mapping of the forest structure by detecting tree crowns, gaps, and individual trees. Further analysis of such low altitude data may lead to the development of tree counts or tree density estimates using this detection of crowns and gaps. Bi-directional reflectance distribution function effects were observed but did not cause a problem for identifying conifer species using the USGS Tetracorder system, in part because the system isolates absorption features using continuum removal. Additional work should be conducted on other imaging spectroscopy data sets for Yellowstone National Park, such as high altitude 1997 AVIRIS data. In addition, further studies in more diverse areas of forest cover are needed in order to develop a robust method of mapping conifers using spectral feature analysis and imaging spectrometer data.

7. REFERENCES

Boardman, J.W. (1999) "Precision geocoding of low altitude AVIRIS data: Lessons learned in 1998," *Summaries of the 8th JPL Airborne Earth Science Workshop,* R.O. Green, Ed., JPL Publication 99-17, pp. 63-68.

Clark, R.N., G.A. Swayze, T.V.V. King, K.E. Livo, R.F. Kokaly, J.B. Dalton, J.S. Vance, B.W. Rockwell, and R. R. McDougal (2001a) "Surface Reflectance Calibration of Terrestrial Imaging Spectroscopy Data: a Tutorial Using AVIRIS," Draft of U.S. Geological Survey Open File Report, available online at: http://speclab.cr.usgs.gov/PAPERS.calibration.tutorial/calibntA.html

Clark, R.N., Swayze, G.A., and King, T.V.V. (2001b) "Imaging Spectroscopy: A Tool for Earth and Planetary System Science Remote Sensing with the USGS Tetracorder System," submitted to *Journal of Geophysical Research.*

Clark, R.N. (1999), Spectroscopy of rocks and minerals and principles of spectroscopy. In *Remote Sensing for the Earth Sciences: Manual of Remote Sensing 3rd Edition, Vol. 3* (A.N. Rencz Ed.), John Wiley and Sons, Inc., New York, pp. 3-58.

Clark, R.N., T.V.V. King, C. Ager, and Swayze, G.A. (1995a) "Initial vegetation species and senescence/stress indicator mapping in the San Luis Valley, Colorado using imaging spectrometer data," *Summaries of the Fifth Annual JPL Airborne Earth Science Workshop,* January 23- 26, 1995, R.O. Green, Ed., JPL Publication 95-1, p. 35-38.

Clark, R.N., G.A. Swayze, Heiebrecht, K.B., Green, R.O., and Goetz, A.F.H. (1995b) "Calibration to Surface Reflectance of Terrestrial Imaging Spectrometry Data: Comparison of Methods," *Summaries of the Fifth Annual JPL Airborne Earth Science Workshop,* January 23- 26, 1995, R.O. Green, Ed., JPL Publication 95-1, pp. 41-42.

Clark, R.N. and Swayze, G.A. (1995c) "Mapping Minerals, Amorphous Materials, Environmental Materials, Vegetation, Water, Ice and Snow, and Other Materials: The USGS Tricorder Algorithm," *Summaries of the Fifth Annual JPL Airborne Earth Science Workshop,* January 23- 26, R.O. Green, Ed., JPL Publication 95-1, p. 39-40.

Clark, R.N., G.A. Swayze, Heiebrecht, K.B., Goetz, A.F.H, and Green, R.O. (1993a) "Comparison of Methods for Calibrating AVIRIS Data to Ground Reflectance," *Summaries of the 4th Annual JPL Airborne Geosciences Workshop, Volume 1: AVIRIS Workshop*, JPL Publication 93-26, pp. 31-34.

Clark, R.N., Swayze, G.A., and Gallagher, A. (1993b) "Mapping Minerals with Imaging Spectroscopy," *U.S. Geological Survey, Office of Mineral Resources Bulletin 2039,* pp. 141-150.

Clark, R.N., G.A. Swayze, A. Gallagher, N. Gorelick, and F. Kruse (1991) "Mapping with Imaging Spectrometer Data Using the Complete Band Shape Least-Squares Algorithm Simultaneously Fit to Multiple Spectral Features from Multiple Materials," *Proceedings of the Third Airborne Visible/Infrared Imaging Spectrometer (AVIRIS) Workshop,* JPL Publication 91-28, 2-3.

Clark, R.N., A.J. Gallagher, and G.A. Swayze, 1990, "Material Absorption Band Depth Mapping of Imaging Spectrometer Data Using a Complete Band Shape Least-Squares Fit with Library Reference Spectra," *Proceedings of the Second Airborne Visible/Infrared Imaging Spectrometer (AVIRIS) Workshop.* JPL Publication 90-54, 176-186.

Clark, R. N. and T.L. Roush, 1984, "Reflectance Spectroscopy: Quantitative Analysis Techniques for Remote Sensing Applications," *Journal of Geophysical Research*, **89**:6329-6340.

Despain, D. G., 1990, Yellowstone Vegetation: Consequences of Environment and History in a Natural Setting, Roberts Rinehart Publishers, Santa Barbara.

Gao, B.C., Heidebrecht, K.B., and Goetz, A.F.H., 1993, "Derivation of Scaled Surface Reflectances from AVIRIS Data," *Remote Sensing of Environment*, **44**:165-178.

Gao, B.C., Heidebrecht, K.B., and Goetz, A.F.H., 1997, "Atmosphere Removal Program (ATREM) Version 3.0 User's Guide," Center for the Study of Earth from Space, University of Colorado at Boulder, pp. 1-27.

Ingle, J.D. (1988), *Spectrochemical Analysis*, Prentice-Hall, Inc., Engelwood Cliffs, New Jersey, pp. 424-425.

Jakubauskas, M.E., 1996, "Thematic Mapper Characterization of Lodgepole Pine Seral Stages in Yellowstone National Park, USA," *Remote Sensing of Environment*, **56**:118-132.

Kokaly, R.F., Despain, D.G., Clark, R.N., and Livo, K.E. (2001) "Spectral feature analysis for mapping vegetation cover and microbial communities in Yellowstone National Park using AVIRIS," submitted to *Remote Sensing of Environment.*

Kokaly, R.F. and Clark, R.N. (1999), Spectroscopic determination of leaf biochemistry using band-depth analysis of absorption features and stepwise multiple linear regression. *Remote Sensing of Environment* **67:** 267-287.

Kokaly, R.F., Clark, R.N., and Livo, K.E. (1998) "Mapping the Biology and Mineralogy of Yellowstone National Park using Imaging Spectroscopy," *Summaries of the 7th Annual JPL Airborne Earth Science Workshop, January12-16, 1998, Volume 1. AVIRIS Workshop*, R.O. Green, Ed., JPL Publication 97-21, pp. 245-254.

Martin, M.E., Newman, S.D., Aber, J.D., and Congalton, R.G., 1998, "Determining forest species composition using high spectral resolution remote sensing data," *Remote Sensing of Environment*, vol. **65**:249-254.

Martin, M.E., and Aber, J.D. (1997), High spectral resolution remote sensing of forest canopy lignin, nitrogen, and ecosystem processes. *Ecological Applications* **7**:431-443.

Mustard, J.F., Staid, M.L., and Fripp, W. (1999) "Atmospheric correction and inverse modeling of AVIRIS data to obtain water constituent abundances," *Summaries of the 8th JPL Airborne Earth Science Workshop,* R.O. Green, Ed., JPL Publication 99-17, pp. 309-315.

Roberts, D.A., Gardner, M., Church, R., Ustin, S., Scheer, G., and Green, R.O., 1998, "Mapping chaparral in the Santa Monica Mountains using multiple endmember spectral mixture models," *Remote Sensing of Environment*, **65**:267-279.

Ustin, S.L., Smith, M.O., Jacquemoud, S., Verstraete, M., and Govaerts, Y. (1999), Geobotany: Vegetation mapping in earth sciences. In *Remote Sensing for the Earth Sciences: Manual of Remote Sensing 3rd Edition, Vol. 3* (A.N. Rencz Ed.), John Wiley and Sons, Inc., New York, pp. 189-248.

Wessman, C.A., Aber, J.D., and Peterson, D.L. (1989), An evaluation of imaging spectrometry for estimating forest canopy chemistry, *International Journal of Remote Sensing* **10**:1293-1316.

Table 1. AVIRIS Data Collection Parameters for High and Low Altitude Acquisitions.

Parameter	High Altitude	Low Altitude
Date	August 7, 1996	October 13, 1998
Time (local)	10:32 am	10:43 am
Platform	NASA ER-2	NOAA Twin Otter
Aircraft Altitude (km)	20.0	3.81
Solar Azimuth (degrees)	139.6	154.4
Solar Elevation (degrees)	44.3	34.3
Nominal pixel size (m)	17.5	1.5
Ground Sampling Distance (m) Cross-track (near nadir)	15.4	1.3

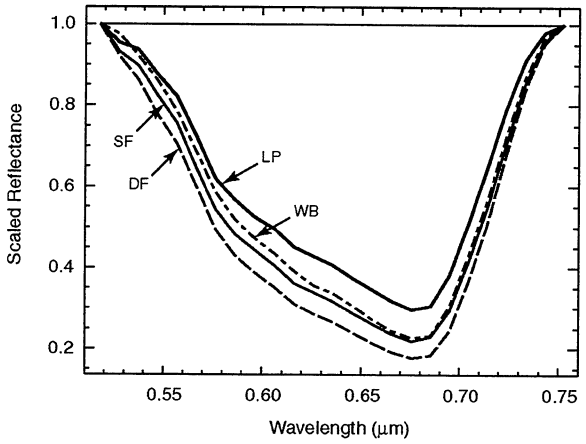

Figure 1. Continuum removed chlorophyll absorption feature of conifer vegetation cover types occurring in Yellowstone National Park (lodgepole pine, LP; Douglas-fir, DF; whitebark pine, WB; and mixed Engelmann spruce/subalpine fir, SF)

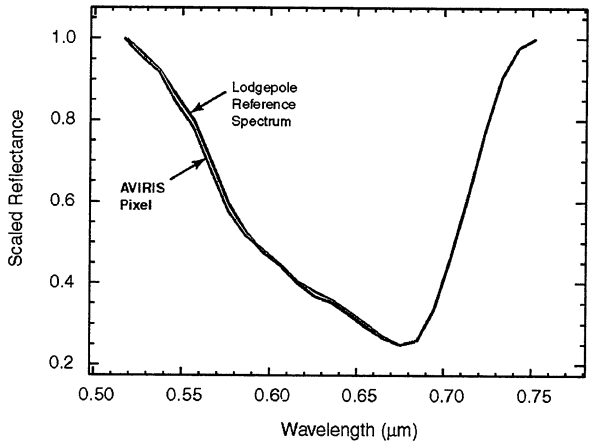

Figure 2. A comparison of the continuum removed and scaled absorption features of the spectrum of an AVIRIS pixel and the vegetation cover type (lodgepole pine) identified by the USGS Tetracorder expert system as the best match.

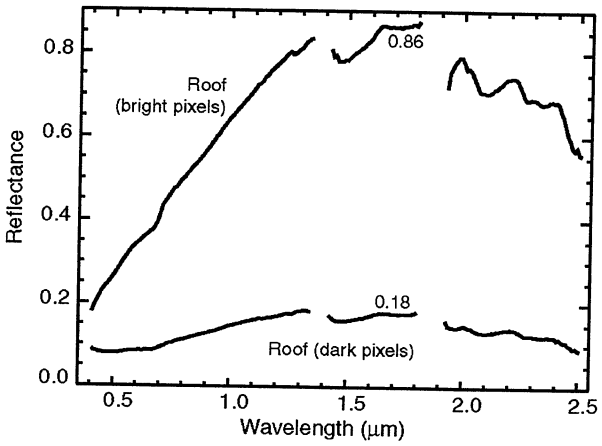

Figure 3. The average AVIRIS 1998 low altitude reflectance spectra for two sides of a pitched roof in the Old Faithful area (Figure 4a). The reflectance value at 1.7 μm is given.

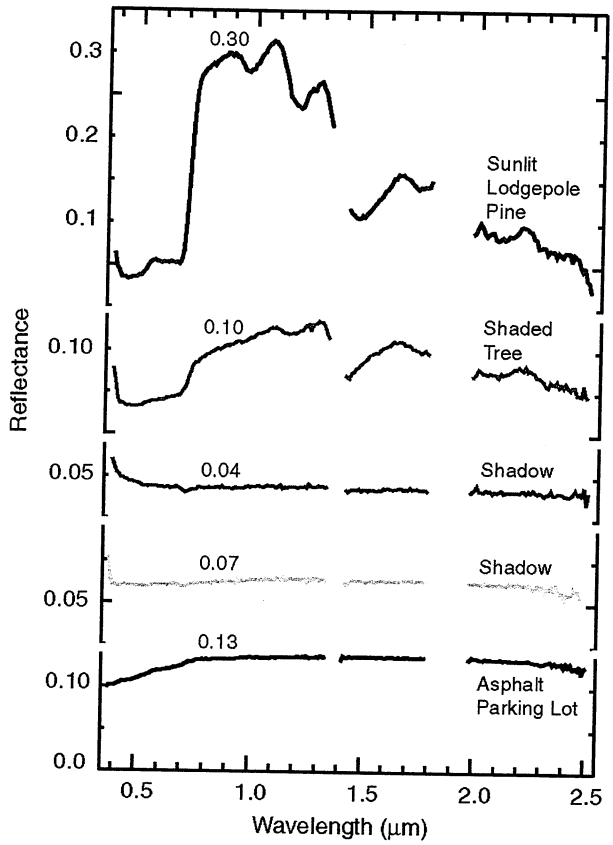

Figure 4. Reflectance spectra of sunlit tree, shaded tree, shaded parking lot, and sunlit parking lot from the AVIRIS 1998 low altitude data.

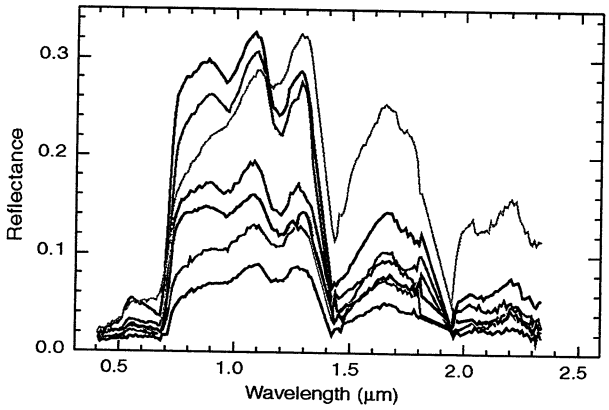

Figure 5. Reflectance spectra of pixels extracted from an area of lodgepole pine just north of Old Faithful geyser.

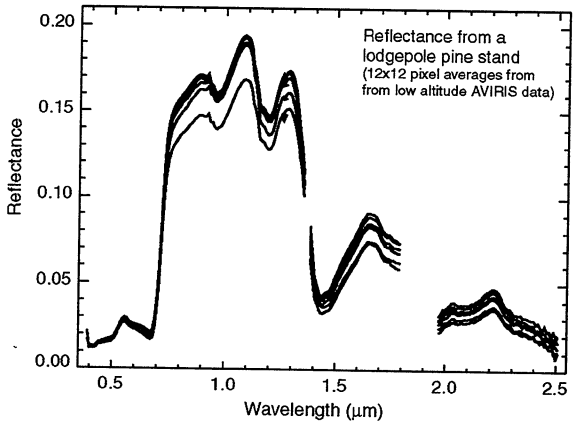

Figure 6. Reflectance spectra of low altitude data averaged in 12x12 blocks for an area of lodgepole pine just north of Old Faithful geyser, which show less variation in their reflectance signatures compared to individual pixels as depicted in Figure 5.

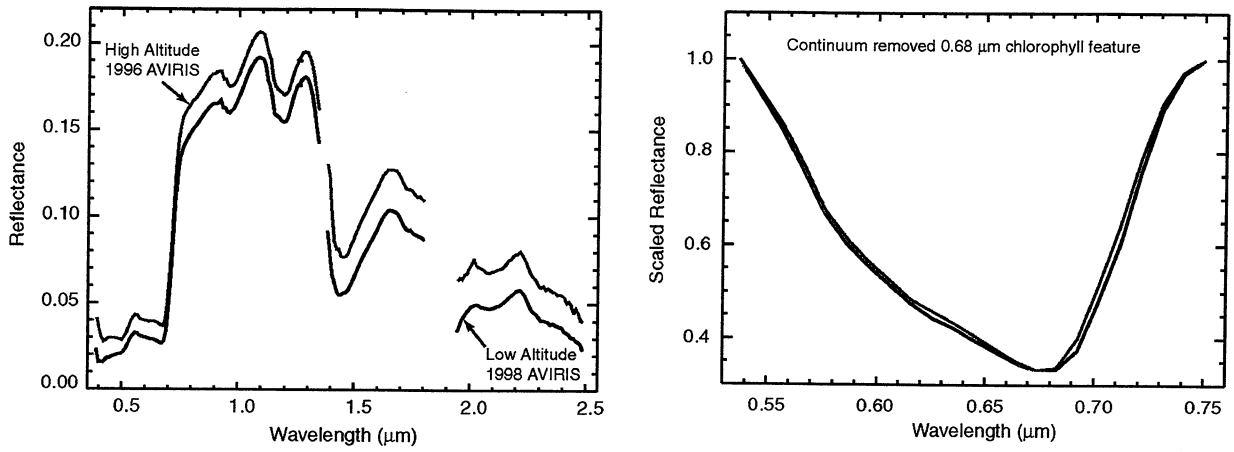

Figure 7. A comparison of the averaged reflectance signatures of the lodgepole pine stand just north of Old Faithful geyser (Figure 7a) and their 0.68 μm chlorophyll absorption feature that has been continuum removed and scaled (Figure 7b)

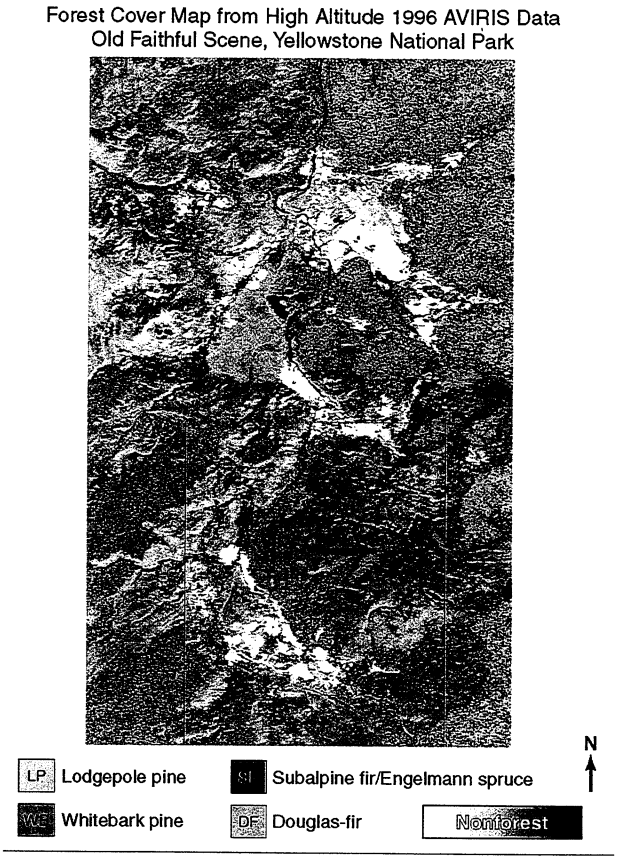

Figure 8. Forest cover map of a 1024 line scene of high altitude 1996 AVIRIS data over the Old Faithful area generated using the USGS Tetracorder expert system.

Figure 9. Forest cover map of a 1024 line scene of low altitude 1998 AVIRIS data over the Old Faithful area generated using the USGS Tetracorder expert system.

Figure 10. Forest cover map of the Old Faithful area taken from a scene of high altitude 1996 AVIRIS data over the Old Faithful generated using the USGS Tetracorder expert system.

PROGRESS REPORT: GEOLOGIC VALIDATION OF EO-1 HYPERION USING AVIRIS

F. A. Kruse,[1] J. W. Boardman,[1] and J. H. Huntington[2]

1.0 Introduction

Over the last few years, the field of imaging spectrometry has grown rapidly as new instruments and analysis techniques have been developed. The launch of Hyperion as part of NASA's EO-1 program represents a significant landmark in the progression of the technology; the first spaceborne imaging spectrometry system. AIG, in cooperation with CSIRO, is evaluating, validating, and demonstrating use of EO-1 Hyperion hyperspectral data for geologic applications. The Airborne Visible/Infrared Imaging Spectrometer (AVIRIS) plays a pivotal role in this effort. This manuscript describes the geologic test sites being used and progress on preparing "ground truth" for anticipated Hyperion data collects using AVIRIS data. Preliminary findings are extrapolated to predict the effect of instrument characteristics and performance on geologic mapping using Hyperion.

2.0 EO-1 Hyperion Summary

Hyperion is a pushbroom/diffraction grating imaging spectrometer launched as part of NASA's EO-1 mission on 21 November 2000. The instrument has 200 spectral bands covering the 0.4 to 2.5 μm range with approximately 10nm spectral resolution and 30 meter spatial resolution. Ground coverage is approximately 7.5 km by 180 km per image (24 second collect). Signal-to-noise ratios are estimated as approximately 100:1 in the VNIR and 50:1 for the SWIR.

3.0 Objectives

Characterization and validation of Hyperion are key tasks in the understanding of its performance, its utility for specific applications, and the planning for future systems. The objectives of the AIG/CSIRO research are to evaluate Hyperion to determine its performance and to validate with respect to requirements for applied and commercial use of space-based hyperspectral data for geologic applications. We are evaluating, validating, and demonstrating Hyperion in the role of geologic mapping and in the context of monitoring the processes that control the occurrence of non-renewable mineral resources, especially mineral deposits. We are also examining the issues of spectral and spatial scaling using Hyperion data, using the data to examine parameters inherent to analysis of satellite hyperspectral data (subpixel detection, identification, quantification, and mapping). Our principle means of validating Hyperion is through comparison with airborne hyperspectral datasets (AVIRIS and HyMap), laboratory and field spectral measurements, and satellite simulations.

4.0 AIG Hyperion Geologic Validation Sites

Three primary test sites representing geologically diverse terrains are being used for the AIG/CSIRO Hyperion validation effort; the N. Grapevine Mountains, Nevada; Oatman, Arizona; and Virginia City, Nevada. Secondary sites in Argentina, Australia, Israel, and New Zealand are also being imaged. Existing AVIRIS/HyMap data and supporting information serve as the baseline for determination of Hyperion spectral, spatial and radiometric properties.

NGM Site: The northern Grapevine Mountains (NGM) site, located in south-central Nevada (Figure 1), consists of about one third of the "West of Gold Mountain" U.S. Geological Survey 7 1/2 minute quadrangle (1:24,000 scale). The site has been studied in detail using field mapping and several remote sensing data sets (Kruse, 1988; Kruse et al., 1993b; Kruse et al., 1999). Existing geologic maps include 1:62,500-scale bedrock mapping by (Wrucke et al., 1984) and mapping of surficial deposits by Moring (1986). More detailed site-specific mapping has also been performed (Kruse, 1988). The NGM site is ideal for Hyperion validation because of the presence of both large (disseminated) and small (vein) alteration zones, common alteration minerals with similar spectral signatures, and the abundance of supporting hyperspectral data (AIS/AVIRIS/HyMap).

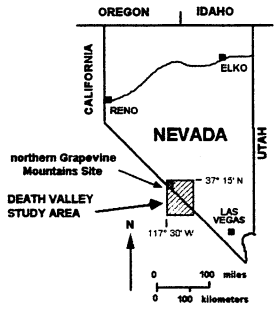

Figure 1: Location map

[1] Analytical Imaging and Geophysics, Boulder, Colorado 80303 (www.aigllc.com)

[2] CSIRO, Sydney, Australia

PreCambrian bedrock in the NGM area consists of limestones, dolomites, sandstones and their contact metamorphic equivalents, however, published geologic maps do not distinguish between the different lithologies. Mesozoic plutonic rocks are mapped primarily as granitic-composition and some age-dates are available (Albers and Stewart, 1972). Mesozoic units mapped in the field during previous investigations include quartz syenite, a quartz monzonite porphyry stock, quartz monzonite dikes, and a granite intrusion (Kruse, 1988). These rocks are cut by narrow north-trending mineralized shear zones containing sericite (fine grained muscovite or illite) and iron oxide minerals (Wrucke et al., 1984; Kruse, 1988). Slightly broader northwest-trending zones of disseminated quartz, pyrite, sericite, chalcopyrite, and fluorite mineralization (QSP alteration) ± goethite occur in the quartz monzonite porphyry. This type of alteration is spatially associated with fine-grained quartz monzonite dikes (Kruse, 1988). There are several small areas of quartz stockwork (silica flooding of the rocks) exposed at the surface in the center of the area, and skarn, composed mainly of brown andradite garnet near contact zones with limestone/dolomite. Complexly faulted, Tertiary volcanic rocks related to the Timber Mountain Caldera in southern Nevada are abundant around the southern periphery of the study area and are overlain by volcaniclastic sedimentary rocks interbedded with rhyolite and basalt (Wrucke et al., 1984). Quaternary deposits include Holocene and Pleistocene fanglomerates, pediment gravels, and alluvium.

Virginia City, Nevada: Virginia City is located in the Virginia Range in west-central Nevada, SE of Reno, Nevada. The Comstock Lode Mining District at Virginia City produced over 200 million oz of silver and 9 million oz of gold during the mid-1800s. The andesitic volcanic rocks that host the ore deposits are extensively altered and bleached. Zones of hydrothermal alteration are widely exposed and identifiable on Landsat MSS and TM images due to their light color and the presence of iron oxide and clay minerals (Hutsinpiller, 1988). Previous remote sensing studies of the Virginia City district have been made by Hutsinpiller, 1988, and Elvidge, 1985. Other studies have been made by Whitebread, 1976, and Thompson, 1956.

Virginia City was chosen as an Hyperion site because of the abundance of hydrothermal alteration minerals, existence of appropriate supporting hyperspectral data (AVIRIS/HyMap), the presence of one of the world's most valuable, historic mineral fields, complex and relatively poorly exposed geology and the complementary nature of the terrain to the other AIG/CSIRO sites. The area is rugged, well vegetated and encompasses extensive old (contaminating) mine activity, dumps and urban development, as well as natural fresh and altered outcrops. Virginia City thus represents a typical site that users of spaceborne hyperspectral data might encounter, more difficult than NGM in many respects, but one that we will have to learn to deal with.

The following geological summary is taken largely from Hutsinpiller (1988). The oldest rocks in the district are Mesozoic meta-sediments and meta-volcanics that have been intruded by Cretaceous granodiorite and granite. Unconformably overlying the Mesozoic rocks are a series of silicic ash-flow tuff. These are overlain by thick andesite flows and breccias of the Miocene Alta Formation, the main host of the orebodies in the district. Dikes and stocks of the Davidson Diorite intrude the Mesozoic rocks and the Alta Formation. Overlying the Alta Formation are andesitic to dacitic flows and associated dikes and stocks of the Kate Peak Formation. During emplacement of the lower member of the Kate Peak Formation normal faulting, mineralization and alteration occurred. The Knickerbocker Andesite unconformably overlies the Kate Peak Formation.

Mineralization and hydrothermal alteration in the Comstock Lode District are mostly confined to the northerly-trending Comstock, Silver City and Occidental fault zones, although some ore was mined in hanging wall faults. The faults dip moderately to the east but are nearly vertical at the surface. Post-mineral faulting has displaced the hanging-wall ore bodies as well as portions of the ore-bodies within the main fault zones. Hudson (1984) defines seven alteration assemblages at Virginia City (Table 1).

Alteration assemblages vary with depth from the palaeo-surface and horizontal distance form the major faults. At the surface, in the hanging wall, narrow alunitic and alsic ledges grade laterally into kaolinitic alteration. The kaolinite zones in turn grade into illitic and finally into propylitic alteration. Illitic and kaolinitic assemblages occur in zones from several meters to over 500 meters in width. Propylitically altered rocks of varying intensity are widespread throughout the district. Patches of sericitic alteration up to 800 meters wide crop out west of Virginia City in the footwall of the Comstock Fault.

Table 1 - Alteration Mineral Assemblages at Virginia City (from Hutsinpiller, 1988)

Alteration Type	Alteration Assemblage	Minerals with SWIR absorptions
Propylitic	albite, chlorite, epidote, calcite, white mica, (illite &/or sericite), quartz, pyrite	Chlorite, epidote, calcite, white mica
Illitic	Illite, quartz, pyrite, mixed-layer illite-montmorillonite	Illite, montmorillonite
Kaolinitic	Kaolinite, quartz, pyrite	Kaolinite
Alsic	Pyrophyllite, quartz, diaspore, kaolinite, pyrite	Pyrophyllite, kaolinite
Alunitic	Quartz, alunite, pyrite	Alunite
Sericitic	Sericite, quartz, pyrite	Sericite
Silicification	Quartz, adularia, calcite	Calcite

Thus it is apparent that many of the minerals we believe Hyperion will be able to map are present in the Virginia City area. It should be noted, however, that much of this information has been derived from detailed petrological work on drill hole samples and it is not clear how much of this mineralogical variety may be evident on the surface rocks, soils and exposures visible from above (as opposed to road-side cuttings).

Oatman, Arizona: The Oatman Mining District lies approximately 160 km south-east of Las Vegas Nevada, mid-way between Needles, California and Kingman, Arizona. The district is about 21 miles long and 7 miles wide and is situated within Tertiary Volcanics of the Black Mountains. Gold was first discovered at Oatman in 1863 in the Moss Vein and subsequent finds in other locations (Gold Road Vein, Tom Reid Vein) led to the development of a town of 10,000 at Oatman after about 1916. Production ceased in the district in 1942 after producing some 2.2 million ounces of gold and 0.8 million ounces of silver.

Oatman was chosen as an Hyperion validation site because of the suite of minerals present (argillic, phyllic and propylitic), its semi-arid nature, being an historic mining center, the existence of appropriate supporting AVIRIS and HyMap data sets and previous mineral mapping research conducted to validate CSIRO ARIES simulation results (Marsh and McKeon, 1983; Huntington et al., 1988; Huntington et al., 1989; Huntington and Boardman, 1995).

The regional geology consists of a thick sequence of Tertiary sub-alkaline, intermediate and silicic volcanic rocks which have been intruded by two epizonal plutons. The Black Mountains are a typical Basin and Range, fault-bounded, Tertiary volcanic sequence composed of trachyte, latite, rhyolite and basalt (Thorson, 1971; Clifton et al., 1980). Oatman lies at the center of a trachyte, latite, rhyolite volcanic complex which contains at least one resurgent caldera. The orebodies are typically low sulfur, epithermal, quartz-calcite +/- adularia lode deposits. Ore deposition has occurred along faults that radiate from a common point within the complex.

An intense and pervasive argillic alteration is evident in the center of the Hyperion study area. Thorson has interpreted this to be a late stage phase of the Moss Porphyry intrusion which has affected both the Lower and Middle Volcanics. More recent studies by Clifton et al. (1980) indicate that the argillic alteration is centered around a previously unmapped rhyolite center located on the eastern margin of the Moss Porphyry. The orebodies of the district occupy dilatant zones within faults structures resulting from dip-slip and strike-slip movements along irregular fault planes. They vary from tabular fissure fillings to complex stockworks of broken, vertically oriented latite slabs separated by quartz calcite veins ranging from an inch to 15 feet wide. Most of these mineralized fractures have a generally similar NW-E orientation, though variations in these trends can be the all important loci for liberalization. In addition to the pervasive argillic alteration there is also significant wall rock alteration which delineates all known ore deposits in the district.

Marsh and McKeon (1983), conclude that there are four distinct alteration assemblages at Oatman which may be directly or indirectly related to the mineralization. These are:

1. pervasive argillic alteration that is characterized by the formation of alunite and sericite (muscovite);

2. spatially restricted, phyllic wall rock alteration which is characterized by the presence of illite. This alteration style extends above the orebodies to the surface in the central district and may coalesce with zones from adjacent veins to form a wider, potentially more visible surface signature;
3. propylitic alteration which introduces chlorite, calcite and epidote into the wall rock;
4. silicification of the wall rock characterized by the introduction of quartz along microfractures.

The above mineralogy and structural control of alteration provides an excellent reference against which to compare and judge the mineralogical mapping capabilities of Hyperion since most of the minerals described should be within the scope of its recognition capabilities.

Other Sites: The November launch of Hyperion and the desire to quickly produce results under optimum acquisition conditions dictated that we acquire data for selected additional southern hemisphere sites. Accordingly, AIG added sites in Australia, New Zealand and Argentina to assist with early Hyperion validation. An AVIRIS data acquisition opportunity during February 2001; AVIRIS deployment to Argentina, also provided the opportunity to collect EO-1 Hyperion support data at a southern hemisphere location coincident with Hyperion data collections. While AIG hasn't conducted any previous mapping at these specific sites, we have proposed to team with other scientists cognizant of site geology (CSIRO for Australia and Perry Remote Sensing (PRS) and a major mining company for Argentina) to assist with evaluation and validation of these data. We have also added an additional site, Makhtesh Ramon, Israel, to take advantage of expertise at Tel Aviv University (Dr. Eyal Ben-Dor) and existing ground and hyperspectral measurements for Hyperion validation. We anticipate that depending upon site coverage and performance, the Hyperion data will provide additional information valuable for geologic understanding of these areas.

5.0 Analysis Example

The NGM site represents the best-case example of a well documented geologic site for Hyperion geologic validation, with both detailed ground information and multiple hyperspectral datasets available. Repeated overflights of the NGM site with a variety of remote sensing instruments were arranged from 1982 through 1999 to evaluate remote sensing technology for resource assessment and to develop advanced analysis methodologies. Remote sensing data available for the NGM site include Landsat MSS and TM, Thermal Infrared Multispectral Scanner (TIMS), MODIS/ASTER (MODIS) Airborne Simulator, JPL Airborne Synthetic Aperture Radar (AIRSAR) and SIR-C. Imaging spectrometer (hyperspectral) data flown for the NGM site include GER Spectral Profiler (1982), Airborne Imaging Spectrometer (AIS) (1984 - 1986), Airborne Visible/Infrared Imaging Spectrometer (AVIRIS) (1987, 1989, 1992, 1994, 1995), Low Altitude AVIRIS (1998), and HyMap (1999). Table 2 summarizes the characteristics of selected datasets and for the planned EO-1 Hyperion.

Table 2: Data acquired and planned for the NGM site, 1982 - 2001

Instrument/Data	Date	Spatial Res.	No. Bands/Spectral Res	SWIR SNR
GER Profiler	1982	20 m	64/~8 nm	500:1
AIS	1984-1986	11-14 m	128/~9.3 nm	~20:1
AVIRIS	1987	20 m	224/~10 nm	15:1
AVIRIS	1989	20 m	224/~10 nm	50:1
AVIRIS	1992	20 m	224/~10 nm	100:1
AVIRIS	1994	20 m	224/~10 nm	100:1
AVIRIS	1995	20 m	224/~10 nm	400:1
AVIRIS	1998	2.4 m	224/~10 nm	400:1
HyMap	1999	3.7 m	126/~17 nm	>500:1+
MASTER	1999	4.3 m	50 (6 SWIR)/~50 – 70 nm	~450:1
EO-1 Hyperion (planned)	2001	30 m	220/~10 nm	50:1

The Mineral Mapping Process: AIG plans to apply the following well-extablished approach to mineral mapping using hyperspectral data to the Hyperion data. These methods have been tested extensively using AVIRIS and other airborne hyperspectral datasets (Boardman and Kruse, 1994; Boardman et al. 1995; Kruse and Huntington 1996; Kruse et al. 1996; and Kruse 1997). The proposed Hyperion data analysis represents the first time that this approach has been applied to satellite hyperspectral datasets.

We believe that hyperspectral data analysis should be cast in the same format as other geophysical data analysis processes. First, the data must be fully calibrated and well characterized. Then instrumental and natural influences on the data, unrelated to our signal of interest, should be modeled and removed via a data reduction step. We use a spectral mixing model to derive the locations and spectral signatures of various key scene components. These derived components, or endmembers, are identified using spectral matching methods and their apparent abundances mapped over the entire hyperspectral scene. Finally, the results are geometrically rectified and map registered (Boardman, 1999). These steps are shown schematically in Figure 2 along with a mapping result. The details of the methodology are described in the following sections.

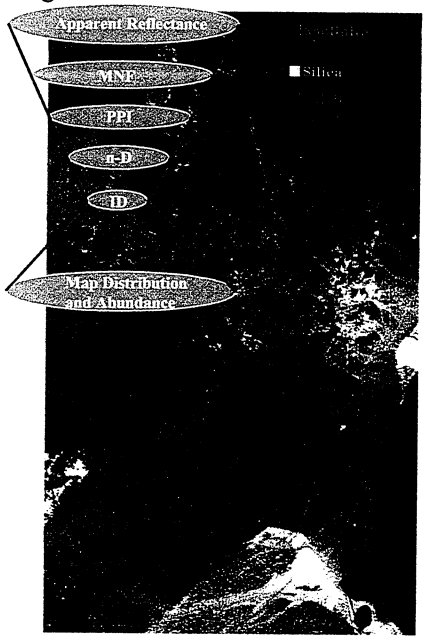

Figure 2: The AIG "Hourglass" method for analysis of hyperspectral data. The underlying image is the result of spectral mapping using "Spectral Feature Fitting', a least-squares fit to endmember spectra, Cuprite, Nevada.

The AIG hyperspectral analysis methodology includes correction of data to apparent reflectance, use of a linear transformation to minimize noise and determine data dimensionality, location of the most spectrally pure pixels, extraction and automated identification of endmember spectra, and spatial mapping and abundance estimates for specific image endmembers. The approach is summarized in more detail below and in Boardman and Kruse (1994), Boardman et al. (1995), Kruse and Huntington (1996), Kruse et al. (1996), and Kruse (1997). A key point of this methodology is the reduction of data in both the spectral and spatial dimensions to locate, characterize, and identify a few key endmember spectra that can be used to explain the rest of the hyperspectral dataset. Once these endmembers are selected, then their location and abundances can be mapped from the original data. The methods described here attempt to derive the maximum information from the hyperspectral data themselves, minimizing the reliance on *a priori* or outside information.

Atmospheric Corrections are a Prerequisite for Most Analysis:

Remote sensing measurements of the Earth's surface are strongly influenced by the atmosphere (Goetz et al., 1985). Both scattering and absorption by gases and particulates affect the amount and wavelengths of light reaching the sensors. Absorption by atmospheric gases is dominated by water vapor with smaller

contributions from carbon dioxide, ozone, and other gases (Gao and Goetz, 1990). Strong atmospheric water absorption bands make the atmosphere opaque in many regions (for example the 1.4 and 1.9 μm regions) and only small atmospheric windows are available for terrestrial remote sensing.

One of the most critical steps in most imaging spectrometer data analysis strategies is to convert the data to reflectance, principally so that individual spectra can be compared directly with laboratory or field data for identification. (If comparison to reflectance isn't required, then this step may be eliminated, but for most work, this is a requirement). Ideally, imaging spectrometer data should be calibrated to absolute reflectance using onboard calibration. Onboard calibration, however, is typically not available. In its absence, one method that comes close to achieving this goal is a radiative transfer model-based technique, "ACORN". ACORN is a commercially available atmospheric correction program (see http://www.aigllc.com) that uses the hyperspectral signature and licensed MODTRAN technology to model the atmosphere and produce apparent reflectance data from hyperspectral radiance measurements. MODTRAN is used to derive and estimate the atmospheric properties for the remote sensing data set on a pixel-by-pixel basis. ACORN corrects for water vapor, oxygen, carbon dioxide, methane, and ozone as well as molecular and aerosol scattering. The software automatically assesses and suppresses artifacts caused by spectral calibration mismatch between the measured data and the radiative transfer calculations. Estimated atmospheric properties are used in an inversion from radiance to apparent surface reflectance. This method makes it possible to quantitatively derive physical parameters and analyze data from different regions and different times without *a priori* knowledge. We can also compare and analyze imaging spectrometry data acquired by different instruments, compare to field and laboratory spectral measurements, or to spectra generated using theoretical models. Correction to reflectance is critical for analysis of the Hyperion data.

MNF Transform

The MNF transformation is a linear transformation related to principal components that orders the data according to signal-to-noise-ratio (Green et al., 1988). The MNF transformation is used to partition the data space into two parts: one associated with large eigenvalues and coherent eigenimages, and a second with near-unity eigenvalues and noise-dominated images (Boardman and Kruse, 1994). In general, the higher numbered MNF bands contain progressively lower signal-to-noise.

Pixel Purity Index (PPI)

Based on the above MNF results, the lower order MNF bands are temporarily discarded and only the higher order bands are selected for further processing. These are used in the "Pixel Purity Index" (PPI), processing designed to locate the most spectrally extreme pixels, which pixels typically correspond to mixing endmembers (Boardman et al., 1995). The PPI is computed by repeatedly projecting n-dimensional scatterplots onto a random unit vector. The extreme pixels in each projection are recorded and the total number of times each pixel is marked as extreme is noted. A PPI image is created in which the digital number of each pixel corresponds to the number of times that pixel was recorded as extreme. A histogram of these images shows the distribution of "hits" by the PPI. A threshold is interactively selected using the histogram and used to select only the purest pixels in order to keep the number of pixels to be analyzed to a minimum. These pixels are used as input to an interactive visualization procedure for separation of specific endmembers.

n-Dimensional Visualization

Spectra can be thought of as points in an n-dimensional scatterplot, where n is the number of bands (Boardman, 1993; Boardman et al., 1995). The coordinates of the points in n-space consist of "n" values that are the spectral reflectance values in each band for a given pixel. The distribution of these points in n-space can be used to estimate the number of spectral endmembers and their pure spectral signatures. In two dimensions, if only two endmembers mix, then the mixed pixels will fall in a line in the histogram. The pure endmembers will fall at the two ends of the mixing line. If three endmembers mix, then the mixed pixels will fall inside a triangle, four inside a tetrahedron, and so on. Mixtures of endmembers "fill in" between the endmembers. All mixed spectra are "interior" to the pure endmembers, inside the simplex formed by the endmember vertices, because all the abundances are positive and sum to unity. This "convex set" of mixed pixels can be used to determine how many endmembers are present and to estimate their spectra.

Mapping Methods

AIG uses a variety of mapping methods depending on the data type and the desired results. These include the Spectral Angle Mapper (SAM) Classification, Spectral Unmixing, Spectral Feature Fitting, Matched Filtering, and Mixture-Tuned Matched Filtering. SAM is an automated method for comparing image spectra to individual spectra (Boardman, unpublished data; Kruse et al., 1993a). The algorithm determines the similarity between two spectra by calculating the "spectral angle" between them, treating them as vectors in a space with dimensionality equal to the number of bands.

Spectral mixing is a consequence of the mixing of materials having different spectral properties within a single image pixel. If the scale of the mixing is large (macroscopic), then the mixing occurs in a linear fashion. A simple additive linear model can be used to estimate the abundances of the materials measured by the imaging spectrometer. Each mixed spectrum is a linear combination of the "pure" spectra, each weighted by their fractional abundance within the pixel, a simple averaging (Boardman, 1989).

Spectral Feature Fitting is an absorption-feature-based methodology for comparing the fit of image spectra to selected reference spectra using a least-squares technique (Kruse et al., 1993b; Kruse and Lefkoff, 1999). This is similar to the "Tetracorder" algorithm developed by the USGS (Clark et al., 1990; Clark and Swayze, 1995), but without the expert system. The reference spectra are scaled to match the image spectra after continuum removal from both data sets. The image and reference spectra are compared at each selected wavelength in a least-squares sense and the root mean square (rms) error is determined for each reference spectrum. The results of Spectral Feature Fitting include a scale image and rms image output for each reference spectrum or a combined "fit" (Scale/RMS) image for each reference spectrum. Best matches to the reference spectrum are easily detected by selecting the high fit scores or by using 2-D scatterplots to select areas with low rms and high scale.

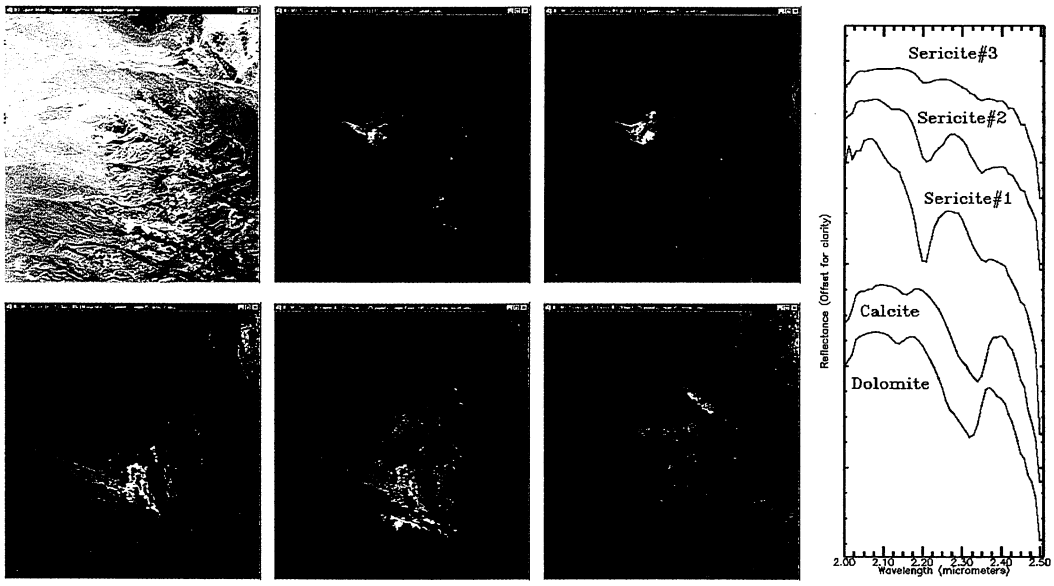

Figure 3: Results for the NGM site showing AVIRIS endmember spectra extracted from the data and identified using a spectral library (right) and Matched Filter mapping results (left). Brighter pixels in the Matched Filter results represent higher abundances.

Mixture-Tuned Matched Filtering is a hybrid method based on the combination of well-known signal processing methodologies and linear mixture theory. The Matched Filter portion of the algorithm maximizes the response of a known endmember and suppressing the response of the composite unknown background (Harsanyi and Chang, 1994) – see Figure 3 below. Mixture-Tuning uses linear spectral mixing theory to constrain the ... to feasible mixtures and reduce false alarm rates (Boardman, 1998a). Figure 4 on the following page shows a visual summary of the NGM mapping results for AVIRIS data collected during 2000 in direct support of Hyperion validation

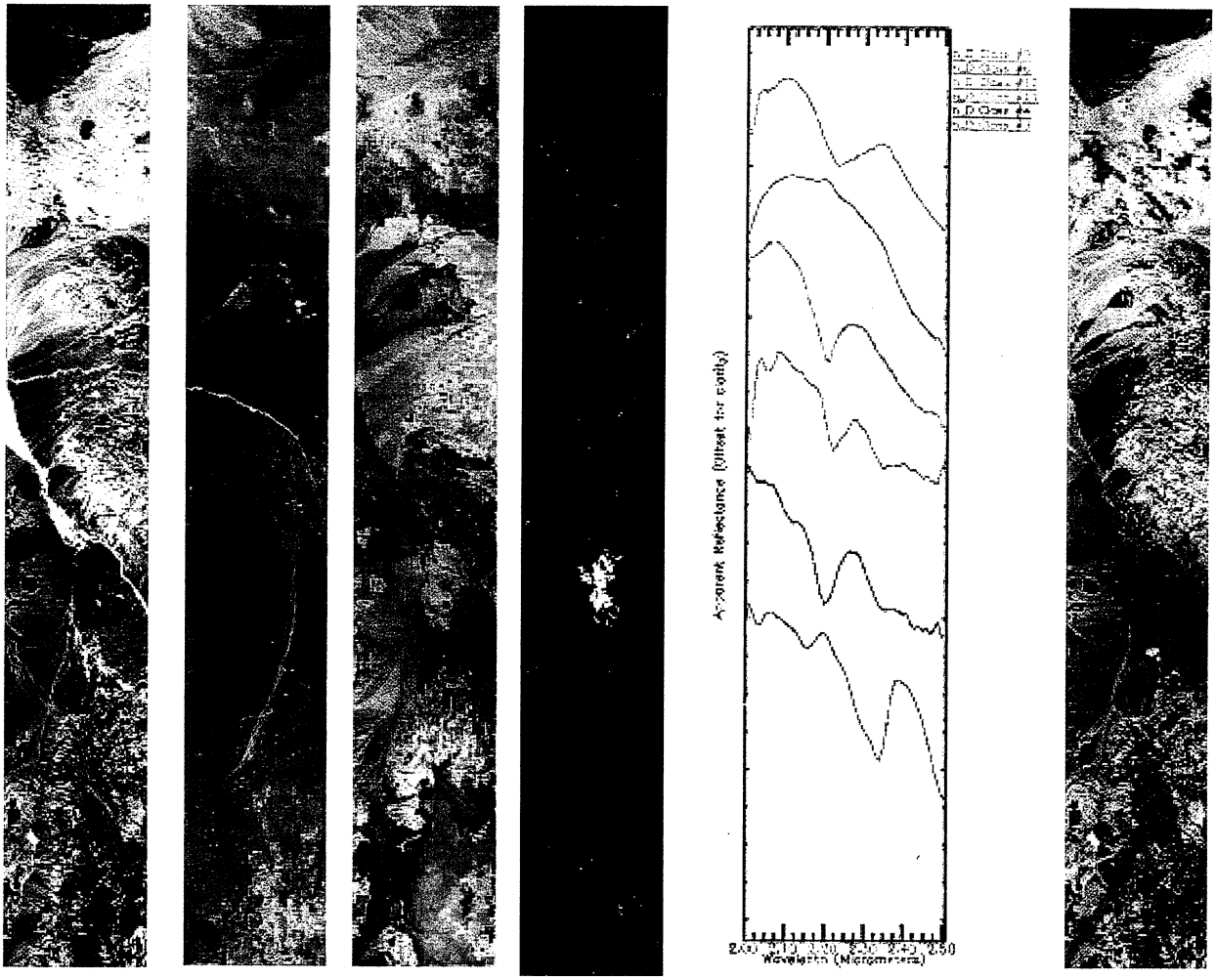

Figure 4: Images and spectra summarizing the AIG approach to analysis of Hyperion data. Images from left to right are: AVIRIS true color image, MNF bands 1, 2, 3 (RGB), MNF bands 4, 5, 6 (RGB), PPI image, extracted endmember spectra, SAM mapping result with class colors corresponding to endmember spectra colors (red=calcite, yellow=dolomite, blue=muscovite#1, brown=muscovite#2, green=muscovite#3, magenta=zeolite, and sea-green=hydrothermal silica).

6.0 Hyperion Validation Plans

Prior to receipt of Hyperion data, we are concentrating on consolidating available AVIRIS and other data for the test sites, compiling mineral maps, and simulating Hyperion performance. We plan to work with the AVIRIS data to generate simulations with Hyperion's 30 meter pixel size and approximate 100:1 (VNIR) and 50:1 (SWIR) signal-to-noise ratios (SNR). We expect that these simulations will answer some of the questions about how Hyperion will perform against our test sites and specific questions of interest for mapping mineral deposits. Questions to be answered include: 1. how will the 30m spatial resolution effect detection of small (vein) occurrences; will subpixel

detection and mapping methods allow us to map critical areas? 2. how will the reduced SNR of Hyperion (as compared to AVIRIS) effect our mapping capabilities?

We have done some direct comparison of the Signal-to-Noise-Ratio (SNR) effects utilizing AVIRIS. AVIRIS data acquired over the period 1989 – 1995 on the ER-2 platform for the NGM site share 20m spatial resolution and approximately 10nm spectral resolution. All data were corrected to apparent reflectance using ATREM (CSES, 1999). SNR for these datasets were not directly computed. Instead, reported SNR for the acquisition year SNR under standard AVIRIS radiance conditions (50% reflectance, solar noon) were used to select a range of representative data. Reported SNR for these data are approximately: 50:1 (1989), 100:1 (1992), and 400:1 (1995) for the D spectrometer (2.0 – 2.5 μm) as reported by Green et al., 1990, 1993, 1996. The 1995 data were also corrected for residual systematic errors utilizing the EFFORT method of Boardman (1998b). This correction is only possible on the 1995 data because of its exceptional signal-to-noise characteristics. Single-pixel spectra were extracted from the data for two key materials at the NGM site; carbonates, and sericitic alteration. Figure 5 shows spectral plots of the 1989, 1992, and 1995 reflectance spectra for calcite and dolomite endmembers. Though there are obvious SNR differences, the position of the diagnostic spectral feature for dolomite near 2.32 mm could be separated from the spectral feature for calcite at all SNR levels. At the 50:1 SNR, there is some calcite/dolomite confusion. It should be clear, that any automated feature-based method will have difficulty picking out the specific absorption features at the lower SNR levels. Figure 6 shows a comparison of spectral plots for single-pixels for sericitic alteration identified at the NGM site. First, note that for both the 1989 and 1992 cases, only two different sericite varieties were distinguishable. The 1995 data indicate that there are actually three distinct species of sericite at the NGM site based on the position of the main feature near 2.2 μm, a fact verified by microprobe analysis (Kruse et al., 1999).

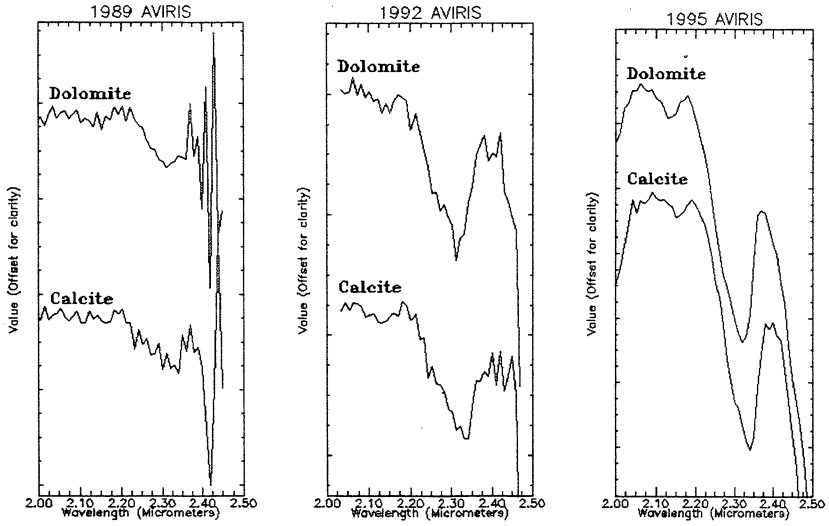

Figure 5: Comparison of 1989 (left), 1992 (center), and 1995 (right) single-pixel AVIRIS spectra for areas identified as calcite and dolomite at the NGM site (from Kruse, 2000).

Plans for analysis of Hyperion data include correction to apparent reflectance utilizing ACORN and analysis using standardized AIG methodologies described above. Validation efforts will concentrate on verifying Hyperion's spatial and spectral resolution as well as SNR performance. We will then compare the Hyperion analysis results for the various sites to those achieved with AVIRIS as well as ground spectral measurements and mapping to determine the utility of Hyperion for geologic applications.

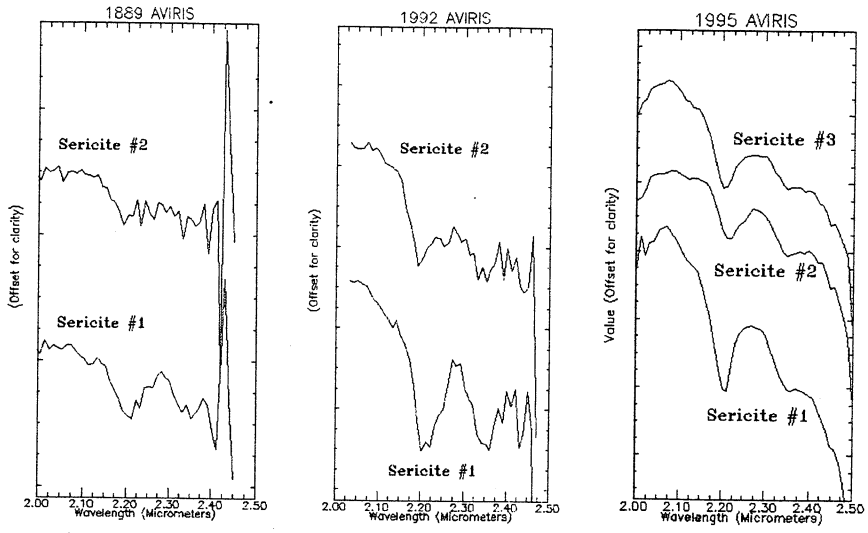

Figure 6 Comparison of 1989 (left), 1992 (center), and 1995 (right) single-pixel AVIRIS spectra for sericitic alteration at the NGM site (from Kruse, 2000).

7.0 Conclusions

We have described our geologic test sites for Hyperion and outlined our analysis approach. The NGM AVIRIS example presented demonstrates the baseline against which the Hyperion data will be judged. This work and other cited references demonstrate that spatial resolution, spectral resolution, and SNR can have dramatic effects on the ability to perform mineral mapping using hyperspectral data. Previous work (Kruse, 2000) indicates that spatial resolution is the key to mapping of detailed, scale-dependent variation. Increasing the pixel size (decreasing the spatial resolution) results in the loss of image detail. There is a tendency to lose small, discrete occurrences of specific materials with larger pixels. The same study indicates that spectral resolution is the key to separation of subtle material differences. Decreasing the spectral resolution results in losses in the ability to distinguish and map fine spectral detail. Coarser spectral resolution can prohibit discrimination and identification of specific minerals. Finally, as shown in Figures 5 and 6, SNR is the key to overall quality of the spectral mapping process. There is decreased capability to define key spectra with decreasing SNR. If the SNR level is inadequate, neither spatial or spectral resolution matters. We expect to validate Hyperion in this context.

Some final comments on expectations for EO-1 Hyperion and future satellite systems: We are NOT expecting Hyperion to perform like 2000 AVIRIS! Hyperion will, however, demonstrate the viability of Satellite Hyperspectral Sensing. A key factor is its potential for site acquisition world-wide. We expect that Hyperion will be useful for geologic mapping on about the level of the 1989 AVIRIS data. Its 30m spatial resolution, 10 nm spectral resolution, and SWIR SNR of 50:1 should produce results similar to those shown for 1989 AVIRIS data in other published work (Kruse, 2000). These capabilities will be combined with airborne systems such as AVIRIS and HyMap to allow scaling of higher spatial and spectral resolution measurements. Future satellite systems should provide sufficient spatial resolution to allow overview coverage (trade off for SNR), spectral resolution around 10 - 20 nm (trade off for SNR), and SNR "as high as possible".

8.0 Acknowledgements

Collection and analysis of support data being used for this Hyperion validation effort were supported over the years by the U.S. Geological Survey, Colorado School of Mines, NASA/JPL, Center for the Study of Earth from Space (CSES, University of Colorado), and Analytical Imaging and Geophysics LLC. Special thanks are due to the JPL AVIRIS team for their dedication and support. Portions of this manuscript and related research were funded by AIG internal research and development (IR&D) in support of NASA EO-1 Hyperion. The 2000 AVIRIS data and additional funding for this research were provided under AIG's EO-1 NASA-funded proposal "EVALUATION AND GEOLOGIC VALIDATION OF EO-1 HYPERION", grant number NCC5-495.

9.0 References Cited

Albers, J. P., and Stewart, J. H., 1972, Geology and mineral deposits of Esmeralda County, Nevada: Nevada Bureau of Mines and Geology Bulletin 78, 80 pages.

Boardman, J. W., 1989, Inversion of imaging spectrometry data using singular value decomposition: in Proceedings, IGARSS '89, 12th Canadian Symposium on Remote Sensing, 4, pp. 2069–2072.

Boardman, J. W., 1993, Automated spectral unmixing of AVIRIS data using convex geometry concepts: in Summaries, Fourth JPL Airborne Geoscience Workshop, JPL Publication 93-26, v. 1, pp. 11–14.

Boardman, J. W., 1998a, Leveraging the high dimensionality of AVIRIS data for improved sub-pixel target unmixing and rejection of false positives: mixture tuned matched filtering, in: Summaries of the Seventh Annual JPL Airborne Geoscience Workshop, Pasadena, CA, p. 55.

Boardman, J. W., 1998b, Post-ATREM polishing of AVIRIS apparent reflectance data using EFFORT: a lesson in accuracy versus precision: in Proceedings of the 8th JPL Airborne Earth Science Workshop: Jet Propulsion Laboratory Publication 99-17, p. 53.

Boardman, J. W., 1999, Precision geocoding of AVIRIS low-altitude data: lessons learned in 1998: in Proceedings of the 8th JPL Airborne Earth Science Workshop: Jet Propulsion Laboratory Publication 99-17, pp. 63–68.

Boardman, J. W., and Kruse, F. A., 1994, Automated spectral analysis: A geological example using AVIRIS data, northern Grapevine Mountains, Nevada: in Proceedings, Tenth Thematic Conference, Geologic Remote Sensing, 9-12 May 1994, San Antonio, Texas, pp. I-407–I-418.

Boardman, J. W., Kruse, F. A., and Green, R. O., 1995, Mapping target signatures via partial unmixing of AVIRIS data: in Summaries, Fifth JPL Airborne Earth Science Workshop, JPL Publication 95-1, v. 1, pp. 23–26.

Clark, R.N. and Swayze, G.A., 1995, Mapping Minerals, Amorphous Materials, Environmental Materials, Vegetation, Water, Ice and Snow, and Other Materials: The USGS Tricorder Algorithm. Summaries of the Fifth Annual JPL Airborne Earth Science Workshop, January 23–26, R.O. Green, Ed., JPL Publication 95-1, pp. 39–40.

Clark, R.N., A.J. Gallagher, and G.A. Swayze, 1990, Material Absorption Band Depth Mapping of Imaging Spectrometer Data Using a Complete Band Shape Least-Squares Fit with Library Reference Spectra: in Proceedings of the Second Airborne Visible/Infrared Imaging Spectrometer (AVIRIS) Workshop. JPL Publication 90-54, pp. 176–186, 1990.

Center for the Study of Earth from Space (CSES), 1999, Atmosphere REMoval Program (ATREM) User's Guide, Version 3.1, Center for the Study of Earth from Space, Boulder, Colorado, 31 pages.

Clifton, C.G., Buchanan, L.J. and Durning, W.P., 1980, Exploration Procedure and Controls of Mineralisation in the Oatman Mining District, Oatman, Arizona: New York, So. Of Mining Engineers of AIME, Reprint, 80-143, 17 pages.

Elvidge, C.D., 1985, Separation of leaf water and mineral absorption in the 2.2 micrometre Thematic Mapper band: Unpublished Ph.D. dissertation, Stanford University, 182 pages.

Gao B. and Goetz, A. F. H., 1990, "Column atmospheric water vapor and vegetation liquid water retrievals from airborne imaging spectrometer data." Journal of Geophysical Research, 95(D-4): pp. 3549–3564.

Goetz, A. F. H., Vane, G., Solomon, J. E., and Rock, B. N., 1985, Imaging spectrometry for earth remote sensing: Science, 228, pp. 1147–1153.

Green, A. A., Berman, M., Switzer, B., and Craig, M. D., 1988, A transformation for ordering multispectral data in terms of image quality with implications for noise removal: IEEE Transactions on Geoscience and Remote Sensing, v. 26, no. 1, pp. 65–74.

Green, R. O., Conel, J. E., Carrere, V., Bruegge, C. J., Margolis, J. S., Rast, M., and Hoover, G., 1990, Determination of the in flight spectral and radiometric characteristics of the Airborne Visible/Infrared Imaging Spectrometer (AVIRIS): in Proceedings, 2nd Airborne Visible/Infrared Imaging Spectrometer (AVIRIS) workshop, JPL Publication 90-54, pp. 15–34.

Green, R. O., Conel, J. E., Helmlinger, M., van den Bosch, J., Chovit, C. and Chrien, T., 1993, Inflight calibration of AVIRIS in 1992 and 1993: in Summaries, 4th Annual JPL Airborne Geoscience Workshop, JPL Publication 93-26, pp. 69–72.

Green, R. O., Conel, J. E., Margolis, J., Chovit, C., and Faust, J., 1996, In flight calibration and validation of the Airborne Visible/Infrared Imaging Spectrometer (AVIRIS): in Proceedings, 6th Airborne Visible/Infrared Imaging Spectrometer (AVIRIS) workshop, JPL Publication 96-4, v. 1, pp. 115–126.

Harsanyi, J. C., and Chang, C. I., 1994, Hyperspectral image classification and dimensionality reduction: An orthogonal subspace projection approach: IEEE Trans. Geosci. and Remote Sens., v. 32, pp. 779–785.

Hudson, D. M., 1984, Geology of the Comstock District, Storey County, Nevada: Report prepared for United Mining Company of Nevada, Virginia City, Nevada, 29 pages.

Huntington, J.F. and Boardman, J.W., 1995, Semi-quantitative Mineralogical and Geological Mapping with 1995 AVIRIS Data, Proc. Spectral Sensing Research '95, ISSSR, Published by the AGPS, 26 Nov–1 Dec, 1995, Melbourne, Australia.

Huntington, J.F., Green, A.A. and Craig, M.D., 1989. Identification - the Goal Beyond Discrimination. The status of mineral and lithological identification from high resolution spectrometer data: Examples and challenges. Invited Keynote paper. In "Remote Sensing: An Economic Tool for the Nineties", IGARSS '89, 12th Canadian Symposium on Remote Sensing, Vancouver, 10-14 July, 1989, Vol.1, pp. 6–11. IEEE#89CH2768-0

Huntington, J.F., Green, A.A., and Craig, M.D., 1988, Mineral and Lithological Mapping with the GER 64 Band Scanner: US and Australian Examples. Poster and presented paper, 6th Thematic Conf. on "Remote Sensing for Mineral Exploration", Houston Texas, May 16-19 1988 pp. 39–40.

Hutsinpiller, A., 1988, Discrimination of Hydrothermal Alteration Mineral Assemblages at Virginia City, Nevada, Using the Airborne Imaging Spectrometer. Remote Sensing of Environment, Vol. 24, pp.53–66.

Kruse, F. A., 1988, Use of Airborne Imaging Spectrometer data to map minerals associated with hydrothermally altered rocks in the northern Grapevine Mountains, Nevada and California: Remote Sensing of Environment, v. 24, no. 1, pp. 31–51.

Kruse, F. A., 1997, Regional Geologic Mapping Along the Colorado Front Range from Ft Collins to Denver Using the Airborne Visible/Infrared Imaging Spectrometer (AVIRIS): in proceedings, 12th Thematic Conference, Applied Geologic Remote Sensing, 17-19 November 1997, Environmental Research Institute of Michigan (ERIM), Ann Arbor, MI, pp. II-91–II-98.

Kruse, F. A., 2000, The effects of spatial resolution, spectral resolution, and SNR on geologic mapping using hyperspectral data, northern Grapevine Mountains, Nevada: in Proceedings of the 9th JPL Airborne Earth Science Workshop: Jet Propulsion Laboratory Publication.

Kruse, F. A., and Huntington, J. H., 1996, The 1995 Geology AVIRIS Group Shoot: in Proceedings, 6th JPL Airborne Earth Science Workshop: Jet Propulsion Laboratory Publication 96-4, v. 1, pp. 155–166.

Kruse, F. A., and Lefkoff, A. B., 1999, Analysis of Spectral Data of Manmade Materials, Military Targets, and Background Using an Expert System Based Approach: In Proceedings, ISSSR'99, 31 October – 4 November 1999, Las Vegas, Nevada.

Kruse, F. A., Huntington, J. H., and Green, R. O, 1996, Results from the 1995 AVIRIS Geology Group Shoot: in Proceedings, 2nd International Airborne Remote Sensing Conference and Exhibition: Environmental Research Institute of Michigan (ERIM), Ann Arbor, v. I, pp. I-211–I-220.

Kruse, F. A., Lefkoff, A. B., Boardman, J. B., Heidebrecht, K. B., Shapiro, A. T., Barloon, P. J., and Goetz, A. F. H., 1993a, The Spectral Image Processing System (SIPS) - Interactive Visualization and Analysis of Imaging Spectrometer Data: Remote Sensing of Environment, Special issue on AVIRIS, May-June 1993, v. 44, pp. 145–163.

Kruse, F. A., Lefkoff, A. B., and Dietz, J. B., 1993b, Expert System-Based Mineral Mapping in northern Death Valley, California/Nevada using the Airborne Visible/Infrared Imaging Spectrometer (AVIRIS): Remote Sensing of Environment, Special issue on AVIRIS, May-June 1993, v. 44, pp. 309–336.

Kruse, F. A., Boardman, J. W., and Huntington, J. F., 1999, Fifteen Years of Hyperspectral Data: northern Grapevine Mountains, Nevada: in Proceedings of the 8th JPL Airborne Earth Science Workshop: Jet Propulsion Laboratory Publication, JPL Publication 99-17, pp. 247–258.

Marsh, S.E. and McKeon, J.B., 1983, Integrated Analysis of High-Resolution Field and Airborne Spectroradiometer Data for Alteration Mapping, Econ. Geol. Vol.78, No.4, pp.618-632.

Moring, B., 1986, Reconnaissance surficial geologic map of northern Death Valley, California and Nevada: U. S. Geological Survey Miscellaneous Field Studies Map MF-1770, 1:62,500, 1 sheet.

Thorson, J.P., 1971, Igneous Petrology of the Oatman Mining District, Mohave County, Arizona, Unpublished Ph.D dissertation, Uni. California, Santa Barbara, 189 pages.

Thompson, J.V., 1956, Geology of the Virginia City Quadrangle, Nevada, USGS Bull. 1042-C, 75 pages.

Whitebread, D.H., 1976, Alteration and Geochemistry of Tertiary Volcanic Rocks in Parts of the Virginia City Quadrangle, Nevada, US Geological Survey Professional Paper No. 936, 43 pages.

Wrucke, C. T., Werschkey, R. S., Raines, G. L., Blakely, R. J., Hoover, D. B, and Miller, M. S., 1984, Mineral resources and mineral resource potential of the Little Sand Spring Wilderness Study Area, Inyo County, California: U. S. Geological Survey Open File Report 84-557, 20 pages.

HYPERSPECTRAL IMAGE CLASSIFICATION USING A SELF-ORGANIZING MAP

P. Martínez,[1] J.A. Gualtieri,[2] P.L. Aguilar,[1] R.M. Pérez,[1] M. Linaje,[1] J.C. Preciado,[1] A. Plaza[1]

1. INTRODUCTION

The use of hyperspectral data to determine the abundance of constituents in a certain portion of the Earth's surface relies on the capability of imaging spectrometers to provide a large amount of information at each pixel of a certain scene. Today, hyperspectral imaging sensors are capable of generating unprecedented volumes of radiometric data. The Airborne Visible/Infrared Imaging Spectrometer (AVIRIS), for example, routinely produces image cubes with 224 spectral bands (Green, 1988-2000). This undoubtedly opens a wide range of new possibilities, but the analysis of such a massive amount of information is not an easy task. In fact, most of the existing algorithms devoted to analyzing multispectral images are not applicable in the hyperspectral domain, because of the size and high dimensionality of the images.

Hyperspectral unmixing or linear pixel unmixing is becoming increasingly popular for the analysis and interpretation of hyperspectral images (Martínez et al., 1999). The basic assumption is that the signal received from each pixel can be considered as a simple linear combination of the spectral contributions of all pixel components. The technique, therefore, decomposes the scene in such a way as to recover the fractional contributions of the fundamental components or "endmembers" (as abundance or fraction images). This provides a means of extracting sub-pixel information from the scenes, which is particularly advantageous when the size of the interesting ground elements is much smaller than the image resolution and there is dominance of "mixed" pixels.

Unsupervised clustering is a challenging problem in many areas of data analysis (Antonille & Gualtieri, 2000). It can be stated as follows: given a set of N data points in a feature space of D dimensions,

$$\{x_1, x_2, ..., x_N\} \in R^D, x_i = (x_{i1}, x_{i2}, ..., x_{iD}), i = 1, ..., N, \quad (1)$$

we wish to characterize K clusters for the data, where K is obtained from statistical information about the data using some distance metric,

$$d_{ij} = d(x_i, x_j). \quad (2)$$

The principal characteristic of unsupervised clustering is that it does not incorporate any previous knowledge about the data. Since ground truth data in remote sensing is expensive and hard to obtain, the use of unsupervised procedures has become more relevant in this field during recent years. In particular, several unsupervised procedures to process hyperspectral data are available in well-known commercial software systems as Research Systems ENVI™.

The application of neural networks to perform unsupervised classification of hyperspectral data has been tested by several authors (Jiménez et al., 1999) and also by us in some previous work (Aguilar et al., 1998; Martínez et al., 1999; Aguilar et al., 2000a, Aguilar et al., 2000b). We have also focused on analyzing the intrinsic capability of neural networks to parallelize the whole hyperspectral unmixing process (Pérez et al., 1999). The results shown in this work indicate that neural network models are able to find clusters of closely related hyperspectral signatures, and thus can be used as a powerful tool to achieve the desired classification.

[1] Departamento de Informática, Universidad de Extremadura, Avda. de la Universidad s/n, 10071 Cáceres, SPAIN
E-mail: pablomar@unex.es

[2] Global Science and Technology at Applied Information Sciences Branch, NASA/GSFC, Greenbelt, Maryland 20771, U.S.A. E-mail: gualt@peep.gsfc.nasa.gov

One of the most widely used unsupervised neural network algorithms is the Self-Organizing Map (SOM), proposed by Kohonen, 1995-1997. This approach has been successfully applied in many different fields, including image analysis and computer vision, handwritten text recognition, analysis and recognition of human voice and telecommunications. Some reasons for using SOM to perform hyperspectral analysis have been described by Bruske and Merenyi, 1999, who highlight the computational speed provided by this method when implemented by hardware in the form of a massively parallel algorithm, surpassing the performance of conventional classification algorithms. Since the Kohonen algorithm is simple and intuitive, highly parallelizable (which can lead to an easy VLSI implementation based on systolic arrays or FPGAs) and is easily extendable to a high number of dimensions, we have selected it as our starting point to deal with hyperspectral data.

The present work discusses the possibility of using a Self Organizing neural network to perform unsupervised classification of hyperspectral images. In sections 3 and 4, the topology of the proposed neural network and the training algorithm are respectively described. Section 5 provides the results we have obtained after applying the proposed methodology to real hyperspectral data, described in section 2. Different parameters in the learning stage have been modified in order to obtain a detailed description of their influence on the final results. Finally, in section 6 we provide the conclusions at which we have arrived.

2. DATA

The hyperspectral unmixing algorithms proposed in this work have been tested using the public domain Indian Pines hyperspectral dataset, which has been previously used in many different studies. This image was obtained from the AVIRIS imaging spectrometer at Northern Indiana on June 12, 1992 from a NASA ER2 flight at high altitude with ground pixel resolution of 17 meters. The dataset comprises 145x145 pixels and 220 bands of sensor radiance without atmospheric correction. It contains two thirds of agriculture (some of the crops are in early stages of growth with low coverage), and one third of forest, two highways, a rail lane and some houses. Ground truth determines sixteen different classes (not mutually exclusive). Water absorption bands (104-108, 150-163 and 220) were removed (Tadjudin and Landgrebe, 1998), obtaining a 200 band spectrum at each pixel. In order to reduce the time of training and testing, we have selected a subscene of the complete Indian Pines dataset (depicted in Figure 1) of size 68 samples x 86 lines at [27-94] x [31-116] in the original image, considering left in the full scene is at (1,1). In the selected subscene there are four known ground truth classes.

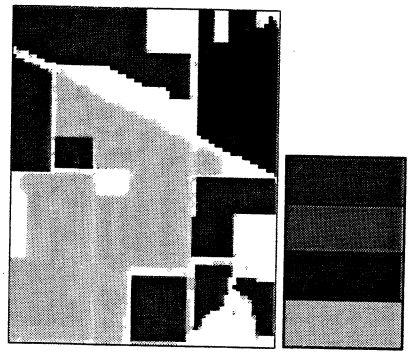

Figure 1. A subset of the Indian Pines hyperspectral dataset with ground truth.

3. TOPOLOGY OF THE PROPOSED NEURAL NETWORK

The Self-Organizing Map (SOM) is based on competitive learning that leads to the construction of topologic maps representing class prototypes. In order to understand the topology of the proposed neural network, we first need to define some basic concepts. A neuron is an information-processing unit. Neurons are connected

by synapses or connecting links, each of them characterized by a weight. Specifically, a signal x_j at the input of synapse j connected to neuron k is multiplied by the synaptic weight w_{kj}.

A neural network is a set of neurons organized in the form of layers. In the simplest form, an input layer projects onto an output layer of neurons. If the input layer has N units and the output layer has M units, each unit in the output layer owns N weights associated to the connections which come from the input layer, so that the set of neural weights is organized in the form of a two-dimensional lattice (W_{MxN}).

Our proposed network architecture is depicted in Figure 2 (Aguilar et al., 2000b). In our case, N corresponds to the number of channels of the hyperspectral image and M is the number of classes or prototypes to be extracted by the network. M must be carefully selected according to some metric (we will insist on this issue later on in the paper). There are feedforward connections from the input layer to the output layer and self-feedback and lateral feedback connections in the output layer. These two types of local connections serve two different purposes:

a) In the classification stage, the weighted sum $x \cdot W_i$ (scalar product) of the input signals x at each neuron i performs feature detection: each neuron produces a selective response to input signals.

b) In the learning stage, lateral and self-feedback connections produce excitatory or inhibitory effects depending on the distance from the corresponding output layer neuron to the winning neuron (Aguilar et al., 2000c). Their associated weights are used to determine the W_i classification prototype for each neuron.

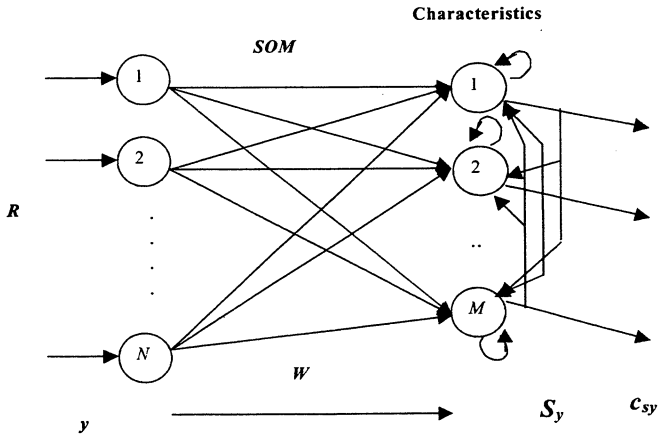

Figure 2. SOM neural network topology including weight matrix W and self-feedback and lateral feedback connections.

4. TRAINING ALGORITHM

There are five basic steps involved in the training algorithm. These steps are repeated until the topological map is completely formed:

a) Initialization: choose random values for the initial weight vectors, $w_i(0), i = 1,2,...M$. It is desirable to keep the magnitude of the weights small.

b) Sampling: choose an input pattern x(n) belonging to a set of learning patterns or references, R. The selection is done randomly.

c) Similarity Matching: find the best-matching (winning) neuron i* at time t, using the minimum-distance criterion as shown in the following equation, where dist is the euclidean distance:

$$i^*[x(n)] = \min_j dist\{x(n), w_j(t)\}, j = 1,2,...,M \quad (3)$$

d) Learning: adjust the synaptic weight vectors of all neurons, using the update formula (4), where $\eta(t)$ is a learning-rate parameter, and $\gamma(t,i,i^*[x(n)])$ is a Gaussian neighborhood function centered around the winning neuron. The size of the neighborhood is determined by the reference distance $\sigma(t)$ (see equation 5).

$$w_i(t+1) = w_i(t) + \eta(t) \cdot \gamma(t,i,i^*[x(n)])(x(n) - w_i(t)) \tag{4}$$

From the different options to select the previously mentioned parameters, taking into account the studies done in Aguilar, 2000, we have selected the following ones:

$$\eta(t) = \frac{1}{t}, \qquad \gamma(t,i,i^*[x(n)]) = \frac{e^{dist(i^*,i)^2}}{\sigma(t)}, \qquad \sigma(t) = \frac{\sigma_0}{t}. \tag{5}$$

e) Continue from step b) until no noticeable changes in the weight space are observed, or until the maximum convergence time is achieved.

In order to analyze a hyperspectral image using this algorithm, the network must be trained with hyperspectral signatures obtained directly from the image.

The weights initially associated with each output layer neuron contain the hyperspectral signatures of some carefully selected pixels on the image (according with their spatial distribution).

5. RESULTS AND DISCUSSION

We have applied our proposed neural network to real hyperspectral data, described in section 2. Since there are several parameters involved in the training algorithm (described in the previous section) in this section we analyze the influence of those parameters in the process of class prototype extraction. In particular, the parameters that we consider in the present study are the number of iterations until convergence of the neural network is reached, the size of neighborhood function γ centered around the winning neuron, which is determined by $\sigma(t)$, and the number of neurons in the output layer of the neural network.

The experiment is performed as follows. We train the network with all the hyperspectral signatures of the image. During the learning stage, we go through all the pixels of the image starting from a random pixel which is different in each of the iterations. Once class prototypes have been extracted, each pixel is classified and the confusion matrix (Chuvieco, 2000) is obtained. This matrix allows us to visualize winning neuron density for each class.

The characteristics of the confusion matrix provides us with a comprehensive visualization of distribution in N-dimensional space, and may indicate the accuracy of the classification. Since each column corresponds to an output neuron, if one column presents high values for different classes, the overall accuracy of the classification should be low. In order to measure the degree of accuracy of the classification, we propose the following metric based on the topology of the confusion matrix:

$$E_i = \frac{Xm_i}{Xs_i}, \qquad Xm_i = \underset{i}{Max}(X_{ij}), \qquad Xs_i = \sum_j X_{ij}. \tag{6}$$

Xm_i is the maximum value for a column of the confusion matrix and Xs_i is the sum of all the values in that column. E_i provides information about the capacity of each neuron to discriminate between the classes, and can be averaged for all the neurons in the network, providing a general measure about the accuracy of the classification.

The performance of the SOM Neural Network depends on a lot of adjusting parameters:

1. **Number of output neurons:** the ideal numbers of output neurons must be equal to the number of ground truth classes, associating exactly one neuron with one class. Usually this fact is not possible if we have a larger number of output neurons that ground truth classes. In this way, one correct classification

uses several neurons for each ground truth class. In the Indian Pines ground-truth image there are 16 classes (plus one class of unclassified pixels).

2. **Weigth initialization:** the weights w_{ij} initially associated with each neuron contain random values.
3. **Order to scan the image:** a random initial point of the image is selected at each iteration.
4. **Neighborhood function:** as mentioned before, our choice for the neighborhood function is the Gaussian function.
5. **Reference distance σ(t):** when the algorithm starts (t=1), the neural lattice is in a random state, the neighborhood function in these first iterations of the algorithm must have similar values for i to include a large number of neurons and obtain some average values (high σ(0) values). When t increases, $\gamma(t,i,i^*[x(n)])$ needs to be adjusted to reduce the number of neighbor neurons. Care must be taken into account to avoid a quickly reduction of the number of neighborhood neurons, this reduction can be accomplished by changing the reference distance $\sigma(t)$. Our choice for the reference distance evolution is $\sigma(t)=(1/t)^2$

The parameters that we analyze in the present study are the number of neurons in the output layer, the number of iterations of the neural network and the neighborhood starting value σ_0. Next, some results obtained for the hyperspectral data described in section 2 are provided. In our first experiment, we have considered 16 neurons in the output layer, 100 iterations and $\sigma_0 = 2$. Table 1 shows the resulting confusion matrix and Figure 3 shows the the resulting classification provided by the neural network using the previously mentioned parameters along with a greyscale representation of the confusion matrix shown in Table 1.

A favorable result would be obtained if neurons activate exclusively for a particular class, discriminating this class from the others. In the confusion matrix, this can be graphically expressed as a row for which several columns present high values. In Figure 3 we can appreciate this situation at four different rows (2,6,10,11 and 17). The fact that column values overlap indicates an inaccurate classification.

Another indicator of the quality of the classification is the continuity of high values in the rows of the confusion matrix (this fact should produce bright contiguous rows in the confusion matrix image). In this experiment, the topology of the resulting classes is not preserved since we can appreciate several discontinuities in the learnt classes. The overall accuracy of the classification obtained in this experiment was 60% according to the measure provided in equation 6. Nevertheless, we have to take into account that class 17 in the confusion matrix (see Table 1) corresponds to pixels which have not been classified during the process, and we are considering these pixels when calculating the overall accuracy (if we do not consider these pixels, accuracy increases to 80%).

		Neurons in the output layer															
		1	2	3	4	5	6	7	8	9	10	11	12	13	14	15	16
Classes	1	0	0	0	0	0	0	0	0	0	0	0	0	0	0	0	0
	CORN-NOTILL - 2	0	0	0	0	0	0	98	245	71	161	162	98	11	1	115	46
	3	0	0	0	0	0	0	0	0	0	0	0	0	0	0	0	0
	4	0	0	0	0	0	0	0	0	0	0	0	0	0	0	0	0
	5	0	0	0	0	0	0	0	0	0	0	0	0	0	0	0	0
	GRASS - 6	242	9	253	160	52	9	0	0	0	0	0	0	1	1	5	0
	7	0	0	0	0	0	0	0	0	0	0	0	0	0	0	0	0
	8	0	0	0	0	0	0	0	0	0	0	0	0	0	0	0	0
	9	0	0	0	0	0	0	0	0	0	0	0	0	0	0	0	0
	SOYBEAN 1 – 10	0	0	0	0	0	0	61	0	137	42	0	180	1	1	28	277
	SOYBEAN 2 – 11	12	0	8	0	0	0	471	3	521	136	8	471	66	6	17	207
	12	0	0	0	0	0	0	0	0	0	0	0	0	0	0	0	0
	13	0	0	0	0	0	0	0	0	0	0	0	0	0	0	0	0
	14	0	0	0	0	0	0	0	0	0	0	0	0	0	0	0	0
	15	0	0	0	0	0	0	0	0	0	0	0	0	0	0	0	0
	16	0	0	0	0	0	0	0	0	0	0	0	0	0	0	0	0
	UNCLASS. - 17	121	66	186	161	101	56	127	19	72	24	54	37	191	165	39	36

Table 1. Resulting confusion matrix for the Indian Pines dataset considering 100 iterations, 16 neurons in the output layer and $\sigma_0 = 2$. Non-zero cells in the matrix are highlighted.

In our second experiment, we consider a smaller number of neurons in the output layer (5), 80 iterations and $\sigma_0 = 4$. Figure 4 shows the resulting classification and the associated confusion matrix. We can appreciate an improvement in the topology of the confusion matrix (horizontal "lines" are more contiguous). In this case, the overall accuracy is 60%, without considering the unclassified pixels.

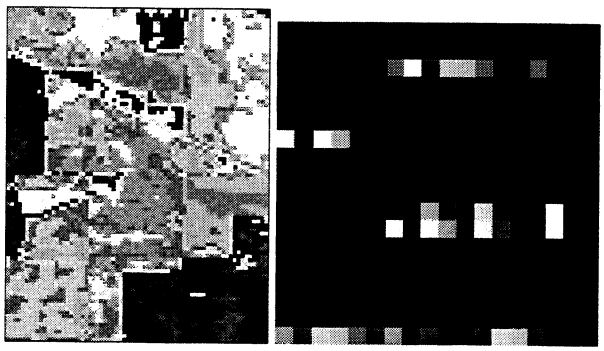

Figure 3. Resulting classification and greyscale representation of the confusion matrix for the Indian Pines dataset considering 100 iterations, 16 neurons in the output layer and $\sigma_0 = 2$. The time used for this computation was approximately 60 minutes in an AMD K-7 600 MHz Processor with 128 Mb of SDRAM memory and IDL 5.4.

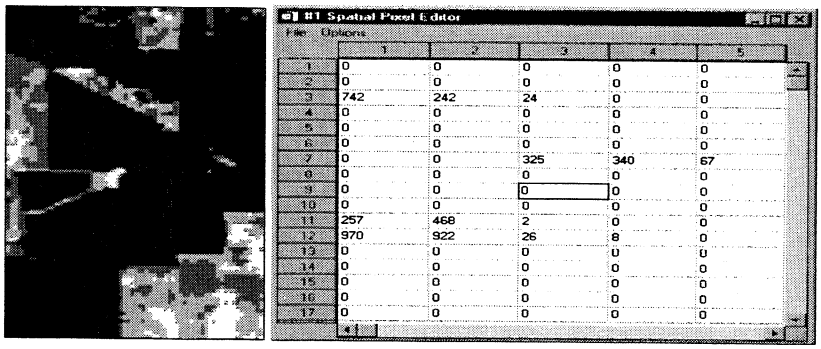

Figure 4. Resulting classification and associated confusion matrix for the Indian Pines dataset considering 80 iterations, 5 neurons in the output layer and $\sigma_0 = 4$. The time used for this computation was 20 minutes in an AMD K-7 600 MHz Processor with 128 Mb of SDRAM memory and IDL 5.4.

Finally, in our last experiment we increase the number of neurons in the output layer (16), we decrease the number of iterations (20) and consider $\sigma_0 = 12$. The results are addressed in Figure 5. A general improvement in the topology is achieved in this experiment, and the overall accuracy in this case is 72%, due to the fact that we compensate the increase in the number of neurons with a subsequent increase in the number of neurons that are considered in the competitive step ($\sigma_0 = 12$). Table 2 shows other experiments we have performed over the Indian Pines hyperspectral dataset.

As we can appreciate in Figure 5, the increase in the number of neurons produces some discontinuities in the topology, but the overall performance increases due to the reduction in the overlapping percentage between bright zones (high values) in the confusion matrix. These facts can be reduced increasing σ_0.

From the previously addressed results, we can conclude:

1. The number of iterations needed to obtain an acceptable accuracy is low compared to other SOM applications. This fact is probably related to the high dimensionality of hyperspectral signatures.

2. It is more efficient, in terms of accuracy, to increase the number of neurons and decrease the number of iterations. As we increase the number of neurons, the overall accuracy increases, but the topology of the classes is poor.
3. When the SOM neural network has a large number of neurons in the output layer, the initial reference distance must be increased in order to maintain similar performance values in the competitive process. In this sense, $\sigma(t)$ plays an important role.
4. Further work is still needed in order to achieve a reasonable compromise between topology preservation, $\sigma(t)$ function and overall accuracy.

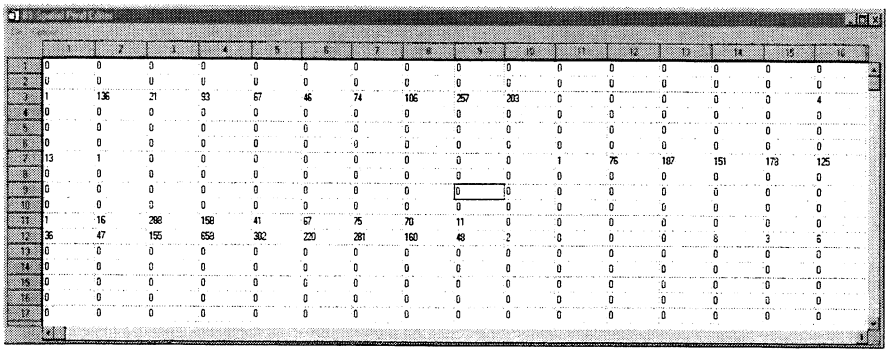

Figure 5. Resulting classification and greyscale representation of the confusion matrix for the Indian Pines dataset considering 20 iterations, 16 neurons in the output layer and $\sigma_0 = 16$. The time used for this computation was 7 minutes in an AMD K-7 600 MHhz Processor with 128 Mb of SDRAM memory and IDL 5.4.

Number of neurons	Number of iterations	Size of neighborhood (σ_0)	Accuracy (%)
16	400	10	74
	150	6	73
	60	2	73
	40	14	73
	20	12	74
8	60	6	70
	60	4	70
6	150	2	66
	60	2	65
	60	2	63
5	80	4	60
	30	1	66

Table 2. Other experiments performed over the Indian Pines dataset.

6. CONCLUSIONS

We have presented a new approach to unsupervised classification of hyperspectral images using a Self Organizing Map. The overall performance of the method has been tested by its application to real hyperspectral data. The availability of ground truth allows us to introduce a new statistical measure to quantify the accuracy of the resulting classification. Since the training stage of the neural network incorporates several parameters, we have studied the influence of some of these parameters on the final result.

ACKNOWLEDGEMENTS

Fundings from Junta de Extremadura (PRI Program, IDUAP Grant) and European Community (LFR Program, TEITORS Grant) are also gratefully acknowledged.

REFERENCES

Aguilar, P.L , Martínez, P., Pérez R.M., Hormigo, A., "Abundance Extractions from AVIRIS Images Using a Self Organizing Neural Network," *Summaries of the IX JPL Airborne Earth Science Workshop*, pp. 281-286, JPL/NASA, 2000a.

Aguilar, P.L., *Cuantificación de Firmas Hiperespectrales Usando Mapas Autoorganizativos*, PhD Thesis, Escuela Politecnica de Cáceres, Universidad de Extremadura, 2000c.

Aguilar, P.L., Pérez, R.M., Martínez, P., Bachiller, P., Merchán, A., "Spectra Evaluation and Recognition in the Mixture Problem Using SOFM Algorithm," *Proc. International Symposium on Engineering of Intelligent Systems, (EIS'98)*, 1998, Vol. 2, pp. 118-124.

Aguilar, P.L., Plaza, A., Martínez, P., Pérez, R.M., "Endmember Extraction by a Self-Organizing Neural Network on Hyperspectral Images," *Proc. International Conference on Automation, Robotics and Computer Vision*, Nanyang Technological Institute, Singapore, 2000b.

Antonille, S. and Gualtieri, J.A., "Visualizing Clusters in High-Dimensional Data with a Kohonen Self Organizing Map," *Technical Report*, 2000.

Bruske, J. and Merényi, E., 1999, "Estimating the Intrinsic Dimensionality of Hyperspectral Images," *Proc. European Symposium on Artificial Neural Network, ESANN'99*, Brussels, Belgium, 21-23 April, 1999, pp. 105-110.

Chuvieco, E., *Fundamentos de Teledetección Espacial*, Ediciones Rialp, Spain, 2000.

Green, R.O., Editor, AVIRIS Earth Science Workshop Proceedings, 1988-2000. Available at http://makalu.jpl.nasa.gov/

Jimenez, L.O., Morales-Morell, A., Creus, A., "Classification of Hyperdimensional Data Based on Feature and Decision Fusion Approaches Using Projection Pursuit, Majority Voting, and Neural Networks," *IEEE Trans. Geoscience and Remote Sensing*, Vol. 37, Issue 3, Part 1, May 1999, pp. 1360 –1366.

Kohonen, T., *Self-Organizing Maps (2nd ed.)*, Springer Series in Information Science. 1.995-1.997

Martínez, P., Pérez, R.M., Aguilar, P.L., Bachiller, P. and Diaz, P., "A Neuronal Tool for AVIRIS Hyperspectral Unmixing," *Summaries of the IX JPL Airborne Earth Science Workshop*, pp. 281-286, JPL/NASA, 1999.

Pérez, R.M., Aguilar, P.L., Bachiller, P. and Martínez, P., "Neural Network Quantifier for Solving the Mixture Problem and its Implementation by Systolic Array," *Microelectronics Journal*, 30 (1), pp. 77-82, 1999.

Taudjin, S. and Landgrebe, D., *Classification of High Dimensional Data with Limited Training Samples*, Doctoral Thesis, School of Electrical Engineering and Computer Science, Purdue University, 1998.

HYPERSPECTRAL REMOTE SENSING IN LONG VALLEY CALDERA: ISSUES OF SCALE, RESOLUTION, AND SIGNAL TO NOISE

Brigette A. Martini,[1] Eli A. Silver,[2] and Donald C. Potts[3]

1. INTRODUCTION

This study focuses primarily on the study, monitoring, and hazard evaluation of active volcanic regions using airborne hyperspectral imagery. The age of hyperspectral satellites is now a reality, and as such, it is important to test this technology's strengths and weaknesses as a viable tool in the hands of volcanologists studying active volcanic regions all over the world. Though one satellite (NASA's Hyperion) is now flying, little data has been seen by the scientific community at large. Other hyperspectral satellites have imminent launch dates; however until more space borne data is available, airborne data that approximates space borne instrument characteristics can be used to study volcanic regions of interest. The datasets used in this study image Long Valley Caldera and the Mono-Inyo Volcanic chain located in central-eastern California. The AVIRIS and HyMap data vary in spatial resolution, instrument signal-to-noise ratios and spectral sampling. Though the exact characteristics of various space borne satellites are not matched, they are close enough to draw important conclusions regarding hyperspectral imaging's abilities as a volcanology tool. We compare spatial resolution of the instruments and relate that to the scale of the problems and phenomena being studied.

2. SETTING

Long Valley Caldera formed approximately 760,000 years ago in an eruption that expelled over 600 km^3 of ash and lava (Bailey et al, 1976). Since this event, several successive eruptive events have covered the region with other volcanic flows and domes including the young north-south trending Mono- Inyo volcanic chains that lie in the western caldera. The rhyodacitic stratovolcano Mammoth Mt. is the southernmost volcanic center of the chain. The most recent volcanic activity in the Inyo occurred ~600 years ago and includes phreatic explosion pits on the north flank of Mammoth Mt.

2.1 Hydrothermal system

The hydrothermal system seen today is the vestige of a 40ka peak in activity (Sorey, 1985). Hydrothermal waters in the caldera appear to have a source in the west from a recharge zone at the Sierra front. The waters flow down along range front faults and caldera ring fractures where they are heated by a magmatic source at depth. Transport of these waters appears to be at approximately 1 km depth, along or just within the top of the Bishop Tuff. Temperatures at depth have been directly measured in wells and reached 214°C at one site, though geothermometry suggests source reservoirs reach 240°C (Sorey, 1991). Transport and discharge of these waters then occurs along various fault systems in the western and central caldera. Once at the surface, the hydrothermal waters flow in a plume-like fashion south-eastwards, populating the eastern caldera with a slightly thermal marsh-like environment. Waters are predominantly alkaline in chemistry throughout the caldera and rarely reach boiling. Temperatures range from ~79-93°C in the central hotter regions and cool to 20-25°C in the eastern caldera. Extensive deposits of travertine and sinter can be seen in these areas, though present deposition is primarily travertine (Lipshie, 1976).

[1] Earth Sciences Department, UCSC, bmartini@es.ucsc.edu
[2] Earth Sciences Department, UCSC, esilver@es.ucsc.edu
[3] Ecology and Evolutionary Biology Department, UCSC, potts@biology.ucsc.edu

Hydrothermal alteration products generally consist of argillic phase kaolinite and montmorillinite with localized distributions of alunite and pyrophyllite.

These pools and creeks are characterized by a classic vegetation zonation pattern. The waters themselves are inhabited by an array of thermophilic algae and bacteria. Grasses surround the pools and creeks. The grasses are in turn encompassed by a narrow swath of rabbit brush, which gives way to sagebrush and occasional Juniper trees.

Fumarolic discharge also occurs in several locales around the caldera, most notably along normal faults in Fumarole Valley, formation contacts at Basalt Fumarole, along faults on the flanks of Mammoth Mt. and faults of the Discovery Fault Zone. Advanced argillic alteration predominates locally in these regions exemplified by distributions of the high temperature sulfate alunite surrounded by kaolinite and montmorillinite.

2.2 Structure

Regional structure in eastern California has been largely influenced by Basin and Range extension and Eastern California Shear Zone tectonics. Locally, Long Valley Caldera is bounded on the west by ring fractures and the large northwest trending normal faults of the Sierra Nevada Fault Zone that have experienced up to 2000 meters of normal displacement. Smaller northwest trending normal faults cut the central resurgent dome region while ring fractures rim the eastern boundary of the caldera. On a still smaller scale, the western caldera is populated by northwest trending normal faults, north-south trending normal faults and northeast trending transtensional faults. The intersections of these fault zones result in enhanced vertical permeability. Not only do these intersections serve as foci for movement of hydrothermal waters and zones of discharge, but they also had a profound effect on the formation of the Inyo volcanic chain itself.

2.3 Recent activity

The past 25 years have witnessed a period of elevated unrest for Long Valley including magmatic CO_2 degassing, increased seismic activity, dike intrusions, and re-inflation of the resurgent dome. Such restlessness has led to extensive research and monitoring efforts in Long Valley due to its importance as one the great calderas of the world and its proximity to a major trucking lane (U.S. Highway 395), a major flight route for western U.S. commercial and cargo flights, and several small but tourist laden towns including Mammoth Lakes which sits on the eastern flank of Mammoth Mt. However, though sophisticated suites of geophysical and geochemical studies and monitoring programs have been and are being done in this region, few remote sensing based studies have been completed.

3.0 DATA AND METHODS

The data used in this study consisted of archival AVIRIS images from September 4, 1992, newly acquired AVIRIS data from September 14, 2000, and seven HyMap flightlines from September 7, 1999. The AVIRIS datasets were both taken on the high altitude platform with spatial resolutions of approximately 17-18m while the HyMap data taken from a Cessna aircraft, has a spatial resolution of 3-5m. The two AVIRIS datasets differ primarily in the SNR values reported for each of the two years. Measurements made in the 2.0-2.5 um range only reached a SNR of 100:1 in 1992 data, while 2000 AVIRIS imagery reports a SNR of 400:1 in this same wavelength range. While a higher SNR is ultimately preferable, the study of the capabilities of 1992 AVIRIS data is key for assessing the abilities of spacebased hyperspectral imagery with similar SNR values. For example, the Hyperion sensor reports a SNR of less than 50:1 for the 2.0-2.5 um range.

We compare spatial resolution and bandwidth for the HyMap and two separate AVIRIS flights. The spatial resolution seen in AVIRIS data more nearly approximates spatial resolutions likely available from spacebased hyperspectral sensors such as Hyperion's 30 m pixel. Other sensors such as Orbview-4 (aka Warfighter) have proposed resolution as low as 8m, however such resolutions face political barriers as well as tradeoffs with SNR. The spectral sampling also differs markedly between the two airborne sensors. The 224 band AVIRIS has a fixed bandwidth of 10nm while the 126-band HyMap sensor has variable bandwidths ranging from 13-17nm across the four separate spectrometers. Space borne sensors such as the 220 band Hyperion have bandwidths of 10nm which is similar to AVIRIS.

All analysis in this study was completed within the software program ENVI. The data was atmospherically corrected using ATREM (Gao et al., 1993). Field samples have been taken, and will eventually be used in further calibration efforts. However, analysis to date is performed on data with only the ATREM correction applied. The data was spatially subset to regions of particular interest including sites on Mammoth Mt., a site within the Discovery Fault Zone, and sites at Rhyolite Hot Spring and Little Hot Creek (see Fig. 1). Each subset was divided into visible-near infrared (VNIR) chunks (0.40-1.8um for AVIRIS and 0.45-1.8um for HyMap) and short-wave infrared (SWIR) chunks (2.0-2.5 um for both sensors). The principal components like Minimum Noise Fraction (MNF) algorithm was applied to segregate noise and emphasize signal (Green et al., 1988). Purest pixels are then isolated using the Pixel Purity Index (PPI) and average spectral signatures extracted from these purest pixel classes for use in further classifications. Both the Spectral Angle Mapper algorithm and the Matched Filter algorithm are used in this study and will be discussed individually per study site.

4.0 ANALYSIS

4.1 SNR comparisons at Rhyolite Hot Spring

Rhyolite Hot Spring is an alkaline hot spring located in the central caldera, just to the east of the 300ka Hot Creek rhyolitic lava flow (see Fig. 1). The spring itself is alkaline, discharging at moderate temperatures of 50-55°C. The spring has been modified both by humans (to construct a recreational hot tub), and by livestock. There are two small pools and limited shallow subsurface flow in the region. Though a zone of low discharge presently, this region was home to much higher discharge levels in the past. Just to the southeast of the present-day Rhyolite Hot Spring, is a set of low hills. These hills are extensive travertine terrace deposits formed by paleo-hot springs.

We analyzed subsets covering the Rhyolite Hot Spring area for both 1992 and 2000 AVIRIS imagery. We wanted to see whether mapping in the 1992 imagery would prove to be as successful as mapping efforts in the 2000 imagery. Although the spatial resolutions are the same, the SNR for both images is quite different as detailed previously. After applying the MNF and PPI algorithms, the image-extracted spectral endmembers were used in the Matched Filter algorithm. Figure 2 shows the distribution of four main mineral species: montmorillinite, travertine, Si-bearing mineral (possibly sinter deposits), and kaolinite. Notice first that the scales are a bit different, however, the distribution and character of mineralization in both images are quite similar. These results illustrate that imagery with a medium spatial resolution (17m) and a poor SNR (100:1 in SWIR) is adequate for mapping major mineral assemblages in volcanic environments. Satellite data has poorer resolution (30m) and SNR (50:1) than 1992 AVIRIS; however, results invoke optimism for satellite-based mineral mapping.

4.2 Vegetation and microorganism mapping at Little Hot Creek

Little Hot Creek is located in the east-central caldera on the eastern flanks of the resurgent dome. It is a west to east flowing hot creek that discharges alkaline waters at temperatures near boiling (90-95°C). Discharge is the second highest in the caldera (behind Hot Creek) at 250 l/s (Sorey, 1985). The Little Hot Creek gorge is bounded on either side by Tertiary sediment cliffs, while the floor of the gorge is home to small travertine terraces, and extensive argillic phase hydrothermal alteration. The pools and creeks of the gorge show thermophilic communities of algae and bacteria. Vegetation species zonation is also seen at this hot creek. The pattern seen at Little Hot Creek and at other creeks and pools around the caldera, is outlined in Figure 3. Microorganisms are found in the waters of the creeks and pools. Grasses surround the pools, which are in turn surrounded by a narrow swath of rabbitbrush. The rabbitbrush then grades into sagebrush. The only trees found near the hot creeks are Junipers. Also shown in Figure 3 is a plot of the spectral signatures of communities of cyanobacteria. The presence of such microorganisms may indicate current hydrothermal discharge. Such communities desiccate when water levels drop; however, their spectral signatures remain intact. Thus, their presence indicates that thermal waters have flowed over the surface either presently or in the near past.

The imagery in Figure 4 tries to answer several questions. First, can we map the vegetation zonation patterns shown in Figure 3? Second, what role does spatial resolution and SNR play in such determinations? We attacked these questions by analyzing three different images from three different years and two different sensors. Each image was spectrally subset to include only the VNIR wavelengths. The far left image shows Spectral Angle Mapper (SAM) results for 1992 AVIRIS imagery. Recall, that this data has a 17-18m pixel and a SNR of roughly

400:1 in the VNIR. The image in the middle is 2000 AVIRIS data, also with a 17-18m pixel, but with a SNR of roughly 900:1 in the VNIR. Finally, the image on the far right is HyMap data that possesses a 3-5m pixel and a SNR of roughly 1200:1 in the VNIR.

We find that the zonation pattern can be discriminated in all three datasets, though the HyMap image possesses the most detail, as would be expected from a 5m pixel. The microorganisms map as the red and magenta colors, while the dark greens are likely grasses and the lighter greens are rabbitbrush. Cyan is a mix of sagebrush and soils, while the blues and yellows correspond to sagebrush found along steep slopes in shade. Second, most of the hot pools are not much larger than approximately $100m^2$. The pixels of AVIRIS produce an area of approximately $300m^2$. It is thus impressive that such small features are map-able in data with lower spatial resolution and degraded signal –to-noise (especially that seen in the 1992 AVIRIS). Not all of these results have been field-checked, however the spectral signature for cyanobacteria has a very distinctive geometry and a prominent absorption at 0.62μm due to the pigment phycocyanin. Image extracted signatures from the red and magenta pixels show this 0.62μm feature, and hence likely contain cyanobacteria mats in some proportion. 1992 AVIRIS data is similar to that data expected from such sensors as Hyperion. Hence these results suggest that simple vegetation zonation patterns and communities of thermophilic organisms indicative of hydrothermal discharge may be identifiable from space-based hyperspectral sensors.

4.3 Hydrothermal mineral mapping in the western caldera with AVIRIS and HyMap

Waters in the western caldera are likely heated by a magmatic source at depth beneath the Mono-Inyo volcanic chain. Such waters are known to discharge in the central caldera along northwest-trending normal faults that cut the resurgent dome. The same waters flow along the caldera floor to the east in a spreading hydrothermal plume. In contrast, no surficial discharge of liquid water is known to occur in the topographically higher western caldera, however, extensive hydrothermal alteration is found here. We have shown in previous HyMap-based work, (Martini et al., 2000), that the most extensive and highest temperature alteration in the Long Valley region is found on the flanks of Mammoth Mt., especially the south-western flank. Linear distributions of alteration indicate faults and/or fractures both previously mapped and newly identified. In this study, 2000 AVIRIS imagery was analyzed, and the same distributions and mineral species were found on the flanks of Mammoth as were found in the 1999 HyMap imagery.

Dissimilarities exist as well. The presence of the sulfate alunite along the Discovery Fault Zone to the northeast of Mammoth Mt. had been mapped previously in the HyMap imagery (Martini et al., 2000). Efforts to map the alunite in the AVIRIS imagery were not as successful. Figure 5 shows the distribution of alunite in the HyMap subset (circled for clarity). Notice that in the AVIRIS imagery, three zones of alunite were not identified that were seen in the HyMap data. We believe this is due simply to differences in pixel size. This region of the caldera is highly vegetated with thick stands of conifers; hence the pixels are highly mixed. Even 5m pixels are mixed, but the 17-18m pixels of AVIRIS simply could not see the limited distributions (10-15 HyMap pixels) of alunite in each of the locations found with the HyMap data.

The northeast-trending faults of the Discovery Fault Zone necessitate modified structural models for the caldera and for genesis of the Mono-Inyo volcanic chain (Suemnicht and Varga, 1988). The presence of high temperature alteration on them indicates crustal weakness and hence either faults and/or fractures. Regional eastern California structure is populated with fault patterns similar to those seen spectrally in Long Valley. Though the scale of a feature may be small (such as those alteration patches found in the Discovery Fault Zone), its implications may be large.

5.0 CONCLUSIONS

This study demonstrates the abilities of hyperspectral imaging to map distributions of vegetation and mineralization in Long Valley caldera. The relative effect of variable SNRs and spatial resolutions between data sources have differing levels of importance. Mineralization is mapped similarly in both 1992 AVIRIS (poor SNR) and 2000 AVIRIS (good SNR). Vegetation zonation patterns indicative of hot spring discharge are mapped by all three datasets, although AVIRIS (17-18m) has a poorer spatial resolution than HyMap (3-5m). Finally, alunite mineralization is detected in both AVIRIS and HyMap, although some deposits were ultimately missed by AVIRIS due to its poorer spatial resolution.

SNR is obviously a controlling factor for success in mapping, however the "poor" SNR of 1992 AVIRIS data did not totally hinder mapping efforts. In fact, the mapping success achieved in 1992 data suggests optimism for space-based hyperspectral mapping efforts. Additionally, spatial resolution is clearly important for biological mapping, and can be critical for some geological applications.

6.0 REFERENCES

Bailey, R.A., G.B. Dalrymple, M.A. Lanphere, 1976, "Volcanism, Structure and Geochronology of Long Valley Caldera, Mono County, California," J. Geo. Res., vol. 81, no. 5, pp. 725-743.

Gao, B.C., K.B. Heidebrecht, A.F.H. Goetz, 1993, "Derivation of scaled surface reflectances from AVIRIS data," Rem. Sens. Env., v.44, pp. 165-178.

Green, A.A., M. Berman, P. Switzer, M.D. Craig, 1988, "A transformation for ordering multispectral data in terms of image quality with implications for noise removal," Rem. Sens. Env., v.26, no.1, pp. 65-74.

Lipshie, S.R., 1976, Geologic guidebook to the Long Valley-Mono Craters region, GSUCLA Field Guide 5, Geol. Soc. of Univ. of Calif., Los Angeles, 184 pp.

Martini, B.A., E.A. Silver, D.C. Potts, W.L. Pickles, 2000, "Geological and geobotanical insights into the hydrothermal structure and magmatic systems of a restless caldera using three meter HyMap imagery: LongValley Caldera, California, USA," Proceedings of the Fourteenth International Conference on Applied Remote Sensing, Las Vegas, NV, v.1, pp. 28-35.

Sorey, M.L., 1985, "Evolution and present state of the hydrothermal system in Long Valley Caldera," J. Geo. Res., v.90, no.13, pp.11219-11228.

Sorey, M.L., G.A. Suemnicht, N.C. Sturchio, G.A. Nordquist, 1991, "New evidence on the hydrothermal system in Long Valley caldera, California, from wells, fluid sampling, electrical geophysics, and age determinations of hot-spring deposits," J. of Volc. and Geotherm. Res., v.48, pp. 229-263.

Suemnicht, G.A. and R.J. Varga, 1988, "Basement structure and implications for hydrothermal circulation patterns in the western moat of Long Valley Caldera, California," J. Geo. Res., v.93, pp. 13191-13207.

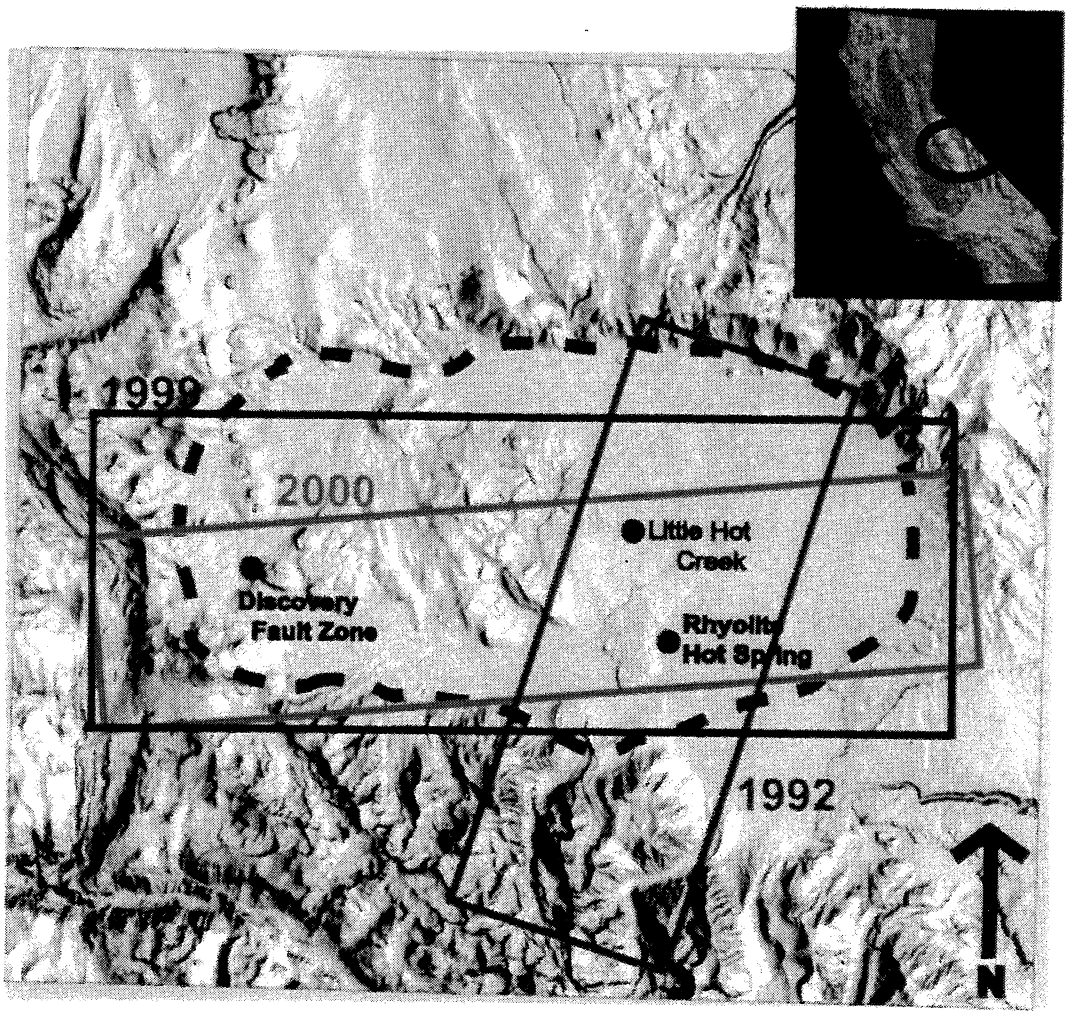

Figure 1. Long Valley caldera outlined in red dashes. The boundaries of the flightlines used in this study shown by rectangles. Specific study sites indicated.

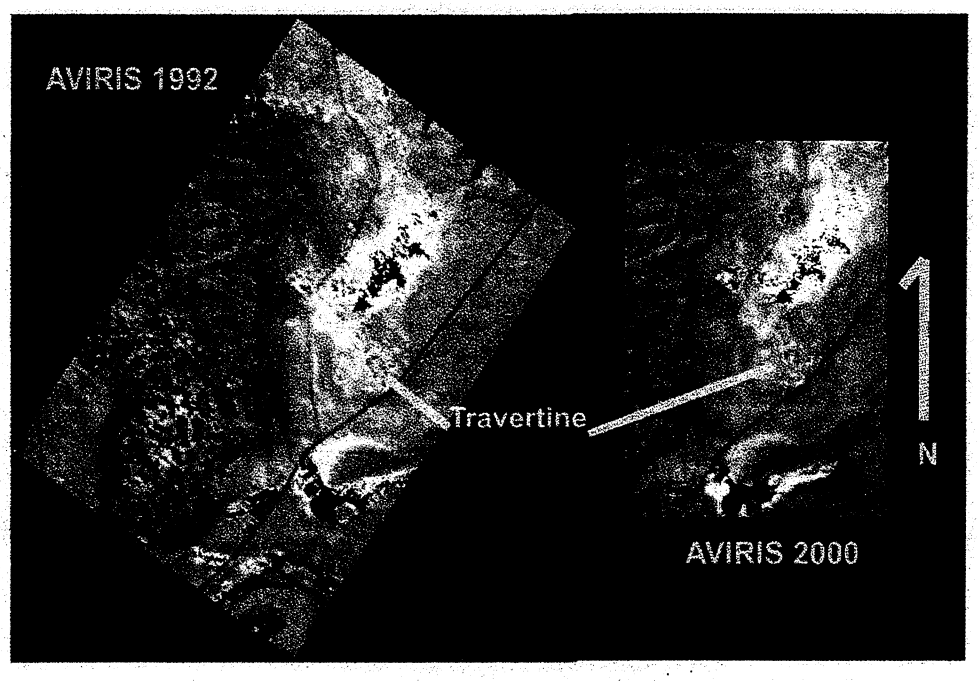

Figure 2. Distributions of mineralization at Rhyolite Hot Springs in the west-central caldera. Classification done in ENVI with Matched Filtering.

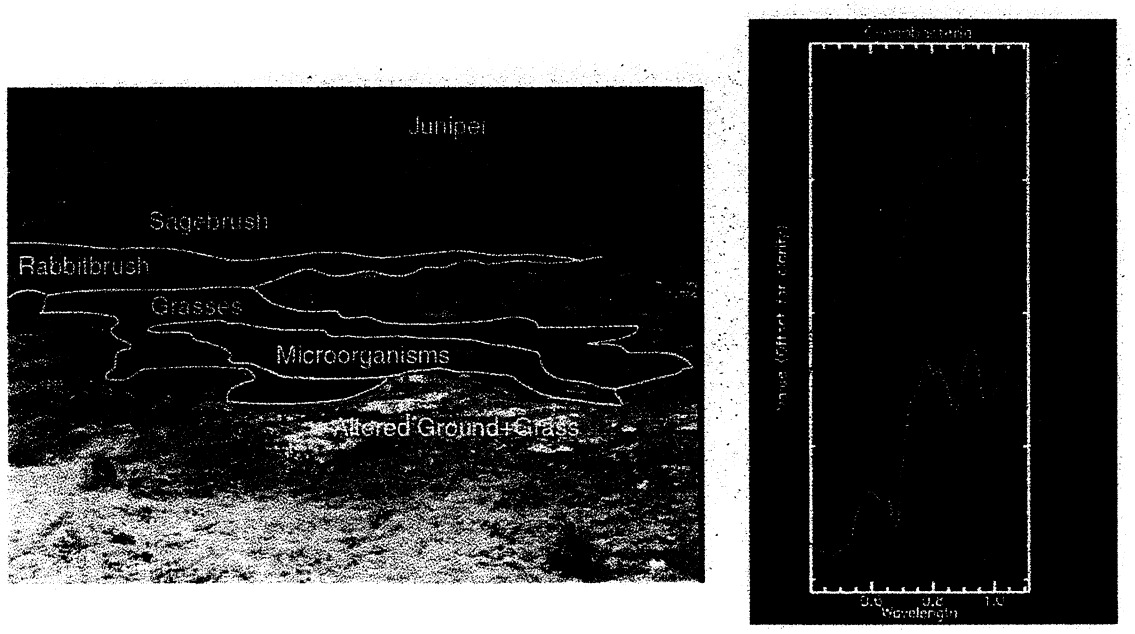

Figure 3. On the right are spectral signatures of microorganisms from each of the datasets, including a GER field spectra. On the left is an image of vegetation zonation patterns found at Little Hot Creek.

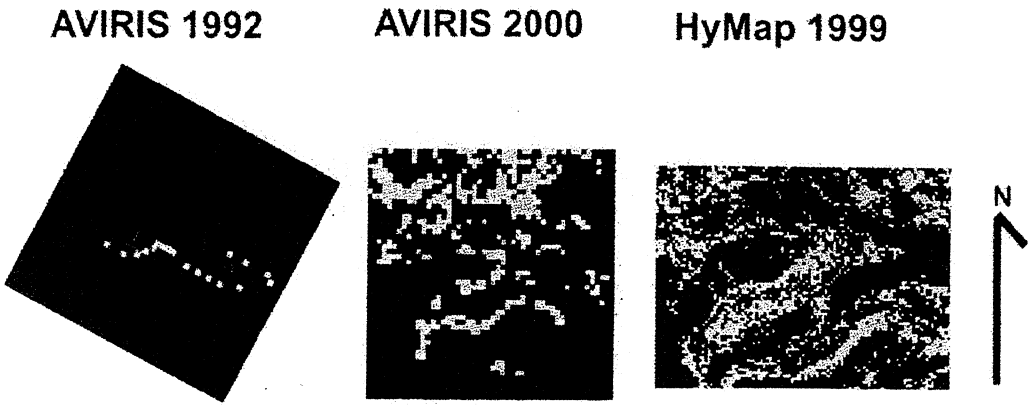

Figure 4. SAM results for both AVIRIS and HyMap data. Differing spatial resolutions, bandwidths, and SNRs effect mapping results. HyMap data clearly has more detail. However, microorganisms in magenta and red map in all three datasets, as well as zonation patterns (albeit crudely in AVIRIS 1992 data).

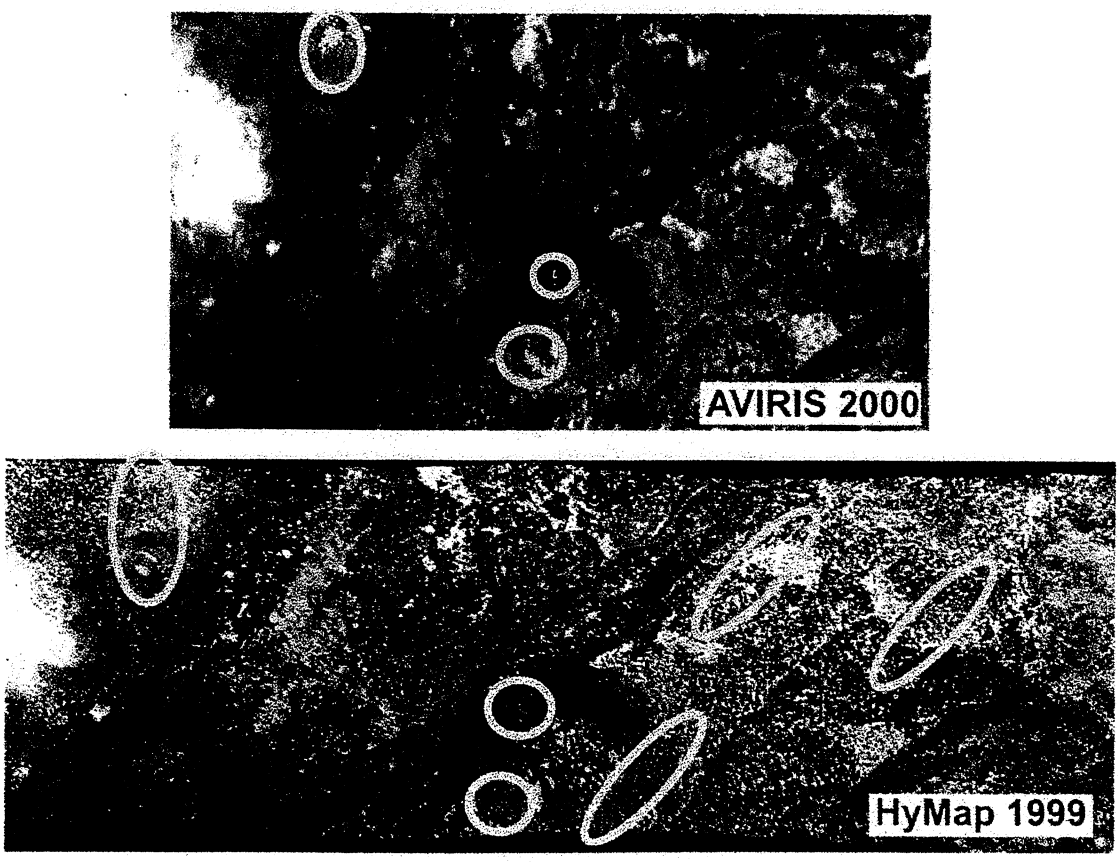

Figure 5. Matched Filter results for AVIRIS and HyMap imagery. Mapped alteration in yellow is alunite. Although the AVIRIS data does reveal alunite, the full distribution is only mapped by HyMap. This is likely due to differences in spatial resolution (17-18m for AVIRIS vs. 3-5m for HyMap).

DECISION TREE CLASSIFICATION OF MULTIDATE AVIRIS DATA FOR MAPPING WOODLAND ENCROACHMENT INTO THE GREAT PLAINS

David Meyer, Bruce Wylie, Cullen Robbins[1]
Lee Vierling, Patrick Kozak[2]

1. BACKGROUND

The Great Plains of North American has experienced a significant increase in woodland cover over the last 200 years. This encroachment of woodlands into grasslands, as well as the "thicketization" of savannas has been observed worldwide (Archer et al., 1995). Several reasons have been offered to explain this transformation. The traditional view holds that changes in land management are the cause, operating through several modes of disturbance. A primary mode is a reduction in burn frequency, coupled with increased grazing and tree planting. Burning tends to favor native prairie species (suppressing encroachment by woodland species), while grazing tends to select for the unpalatable woodland species (Reich et al., 2000). Under these conditions, species introduced as shelterbelts and windrows can spread into prairie ecosystems. A secondary mode of disturbance is the abandonment of agricultural land, which, coupled with fire suppression, favors the development of woodland cover. Climatic factors have also been proposed. For example, the replacement of C_4 grasses by C_3 shrubs in North America inferred over the last 200 years could either be due to systems that were established at the end of the "little ice age" and only marginally supported climatically at the time of settlement (Neilson, 1986), or due to post-industrial CO_2 fertilization (Idso, 1992). The latter proposition is difficult to support, however. Even though the global nature of encroachment supports the fertilization hypothesis, a number of alternative explanations are available (), undermining this point of view.

The implication of these changes is still poorly understood. A simple view holds that the transformation of grassland to woodland increases carbon sequestration. Indeed, the expansion and densification of woodlands has been proposed as an explanation for up to 50% of the total US carbon sink associated with land cover changes (Houghton et al., 1999). This transformation has been implicated in changes in meteorological and climatic patterns within the Great Plains, resulting from alterations to water and energy fluxes between the surface and the atmosphere, as well disturbances to the carbon and nitrogen exchange cycles as grasslands give way to wooded cover. Although carbon sequestration is an important tool for reducing greenhouse gases, this sequestration occurs at the expense of soil carbon (Sage et al., 1999) as grasslands are transformed. In areas prone to droughts and frequent fires, the resilience of carbon stored in tree biomass (wood) as compared to soil carbon is questioned.

In an attempt to monitor this encroachment, it is important to map the distribution of species that may indicate the early onset of grassland-woodland transformation. One such species is the eastern red cedar (*Juniperus virginiana*). Extensive throughout the eastern and central US, this juniper species has spread extensively into the central Great Plains. Because it's drought resistance, highly adaptive physiology and extensive root system, the eastern red cedar has been widely used to control soil erosion and to reduce the desiccating effects of wind. Introduced as windrows and shelterbelts, the species will usually give way to climax deciduous and conifer species. Although considered shade intolerant, eastern red cedar can still flourish under lower- to mid-density deciduous stands, due to it's low capacity for water loss and ability to photosynthesize adequately during leaf-off overstory conditions. The species is highly sensitive to fire, it's primary control, but as fire is suppressed the juniper can spread from shelterbelts into the surrounding pastureland and abandoned cropland. Once established in these new areas, they are usually replaced by more fire-tolerant hardwoods and pines, although they can occasionally outlive competing hardwoods through allelopathy and a highly competitive physiology in marginal soil and climatic conditions.

---

[1] Raytheon Corp. USGS EROS Data Center (dmeyer@usgs.gov)
[2] South Dakota School of Mines and Technology

Mapping the eastern red cedar throughout the Great Plains using remote observation techniques can be problematic for several reasons. First, in the early stages of encroachment, the species is either hidden under deciduous overstory, or expressing itself only through isolated, patchy occurrences in open areas. Its spectral signature is not always distinct from other conifer species as viewed by lower-dimensional multispectral instruments, although throughout much of the plains, there are few other conifers co-occurring with the juniper in large numbers. However, one of its prime expansion corridors is along the riparian systems that cut west-to-east across the central plains. At some point, the eastern red cedar can co-occur with western conifers, such as the ponderosa pine. This is the case along the Niobrara River in Nebraska, a unique riparian system where eastern hardwoods can intermix with western conifers. The Niobrara and other rivers are important conduits to juniper expansion to the west, but present all the problems associated with remote detection: patchiness, overstory obscuration and spectral confusion. The problem of remote detection is approached here using high spectral resolution to improve spectral discrimination, and leaf-on, leaf-off data acquisitions at high spatial resolution to identify the eastern red cedar under varying conditions of background spectra and overstory obscuration. The primary instrument for this study is the Advanced Visible and Infrared Imaging Spectrometer (AVIRIS) coupled with field observations of juniper stands.

2. AVIRIS DATA COLLECTION AND PREPARATION

The geographic focus of this study is the Niobrara Valley Nature Preserve in north central Nebraska, owned and managed by The Nature Conservancy. The preserve includes the intermixed riparian woodland described above, as well as extensive tracts of the Nebraska Sand Hills to the south of the river. Two low-altitude (15,500 ft above mean terrain) Twin Otter AVIRIS acquisitions occurred in 1999: July 22 and November 11. The first acquisition captures the grassland and woodlands under conditions of maximum green cover (the native prairie grasses are dominant warm-season), while the latter captures senesced grasses and leafless hardwood stands. Over 600 field control points were measured over the preserve to include a variety of cover types: grasslands, woodland, shrub (primary sumac), and bare soil. The woodland class was further subdivided into deciduous, conifer-ponderosa pine, conifer-juniper and mixed classes. These field points were located to an accuracy of around 2 meters and used to train the classification described below.

Although the AVIRIS data were geometrically corrected before delivery, the inherent errors were sufficiently large to require further correction. Both the scenes were re-transformed using a standard US Geological Survey digital orthophoto quadrangle (DOQ) as control. Although the scene-to-scene accuracies were high after correction, the DOQ's intrinsic locational uncertainty of around 6 meters must be considered in light of the AVIRIS image's 2.7 meter resolution and the locational accuracies of the field control used in the classification. These problems come into play during the classification accuracy assessment described later. Using field spectroscopy measurements, the radiance-calibrated imagery were corrected for the atmosphere and converted to (isotropic) surface reflectance. Minimum noise fraction (MNF) transformations were applied to both data sets, and an MNF threshold of 2.0 was used to retain MNF components for classification.

3. CLASSIFICATION METHODOLOGY

Two supervised classification methods were used, one using matched filtering for each cover type under investigation, and the other using decision trees (Friedl et al., 1999). For the matched filtering approach, regions of interest (ROIs) were extracted from the imagery using the global positioning system (GPS) locations acquired during the field survey. Image spectra from these ROI's were used as reference spectra for the matched filter algorithm, and a matched filter image was computed for each of the cover types under study. The performance of this approach was used by observing the value of the matched filter values for the different classes at control GPS field survey locations withheld from the training set locations for the purpose of validation. The means by which the performance of this method is measured is described in the next section. The matched filtering approach for the November dataset was not complete at this writing and is not included here.

The decision tree approach used the C5.0 univariate decision tree algorithm. Decision tree classifiers have become increasingly popular for several reasons. First, they are non-parametric, requiring no prior assumptions regarding probability density functions of a given data ensemble. Also, they are considered to be relatively robust with respect to nonlinear and noisy interrelationships between features expressed in a given data set (Friedl et al., 1999). The decision tree algorithm works by computing a metric known as the information gain ratio, a measure of the reduction in entropy produced by subdividing ("splitting") data into subsets based on feature vector decision thresholds, based on a given set of training signatures. The "tree" nomenclature describes the morphology of the splitting process: recursive binary decisions resulting in a number of subdivision. The final tree configuration is achieved by maximizing the information gain threshold at each node (binary decision) in the tree. Performance of the classification is based on standard classification validation procedures.

The July 22 classification was described previously and is synopsized in the next section. For the classification of the November 11 data set, two classification schemas were used. The first was for a general classification scheme dividing the image into 5 basic types (shadow, bare, water, woody, and grass), and the second was a woody-specific division to determine which types of woody species were present (cedar, pine, deciduous, shrub, and mixed (dec. and cedar)). The desired separations were run through the C5.0 decision tree to determine the accuracy and usefulness of the separation. The following separations were run: general classification, cedar/other/mixed, woody/other separation. Cross-validation was used to estimate error rates of various landcovers with different decision tree parameters. Boosted decision trees () produced the most useful results. When the results were determined to be meaningful, the decision tree was run on the entire 32-band MNF image, since it had been trained by the points. This produced classified images and confidence maps.

Due to lower accuracy than expected in some of the images, it was decided to aid improve classification using results from the July classification. Only the woody class was used from the July result as a pre-stratification for the November classification. The mixed class from the July result was excluded to reduce training errors. The training points were again used to estimate the ability of decision tree to classify the image using cross-validation. The decision tree was then run spatially on the entire 32-band November MNF image. The corresponding woody points for both the leaf on and leaf off images were matched up and run through decision tree in an attempt to improve our woody separation. This decision tree was also run spatially on both images and a composite was produced.

A final classification was then produced using a decision model combining the aforementioned results. The general classification was used for the classes shadow, bare, water, and grass. If the leaf-on result called a pixel deciduous and the leaf-off called it cedar or mixed, it was put in a mixed class. If a pixel was deciduous in the leaf-on and pine in the leaf-off, it was also added to the mixed class. Of the remaining pixels, if it was deciduous in the leaf on, it was given a deciduous class. If it was cedar in leaf-off, it was classified as cedar. Likewise, if it was pine or shrub in leaf off, these classes were created and named correspondingly. If a pixel was classified as mixed in the leaf off, it was added to the mixed class. The remaining pixels were classified according to how they were classified in the on and off composite image. (Fig. 1)

4. RESULTS

The results from the July 22 classification, reported previously reported that both the matched filter and decision tree approaches were able to discriminate between cedar from other cover types with accuracies of about 85%.

The cross-validation step in the decision tree provides statistics in the form of a confusion matrix with which an accuracy assessment can be done. The matrices from all of the different decision tree outputs were combined using area weighting to produce an accuracy assessment for each class in the final image. The overall accuracy of the classification is 84 %. The shadow and water classes had the highest accuracies, 94 % and 93 %, respectively. The bare and grass classes had accuracies of 83% and 89%, respectively. Cedar was accurately classified 52% of the time, while the mixed class was accurately classified 35% of the time. Coniferous trees were accurately classified 46% of the time. Deciduous trees and shrubs were accurately classified 64% and 62% of the time, respectively. The following chart shows the breakdown of the above:

Table 1: decision tree results

class	% accuracy
Shadow	94
Water	93
Bare	83
Grass	89
Cedar	52
Coniferous	46
Deciduous	64
Shrub	62
Mixed	35
Overall	84

5. DISCUSSION

The low cedar classification accuracy for the November 11 acquisition is the result of several complicating factors. A primary factor is the overall locational uncertainties in the surveyed control points and the imagery used for analysis (including the reference DOQ). Because of the patchiness of the exposed juniper stands and the 2.7 m resolution of the Twin Otter AVIRIS data, small locational errors in field surveys and imagery all could lead to large errors in a supervised, multi-date classification strategy. Another influence is the general illumination conditions of the November 11 overflight: low sun (shadowing, anisotropic reflectance effects). Also, attempts to measure through obscuring hardwood canopies may be somewhat ambitious, even under leaf-off conditions. Finally, the quality of the field observations must be considered: in a very patchy environment, what is considered "quality" control? Stands of pure juniper, large enough to be spectrally unambiguous, are extremely rare.

Methods for mitigating these factors include the use of precise control for image registration, more accurate field measurements and better examples of "target" spectral signatures for classification. Due to the reasons mentioned above, pure spectral signatures may be unobtainable from the image, so strategies employing the use of reference field spectra along with unmixing strategies should be pursued further.

6. REFERENCES

Archer, S., D.S. Schimel and E.A. Holland, 1995, "Mechanism of Shrubland Expansion: Land Use, Climate or CO_2?," Climate Change, vol. 29, p. 91-99.

Friedl, M.A., C.E. Brodley and A.H. Strahler, 1999, "Maximizing Land Cover Classification Accuracies Produced by Decision Trees at Coontinental to Global Scales," IEEE Trans. Geoscience & R.S. vol. 37, no. 2, pp. 969-982.

Houghton, R.A., J.L. Hackler, and K.T. Lawrence, 1999, "The US Carbon Budget: Contributions from Land-Use Change," Science, vol. 285, pp. 574-578.

Idso, S.B., 1992, "Shrubland Expansion in the American Southwest," Climate Change, vol. 22, p. 85-86.

Neilson, R.P., 1986, "High Resolution Climatic Analysis and Southwest Biogeography,", Science, vol 232, pp. 27-34.

Reich, P.B., D.W. Peterson, D.A. Wedin, and K. Wragge, 2000, "Productivity and Nitrogen Cycling across a Fire Dominated Forest-Grassland Continuum," Ecology, in press.

Sage. R.F., D.A. Wedin, and M. Li, 1999, "The Biogeography of C_4 Photosynthesis: Patterns and Controlling Factors," in R. F. Sage and R.K. Monson, The Biology of C_4 Photosynthesis, Academic Press, pp. 313-373.

7. FIGURES

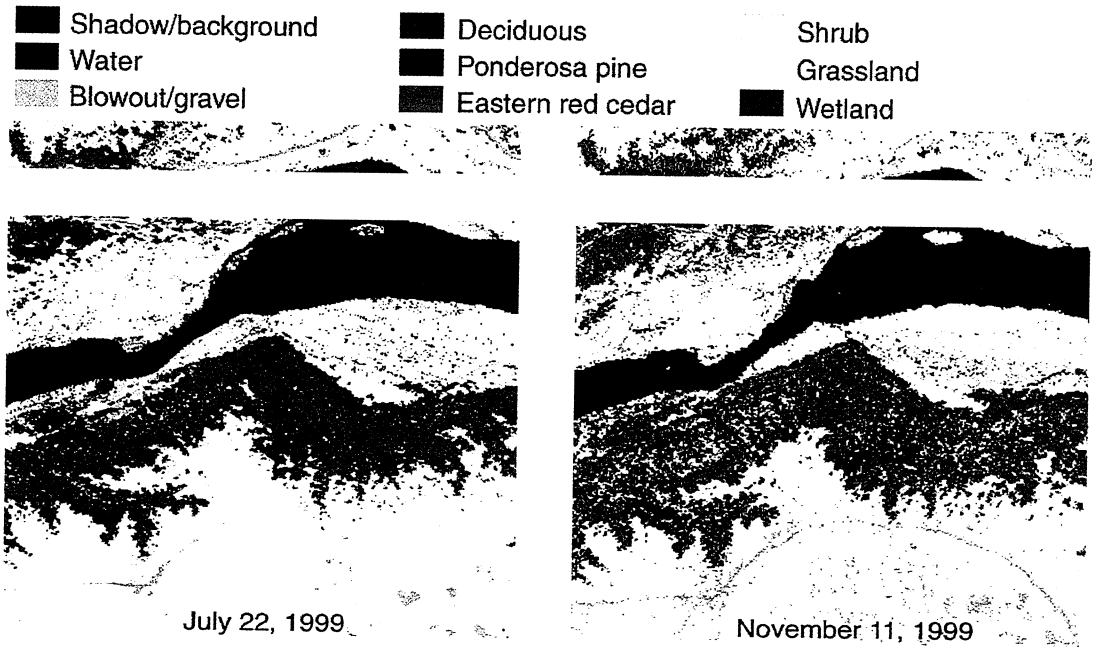

Figure 1.
Classification results from the univariate decision tree for both dates.

Using AVIRIS Data to Map Geologic Signatures of Copper Flat Porphyry Copper Deposit, Hillsboro, New Mexico

Brian S. Penn
Boeing-Autometric, Inc.
Colorado Springs, Colorado 80910
brian.s.penn@boeing.com

K. Eric Livo
United States Geological Service
Lakewood, Colorado 80225

Introduction

The most popular software package for processing hyperspectral imagery is the Environment for Visualizing Imagery (ENVI) available from Research Systems, Inc. Other lesser-known software packages are available including the system developed at the U.S.G.S. Spectroscopy Laboratory call Tetracorder (previously known as Tricorder). Tetracorder does not enjoy the notoriety of ENVI primarily because Tetracorder is a U.S.G.S. in-house tool used almost exclusively by the members of the U.S.G.S. Spectroscopy Laboratory. Tetracorder has been used successfully on a number of studies including the Summitville mine in southwestern Colorado (King, et al., 1995), the Leadville superfund site (Swayze, et al., 1996) and Yellowstone Park (Kokaly, Clark, and Livo, 1998). Another relatively unknown approach, but of interest because of its unique classification capabilities are Kohonen self-organizing maps (SOM).

Each of these techniques was applied to the AVIRIS imagery of Copper Flat porphyry copper deposit (CFPCD) in south-central New Mexico. The ENVI process is well documented, but it is still reviewed here. Since Tetracorder has not been publicly released, only the essential elements are described in any detail. The details of SOM are shown below. Athough SOM are not a complete system, when used in conjunction with ENVI, they prove to be a useful addition to any hyperspectral toolkit.

Hyperspectral Data Set – Site Description

NASA's AVIRIS sensor was flown over the Copper Flat porphyry copper deposit in the summer of 1998. The Copper Flat mine is 8 km NNE of the town of Hillsboro, New Mexico (Figure 1). The Copper Flat mine is located in the Animas Hills and is part of the Hillsboro mining district of Western Sierra County, NM and is one of the older Laramide porphyry-copper deposits in the Arizona-Sonora-New Mexico porphyry-copper belt (McLemore, 1999). The Animas Hills consist of a horst block located just west of the axis of the Rio Grande rift and are underlain by a circular block of andesite nearly 4 miles in diameter. The thickness of the andesite and circular shape suggest that the andesite is a remnant of a Cretaceous caldera. $^{40}Ar/^{39}Ar$ data establish the age of the andesite at $\geq 74.93 \pm .066$ Ma (McLemore, et al., 1999). A relatively small body of quartz monzonite intruded the andesite forming the entire CFPCD. CFPCD is predominantly a low-grade hypogene deposit with thin veneer of supergene enrichment at the surface (McLemore, et al., 1999). The numerous latite dikes radiating from the CF quartz monzonite also show significant mineralization. The CFPCD has produced large quantities of Au, Ag, and Cu since the late 1800s.

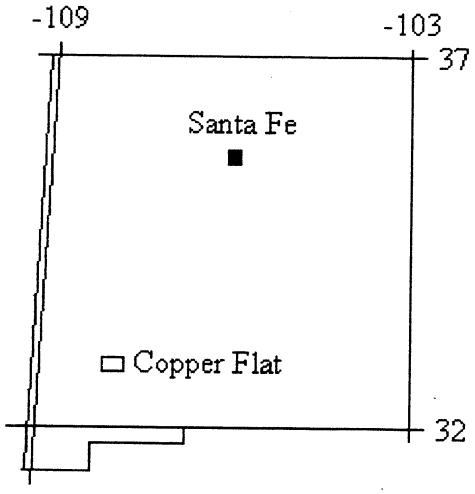

Figure 1 – Location of CFPCD in New Mexico. The deposit is located about 15 km west of Truth or Consequences, NM.

Preprocessing

To properly correct for atmospheric influences on the upwelling reflectance spectra, ground verification data was collected at the CFPCD mine site. Ground verification areas were selected using the following constraints:

1) Low relief;
2) Spectrally flat;
3) High reflectance;
4) Cloudless sky;
5) Solar Noon ± 1 hour;
6) Sufficiently large area of uniform composition (greater than or equal to one pixel (20m x 20m));
7) Ground verification data collected at the same time as the AVIRIS overflight occurred.

Unfortunately, condition five could not be met during the 1998 AVIRIS overflight of CF. Nonetheless, within a few weeks on sight measurements were made using an ASD-FR spectrometer. Two bulldozed areas located adjacent to the CF mine proved suitable for collection of spectra. These spectra were used to refine the output from the atmospheric compensation software.

Tetracorder, ENVI, or SOM require proper atmospheric corrections. All three software techniques work well with the output from ATREM (ATmospheric REMoval Program) from the Center for the Study of Earth From Space (CSES) at the University of Boulder at Colorado (Gao and Goetz, 1990; Gao, Heidebrecht, and Goetz, 1999). But there are a few problems with ATREM output requiring remediation.

ATREM does not account for atmospheric path length on a pixel-by-pixel basis and it also overcorrects for the path radiance scattering in the atmosphere at blue to UV wavelengths yielding negative values. These shortcomings are obviated using the following two-step approach:

1. A radiative transfer correction is performed that tracks changing atmospheric water absorptions from pixel to pixel and removes the absorptions due to water

and other atmospheric gases, scattering in the atmosphere, and the solar spectrum.

2. The reflectance of known targets in the scene are used to correct the artifacts from the imperfect radiative transfer correction. The success of this method depends upon the accurate reflectance characterization of field calibration sites.

These corrections produced a radiative transfer ground corrected image that formed the basis of this study.

The Environment for Visualizing Images (ENVI)

The ENVI approach for processing hyperspectral data consists of winnowing down the vast amount of information into a manageable subset. ENVI treats the classification of the imagery data as a search. As with most search strategies, the name of the game is to constrain the domain. Constraining the search space makes finding a solution easier. This constraining process results in likely endmembers, which are then used to classify the individual spectrum. An endmember represents the purest "homogeneous" material from which other materials are created. The data are then analyzed using the endmembers through a process of linear unmixing.

The basis of linear unmixing is that most pixels are mixtures of substances. Once all the endmembers are found in an image, all the remaining pixels are considered linear combinations of these endmember pixels. While not absolutely true, it is a good first approximation.

In reality, the world is populated with intimate mixtures, i.e., mixtures of materials whose reflectance spectrum is a product of nonlinear mixtures of reflectance spectra from different materials. Unmixing these type of spectra is quite difficult and beyond the scope of this article.

The first step in ENVI is to reduce the dimensionality of the hyperspectral data from, in the case of AVIRIS data, 224 channels down to 10-15 relevant channels containing 95-98% of the information in the image. This is accomplished via a Minimum Noise Fraction (MNF) transform (Boardman and Kruse, 1994). To prevent the MNF from focusing on the variation in the 1.4 & 1.9 um water absorption bands these portions of the spectra were omitted from MNF processing.

Stated simplistically, the MNF transform is a cascade of translation, rotation, scaling and another rotation (essentially an affine transform). MNF is a series of two Principal Components (PC) transformations resulting in a change of basis for the vector space as defined by the number of bands for each pixel in an image. Most imagery data exhibit high band-to-band correlation (Figure 2). Principal Component analysis significantly reduces band-to-band correlation. This is achieved by rotating the coordinate axes so that the first axis is parallel to the maximum variance in the dataset. The second axis (orthogonal to the first) is rotated around so that it is parallel to the next highest variance. Subsequent orthogonal axes are rotated around so that they are parallel to smaller and smaller amounts of variance in the data. The net result is that the first few PC contain most of the information in the data and the remaining PC axes contain most of the noise. The dataset is thus reduced from 224 channels to 10-15 relevant channels. The resulting PC channels, because they are no longer related to a specific wavelength, do not correlate to specific absorption features in reflectance space.

The next step in ENVI hyperspectral processing procedure is based on fitting a simplex around a convex hull (Boardman, 1993). A convex hull encloses all the data points in the *n*-dimensional space of a hyperspectral image. Theoretically, apices of the hypervolume represent pixels composed purely of one material or endmember. These apices are located by repeatedly projecting the data space onto a unit vector (Boardman, Kruse, and Green, 1995). Pixels located the farthest out on the unit vector are counted as potential endmembers. Those pixels with the highest number of occurrences as an outlying pixel are considered apex or endmember pixels. Endmember pixels are further narrowed by visualizing the *n*-dimensional space and projecting

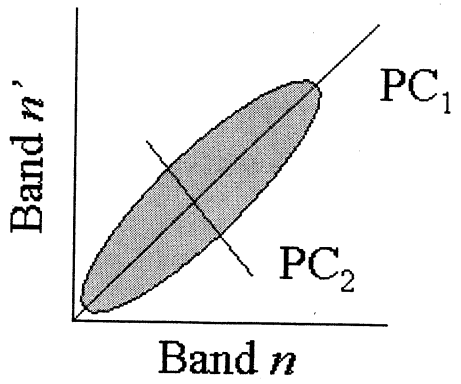

Figure 2 – Highly correlated data and the resulting principal component axes.

them into 2-dimensional space. This process greatly aids the location of endmembers by permitting similar pixels to be grouped together.

At this point, endmember pixels of the purest material content have been found. The next step is to classify the imagery. There are numerous methods available within ENVI, but we chose to use the ENVI's implementation of the Cauchy-Schwarz Inequality (CSI) called Spectral Angle Mapper (SAM). A chief advantage of CSI is that it ignores variations in albedo, so pixels with similar spectral shapes, but different reflectance intensities are considered the same. CSI is based on the relationship that the cosine of the angle between two vectors is the quotient of inner dot product of two vectors divided by the product of the magnitude of those two vectors (Equation 1). CSI generates the angle between two vectors as a measure of their similarity, i.e., the smaller the number, the more similar the spectrum between pixels.

$$\cos\theta = \frac{\langle u,v\rangle}{\|u\|\|v\|} \text{ where } 0 \le \theta \le \pi \tag{1}$$

ENVI is fast and the method is intuitive. Endmembers are readily identified, but actually determining the mineralogy within each pixel is not easy even using ENVI's built-in expert system, the Spectral Analyst.

The results of applying ENVI to the CF AVIRIS imagery are shown in Figure 3. The primary endmember spectra plots are shown in Figure 3.

Self-Organizing Maps

A Kohonen Self-Organizing Map (SOM) is an array (1 or more dimensions) of nodes (Kohonen, 1986). Each node is composed of a unit vector pointing in a random direction in *n*-dimensional space. After normalization, multi-dimensional data are presented to each of the individual nodes. Using a "winner-take-all" learning strategy, the node whose vector most closely matches the input data is found. This winning vector incorporates, or adjusts, its vector weights to match the input data. Vectors in the nodes surrounding the winning node are modified to look less like the input vector. In this manner, each node in the SOM internally develops the ability to recognize vectors similar to itself. This is referred to as self-organization, i.e., no external information is supplied to lead to correct classification.

Two useful features of a SOM are its topology preserving capability and the automatic generation of probabilities for a dataset. Topology preserving means that the original relationships between the data points remain intact after processing. This is exactly the desired result when working with hyperspectral data because it maintains the spectral relationships between pixels. Secondly, as a SOM evaluates the data, it builds a statistical model or probability

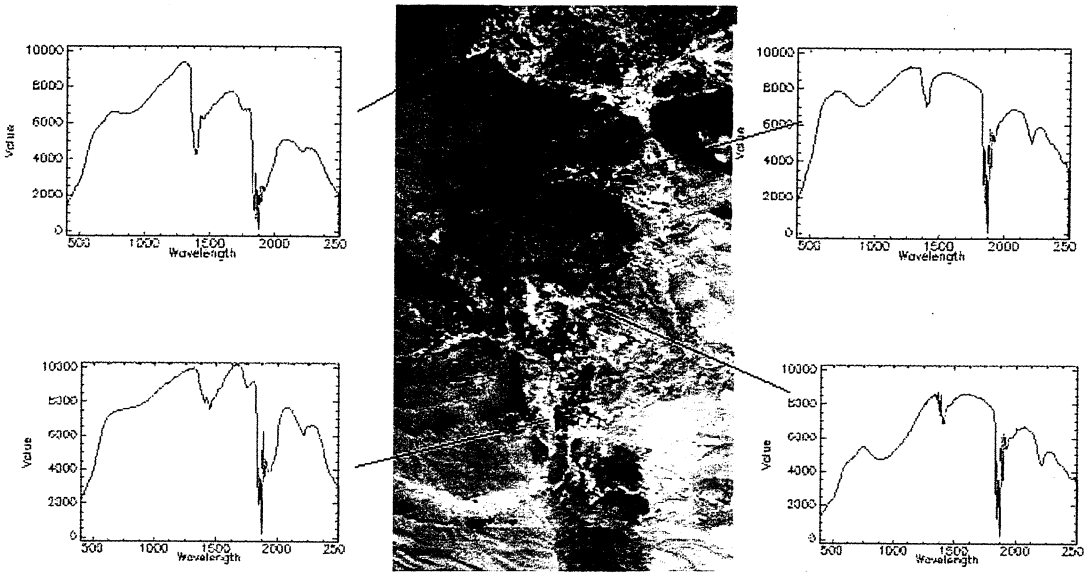

Figure 3 – Showing Fe-Clay endmembers resulting from ENVI processing. The Fe absorption near 1000 nm and the Clay features near 2250 nm are evident in the endmember spectra.

distribution, of the dataset spontaneously. SOM perform this statistical modeling, even in cases where no closed form analytic expression can describe the distribution (Caudill, 1988).
The SOM approach is an unsupervised clustering approach similar to the Iterative Self-Organizing Data Analysis Technique (ISODATA) of Tou and Gonzalez (1974). ISODATA interatively evaluates the imagery based on spectral distance. Initially, the user specifies the number of nodes. These nodes are then treated as cluster centers and pixels are included in the clusters based on user specified thresholds. After each iteration, a new cluster mean is computed based on the actual spectral locations of pixels. These new means are used in the next iteration. The process continues until there is little change between iterations.

SOM are similar to ISODATA, but operate in a much more flexible manner. Cluster centers are allowed to move about to account for topological relationships in the dataset.

Output from the SOM is a series of spectra containing the average spectra for each cluster group. For this example, the first 20 MNF transformed data bands were normalized to remove variation due to albedo and then presented to the SOM with the results shown in Figure 4. The first 20 MNF bands accounted for >95% of the variation within the dataset. The SOM process classified the imagery into fifteen clusters, with thirteen having significant membership (more than 2 members).

Tetracorder

Tetracorder is a hyperspectral image processing software package developed at the U.S.G.S. Spectroscopy Laboratory. Tetracorder is an extensible set of algorithms. Because Tetracorder is a U.S.G.S. Spectroscopy Laboratory in-house tool it is not as well-known as ENVI. Tetracorder was used for a number of studies including the Summitville mine in southwestern Colorado (Kinget al., 1995), the Leadville superfund site (Swayzeet al., 1996) and Yellowstone Park (Kokaly, Clark, and Livo, 1998). The purpose of Tetracorder is to identify objects in imagery with certain absorption features using a spectral identification algorithm called the Band Mapping Algorithm (BMA) (Clarket al., 1990). The basis for BMA is feature fitting. BMA fits each spectral feature in a spectral library to the current spectrum of interest using a least-squares approach to absorption feature identification.

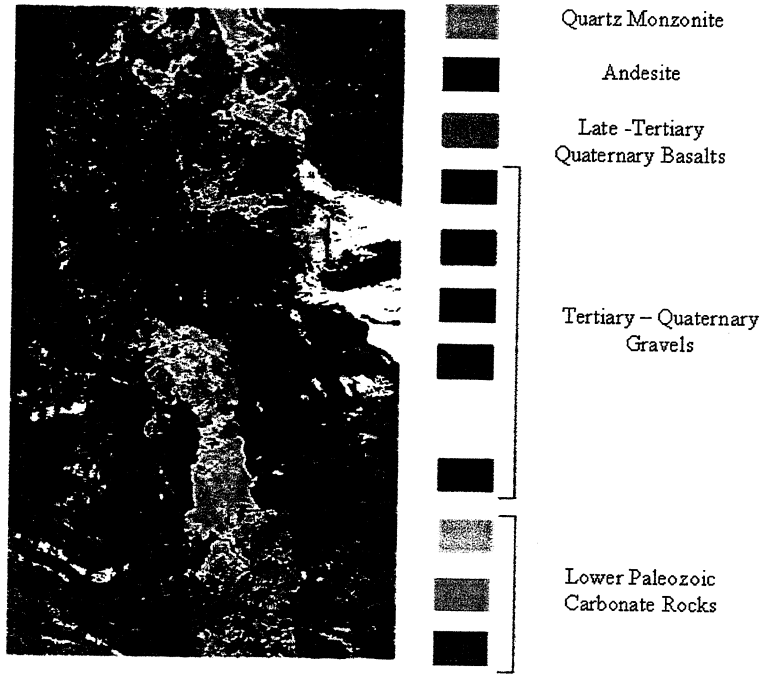

Figure 4 – Classification results from Self Organizing Map. This image results primarily from variations in reflection intensity

The BMA measures the goodness of fit between a library reference spectrum and an unknown spectrum. In preparation for using BMA, unique continua are created for each known mineral in a library of laboratory spectra. The process of identifying an unknown mineral begins by removing the unique continuum from a "candidate spectra" in a spectral library. Next, a continuum is calculated and removed from the unknown spectrum. The two resulting continua-removed spectra are compared and a goodness of fit value is calculated using a least-squares algorithm. The correlation coefficient produced by the least-squares equation is the fit. Multiple fits for different possible mineral candidates are calculated and compared with the best fit to determine the possible mineral present. Final mineral selection is based on additional factors such as albedo and continuum slope. The depth of the absorption feature from the continuum indicates relative abundance of a material and also serves as quality control related to spectral abundance. From these calculations a fractional map indicating mineralogy and relative abundance is generated. BMA has been subsequently expanded to simultaneously analyze multiple features in an unknown spectrum (Clark, et al., 1991).

The preliminary results of applying Tetracorder to the CFPCD imagery are shown in Figure 5 (1 μm) and Figure 6 (2 μm) where identified Fe- and clay-bearing minerals were identified; respectively. The results from the ENVI classification are similar to the Tetracorder results, but without the differentiation into the respective chemical constituents. Tetracorder is only limited by its reference spectra library. In the event that an observed spectrum (or absorption feature) is not in the reference library, then Tetracorder cannot readily identify the mineral.

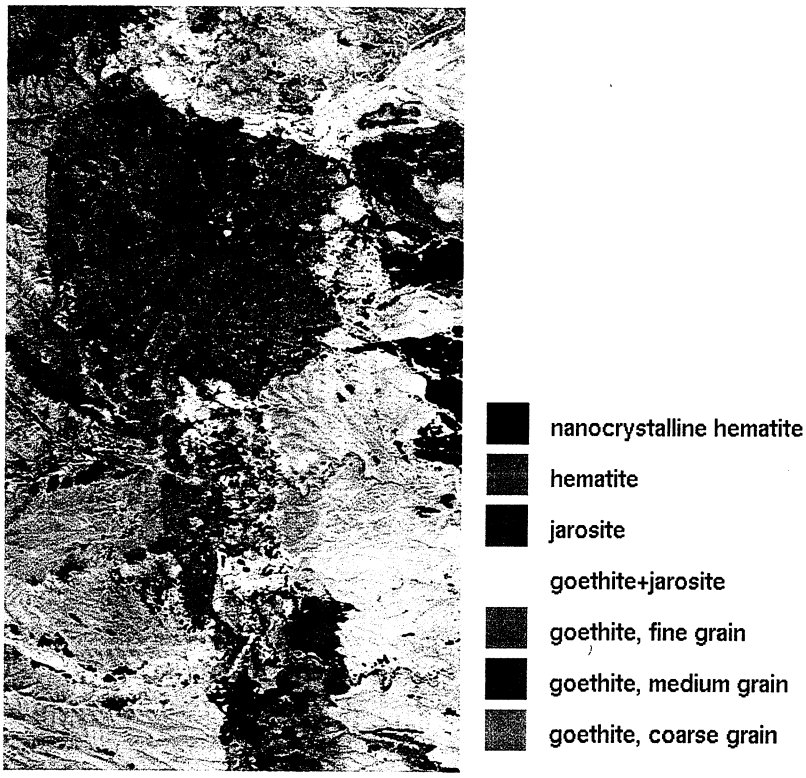

Figure 5 – 1 µm classification output from Tetracorder.

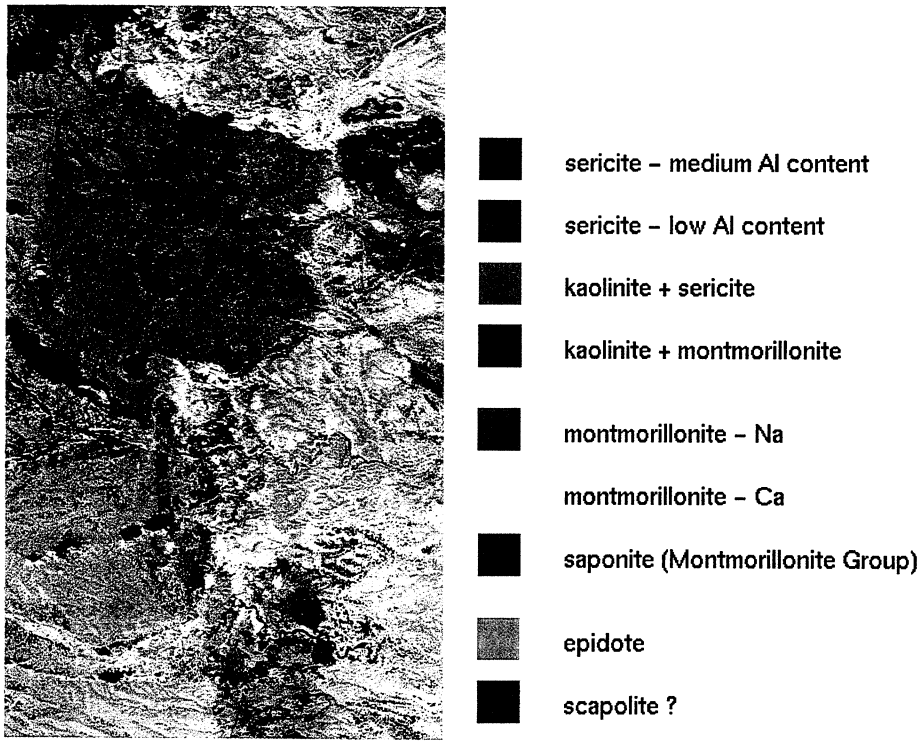

Figure 6 – 2 µm output from Tetracorder.

Discussion

The results presented here are meant to highlight the primary techniques for processing hyperspectral imagery (HSI) data available today. The techniques employed by ENVI and Tetracorder were developed along with the AVIRIS sensor. In general ENVI and Tetracorder represent different approaches to processing and exploiting hyperspectral data. ENVI relies heavily on endmembers, while Tetracorder does not (Figure 7).

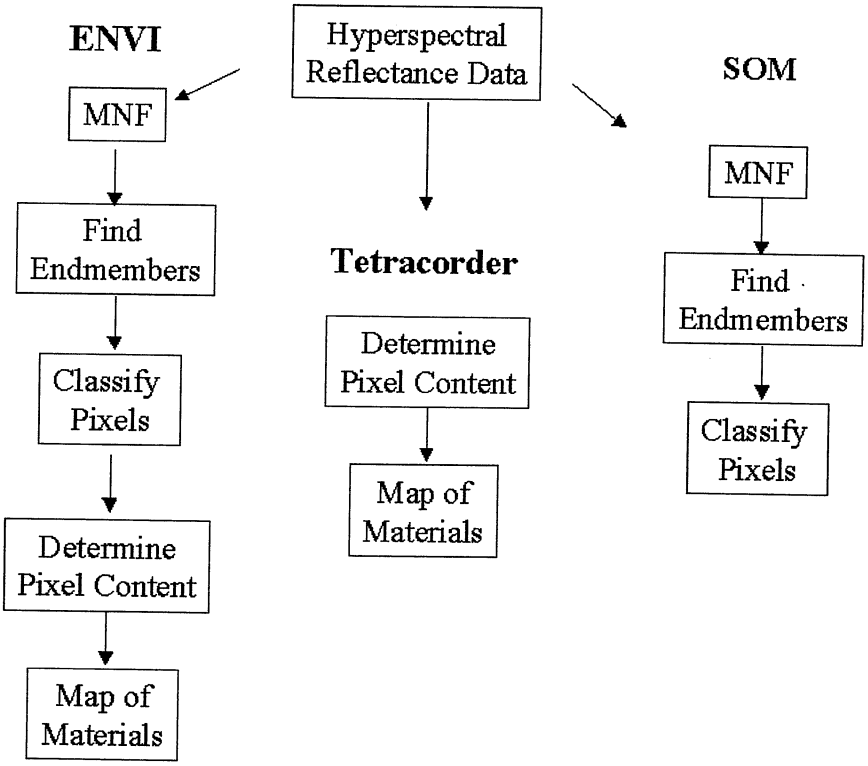

Figure 7 – Hyperspectral data processing flow showing where the respective software process is introduced to the data.

Finding endmembers represents a possible precursor to determining a pixel's content(s), but generally falls short of an actual pixel's content identification. Finding endmembers requires no *a priori* knowledge regarding image or pixel content. In general, classification does not depend upon knowing the content of a pixel. In this situation, the basic assumption is that all pixels are linear combinations of endmembers found at the apices of a convex hypervolume enclosing all the data. Endmembers allow a user to group similar pixels in an image and determine pixel content later. In ENVI, a user develops an *n*-dimensional solution space based on the whole spectrum. Nothing more need be known about the spectra to group the data. The user simply finds the endmembers and classifies the imagery based on a linear endmember mixing model. If an endmember corresponds to a specific mineral, so much the better, but this is not often the case because very few pixels are homogeneous. Subsequent processing is required to decompose and identify the constituents of each derived endmember. ENVI tries to ameliorate this requirement by providing the Spectral Analyst, an expert system for identifying the contents of individual spectra.

Tetracorder's approach is to focus only on a pixel's absorption features to directly assess a pixel's content. This has the limitation of not always being able to classify a pixel. If Tetracorder does not have a desired absorption feature in it's database of known spectra, it cannot identify the spectra and no solution is given.

SOM are strictly a classification method that does nothing regarding absolute interpretation of pixel content. The result of using SOM is that larger aggregates of minerals, i.e., rocks, are discernable in HSI data. SOM represent another classification paradigm offering significant benefits for unsupervised image classification.

Conclusions

Tetracorder, ENVI, and SOM are all effective methods for gleaning information from hyperspectral imagery. Each has its strength and weakness. ENVI and SOM use endmembers while Tetracorder does not. Tetracorder is better at finding individual minerals based upon absorption features. None of these approaches is really a blackbox; most require a significant understanding of mineral spectroscopy and the process of hyperspectral remote sensing.

References

Boardman, J. W. (1993) Automated Spectral Unmixing of AVIRIS data using convex geometry concepts in Summaries, Fourth JPL Airborne Geoscience Workshop, JPL Publication 93-26, v. 1, pp. 11-14.

Boardman, J.W., and Kruse, F.A. (1994) Automated spectral analysis: a geological example using AVIRIS data, North Grapevine Mountains, Nevada, Proceedings, ERIM Tenth Thematic Conference on Geologic Remote Sensing, Environmental Research Institute of Michigan, An, Arbor, pp. 1407-1418.

Boardman, J.W., Kruse, F.A., and Green, R.O. (1995) Mapping Target signatures via partial unmixing of AVIRIS data in Summaries, Fifth JPL Airborne Earth Science Workshop, JPL Publication, 95-1, v. 1. p. 23-26.

Caudill, M. (1988) Neural Networks Primer, Part IV, AI Expert, vol. 3(8), August 1988, pp. 61-67.

Clark, R.N. A.J. Gallagher, and Gregg A. Swayze (1990) Material Absorption Band Depth Mapping of Imaging Spectrometer Data Using a Complete Band Shape Least-Squares Fit with Library Reference, Proceedings of the Second Airborne Visible/Infrared Imaging Spectrometer (AVIRIS) Workshop. JPL Publication 90-54, 176-186, 1990.

Clark, R.N., G.A. Swayze, A. Gallagher, N. Gorelick, and F. Kruse (1991) Mapping with Imaging Spectrometer Data Using the Complete Band Shape Least-Squares Algorithm Simultaneously Fit to Multiple Spectral Features from Multiple Materials, Proceedings of the Third Airborne Visible/Infrared Imaging Spectrometer (AVIRIS) Workshop, JPL Publication 91-28, 2-3, 1991.

Gao, B.C., and Goetz, A.F.H. (1990) Column atmospheric water vapor and vegetation liquid water retrievals from airborne imaging spectrometer data, Journal of Geophysical Research, **95**, 3549-3564.

Gao, B., Heidebrecht, K.B., and Goetz, A. F. H. (1999) Atmosphere Removal Program (ATREM) User's Guide, Version 3.1, Center for the Study of Earth from Space, 31p.

King, T.V.V., Clark, R.N., Ager, C., and Swayze, G.A. (1995) Remote mineral mapping using AVIRIS data at Summitville, Colorado and the adjacent San Juan Mountains. Proceedings: Summitville Forum '95, H.H. Posey, J.A. Pendelton, and D. Van Zyl Eds., Colorado Geological Survey Special Publication 38, p. 59-63.

Kohonen, T. 1986. Representation of Sensory Information in Self-Organizing Feature Maps and Relation of these Maps to Distributed Memory Networks, Proceedings of SPIE Advanced Institute on Hybrid and Optical Computing, vol. 634.

Kokaly, R.F., Clark, R.N., Livo, K.E. (1998) Mapping the Biology and Mineralogy of Yellowstone National Park using Imaging Spectroscopy, Summaries of the 7th Annual JPL Airborne Earth Science Workshop, R.O. Green, Ed., JPL Publication 97-21. Vol. 1, AVIRIS Workshop, conducted Jan 12-16, 1998, pp. 245-254, Dec. 1998.

McLemore, V.T., Munroe, E.A., Heizler, M.T., and McKee, C. (1999) Geochemistry of the CopperFlat porphyry and associated deposits in the Hillsboro mining district, Sierra County, New Mexico, USA, Journal of Geochemical Exploration, vol. 67, pp. 167-189.

Swayze G.A., Clark, R.N., Pearson, R.M., and Livo K.E. (1996) Mapping Acid-Generating Minerals at the California Gulch Superfund Site in Leadville, Colorado using Imaging Spectroscopy, in Summaries of the 6th Annual JPL Airborne Earth Science Workshop March 4-8, 1996.

Tou, Julius T., and Gonzalez, R.C. (1974) Pattern Recognition Principles, Reading, Massachusetts, Addison-Wesley Publishing Company, New York.

LAND COVER IMAGE ENDMEMBERS IN AVIRIS IMAGERY IN THE NEUSE RIVER BASIN, NORTH CAROLINA[1]

Andrew Pilant,[2] Ross Lunetta,[2] Terrence Slonecker,[3] John Streicher,[4] and John Iiames[2]

1. INTRODUCTION

The U.S. Environmental Protection Agency (EPA) National Exposure Research Laboratory (NERL) is conducting hyperspectral remote sensing (imaging spectroscopy) methods development research in the Neuse River Basin, North Carolina. Science objectives have focused on the potential applications of hyperspectral imagery for vegetation discrimination in biologically diverse ecosystems. Imagery was collected by NASA's Airborne Visible/Infrared Imaging Spectrometer (AVIRIS) on July 20, 1999 along a single northwest-southeast oriented flight line in the Atlantic Coastal Plain between New Bern and Kinston, North Carolina. Overall research goals include the evaluation of well-characterized and high signal-to-noise AVIRIS data for vegetative community discrimination and to evaluate (simulation) the potential application of MODIS-based spectral unmixing for vegetation discrimination in the broader Albemarle-Pamlico Basin (APB).

The analysis presented here was directed at extracting a suite of AVIRIS-derived spectral image endmembers from a full scene and determining the land cover class of pixels belonging to each endmember. Image endmembers are the purest pixels in a scene, and can be used as reference spectra in spectral unmixing and land cover mapping. The sections that follow detail the reflectance calibration, the data reduction process, the interactive selection of endmembers, and the land cover class labeling of endmember pixels by comparison with a coregistered land cover / land use (LCLU) map. We close with a discussion of the resultant AVIRIS image endmembers and factors that contributed to endmember emergence from the background data.

2. DATA COLLECTION

The AVIRIS data system is described by Green, et al. (1998). One AVIRIS flight line was collected on July 20, 1999 (14:00 GMT) in the New Bern-Kinston stretch of the Neuse River, immediately upstream of the Neuse Estuary (Fig. 1). Aircraft motion geometric distortions are minimal. Minor haze and clouds (highlighted in images at 1882 nm) are considered negligible for this analysis. The single scene analyzed here (f990720t01p02_r02_sc06.v1.img) is dominated by agriculture and wetland forest flood plain, and is almost entirely vegetated, except for fallow agricultural fields, rivers, ponds, pavement and buildings.

---

[1]**Notice:** This paper has been reviewed in accordance with the U.S. Environmental Protection Agency's peer and administrative review policies and approved for presentation and publication. Mention of any trade names or commercial products does not constitute endorsement or recommendation for use.

[2] U.S. EPA National Exposure Research Laboratory, Landscape Characterization Branch, 79 T.W. Alexander Drive MD-56, Research Triangle Park, North Carolina 27711, pilant.drew@epa.gov

[3]U.S. EPA National Exposure Research Laboratory, Landscape Ecology Branch, Environmental Photographic Interpretation Center, 12201 Sunrise Valley Drive, 555 National Center, Reston, Virginia 20192

[4] National Oceanic and Atmospheric Administration, U.S. EPA National Exposure Research Laboratory, Landscape Characterization Branch, 79 T.W. Alexander Drive MD-56, Research Triangle Park, North Carolina 27711

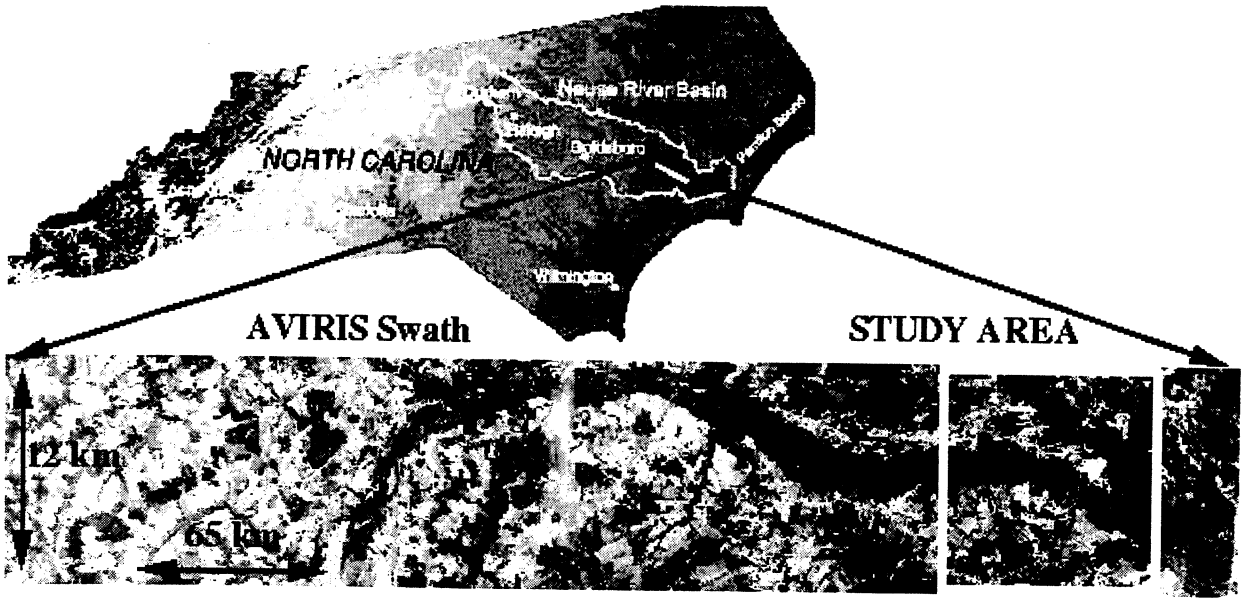

Figure 1. Location of AVIRIS swath and study area in the Neuse River Basin, North Carolina.

2.1 Field Spectroscopy

Fifteen close range field spectra were acquired on November 1-2, 2000 for calibrating the AVIRIS radiance data to apparent reflectance. Calibration targets were selected for optimal performance, i.e., homogenous materials, spectrally flat, time invariant, identifiable in the AVIRIS scene, and preferably spanning a range of low to high reflectance. Candidate pixels for light and dark calibration targets were first screened by examining images showing the darkest and brightest 20% of pixels at four wavelengths (459, 654, 1564, 2192 nm). Potential targets were identified in the northwest and southeast portions of the swath (those areas most anthropogenically developed): airport runway, factory rooftops, water treatment pond, soil baseball infield, and parking lots.

Field spectra were acquired using an Analytical Spectral Devices Full Range Field Spectrometer (Fig. 2) recording upwelling radiance from 350-2500 nm. The instrument was mounted on a tripod approximately 30 cm above the ground, sampling within a 2-4 m^2 region around a central point. Reference spectra of a calibrated Spectralon™ tablet were collected before and after each 5 target spectra. The mean spectrum of five spectra for each target was used in the subsequent image calibration. Field site locations were measured with a Trimble TDC1 GPS in differential corrected mode, accurate to 1.0 m horizontal.

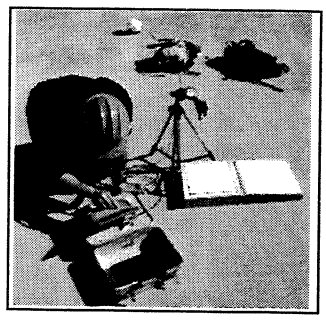

Figure 2. Field spectrometer, Spectralon tablet and GPS.

Atmospheric and solar conditions differed between the AVIRIS acquisition (July 20, 1999; 14:08 GMT) and field spectroscopy (November 1-2, 2000; 15:00-20:00 GMT). The July atmosphere was more humid than November, with visible haze and some cirrus clouds. The solar geometry was as follows: July (elevation: 48°; azimuth 98°); November (elevation: 36°, azimuth: 155°, 17:00 GMT).

2.2 Endmember LCLU Linkages

A recently compiled (U.S. EPA), remote-sensing based Neuse River Basin LCLU map was used to identify the land cover class of pixels identified as AVIRIS spectral image endmembers. The map was produced from 1998-99 SPOT 4 XS and Landsat 7 ETM^+ scenes, plus GIS input data (roads and wetlands). It has a pixel size of 15 m, with a 0.4 ha minimum mapping unit (MMU) (0.1 ha MMU in riparian zones). Overall Level I accuracy as verified

by a virtual field reference database[5] is 88% (n=1360 validation sites) with a Kappa statistic (KHAT) of 0.82 (n=1360).

3. AVIRIS DATA PROCESSING

The goal of the AVIRIS processing (Fig. 3) was to calibrate the raw AVIRIS radiance data to apparent surface reflectance, identify the most spectrally pure pixels, extract endmembers, and determine the class identity for each endmember based on the NRB LCLU map and visual interpretation of the AVIRIS imagery.

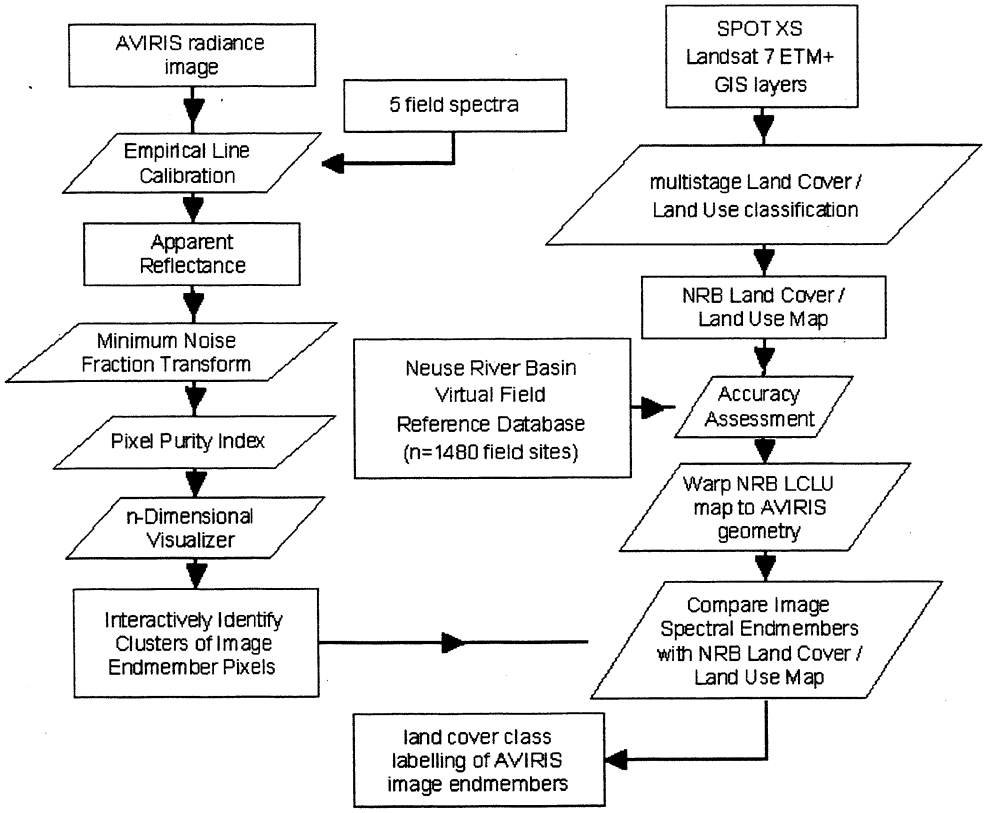

Figure 3. Flowchart of AVIRIS processing steps (left column).

3.1 Empirical Line Calibration

The technique used for calibrating radiance data to apparent reflectance was the Empirical Line Calibration method (Farrand, et al., 1994). A linear regression was performed to relate field spectra reflectance to AVIRIS radiance for corresponding pixels in the image. Generally, at least two field spectra are used: one bright and one dark target. Additional field spectra improve calibration quality.

Five field spectra were used in calibration of this scene: three factory roof targets, one gravel parking lot, and one pond. The gravel pixel and pond pixels were spectrally pure. However, it proved difficult to distinctly locate the roof targets in the image due to their limited areal extent and spectral similarity to surrounding pixels. It was necessary to use these roofs due to the absence of suitably large calibration targets in the scene. Fortunately, the

[5] The Virtual Field Reference Database is available online at www.epa.gov/nerlesd1/lcb/nrb/VFRDB/

surrounding roof and pavement pixels were spectrally similar, thus limiting the problem of mixed pixels. A scaling artifact was evident in the blue and green wavelengths, where reflectance dipped to negative 10%. This may have been due to a greater degree of Raleigh scattering under July sky conditions during the AVIRIS acquisition, relative to drier November sky conditions (less scattering) for the field spectra collection.

3.2 Minimum Noise Fraction Transform

The Minimum Noise Fraction (MNF) Transform is a sequence of two cascaded principal component transforms that results in a series of transformed bands ordered by decreasing signal to noise ratio (Green, et al., 1988; Boardman and Kruse, 1994). The analyst selects those bands with the highest signal-to-noise ratio (SNR) for further processing, and omits the remaining lower SNR bands. High SNR bands typically have eigenvalues > 1.0, and the images appear coherent, whereas the low SNR bands are dominated by noise (typically of a speckle nature). For this data set, the MNF image quality was significantly degraded for MNF bands 30 and greater (eigenvalues > 1.45)

3.3 Pixel Purity Index

MNF bands 1-30 were input to the Pixel Purity Index™ (PPI) algorithm (ENVI, 1999). The PPI algorithm finds the more spectrally pure pixels in scene by iteratively projecting the pixels onto a unit vector in n-dimensional space. Each time a pixel was found to be 'extreme', its count was increased by one. The output was an image with a PPI count assigned to each pixel. Then those pixels below some heuristically estimated threshold value were discarded to create a subset of the most spectrally pure pixels in the scene. This subset was then input to the n-Dimensional Visualizer™ algorithm (ENVI, 1999).

3.4 Interactive Selection of Image Endmembers

At this point in the processing flow the most spectrally pure pixels in the scene had been identified. Next, those pixels were interactively grouped to define image endmembers using an animated n-dimensional scatter plot (n-Dimensional Visualizer™ (*ibid.*)). Numerous bands were selected for input to the n-Dimensional Visualizer™ (three to six at a time generally worked well), then interactively grouped into clusters of pixels in a 3-D display using the mouse as the n-dimensional data cloud rotates on the computer screen. Through this process, 28 endmembers were extracted, with n=1 to 518 pixels (spectra) per endmember. Figure 4 graphs the mean spectrum of each endmember. Three endmembers were artifacts and were omitted from the discussion below. Figure 5 is a true color image of the AVIRIS scene showing color-coded locations of endmember pixels.

3.5 Determining LCLU Class of Image Endmembers

The land cover class of each endmember was determined by comparison with the coregistered cover type map. The NRB LCLU map was warped using ground control points to coregister with the unrectified AVIRIS scene (RMSE < 0.5 pixel). This preserved spectral fidelity by avoiding resampling reflectance values in a geometric warp. The analyst examined each pixel in each endmember, and noted the land cover class of the pixel as indicated by a) the NRB LCLU map and b) a true color composite of AVIRIS bands.

In many cases, multiple cover classes were captured by a single endmember; the dominant class(es) type determined the label. For example, endmember #3 contained 18 pixels distributed as follows: soy (11), cotton (2), pasture/hay (4), woody-mixed (1), and was labeled Agriculture- soy/pasture. In a similar manner, a label was applied to each endmember according to the dominant land class types indicated by the NRB LCLU map.

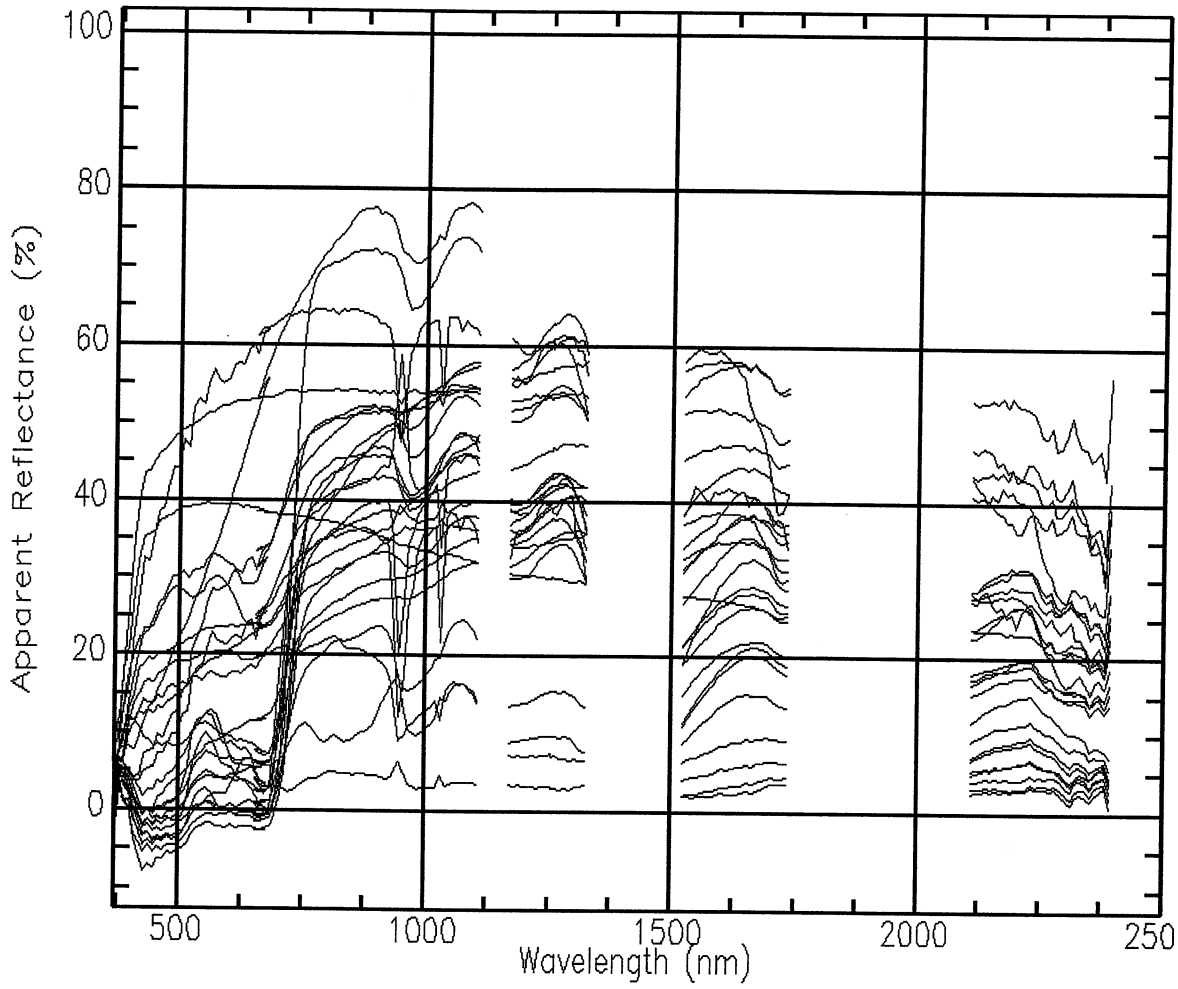

Figure 4. AVIRIS image endmember spectra. Each spectrum is the mean of all spectra for each endmember. The three Edge Artifact spectra are omitted.

4. RESULTS

The processing steps outlined in Figure 3 (left column) yielded 28 endmembers. They were distributed among the LCLU classes as follows:

- Urban (11 endmembers)
- Agriculture (9)
- Edge Artifacts (3)
- Mixed (2)
- Woody Vegetation (1)
- Water (1)
- water treatment pond Aerator Foam (1).

Figures 6-8 show example spectra for selected endmembers. Eleven endmembers were labeled urban. This class is defined as impervious surfaces plus unpaved roads (e.g., roofs (Fig. 6A), pavement, roads). Nine were labeled agriculture, and were further identified as cotton, corn, tobacco, soy or pasture. Most vegetation endmember spectra exhibited a green peak, red edge and near infrared plateau. Some appeared to be mixed with urban spectra

Figure 5. AVIRIS scene f990720t01p02_r02_sc06.v1.img and locations of image endmember pixels. Above: AVIRIS image (visible bands) with endmember pixels plotted. Below: endmember pixels only (image removed).

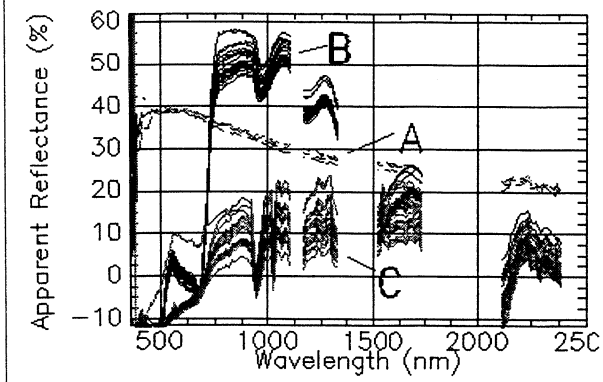

Figure 6. Endmember spectra. A: roof. B: cotton field. C: gravel/soil road.

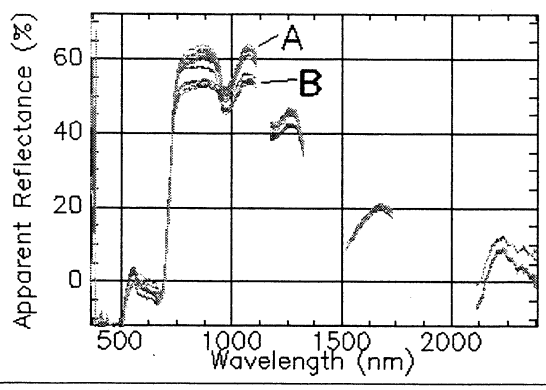

Figure 7. Corn field endmembers.

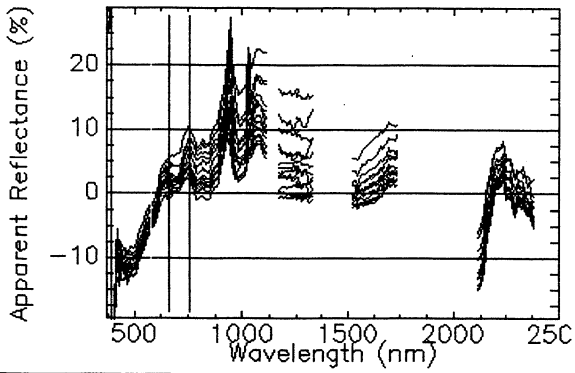

Figure 8. Fallow agricultural field endmember.

(e.g., agricultural fields adjacent to roads, buildings, gravel) (Figs 6.c, 8). At the detailed level (e.g., corn field), no endmembers were purely one crop type.

Three endmembers were labeled edge artifacts. They appeared as a discontinuous column of pixels occupying the right margin of the image (Fig. 5, right margin). Their location and unnatural linear spatial pattern indicated that they did not correspond to any feature of this landscape. Two endmembers were labeled mixed; significantly different land cover classes were contained within a single image endmember (e.g., agriculture and urban). Visual inspection of graphs of all spectra contained in mixed endmembers showed that multiple land cover classes were present (e.g., a group of characteristic vegetation spectra, and another group of characteristic urban spectra). One endmember was labeled woody vegetation, which includes deciduous, evergreen and mixed tree categories. One endmember was labeled water, corresponding to a clear, dark water pond (the water calibration target). One endmember was labeled aerator foam, corresponding to patches of froth and foam around several aerators in a water treatment pond.

5. DISCUSSION

The objective of this experiment was to calibrate an AVIRIS scene, and extract a suite of image endmembers, in preparation for further analysis including spectral unmixing and land cover mapping. The results were encouraging in that the linkages between endmembers and functional land cover classes were reasonably strong, despite a number of potential error sources, which include potential errors in image coregistration, changes in cover type status between the AVIRIS acquisition (1999) and NRB LCLU map (1998-99), the complex nature of vegetation reflectance, and subjectivity in the endmember selection process.

Inspection of spectra at 650 nm shows the endmembers to break into three groups (Fig. 4):

- 40-60 % reflectance, urban (n=4);
- 18-40 % reflectance, urban and mixed (n=8); and
- 0-10% reflectance, vegetation and water (n=13).

Urban endmembers (Group 1) comprised 11 of the 28 endmembers, and were distinct in overall high albedo and rapid increase in blue reflectance. Their relative abundance can be interpreted to mean that urban spectra tend to be more pure than other land cover class spectra in this scene. This results from a number of factors, including the typical spectral homogeneity of urban surfaces, high albedo (thus high signal to noise), and perhaps the fact that urban targets tend to have linear or otherwise distinct (non-diffuse) boundaries (which reduces the effect of intimately mixed pixels). Group 2 endmember spectra showed characteristics of both vegetation and urban spectra. Fallow agricultural fields and farm roads fell in this group, showing contributions from both vegetation and soil components. Vegetation endmembers (Group 3) displayed characteristic green vegetation spectral features: green peak, red edge, infrared plateau, low visible albedo. It is interesting to note that the Neuse River did not produce an endmember, yet it was visually distinct (Fig. 5). The Neuse River is highly turbid with suspended red clay, derived from sediments evident in nearby fields and farm roads. Thus its spectrum is inherently mixed, a combination of water and soil components, and thus less likely to emerge as an endmember in this scene.

Also of interest is the single woody vegetation (i.e., forest) endmember. For our purposes, additional woody vegetation endmembers would be useful in mapping forest associations. Though not strongly expressed in visible wavelengths (Fig. 5), subtle differences in Neuse River flood plain forest areas are well expressed in decorrelation-stretched images for certain wavelength combinations (e.g., 1684, 1614, 1555 nm red, green, blue). The subtle differences among forest pixels were lost in this analysis, overwhelmed by the greater magnitude differences (spectral separability) between urban and vegetation pixels. In order to better extract endmembers for forest pixels, image segmentation is required. By omitting all but forest pixels prior to the MNF transform, the algorithms would operate on a reduced, forest-only set of statistics and produce a different, forest-focused set of endmembers.

The mixed class of endmembers (most apparent in Group 2 spectra) resulted from two primary factors. First, certain pixels are inherently mixed, such as those encompassing both farm roads and adjacent agricultural fields. The second factor was processing related. The interactive grouping of pixels to form endmembers in the n-Dimensional Visualizer™ has inherently subjective components. Results depend on the combination of input bands used, and the analyst's visual perception of relationships among pixels in the animated scatterplot. This step can be refined heuristically as the analyst develops skill through multiple iterations of the technique.

6. CONCLUSIONS

An AVIRIS scene of a densely and diversely vegetated area in the Neuse River Basin of the North Carolina coastal plain was calibrated to apparent reflectance using field acquired reference spectra, and processed to yield 28 image endmembers. The composition of each endmember was identified using an independently-developed NRB LCLU map, in parallel with visual analysis of the original AVIRIS scene. Urban endmembers were the most abundant, followed by agriculture, edge artifacts, mixed, woody vegetation and water. The entire scene was input for processing, and this population of pixels influenced the nature of the output endmembers. If additional endmembers are desired from a particular cover type (e.g., forest), image segmentation to isolate pixels of only that cover class should be performed prior to the MNF transform step. Also, the identity and purity of endmembers are influenced by the band combinations used in the n-Dimensional Visualizer™, and the analyst's visual perception of relationships among pixels. Analyst experience with this step plays a role in endmember extraction.

7. ACKNOWLEDGMENTS

The authors thank Brad Chesson of Weyerhaueser and Clifford Lee of Dupont for assistance in accessing field spectra collection sites, Jayantha Ediriwickrema for land cover data, Jill Crotwell for assistance in image rectification, Dr. Mark Karaska of Applied Analysis, Inc. for assistance in the data acquisition, and the NASA-JPL AVIRIS team for their ongoing efforts.

8. REFERENCES

Boardman, J.W., and F.A. Kruse, 1994. "Automated spectral analysis: a geologic example using AVIRIS data, north Grapevine Mountain, Nevada". Proceedings, Tenth Thematic Conference on Geologic Remote Sensing, Environmental Research Institute of Michigan, Ann Arbor, Michigan. I- 407-418.

ENVI, 1999. ENVI Tutorials: "Chapter 11, Advanced Hyperspectral Analysis". Better Solutions Consulting, Inc, Boulder, CO, p. 261-286.

Farrand, W.H., R.B Singer, and E. Merenyi, 1994. "Retrieval of apparent surface reflectance from AVIRIS data: a comparison of empirical line, radiative transfer, and spectral mixture methods". Remote Sensing of Environment, 47, 311-321.

Green, A.A., M. Berman, P. Switzer, and M. Craig, 1988. "Transformations for ordering multispectral data in terms of image quality and implications for noise removal". IEEE Transactions on Geoscience and Remote Sensing, 28(1), 65-74.

Green, R.O., M.L. Eastwood, C.M. Sarture, T.G. Chrien, M. Aronsson, B.J. Chippendale, J.A. Faust, B.E. Pavri, C.J. Chovit, M. Solis, M.R. Olah, and O. Williams, 1998. "Imaging spectroscopy and the Airborne Visible/Infrared Imaging Spectrometer (AVIRIS)". Remote Sensing of Environment, 65, 227-248.

SPATIAL/SPECTRAL IDENTIFICATION OF ENDMEMBERS FROM AVIRIS DATA USING MATHEMATICAL MORPHOLOGY

Antonio Plaza,[1] Pablo Martínez,[1] J. Anthony Gualtieri,[2] and Rosa M. Pérez[1]

1. INTRODUCTION

During the last several years, a number of airborne and satellite hyperspectral sensors have been developed or improved for remote sensing applications (Green, 1988-2000; Vane et al., 1993; Kruse & Boardman, 1999). Imaging spectrometry allows the detection of materials, objects and regions in a particular scene with a high degree of accuracy. Hyperspectral data typically consist of hundreds of thousands of spectra, so the analysis of this information is a key issue (Landgrebe, 1997).

A very useful and commonly accepted approach to analyze hyperspectral data has been the identification of the purest spectra, or "endmembers" (Kruse, 1998). Some researchers have taken the approach of constructing spectral libraries of pure elements that can be matched with every spectrum in a hyperspectral image in order to classify the scene (Roberts et al., 1999). This processing is suitable when pure materials, contained in the library, are on the ground, but in real-world situations, since materials are spatially or intimately mixed, only the strongest features are matched. As a result, the most widely used technique is to determine endmember spectra directly from the image. Once the individual endmembers have been identified, several methods can be used to map their spatial distributions, associations and abundances (Boardman & Kruse, 1994; Kruse et al., 1996).

A large variety of methodologies have been proposed in the literature in order to find endmembers in the data cube (Winter & Winter, 1999). One of the most successful approaches is the Pixel Purity Index™ (PPI) algorithm (Boardman et al., 1995), which finds the "purest" pixels in the scene through a series of repeated projections on to randomly oriented lines in N-dimensional space. These potential endmember spectra are loaded into an N-dimensional scatterplot and rotated in real time until a trained analyst selects extremities in the data cloud that likely correspond with scene endmembers. This procedure, based on the geometry of convex sets, is widely accepted (available in the commercial software system ENVI®, the Environment for Visualizing Images), but it is time-consuming and highly interactive.

Several methods for autonomous extraction of endmembers have been recently proposed in the literature. The N-FINDR algorithm (Winter & Winter, 1999) finds the simplex of maximum volume that can be enclosed within all the points of the data cloud. The ORASIS algorithm (Palmadesso et al., 1999) uses a process called Exemplar Selection to thin the data set by rejecting any "redundant" spectra (this requires the calculation of the angle between spectral vectors). The Iterative Error Analysis (IEA) approach (Szeredi et al., 1999) performs a series of constrained unmixings and chooses as endmembers those pixels that minimize the error in the unmixed image. In addition to these physically based methods, there are several statistically based approaches that rely on clustering algorithms (Beaven et al., 1999). The major drawback of all the previously addressed methods is that they only consider the spectral information contained in the data cube. Spatial information has not been fully exploited yet, specially in unsupervised classification. The integration of both spatial and spectral information is becoming more relevant as the sensors used in spaceborne platforms tend to increase the spatial resolution (Jiménez & Rivera-Medina, 1999).

Mathematical morphology theory (Serra, 1982) is a widely used non linear technique for image analysis and pattern recognition. Although it is especially well suited to segment binary or grayscale images with irregular and complex shapes, its application in the classification/segmentation of multispectral or hyperspectral images has been quite rare (Soille, 1996; Lambert & Channusot, 2000). In this paper, we discuss a new completely automated methodology to find endmembers in the hyperspectral data cube using mathematical morphology.

[1] Departamento de Informática, Universidad de Extremadura, Avda. de la Universidad s/n, 10071 Cáceres, SPAIN
E-mail: {aplaza, pablomar, rosapere}@unex.es

[2] Global Science and Technology at Applied Information Sciences Branch, NASA/GSFC, Greenbelt, Maryland 20771, U.S.A.
E-mail: gualt@peep.gsfc.nasa.gov

The extension of classic morphology to the hyperspectral domain allows us to integrate spectral and spatial information in the analysis process. In Section 3, some basic concepts about mathematical morphology and the technical details of our algorithm are provided. In Section 4, the accuracy of the proposed method is tested by its application to real hyperspectral data obtained from the AVIRIS imaging spectrometer. Some details about these data and reference results, obtained by well-known endmember extraction techniques, are provided in Section 2. Finally, in Section 5 we expose the main conclusions at which we have arrived.

2. DATA

We have applied our endmember extraction algorithm to real hyperspectral data obtained from the AVIRIS imaging spectrometer for a particular scene: Salinas 98 taken in the Salinas Valley, California on October 9, 1998 (Gualtieri et al., 1999). This data was available only as at-sensor radiance data and includes vegetables, bare soils and vineyard fields. We have selected a subscene of the Salinas 98 dataset called Salinas A, which comprises 83x86 pixels and includes six classes. Ground truth is available for this image (see Figure 5 at the end of the paper).

The spatial characteristics of the Salinas A dataset make it particularly suitable for testing the accuracy of our method. Ground truth information reveals zones where broccoli with weeds, senesced corn and romaine lettuce are present. The romaine lettuce is at different weeks since planting and with growth increasingly covering the soil.

A reference dataset of endmembers was obtained for this particular image using the Pixel Purity Index™ (PPI) procedure as implemented in the commercial software system ENVI®. The endmembers extracted by this widely accepted supervised methodology will be compared to those found by our algorithm. The full ENVI process is detailed next.

First, the spectral data volume of the hyperspectral dataset was reduced by using the Minimum Noise Fraction (MNF) transformation. The top MNF bands, which contain most of the spectral information, were used to determine the most likely endmembers by using the PPI procedure. These potential endmember spectra were loaded into an N-dimensional scatterplot and rotated in real time through the N-Dimensional Visualizer™ until extremities on the scatterplot were found. The resulting projections were annotated and exported to the image using Region-of-Interest (ROI) definition procedures. Mean spectra were extracted for each ROI to act as endmembers for mapping through Linear Spectral Unmixing, which results in a series of grayscale abundance maps (rescaled to lie in the range from 0 to 255), representing the fractional composition of endmember materials in the scene (darker pixels indicate more concentration of the endmember material). The results of applying this methodology to the Salinas A dataset are depicted in Figure 7, where 7.a shows the resulting endmembers and 7.b to 7.e show their correspondent abundance maps.

3. METHODS

In this section we provide some basic concepts about mathematical morphology theory and describe a schema to extend morphological operators to the hyperspectral domain. Finally, we propose an automated methodology, based on morphology, to extract endmembers from the data cube.

3.1 Classic Mathematical Morphology

Mathematical morphology theory (Serra, 1982) has now become an useful tool for image analysis and pattern recognition. In binary morphology, images are represented as sets, where pixels in the image foreground are members of a set X and pixels in the background belong to the complementary set X^C. The two basic operations of mathematical morphology consist of the transformation of an image by another set K, known as the structuring element. The shape and size of the structuring element determine the spatial characteristics of the resulting image. The two basic morphology operations, dilation and erosion, are defined respectively as follows:

$$X \oplus K = \{s \mid K_s \cap X \neq \varnothing\} \tag{1}$$

$$X \otimes K = \{s \mid K_s \subseteq X\} \tag{2}$$

Erosion and dilation are said to be dual to each other with respect to complementation. We call the *opening* of X with respect to K the following set:

$$X_K = (X \otimes K) \oplus K \tag{3}$$

Similarly, we call the *closing* of X with respect to K the following set:

$$X^K = (X \oplus K) \otimes K \tag{4}$$

The opening of X by K is thus defined in terms of an erosion followed by a dilation. Similarly, the closing of X by K is defined in terms of a dilation followed by an erosion.

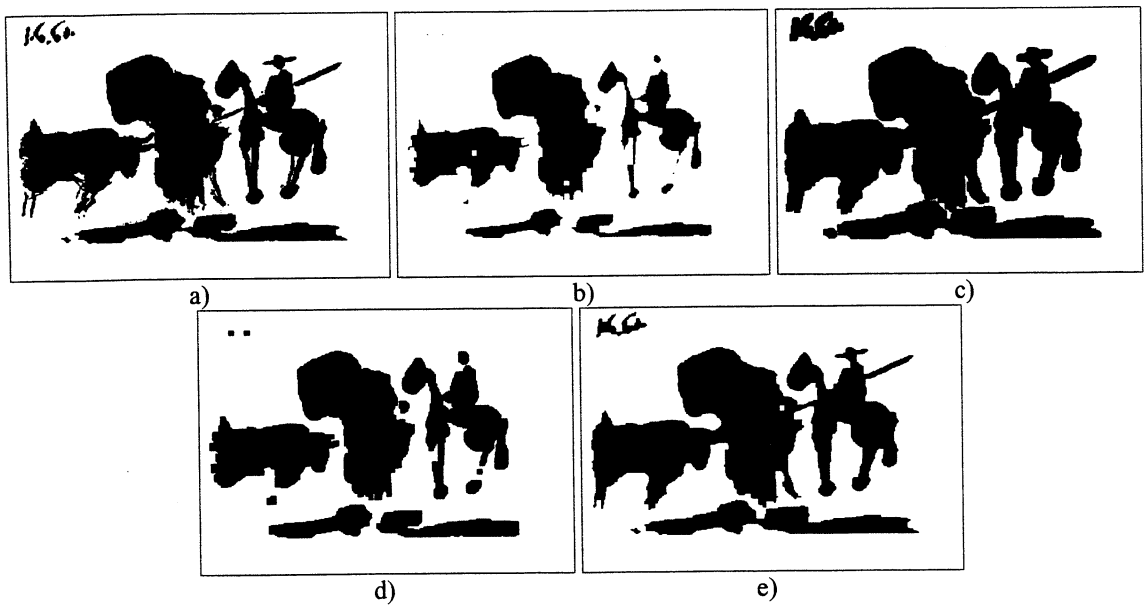

Figure 1. Binary mathematical morphology example.

Figure 1 shows the effect of applying erosion and dilation operations to a simple binary image corresponding to an original Pablo Picasso painting: "Pass with the cape," 1960 (Figure 1.a). In 1.b and 1.c, the results of applying a binary erosion and a binary dilation to 1.a with a 5x5 square-shaped structuring element are respectively addressed. Finally, in 1.d and 1.e the effect of opening and closing image 1.a with the same structuring element are shown. As depicted in Figure 1, after having eroded X by K, it is not possible, in general, to recover the initial set by dilating the eroded set by the same K, i.e. $(X \otimes K) \oplus K$. This dilate reconstitutes only a part of X which is simpler and has less details, but the new set, called the *opening* of X, actually filters out a subset of X which is extremely rich in morphological and size distribution properties (Serra, 1993).

The principles of mathematical morphology have also been extended to the grayscale image case (Sternberg, 1986). Greyscale images are described as a grey level function $f(x, y)$ on the points of Euclidean 2-space. Grayscale dilation, erosion, opening and closing are respectively defined as follows:

$$(f \oplus k)(x, y) = \underset{(s,t)\in k}{\text{Max}} \{f(x-s, y-t) + k(s, t)\} \tag{5}$$

$$(f \otimes k)(x, y) = \underset{(s,t)\in k}{\text{Min}} \{f(x+s, y+t) - k(s, t)\} \tag{6}$$

$$f_k(x, y) = ((f \otimes k) \oplus k)(x, y) \tag{7}$$

$$f^k(x, y) = ((f \oplus k) \otimes k)(x, y) \tag{8}$$

The expressions for greyscale dilation and erosion bear a marked similarity to the convolution integral encountered frequently in digital image processing, with sums and differences replacing multiplication and minimum and maximum replacing summation. Figure 2 illustrates the effect of applying greyscale erosion (2.b), dilation (2.c), opening (2.d) and closing (2.e) to a simple greyscale image (2.a), using a 5x5 square-shaped structuring element. As it can be infered from this example, image processing through iterative morphological transformation is a process of selective information removal where irrelevant image content is irrecoverably destroyed, enhancing the contrast of image features of certain spatial characteristics (in this sense, the structuring element acts as a *matching pattern* that performs a filtering operation).

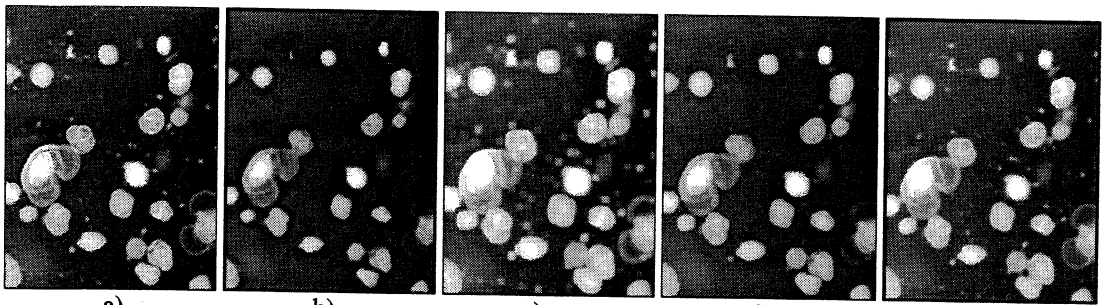

Figure 2. Greyscale mathematical morphology example.

3.2 Extending mathematical morphology to N-dimensional space

Mathematical morphology definition requires an algebraic structure T (complex lattice) such that:

a) T is induced by a (partial) ordering relation, and

b) For any family of elements in T, there exists a smallest majorant or *supremum* and a greatest minorant called the *infimum* (Lambert & Chanussot, 2000).

In the case of hyperspectral images, these two properties are missing because there is no natural means for total ordering of multivariate pixels. Two main strategies have been considered in order to solve this:

a) The first one consists of processing each channel of the hyperspectral image separately. This *marginal* approach is not satisfying because it does not take into account the existing correlation between the individual channels.

b) The second one uses a purely vector approach to process the hyperspectral channels all at once. This strategy requires the definition of a vector ordering relation to determine the *supremum* and the *infimum* of any family of N-dimensional vectors.

The definition of a vector ordering relation can be done as follows. Let x_1, x_2, ..., x_n be the hyperspectral image pixels within a filtering window that represents the structuring element of a morphological operation. We can define a measure of the dissimilarity between two of those pixels, x_a and x_b by:

$$\mathrm{dist}(x_a, x_b) = \cos^{-1}\left(\frac{x_a \cdot x_b}{\|x_a\| \cdot \|x_b\|}\right) \tag{9}$$

This is the angular distance function, expressed in radians. The following scalar quantity can be calculated to measure the global distance between a particular pixel x_i and a set $x_j, j = 1...m$ of neighboring pixels.

$$d_i = \sum_{j=1}^{m} \mathrm{dist}(x_i, x_j) \tag{10}$$

The *supremum* and *infimum* of a set of $x_i, i = 1...n$ hyperspectral pixels are respectively defined:

$$\sup(x_i) = h = \arg\max_i d_i \tag{11}$$

$$\inf(x_i) = l = \arg\min_i d_i \tag{12}$$

Now it is easy to determine basic morphology operations such as erosion and dilation by *maximum* and *minimum* operations, as described in the previous subsection. While *h* is the most spectrally singular pixel in a spatial neighborhood, *l* is nothing else than the median of the pixels the neighborhood, according to the classical vector median definition (Lambert & Chanussot, 2000).

3.3 Autonomous morphological endmember extraction (AMEE)

We propose a morphology-based automated algorithm to extract endmembers from hyperspectral images. The input to this process is the full hyperspectral image cube, with no previous dimensionality reduction or pre-processing. The procedure must examine the full dataset to find those pure pixels that can be used to describe the various mixed pixels in the scene. This is done in the following steps.

3.3.1 Application of morphological operators

Let X be the original image and K a structuring element. We propose the following morphological operator to identify endmembers:

$$X\Phi K = \mathrm{dist}(X, X^K) = \mathrm{dist}(X, (X \oplus K) \otimes K) \tag{13}$$

This operator works as follows: firstly, a hyperspectral closing operation is applied to the original image; then, a measure of the dissimilarity between each pixel of the original image and the correspondent pixel in the closed image is calculated by the angular distance function.

It is important to emphasize that Φ extracts spectral information using a pixel by pixel basis, much like other existing methods, but the process is guided by spatial information. As a result, the spatial and spectral response is considered simultaneously in the analysis process.

Let K be a square-shaped, 3x3 structuring element. Figure 3 illustrates the working procedure of the operator when applied to a target pixel E in the original image using K as structuring element. Firstly, the most spectrally pure hyperspectral pixel (Q) in a spatial neighborhood of the target pixel is selected after projecting each pixel against all its spatial neighbors. This procedure is repeated for every pixel in X, leading to a new image $X \oplus K$. From this image, only the pixels that provide a good representation of their neighbors are selected by the minimum operator, which in our case is equivalent to a vector median filtering. The pixels in $(X \oplus K) \otimes K$ match the definition of an endmember, i.e. a spectrally pure pixel that can be used to describe several mixed pixels in the scene. Finally, the dissimilarity between E, the target pixel in the original image, and V, the pixel selected by the operator, is calculated to check if the target pixel is likely to be an endmember.

The previously described operation is repeated using structuring elements of progressively increased size, in order to obtain a detailed information of the spatial context associated to each hyperspectral pixel. The overall result of applying a sequence of morphological operators to the original image is a spatial/spectral signature associated to each pixel of the scene. From this information, a 2-dimensional grayscale rule image is generated following the basic idea of the Pixel Purity Index algorithm: those pixels that have been repeatedly selected by the operator during the process increase their probability of being declared "pure".

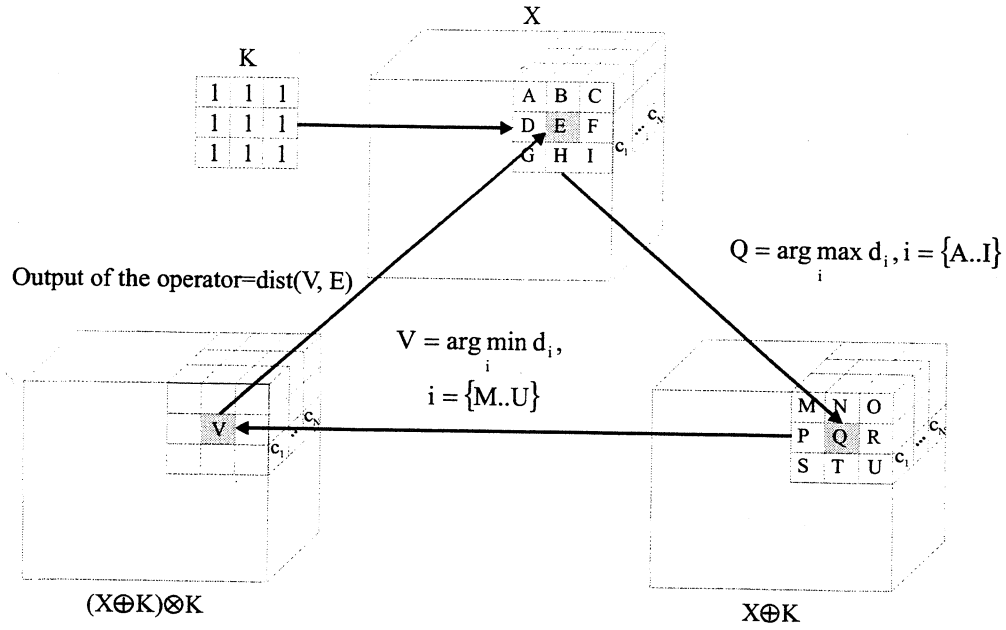

Figure 3. Working procedure of Φ hyperspectral morphological operator.

3.3.2 Endmember selection

Individual endmember spectra can be selected by automatically thresholding the previously obtained rule image. Once the automatical thresholding has been performed, mean spectra can be extracted from the resulting regions to act as endmembers for spectral mapping.

Several methods for automatic thresholding of grayscale images are available in the literature (Sahoo et al., 1988). In our particular case, we have found satisfactory results using Otsu method (Otsu, 1979), which is based on the minimization of the weighted sum of group variances. Let σ_w^2, σ_b^2 and σ_t^2 be the within-class, between-class and total variance, respectively. An optimal threshold v can be determined by maximizing one of the following criterion functions with respect to v:

$$\lambda = \frac{\sigma_b^2}{\sigma_w^2} \qquad \eta = \frac{\sigma_b^2}{\sigma_t^2} \qquad \kappa = \frac{\sigma_t^2}{\sigma_w^2} \tag{14}$$

3.3.3 Redundant endmember thinning

Thresholding of the rule image may result in several unconnected regions with very similar mean spectra, so a procedure to reject redundant endmembers must be performed. We propose to apply a spatial/spectral seeded region growing from those regions, following the approach of Bateson et al., 1998 to create endmember bundles.

The process is as follows: neighboring pixels are incorporated to each region if their spectra are sufficiently correlated to the mean spectrum of the region (a threshold angular distance value A=0.001 is previously set). Once the region growing process has finished, mean spectra associated to the resulting regions are stored in a dataset. If several regions merge during the process, redundant endmember spectra are automatically thinned from the original dataset.

The previously described algorithm performs a spatial/spectral processing of the original image. Spectral information at each pixel is analyzed regarding its spatial context, which guides the fully automated endmember extraction process.

4. RESULTS AND DISCUSSION

In this section, the application of the Autonomous Morphological Endmember Extraction (AMEE) algorithm to hyperspectral data collected by the AVIRIS sensor is discussed. In particular, the Salinas A dataset (see Figure 1) is analyzed. The results obtained by our method are compared to those found using the Pixel Purity Index (PPI) algorithm implemented in the software system ENVI (a detailed explanation of this ENVI-based analysis process can be found in Section 2).

The full AMEE process for this particular image was accomplished in approximately 50 seconds using a Pentium III 500 MHz personal computer with 128 Megabytes of RAM. A sequence of morphological Φ operators with square-shaped structuring elements of size ranging from N_1xN_1 to N_2xN_2 (N_1=3 and N_2=30) was applied to the image in order to create a rule image. Seed regions were extracted by automatically thresholding the rule image and a preliminary set of endmembers was generated. Redundant endmembers were thinned using a seeded region growing process with angular distance parameter A=0.001 (refer to subsection 3.3 for a detailed description of each step).

Figure 4 shows some intermediate results of the processing. The resulting endmembers of applying our methodology to the Salinas A dataset are shown in Figure 6.a, along with grayscale abundance maps (6.b to 6.e) representing the fractional composition of endmember materials in the scene. These maps have been obtained by the Linear Spectral Unmixing procedure using the extracted endmembers, and have been rescaled to lie in the range from 0 to 255. Our results can be visually compared with those found using PPI (Figure 7).

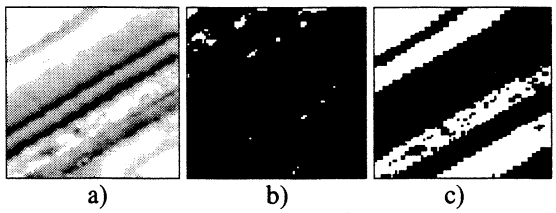

a) b) c)

Figure 4. Intermediate results of processing the Salinas A image with AMEE method. a) Probability image after applying morphological operators to the full hyperspectral dataset. b) Resulting image after automatically thresholding *a* with Otsu method. c) Resulting image after spatial/spectral growing of the seeds obtained in *b*.

For the purpose of comparison, Table 1 shows the correlation matrix between the endmembers obtained by AMEE and PPI methods. This table reveals very high correlation values for endmembers 1, 2 and 3, and a reasonably high correlation value for endmember 4. The availability of ground truth allows us to identify the zones that those endmembers represent: in particular, endmembers 1, 2 and 3 correspond to broccoli, romaine lettuce at 4 weeks and romaine lettuce at 7 weeks. Endmember 4 corresponds to the corn senesced and green weeds zone (there is some variability for this endmember as it can be appreciated in Table 2).

Table 1. Correlation matrix between the endmembers obtained by AMEE and PPI (ENVI-based) methods.

		AMEE endmembers			
		1	2	3	4
PPI Endmembers	1	**0.999**	0.973	0.72	0.735
	2	0.980	**0.999**	0.839	0.852
	3	0.718	0.85	**0.999**	0.998
	4	0.902	0.917	0.938	**0.966**

In order to analyze if the abundance maps shown in Figure 6 are meaningful, we have taken into account the following simple reasoning. Let $P(i, j, \lambda)$ be the radiance at pixel x_{ij} of the original image and wavelength λ. Also, let $p_k(\lambda), k = 1..n$ be the extracted endmember spectra and $a_k(i, j), k = 1..n$ the fractional endmember amounts at hyperspectral pixel x_{ij}. If the selected *n* endmembers are correct, all hyperspectral pixels in the original image can be expressed as a linear combination of fractional endmember amounts, i.e.:

$$\forall i, j, \sum_k a_k(i, j) \cdot p_k(\lambda) = P(i, j, \lambda) \tag{15}$$

The following experiment analyzes the "quality" of the endmembers extracted by both PPI and AMEE methods. According to our previous reasoning, if the endmembers are properly constructed, they represent approximations to the signature patterns of the actual constituents of the scene being observed, i.e. a linear combination of fractional endmember abundances at each pixel of the image must account for all of the original hyperspectral cube radiance. Then, a reconstruction of the original hyperspectral image (or "test" image) can be generated by the dataset of extracted endmembers and their resulting abundance maps, using equation 15. A set of endmembers would be "good" if we can obtain a test image that is very similar to the original. In fact, this remark provides us with a powerful mechanism to compress the full hyperspectral dataset.

Table 2 shows the results of measuring the mean quadratic error (sum of the quadratic error at each pixel divided by the number of pixels) between the original hyperspectral dataset and "test" images generated by PPI and AMEE endmember sets.

Table 2. Mean quadratic error between test images, generated using both PPI and AMEE endmember sets, and the original Salinas A dataset.

	PPI Test Image	*AMEE Test Image*
Original Image	5.66	5.71

The results shown in Table 1 and Table 2 indicate that the proposed methodology is able to obtain very similar results to those found using the supervised procedure implemented in ENVI, but without the necessity of human supervision. This fact leads to an important reduction in the overall analysis time. Although the results obtained for the Salinas A dataset are encouraging, some work is still needed in order to extrapolate our conclusions to other hyperspectral datasets.

5. CONCLUSIONS

We have presented a new autonomous method to find endmembers in hyperspectral remote sensing data based on mathematical morphology concepts. Although no previous dimensionality reduction or data thinning is performed, it is capable of accurate and rapid determination of endmember spectra from high dimensional hyperspectral images. Some preliminary results obtained after applying this algorithm to AVIRIS sensor data show that it is successful in the task of integrating spatial and spectral information in the analysis process.

REFERENCES

Bateson, C.A., Asner, G.P., Wessman, C.A., "Incorporating Endmember Variability into Spectral Mixture Analysis through Endmember Bundles," *Summaries of the Seventh JPL Airborne Earth Science Workshop*, 1998.

Beaven, S., Hoff, L.E., Winter, E.M., "Comparison of SEM and Linear Unmixing Approaches for Classification of Spectral Data", *Proc. SPIE*, 1999.

Boardman, J.W. & Kruse, F.A., "Automated Spectral Analysis: A Geological Example Using AVIRIS Data, Northern Grapevine Mountains, Nevada," *Proc. 10th Thematic Conference, Geologic Remote Sensing*, San Antonio, TX, May 1994.

Boardman, J.W., Kruse, F.A. & Green, R.O., "Mapping Target Signatures via Partial Unmixing of AVIRIS Data," *Summaries of the Fifth JPL Airborne Earth Science Workshop*, 1995.

Green, R.O., Editor, AVIRIS Earth Science Workshop Proceedings, 1988-2000. Available at http://makalu.jpl.nasa.gov/

Gualtieri, J.A., Chettri, R., Cromp, R.F., Johnson, L.F., "Support Vector Machine Classifiers as Applied to AVIRIS Data," *Summaries of the Eighth JPL Airborne Earth Science Workshop*, 1999.

Jiménez, L.O. & Rivera-Medina, J., "On the Integration of Spatial and Spectral Information in Unsupervised Classification for Multispectral and Hyperspectral Data," *Part of the EUROPTO Conference on Sensors, Systems and Next-Generation Satellites, Proc. SPIE*, Florence, Italy, Sep. 1999.

Kruse, F.A. & Boardman, J.W., "Fifteen Years of Hyperspectral Data: Northern Grapevine Mountains, Nevada," *Summaries of the Eighth JPL Airborne Earth Science Workshop*, 1999.

Kruse, F.A., "Spectral Identification of Image Endmembers Determined from AVIRIS Data," *Summaries of the Seventh JPL Airborne Earth Science Workshop*, 1998.

Kruse, F.A., Huntington, J.H. & Green, R.O., "Results from the 1995 AVIRIS Geology Group Shoot," *Proc. 2nd International Airborne Remote Sensing Conference and Exhibition*, 1996.

Lambert, P. & Chanussot, J., "Extending Mathematical Morphology to Color Image Processing," *CGIP'2000,* Saint-Etienne, France, 2000.

Landgrebe, D., "On Progress Toward Information Extraction Methods for Hyperspectral Data," *Proc. SPIE*, San Diego, CA, Aug.1997.

Otsu, N., "A Threshold Selection Method from Gray-Level Histograms," *IEEE Trans. Systems, Man, and Cybernetics*, Vol.SMC-9 No. 1, Jan. 1979.

Palmadesso, P., Antoniades, J., Baumback, M., Bowles, J. & Rickard, L.J., "Use of Filter Vectors and Fast Convex Set Methods in Hyperspectral Análisis," *Proceedings of SPIE*, 1999. Available at http://nemo.nrl.navy.mil/public/publications.html

Roberts, D.A., Dennison, P., Ustin, S., Reith, E., Morais, M., "Development of a Regionally Specific Library for the Santa Monica Mountains Using High Resolution AVIRIS Data," *Summaries of the Eighth JPL Airborne Earth Science Workshop*, 1999.

Sahoo, P.K., Soltani, S. & Wong, A.K.C., "A Survey of Thresholding Techniques," *Computer Vision, Graphics and Image Processing*, 41, pp. 233-260, 1988.

Serra, J., *Image Analysis and Mathematical Morphology*. Academic Press, London, 1982.

Serra, J., *Image Analysis and Mathematical Morphology, Volume 1*. Academic Press, London, 1993.

Soille, P., "Morphological Partitioning of Multispectral Images," *Journal of Electronic Imaging*, Vol. 5(3), pp. 252-265, July 1996.

Sternberg, S.R., "Greyscale Morphology," *Computer Vision Graphics and Image Processing*, 35, 283-305, 1986.

Szeredi, T., Staenz, K. & Neville, R., "Automated Endmembers Selection: Part I Theory," *Remote Sensing of Environment, 1999.*

Vane, G., Green, R.O., Chrien, T.G., Enmark, H.T., Hansen, E.G., Porter, W.M., "The Airborne Visible/Infrared Imaging Spectrometer (AVIRIS)," *Remote Sensing of Environment*, Vol. 44, pp. 127-143, 1993.

Winter, E.M. & Winter, M.E., "Autonomous Hyperspectral End-member Determination Methods," *Part of the EUROPTO Conference on Sensors, Systems and Next-Generation Satellites, Proc. SPIE*, Florence, Italy, Sep.1999.

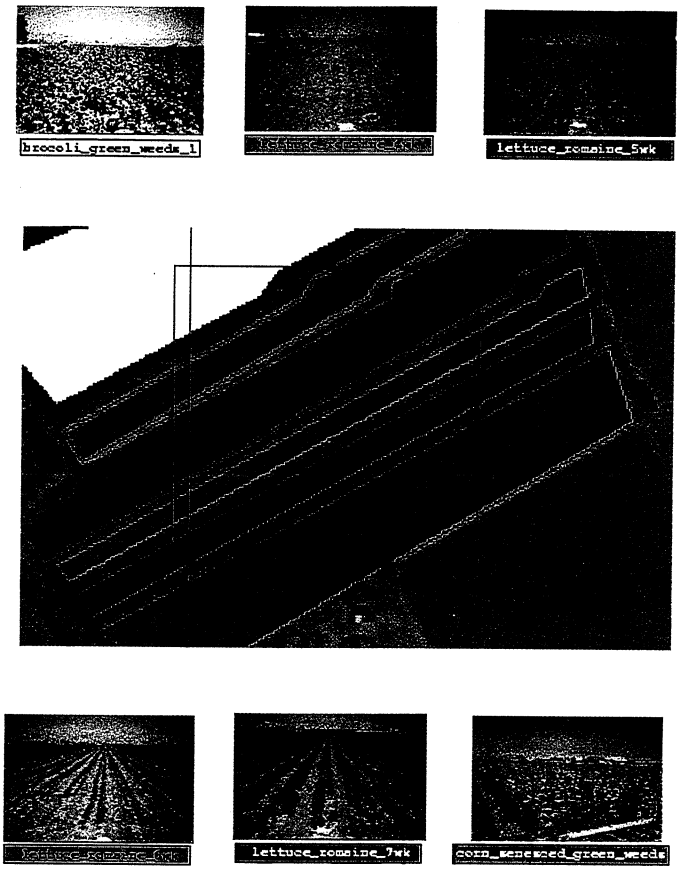

Figure 5. A subscene of the Salinas 98 dataset, showing known ground truth as polygons containing solid colors bounded by black lines and surrounded by thumbnail figures of the ground truth taken at the time of the data acquisition. The outlined box in red shows the subscene boundaries of the scene called Salinas A.

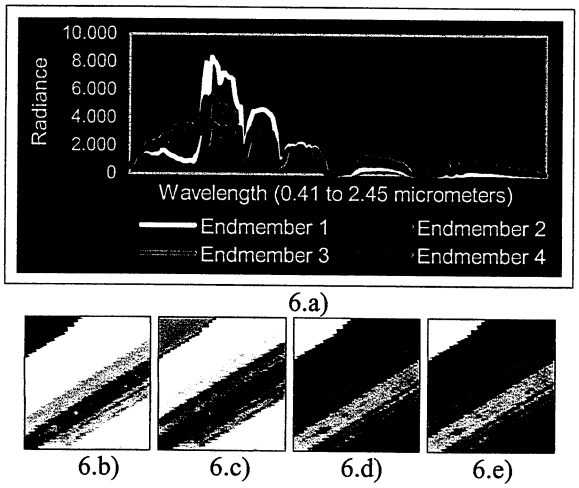

6.a)

6.b) 6.c) 6.d) 6.e)

Figure 6. Resulting endmembers after applying AMEE method to the Salinas A dataset (a) and correspondent abundance maps (b-e).

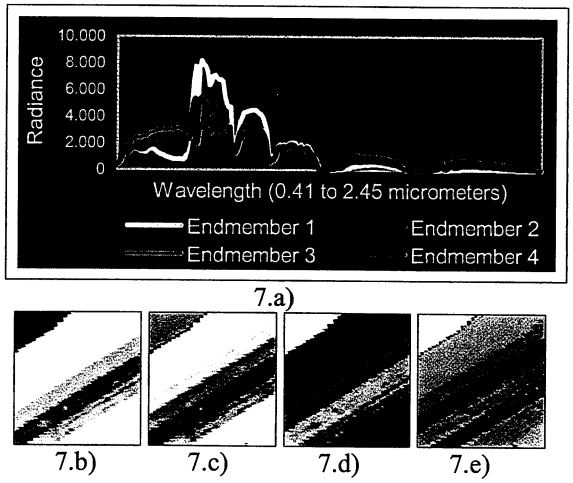

7.a)

7.b) 7.c) 7.d) 7.e)

Figure 7. Resulting endmembers after applying PPI method to the Salinas A dataset (a) and correspondent abundance maps (b-e).

DETERMINING ATMOSPHERIC COLUMN WATER VAPOUR IN THE 0.4 – 2.5μm SPECTRAL REGION

Andrew Rodger,* Mervyn. J. Lynch*

1 Introduction

To derive the surface spectral reflectance $\rho(\lambda)$ from the radiance received at-sensor $L(\lambda)$, correction is required for the effects of scattering and absorption. In the 400 to 2500 nm spectral region there are five major absorbing species, with the largest absorber being atmospheric water vapour (Green *et al*, 1991). The atmospheric water vapour is highly variable both spatially and temporally (Green, 1998) and has the effect of modifying the solar irradiance at the surface, which leads to the requirement to estimate the atmospheric column water vapour on a per pixel basis.

Current methods for water vapor estimation include the Continuum Interpolated Band Ratio (CIBR) (Bruegge *et al*, 1990) and the Narrow/Wide and Atmospheric Pre-Corrected Differential Absorption (APDA) (Borel *et al*, 1996; Schläpfer *et al*, 1996) technique. All of the methods make use of differential absorption techniques (Carrere *et al*. 1993), though a limiting factor is the way they are applied across a given atmospheric water vapour absorption feature; usually the 940 and 1130 nm absorption features. The accepted techniques use measurement channel/s and reference channel/s as described by Schläpfer (1996). One of the limiting factors of the traditional techniques is that only one estimate of column water vapor is gained for each water vapor absorption feature. This doesnt allow rejection schemes to be utilized or outliers to be readily identified. The use of linear interpolation across a given absorption feature to provide background surface reflectance slopes can also lead to problems when the surface under consideration has surface absorption features close to the atmospheric water vapour absorption features, this occurs with vegetated surfaces etc. Both of these problems may be overcome by modifying the form of the differential technique used, which in turn allows more of the 400 to 2500 nm spectral region to be utilised for the estimation of atmospheric column water vapour.

2 Radiative Transfer (RT) Theory

The spectral radiance at the sensor $L(\lambda)$ may be expressed as the sum of the surface reflected radiance and the atmospheric path radiance $L_p(\lambda)$ (Liou, 1980). This is shown in equation (1).

$$L(\lambda) = \frac{\rho(\lambda)\mu_o E_o(\lambda)}{(1-\rho_b \bar{r})\pi}\gamma(\mu_o)\gamma(\mu) + L_p(\lambda), \tag{1}$$

where, the first term on the right hand side is the surface reflected radiance, $\rho(\lambda)$ is the surface spectral reflectance at wavelength λ, μ_o is the solar zenith angle, μ is the sensor zenith angle, ρ_b is the background reflectance, $\bar{r}$ is the spherical albedo, $\gamma(\mu_o)$ is the downward transmittance, direct plus diffuse, at solar zenith angle μ_o and $\gamma(\mu)$ is the upward transmittance, direct plus diffuse, at zenith angle μ.

3 Power Series Form of the RT equation

If a single scattering regime is assumed, we have shown equation (1) may be recast, for a given surface spectral reflectance $\rho(\lambda)$ in terms of the atmospheric column water vapor W and expressed as a power series of the following form (Rodger, 2000),

* Andrew Rodger <andrew_marie@bigfoot.com>, Mervyn. J. Lynch <tlynchmj@cc.curtin.edu.au>: Remote Sensing and Satellite Research Group. Curtin University of Technology, Perth, Western Australia

$$L(W,\lambda) = \sum_{k=0}^{n} a_k(\lambda) W^k \,, \tag{2}$$

where, $a_k(\lambda)$ is the k^{th} order coefficient at wavelength λ and W^k is the atmospheric column water vapor W raised to the k^{th} power. Equation (2) can be thought of as an approximating polynomial whose order is dependent on the spectral region under consideration. For example, in an atmospheric window region for a given wavelength λ and spectral surface reflectance $\rho(\lambda)$, equation (2) reduces to a constant. As a water vapor absorption feature is approached the order required to represent the at-sensor radiance with equation (2) increases. In most cases the highest order required has been found to be a fourth order approximating polynomial. Further, if the radiance is represented as a function of atmospheric column water vapor W for j different values of water vapor, equation (2) becomes,

$$L_j(W,\lambda) = \sum_{k=0}^{n} a_{kj}(\lambda) W_j^{\,k} \,, \tag{3}$$

where j is used to differentiate between different atmospheric column water vapor amounts. Therefore, if a known surface reflectance $\rho(\lambda)$ is used in conjunction with known viewing and solar geometry, the radiance at a particular wavelength may be synthetically generated for a series of differing water vapor amounts (see figure 1). This is precisely what is applied to produce reference curves that allow the atmospheric column water vapor to be determined for a given $L(\lambda)$.

4 Procedure Outline

To determine the water vapor W for an at-sensor radiance signal the following assumptions are made

- Single Scattering Regimes unless stated otherwise
- All reflectance calculations use atmospheric multiple scattering
- If aerosol is present an estimate of the visibility is known
- The navigation data and solar and viewing geometries for a given scene is known
- An accurate estimate of surface reflectance may be determined in spectral regions where the optical depth is small, (ie in the atmospheric window regions)

The following procedure is then implemented to estimate the atmospheric column water vapor W,

1. Estimate the surface spectral reflectance $\rho(\lambda)$ in the atmospheric window regions (Table 1) using equation (7). (see section **5**).
2. Forward model j synthetic at-sensor spectral signals, using a standard atmospheric type suitable to the time and region, and where each synthetic signal has a different amount of atmospheric column water vapor W and where each estimate uses the estimate of surface spectral reflectance $\rho(\lambda)$ that was determined in 1.
3. Scale the synthetic at-sensor spectral radiance and the measured at-sensor spectral radiance signal $L(\lambda)$ using equation , (10) for each signal. (see section **6**).
4. Establish spectrally dependent reference curves, using the synthetic signals from 3 using equation (15) (see section 7).
5. Estimate the atmospheric column water vapor, at reference wavelength λ, of the scaled measured at-sensor radiance using the reference curve that was established in 4.
6. Use the estimate of atmospheric column water vapor to repeat from steps 1 to 5 until an acceptable level of convergence has been reached[†].

5 Reflectance Determination in the Atmospheric Window Regions

To allow the accurate retrieval of atmospheric water vapor to proceed, estimates of the surface spectral reflectance in the atmospheric window regions is required. The purpose of this is to permit the generation of synthetic at-sensor scaled signals. The surface reflectance estimate is used in conjunction with an atmospheric

[†] When the procedure is repeated the estimate of atmospheric column water vapor that is determined in step 7 is used to forward model the synthetic signal that is used in step 1, and Table 1 has its limits changed to those given in Table 2.

modelling program, such as MODTRAN4.0 (Berk et al, 1999; Adler-Golden et al, 1999) to produce a series of synthetic at-sensor radiances that differ only in the amount of atmospheric water vapor. For the purpose of the following procedure, the atmospheric windows are defined in Table 1. It should be noted that the definition of the atmospheric windows in Table 1 are only used for an initial estimate of the atmospheric column water vapor W. After the initial estimate, the start and stop wavelengths/channels for each region are redefined and are shown in Table 2. The extended limits on the atmospheric window regions allow the retrieval of surface reflectance to take place within the wings of the atmospheric water vapor absorption features. This is possible because the first estimate of atmospheric column water vapor provides an improved estimate of the surface reflectance, and hence allows the estimation of surface reflectance to proceed into the wings.

It can be shown (Rodger, 2000) that a good estimate of surface reflectance in the atmospheric window regions can be found by performing the following procedure. Firstly, an estimate of the atmospheric path radiance $L_{mp}(\lambda)$ is removed from the at-sensor signal $L(\lambda)$ and from a synthetic signal $L_m(\lambda)$ that has a constant surface reflectance. Accordingly,

$$L(\lambda) - L_{mp}(\lambda) = \frac{\rho(\lambda)\mu_o E_o(\lambda)}{(1-\rho_b \bar{r})\pi}\gamma(\mu_o)\gamma(\mu), \text{ and} \tag{4}$$

$$L_m(\lambda) - L_{mp}(\lambda) = \frac{\rho_m \mu_o E_o(\lambda)}{(1-\rho_{mb} \bar{r}_m)\pi}\gamma_m(\mu_o)\gamma_m(\mu), \tag{5}$$

where, it is assumed that the solar zenith angle μ_o and the sensor zenith angle μ are known. Further, it is assumed that the spectral solar irradiance $E_o(\lambda)$ at wavelength λ is the same in the atmospheric modelling program of choice and the actual spectral solar irradiance observed on the day of acquisition. $L_{mp}(\lambda)$ is a synthetically generated estimate of the path radiance, and ρ_m is given as,

$$\rho_m = \text{constant}. \tag{6}$$

All other terms in equation (4) have been previously described. The terms in (5) have the subscript m added to signify a synthetically generated term or modelled quantity. As part of the scaling process equation (4) is divided by equation (5), and multiplied by equation (6), to produce equation (7). It is assumed that, since the regions of interest in atmospheric window regions, the optical depth and hence, gaseous absorption is minimal (Kaufman, 1989, 1984) and therefore the value of $\gamma(\mu_o)\gamma(\mu)/\gamma_m(\mu_o)\gamma_m(\mu)$ is close to unity. This can also be shown formally (Rodger, 2000). Further, the spherical albedo $\bar{r}$ multiplied by the background surface reflectance ρ_b is considered to be small (Kaufman, 1989) and as such is neglected. Therefore, the surface spectral reflectance $\rho(\lambda)$ in the atmospheric window regions is given as,

$$\rho(\lambda) = \rho_m \left(\frac{L(\lambda) - L_{mp}(\lambda)}{L_m(\lambda) - L_{mp}(\lambda)} \right). \tag{7}$$

The estimate of surface reflectance $\rho(\lambda)$ {see figure 2(a)} now is then used to write a spectral albedo file that is compatible with the atmospheric modelling program, MODTRAN4.0 in this case. In the spectral areas between the regions outlined in Table 1 and Table 2, MODTRAN4.0 will interpolate between the end values, so for example MODTRAN4.0 will interpolate between the 884nm reflectance value and the 1009nm reflectance value. Thus, an estimate of the reflectance in the absorption feature is gained. The estimate in the absorption feature is only deemed to be an approximation and is improved by implementing this procedure on an iterative basis. It is this estimate though that lends itself to accuracy when determining the column water vapor.

6 Transmittance Slope Ratio (TSR)

With techniques such as the CIBR and APDA, weighting is performed on the reference channels so as to provide a mean weighted radiance at the centre of an absorption feature. Rather than weight the reference channels it

is preferable to weight consecutive absorption features (ie the measurement channels). This can be thought of as a transmittance slope and is analogous with the reflectance slope that is used in other methods. The weighted mean radiance is given as,

$$\overline{L}_j(W,\lambda) = X_1(\lambda)L_{1j}(\lambda_1) + X_2(\lambda)L_{2j}(\lambda_2)\,, \tag{8}$$

where, $L_{1j}(\lambda_1)$ is the radiance at measurement channel 1 and wavelength λ_1 for the j^{th} value of atmospheric column water vapor, and $L_{2j}(\lambda_2)$ is the radiance at measurement channel 2 and wavelength λ_2 for the j^{th} value of atmospheric column water vapor. The weighting factor $X_1(\lambda)$ and $X_2(\lambda)$ are given as,

$$X_1(\lambda) = \frac{\lambda_2 - \lambda_i}{\lambda_2 - \lambda_1} \qquad \text{and} \qquad X_2(\lambda) = \frac{\lambda_i - \lambda_1}{\lambda_2 - \lambda_1}\,, \tag{9}$$

To produce a scaled radiance signal, or TSR value, equation , (10) is used {see figure 2(b)}, namely,

$$L_{s,j}(W,\lambda_i) = \frac{\overline{L_j}(W,\lambda_i)}{L_j(W,\lambda_i)}\,, \tag{10}$$

where, $L_{s,j}(W,\lambda_i)$ is the scaled radiance at wavelength λ_i and for atmospheric column water vapor value j.

7 Atmospheric Water Vapor as a Function of Radiance

To estimate the atmospheric column water vapor W for a given wavelength λ_i, the change in scaled radiance as a function of water vapor needs to be established. Writing the scaled at-sensor radiance of equation , (10) in a power series form yields the following,

$$L_{s,j}(W,\lambda_i) = \frac{X_1(\lambda_i)\left(\sum_{k=0}^{\infty} a_{1,k}(\lambda_1)W^k\right) + X_2(\lambda_i)\left(\sum_{k=0}^{\infty} a_{2,k}(\lambda_1)W^k\right)}{\sum_{k=0}^{\infty} a_k(\lambda_i)W^k}\,, \tag{11}$$

where, the numerator represents an approximating polynomial of a power series, as does the denominator. The numerator in equation (11) can be recast as a single power series, and as such, (11) is reduced to single power series given by,

$$L_{s,j}(W,\lambda_i) = \sum_{k=0}^{\infty} c_k(\lambda_i)W^k\,, \tag{12}$$

where,

$$\sum_{k=0}^{\infty} c_k(\lambda_i)W^k = c_0 + c_1W + c_2W^2 + \ldots + c_kW^k + \ldots \tag{13}$$

To retrieve the unknown water vapor W, equation (13) must be solved. This is not necessarily an easy task when it is in the form shown. Therefore, equation (13) is used in a form that has the dependent and independent variables interchanged such that now,

$$W = f(L_s(\lambda_i))\,, \tag{14}$$

$$W = \sum_{k=0}^{\infty} d_k(\lambda_i)[L_s(\lambda_i)]^k = d_0 + d_1[L_s(\lambda_i)]^1 + d_2[L_s(\lambda_i)]^2 + \ldots + d_k[L_s(\lambda_i)]^k + \ldots \tag{15}$$

where, $L_s(\lambda_i)$ is the TSR value for an unknown water vapor W. The coefficients of equation (15) are found from a least squares fit to synthetically generated TSR values of differing atmospheric column water vapor {see figure 2(c)}. The minimum order required for the approximating polynomial of equation (15) may also be found from the least squares fit, to date a third order has been found to be sufficient.

8 **Measurement Channels**

Three spectral sections are defined for the determination of atmospheric column water vapor. Each section contains two measurement channels and a number of reference channels. Located between the measurement channels, for a given section, are the reference channels. Shown in Table 3 are the channels that are used with AVIRIS as measurement channels and shown in Table 4 are the channels for each section that are defined as reference channels. It can be seen that if all three sections are utilised for the estimation of atmospheric column water vapor a total of 6 measurement channels and 32 reference channels are available, with each reference channel providing an estimate of atmospheric column water vapor.

9 **Performance & Evaluation**

Figures 3 and 4 show the results of using the procedure outlined. It is seen that it is effective over a range of targets, such as water {figure 3(a) and figure 4(b)}, vegetation {figure 3(c)} and other targets for all three sections. All targets (all charts in figures 3 and 4) show good agreement between all sections in the determination of water vapor. Differences between sections for a given pixel are attributed to surface absorption features located in the water vapor absorption features. These are not surface features that are close to the water vapor feature, rather they are surface features that overlay the water vapor absorption features. The ability of the procedure to work across a larger part of the spectrum is advantageous for a number of reasons. Firstly, a greater range of reference channels is utilised and hence a greater number of water vapor estimates are made from any given pixel. Secondly, preliminary testing suggests that section three is less prone to the effects of atmospheric aerosol and hence allows an estimate of water vapor to be made even if the aerosol loading is not known. Thirdly, the larger spectral freedom allows, in some cases, absorption features that are present in the water vapor absorption features to be verified as was illustrated in figure 4a. While not discussed in this paper, some caution should be observed when using sections two and three due to broad surface absorption features. These involve the use of small linear extrapolations. It should be remembered that the inclusion of surface reflectance estimates from the window regions is one of the major factors governing the success of this scheme and helps to overcome some of the major obstacles encountered by other methods.

10 **Conclusion and Recommendations**

The effectiveness of the procedure for determining atmospheric column water vapor in the 0.4 –2.5μm spectral region has proven to be highly successful. The procedure has been evaluated over different spectral materials and to date has not shown any major failures. A limitation to date is that no ground truth have been available to validate the procedure, and as such, it is recommended that in future work ground truth spectra be acquired and tested in conjunction with this procedure for the purposes of evaluation. All results shown also include output reflectance spectra from the commercial correction package ACORN as a form of validation. The performance of the procedure over dark targets has proven highly successful and has yielded results that are consistent with the surrounding water vapor for a given scene. It is recommended that over dark targets that the procedure is run for one iteration only. This provides a good estimate of atmospheric column water vapor and prevents looping of the estimate due to the dark nature of the target. Tests carried out on synthetic data sets to evaluate the accuracy of the procedure have shown an accuracy of around 1-2%, in reality though this is expected to be higher due to incorrect modelling and other factors such as aerosol contamination and random instrument effects. It is expected that this procedure can be used in a Look Up Table (LUT) procedure. A comprehensive sensitivity analysis will also be carried out in the near future.

11 Acknowledgments

Many thanks to Dr Thomas Cudahy from CSIRO Exploration and Mining Division, Floreat Park, Perth Western Australia, for financial assistance for one of the authors (AR) to attend the 2001 AVIRIS workshop and for being a great sounding board for ideas. Thanks to Gail Anderson from NOAA for answering AR's endless questions about MODTRAN4.0, and many thanks to Robert. O. Green from the AVIRIS science team at NASA JPL for also answering the never-ending stream of questions concerning AVIRIS.

12 References

Adler-Golden, S.M., M.W. Matthew, L.S. Bernstein, R.Y. Levine, A. Berk, S.C. Richtsmeier, P.K. Acharya, G.P. Anderson, G. Felde, J. Gardner, M. Hoke, L.S. Jeong, B. Pukall, J. Mello, A. Ratkowski, H.-H. Burke, (1999), Atmospheric Correction For Short-Wave Spectral Imagery Based On MODTRAN4, Airborne Visible/Infrared Imaging Spectrometer (AVIRIS) 1999 Workshop Proceedings, Jet Propulsion Laboratory, Pasadena, CA

Berk, A., G.P. Anderson, L.S Bernstein, P.K. Acharya, H. Dothe, M.W. Matthew, S.M. Adler-Golden, J.H. Chetwynd, Jr., S.C Richtsmeier, B. Pukall, C.L. Allred, L.S. Jeong, M.L. Hoke, (1999), MODTRAN4 Radiative Transfer Modeling For Atmospheric Correction, Airborne Visible/Infrared Imaging Spectrometer (AVIRIS) 1999 Workshop Proceedings, Jet Propulsion Laboratory, Pasadena, CA

Borel, C.C., D. Schläpfer, (1996), Atmospheric Pre-Corrected Differential Absorption Techniques To Retrieve Columnar Water Vapor: Theory And Simulations, Airborne Visible/Infrared Imaging Spectrometer (AVIRIS) 1996 Workshop Proceedings, Jet Propulsion Laboratory, Pasadena, CA

Bruegge, C.J., J.E. Conel, J.S. Margolis, R.O. Green, G. Toon, V. Carrère, R.G. Holm, G. Hoover, (1990), 'In-Situ Atmospheric Water-Vapor Retrieval in Support of AVIRIS Validation', *Imaging Spectroscopy of the Terr. Environ, SPIE* **1298**, 150-163

Carrère, V., J.E. Conel, (1993), 'Recovery Of Atmospheric Water Vapor Total Column Abundance From Imaging Spectrometer Analysis And Application to Airborne Visible/Infrared Imaging Spectrometer (AVIRIS) Data', *Remote Sens. Environ*, **44**, 179-204

Green, R.O., J.E. Conel, J.S. Margolis, C.J. Bruegge, G.L. Hoover, (1991), An Inversion Algorithm for Retrieval of Atmospheric and Leaf Water Absorption From AVIRIS Radiance With Compensation for Atmospheric Scattering, Airborne Visible/Infrared Imaging Spectrometer (AVIRIS) 1991 Workshop Proceedings, Jet Propulsion Laboratory, Pasadena, CA

Green, R.O., (1998), Apparent Surface Reflectance of the DOE ARM SGP CART Central Site Derived from AVIRIS Spectral Images, Airborne Visible/Infrared Imaging Spectrometer (AVIRIS) 1998 Workshop Proceedings, Jet Propulsion Laboratory, Pasadena, CA

Kaufman, Y.J, (1984), 'Atmospheric Effects On Remote Sensing Of Surface Reflectance', *SPIE*, **475(6)**, 20-33

Kaufman, Y.J, (1989), *Theory and Applications of Optical Remote Sensing*, John Wiley and Sons, New York, chapter The Atmospheric Effect on Remote Sensing and Its Correction, 336-428

Liou, K., (1980), *An Introduction to Atmospheric Radiation*, Academic Press, Inc. New York, chapter Principle of Multiple Scattering in Plane-Parallel Atmospheres, 176-230

Rodger, A., (2000), Estimation of Atmospheric Column Water Vapor and Surface Reflectance Determination Using Remotely Sensed Hyperspectral Data, Report No: SPS 714/2000/AP97, School of Physical Sciences, Curtin University, Perth, Western Australia.

Schläpfer, D., C.C. Borel, J. Keller, K.I. Itten, (1996), Atmospheric Pre-Corrected Differential Absorption Techniques To Retrieve Columnar Water Vapor: Application To AVIRIS 91/95 Data, Airborne

Visible/Infrared Imaging Spectrometer (AVIRIS) 1996 Workshop Proceedings, Jet Propulsion Laboratory, Pasadena, CA

13 Tables and Figures

Table 1: The defined atmospheric window regions that are used to determine surface reflectance in preperation for the estimation of atmospheric column water vapor.

Region	Start Wavelength (nm)	End Wavelength (nm)	Start AVIRIS Channel	End AVIRIS Channel
1	875	884	55	56
2	1009	1067	69	75
3	1230	1284	92	100
4	1543	1702	126	142
5	2078	2088	181	182

Table 2: The defined atmospheric window regions that are used to determine surface reflectance in preperation for the estimation of atmospheric column water vapor after an initial estimate has been made.

Region	Start Wavelength (nm)	End Wavelength (nm)	Start AVIRIS Channel	End AVIRIS Channel
1	875	913	55	59
2	961	1105	64	79
3	1163	1314	85	103
4	1463	1722	118	144
5	1978	2088	171	182

Table 3: Consecutive measurement channels used to define an section. An interval has the measurement channels at the start and end of each section and contains the reference channels within each section.

Section	M1 Wavelength (nm)	M2 Wavelength (nm)	Measurement Channel 1	Measurement Channel 2
1	942	1124	62	81
2	1124	1334	81	105
3	1443	1782	116	150

Table 4: The reference channels available for each section outlined in Table 3.

Section	Reference Channels (nm)	Reference Channels
1	980 – 1086	66 – 77
2	1201 – 1274	89 -99
3	1563 - 1642	128 - 136

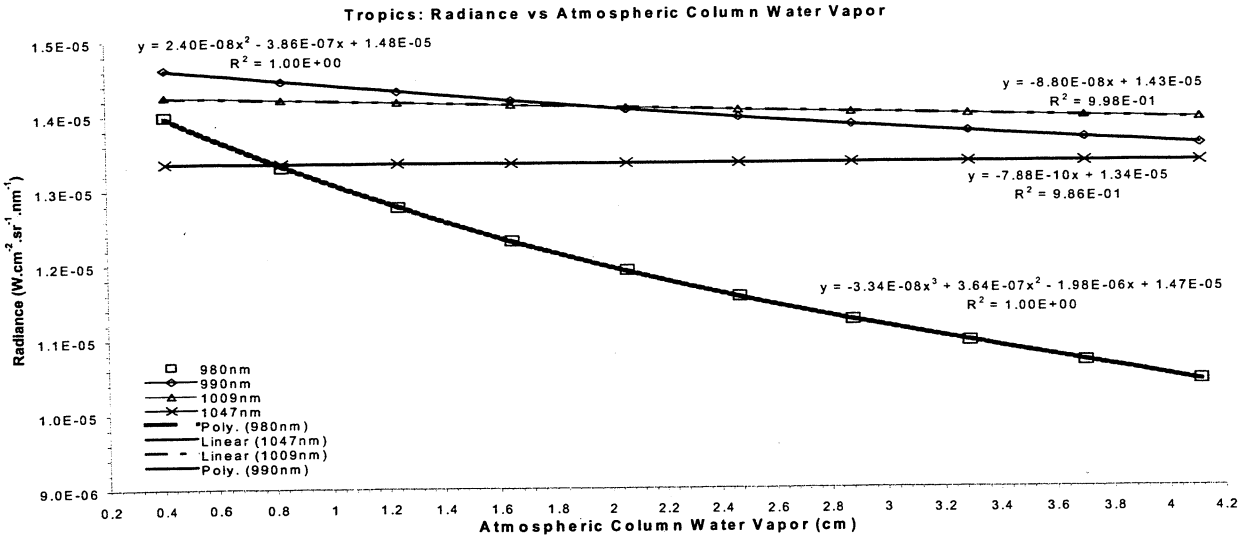

Figure 1: The radiance at-sensor as a function of atmospheric column water vapor and for a given surface spectral reflectance. Four different wavelengths are shown, they demonstrate that the radiance can be represented by an approximating polynomial. The order of which is dependent on the region under consideration. As the water vapor absorption feature (940nm) is approached the order of the polynomial is seen to increase.

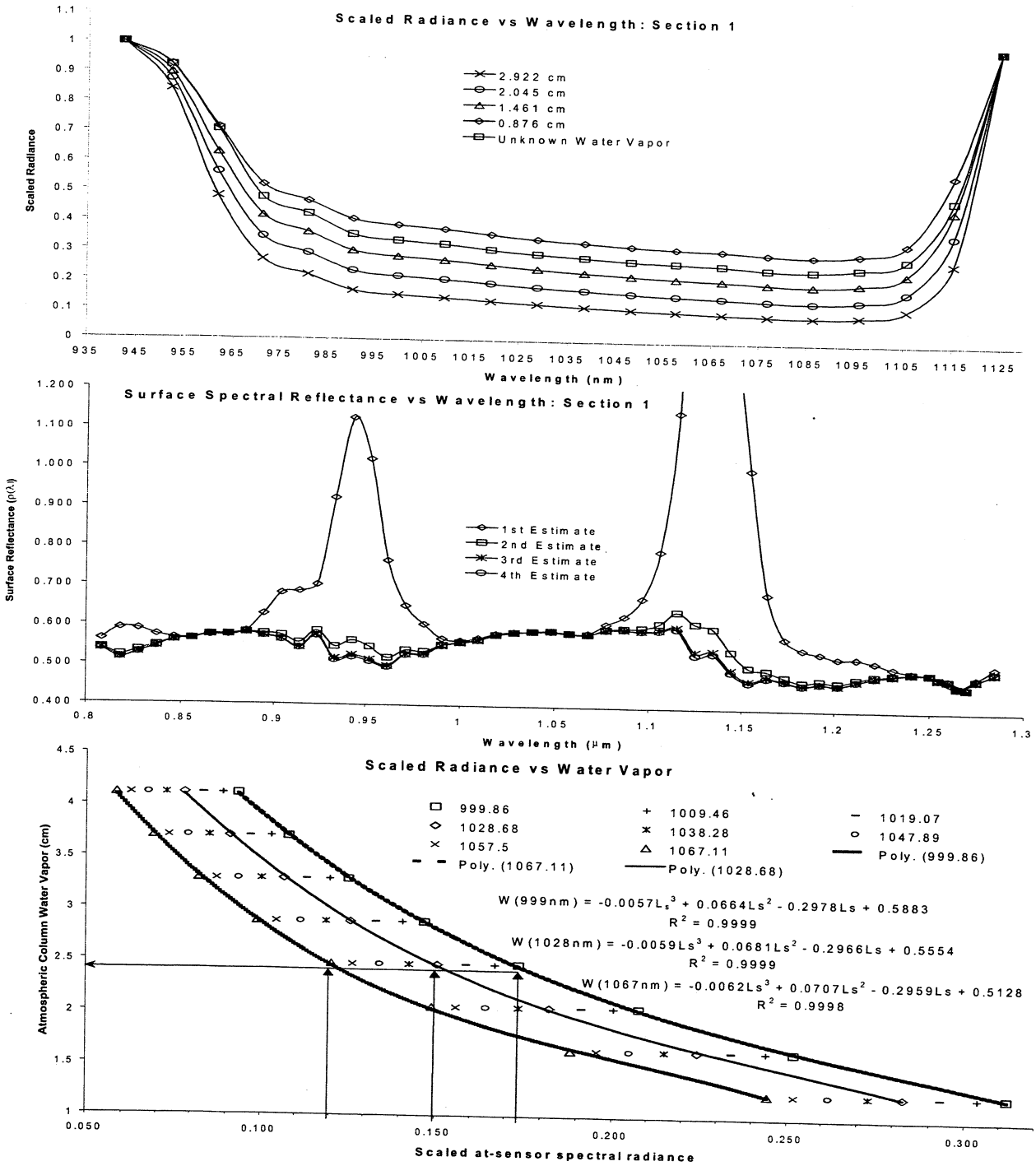

Figure 2: Top (a), Retrieval of surface reflectance with increasingly improved estimates of atmospheric water vapor. Only the wavelengths shown in Table 1 and 2 are used. When Table 2 is used the retrieval effectively occurs in the wings of the atmospheric water vapor absorption feature as well. **Middle (b)**, Scaled radiance as a function of wavelength. An estimate of surface reflectance has been made and used to produce synthetic at-sensor radiance with the different atmospheric column water vapor amounts shown. The at-sensor signal of unknown atmospheric column water vapor is seen to lie between 1.461 and 0.876 cm of water vapor. **Bottom (c)**: Reference curves used to estimate atmospheric water vapor of a pixel that has had the surface reflectance estimated in the atmospheric windows. The arrows indicate the direction of the estimate. A scaled at-sensor radiance (measured) value is determined for a given wavelength, which is related to an amount of atmospheric column water vapor.

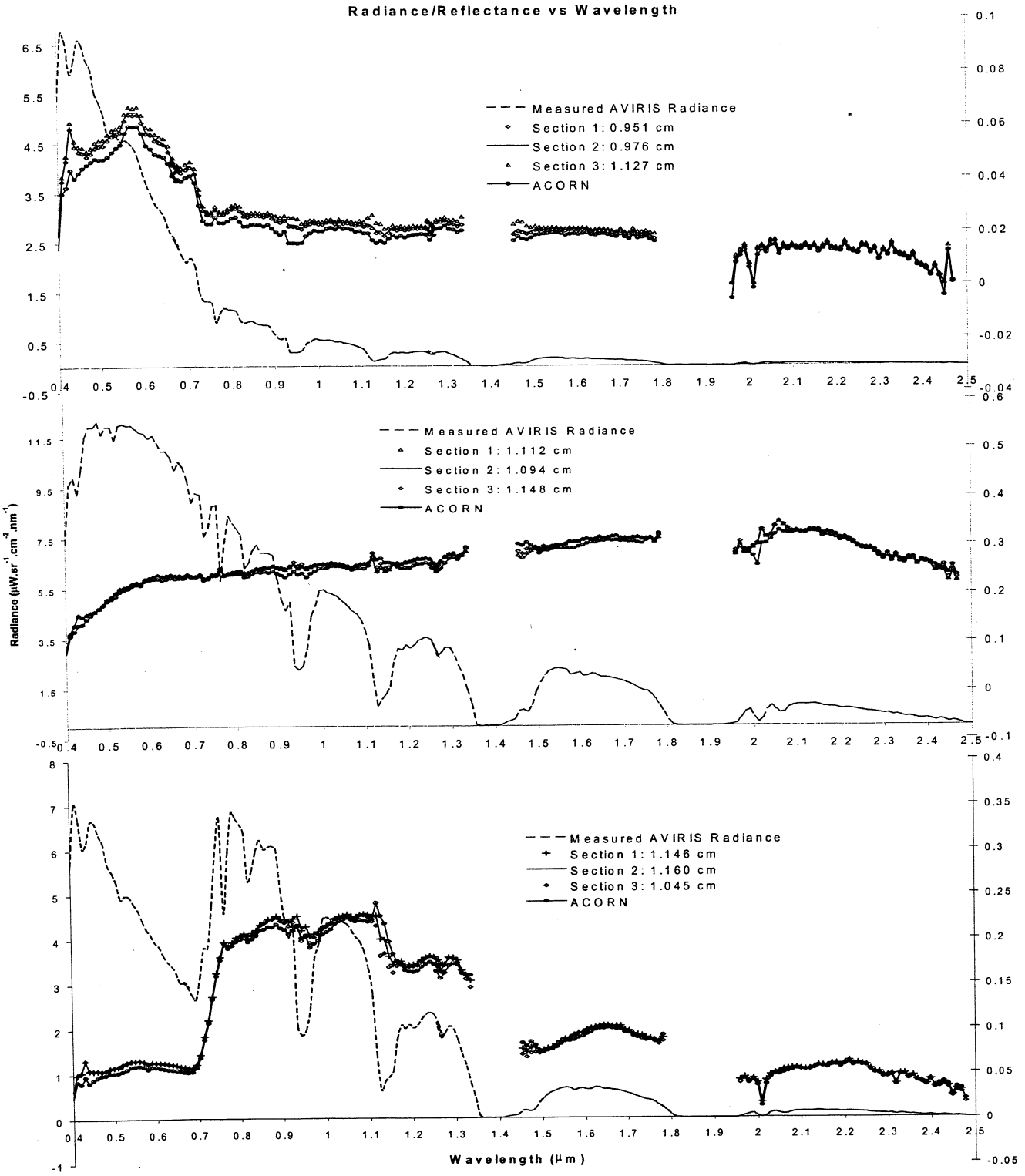

Figure 3: Moffett Field 1997. Derived surface reflectance for all 3 section. **Top (a)**, Pixel 188 line 93 scene3. Standing water target. **Middle (b)**, Pixel 503 line 165 scene3. Tarmac located at Moffett field airbase. **Bottom (c)**: Pixel 602 line 19 scene3. Vegetation target

All three figures (a), (b) and (c) show the amount of water vapor, in cm, derived for each section. The agreement, for atmospheric column water vapor, between the three different intervals is good except in the case of the standing water, where section 3 shows a higher water vapor value. The pixel in (c) is over shallow water and therefor the higher value in section 3 may indicate a surface absorption feature at 1.4 micron.

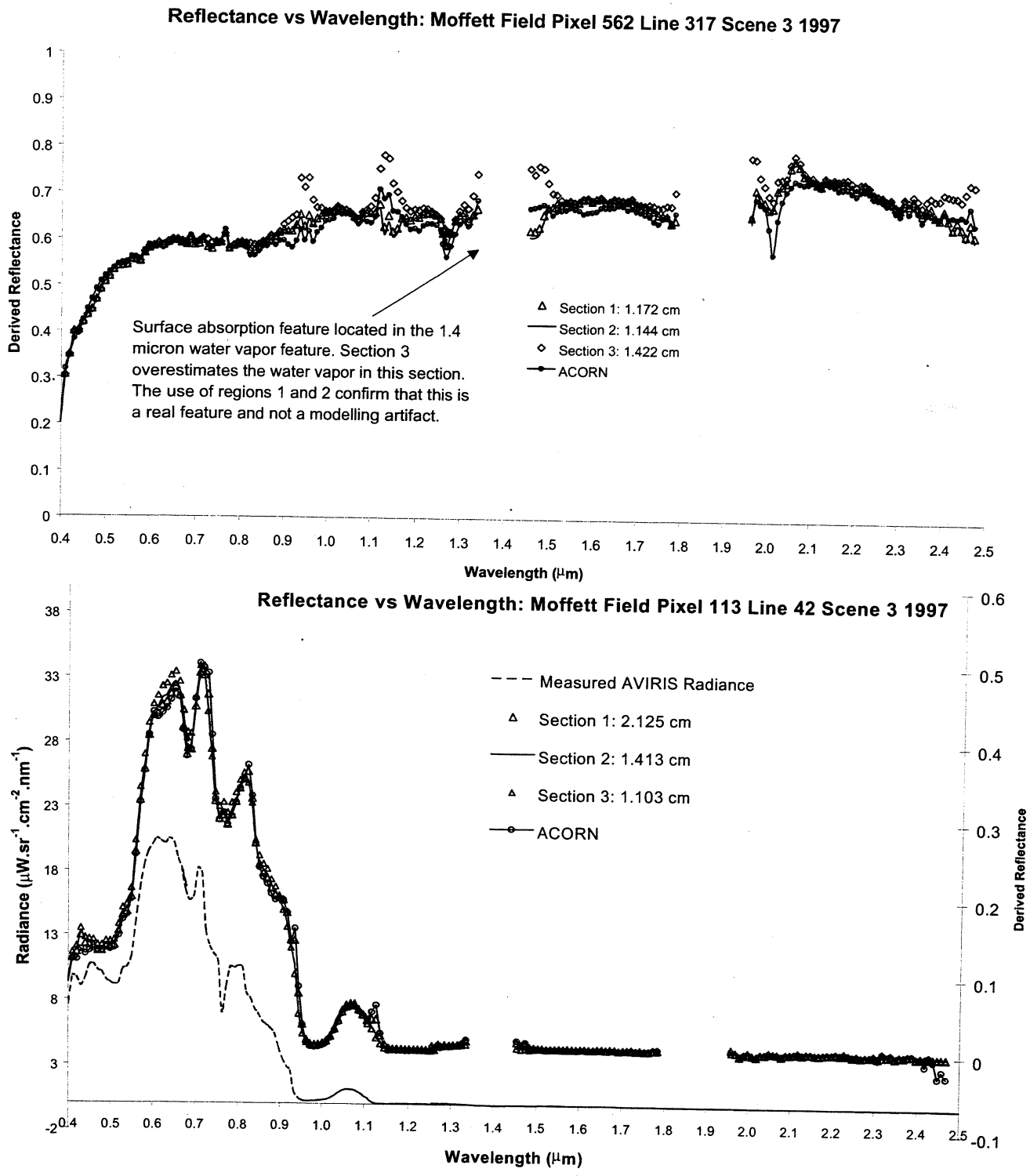

Figure 4: Moffett Field 1997. Derived surface reflectance for all 3 sections **Top (a)**, Roofing material. Note the agreement from sections 1 and 2 for atmospheric column water vapor, thus confirming a surface absorption feature located in the 1.4 micron water vapor absorption feature. The surface absorption feature causes section 3 to overestimate water vapor. **Bottom (b)**: Salt+standing water in the salt reservoirs at Moffett Field. Again a large surface absorption feature in the 0.94 micron region causes and overestimation of water vapor. This is confirmed with consistent results for sections 2 and 3. It should be remembered that each estimate from each section is an average of approximately 10 separate estimates of water vapor. A suitable rejection scheme would discount outlier results caused by deep surface absorption features locate din the water vapor absorption features.

HYPERSPECTRAL TECHNOLOGY TRANSFER TO THE U.S. DEPARTMENT OF INTERIOR: SUMMARY OF RESULTS OF THE NASA/DOI HYPERSPECTRAL TECHNOLOGY TRANSFER PROJECT

Ralph Root[1] and Diane Wickland[2]

1. Abstract

In 1997 the Office of Biological Informatics and Outreach (OBIO), Biological Resources Division, U.S. Geological Survey and NASA, Office of Earth Science (OES), initiated a coordinated effort for applying Airborne Visible and Infrared Imaging Spectrometer (AVIRIS) data and analysis, as a technology transfer project, to critical DOI environmental issues in four study sites throughout the United States. This work was accomplished by four U.S. Department of the Interior (DOI) study teams with support from NASA/OES principal investigators and the Office of Earth Science programs. The studies, including personnel, objectives, background, project plans and milestones were documented in a project website at <http://biology.usgs.gov/hwsc>. This report summarizes the final outcomes of the project, detailing accomplishments, lessons learned, and benefits realized to NASA, the U.S. Geological Survey, and the participating DOI bureaus.

2. Introduction and background

A project steering committee was formed in early 1997 consisting of NASA and USGS scientists and representatives of four DOI bureaus. In April 1997 the committee solicited proposals from DOI bureaus for studies relating to current DOI initiatives that addressed significant environmental issues from several diverse ecosystem areas that could benefit from application of hyperspectral imaging technology.

Descriptions of these study sites including personnel, objectives, background, project plans, milestones and first and second year status reports (Getter and Wickland, 1998, Root and Wickland, 2000) were posted on a website produced specifically for this project <http://biology.usgs.gov/hwsc>. This report summarizes the three-year project with a final synopsis of accomplishments, lessons learned, and benefits realized by participating DOI bureaus.

The goals of this undertaking, as originally developed by the project's steering committee were: (1) Provide DOI technical and resources management personnel information and technical assistance on hyperspectral systems and advanced technologies, (2) Focus on a limited number of resource issues or problems of interest to DOI that could potentially be addressed using hyperspectral remote sensing technologies, and (3) Use workshop formats and partnerships for introducing DOI resource and line management personnel to hyperspectral technologies, and to evaluate the results of the four pilot studies.

[1] USGS Rocky Mountain Mapping Center (ralph_root@usgs.gov)
[2] NASA Office of Earth Science (diane.wickland@hq.nasa.gov)

These studies were conducted only with funds and/or resources committed by the participating bureaus. Studies were selected on the basis that baseline information pertinent to each of the studies proposed was already well developed and readily available. NASA contributed AVIRIS missions for each of the selected sites, and provided technical assistance both directly and through partnering organizations.

In July 1997, the selected DOI and NASA Principal Investigators held an organizational workshop in Denver, Colorado to discuss each study. Work plans were devised to include description of the area, existing baseline data, ancillary data collection efforts, analysis capability, knowledge of the technologies involved, milestones to be achieved, resource availability, logistics and expectations. Robert Green, NASA/JPL provided an overview of the AVIRIS platform, hardware, software and analysis capabilities along with an appreciation for flight planning logistics. The outcome of the workshop was construction of a framework enabling the DOI and NASA PI's to develop implementation plans defined well enough to carry out those activities necessary for the data collection, analysis and evaluation of hyperspectral technology on their respective environmental parameters to be measured. Planning efforts on flight line parameters were sufficiently developed so that information could be transmitted to the NASA Airborne Science and Applications Program flight control group for mission planning for 1998 and 1999.

3. Information transfer

The entire project, including all technical and logistical aspects, has been documented by two published progress reports (Getter and Wickland, 1998, Root and Wickland, 2000), and by establishment of a project web site documenting the entire project history and accomplishments <biology.usgs.gov/hwsc>. The contents of this page consists of the steering committee membership list, the four implementation plans, a hyperspectral imaging searchable bibliography, a list of 200 URL's with hyperspectral information, links to the USGS Spectroscopy Lab, NASA AVIRIS Data Facility, AVIRIS flight line map and some University and vendor sites. It is the intent to use this page as a vehicle for communication to interested parties regarding these study efforts and outcomes. It is also anticipated that results of the research for each of the studies will be published in appropriate venues in the scientific literature by each of the respective teams of principal investigators.

As a method for porting the technology to the DOI/Bureau technical line manager, a second workshop, jointly sponsored by NASA and the DOI was proposed to convert the experience gained in these selected studies into a forum that would provide for a tutorial of the advanced systems covering: 1) characterization of hyperspectral hardware and software systems, 2) characterization of hyperspectral data, 3) exploitation and expectations of the data, and 4) data fusion techniques, degrees of difficulty encountered, and known successes and failures in the use of the data and/or technology. Unfortunately funding limitations did not permit the implementation of this last element of the technology transfer project.

4. Summary of study sites

A summary of each of the four study sites is provided below including the personnel involved, objectives, and brief background information. Accomplishments, benefits to DOI land managers and study site partners, and lessons learned are discussed.

Study site 1 - Mapping vegetation alliances, Congaree Swamp National Park (COSW), South Carolina.

Personnel:
PI's: Mike Story of the National Park Service and Dr. Mary Martin, University of New Hampshire.

Objectives:
The primary objective of this project is to incorporate the use of AVIRIS imagery with existing aerial photography and field collected vegetation data in order to evaluate the ability of the AVIRIS data to accurately map the variety of tree species found at COSW.

Background:
The COSW project includes approximately 30,000 acres of old-growth forest just Southeast of Columbia, SC. It contains a complex mosaic of wetland and upland communities. COSW is subjected to occasional hurricanes that can cause severe destruction to these communities. An important element of the NPS mission to manage the resources at COSW includes understanding the complex relationships of these communities and the changes that occur as a result of the destructive winds.

Accomplishments:
Low altitude AVIRIS data were acquired October 24, 1998 during fall leaf change, which is an ideal time to optimize species distinction. High altitude AVIRIS data were also acquired on May 17, 1999. Limited field spectra were obtained in July, 1998. Color composites of selected bands and 3-color composites of selected principal components show strong spectral contrasts. Detailed forest canopy texture is visible in the low altitude data. Preliminary spectral analysis of both low and high altitude data sets have yielded very promising results for mapping at the vegetation alliance level, and in some cases the species level.

Benefits realized to DOI land managers and study site partners:
These data are helping land managers at Congaree Swamp better understand the complexity of the distribution of old growth tree species within the park and NPS personnel are gaining experience in hyperspectral imaging analysis.

Lessons learned:
Hyperspectral characteristics of AVIRIS can contribute to the understanding and mapping of species and vegetation associations. However, multidirectional geometric anomalies of up to 2 to 3 pixel widths, which were found in both the low and high altitude data are inhibiting use of the data for mapping purposes. Both scenes were found to contain non-systematic geometric characteristics that cannot be eliminated via traditional registration techniques.

Study site 2 - Estimating the effect of invasive woody species on grasslands, Great Plains Basin.

Personnel:

PI's: Dr. Dave Meyers, B. Wylie, M. Choate, US Geological Survey, EROS Data Center and Dr. Carol Wessman, University of Colorado with The Nature Conservancy, Augustana College, North Dakota State University, the University of Toronto, the University of Nebraska, and Oklahoma State University.

Objectives:

The objective of this study is to use spectral signature analysis and linear spectral mixing models to determine the degree to which a grassland spectral signature is influenced by woody species. Ultimately, these results will provide a means to quantify species gradients, allowing the isolation of the woody components in land cover mapping over the grasslands.

Background:

The focus of this study is to investigate the effectiveness of AVIRIS for mapping the encroachment of woody species on grasslands in the Great Plains. Several test sites, owned by the Nature Conservancy, were chosen to map specific invasive plants: Tallgrass Prairie Preserve (OK) and Konza Prairie Preserve (KS) for mapping oak and juniper species, and the Niobrara Valley Preserve (NE) for mapping sumac and juniper species. The preliminary work reported here focuses on the Niobrara site, because the intermixing of eastern red cedar with ponderosa pine poses a particularly difficult spectral discrimination problem.

Accomplishments:

The 1999 data acquisition season was highly productive, with extensive ER-2 (high altitude) coverage over all three sites (Niobrara on 7/7/1999, Tallgrass on 7/13/1999 and 7/19/1999, and Konza on 7/13/1999), and multiple Twin Otter (low altitude) visits to Niobrara (7/22/1999 and 11/11/1999). Work began on the 7/22 low-altitude acquisition at Niobrara, because necessary geolocation information was missing from the other acquisitions that are required for identifying GPS measured reference points in the imagery. An agreement with JPL will give us access to geolocation information in the future, allowing us to (1) reproduce the JPL geocoding technique, and (2) add terrain correction to the JPL method to remove site-specific geometric artifacts.

The 7/22 low-altitude AVIRIS data at Niobrara was used to develop several methods for discriminating the eastern red cedar (a juniper) from ponderosa pine. The georectified data were corrected for atmospheric effects using ATREM, bands associated with water vapor and ultraviolet ozone absorption were removed, and a minimum noise fraction (MNF) transformation within ENVI (Environment for Visualizing Images) was applied to prepare the data for analysis. For our purposes, an MNF threshold of 2.0 was chosen, yielding 23 MNF bands.

The first analysis followed the "spectral endmember" approach: (1) find "pure" pixels, (2) identify endmember via "n-dimensional visualization" tools, identify endmembers then perform unmixing. Up to 40,000 iterations of the "pixel purity index" algorithm was run in an attempt to find endmembers associated with the different species, without success. We attribute this failure largely to our inexperience with hyperspectral data, coupled with the difficulty in separating juniper from pine as endmembers. In another approach, field training sets of different woody types (juniper, pine, deciduous and sumac) were used in a "matched

filtering" scheme on MNF transformed data. Errors of omission and commission were reasonable using this approach.

A third approach, employing decision trees, met with considerable success, the results of which were presented at the Ninth JPL Airborne Science Workshop (Wylie et al., 2000). This uses hyperspectral data in a manner similar to the classification techniques used to generate the Multiresolution Land Cover (MRLC) classification, with considerable success.

We look forward to analyzing the 11/11/1999 acquisition, because the deciduous leaves were off at that time, exposing the junipers under the canopy. This is a common propagation method for the junipers: develop in the understory, then spread into the grasslands. Also, the junipers dried down more rapidly than the ponderosas, causing a significant color difference between the two species. This provides ideal conditions for identifying junipers distinctly from pines.

Future plans: (1) develop precision corrections for ER-2 and Twin Otter, (2) complete the 7/22 analysis, (3) analyze the 11/11 data, (4) analyze the ER-2 data, (5) post-validation of results.

Benefits realized to DOI land managers and study site partners:
Ability to remotely distinguish between exotic eastern red cedar and native ponderosa pine is of significant value to a variety of Great Plains land managers committed to monitoring and/or controlling increasing populations of invasive eastern red cedar.

Lessons learned:
End-member pixel unmixing analysis appeared to have limited usefulness for separating eastern red cedar from ponderosa pine, possibly because of the study team's inexperience with the technique, but more likely because of the closeness of their spectral signatures.

Matched filtering and the MRLC decision tree classification techniques both appear to be effective for separating eastern red cedar and ponderosa pine.

In order to effectively validate classification results, geocoding techniques applied to AVIRIS data need to be refined to handle localized geometric artifacts and provide for terrain correction.

Study site 3 - Identify and map leafy spurge infestations, Theodore Roosevelt National Park, North Dakota

Personnel:
PI's are Dr. Ralph Root, U.S. Geological Survey, Steve Hager, Theodore Roosevelt National Park, Dr. Gerald Anderson, Agricultural Research Service, Dr. Susan Ustin, Dr. Pablo J. Zarco-Tejada, Michael O'Neill, and Geogre Scheer, University of California – Davis.

Objective:
The objective of this project is to determine the extent to which hyperspectral imaging can be used to develop automated methods for detecting and mapping the extent of leafy spurge (*Euphorbia esula L.*) infestations in Theodore Roosevelt National Park

Background:
Leafy spurge (*Euphorbia esula L.*) is a troublesome invasive non-native plant on the Northern Great Plains of the United States. Current research shows that leafy spurge is a

serious invader into the south unit of Theodore Roosevelt National Park near Medora, North Dakota. This aggressive invasion has displaced many native plant species. In addition to destroying the rich species diversity unique to the badlands, significant ecological impacts are resulting. Infestations have grown from 13 ha. in 1972 to an estimated 702 ha. in 1993, 4% of the park's 18,680 ha. land base. Currently, leafy spurge is the number one resource threat to the park and environs. The Resource Management Plan of Theodore Roosevelt National Park identifies a requirement of intensive management to reduce and contain these infestations in keeping with the "preserve and protect" mandate of the National Park Service.

Accomplishments:

Low altitude AVIRIS data were acquired in October, 1998 and high altitude AVIRIS data were acquired in July, 1999. Ground calibration and field spectra were collected in support of both data collection events. Leafy spurge has been successfully extracted from the 1999 data by spectrum matching to minimum noise fraction components employing the ENVI spectral angle mapper algorithm using carefully selected training spectra from a calibrated version of the imagery (O'Neill et al., 2000). Initial analysis covered a two-cube data set selected from one of the four 1999 AVIRIS flight lines. Further work will extend this analysis to all four flight lines covering the entire south unit of the park. Results will be validated via a quantitative accuracy assessment using ground data delineated by sub-meter global positioning systems. An initial accuracy assessment revealed difficulties with consistent geo-positioning on both the AVIRIS data and photo-interpreted verification data, making quantitative accuracy assessment a problematic issue. Future studies will examine refinements in orthorectification to bring geo-locational error to less than +/- 1 pixel (17 m).

Benefits realized to DOI land managers and study site partners:

The initial study team introduced some new technologies to address the park's top priority resource management problem, which is controlling highly aggressive leafy spurge infestations. As a result of this study, the park's visibility in the scientific community has been elevated as its challenges in managing leafy spurge are communicated to many of the nation's leading remote sensing specialists. Partners involved in the study are learning a valuable and potentially effective new technology for invasive species management. An additional by-product of this study was the development of the Spectral Analysis Management System (SAMS) by the Center for Spatial Technologies and Remote Sensing at UC Davis. SAMS permits a user to browse, sort, and analyze/combine large numbers of ground spectra in support of hyperspectral image analysis.

Two additional studies have been spawned as a result of the current study. Detection and mapping of leafy spurge using orbital hyperspectral imaging in comparison with AVIRIS was selected as one of three invasive plant studies on NASA's EO-1 Validation Team. A second high altitude AVIRIS mission will be flown over the park in 2001 as a part of this study. A more regional study, sponsored by TEAM (The Ecological Area-wide Management) Leafy Spurge in North Dakota <http://www.team.ars.usda.gov/> is comparing the cost effectiveness of a cross section of remote sensing techniques and scales for mapping leafy spurge annually on a regional basis. Two Ph.D. studies also developed as an outcome of the original study. The first will develop an expert system that models environmental factors controlling the occurrence of leafy spurge to predict likely areas for future infestation. The second will produce park-wide leafy spurge maps from both the 1999 and 2001 AVIRIS data sets, conduct change detection between the two, and relate cause/effect of the changes

with spatially documented leafy spurge control measures compiled by the park since the mid-1990's. A master's thesis study has also started in 2001 that will analyze the 1999 AVIRIS data for development of a fire fuels map over the park. Yet another study will be started in 2001 by the USGS to analyze the 1998 and 1999 AVIRIS data for mineralogical characteristics of geological formations related to burnable coal seams in the park.

Lessons learned:
Field activities in support of hyperspectral imaging are costly in terms of equipment, people, and time required. Because of the need to be in the field at the time of aerial data collection, effective planning and coordination of fieldwork is critical. The timing of overflights in relation to growing season characteristics and field crew logistics are vital to successful data collection.

The study team found that having a state-of-the-art well equipped geospatial laboratory on-site was extremely valuable for nightly downloads and near real-time review/evaluation of ground data collected each day.

The study team's first attempt at constructing a quantitative accuracy assessment revealed geo-locational problems in both the AVIRIS data and in the manually interpreted verification data. This underscores the importance of developing consistent and accurate geo-positioning in AVIRIS missions if the data are to be effectively used for mapping applications and merged with other types of geodata in land manager's GIS data bases.

The project, especially in its early stages, frustrated park managers as things did not happen any faster than they did, in the context of a time-sensitive and pressing resource problem. As the project evolved and promising results emerged, the relation between pragmatic time sensitive management needs and the characteristic longer-term nature of research came into perspective. The two additional studies and 3 student research projects that grew from the initial technical transfer study has created an ongoing research program in the park that will continue to provide information and guidance to managers far beyond the original scope of the NASA/DOI study.

Study site 4 - Mapping of mercury-containing mineral sources in the Owyhee Reservoir watershed, Oregon

Personnel:
PI's Ron Pearson, Douglas Craft, and David Zimmer, Bureau of Reclamation, Dr. Roger N. Clark, U.S. Geological Survey, and Paul Seronko, Bureau of Land Management

Objectives:
This study proposes to include Landsat TM and AVIRIS mineral classification as a cost effective means for mapping the (largely) exposed surface mineralogy of the watershed and identifying source areas for naturally occurring Mercury containing minerals. Due to the extent of the Owyhee watershed, an initial assessment of tributary basins will be conducted using Landsat TM imagery to identify those tributary basins with geological and mineralogical anomalies related to mining and geologic formations associated with mercury. AVIRIS data will then be acquired over those specific watershed tributaries and the reservoir basin to identify specific suspected sources at the much higher spectral and spatial resolution of AVIRIS. The AVIRIS mapping will be used to develop land management plans and

reservoir watershed management alternatives to limit the amount of Mercury influent to the reservoir and to verify the validity of making direct remote measurements of water quality in the reservoir, in terms of total suspended solids and chlorophyll content.

Background:

Owyhee Reservoir was constructed during the 1930's by the Bureau of Reclamation, and covers approximately 13,900 acres over a lateral distance of 50 miles. Research projects and data collection activities have been limited. While anthropogenic Mercury source areas have been generally identified, very little is known regarding natural sources in the area. The Bureau of Reclamation is currently performing a baseline survey of Owyhee Reservoir for general chemistry and Mercury fate and transport. The reservoir study is evaluating the fate, transport, and transformation of Mercury in Owyhee Reservoir and inflow streams, and is interested in developing a more detailed knowledge of naturally occurring geologic Mercury source areas in the reservoir watershed. The natural and anthropogenic sources of Mercury in the watershed have produced Mercury bioaccumulation problems in local reservoirs, streams, and water bodies. Both Oregon and Idaho public health organizations have issued fish consumption advisories for Owyhee Reservoir, Antelope Reservoir, and several other watershed streams. The reservoir study is also evaluating the ability of AVIRIS to make remote water quality measurements through analysis of spectral characteristics associated with dissolved solids and amounts of chlorophyll present in the near-surface water layer.

Accomplishments:

An AVIRIS overflight was successfully completed in July, 1998 and the data were received in mid-1999. Field spectrometer ground calibration and water quality data were successfully collected with USGS Spectroscopy Laboratory and USBR Research Chemistry Laboratory cooperators. After receiving the data in late-1999 they were atmospherically corrected using ACORN (Atmospheric CORrection Now), a commercial off-the-shelf version of MODTRAN-4. A portion of the data over the reservoir was successfully georeferenced using field-collected control data (to +/- 1 pixel) allowing surface water quality measurements to be linked with corresponding pixels within the AVIRIS image. ACORN was again used to simulate TM spectra from the AVIRIS data, and the results were compared with chlorophyll & suspended solids data collected at the surface by both field spectrometer and chemical sampling during the AVIRIS overflight. Overall results of regression analysis produced an r^2 of 0.76 between AVIRIS and ground based water quality measurements. Methodology included determining best ways to compensate for sun glint on the reservoir surface, and experimentation with both unmixing and spectrum matching tools for mapping water quality measures. The study still plans to map rock mineralogy using continuum removal & spectrum matching tools within the USGS Spectroscopy Laboratory's Tetracorder algorithm. Field data will then be used to validate results.

Benefits realized to DOI land managers and study site partners:

If Mercury-rich volcanic source materials are successfully located and mapped, their contributions to reservoir Mercury levels might be more accurately quantified. Knowing where the sources are, managers may find new options for locally controlling, reducing, or diverting Mercury-laden runoff into the reservoir. As hyperspectral data becomes more available and less expensive (e.g. orbital sensors), this study has verified that hyperspectral imaging can be used directly or indirectly to routinely assess the health of reservoirs.

A significant outcome of this study was BOR's decision to acquire a full-range field spectrometer after seeing the demonstrated potential of imaging spectroscopy for assisting with research on developing remote water quality measures. The Bureau of Reclamation is now collecting spectra on other reservoirs in the western United States to simulate performance of airborne/orbital sensors. The USGS Spectroscopy Laboratory also benefited from this study by increasing their own experience in use of imaging spectroscopy for water quality measurements, while the BOR is learning about the capabilities of Tetracorder to identify and map mineralized features relating to the presence of Mercury.

Although this hyperspectral technical transfer project reached completion in early 2001, certain aspects of this study will continue throughout the year, and new studies based on the findings of this study will continue in years following.

Ultimately, both aspects of this study will benefit managers and users of reservoirs and surrounding lands as water quality is more frequently and accurately monitored.

Lessons learned:
Analysis and interpretation of the AVIRIS data obtained for this study underscored to the investigators how different the tools are from techniques applied to MSS data. Use of hyperspectral imaging (as well as collection of field spectra) was found to be of great value in predicting the potential performance of the other types of lower spectral resolution sensors for the specific applications of this study. There was a definite learning curve and investment of time and resources to implement the effective use of hyperspectral analysis tools. Because of their value, however, a significant investment was made in hardware (a full-range field spectrometer) and software (ENVI and ACORN) with the anticipation of expanding this work to make similar determinations (particularly with the water quality measurements) at other reservoirs.

5. Anticipated outcomes

The primary overall result of the NASA/DOI hyperspectral technical transfer project was the successful demonstration of AVIRIS hyperspectral imaging capabilities to land managing bureaus within the Department of the Interior for:

(1) Detection/mapping of multiple types of invasive plants
(2) Distinguishing eastern deciduous forest community types
(3) Demonstration of two remote measures of public reservoir water quality

All of the above confirmed the effectiveness of applying hyperspectral imaging technology to several timely and pertinent DOI land managing issues and problems. This potentially marks the early stages of a transition of hyperspectral imaging from a research-oriented technology to an applied land management tool. As a direct result of this project scientists within several DOI bureaus have acquired new knowledge and insights into some pragmatic land management applications of hyperspectral imaging technology.

As expected, the activities extending from this project gained broad public visibility through the project web site, which has been active for 3 years, and continues to be updated with results from each of the individual studies. Also, as hoped, increased dialog about the capabilities and potential applications of hyperspectral imaging has grown within and between each of the participating DOI bureaus, NASA, the USGS, and academic partners.

6. Unexpected outcomes and benefits

In addition to meeting most of the project objectives, some very significant outcomes resulted that went well beyond the initial expectations of the steering committee. These unexpected and beneficial outcomes occurred in the areas of (1) partnering, (2) science integration, (3) spawning of new, additional projects, and (4) substantial commitments/investments of project participants in hyperspectral imaging technology.

(1) Partnering: Although the project was intentionally designed to link DOI participants with experienced users of hyperspectral imaging technology, development of proposals submitted to the steering committee stimulated the formation of some broad alliances of scientists and natural resource managers between federal agencies and academia that otherwise might never have taken place. For example, the study at Theodore Roosevelt National Park brought a wide range of scientists together from NASA, the USGS, the USDA Agricultural Research Service, and the University of California at Davis. Similar alliances developed in related ways for each of the studies to some extent.

(2) Science integration: In a broad sense, this project brought federal as well as academic scientists together from many diverse specialties and disciplines, illustrating and underscoring the synergy that can result when individuals with many complementary backgrounds and skills are charged to work toward a common goal. More specifically, science integration took on particular meaning to project participants from the USGS. Coincidentally, within the same time frame as the hyperspectral technical transfer project, the USGS undertook a broad and ambitious re-organization with strong emphasis on integrating activities and functions of its four scientific disciplines: Geology, Mapping, Biology and Water. USGS scientists involved over the duration of this project represented three of the four USGS disciplines, and their activities and communications served as an early and successful demonstration of the purpose, spirit, and benefits of integrated science. These internal cross-disciplinary connections within the USGS have not only continued but have strengthened, underscoring the efficacy of the bureau's re-organization concept.

(3) Spawning of new, additional projects: In at least two of the four studies undertaken in this project additional research projects have resulted. For example, success of water quality measurements by the Bureau of Reclamation at Owyhee Reservoir has lead to the BOR deciding to pursue similar work at other reservoirs under their jurisdiction. The study to detect/map leafy spurge at Theodore Roosevelt National Park led to another NASA-sponsored study to compare AVIRIS data with orbital imaging spectrometer data from the EO-1 Hyperion sensor as part of the EO-1 Science Validation Team. A second new leafy spurge study was sponsored by the USDA Agricultural Research Service as part of TEAM Leafy Spurge to demonstrate and validate regional methods for remote detection and mapping. Two Ph.D. studies also resulted as further ramifications of the initial leafy spurge investigation. The first is developing an expert system model to predict locations of future leafy spurge infestations, and the second is using data from AVIRIS missions two years apart to determine changes in leafy spurge distributions in connection with biological and

chemical control measures undertaken by the park. Another Master's thesis project will interpret the 1999 AVIRIS data over Theodore Roosevelt NP to develop fire fuel models, and yet another scientist from the USGS will analyze the 1999 AVIRIS data at the park for extracting locations of burnable coal seams. The original investigation team at Theodore Roosevelt NP had no way of anticipating the degree of interest and variety of research opportunities that would be generated from the NASA sponsored AVIRIS missions resulting from the original technology transfer study.

(4) Investments in the technology: Each of the four studies resulted in participants making investments in hyperspectral imaging technology, to one extent or another. The National Park Service, in response to both the Congaree Swamp study and the Theodore Roosevelt study invested in hyperspectral imaging software and ongoing maintenance for use by their project participants. Partly as a result of early success in leafy spurge detection/mapping, the USDA Agricultural Research Service made a major decision to invest in a complete hyperspectral imaging system (a Compact Airborne Spectrographic Imager), a full-range field spectrometer, and hyperspectral imaging software. The Bureau of Reclamation also purchased a full-range field spectrometer in support of its decision to use imaging spectroscopy for making water quality measurements in several more reservoirs under its jurisdiction. The BOR also purchased hyperspectral imaging software, and tools based on NASA's MODTRAN-4 for atmospheric correction – ACORN (Atmospheric CORrection Now). The USGS, after starting yet another project to use hyperspectral imaging to enhance the mapping of fire fuels also decided to purchase a full-range field spectrometer, and obtained funds to support an AVIRIS mission over Yosemite National Park. The USGS also purchased four additional licenses for hyperspectral image processing and ACORN calibration software. These levels of commitment to hyperspectral imaging tools were not anticipated by the original study, but they clearly demonstrate the degree to which participants literally bought into the technology, underscoring the success of the original technology transfer project.

7. Summary

The joint partnering effort between NASA and the USGS to demonstrate and transfer the technologies related to hyperspectral imaging to DOI bureaus were largely successful in the context of the envisioned project goals. Although the project itself was conceived and implemented in a partnering environment, the additional integration and collaborations that resulted went far beyond initial project expectations. USGS re-organizational vision and goals for future science directions were reinforced in a beneficial time-coincident manner, and internal connections between individual scientists and bureau disciplines were enhanced. Participants from all projects made ongoing commitments to the technology ranging from obtaining hyperspectral imaging software to procuring entire ground and aerial data acquisition systems. In two instances, study participants are continuing their work through partnering efforts, and by providing their own resources and support.

8. Bibliography

Getter, James R., and Diane Wickland. 1998. DOI Use of AVIRIS Data In Natural Resources Management – A Technology Transfer Project – Status Report. Summaries of the Seventh JPL Airborne Earth Science Workshop. January 12-16, 1998. National Aeronautics and Space Administration, Jet Propulsion Laboratory. California Institute of Technology, Pasadena, California. Volume 1. AVIRIS Workshop 149-157.Pp. 149-157.

O'Neill, M., S. L. Ustin, S. Hager, and R. Root. 2000. Mapping the Distribution of Leafy Spurge at Theodore Roosevelt National Park Using AVIRIS. Proceedings of the Ninth JPL Airborne Earth Science Workshop. National Aeronautics and Space Administration, Jet Propulsion Laboratory. California Institute of Technology, Pasadena, California. JPL Publication 00-18. Pp. 339-347.

Root, Ralph R., and Diane Wickland. 2000. Hyperspectral Technology Transfer to the U.S. Department of the Interior:Status and Results of the NASA/Department of Interior Hyperspectral Technology Transfer Project. Proceedings of the Ninth JPL Airborne Earth Science Workshop. National Aeronautics and Space Administration, Jet Propulsion Laboratory. California Institute of Technology, Pasadena, California. JPL Publication 00-18. Pp. 419-427.

Wylie, B. K., D. J. Meyer, M.J. Choate, L. Vierling, and P.K. Kozak. 2000. Mapping Woody Vegetation and Eastern Red Cedar in the Nebraska Sand Hills Using AVIRIS. Proceedings of the Ninth JPL Airborne Earth Science Workshop. National Aeronautics and Space Administration, Jet Propulsion Laboratory. California Institute of Technology, Pasadena, California. JPL Publication 00-18. Pp. 491-500.

MODO: AN INTERFACE TO MODTRAN FOR THE SIMULATION OF IMAGING SPECTROMETRY AT-SENSOR SIGNALS

Daniel Schläpfer

1) Remote Sensing Laboratories (RSL),
Department of Geography, University of Zurich, CH-8057 Zurich, Switzerland
Phone: +41 1 635 52 50, Fax: +41 1 635 68 46, E-mail: dschlapf@geo.unizh.ch

2) ReSe Applications Schläpfer,
Langeggweg 3, CH-9500 Wil, Switzerland, http://www.rese.ch

1. INTRODUCTION

The radiative transfer code MODTRAN, version 4 (Berk et al., 1998; 2000) has been established as de-facto standard for the simulation of imaging spectrometry data and for quantitative modelling of the signal at the sensor level. The original interface of MODTRAN consisting of ASCII-file based inputs leads often to misunderstandings and mistakes in such analyses. Almost every frequent user of MODTRAN has therefore some tools available to ease the setup of the inputs.

The MODTRAN interface described in this paper includes an extensive translation of the logical structure and the parameters of the input tape5 as well as utilities for the extraction and convolution of radiation component spectra. It also supports surface reflectance spectra from external data sources. Its functionality including the workflow is described first. Some examples for the simulation of imaging spectrometry radiance levels follows.

2. INTEGRATION WITH MODTRAN

The MODTRAN code as provided by the Air Force Geophysics Laboratory (AFGL) is written in the FORTRAN computing language. It is handled by rigidly formatted ASCII input files: The "tape5" is used for the definition of the atmosphere and the geometry while the file 'spec_alb.dat' (e.g.) defines the background reflectance characteristics. Other optional input files concern the solar irradiance or the spectral band model. The direct handling of these files is very sensitive and requires experience with the code. This also bears the danger of introducing errors in at-sensor data simulations. The goals of the efforts described herewith was to ease the use of MODTRAN by providing a graphical user interface for the creation of the input files as well as for the treatment of the outputs with respect to hyperspectral remote sensing. The efforts resulted in the MODO ('MODTRAN Organizer') concept. The interface is based on the IDL (IDL, 2001) programming language which has been established as de-facto standard for hyperspectral image processing. The design has been optimized for research applications and thus does not support high degrees of automatism, avoiding 'black box' mechanisms. The MODO concept as shown in Figure 1 is based on the standard distribution of MODTRAN by interfacing with the inputs 'tape5' and 'spec_alb.dat' and evaluating the outputs 'tape7' and 'flux'.

The core interface of the procedure is the tape5 editor window. It allows to set most of the input parameters using pull-down menus instead of manually editing the rigidly formatted ASCII file. Logics within the tape5 are considered, such that if, e.g., the transmittance mode has been selected it is not possible to set the irradiance source options. Sub-interfaces will pop up for supported special functions such as the import of user defined atmospheres, the selection of the surface reflectance, or the definition of the four standard aerosol layers. The interface is grouped in the same way

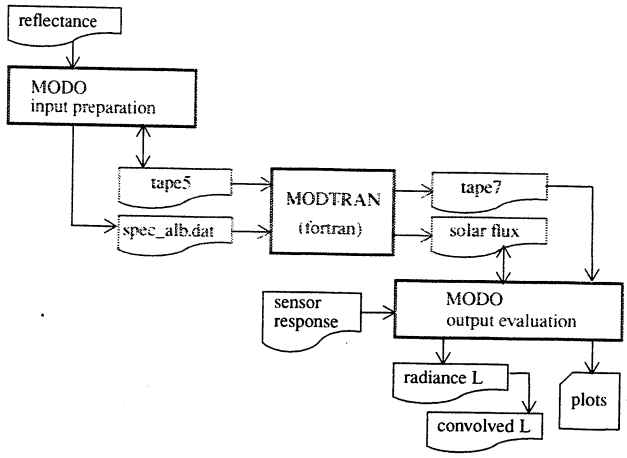

Figure 1: **Integration of the MODTRAN standard code with the MODO interface.**

as in the original tape5 to be consistent with the documentation as provided with MODTRAN. If one or more parameters shall be varied, the setup of 'multiple run' tape5s has proven to be very useful. Each run within such tape5s can be accessed, edited, or deleted individually by browsing through the tape5. Some dedicated save options help to keep various tape5s organized. A sample of the MODO tape5 editor window is shown in Figure 2.

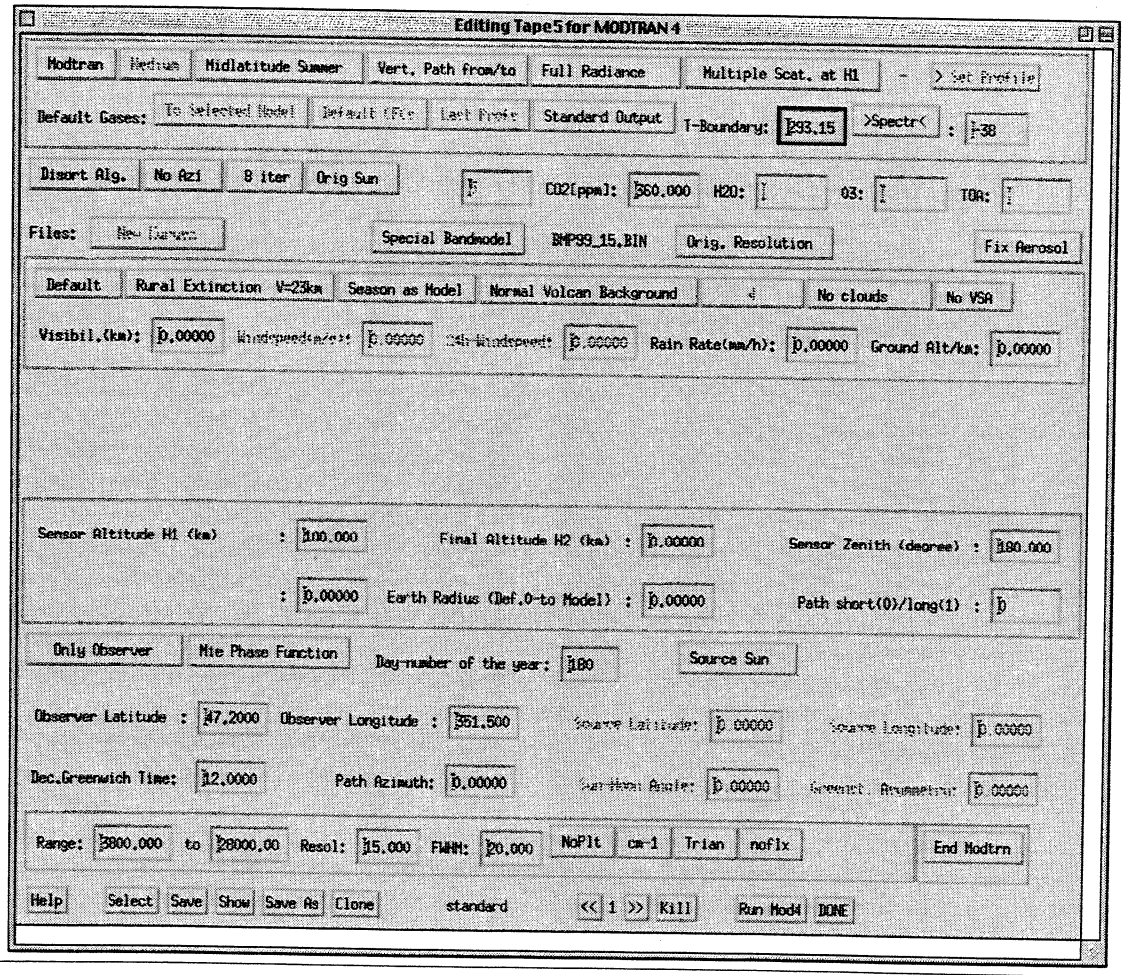

Figure 2: **Example of the MODTRAN interface 'MODO'; translator and organizer for the ASCII input file 'tape5'.**

The inclusion of surface reflectance spectra has become of high importance for modelling at-sensor radiance values for known targets. An interface has therefore been included for importing reflectance data into MODTRAN from ENVI (ENVI, 2001) spectral libraries or ASCII reflectance files. The spectra can afterwards be selected for the target as well as for the background if adjacency effects shall be studied (see Figure 3).

The startup of the original MODTRAN executable is managed by a UNIX child process from within MODO. A UNIX shell script is invoked which automatically links the original MODTRAN DATA directory and its contents to the startup location if no DATA reference is available there. This allows to use MODTRAN from whatever directory the tape5 has been saved to. On non-Unix operating systems, MODTRAN still may be invoked externally after saving the tape5 from the MODO interface.

Additional interfaces are included for the following tasks:

- plotting of the spectral output (tape7 or solar flux),
- calculation of solar angles for time and date,
- save/restore of settings,
- extraction of single spectra from the whole output,
- convolution to hyperspectral (Gaussian) channel characteristics, and
- export of radiance spectra to ENVI spectral libraries.

All these utilities have been developed in support of a flexible handling of the MODTRAN inputs and outputs for a fast simulation of at-sensor radiance values.

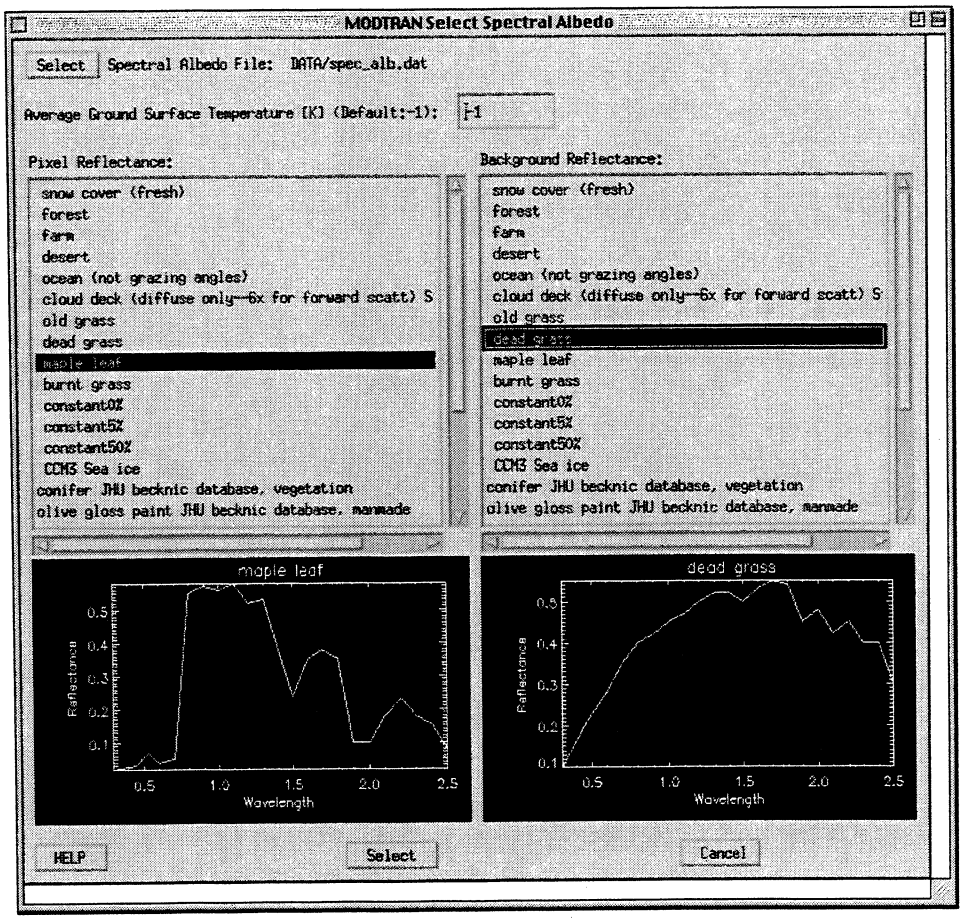

Figure 3: Interface for the selection of spectra from the spectral albedo file for the MODTRAN background reflectance option.

3. PROCEDURES

The typical workflow using the MODO utility depends on the task to be performed. In imaging spectroscopy, the normal case starts with known surface reflectance spectra which need to be transposed to at-sensor radiance values. For the creation of spectral databases or Look-Up-Tables for later inversion, standard setting for reflectance and discrete values for parameter variation are taken as basic input. An overview of a typical data simulation workflow is given in Figure 4.

3.1 MODTRAN Setup

After the surface reflectance has been defined, the various parameters need to be set in the tape5 window. One may choose to vary certain parameters and create a multiple run tape5. At this point, additional knowledge of the geometric and meteorologic situation to be simulated is required. Furthermore, some basic comprehension of the MODTRAN functionality helps to create inputs to MODTRAN making physical sense.

MODTRAN can be run afterwards in one of its four major modes, as radiance, transmittance, solar irradiance, or thermal radiance. Depending on the settings for the DISORT option and the wavelength resolution, such runs may be very time consuming for the radiance options. The first run in the standard output tape7 or in the optionally created ".flx" file may be plotted directly afterwards for quick visualization of the outputs.

3.2 Data Extraction

In normal cases, the total radiance at the sensor is the main output component to be read afterwards from the MODTRAN outputs. Other components such as the path scattered radiance, specific transmittance values, or the solar irradiation are of specific interest for atmospheric applications and corrections routines as well as for validation of the cross sensitivity of the simulated spectra to atmospheric influences. The components are then read from the outputs and converted to SI standard units [W/(m^2 sr nm)] from the original units being [W/(cm^2 sr cm^{-1})]. This conversion is based on the well-known relationship between wavelength λ and wavenumber ν:

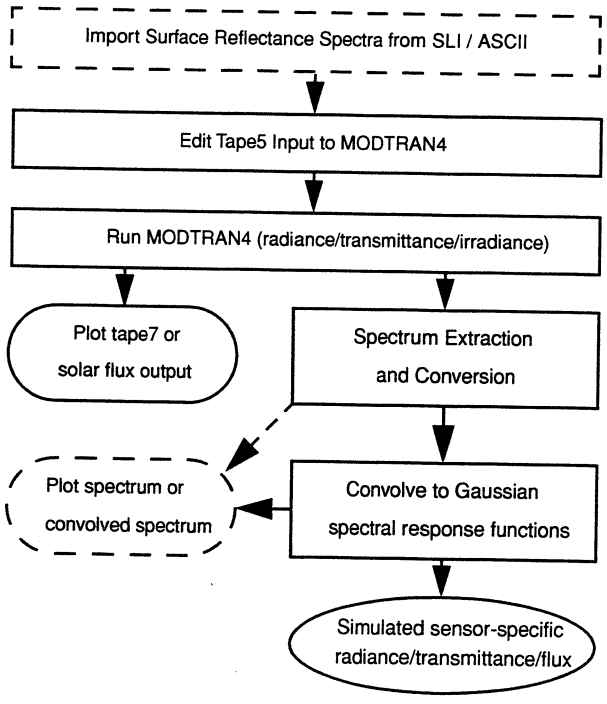

Figure 4: MODO typical workflow structure as used for the simulation of imaging spectrometer data.

$$\lambda = \frac{1}{\nu}, \tag{1}$$

The wavenumber is converted to its equivalent wavelength through the following relationship:

$$|\lambda|[nm] = \frac{1}{|\nu|[cm^{-1}]} = \frac{10^7}{|\nu|}[nm]. \tag{2}$$

The relation between the wavelength interval and the wavenumber interval is given by:

$$d\lambda = -\frac{1}{\nu^2}d\nu \text{ and } d\nu = -\nu^2 d\lambda. \tag{3}$$

The generic relation between the radiance per wavelength and the radiance per wavenumber is derived from the respective definitions:

$$L_{S,\nu} = \frac{d\phi}{dAd\Omega d\nu} \text{ ,and with (1): } L_{S,\lambda} = \frac{d\phi}{dAd\Omega d\lambda} = \frac{d\phi\nu^2}{dAd\Omega d\nu}. \tag{4}$$

The unit conversion is derived as follows, where $|L_{S,\lambda}|$, and $|L_{S,\nu}|$ denote data values for the same radiance equivalents and $|\nu|$ the wavenumber value in inverse centimeters:

$$|L_{S,\lambda}|\left[\frac{W}{m^2 srnm}\right] = |\nu|^2|L_{S,\nu}|\left[\frac{W(cm^{-1})^2}{cm^2 sr(cm^{-1})}\right] = |\nu|^2|L_{S,\nu}|10^4\left[\frac{W(cm^{-1})}{m^2 sr}\right] = |\nu|^2|L_{S,\nu}|10^{-3}\left[\frac{W}{m^2 srnm}\right]. \tag{5}$$

The standard unit in cm^{-1} is given as the original MODTRAN wavenumber reference which may be related closely to the energy levels of the simulated photons. In imaging spectrometry and spectroscopy of the visible/near infrared part of the spectrum, the usually used wavelength reference are microns or nanometers. As the resolution of current imaging spectrometers is in the range of 5 to 20 nanometers, it has been decided to select the wavelength in nanometers as generic reference for data simulation within MODO.

3.3 Convolution

The MODTRAN data usually is derived in wavelength units using a triangular slit for convolution to the original band data. Since version 3.7 of MODTRAN, an option is included which allows the direct convolution of the MODTRAN outputs to sensor specific response functions. This option is not fully supported within MODO. A separate convolution function convolves extracted and possibly joined spectra to sensor characteristics using a Gaussian approximation of the sensor function. This option leaves higher flexibility for research purposes if, e.g., the response function needs to be varied. The convolved radiance values L_i in a band i are calculated as:

$$L_i = \frac{\int L_S(\lambda)r_i(\lambda)d\lambda}{\int r_i(\lambda)d\lambda} \approx \frac{\sum_j L_S(\lambda_j)r_i(\lambda_j)\Delta\lambda_j}{\sum_j r_i(\lambda_j)\Delta\lambda_j}, \tag{6}$$

where $r_j(\lambda)$ is the spectral response function of the sensor's band. A stepwise assumption is taken for the convolution if the number of raw data values j is sufficient within the width of the spectral band. If the original resolution is not sufficient, a polynomial is calculated through the original data points $L_s(\lambda_j)$ for better approximation of the spectrum and summarized through a number of $k = 100$ interpolated data points, i.e:

$$L_i \approx \frac{\sum_k Poly(L_S(\lambda_j))_k r_i(\lambda_k)\Delta\lambda_k}{\sum_k r_i(\lambda_k)\Delta\lambda_k}. \tag{7}$$

A minimal number of 2 data points within the range of the target bands is required for a sufficient calculation of the convolved data values in any case.

4. EXAMPLE APPLICATIONS

4.1 Simulation of Atmospheric Signatures

The most straight-forward simulation of atmospheric signatures using MODTRAN is the calculation of the transmittance of a specific optical path (see example of such an output in Figure 5). Transmittance curves are derived for the characterization of atmospheric scatterers and gases such as water vapor (cf. Schläpfer et al., 1998). Anyhow, the transmittance runs do not include all effects of multiple scattering on the path. It is thus preferred to use radiance simulations under well known atmospheric parameter variations for realistic results. At-sensor radiance values are then evaluated with respect to the variation of atmospheric parameters available within MODTRAN such as the visibility, cirrus or cloud coverage, humidity, and ozone content or with respect to geometric constraints such as sensor altitude, ground altitude, sun zenith angle, or sensor zenith angle.

Such variations may be combined for building Look-Up-Tables for atmospheric correction as it has been done within the ATCOR programs (Richter, 1997; 2000). The MODO interface does not support directly the construction of such lookup tables but its internal functionality can be used to ease their creation.

4.2 Simulation of At-Sensor Radiance

The at-sensor radiance is the critical parameter for the physical investigation of imaging spectrometry data. It is derived by calibration of a sensor system and needs to be compared to the expected radiance levels. An example of simulated at sensor radiance components is shown in Figure 6. The components of the signal are to be considered for validation of the relative sensitivity of the radiance to atmospheric and surface parameters. Usually, a series of simulations needs to be set up in order to obtain the variation of the signal. This approach may be chosen to simulate the expected radiance levels at sensors to be constructed.

4.3 Evaluation of Sensor Specifications

For the design of new instruments, the specifications need to be fixed based on simulated at-sensor radiance values. The simulations may be done by comparison to measured values of existing instruments (Schläpfer et al., 1999) or by

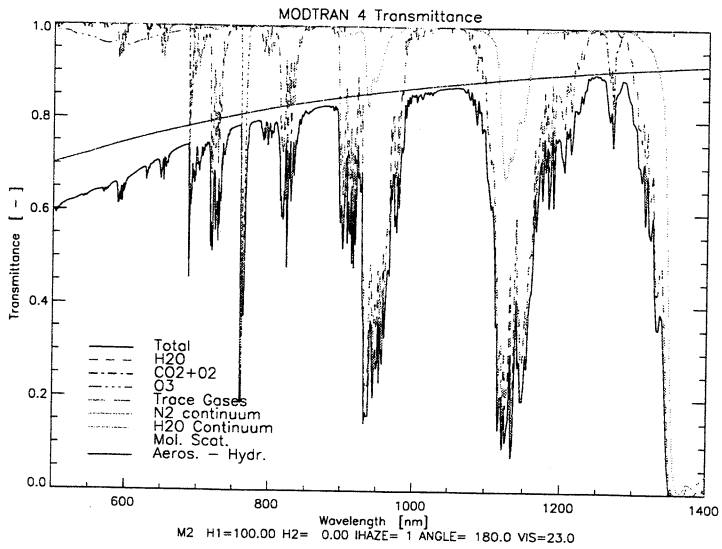

Figure 5: Simulation of atmospheric transmittance using the direct transmittance calculation - Standard MODO output.

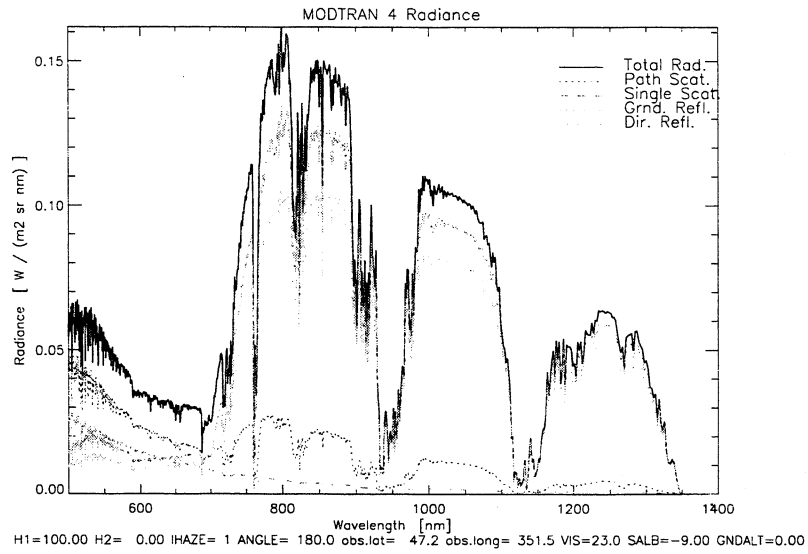

Figure 6: At-sensor radiance simulation raw data over vegetation after MODTRAN simulation - MODO Standard tape7 plot.

fully physical based simulation. MODTRAN has been established as a standard tool for such simulations for imaging spectrometry data. The MODO utility can be used in a supportive manner to derive the following critical parameters:

- Typical and extreme at-sensor radiance levels,
- Application-specific reflectance based signal (delta radiance) simulations,
- Noise equivalent delta radiance specification,
- Spectral resolution (FWHM), and
- Spectral sampling interval requirement.

FWHM spectral resolution and spectral sampling interval are derived by series of convolutions to potential spectral response functions. The sensitivity, e.g., within absorption features may then be characterized to derive recommenda-

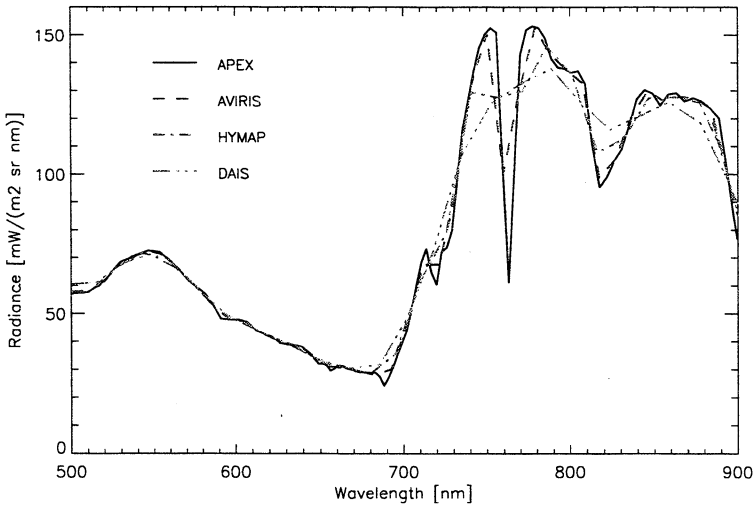

Figure 7: Total at-sensor radiance over vegetation convolved to specifications of the APEX instrument and to reference instruments (AVIRIS, HYMAP, and DAIS 7915).

tions for spectral resolution. An example is given in Figure 7 where the spectral characteristics of existing imaging spectrometers are compared to potential resolution specifications of the upcoming APEX instrument (Itten et al., 1997).

However, the presented approach does not compare to measured data values. If the real signals after optics and electronics are to be simulated, more sophisticated tools such as SENSOR (Börner et al., 1999) are required.

5. CONCLUSIONS

An interface to MODTRAN has been presented which eases the use of this radiative transfer code substantially. It has been optimized for research applications in imaging spectroscopy. The MODO interface has been designed on the actual version of the IDL (RSI, Inc., 2000) programming language. It is available 'as is' from the internet as shareware code[1] while MODTRAN itself still needs to be ordered through the Air Force Research Laboratories.

Functionality which might be included in the future is the convolution to multispectral response functions, the support for creating Look-Up-Tables for atmospheric correction, or the inclusion of BRDF modelling approaches. MODO is currently used operationally for the simulation of at-sensor radiance values of the European APEX airborne imaging spectrometry system and will be further developed in support of such simulations.

6. ACKNOWLEDGEMENTS

This work has been supported by the Remote Sensing Laboratories of the University of Zurich. Special thanks go to Stephan Bojinski, Michael Schaepman, and Peter Keller who provided valuable input for the development.

7. REFERENCES

Berk, A., Bernsten L.S., and Robertson D.C., 1989: *MODTRAN: A Moderate Resolution Model for LOWTRAN7*. Air Force Geophysics Laboratory, Hanscom AFB, MA, GL-TR-89-0122, pp. 38.

Berk, A., Bernstein, L.S., Anderson, G.P., Acharya, P.K., Robertson, D.C.,Chetwynd, J.H., and Adler-Golden, S.M., 1998: MODTRAN cloud and multiple scattering upgrades with application to AVIRIS, *Remote Sens. Environ.*, 65:367-375.

Börner, A., Schaepman M., Schläpfer D., Wiest L., and Reulke R., 1999: The Simulation of APEX Data: The SENSOR approach. Imaging Spectrometry V, Denver, SPIE Vol. 3753:235-246.

ENVI, 2001: *The Environment for Visualizing Images*, Version 3.4. Research Systems, Inc., Boulder, Colorado, USA.

IDL, 2001: *Interactive Data Language (IDL)*, Version 5.4. Research Systems, Inc., Boulder, Colorado, USA.

Itten, K.I., Schaepman M., De Vos L., Hermans L., Schlaepfer H., and Droz F., 1997: APEX-Airborne Prism Experiment a New Concept for an Airborne Imaging Spectrometer. Proceedings of the Third International Airborne Remote Sensing Conference and Exhibition, ERIM International Inc., Copenhagen (DK), Vol. I, pp. 181-188.

Richter, R., 1997: Correction of atmospheric and topographic effects for high spatial resolution satellite imagery. *Int. J. Rem. Sens.*, 18(13):1099-1111.

Richter, R., 2000: *Atmospheric / Topographic Correction for Wide FOV Airborne Imagery: Model ATCOR4*. DLR Internal Report, DLR-IB 552-05/00, pp. 62.

Schläpfer, D., Borel C.C., Keller J., and Itten K.I., 1998: Atmospheric Pre-Corrected Differential Absorption Techniques to Retrieve Columnar Water Vapor. *Remote Sens. Environ.*, Elsevier, **65**(3):353-366.

Schläpfer, D., Boerner A., and Schaepman M., 1999: The Potential of Spectral Resampling Techniques for the Simulation of APEX Imagery based on AVIRIS Data. Summaries of the Eighth JPL Airborne Earth Science Workshop, JPL, Pasadena (CA), **99-17**:377-384.

1. URL: http://www.rese.ch

Characteristics of AVIRIS Band Measurements in Desert Agroecosystems in the Area of Blythe, California: I. Studies of Cotton Spectra

Safwat H. Shakir Hanna
Texas Gulf Coast Environmental Data Center (TEXGED)
Prairie View A&M University
P.O. Box 235
Prairie View, Texas 77446

ABSTRACT

AVIRIS data from Blythe, California, were acquired in June 1997 to study agricultural spectra from different crops and to identify crops in other areas with similar environmental factors and similar spectral properties. The main objectives of this study are: 1) to compare the spectral and radiometric characteristics of AVIRIS data from agriculture crops with ground spectra measured by a FieldSpec® ASD spectrometer; 2) to explore the use of AVIRIS spectral images for identifying agricultural crops; 3) to study the spectral expression of environmental factors on selected crops; and 4) to build a spectral library for the crops that were studied. A long-term goal is to extend the spectral library for different vegetation or crops in different stages of growth.

To support our study, on July 18 and19, 2000, we collected spectra using the FieldSpec® spectrometer from selected fields with different crops in the Blythe area of California (longitude 114° 33.28 W and latitude 33° 25.42 N to longitude 114° 44.53 W and latitude 33° 39.77 N). These crops were cotton in different stages of growth, varieties of grass pure or mixed, Sudan grass, Bermuda grass, Teff grass, and alfalfa. Some of the fields were treated with different types of irrigation (i.e., wet to dry conditions). Additional parameters were studied such as the soil water content (WC), pH, and organic matter (OM).

The results of this study showed that for crops known to be similar, there is a significant correlation between the spectra that were collected by AVIRIS in 1997 and spectra measured by the FieldSpec® spectrometer in 2000. This correlation allowed development of a spectral library to be used in ENVI-IDL analysis software. This library was used successfully to identify different crops. Furthermore, using IDL algorithms of Spectral Angle Mapper classification (SAM), spectral feature fitting (SFF) and spectral binary encoding (SPE) showed that there is excellent agreement between the predicted and the actual crop type (i.e., the correlation is between 85–90% match). Further use of the AVIRIS images can be of a value to crop identification or crop yield for commercial use.

INTRODUCTION

The goal of this research project was to explore the use of spectral measurement for agricultural crops, using AVIRIS data that were collected from the Blythe, California area, in June 1997. Another goal was to evaluate the temporal and spatial behavior of the spectral signatures for different crop types. In addition, for this research, ground spectral measurements were made using a handheld spectrometer to compare with the remotely sensed data of AVIRIS. This study explores several additional factors affecting crops. These include a water stress experiment, with several water treatments over a range of crop-development stages. An additional aspect of the study was to develop a spectral library for the different crops studies, to be used in the IDL_ENVI program. These measurements and analyses may be used in future studies of the spectra characteristics of the crops.

MATERIALS AND METHODS

Studied sites

The study sites were located in the area of Blythe, on the eastern border of California, at 114° 33.28 to 114° 44.53 W and at 33° 25.42 N to 33° 39.74 N (the details of location of selected crops are presented in Table 1 [all tables are at the end of this paper] and Plate 1). The Blythe agricultural area is characterized by high temperatures that often exceed 46 C during the summer season. The fields are irrigated regularly at specific intervals (i.e., every one to two weeks). The field sites were selected with the help of the farm advisor of the Riverside County Extension Research Facility. The field plots that were selected have been planted with Bermuda grass, Sudan grass, Alfalfa, Kenaf grass, Teff grass, and cotton. Bare soil data also were taken for the comparison between vegetated fields. The studied fields include a range of water irrigation treatments, and varieties of crops at different stages of maturity. Spectral data are planned to be analyzed for every crop and every treatment. The work presented in this paper is concentrated on the cotton crop.

Characteristics of the Cotton crop

Cotton (*Gossypium hirsutum*) is a perennial, tropical plant that has been bred and adapted for annual crop production in temperate climates. Cotton develops on a somewhat predictable schedule, although water and temperature stress have effects on the rate of growth. The cotton plantation depends on adequate soil moisture and warm soil temperature. In addition, cotton requires considerable care in the field with treatments of fertilizer and insecticides.

Spectral Field Measurements

Spectral data were collected with an ASD FieldSpec® hand-held spectrometer unit that measures the wavelength range from 350 nm to 2500 nm. The reported spectral sampling is 1 nm. For analysis, the data were resampled to 5 nm. For crop and soil target measurements, the instrument operator walked the length of the plot and pointed the spectrometer probe at the area to be measured. For the reflectance standard measurements, the probe was positioned approximately 10–15 cm above the surface and pointed straight down. The position of the operator and probe relative to the spectralon was chosen to minimize shadowing and reflection from the operator.

AVIRIS Data Collections

AVIRIS data were measured over Blythe, California, on June 26, 1997. The data were acquired at the altitude of 20 km during the dry season. The data were collected in 224 channels (10 nm in width) in the range of 369-2500 nm spectral interval (Green et al., 1998). AVIRIS uses a scanning mirror to sweep back and forth in a whiskbroom fashion, producing 614 pixels for each scan. Each pixel produced by the instrument covers approximately 20 x 20 m^2 on the ground (with some overlap between pixels). The ground swath width is approximately 10 km for an ER-2 flight altitude of 20 km (Vane, 1987 and Vane et al., 1984). The effects of atmospheric absorption and scattering on the calibrated radiance data were compensated for by using a MODTRAN-based method (Green et al., 1993).

Methodology

Exploration of Reflectance Factors and Vegetation Indices

There are may commonly used vegetation indices (VI): perpendicular (PVI) (Richardson and Wiegand, 1977), normalized difference (NDVI) (Rouse et al., 1974), NIR/RED ratio (RVI) (Tucker, 1979; Pearson and Miller, 1972), and soil adjustment (SAVI), which includes a soil-adjustment factor (L) to account for first-order soil background variations (Huete, 1988), transformed soil adjusted (TSAVI) (Baret et al., 1989), ATSAVI (Baret and Guyot, 1991), and water band (WBI). They were calculated as follows:

$$NDVI = (R750-R600)/(R750 + R600) \quad (1)$$
$$WBI = (R900/R970) \quad (2)$$
$$PVI = (NIR-RED) \quad (3)$$
$$RVI = (NIR/RED) \quad (4)$$
$$SAVI = ((NIR-RED)/(NIR + RED + L))X\ (1-L) \quad (5)$$
$$TSAVI = a[NIR-a(RED)-b]/[RED + a(NIR)-ab] \quad (6)$$
$$ATSAVI = a[NIR-a(RED)-b]/[a(NIR) + RED - a*b + X(1 + a^2)] \quad (7)$$
$$NIR = a\ (RED) + b \quad (8)$$

where Rxxx represents reflectance at the indicated wavelength (xxx in nm). Data were analyzed using statistical analysis software (SAS) package.

RESULTS AND DISCUSSION

Table 1 represents the collected spectra data from different crops and different treatments, in the area of Blythe, California, on July 18 and 19, 2000. The table also shows the latitude and longitude of the field sites and also the time of spectral collection. The collection of data comes from healthy cotton, wilted cotton, and cotton at the bloom stage without open bolls. These spectra provide a basis for building a library to explore the cotton vegetation from the AVIRIS images (Plates 1-4). Table 2 shows the soil parameters that were collected. This table shows stressed conditions of the soil moisture as 0.96-1.4 % and unstressed conditions of the soil moisture as 8.0 %. The pH was 8.35; organic matter (OM%) was 1.9–2.5%. The plants were in a mature stage, dry, and some of the bolls and leaves were green. The time of collected data and the reflectance and wavelength of the cotton in different maturity stages are presented in Tables 3 and 4. The reflectance and wavelength were organized according to different spectral regions. The selected ranges of wavelengths are 350–650, 650–950, 950–1250, 1250–1550, 1550–1850, 1850–2150, and 2150–2500 nm.

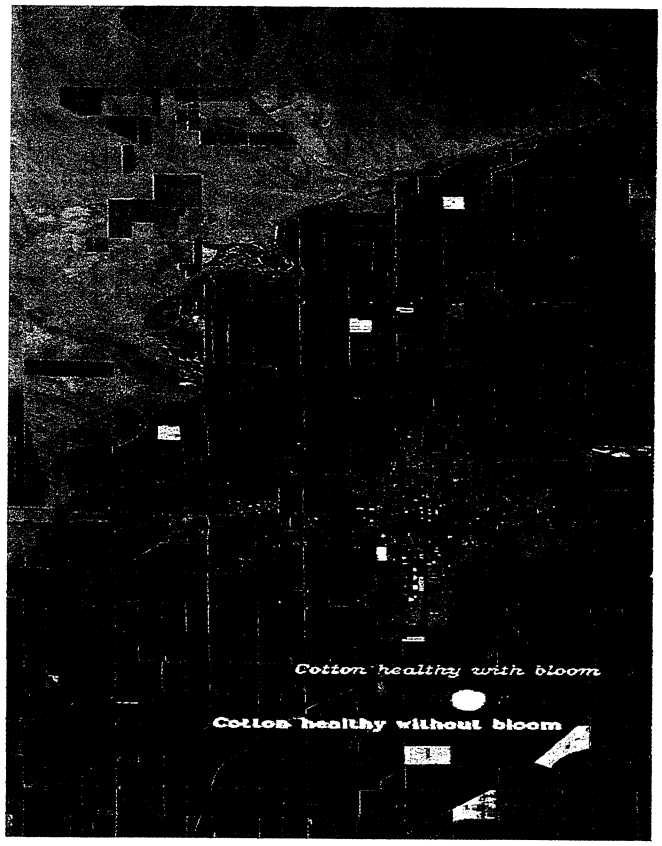

Plate 1. AVIRIS Image

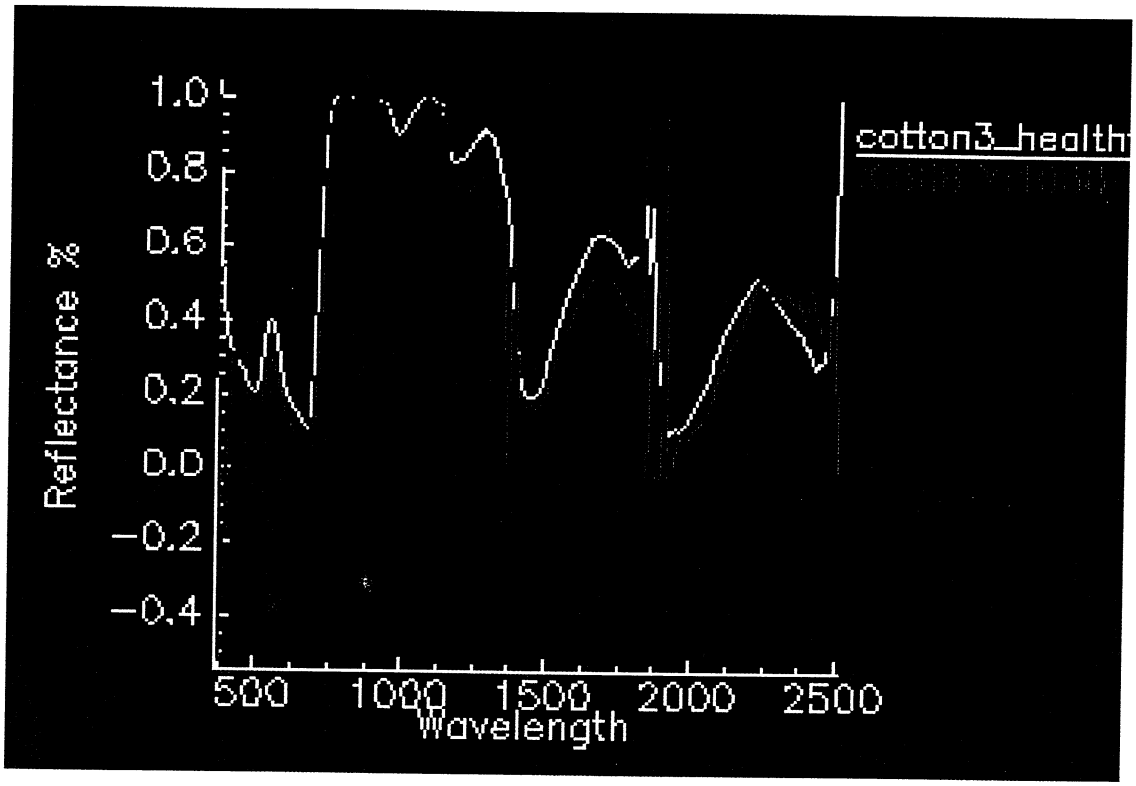

Plate 2. Spectral data from AVIRIS compared with cotton healthy bloom (a)

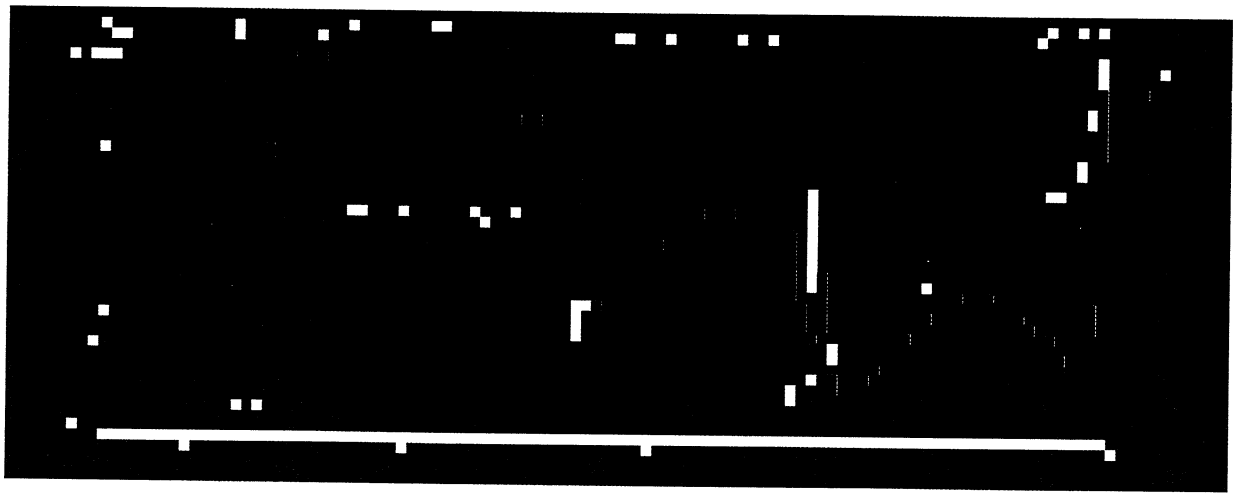

Plate 3. Spectral data from AVIRIS compared with cotton healthy bloom (b)

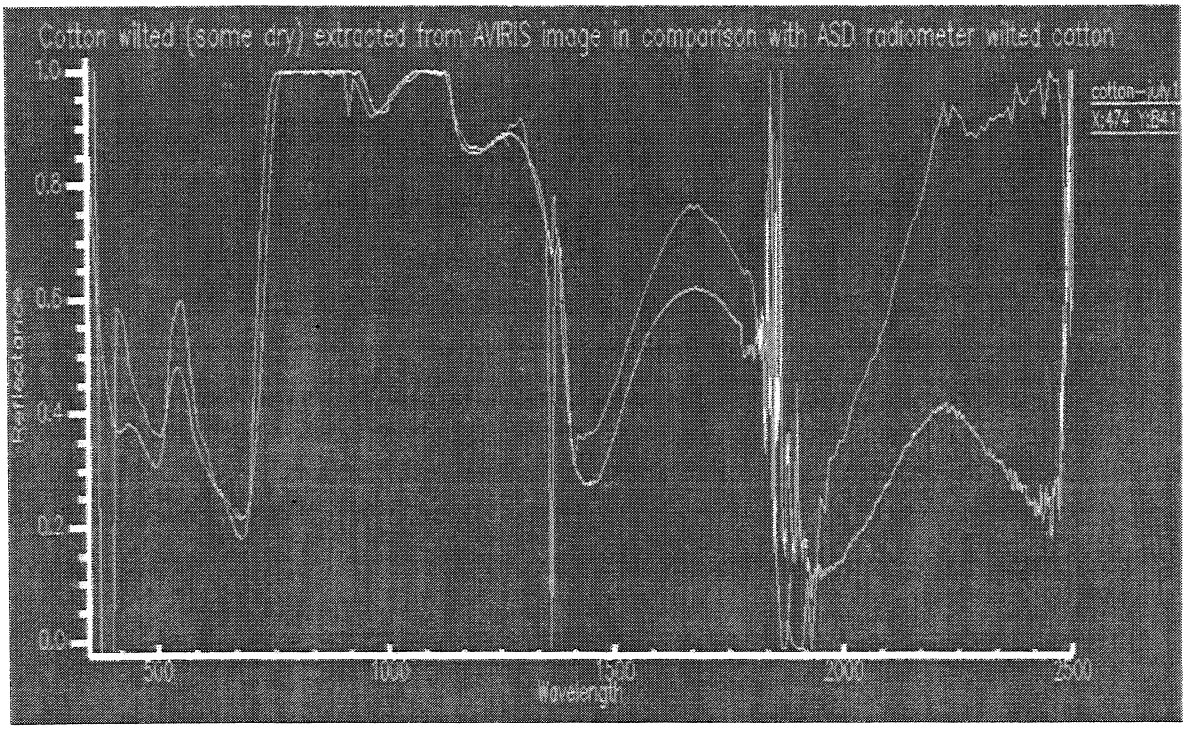

Plate 4. Cotton wilted (Some Dry) extracted from AVIRIS Image in Comparison with Data from ASD radiometer wilted cotton

Characteristics of Cotton Spectra

The wavelength range reflectance values of healthy cotton were analyzed (Table 3). The vegetation indices were analyzed as well. The normalized difference vegetation index (NDVI) and water band index (WBI) (Fig.1) showed a positive correlation ($r^2 = 0.86$ $P<0.01$). The indices NIR, NDVI, RVI, PVI also were calculated using the relationship between the reflectance of NIR and RED spectra in the acquired reflectance from the healthy cotton and relatively stressed cotton using the spectrometer data. The factors (a) and (b) were calculated using a regression procedure (Table 4). These factors represent the slope and intercept, respectively, of the soil line. From these results L is calculated, which is used for the vegetation indices TSAVI, PVI, NDVI, and RVI.

Analysis of AVIRIS Image

Significant correlation was found between the AVIRIS 1997 data and spectral data collected by the FieldSpec® spectrometer. This allowed development of a spectral library to be used in ENVI-IDL analysis software. This allowed identification of different crops using primarily the visible part of the spectra. The AVIRIS data are in agreement with FieldSpec® spectrometer data (Figures 2–4). Regression analysis gave positive correlation coefficients ($r^2 = 0.80$- 0.87). Crop identification was explored using Spectral Angle Mapper classification (SAM), spectral feature fitting (SFF) and spectral binary encoding (SPE). Excellent agreement as found between the predicted and the actual crop type (i.e., the correlation is between 85–90% match). Additional analysis of the healthy cotton showed six local maxima.

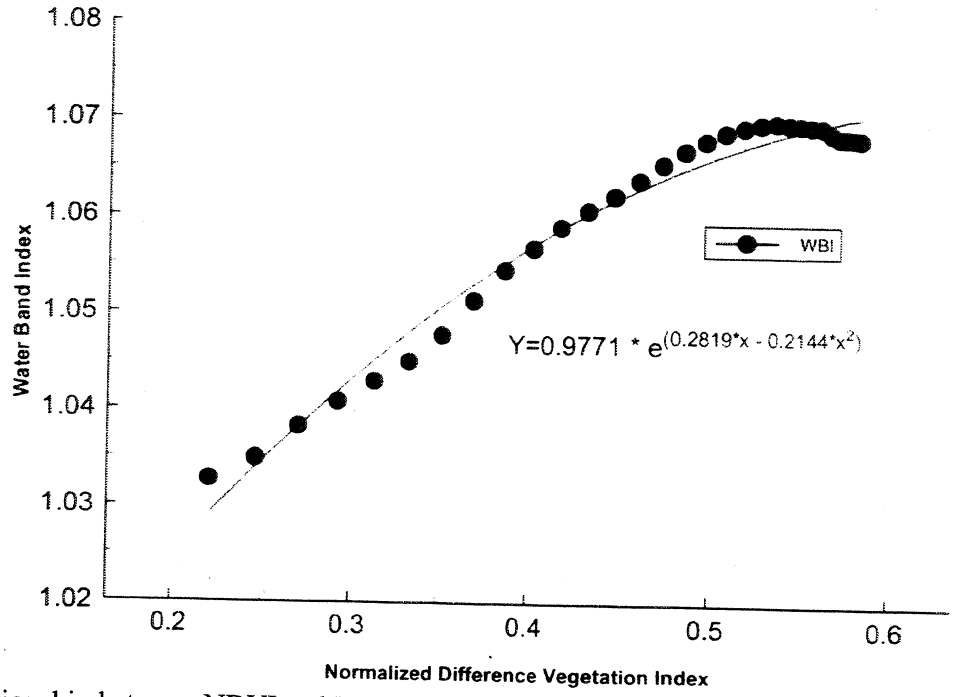

Fig. 1. Relationship between NDVI and WBI in healthy cotton in the area of Blythe, California, at longitude 114° 44.53 W and latitude 33° 25.42 N full-bloom cotton and no bolls open

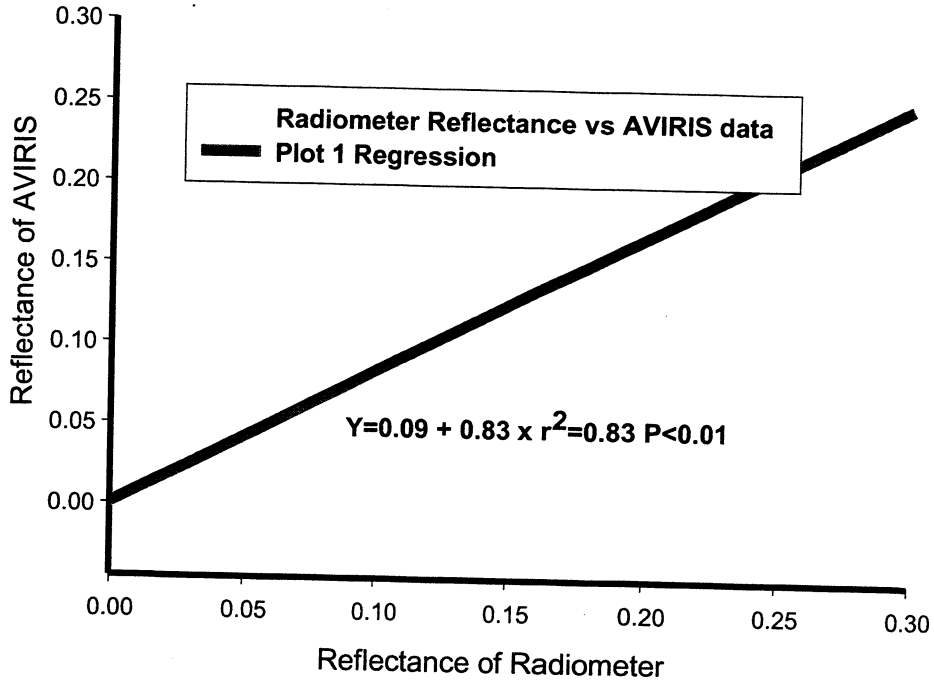

Fig. 2. Relationship between reflectance extracted from AVIRIS images for healthy cotton and reflectanced data obtained from the ASD Radiometer

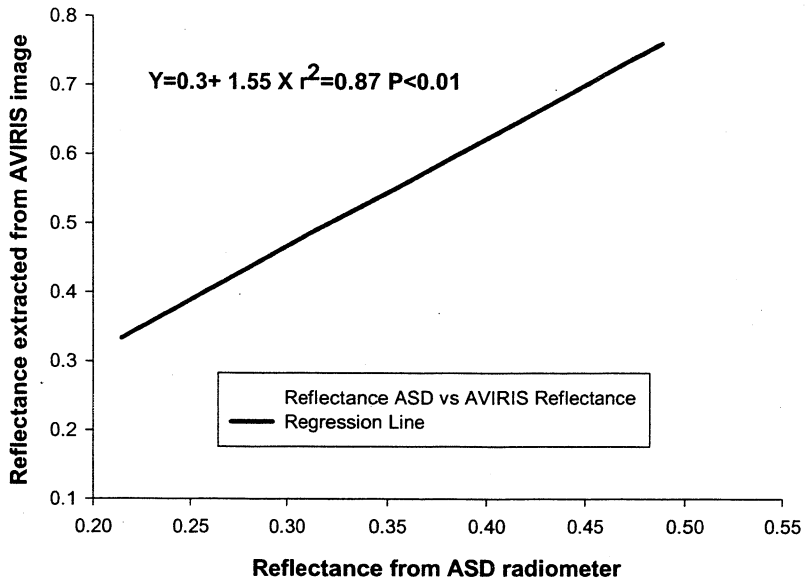

Fig. 3. Relationship between reflectance extracted from the AVIRIS image for healthy cotton with bloom and reflectanced data obtained from the ASD Radiometer

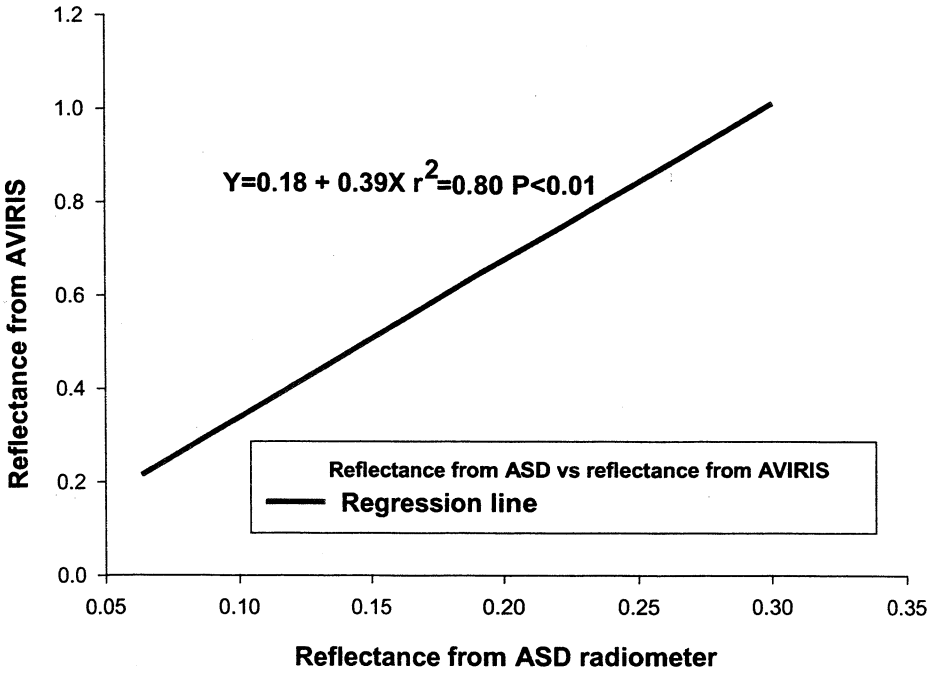

Fig. 4. Relationship between reflectance extracted from the AVIRIS image for wilted cotton and reflectanced data obtained from the ASD radiometer

These peaks are in the wavelength regions of 486.58, 780.57, 880.31, 1043.6, 1851.6, and 2500 nm. In these regions healthy cotton has lower reflectance in the visible and higher peek reflectance in the RED and NIR.

The spectral peaks of healthy cotton from the AVIRIS image and from the ASD FieldSpec® (Figs. 5 and 6) are consistent with analyses that have shown high information content for vegetation spectra (Collins, 1978). The spectral reflectance of vegetation in this wavelength region is characterized by low reflectance in the red part of the spectrum and high reflectance at 780-880 nm wavelengths. This is generally referred to as the ""red edge." Several studies have shown that measures based on the red edge position or shape are well correlated with biophysical parameters at the canopy level, but less sensitive to noise effects caused by the soil background and the atmosphere effects (Baret et al., 1992; Demetriades et al., 1990; Guyot et al., 1989; and Mauser and Bach, 1995).

Healthy cotton in the ground has a dense vegetation canopy completely covering the soil. In the spectral region beyond 1000 nm, water has a dominant effect, but has little effect on the spectral properties in the visible (VIS) and NIR regions short of this wavelength. However, variations of leaf dry matter content in relatively stressed cotton vegetation (Figs.7 and 8) may affect canopy reflectance. It is assumed that for studies in remote sensing, this affect is negligible, because the within-crop variation of leaf dry matter content is stable. In summary, the data that were collected from the fields using the ASD FieldSpec® showed general agreement with the data acquired from the AVIRIS Images.

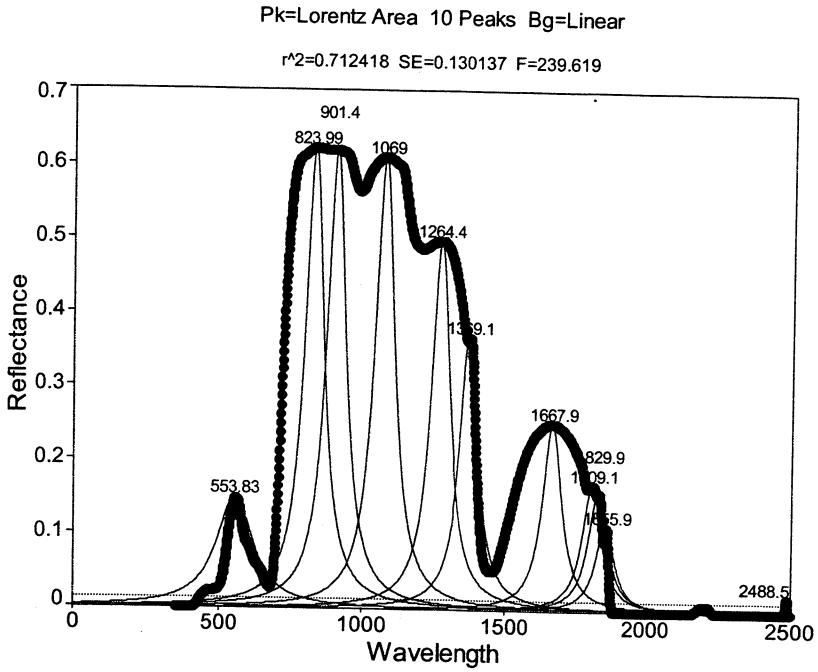

Fig. 5. Healthy cotton peaks that were collected by the ASD FieldSpec®.

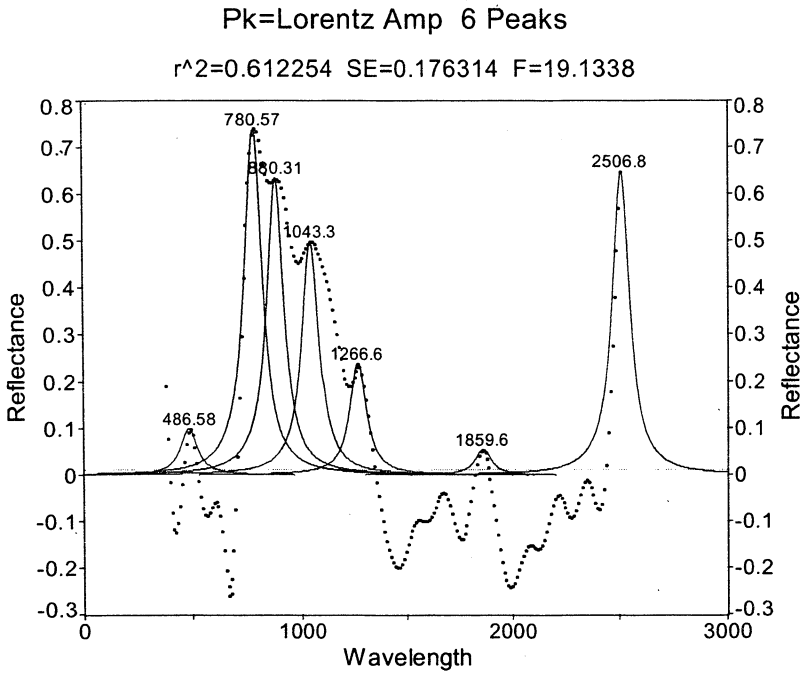

Fig. 6. AVIRIS image: healthy cotton peaks of reflectance against wavelength in the Blythe area.

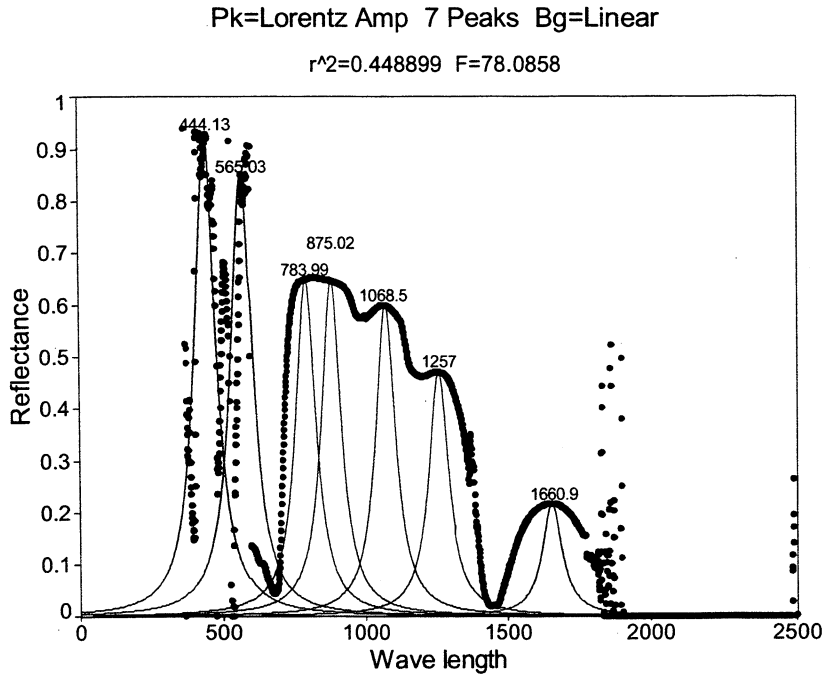

Fig. 7. Data extracted from AVIRIS image on relatively stressed cotton.

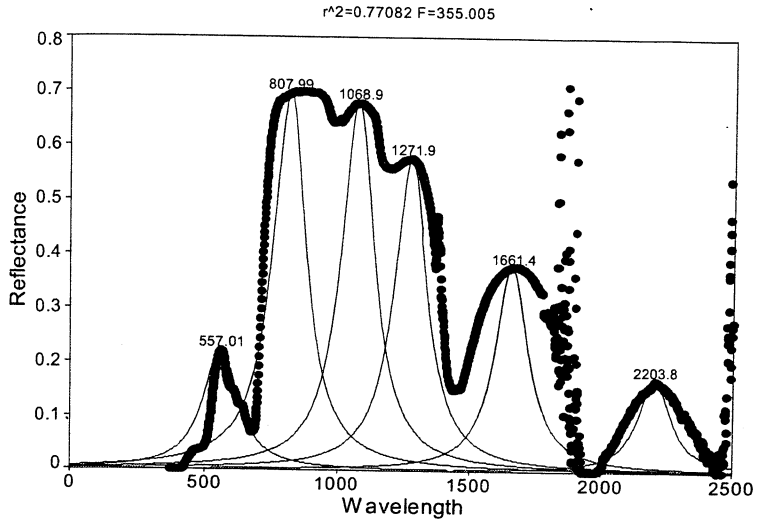

Fig. 8. Data collected from the ASD FieldSpec® radiometer on relatively stressed cotton.

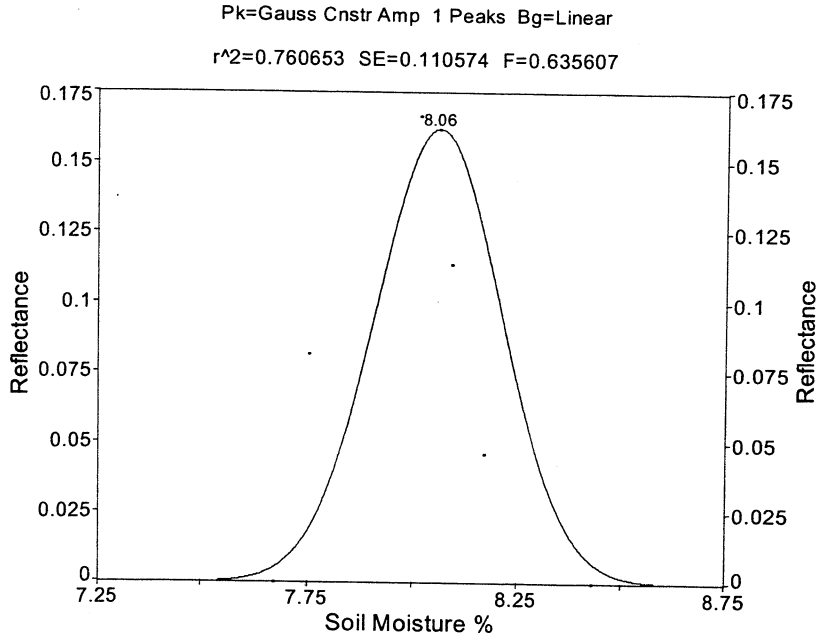

Fig. 9. Peak relationship between soil moisture and reflectance in healthy cotton.

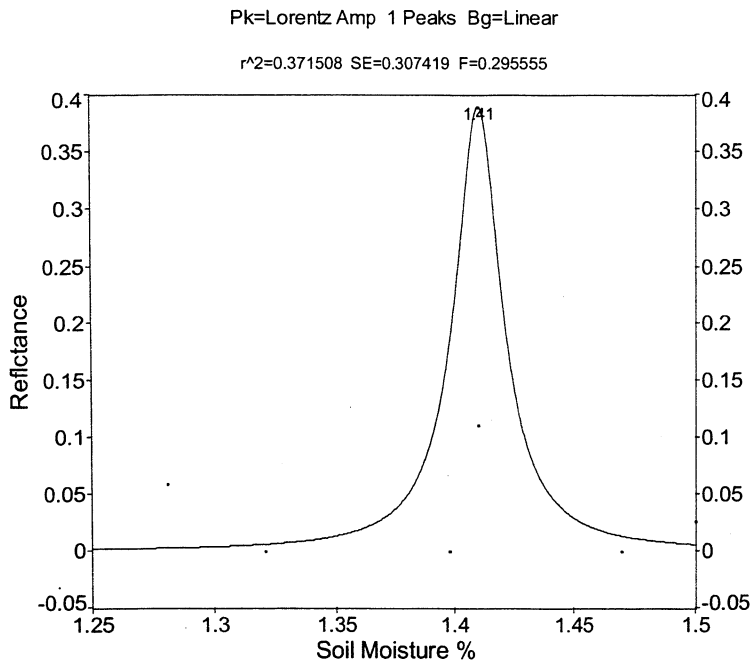

Fig. 10. Peak relationship between soil moisture and reflectance in stressed cotton.

Soil moisture can affect the reflectance signals in stressed and healthy cotton in the form of peaks (Figures 9 and 10). The graphs indicate that in the in the stressed cotton, the reflectance is higher (i.e., reflectance is 40%) when soil moisture reaches 1.4–1.42% than in the healthy cotton (i.e., reflectance is 17%) when the soil moisture reaches the 8% level. The higher reflectance data in stressed crops are in the area of wavelength 500–700 nm and the lower reflectance data in unstressed crop are in the 500–700 nm range. This indicates that water stress will be revealed in the region of 500–700 nm.

CONCLUSIONS

Reflectance spectra from an AVIRIS image acquired in 1997 and ground spectral data collected in the year 2000 by the FieldSpec® spectrometer have been examined and analyzed. Simple direct comparison of reflectance spectra for like crops in similar growth stages showed good correlation. These results support the use of these types of reflectance data for agricultural crop investigations and development of advanced applications.

In addition, these data were used to reproduce various vegetation indices. The response of these vegetation indices were examined for healthy and stressed cotton plants. Differences in the indices response were identified. The visible and near-infrared portion of the spectrum between 400 and 1000 nm was found to contain significant variation associated with vegetation type and condition. The effect of vegetation water appeared to dominate the spectrum beyond 1000 nm.

Overall, the measured spectral reflectance signatures showed variation associated with different crops at different stages of development. This supports the continued research into use of reflectance spectra in the AVIRIS spectral range for agricultural applications. Future efforts will be directed to extend this research to other crop types and agricultural regimes.

ACKNOWLEDGEMENTS

NASA has supported this research under grant NAG-13. Also, the Summer Faculty Program sponsored by NASA/JPL supported the PI of the TEXGED Center. The author also recognizes the help and support of Michael D. Retwisch, Agriculture & Natural Resources, Cooperative Extension, Riverside County, University of California, during the collection of spectra from the Blythe area, California.

Part of this research was carried out at the Jet Propulsion Laboratory, California Institute of Technology, under contract with the National Aeronautics and Space Administration

REFERENCES

Baret, F., Jacquemoud, S., Guyot, G. and Leprieur, C., 1992. Modelled analysis of the biophysical nature of spectral shifts and comparison with information content of broad bands. Remote Sensing of the Environment 41, pp. 133–142.

Baret, F. and Guyot, G., 1991. Potentials and limits of vegetation indices for LAI and APAR assessment. *Remote Sensing of the Environment* 35, pp. 161-173.

Baret, F., Guyot, G. and Major, D. J., 1989. TASVI: A vegetation index which minimizes soil brightness effects on LAI and APAR estimations. In: *Quantitative Remote Sensing for the Nineties*, Proc. IGARSS '89, Vancouver, Canada, Vol. 3 pp. 1355-1358.

Collins, W., 1978. Remote sensing of crop type and maturity. *Photogrammetric Engineering and Remote Sensing* 26, pp. 43-55.

Demetriades-Shah, T.H., Steven, M.D. and Clark, J.A., 1990. High resolution derivative spectra in remote sensing. *Remote Sensing of the Environment* 33, pp. 55-64.

ENVI-IDL (1999). The Environment for Visualization Images. ENVI User Guide ENVI 3.2 version. Research System 864 pp.

Guyot, G., Baret, F. and Jacquemoud, S., 1989. Imaging spectroscopy for vegetation studies. In: Toselli, F. and Bodechtel, J., Editors, 1989. *Imaging Spectroscopy: Fundamentals and Prospective Applications*, Kluwer Academic Publishers, Dordrecht, The Netherlands, pp. 145-165.

Green, R.O., Eastwood, M.L., Sature, C.M., Chrien, T.G., Aronsson, M., Chippendale, B.J., Faust, J.A., Pavri, B.E., Chovit, C.J., Solis, M., Olah, M.R. and William, O., 1998. Imaging spectroscopy and airborne visible/infrared imaging spectrometer (AVIRIS). *Remote Sens. Environ.* 65:227-248.

Green, R. O., Conel, J.D., and Roberts, D. A., 1993. Estimation of aerosol optic depth pressure elevation, water vapor, and calculation of apparent surface reflectance from radiance measured by the airborne visible/infrared imaging spectrometer (AVIRIS) using a radiative transfer code. In proceedings of the International Society of Optical Engineering, SPIE 1937, Orlando, Florida, pp. 2-11.

Huete, A.R., 1988. A Soil-Adjusted Vegetation Index (SAVI). *Remote Sensing of the Environment* 25, pp. 295–309.

Mauser, W. and Bach, H., 1995. Imaging spectroscopy in hydrology and agriculture -- determination of model parameters. In: Hill, J. and Megier, J., Editors, 1995. *Imaging spectrometry -- A Tool for Environmental Observations*, Kluwer Academic Publishers, Dordrecht, The Netherlands, pp. 261-283.

Pearson, L. and Miller, L.D., 1972. In: Remote mapping of standing crop biomass for estimation of the productivity of the short-grass Prairie, Pawnee National Grasslands, Colorado, ERIM, Ann Arbor, Michigan, pp. 1357–1381.

Richardson, A. J. and Wiegand, C.L., 1977. Distinguishing vegetation from soil background information. *Photogramm. Eng. Remote Sens.* 43:1541-1552.

Rouse. W., Haas, R. H., Schell, J. A., Deering, D. W., & Harlan, J. C., 1974. Monitoring the vernal advancement of retrogradation of natural vegetation. NASA/GSFC, Type III, Final Report, Greenbelt, Maryland, USA, pp. 1-371.

Tucker, C. J.,1979. Red and photographic infrared linear combinations for monitoring vegetation. *Remote Sens. Environ.* 8:127-150.

Vane, G., 1987. *Airborne Visible Infrared Imaging Spectrometer (AVIRIS).* JPL Publication 87-38, Jet Propulsion Laboratory, Pasadena, California.

Vane, G., Chrisp, M., Enmark ,H., Macenka, S. and Solomon, J., 1984. Airborne Visible Infrared Imaging Spectrometer. An advance tool for Earth remote sensing. *Proc. IEEE Int'l Geosc.& Rem. Sens. Symp. SP215*, 751-757.

Table 1. Data collected from the Blythe area in California on July 18 and 19, 2000

Field	Latitude	Longitude	Time	Treatment
Bare soil	33° 39.69 N	114° 34.30 W	1:00 pm July 19,2000	Soil is empty of any vegetation
Relatively stressed cotton	33° 25.76 N	114° 44.42 W	11:00 am July 18,2000	Healthy cotton but stressed
Healthy cotton	33° 25.42 N	114° 44.53 W	12:13 pm, July 18, 2000	Full bloom, no balls of cotton yet open

Table 2. Soil moisture content: %, pH, soil organic matter, and yield of plants (kg/ha) from Blythe, California

Field	Soil Moisture%	PH	Soil organic matter%	C%	N%	C/N Ratio
Relatively stressed cotton	1.398	8.35	2.560	1.520	0.0300	50.66:1
Healthy cotton	8.013	8.35	1.990	1.158	0.0340	34.05:1

Table 3. Wavelength and reflectance data in the different fields and treatments using a hand-held radiometer from Blythe, California

Field	350.0–650nm	650–950 nm	950–1250 nm	1250–1550 nm	1550–1850 nm	1850–2150 nm	2150–2500 nm
Relatively stressed cotton, wilted cotton	0.1641	0.6502	0.7124	0.4371	0.4340	0.1810	0.2145
Healthy cotton	0.1339	0.6112	0.6889	0.4129	0.4004	0.1557	0.1875

Table 4. Soil line and vegetation index equations by site and radiometer

Field	Latitude	Longitude	Time	Treatment	Soil line and vegetation index equations
Bare soil	33° 39.69 N	114° 34.30 W	1:00 pm, July 19,2000	Soil is empty from any vegetation	Cotton healthy but relatively stressed
Cotton healthy but relatively stressed	33° 25.76 N	114° 44.42 W	11:00 am, July 18,2000	Healthy cotton but relatively stressed	NIR=0.8171 – 0.2252 RED r^2=0.84
Cotton healthy but relatively stressed	33° 25.76 N	114° 44.42 W	11:00 am, July 18,2000	Healthy cotton but relatively stressed	PVI=0.1666-0.6046 RED +0.74 NIR
Cotton healthy but relatively stressed	33° 25.76 N	114° 44.42 W	11:00 am, July 18,2000	Healthy cotton but relatively stressed	TSAVI=0.8171[NIR-0.8171*RED-(-.2252)]/[0.8171*NIR+RED-(-0.1840)]
Cotton healthy	33° 25.42 N	114° 44.53 W	12:13 pm, July 18, 2000	Full bloom, no bolls of cotton yet open	NIR=Y=0.7865 –0.3176*RED r^2=0.86
Cotton healthy	33° 25.42 N	114° 44.53 W	12:13 pm, July 18, 2000	Full bloom, no bolls of cotton yet open	PVI=0.2500 – 0..6193 RED +0.7874NIR
Cotton healthy	33° 25.42 N	114° 44.53 W	12:13 pm, July 18, 2000	Full bloom, no bolls of cotton yet open	TSAVI=0.7865[NIR-0.7865*RED-(-.3176)]/[0.7865*NIR+RED-(-0.2498)]

Preliminary Results of Hydrothermal Alteration Assemblage Classification in Aurora and Bodie Mining Districts, Nevada and California, with Airborne Hyperspectral Data

Amer Smailbegovic, James V. Taranik and Wendy M. Calvin
Arthur Brant Laboratory for Exploration Geophysics
University of Nevada, Reno

ABSTRACT

The Aurora and Bodie mining districts are located in Bodie Hills, north of Mono Lake, on opposite sides of the Nevada-California state line. From the standpoint of economic geology, both deposits are structurally controlled, low-sulfidation, adularia-sericite precious metal vein deposits with an extensive alteration halo. The area was exploited from the late 1870's until 1988 by both underground and minor open pit operations (Aurora), exposing portions of ore-hosting altered andesites, devitrified rhyolites as well as quartz-adularia-sericite veins. Much of the geologic mapping and explanation was ad-hoc and primarily in support of the mining operations, without particular interest paid to the system as a whole. The University of Nevada, Reno has acquired both high- and low-altitude AVIRIS data of the region. Low-altitude data was acquired in July 2000, followed by high-altitude collection in October 2000. The AVIRIS coverage was targeted on the main vein system in Aurora (Prospectus and Humboldt Vein), East Brawley Peak prospect (midpoint between Aurora and Bodie) and "Bonanza Zone" (Bodie Bluff and Standard Hill) in Bodie, where the hydrothermal alteration zones appear to be the most pervasive. The ground-observations and mining/prospecting reports suggest propylitic alteration throughout the Bodie Hills, argillic and potassic alteration in Aurora and Bodie, (low-sulfidation system) and alunitic alteration (high-sulfidation system) on East Brawley Peak.
The AVIRIS data allows identification of alteration zones containing dominant kaolinite, sericite (Aurora), alunite (E. Brawley Peak) and Na and Ca-montmorillonite (Bodie), which have been verified with ASD spectrometer and XRD analysis on field collected samples. Spectral mapping is somewhat hindered by anthropogenic factors (mine dumps and reclamation efforts) and coatings (heavy varnish and pyroclastic "sand" from Inyo Craters). We will present the mapping results from the high-altitude data set and an initial comparison to the low-altitude scene.

AREA and GEOLOGY

Aurora:

The Aurora district, formerly known as the Esmeralda Mining District, was discovered in 1860 by J. M. Braly, E. R. Hicks and J. M. Cory. Most of the estimated 1.6 million ounces of gold and 2.4 million ounces of silver was produced in the heyday of the district between 1862 and 1865 with sporadic production up to 1988. The district is located in the Bodie Hills, south of Hawthorne, Nevada (via Lucky Boy Pass) and northeast od Bridgeport, California (via Bodie Road) (Figure 1). The area is mountainous

with elevations ranging from 1,716 m (5,150 ft) at Fletcher Valley to (3,675) 11,015 on Potato Peak and characterized by semi-arid climate and vegetation characteristic for Great Basin (Sagebrush, Rabbitbrush, Mormon tea, Cacti, Pinon pine, Jeffrey pine and Juniper).

The oldest rocks in the district are metavolcanics of the Mid-Triassic Excelsior Formation, intruded by Cretaceous Sierra Nevada Granites. Tuffs (15 Ma?) and andesitic lava flows and breccias (14.8 Ma) of East Brawley Peak are resting unconformably upon the granitic and metavolcanic basement. The East Brawley Andesites (Aurora Andesites 13 Ma) are the main body of mineralized andesites found in the Aurora district. Del Monte shaft, sank to a depth of 700 m (2200 ft), had not reached the lower contact of the Aurora Anesdite sequence. An episode of rhyolitic volcanism occurred at about 11.2 Ma intruding the andesites and tuffs, followed by hydrothermal activity, alteration and most likely precious metal mineralization in the Aurora area (at 10.2 Ma). Approximately 3 .Ma ago, the style of volcanism shifted from Calc-alkaline to alkalic-calcic. Another episode of rhyolitic volcanism occurred around 2.5 Ma with emplacement of Aurora Peak and Martinez Hill. The volcanism in the district ceased with emplacement of Aurora Crater basalts (25 Ka) (Breit, 2000; Al-Rawi, 1970). The district mineralization itself, appears to be structurally controlled and related to N20E trending right-lateral strike slip faults (Osborne, 1986). The most significant alteration assemblages (sericitic, argillic) appear to be closely associated with the fault-contact between 13 Ma Andesite and 11 Ma rhyolite, although almost all of the Aurora Andesite in the district appears to be altered to a degree (Field observations, Larson, L.T. Pers. Comm). The mineralized veins in the district appear to follow zones of earlier structural weaknesses and most likely have been deposited from meteoric hydrothermal waters, contemporaneous with the emplacement of Rhyolite flow dome, which may have provided the heat to drive the hydrothermal system. The system at Aurora is classified as a Quartz - Sericite - Adularia type gold deposit. Thin sections reveal that the veins are dominantly Quartz with a few percent or less of Sericite and a fraction of a percent or less of adularia (K-feldspar). Adularia appears to be replacing earlier bladed, hydrothermal calcite. The dominant ore mineral in the veins is electrum with associated trace amounts of the silver sulfides: acanthite, aguilarite, proustite, pyragyrite, and pearcite. Gangue minerals include pyrite, goethite, and in some veins trace amounts of arsenopyrite and sphalerite. The type of ore found in the veins varies: disseminated electrum in a coarse grained quartz, electrum deposited along the boundaries of well defined bands or ribbons of quartz and occasionally, electrum encapsulated in pyrite and/or goethite (Nevada Goldfields Internal Report, 1988).

Bodie:

The Bodie Mining District was incorporated in 1860, and several reports were written in the years that followed, most notably by Joseph Watson, who had prepared a preliminary report for members of the New York Bullion Club and H.A. Whiting's report to the USGS and Bodie Consolidated Mining Company in 1888 (State Mineralogist Report, 1888). Empire Mill and Mining Co. of New York, NY incorporated and consolidated earlier claims and invested large sums of money in the district in 1863. By 1865, no substantial ore was found. Empire abandoned the operation and the district was held in very low regard until 1872 when rich ore was struck. In 1876, San Francisco

venture capitalists bought the mines and ran the operation until 1883. The mining in the district ceased in 1947. Bodie is now a part of the California State Park system.

The rock units found around Bodie are mainly composed of tuff breccias, dacite flows and some intrusive dacite. Volcanism commenced in Bodie Hills and eastward, approximately ~17 Ma ago with eruptions of calc-alkaline andesite, dacite and rhyodacite onto topographically flat surface (presumably of sedimentary origin) (Kleinhampl et al., 1975). Initial geothermal activity began at Masonic District (northern Bodie Hills, ~20km NE of Bodie). Two distinct episodes of geothermal activity at ~7.8 Ma and ~7.2 Ma (Silberman, et al., 1972), produced economic mineralization in Bodie District, although some hydrothermally altered areas at Bodie may be related to an earlier, non-economic, hydrothermal activity of 8.4 Ma (Chesterman et al., 1986). The mineralizing events in Bodie are geochemically and minerologically distinct (Brown, 1907; Silberman, 1995) and are localized on the southeast flank of the alkali-calcic Bodie Mountain – Potato Peak stratovolcanoes (Chesterman et al., 1986). The hydrothermal alteration in Bodie is widespread and appears to have had four major episodes, beginning with propylitic and following, in succession, by argillic, potassic and silicic. Propylitic alteration is widespread over 9 square mile radius and appears to have affected all rock types regardless of composition or structure. Argillic alteration is characterized by montmorillonite, kaolinite and minor sericite and appears to be concetrated along joints and fractures. Potassic alteration appears to be confined to the rocks in and surrounding the Bodie Bluff-Standard Hill. Silicic alteration is, most likely, the last stage of the hydrothermal activity and perhaps a factor in the formation of quartz veins. Similar to Aurora, Bodie is classified as a low-sulfidation epithermal vein depost.

AVIRIS FLIGHTS and PREVIOUS WORK

Bodie was targeted for 1992 AVIRIS overflight and the data have been processed by Crosta, Sabine and Taranik (1998) and USGS (Trude King, unpublished report). Both parties were successful in extracting Ca and Na-montmorillonite spectra from the 1992 imagery as well as spectra of Fe-oxides and hydroxides. The goal of the project was to compare the alteration systems at Bodie and Paramount (a small mercury mine west of Bodie) and methods of spectrally classifying the deposits (using SAM and Tricorder). The zones of iron and clay enrichment were corresponding with the mineralized areas in Bodie. The University of Nevada Reno proposed both high altitude and low altitude flights over Bodie and Aurora for the 2000 flight season. The low altitude data were acquired on July 9, 2000 and high altitude on September 19, 2000. The AVIRIS data are to be used in conjunction with other data sets and extensive field observations in understanding the structural and lithologic constraints to mineralization in the districts.

IMAGE PROCESSING

Both high and low altitude data sets were ATREM corrected, but only the high altitude set was EFFORT polished; the procedure has created significant artifacts in the low altitude set. For the preliminary analysis, both sets were subsetted to SWIR range and individual scenes mosaicked. A Minimum Noise Fraction (MNF) transformation was

used to produce spectral bands free of instrumental and/or atmospheric noise. A Pixel Purity Index (PPI) routine was then used to select all of the pixels in the image that are above the noise floor and appear to contain unique spectra that can be further used to determine spectral "end members." The term "end member" is used to denote a pixel that contains unique spectra that is representative and characteristic of a dominant mineral, or intimate mixtures of minerals. The improved signal to noise of AVIRIS allowed 11 characteristic end members to be selected from the high altitude and 16 from the low altitude data. These end members were used to further process the image using the Mixture Tuned Matched Filtering (MTMF) and Spectral Angle Mapper (SAM) algorithms. The results from the application of these algorithms, and comparison with the USGS spectral library produced relative mineral abundance thematic displays for the main mineral constituents, including alunite, kaolinite, illite, muscovite (sericite), and na, ca-montmorillonite. Additionally, the low-altitude data have the inherent geometric distortions and under sampling in the down-track direction because of aircraft pitch, yaw and roll and instrument constraints. The low-altitude scene was co-registered to a special reference file compiled by AIG for NASA. This file contains information on actual and "artificial" pixels used to georectify the flight line. The reference file was used to create an image mask to drape over the image thus highlighting only actual spectral measurements for classification.

RESULTS

The analysis of high altitude data allowed indentification of alunite, kaolinite and sericite in the Aurora-Bodie transect (Figure 2). The main body of hydrothermal alteration in Aurora, is associated with the main vein system.The mineral classes include sericite (in proximity to the veins), illite and kaolinite associated with the vein alteration halo, kaolinite distributed throughout the district, but particularly evident in the section of altered rhyolites, immediately west of the main mine works. It was also possible to distinguish some exposed quartz-veins by their lack of spectral features in SWIR. Similarly, in Bodie it is possible to distinguish the zones of Ca-Na montmorillonite and Kaolinite with minor sericite. The main body of alteration is constrained in the so-called "Bonanza Zone;" an extensional graben including the Bodie Bluff and Standard Hill with a minor splay on Queen Bee Hill (south of the Bonanza Zone and delineated by the Red Cloud fault). Aside from the mining district, it is also possible to distinguish alunite associated with the high-sulfidation hydrothermal system on East Brawley Peak, illite and kaolinite associated with sections of altered granites near Spring Peak and rhyolites near Rough Creek.

The low altitude data, centered at the districts themselves allow better spectral classification with the improved spatial resolution. In Aurora, it is possible to distinguish the areas of sericitic alteration and display them in the more field-observable context. Furthermore, it is possible to trace the argillic alteration (kaolinite, illite) along the length of Prospectus fault (which may be the primary structure responsible for the mineralization in the district) and trace it in the areas where it may not be well exposed (the actual extent of the fault is a point of violent dispute among the mine geologists in Aurora). The low-altitude data also allows identification of, what appears to be supergene, clay in the tuffaceous sediments ringing the Martinez Hill. In Bodie, it is

possible to map the distribution of kaolinite on Bodie Bluff and Ca-Na montmorillonite on Standard Hill with a sericitic zone in between. Relatively sharp contact between the mineralogic units appears to be congruent with the normal faults defining the "Bonanza Zone." In particular the distribution of sericite corresponds with the approximate location of mineralized veins at depth.

The AVIRIS spectral measurements were checked with field-measured spectra and XRD diffraction on select samples (Figure 3). Both XRD spectra and ASD field-spectra support the results obtained from AVIRIS.

DISCUSSION AND CONCLUSIONS

Most of the mining in Aurora and Bodie was concentrated on "chasing the veins" through the district where the miniscule structural features or surficial expressions of the vein at depth (alteration) made the difference in choosing the mineralized versus barren vein. The high altitude AVIRIS data gives an excellent overview of the terrain, with predominat alteration types on the district level. However, the integration with the low-altitude data sets allows interpretation and characterization at the sub-district level, which was the historic way of exploring the district. The high altitude data tends to clump the spectral measurements and masks them with the robust spectral signature of the dominant material (the mixed pixel problem). In Aurora and Bodie it is very difficult to hone in on sericite – its features are often masked by much more dominant clay absorption features. However, the increased spatial resolution of the low altitude data set allows for the effective mapping of sericite and interpretation of how it fits within the vein system. Further, it is possible to observe the zones that may be associated with the fault system in the district, most notably the extent of the Prospectus Fault (through argillized fault breccia) and its relation to the mineralization in the district.

When compared to the 1992 data over Bodie, the 2000 data set presents a dramatic improvement in both spectral and spatial domains . The addition of the low-altitude data enhances the mapping potential and allows an easy integration with the field orientation and mapping. Mineralogic assignments corresponding to structural boundaries are a tremendous asset in use and application of the data and may help resolve differing interpretation of fault location and extent.

ACKNOWLEDGMENTS

This research was made possible by the Arthur Brant Endowment and Nevada Space Grant Consortium. Special thanks to Bill Silberman and Fred Breit in discussing Aurora and Bodie geology and to Stuart Miles for help with the fieldwork and mapping.

FIGURES:

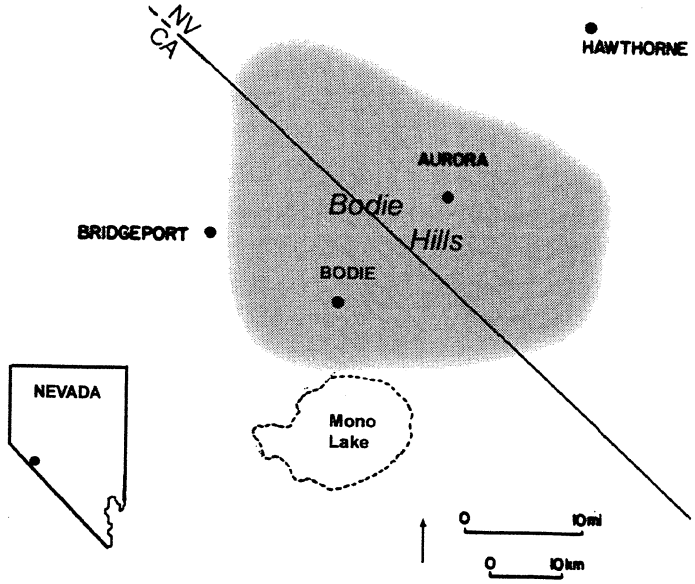

Figure 1 – Area Location

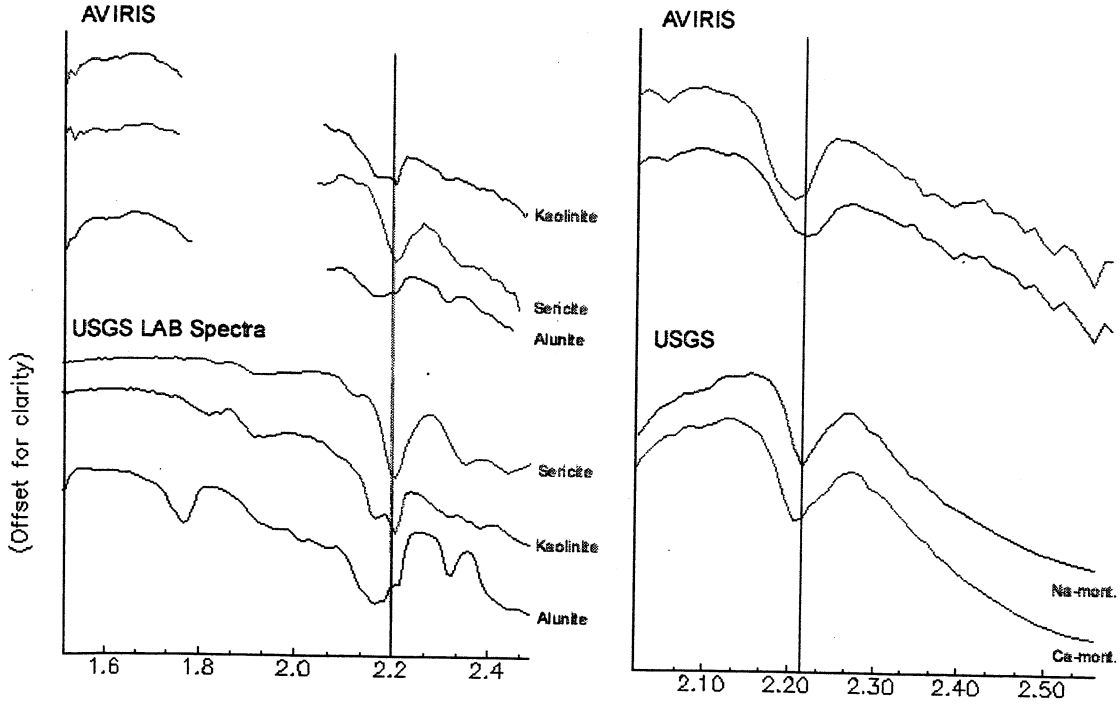

Figure 2 – AVIRIS and LAB Spectra

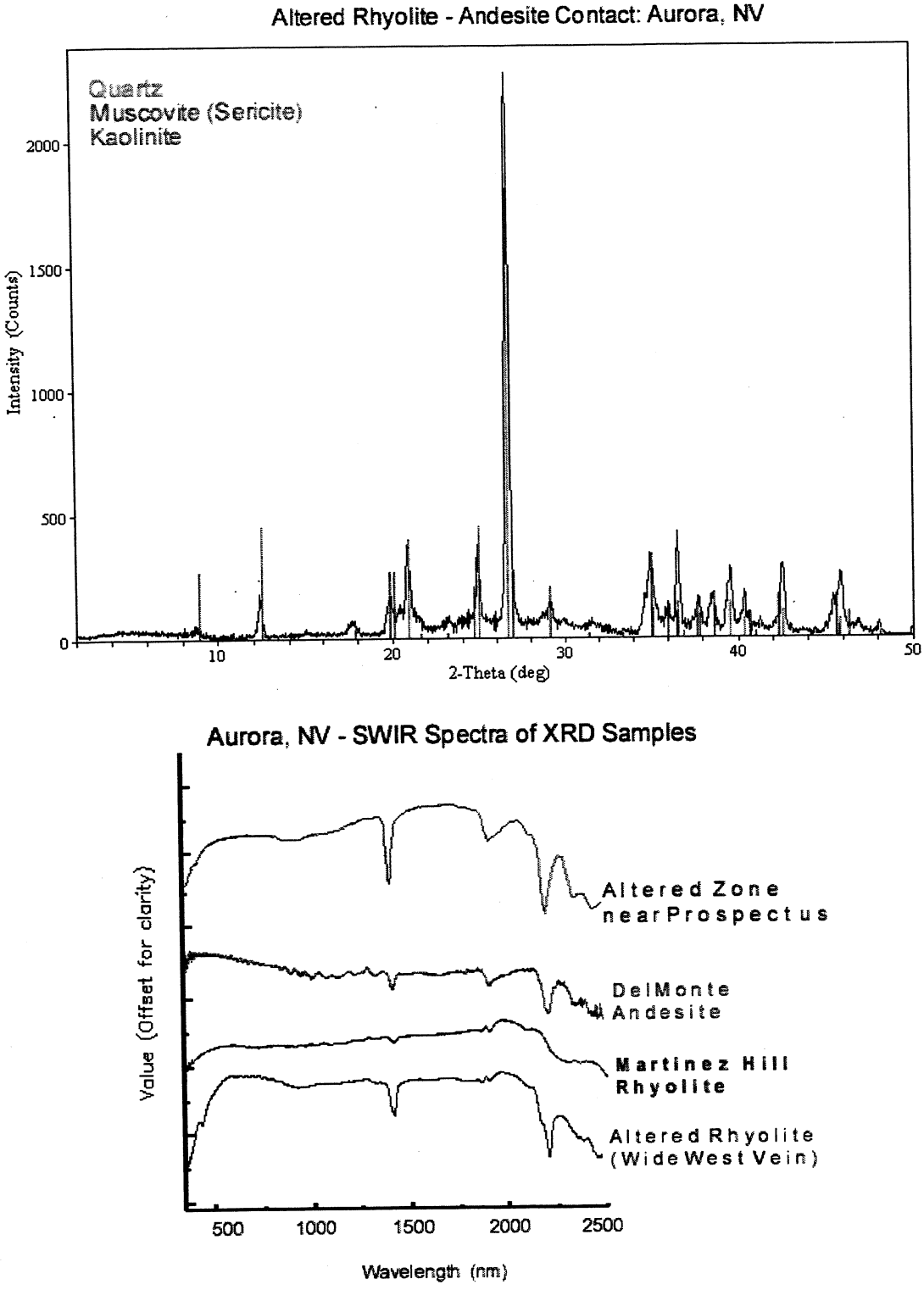

Figure 3 – XRD Spectra and ASD Field Spectra on XRD samples.

REFERENCES CITED

Al-Rawi, Yehya. 1970. Paleomagnetic study and K-Ar age od Pliocene volcanics, Bodie District, California. GSA Special Paper, p. 478-479.

Breit, Frederick, J. 2000. Structural and Temporal Relationships and Geochemical Characteristics of the East Brawley Peak Acid-sulfate Prospects and the Adjacent Aurora Adularia-Sericite System. M.S. Thesis. Mackay School of Mines, University of Nevada, Reno.

Crosta, A., Sabine, C. and Taranik, J.V. 1998. Hydrothermal Alteration Mapping at Bodie, California, Using AVIRIS Hyperspectral Data. Rem. Sens. Env. Vol 65, p. 309-319.

Chesterman, Charles, Chapman, Rodger and Gray, Clifton. 1986. Geology and Ore Deposits of the Bodie Mining District, Mono County, California. California Bureau of Mines and Geology – Publication 206.

Kleinhample, F.J. Davis, W.E. Silberman, M.L., Chesterman, C.W. Chapman, R.H. Gray, C.H. Jr. 1975. Aeromagnetic and limited gravity studies and generalized geology of the Bodie Hills region, Nevada and California. USGS Bulletin 1384, p.38.

Silberman, M.L., Chesterman, C.W. Kleinhampl, F.J., Gray C.H. Jr. 1972. K-ar Ages of Volcanic Rocks and Gold Bearing Quartz-Adularia Veins in the Bodie Mining District, Mono County, California. Economic Geology, Vol.67, p. 597-603.

State Mineralogist Report. 1888. California Mining Bureau, p. 382 – 392.

Spectral Dimensionality and Scale of Urban Radiance

Christopher Small

Lamont Doherty Earth Observatory
Columbia University
Palisades, NY 10964 USA
small@LDEO.columbia.edu

Abstract

Characterization of urban radiance and reflectance is important for understanding the effects of solar energy flux on the urban environment as well as for satellite mapping of urban settlement patterns. Spectral mixture analyses of Landsat and Ikonos imagery suggest that the urban radiance field can very often be described with combinations of three or four spectral endmembers. Dimensionality estimates of AVIRIS radiance measurements of urban areas reveal the existence of 30 to 60 spectral dimensions. The extent to which broadband imagery collected by operational satellites can represent the higher dimensional mixing space is a function of both the spatial and spectral resolution of the sensor. AVIRIS imagery offers the spatial and spectral resolution necessary to investigate the scale dependence of the spectral dimensionality. Dimensionality estimates derived from Minimum Noise Fraction (MNF) eigenvalue distributions show a distinct scale dependence for AVIRIS radiance measurements of Milpitas, California. Apparent dimensionality diminishes from almost 40 to less than 10 spectral dimensions between scales of 8000 m and 300 m. The 10 to 30 m scale of most features in urban mosaics results in substantial spectral mixing at the ~20 m scale of high altitude AVIRIS pixels. Much of the variance at pixel scales is therefore likely to result from actual differences in surface reflectance at pixel scales. Spatial smoothing and spectral subsampling of AVIRIS spectra both result in substantial loss of information and reduction of apparent dimensionality, but the primary spectral endmembers in all cases are analogous to those found in global analyses of Landsat and Ikonos imagery of other urban areas.

Introduction

Recent estimates indicate that over 45% of the world's human population now lives in urban areas with over 60% projected by 2030 (*United Nations, 1999*). As the size and number of urban agglomerations increases, so does the relative importance of the urban environment to the global population. Remote sensing can serve (at least) two important roles in the study of the urban environment. Moderate resolution, broadband optical sensors on the Landsat and Spot satellites provide a 30 year time series with which to quantify urban growth and settlement patterns worldwide. In order to map urban growth with optical sensors, it is necessary to distinguish the reflectance properties of the urban surfaces from those of other landcover types. This is an inherently difficult task because urban areas incorporate spectrally identical land covers from other environments and because built urban surfaces are often composed of materials extracted from nearby surroundings. The scale and texture of urban reflectance is, however, often distinct from other landcovers so the combination of reflectance and textural properties is more informative. This requires a robust characterization of urban reflectance properties at different scales. The synoptic view of the urban mosaic provided by satellite and airborne sensors is also an important complement to *in situ* measurements of physical characteristics of the urban environment. The spectral reflectance properties of the urban mosaic have a strong influence on energy flux through the urban environment and the microclimatic variations that result (*Landsberg, 1981*). Since much of the reflectance of the built environment is subject to human modification, understanding

scale dependent optical properties of existing urban settlements may influence future design decisions. Characterization of urban spectral reflectance serves both of these objectives.

Analysis of reflectance properties in different urban environments may provide a basis for a general characterization of urban reflectance. Comparative analyses of Landsat and Ikonos imagery for a variety of cities worldwide indicates that spectral heterogeneity at scales of tens of meters is the most consistent characteristic of broadband spectral reflectance of urban areas (*Small, 2001b*). In spite of the lack of a single characteristic urban reflectance spectrum, almost all of the urban areas considered could be described as spectral mixtures of three or four endmembers as resolved by the Ikonos, Landsat TM and ETM+ sensors (*Small, 2001a*). In contrast, many of the areas surrounding these cities are characterized by more complex mixing spaces with larger numbers of spectral endmembers. Representation of urban reflectance with a simple spectral mixing model (e.g. *Adams et al, 1986, 1993; Smith et al, 1990; Gillespie et al, 1990*) would be desirable because it could accommodate the spectral heterogeneity with a physically based description consistent with the variety of reflectances observed in urban environments. This requires a more thorough understanding of the relationship between the true spectral dimensionality of the urban mosaic and the low dimensional projection of this mixing space that is resolved by broadband sensors like Landsat. The representation of the mixing space provided by broadband imagery is incomplete because these operational sensors lack the spectral resolution necessary to distinguish among materials with narrow absorption bands resolvable by imaging spectrometers like AVIRIS.

An analysis of high resolution AVIRIS imagery by *Green and Boardman, (2000)* found that a flight line collected of San Diego California had higher spectral dimensionality than datasets collected in other environments. This prompts the question of whether urban areas can really be characterized with simple linear mixing models or whether the true high spectral dimensionality of the urban mosaic will preclude development of a general characterization of urban reflectance. In order to resolve this question, it is necessary to consider the spatial scale of the observations. The objective of this analysis is to investigate the relationship between spatial scale and spectral dimensionality in an urban environment. The focus of the analysis in on the use of eigenvalue decomposition for multiscale estimation of spectral dimensionality.

Data and Analysis

This analysis used AVIRIS radiance and reflectance data collected over Milpitas California on 20 June 1997. These data are available as AVIRIS standard data products from *popo.jpl.nasa.gov*. The study area, shown in Figure 1, consists of undeveloped land, suburban residential areas and urban industrial areas. The primary spectral endmembers, derived from the analyses described below, are shown in Figure 2. These endmembers were selected using the methodology described by *Boardman (1993)* and *Boardman and Kruse (1994)*. Endmember spectra are shown in scaled reflectance for ease of interpretation, but all dimensionality estimates were made using calibrated radiance data so the information content is determined by both the surface reflectance characteristics and the atmospheric interactions.

Spectral dimensionality estimates are based on eigenvalue distributions obtained from principal component analyses as described by *Boardman and Green (2000)* and *Green and Boardman (2000)*. The Minimum Noise Fraction (MNF) transformation (*Green et al, 1988; RSI, 2000*) is used because it accommodates band-to-band differences in signal and noise amplitude and because the resulting eigenvalues provide an indication of the information and noise content of the data. All analyses shown here were done with ENVI image processing software. The MNF implemented in ENVI is similar to that Maximum Noise Fraction transformation described by *Green et al (1988)* but differs in the scaling of the resulting eigenvalues. The eigenvalues produced by ENVI's MNF are scaled in sigma noise units analogous to a signal-to-noise ratio so the number of eigenvalues greater than unity gives an estimate of

the number of dimensions with variance larger than the amplitude of the noise estimate. One advantage of the Minimum Noise Fraction transformation is that it accounts for the fact that the noise in some bands may be larger than the signal in other bands. Rather than basing the rotation on variance alone, the ENVI MNF attempts to "prewhiten" the data by performing an initial rotation to diagonalize the noise covariance and by rescaling the eigenvalues of the second rotation to sigma noise units (*RSI, 2000*).

In order to compare dimensionality estimates from different areas, it is necessary to use a consistent noise estimate. For this analysis, the noise estimate is based on a subimage acquired over the Calaveras reservoir in the same AVIRIS scene as the study area. By using the same noise covariance for all MNF rotations, differences in the resulting eigenvalue distributions should more accurately reflect differences in the signal content of each subscene. The noise covariance estimate is derived from differences in spectra of adjacent pixels so a dark, uniform target provides a crude approximation of a dark current noise source. The approximation is imperfect, however, because it includes actual differences in radiance related to spatial variations in surface reflectance and path radiance at scales of ~20 meters.

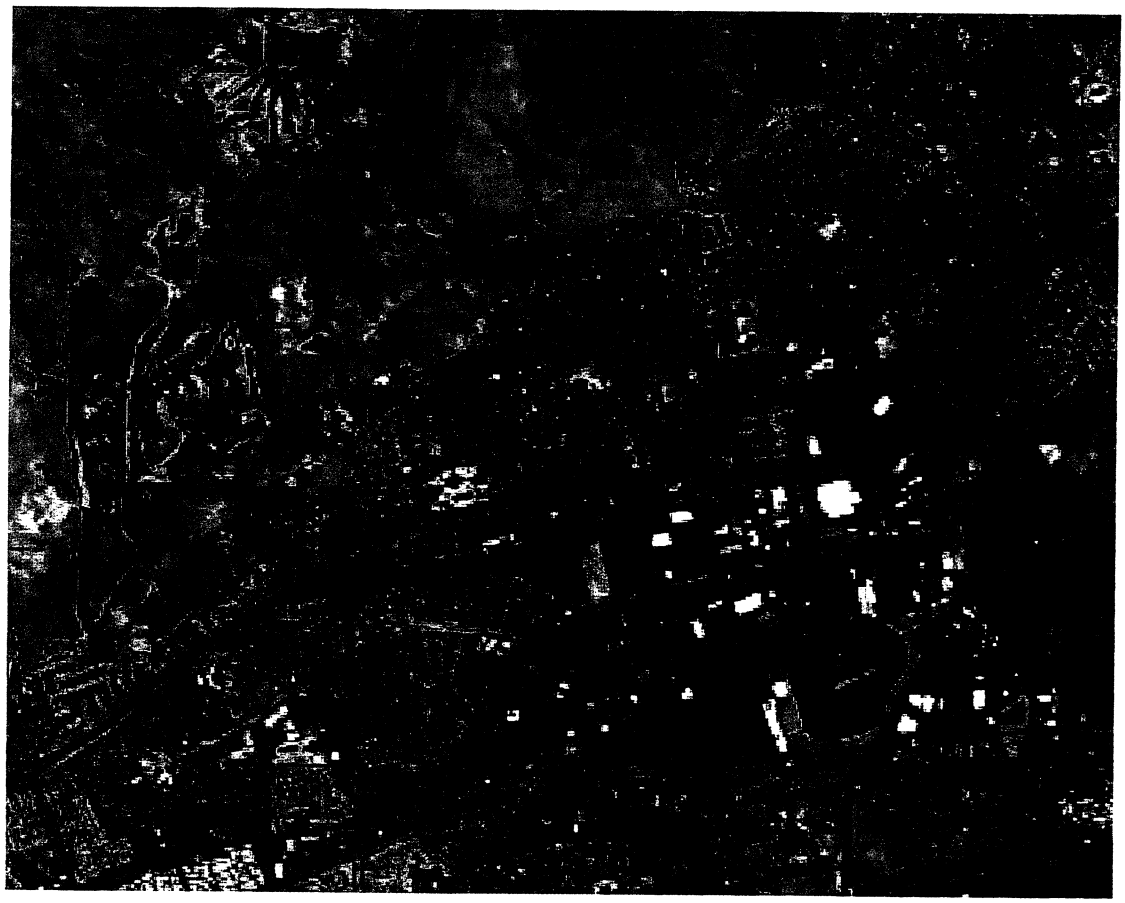

Figure 1. *AVIRIS false color composite of Milpitas California acquired in 1997. The Red, Green and Blue layers correspond to the 2.21 μm, 0.81 μm and 0.66 μm wavelength bands respectively. The image is 6 x 8 km and each pixel is approximately 20x20 m. The spectral dimensionality of the mosaic of urban, subruban and undeveloped areas varies at scales larger and smaller than the Ground Instantaneous Field Of View (GIFOV) of the AVIRIS sensor.*

Color image available from: *www.LDEO.columbia.edu/~small/Urban.html*

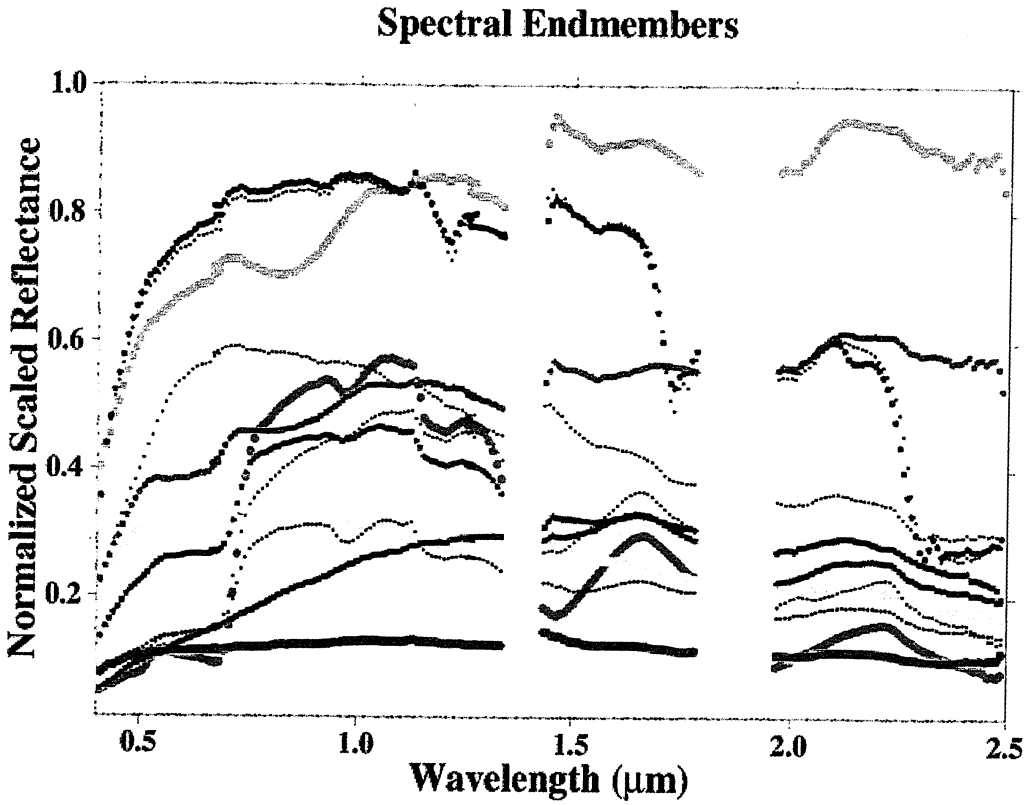

Figure 2. *Primary spectral endmembers for the AVIRIS reflectance image of Milpitas California. Spectra plotted with thicker curves and warmer colors are associated with the extrema of the low order dimensions of the mixing space. Thinner curves correspond to higher order dimensions. Each endmember is an average of 10 to 100 individual spectra residing at the apexes of the mixing space. The primary endmembers (high albedo, low albedo, soil and vegetation) span the mixing space of the three low order dimensions and describe 97.5% of the variance in a variance maximizing principal component rotation of the image. These endmembers are analogous to those found in spectral mixture analyses of other urban areas investigated with Landsat and Ikonos imagery. AVIRIS resolves many more distinct endmembers because the high spectral resolution discriminates subtle differences such as those seen in the different vegetation endmembers above.*

Color image available from: *www.LDEO.columbia.edu/~small/Urban.html*

The relationship between spatial scale and spectral dimensionality was quantified by comparison of 40 subscenes within the study area. Nine adjacent 100x100 pixel subscenes covering the built up area were used for the first stage of the analysis. Each of these ~2x2 km areas contained a variety of landcover types. Within these nine subscenes, ten 30x30 pixel subscenes were chosen in areas of undeveloped hillslopes, suburban residential and urban industrial development. An additional twenty 15x15 pixel subscenes allowed each of these landcover types to be further isolated in smaller areas.

Spatial averaging attenuates both noise and information to varying degrees while spectral resampling should preferentially attenuate the information content of the signal. The effects of spatial averaging and spectral resampling were tested in a 200x170 pixel subscene containing a combination of industrial and residential landcovers. Spatial averaging was done with a series of gaussian kernels ranging from 5x5 to 45x45 pixels. Spectral resampling was done using every Nth band of the original AVIRIS radiance dataset for N ranging from 2 to 16.

Results

Spectral endmembers bounding the mixing space of the lower order MNF dimensions are analogous to the endmembers found in analyses of other urban areas. Figure 2 shows 12 endmembers bounding the six primary dimensions of the mixing space. The endmember spectra bounding the lowest three dimensions correspond to vegetation, soil, high albedo roofing material and low albedo pavement. The endmembers spanning the low order dimensions are almost identical to those derived from a standard principal component analysis, indicating that a simple four component mixing model accounts for the vast majority of variance (97.5%) in the radiance field. The endmembers associated with the higher order dimensions are certainly significant but would not be resolved by broadband sensors.

The analysis of the 40 subscenes indicates a correspondence between area and dimensionality. When plotted in log-linear space, the eigenvalue distributions in Figure 3 all have a similar shape with a sharp break in slope separating the primary dimensions associated with higher, but rapidly diminishing, spatial autocorrelation from a long tail of gradually diminishing signal to noise levels. The break in slope corresponds to a transition from spatially coherent to spatially incoherent eigenimages. Figure 4 shows an example of this transition for a spectrally diverse subscene containing a variety of landcovers at different spatial scales. The transition from spatially coherent to spatially incoherent eigenimages occurs between dimension 31 and 35 but there are still isolated coherent features visible in these higher dimension eigenimages. These isolated features have distinct spectra and therefore represent useful information about the smaller features in the image.

The number of MNF eigenvalues larger than unity is often used as an indication of the inherent dimensionality of a hyperspectral image (e.g. *Boardman and Green, 2000, Green and Boardman, 2000, RSI, 2000*). Numerically, the eigenvalues larger than unity are associated with dimensions having variance greater than that of the noise estimate. In Figure 3, the eigenvalue distributions cluster in accordance with the size of the subimage. If the unity threshold is adopted, the results imply that the full image contains almost 200 spectral dimensions and that the 100x100 pixel subimages are also of comparable dimensionality. The apparent dimensionality drops somewhat for the 30x30 pixel subimages and more appreciably for the 15x15 pixel subimages. As pointed out by *Boardman and Green (2000)*, eigenvalue distributions are, however, merely a statistical proxy for dimensionality. In this study, the higher dimensions associated with the tail of the eigenvalue distribution do generally contain some small, spatially coherent features in the associated eigenimages that may correspond to distinct spectral features.

A more conservative criterion of spectral dimensionality would be the break in slope distinguishing the low order eigenvalues with coherent eigenimages associated with greater spatial coherence. This criterion also indicates a similar scale dependence in dimensionality. The full image and the 100x100 pixel subimages have transitions between 25 and 30 while the 30x30 pixel subimages have a transitions between 20 and 25. The 15x15 pixel subimages are small enough to contain more spectrally homogeneous areas and show a wide range of transitions between 10 and 25 dimensions. Using this "breakpoint" criterion, the hillslope subimages have the lowest dimensionality, and the suburban residential subimages have the highest dimensionality.

Spatial filtering of a high dimensional subscene results in both suppression of noise and dilution of spectral dimensionality. Figure 5 shows the eigenvalue distribution (labelled Raw) corresponding to the eigenimages shown in Figure 4. The raw image was smoothed with a succession of gaussian lowpass filters to investigate the effect of variance attenuation on the apparent dimensionality. The same unfiltered noise source was used for each MNF rotation. The effects of increased smoothing are 1) a successive reduction of variance (relative to the noise source) and 2) a shift in the breakpoint between the rapidly diminishing low-order eigenvalues and the gradually diminishing tail of higher order eigenvalues. The successive reduction in the number of eigenvalues greater than unity is a direct consequence of the

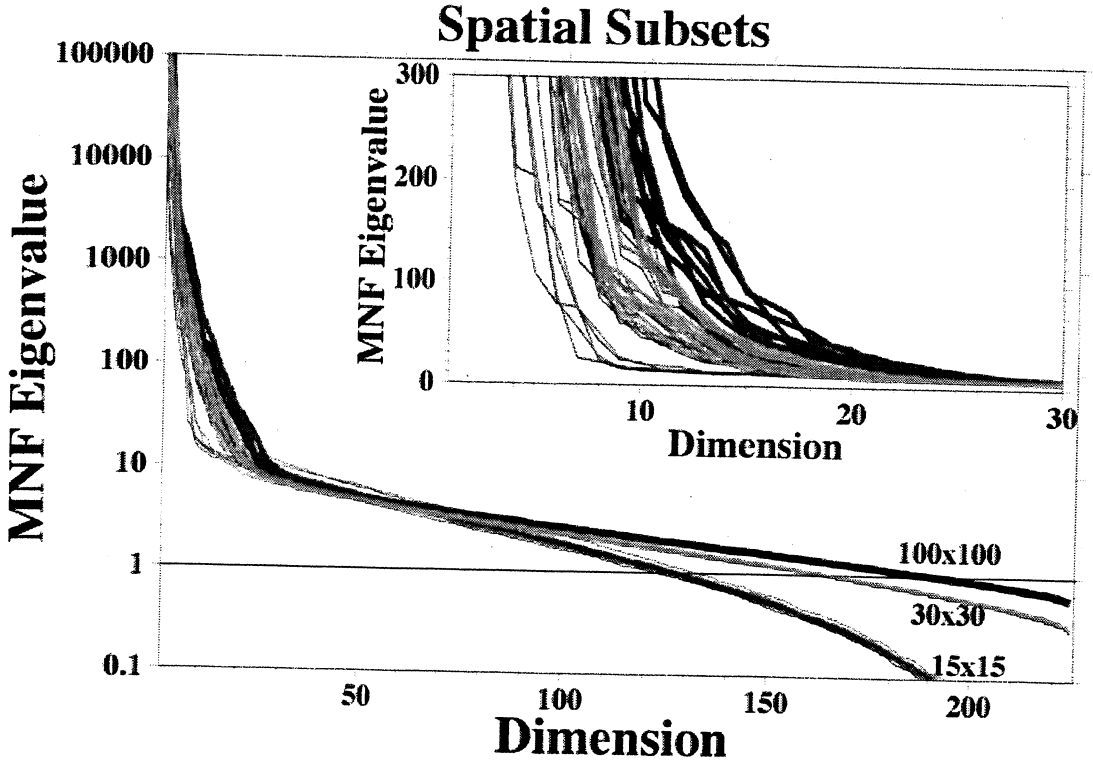

Figure 3. *Scale dependence of spectral dimensionality. The Minimum Noise Fraction (MNF) eigenvalue distributions correspond to spatial subsets of the AVIRIS image shown in Figure 1. The eigenvalues are scaled in sigma noise units so those smaller than unity are associated with noise-dominated eigenimages. The eigenvalues larger than unity are associated with dimensions with variance greater than the amplitude of the noise estimate. The break in slope near eigenvalues of 10 corresponds to a transition from spatially coherent to spatially incoherent eigenimages as shown in Figure 4. The thick black curve shows the distribution for the entire image shown in Figure 1. Increasingly thinner curves correspond to subimages 100, 30 and 15 pixels on a side. Spectral dimensionality diminishes with size of the subimage but there is significant variation in the dimensionality of subimages of the same size. The undeveloped areas in the upper left of Figure 1 have the lowest dimensionality while the developed areas in the lower right tend to have the highest dimensionality - at the range of scales considered here.*

Color image available from: *www.LDEO.columbia.edu/~small/Urban.htm*

reduction of variance (relative to the noise source) resulting from the smoothing operator. For the 5x5 and 11x11 gaussian filters, the rightward shift of the breakpoint in the eigenvalue distributions is accompanied by a corresponding increase in the number of spatially coherent eigenimages. For the 23x23 and 45x45 filters the breakpoint shifts back to lower dimensions and becomes less pronounced. Spatial smoothing attenuates variance at higher wavenumbers shifting the transition between the larger, more spatially coherent spectral features with higher variance and the succession of less spatially coherent features with lower variance. To the extent that some of this attenuated variance is noise, this is analogous to an increase in signal-to-noise ratio. Some of the attenuated variance would, however, be expected to correspond with actual spectral variability at the ~20m pixel scale. The larger filters may also be attenuating actual spectral endmembers and thereby reducing the dimensionality of the dataset and causing the breakpoint in the eigenvalue distribution to shift back to lower dimensions.

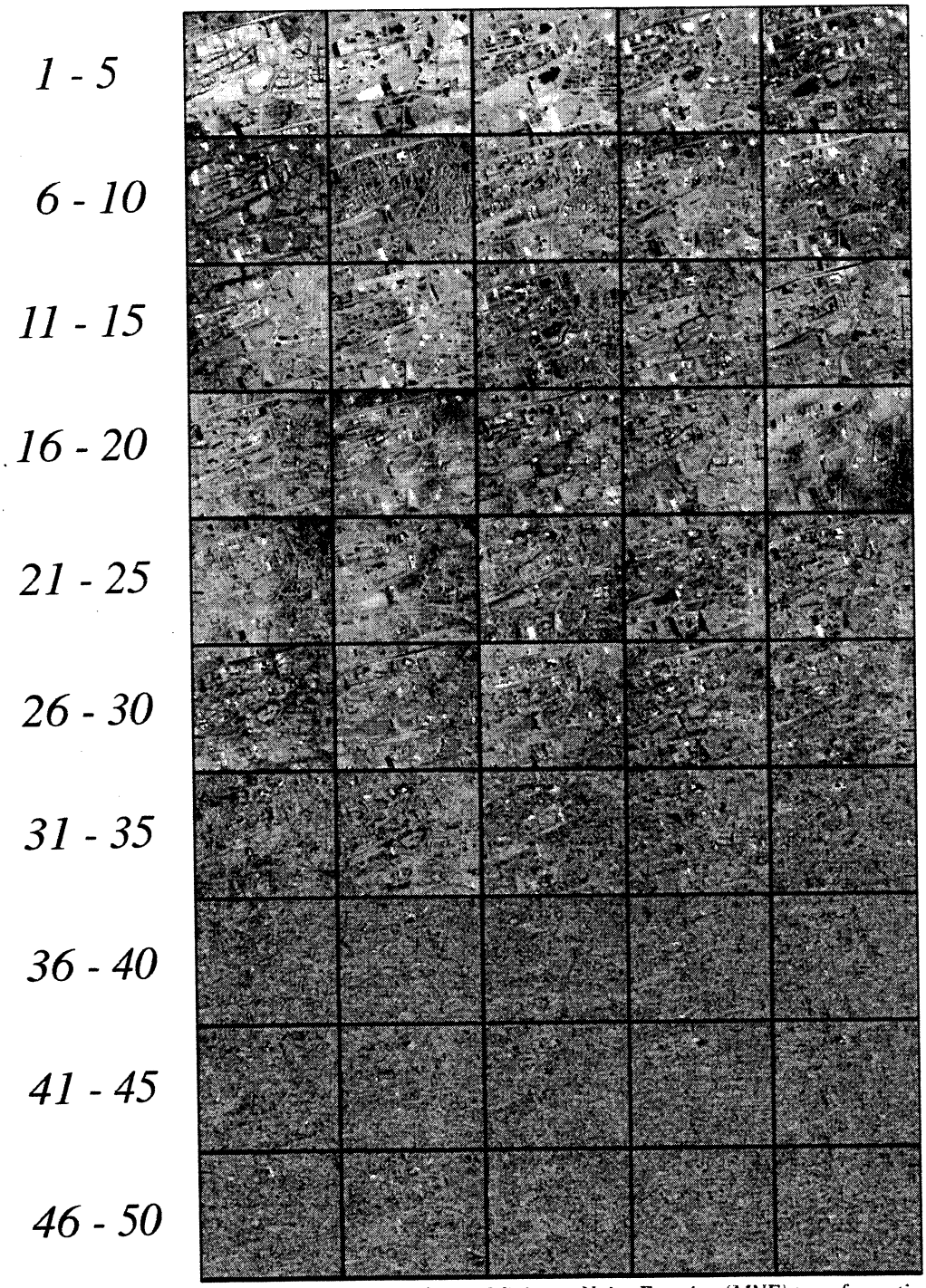

Figure 4. *Principal component images from a Minimum Noise Fraction (MNF) transformation of a subset of the AVIRIS image shown in Figure 1. The subset, from the lower right corner of Figure 1, contains residential, industrial and undeveloped areas. The transition from spatially coherent to spatially incoherent images occurs between 31 and 35 - consistent with the eigenvalues in Figure 3.*

Higher resolution image available from: *www.LDEO.columbia.edu/~small/Urban.htm*

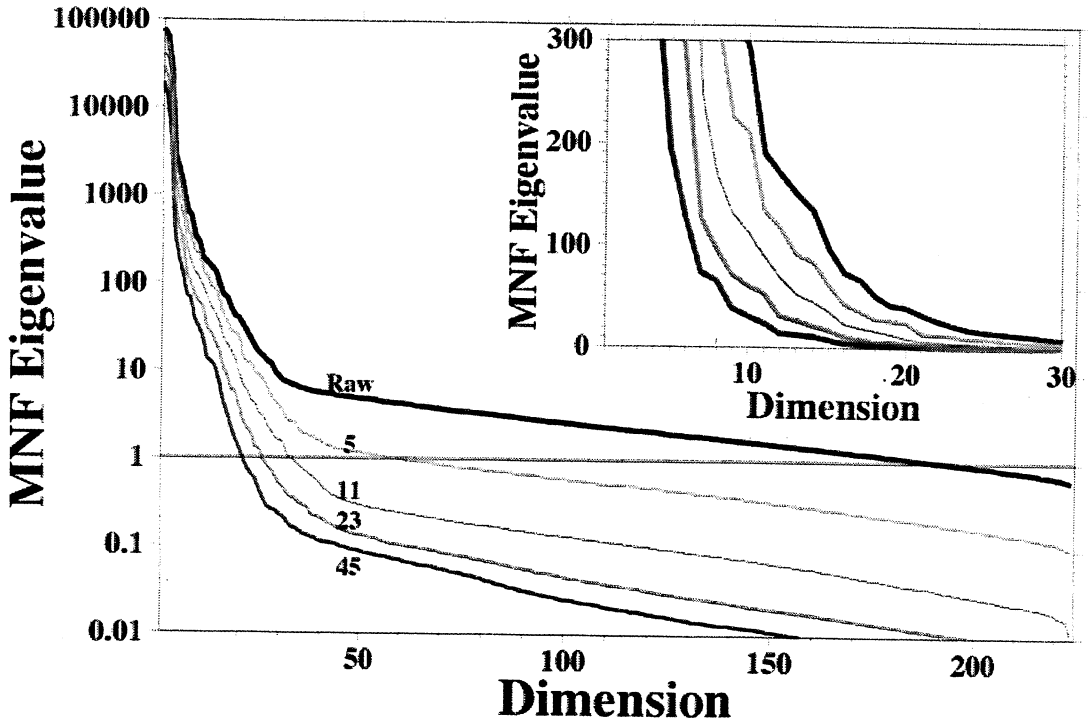

Figure 5. *Suppression of noise and dilution of spectral dimensionality. Spatial averaging with successively larger gaussian kernels simultaneously reduces both noise and information content at pixel scales. The 5x5 and 11x11 kernels increase the number of spatially coherent eigenimages and shift the breakpoint in the eigenvalue distribution to higher dimensions but the 23x23 and 45x45 kernels begin to attenuate some spectral endmembers and shift the breakpoint back to lower dimensions. Successively larger kernels attenuate increasing variance at high wavenumbers relative to the covariance of the noise estimate on which the MNF transformation is based.*

Color image available from: *www.LDEO.columbia.edu/~small/Urban.htm*

Spectral resampling results in appreciable loss of spectral dimensionality. The maximum dimensionality of the image is constrained by the number of spectral bands it contains. As would be expected, reducing the number of bands results in a direct loss of dimensionality without changing the signal-to-noise ratio in the remaining bands. Figure 6 indicates that subsampling by a factor of two significantly reduces the number of dimensions with variance greater than the noise estimate but does not change the breakpoint between the spatially coherent and spatially incoherent eigenimages. Subsampling the specra by a factor of four further reduces the spatially incoherent dimensions but also causes the breakpoint in the eigenvalue distribution to shift to a lower dimension. Resampling the spectra by factors of 8 and 16 has a pronounced effect on the dimensionality of the image - effectively eliminating some of the spectral dimensions and all but one or two spatially incoherent eigenimages. This reduces the number of spectral endmembers that can be represented uniquely. The loss of dimensionality occurs because many of the higher order spectral endmembers are characterized by subtle features that cannot be distinguished from one another without the fine spectral resolution provided by AVIRIS narrow spectral bandwidths.

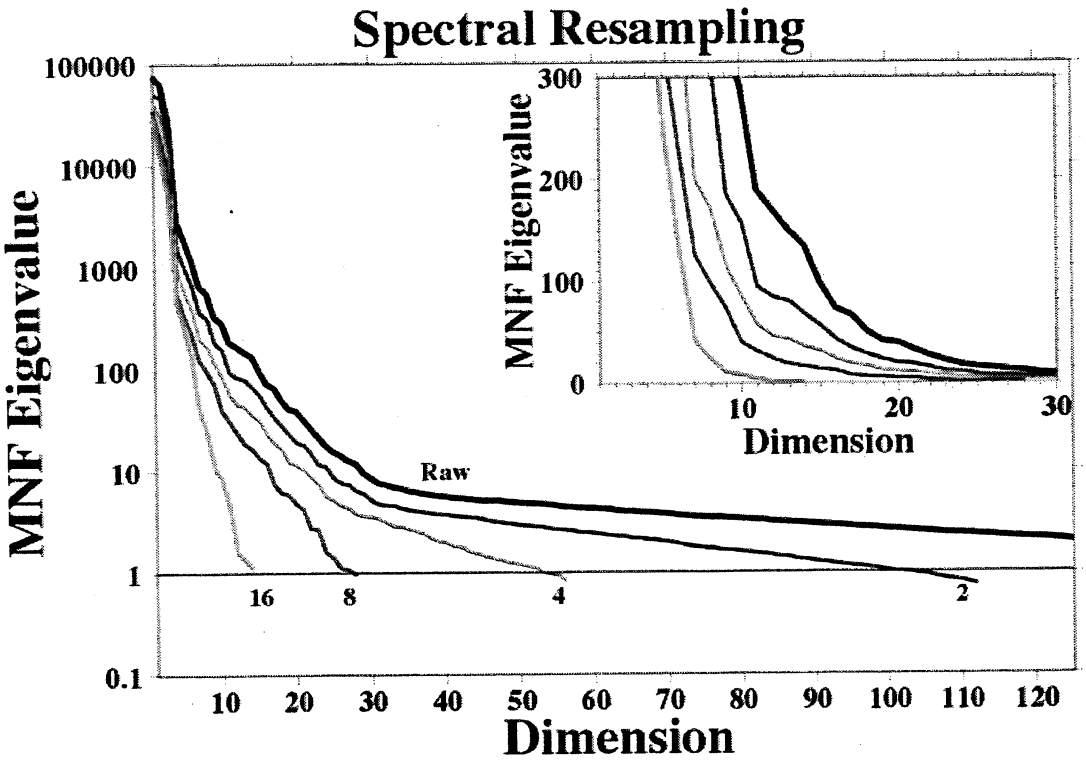

Figure 6. *Spectral resampling and loss of dimensionality. Resampling AVIRIS spectra by factors of 1/n for n= 2, 4, 8, and 16 rapidly reduces spectral dimensionality. Resampling by a factor of 1/4 results in some loss of significant dimensions as indicated by the leftward shift of the breakpoint in the eigenvalue distribution. Resampling by factors of 1/8 and 1/16 results in greater losses of spectral endmember resolution with spatially coherent eigenimages for all but the highest one or two dimensions.*

Color image available from: www.LDEO.columbia.edu/~small/Urban.html

Implications

The eigenvalue distributions have a consistent form for all of the subimages. They are all characterized by rapidly diminishing amplitude in the low order dimensions and a longer tail of gradually diminishing amplitude in the higher dimensions. When plotted in log-linear space, a distinct break in slope separates the two parts of the eigenvalue distribution. This transition between distinct log-linear eigenvalue distributions is analogous to that commonly observed in physical processes characterized by scaling relationships in the presence of noise processes. In this case, the low order eigenvalues are associated with spatially coherent eigenimages and the high order eigenvalues are associated with spatially incoherent eigenimages. Within the Milpitas study area, the spatially coherent eigenimages span approximately 30 spectral dimensions. The spectral endmembers associated with the extrema of the low order dimensions represent soil, vegetation, and a variety of high and low albedo anthropogenic endmembers. Despite the high spectral dimensionality of the urban mosaic, the low order dimensions with the highest spatial autocorrelations are associated with the hyperspectral equivalents of the spectral

endmembers that characterize broadband imagery of Milpitas and many other urban environments observed with Landsat and Ikonos imagery.

Variance at pixel scale represents a combination of noise and signal. The characteristic scale of urban reflectance is generally between 10 and 30 meters (*Small, 2001b*) so many of the 20-m AVIRIS pixels in the study area are likely to be spectral mixtures of at least two endmembers. This results in appreciable spectral variability at pixel scales and contributes to the higher order principal components whose eigenimages are not spatially coherent. Successive smoothing of the image suggests that apparent dimensionality increases somewhat as noise related variance is attenuated. More severe smoothing reduces apparent dimensionality as isolated spectral endmembers are attenuated. The first rotation applied by the MNF is based on the assumption that signal is strongly correlated among adjacent pixels and that noise is spatially uncorrelated at pixel scales. In urban environments where significant variations in reflectance occur at pixel scales, much of the pixel scale variance is not noise. Pre-rotation to diagonalize the noise covariance matrix therefore accommodates the spatially uncorrelated variance associated with the noise estimate but does not account for actual spectral variability at pixel scales. By ordering the resulting eigenimages by decreasing spatial autocorrelation, the MNF rotation emphasizes the spectral endmembers occurring at larger spatial scales and relegates the isolated and mixed spectra to the higher order dimensions. The scaling of eigenvalues in sigma noise units is convenient because it provides a benchmark for the amplitude of the instrument noise relative to pixel scale variance in the radiance field.

The apparent reduction in dimensionality with spatial scale is a consequence of the characteristic scales of the urban mosaic. The larger subimages generally contain a greater diversity of spectral endmembers and thus have higher dimensionality. The smaller subimages have higher dimensionality in residential suburbs and transitional areas and lower dimensionality in more spectrally homogeneous areas. In spite of the high spectral dimensionality of the urban mosaic, the majority of variance (97.5%) can be described with a four-endmember mixing model spanning the three low order dimensions of the mixing space. The consistency of endmembers suggests that the low dimensional projections of the mixing space resolved by broadband sensors does represent the true dominant endmembers even if they cannot represent the true spectral diversity of the urban mosaic. The scale analysis indicates that relatively high dimensionality is retained at least down to scales of 300 meters for high altitude AVIRIS in this area. Higher spatial resolution AVIRIS imagery may reveal higher spectral dimensionality at the same scales however. This method could also be used to quantify the spectral scaling properties of other environments. For instance, spatial scaling of reflectance spectral in forest canopies may provide insights into species diversity and forest succession dynamics.

Acknowledgments This work was funded, in part, by the Environmental Protection Agency - STAR program and the Columbia Earth Institute in association with the NASA SocioEconomic Data and Applications Center (SEDAC). The support of the Palisades Geophysical Institute and the Doherty Foundation is also gratefully acknowledged. Many thanks to Dave Hulslander for insights regarding ENVI's MNF algorithm.

References

Adams, J. B., M. O. Smith, and P. E. Johnson, Spectral mixture modeling; A new analysis of rock and soil types at the Viking Lander 1 site, *J. Geophys. Res.*, *91*, 8098-8122, 1986.

Adams, J. B., M. O. Smith, and A. R. Gillespie, Imaging Spectroscopy: Interpretation based on spectral mixture analysis. in Remote Geochemical Analysis: Elemental and Mineralogical Composition, edited by C.M. Pieters and P. Englert, 145-166, Cambridge University Press, New York, 1993.

Boardman, J. W. (1993). Automating spectral unmixing of AVIRIS data using convex geometry concepts. Fourth Airborne Visible/Infrared Imaging Spectrometer (AVIRIS) Airborne Geoscience Workshop, Jet Propulsion Laboratory, Pasadena, CA, p.11-14.

Boardman, J.W. and R.O. Green, Exploring the spectral variability of the earth as measured by AVIRIS in 1999, *Proceedings of the Ninth JPL Airborne Earth Science Workshop*, edited by R.O. Green,, Jet Propulsion Laboratory, Pasadena, CA, 195-206, 2000.

Boardman, J. W. and F. A. Kruse (1994). Automated spectral analysis: a geologic example using AVIRIS data, north Grapevine mountains, Nevada. Tenth Thematic Conference on Geologic Remote Sensing, Ann Arbor, MI, Environmental Research Institute of Michigan.

Gillespie, A. R., M. O. Smith, J. B. Adams, S. C. Willis, A. F. Fischer, and D. E. Sabol, Interpretation of residual images: spectral mixture analysis of AVIRIS images, Owens Valley, California, Proceedings of the 2nd Airborne Visible/Infrared Imaging Spectrometer (AVIRIS) Workshop, Pasadena, CA, 243-270, 1990.

Green, A. A., M. Berman, P. Switzer, and M. D. Craig, A transformation for ordering mutispecral data in terms of image quality with implications for noise removal, *I.E.E.E. Transactions on Geoscience and Remote Sensing*, *26*, 1, 65-74, 1988.

Green, R. O., and J. W. Boardman, Exploration of the relationship between information content and signal/noise ratio and spatial resolution in AVIRIS spectral data, *Proceedings of the Ninth JPL Airborne Earth Science Workshop*, edited by R.O. Green, Jet Propulsion Laboratory, Pasadena, CA, 195-206, 2000.

Landsberg, H. E., The Urban Climate. New York, Academic Press, 1981.

Research Systems Incorporated, ENVI 3.4 User's Guide, Boulder, CO, 930pp. 2000.

Small, C., Estimation of Urban Vegetation Abundance by Spectral Mixture Analysis, *International Journal of Remote Sensing*, *22*, 7, 1305-1334, 2001a.

Small, C., Multiresolution analysis of urban reflectance, *IEEE/ISPRS Conference on Remote Sensing of Urban Areas*, Rome, Italy, 2001b.

Smith, M. O., S. L. Ustin, J. B. Adams, and A. R. Gillespie, Vegetation in deserts: I. A regional measure of abundance from multispectral images, *Remote Sensing of Environment*, *31*, 1-26, 1990.

United, Nations, Prospects for Urbanization - 1999 Revision. United Nations, (ST/ESA/SER.A/166), Sales No. E.97.XIII.3, 1999.

LOW-ALTITUDE AVIRIS DATA FOR MAPPING LAND COVER IN YELLOWSTONE NATIONAL PARK: USE OF ISODATA CLUSTERING TECHNIQUES

Joseph P. Spruce*

1. INTRODUCTION

Northeast Yellowstone National Park (YNP) has a diversity of forest, range, and wetland cover types. Several remote sensing studies have recently been done in this area, including the NASA Earth Observations Commercial Applications Program (EOCAP) hyperspectral project conducted by Yellowstone Ecosystems Studies (YES) on the use of hyperspectral imaging for assessing riparian and in-stream habitats. In 1999, YES and NASA's Commercial Remote Sensing Program Office began collaborative study of this area, assessing the potential of synergistic use of hyperspectral, synthetic aperture radar (SAR), and multiband thermal data for mapping forest, range, and wetland land cover. Since the beginning, a quality "reference" land cover map has been desired as a tool for developing and validating other land cover maps produced during the project. This paper recounts an effort to produce such a reference land cover map using low-altitude AVIRIS data and unsupervised classification techniques.

The main objective of this study is to assess ISODATA classification for mapping land cover in Northeast YNP using select bands of low-altitude AVIRIS data. A secondary, more long-term objective is to assess the potential for improving ISODATA-based classification of land cover through use of principal components analysis and minimum noise fraction (MNF) techniques. This paper will primarily report on work regarding the primary research objective.

This study focuses on an AVIRIS cube acquired on July 23, 1999, by the confluence of Soda Butte Creek with the Lamar River (Figure 1). Range and wetland habitats dominate the image with forested habitats being a comparatively minor component of the scene. The scene generally tracks from southwest to northeast. Most of the scene is valley bottom with some lower side slopes occurring on the western portion. Elevations within the AVIRIS scene range from approximately 1998 to 2165 meters above sea level, based on U.S. Geological Survey (USGS) 30-meter digital elevation model (DEM) data. Despain (1991) and the National Park Service (NPS) (2000) provide additional description of the study area.

2. RESEARCH RATIONALE

Although undersampled in the along-track direction, the 1999 low-altitude AVIRIS data was employed for this study because of its well-known overall high spectral quality, its ability to be georeferenced, and its sufficiently large areal extent. The unsupervised classification approach was selected over the supervised method because of the great diversity and complexity of land cover types within the study area. During this project, several YES research collaborators assessed various supervised classification methods for mapping targeted cover types in the area. These studies produced impressive maps of specific riparian and in-stream habitats (Crabtree et al., in press) but apparently did not yield wall-to-wall land cover maps. The latter can be constructed with the ISODATA unsupervised classification routine now resident in most commercial-off-the-shelf software packages. In essence, the acronym ISODATA means the Iterative Self-Organizing Data Analysis Technique Algorithm. It is often used for processing multispectral image data into effective land cover maps. ISODATA has worked well for mapping land cover from broad-band multispectral data sets, which tend to include 3 to 15 bands and spectral coverage in the visible, near infrared (NIR), and short-wave infrared (SWIR) regions. Therefore, ISODATA should also be effective for classifying land cover from narrow-band hyperspectral imagery with 15 bands or less in comparable regions of the electromagnetic spectrum.

* Lockheed Martin Space Operations – Stennis Programs, John C. Stennis Space Center (Joseph.Spruce@ssc.nasa.gov)

A literature review revealed a lack of publications discussing the effect of total number of input hyperspectral bands on ISODATA classification success. Sensor, application, and scene characteristics can individually or collectively affect the optimum number of bands needed for ISODATA classification success. The review did show some studies that successfully employed AVIRIS band subsets for effective land cover classification. For example, Martin et al. (1998) reported that 11 bands of AVIRIS data were effective for supervised classification of forest cover types within the Harvard Experimental Forest. Fuentes et al. (2000) produced boreal forest habitat maps that showed improvement over Landsat-based mapping. Fuentes used a subset of AVIRIS bands, data stacks of band ratios, and other indices, plus maximum likelihood supervised classification.

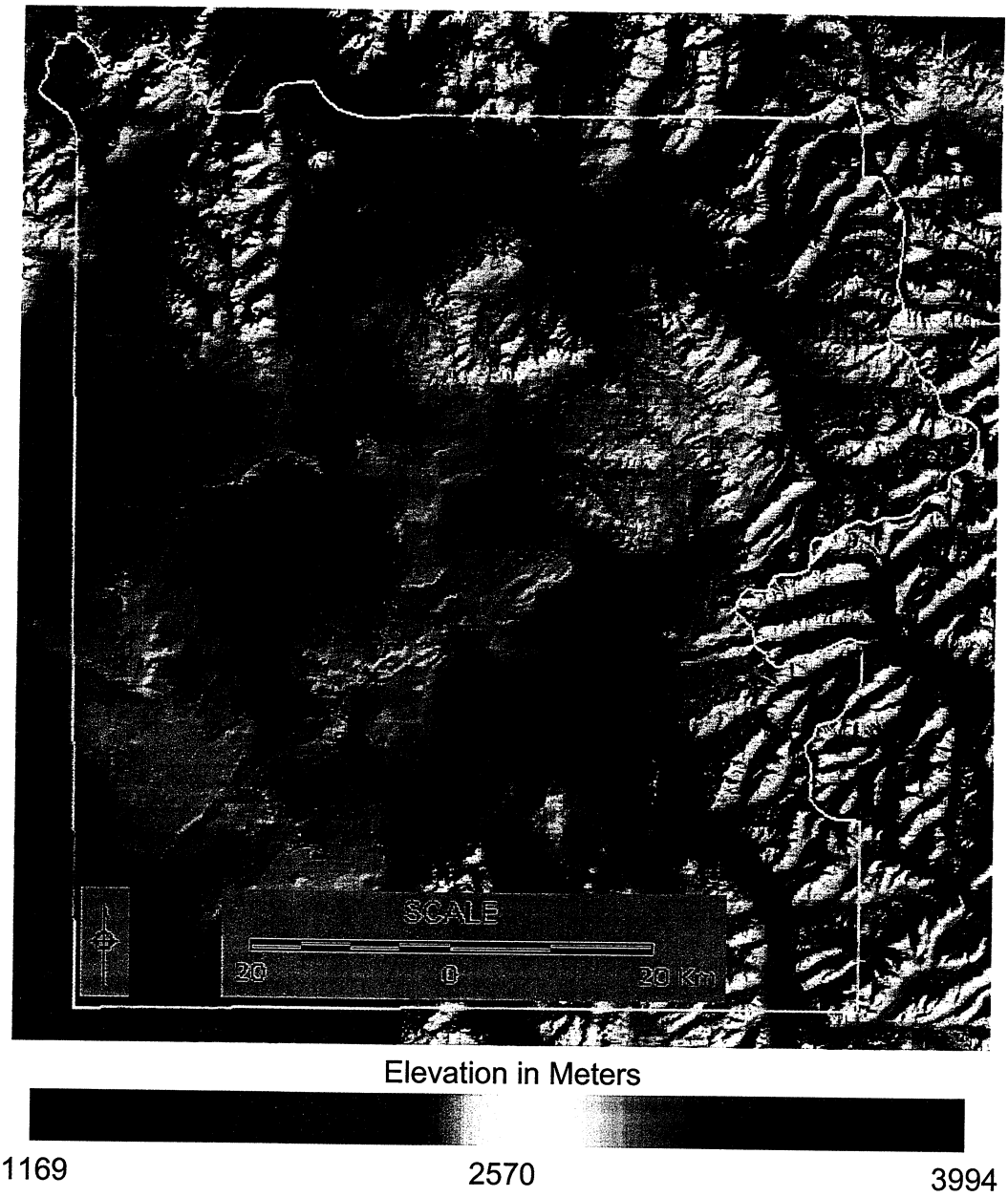

Figure 1. Location of study area within Yellowstone National Park. The graphic shows a hillshaded 90-meter DEM from the USGS with the AVIRIS scene boundary outlined in red.

The number of bands clearly affects the amount of time needed to perform ISODATA classifications. Based on first-hand experience, the amount of time needed to run an ISODATA classification on a whole AVIRIS

cube is substantially greater than for the time needed to classify 10-15 bands. An initial classification of the entire low-altitude AVIRIS cube used in the Yellowstone study took about 20 times longer to compute than did classification of the same image with only 11 subset bands (7 hours as opposed to 20 minutes). The input data volume for the 11-band data set contains 78 megabytes, while the full AVIRIS cube includes 1600 megabytes. These classifications employed an SGI Onyx2 workstation with four CPU's and five Gigabytes of RAM.

One clear advantage of ISODATA is that it can be used in a supervised manner to generate spectral signatures, which can later be subject to a supervised classifier, such as the maximum likelihood routine. In addition, ISODATA can be used in the classification refinement process known as cluster busting to effectively reclassify "confused" cluster classes (Jensen, 1996). Such reclassification runs using all of the AVIRIS bands would be extremely time consuming and would generate excessively large volumes of intermediate raw data files. It would be quite advantageous if an accurate, detailed land cover classification could be computed with ISODATA clustering on a relatively modest subset of representative bands.

3. DATA ACQUISITION

The related NASA EOCAP hyperspectral project with YES enabled acquisition of and access to a wealth of remote sensing data, much of which was also acquired in 1999 (Table 1). These data sets included Probe-1 hyperspectral data at various resolutions, ATLAS multispectral data with multiple thermal bands, very high resolution color infrared (CIR) aerial photography scanned at 0.5 meters, plus synthetic aperture radar imagery collected by the AIRSAR and STAR-3*i* sensors. In addition, the study also employed several geographic information system (GIS) compatible field surveys and thematic maps generated by the USGS, the NPS, and others (Table 2).

Table 1. Remote sensing data available for study.

AVIRIS Hyperspectral data	7/23/99	1.6 by 4.8m
ATLAS Multispectral/Thermal data	8/17/99	2.5m
Zeiss CIR Aerial Photo data	8/17/99	scanned at 0.5m
Positive Systems Multispectral data	early 10/99	0.5m
USGS DOQQ data	mid 1990s	1m
Probe-1 Hyperspectral data	summer 1999	1 to 8m
STAR-3*i* X-Band SAR data	fall 1999	2.5m
AIRSAR data	5/28/99	10m
Landsat ETM+ data	7/13/99	30m

Table 2. Field reference data.

Analytical Spectral Devices spectra	point	NASA/YES
Field checks and photos	point	NASA/YES
40x40m vegetation plots	polygon	YES
DEM data - 10 to 30m	raster	USGS, EarthWatch
Digital line graph data	polygon	USGS
Digital raster graphic data – multiple scales	raster	USGS
National wetlands inventory	polygon	U.S. Fish and Wildlife Service National Wetlands Inventory
Habitat map	raster	NPS
Vegetation map	raster	NPS
Fire intensity - 1988 wildfire	raster	NPS

4. METHODS

ATREM and EFFORT software were used to compute ground reflectance from the AVIRIS data. Afterwards, an additive offset was applied to eliminate negative reflectance values in waters and shadows. The AVIRIS data was later georeferenced with software developed by Analytical Imaging Geophysics and subsequently co-registered to USGS digital orthophoto quarter quadrangles (DOQQ's) using 80 ground control points and a second-order polynomial transformation. Output imagery contained an across-track resolution of 1.6 meters, an along-track resolution of 4.8 meters, and an overall root mean square error fit of 2.70. This unusual resolution is due to along-track undersampling (i.e., skip) from the plane's not flying high enough to permit sampling at the same resolution as in the cross track. Future collects should not have this problem as the AVIRIS data can now be collected at sufficiently high altitudes to avoid along-track skip.

Prior to classification, the author conducted a literature review to identify spectral bands or regions important for classification of vegetation, soil, and water conditions. Relevant publications include Ahern (1988), Guyot et al. (1992), Penuelas et al. (1994), Clark et al. (1995), Goetz and Boardman (1995), Carter et al. (1998), Kokaly et al. (1998), Martin et al. (1998), Sampson et al. (2001), Adams et al. (1999), Zarco-Tejada et al. (1999), Fuentes et al. (2000), Jensen (2000), Mohammed et al. (2000), and Thenkabail et al. (2000). This review led to the selection of 11 bands for classification, including six bands in the visible, three bands in the NIR, one in the "Landsat" short wave infrared-1 (SWIR-1), and one in the "Landsat" SWIR-2 region (Table 3). Selection included representative bands indicative of healthy, stressed, and dead vegetation. Bands sensitive to vegetation health and biomass help to promote detection of several grassland types growing along a topographic moisture gradient. Selection also consisted of blue and green bands for aiding separation of forest types as well as for mapping water. In addition, selection included one SWIR-1 band for adding information on soil and vegetation moisture and one SWIR-2 band for enhancing detection of vegetation moisture, dead forest, woody debris, exposed soil, rock, mineral deposits, and alluvial surfaces. Band selection avoided bands with known significant atmospheric influence.

The 11 selected bands were subset from the path-oriented yet georeferenced output. Classification analyses required at least some initial georeferencing because the non-georeferenced data could not be effectively related to field surveys. In particular, classification products could not be most effectively assessed without visual comparison to the ground reference data. The use of the path-oriented raw data and the band reduction collectively also enabled significant reductions in data volume and expedited classification run times.

Table 3. Bands selected for ISODATA classification.

13	488.37	Blue	soil, water, and vegetation
17	527.67	Green	vegetation - chlorophyll reflectance – in left side slope
20	557.14	Green	vegetation - "green peak" for chlorophyll reflectance
23	586.61	Yellow	vegetation – reflectance of chlorotic foliage
27	625.90	Orange	vegetation – reflectance - early phase necrotic foliage
37	692.33	Red	vegetation – right side of red "chlorophyll absorption well"
42	740.03	Red/NIR	vegetation - band located in far red portion of "red edge"
51	825.93	NIR Plateau	vegetation condition, soil moisture, and water body detection
70	1012.21	NIR Plateau	vegetation condition, soil moisture, and water body detection
137	1654.04	SWIR-1	clouds, snow, soil moisture, and vegetation moisture
194	2211.8	SWIR-2	mineral, rock type, and vegetation moisture

Classifications were performed with ERDAS IMAGINE software as follows: ISODATA was used to generate an initial classification of 30 cluster classes using settings of 50 iterations, 99% convergence, means initialization along the first PC axis, automatic scaling, and sampling every pixel. The 30-class output was compared to assorted reference data (e.g., aerial photographs and field survey data) and then recoded into 9 broad classes.

For the most part, at least some visually apparent confusion occurred in each broad class of the regrouped initial classification. Consequently, cluster-busting techniques were applied to reduce misclassification. In doing so, masking was performed to isolate raw data for each broad class. These raw data sets were then reclassified with ISODATA clustering. The settings for these follow-up "runs" were identical to the initial classification, except with respect to the number of classes. For each raw data mask, the number of classes was set to twice the apparent number of distinct spectral tones evident on representative RGB color composite displays. This reclassification process worked well for most situations but did not usually separate targeted classes that were locally common yet regionally rare. To break out the latter, area of interest (AOI) polygons were screen delineated and later used to guide ISODATA clustering within AOI's. In paved highway, AOI's had to be defined around the category of interest as well as the category with which it was confused. Running ISODATA on both confused features enabled spectrally similar but distinct signatures to be identified. In the reclassification process, "keeper" cluster classes refer to those not needing cluster busting. Such classes contain minimal apparent confusion between spectrally similar land cover types.

Reclassification led to several secondary classifications being output as classification imagery and signature files. All of the "keeper" secondary classification signatures were appended into one master signature file. The master signature file and the original 11-channel subset were then subject to the maximum likelihood classifier to produce a classification image containing 147 cluster classes. The latter represented 33 specific land cover categories falling under 13 general classes: 1) wet herbaceous cover, 2) moist to seasonally wet herbaceous cover, 3) moderately moist grassland without and with sage, 4) dry sage habitats without and with dry grassland, 5) dry grassland without sage, 6) very dry grassland on exposed sites, 7) coniferous forest – alive and dead, 8) deciduous forest and shrubs, 9) woody debris, 10) bare rocks and coarse soil, 11) bare alluvial deposits, 12) water, and 13) shadowed non-forested areas.

The 147-class image was regrouped to 33 classes that were subsequently filtered using IMAGINE's ELIMINATE routine and a 9-pixel elimination threshold (Figure 2). Areal extent for each of 33 categories in the "final" classification was summarized (Table 4). The final classification was then evaluated qualitatively through comparison with large-scale CIR aerial photographs and field survey data. The latter includes field-annotated hardcopies of the aerial photography as well as Global Positioning System referenced field photographs. Time scheduling did not permit for results of a quantitative accuracy assessment to be presented at the workshop.

5. PRELIMINARY ANALYSIS OF FINAL CLASSIFICATION

This classification includes not only distinct land cover types but also variants (i.e., subclasses) in some cases. In doing so, the classification scheme includes ecological and/or spectral subclasses to aid qualitative and quantitative accuracy assessment, plus the editing of class descriptions.

Rangeland cover types dominate the scene, collectively composing about 67 % of the total mapped area. The final map clearly shows the main herbaceous plant and sage communities occurring along the topographic moisture gradient readily seen in the field. In general, the classification separates extremely dry grassland, dry grassland, moist grassland, moderately moist grassland, and moist to seasonally wet herb-dominated grassland as well as sage/grasslands growing in moderately moist to dry sites (Figure 2 and Figure 3).

Wetland habitats commonly occur in some parts of the scene. The classification identifies several types of herb-dominated wetlands, including sedge-dominated communities and mixed grass/forbs with Canada thistle, an exotic species. The latter is a land cover condition of interest to the NPS for its program to combat invasive plant species (NPS, 1999). The rush cover type is not mapped, probably because of the rareness of the cover type in the study area. It tends to occur as very small patches in close proximity to the waterlogged sedge sites. The sedge types represent multiple spectral conditions, apparently due to variations in site moisture. In effect, the sedges occur on wet to very wet sites with standing water apparent in the extreme cases. The classification does not map wetland forest (cottonwood) and shrub (willow) types as well as desired, in part due to the rarity and very small patch size of these features within the AVIRIS scene. The largest patch of willow observed in the study area is only 10 meters by 10 meters, which is much smaller than a 0.25-acre minimum-mapping unit. The time of year probably imposes a negative influence on the detection of willow communities. The willows tend to occur among sedges that are spectrally similar to willows on the AVIRIS scene. A scene acquired later in the year probably would have better

separation, based on the fact that these types are distinct on October multispectral data from Positive Systems' ADAR system. Undoubtedly, the undersampling of the AVIRIS data in the along-track direction also impeded the detection of these very fine-scaled features.

In general, this author found the non-forested wetland cover types to have impressive exploitable spectral variability, but they posed great difficulties in mapping because of the spectrally subtle tones of certain wetland types on the CIR aerial photographs and because of the fine-scaled nature of many wetland sites (Figure 3). Certain AVIRIS RGB displays show wetland types better than the CIR aerials do, although it was best to view both data types compared to ground reference data. While we had considerable in-situ data, the description and accuracy assessment of the wetland types would benefit greatly from additional field validation.

The AVIRIS classification also largely identifies live and dead softwood forest, plus dead woody debris. The last tends to be a fine-scaled feature occurring on alluvial surfaces, such as gravel and sandbars (Figure 3). Mapping woody debris is important to the NPS for enhanced understanding of the region's riparian ecology and for better park management (NPS, 1999). The attempt to map aspen yielded mixed success, again apparently because of very small patch size and rarity within the scene. The AVIRIS also readily identifies many non-vegetated surfaces, such as multiple alluvium types, surface water, pavement, and bare rock outcroppings. Pavement is mapped well, though doing so required considerable additional effort using subset AOI's in conjunction with masking and reclassification. The classification shows a very small amount of non-forested shadow. The shadowed forest largely pertained to softwood forest and subsequently recoded as such in the final classification.

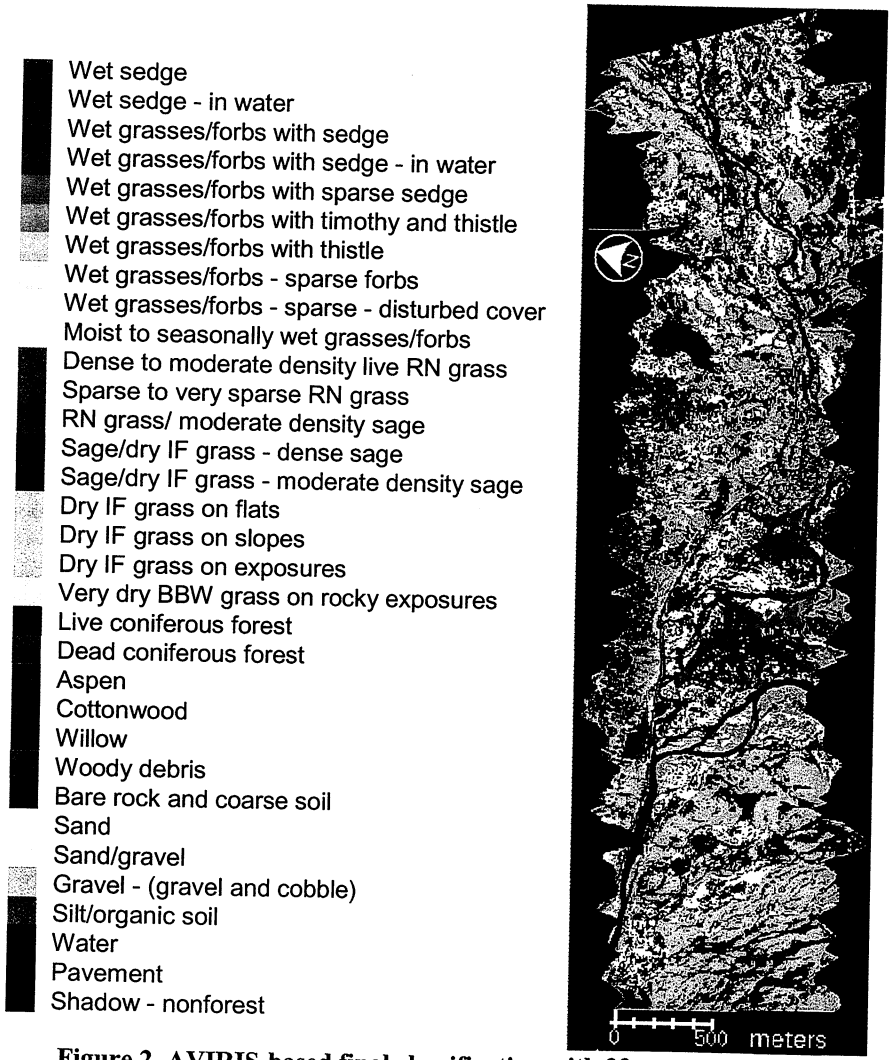

Figure 2. AVIRIS-based final classification with 33 map categories.

Table 4. Summary area for map categories in final classification.

1	Wet sedge	13.62	2.69
2	Wet sedge - in water	7.19	1.42
3	Wet grasses/forbs with sedge	17.53	3.47
4	Wet grasses/forbs with sedge - in water	7.76	1.53
5	Wet grasses/forbs with sparse sedge	14.17	2.80
6	Wet grasses/forbs with timothy and thistle	3.14	0.62
7	Wet grasses/forbs with thistle	0.72	0.14
8	Wet grasses/forbs - sparse forbs	4.69	0.93
9	Wet grasses/forbs - sparse - disturbed cover	20.22	4.00
10	Moist to seasonally wet grasses/forbs	60.52	11.96
11	Dense to mod. dense live RN grass[1]	36.17	7.15
12	Sparse to very sparse RN grass	46.56	9.20
13	RN grass/moderate density sage	14.45	2.86
14	Sage/dry IF grass - dense sage[2]	18.43	3.64
15	Sage/dry IF grass - moderate density sage	39.47	7.80
16	Dry IF grass on flats	52.84	10.45
17	Dry IF grass on slopes	53.05	10.49
18	Dry IF grass on exposures	12.93	2.56
19	Very dry BBW grass on rocky exposures[3]	3.91	0.77
20	Live coniferous forest	14.40	2.85
21	Dead coniferous forest	1.98	0.39
22	Aspen	0.33	0.06
23	Cottonwood	0.14	0.03
24	Willow	0.05	0.01
25	Woody debris	1.15	0.23
26	Bare rock and coarse soil	4.83	0.95
27	Sand	0.62	0.12
28	Sand/gravel	2.54	0.50
29	Gravel - (gravel and cobble)	17.39	3.44
30	Silt/organic soil	6.24	1.23
31	Water	23.01	4.55
32	Pavement	3.40	0.67
33	Shadow – nonforest	2.38	0.47
N/A	Grand Total	505.82	100.00

[1]RN denotes grassland community with Richardson's needlegrass
[2]IF denotes grassland community with Idaho fescue grass
[3]BBW denotes grassland community with bluebunch wheatgrass

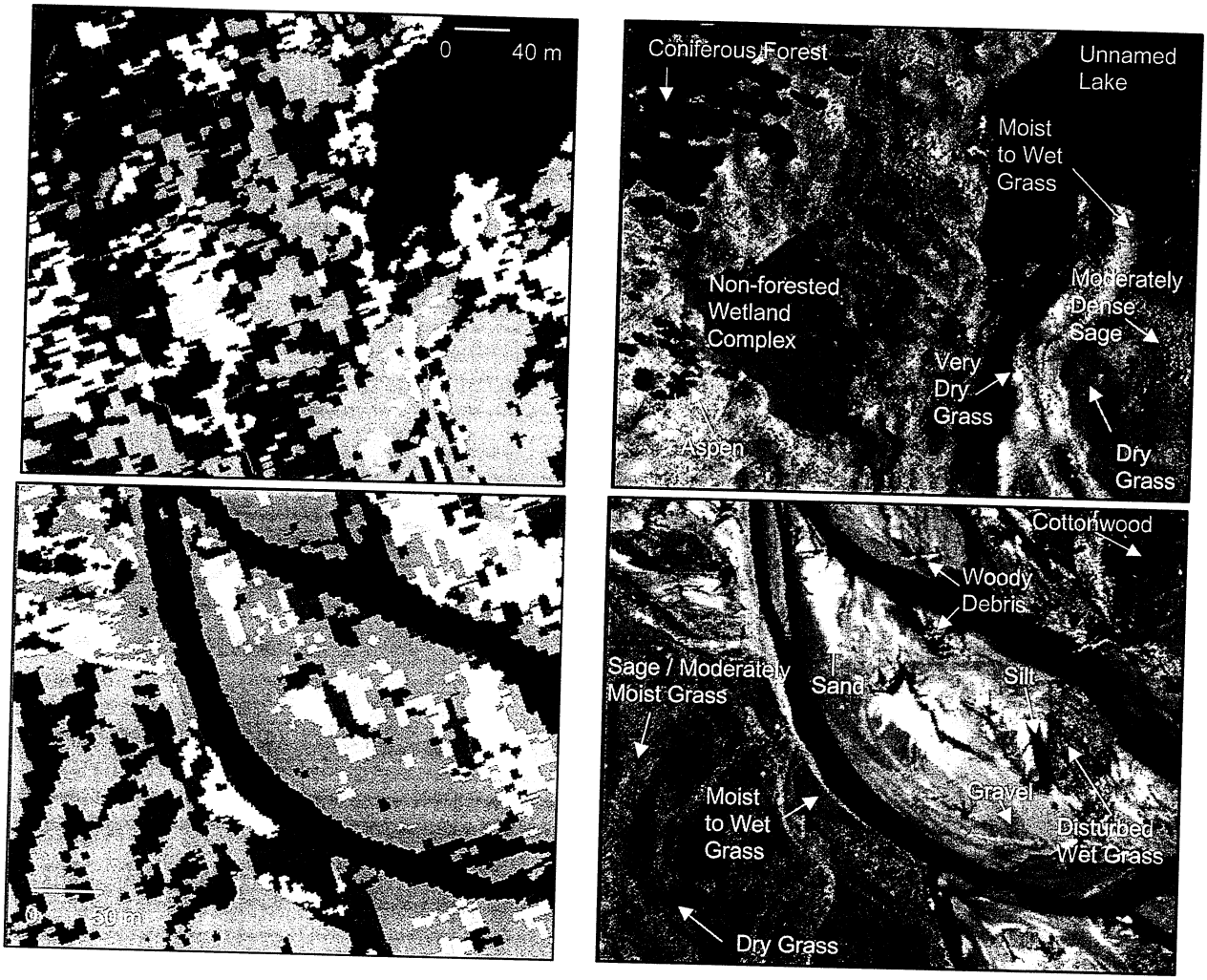

Figure 3. Visual comparison of final classification to scanned 1:8,000 color infrared aerial photographs.

6. CONCLUDING REMARKS

The results of this study provide insight into the apparent feasibility of using an 11-band subset of AVIRIS data and ISODATA techniques for classification of forest, range, and wetland habitats. The author observed consistent classification success for the most common cover types based on qualitative comparison to ground reference data. Classification success also occurred for some scarce, fine-scaled and/or comparatively rare habitats. However, classification confusion took place for other scarce, fine-scaled cover types. Herb-dominated wetlands appear to be well classified in general, although additional ground reference data is needed to determine the level of detail that can be extracted with the ISODATA classification approach as well as through interpretation of the CIR aerial photographs.

The ISODATA classification approach appears to be quite useful for computing wall-to-wall land cover maps from AVIRIS-quality hyperspectral data. The approach does not require all the bands and may or may not be improved using more bands. In terms of a first-cut classification, ISODATA classification using all bands did not appear to improve results when compared to ISODATA classification of 11 select bands. In addition, using all the bands takes about 20 times longer to perform a classification run and requires much more disk space to run. The disk space requirement for running ISODATA cluster busting on all the bands is probably too great for usage in an operational setting. However, an 11-band subset or a similar sized subset would be much easier to process from a data volume management perspective.

It is quite possible that there are other comparable or even better ways to compute wall-to-wall land cover maps from AVIRIS data. For example, some preliminary work by the author indicates that use of the 15 most signal-rich MNF bands instead of 11 select bands may improve ISODATA classification success. It also maybe possible to increase the number of raw bands to 25 without significantly slowing run times and without increasing data volumes to excessively large amounts. There are other bands that probably would be useful for band selection in regard to ISODATA classification. For example, Kokaly and Clark (1999) identify spectral regions important for estimating nitrogen, lignin, and cellulose levels in vegetation. Additional bands from these spectral regions could help improve classification results. Some of the bands selected for classification may not have been optimal. Consequently, better band selection may also improve results.

The classification of problematic scarce, fine-scaled features maybe better mapped with subpixel classification techniques. ISODATA may not always provide a sufficiently effective means to map rare and spectrally subtle features, although it appears to be well suited for land cover classification of common types within the scene. The study area of Northeast Yellowstone National Park largely consists of cover types common to the Northern Rocky Mountains. Consequently, the results from this study should be quite applicable to comparable mapping studies in this region of North America.

Additional work is being done to complete a quantitative map accuracy assessment, using a stratified random sampling of the classification in conjunction with CIR aerial photograph interpretation and field surveys. The results of this assessment will be reported at later date.

7. ACKNOWLEDGEMENTS

This work was supported by the NASA Geospace Applications and Development Directorate under contract number NAS 13-650 at the John C. Stennis Space Center, Mississippi. Several researchers affiliated with Yellowstone Ecosystems Studies (YES) provided invaluable assistance, including Dr. Bob Crabtree of YES, Kerry Halligan of YES and the University of California at Santa Barbara, and Dr. Don Despain of the USGS.

8. REFERENCES

Adams, M. L., W. D. Philpot, and W. A. Norvell, 1999, "Yellowness Index: An Application of Spectral Second Derivatives to Estimate Chlorosis of Leaves in Stressed Vegetation," Int. J. Remote Sens., 20(18):3663-3675.

Ahern, F. J., 1988, "The Effects of Bark Beetle Stress on the Foliar Spectral Reflectance of Lodgepole Pine," Int. J. Remote Sens., 9(9):1451-1468.

Carter, G. A., M. R. Seal, and T. Haley, 1998, "Airborne Detection of Southern Pine Beetle Damage Using Key Spectral Bands," Can. J. Forest Res., 28(7):1040-1045.

Clark, R. N., T. V. V. King, C. Ager, and G. A. Swayze, 1995, "Initial Vegetation Species and Senescence/Stress Mapping in the San Luis Calley, Colorado Using Imaging Spectrometer Data," Proceedings: Summitville Forum '95, H. H. Posey, J. A. Pendelton, and D. Van Zyl, eds., Colorado Geological Survey Special Publication 38, pp. 64-69.

Crabtree, B., A. Marcos, J. Boardman, R. Aspinall, W. Minshall, and D. Despain, in press, "Validation of High-Resolution Hyperspectral Data for Stream and Riparian Habitat Analysis," EOCAP Hyperspectral Workshop, January 16-18, 2001, NASA Geospace Applications and Development Directorate, John C. Stennis Space Center, Mississippi, CD-ROM.

Despain, D. G., 1991, Yellowstone Vegetation: Consequences of Environment and History in a Natural Setting, Roberts Rinehart Publishers, Santa Barbara, 239 pp.

Fuentes, D. A., J. A. Gamon, H-L. Qiu, D. Sims, and D. A. Roberts, 2000, "Mapping Vegetation Cover Types in the Canadian Boreal Forest Using Pigment and Water Absorption Features Derived from AVIRIS,"

Summaries of the Ninth JPL Airborne Earth Science Workshop, February 23-25, Jet Propulsion Laboratory, Pasadena, CA.

Guyot, G., F. Baret, and S. Jacquemoud, 1992, "Imaging Spectroscopy for Vegetation Studies," in Imaging Spectroscopy: Fundamentals and Prospective Applications (F. Toselli & J. Bodechtel, eds), ECSC, EEC, EAEC, Brussels and Luxembourg, pp. 145-165.

Goetz, A. F. H, and J. W. Boardman, 1995, "Spectroscopic Measurement of Leaf Water Status," Geoscience and Remote Sensing Symposium IGARSS '95: Quantitative Remote Sensing for Science and Applications, Volume 2, pp. 978-980.

Jensen, J. R., 1996, Introductory Digital Image Processing: A Remote Sensing Perspective, Prentice-Hall, Inc., 231 pp.

Jensen, J. R., 2000, Remote Sensing of the Environment: An Earth Resource Perspective, Prentice Hall, Upper Saddle River, NJ, 316 pp.

Kokaly, R. F., R. N. Clark, and K. E. Livo, 1998, "Mapping the Biology and Mineralogy of Yellowstone National Park using Imaging Spectroscopy," Summaries of the 7th Annual JPL Airborne Earth Science Workshop, R.O. Green, ed., JPL Publication 97-21, January 12-16, Vol. 1: AVIRIS Workshop, pp. 245-254.

Kokaly, R. F., and R. N. Clark, 1999, "Spectroscopic Determination of Leaf Biochemistry Using Band-Depth Analysis of Absorption Features and Stepwise Linear Regression," Remote Sens. Environ., 67:267-287.

Martin, M. E., S. D. Newman, J. D. Aber, and R. G. Congalton, 1998, "Determining Forest Species Composition Using High Spectral Resolution Remote Sensing Data," Remote Sens. Environ., 65:249-254.

Mohammed, G. H., T. L. Noland, D. Irving, P. H. Sampson, P. J. Zarco-Tejada, and J. R. Miller, 2000, Natural and Stress-induced Effects on Leaf Spectral Reflectance in Ontario Species, Ontario Ministry of Natural Resources, Ontario Forest Research Institute , Sault Ste. Marie, Ontario, Forest Research Information Paper No. 156, 42 pp. Downloadable at: http://www.cciw.ca/forest-health/reports/sustainability-bioindicators/frr156.pdf.

National Park Service, 1999, Yellowstone National Park - State of the Park 1999, National Park Service, Mammoth Hot Springs, Wyoming.

National Park Service, 2000, Resources and Issues Handbook 2000, National Park Service, Mammoth Hot Springs, Wyoming, 165 pp. Downloadable at: http://www.nps.gov/yell/publications/pdfs/handbook/handbook.pdf.

Penuelas, J., J. A. Gamon, A. L. Fredeen, J. Merino, and C. Field, 1994, "Reflectance Indexes Associated with Physiological-changes in Nitrogen-limited and Water-limited Sunflower Leaves," Remote Sens. Environ., 48:135-146.

Sampson, P. H., G. H. Mohammed, P. J. Zarco-Tejada, J. R. Miller, T. L. Noland, D. Irving, P. M. Treitz, S. J. Colombo, and J. Freemantle, 2001, "The Bioindicators of Forest Condition Project: A Physiological, Remote Sensing Approach," Forest Chron., 76(6):941-952.

Thenkabail, P., R. Smith, and E. Pauw, 2000, "Hyperspectral Vegetation Indices and their Relationships with Agricultural Crop Characteristics," Remote Sens. Environ., 71:158-182.

Zarco-Tejada, P. J., J. R. Miller, G. H. Mohammed, T. L. Noland, and P. H. Sampson, 1999, "Canopy Optical Indices from Infinite Reflectance and Canopy Reflectance Models for Forest Condition Monitoring: Application to Hyperspectral CASI Data," Geoscience and Remote Sensing Symposium, IGARSS '99 Proceedings, IEEE International, Volume 3, pp. 1878-1881.

THE ROLE OF HYPERSPECTRAL DATA IN UNDERSTANDING THE GLOBAL CARBON CYCLE

Susan L. Ustin,[1] Pablo J. Zarco-Tejada,[1] and Gregory P. Asner[2]

1. Introduction

A major challenge in predicting the consequences of global climate change is to accurately estimate carbon stocks and to predict future CO_2 sequestration and dynamics (NRC, 1999). Climate dynamics and human activities drive changes in land cover and land use, creating unpredictable patterns of disturbance and environmental stresses in natural and managed ecosystems. These changes affect carbon storage, the distribution of carbon in above and below ground compartments, ecosystem productivity, and biogeochemical cycles. A wide range of information is needed to monitor the carbon cycle from properties that regulate fluxes of CO_2, to estimates of standing biomass, land cover types, and land use history. Satellite observations provide the only practical means to obtain a synoptic view of the Earth's ecosystems, their spatial distribution, extent, and temporal dynamics.

Four priority areas have been identified where improved satellite observations of terrestrial landscapes could contribute to greatly reducing the uncertainties in the global carbon budget. These are: (1) land cover characterization at improved spatial resolution, (2) above-ground biomass estimates, (3) areal estimates of disturbance, disturbance type, and time period since the last disturbance, and (4) improved estimates of productivity and controls on productivity. While these categories do not exclusively require hyperspectral data, it can contribute to significant improvements in reducing uncertainties in each area.

Among most important information that satellite observations can contribute is the distribution of land cover types, in particular vegetation, and their spatial variability. For terrestrial biomes, information is needed on the growth form, the cover fraction, canopy density, seasonality and duration of the growing season, the leaf type (conifer, broadleaf) and the photosynthetic pathway (producing four-carbon (C4) or three carbon (C3) carbohydrate products) associated with specific carbon uptake characteristics (DeFries *et al.* 1995; 1999). To understand the consequences of land cover and land use change on the carbon budget, both the biophysical and the human factors that drive land cover and land use changes must be addressed. Natural disturbances (such as wildfire, floods, insect infestations), and human-induced disturbances (e.g., agriculture, urbanization, and logging) may change large areas of the Earth's surface, but more subtle changes may also result in habitat degradation and fragmentation (e.g., selective logging, soil erosion, and pollution). The introduction of non-native species can lead to significant changes at the ecosystem scale in carbon storage and fluxes, redistribution of species, and/or losses of biodiversity. Current satellite observations are inadequate to characterize and verify land cover at the spatial scales needed to assess their impacts on the carbon budget.

Land cover characteristics influence many of the mass and energy exchange processes at the land-atmosphere interface (Cihlar *et al.*, 1997) with a functional dependency on the land cover type. Land use changes play an important additional role because these cause uncertainty in the net flux of CO_2 and the required size of a terrestrial sink (Schimel, 1995). Therefore accurate spatial distribution and percent aerial coverage of the major cover types is essential for correct process modeling. However, current land cover maps derived from AVHRR are coarse at the global scale (e.g., 0.5° - 1°), and primarily rely only on NDVI or a monthly time series to differentiate land cover characteristics (DeFries *et al.*, 1999; Potter *et al.*, 1998; Veroustraete *et al.*, 1996). These NDVI maps are used to generate estimates of multiple model parameters including carbon fluxes, carbon stores, carbon turnover rates, and other land cover properties that impact the carbon budget. Furthermore, NDVI is also used to estimate carbon assimilation processes using fraction of absorbed photosynthetically active radiation (fPAR), net primary productivity (NPP) and net ecosystem productivity (NEP).

Hyperspectral data, having many more spectral bands, provide more independent measures of land surface characteristics. Boardman and Green (2000) explored the intrinsic dimensionality of 510 AVIRIS scenes having a

[1] Center for Spatial Technologies and Remote Sensing (CSTARS), Department of Land, Air and Water Resources (LAWR), University of California, Davis.
[2] Department of Geological Sciences, University of Colorado, Boulder.

range of land cover characteristics and found at least 60-70 above a conservative noise floor, with many individual scenes exceeding 50 spectral dimensions. Because of the scale of variability in ecosystem properties, high spatial resolution (10-100m) is considered critical to developing land cover characterizations, at least for developing appropriate and testable scaling methods to understand the non-linearities in aggregating land cover properties to 1° grids. Green and Boardman (2000) investigated data dimensionality in AVIRIS data and found that the increased signal-to-noise obtained in larger pixels (in this case from 4m to 32m) enhanced the dimensionality despite loss of spatial resolution. This suggests that hyperspectral instruments would not require hyperspatial pixel resolutions. This paper discusses the approaches and variables used for estimating the carbon budget on terrestrial surfaces and the improvements that a hyperspectral satellite sensor could make to reducing the overall uncertainty in the carbon budget.

2. The role of hyperspectral sensors for carbon estimates by improving land cover classification

Key variables are mapping land cover, land use, and land cover conversions, either occurring naturally or due to human disturbances. In all cases where instruments have been compared, HSI instruments provide more detailed information about land cover. For example, predicting whether a boreal forest will become a carbon sink or source demands an accurate knowledge of the distribution of the cover classes in this ecosystem (Steyaert *et al.*, 1997). Ustin and Xiao (2001) compared boreal forest classifications from SPOT and AVIRIS and showed much greater delineation of types and fidelity to a pre-existing field-based map despite similar spatial resolution.

Obtaining baseline maps of the composition of the boreal landscape is of high priority due to predictions for large increases in temperature in this century (IPCC, 1996), the relative inaccessibility of the region, and the potential for feedbacks with other trace gases, e.g., CH_4 production. Landscape heterogeneity (e.g. deciduous and evergreen forests, fens, bogs and small lakes) in boreal ecosystems call into question coarse spatial resolutions between 1 km and 1° x 1°, land cover classification provided by multi-temporal AVHRR data, and persist even with higher spatial resolution Landsat TM data (Steyaert *et al.*, 1997). These issues have been continuously addressed within the BOReal Ecosystem-Atmosphere Study (BOREAS) since a critical contribution to remote sensing science in BOREAS was the development of accurate land cover information at local and regional scales (*BOREAS Experiment Plan,* 1994; Sellers *et al.* 1995). Land cover was mapped at 30m with Landsat TM utilizing a physically-based classification algorithm that employed geometric canopy reflectance models (Hall *et al.*, 1995; 1997). Nevertheless, classification accuracies using such an approach remained low for fens (a major source of methane) and upland conifers. Improvements in land cover mapping were identified as a priority and enhancements were attempted using physical-modeling approaches (Hall *et al.*, 1997; Peddle *et al.*, 1997), and neural networks (Benediktsson *et al.*, 1990; Duguay and Peddle, 1996). Zarco-Tejada and Miller (1999), and by Fuentes *et al.* (in press), exploited systematic species differences using hyperspectral instruments and exploiting wavelength regions sensitive to foliar chemistry to obtain significant improvements in land cover characterization of the BOREAS region. Zarco-Tejada and Miller (1999) improved land cover classification (Figure 1) using 16 CASI bands at the TM spatial resolution (originally 3m resampled to 30m) based on three red-edge spectral parameters: the red-edge inflection point (λ_p), the wavelength at the reflectance minimum (λ_o), and a shape parameter (σ), as defined by the inverted-gaussian red-edge curve-fit model (e.g. Hare *et al.*, 1984), and discussed by Miller *et al.* (1990; 1991).

Their approach was based on the separation of land cover types using variables known to affect red edge spectral parameters: vegetation chlorophyll content, canopy structure and canopy cover. An extension of this work by Fuentes *et al.* (in press) (Figure 2) used pigment classes in a spectral unmixing procedure to map the relative abundance of pigments, and seven indices of vegetation structure and physiological function related to the pigment content and calculated from water absorption features. Indices such as the water band index (WBI, Peñuelas *et al.*, 1997), and the normalized difference water band index (NDWI, Gao, 1996) have been shown to be good indicators of leaf and canopy water content, which vary with vegetation type, LAI, and physiological state (Ustin *et al., 1998;* Gamon and Qiu, 1999; Serrano *et al.*, 2000). Accuracy assessment of the resulting land cover map, when compared to forest inventory classifications, showed significantly improved classification accuracy with red-edge indices, which exceeded 68% for all classes (Zarco-Tejada and Miller, 1999) and improved to 66.6-80.1% (Fuentes *et al.*, in press) by including water-based indices.

Therefore, hyperspectral sensors enable the use of individual spectral features related to pigment composition (Gitelson and Merzylak, 1996, 1997; Gamon and Surfus, 1999), canopy water content (Peñuelas *et al.*,

1997; Ustin *et al.*, 1998; Serrano *et al.*, 2000), canopy dry plant litter and/or wood (Roberts *et al.*, 1993; Ustin *et al.*, 1993, 1996, 1998, Asner *et al.*, 1998), and forest composition as function of foliar chemistry (Martin *et al.*, 1998; Zarco-Tejada and Miller, 1999; Fuentes *et al.*, in press) achieving better discrimination of vegetation classes than possible from broadband sensors.

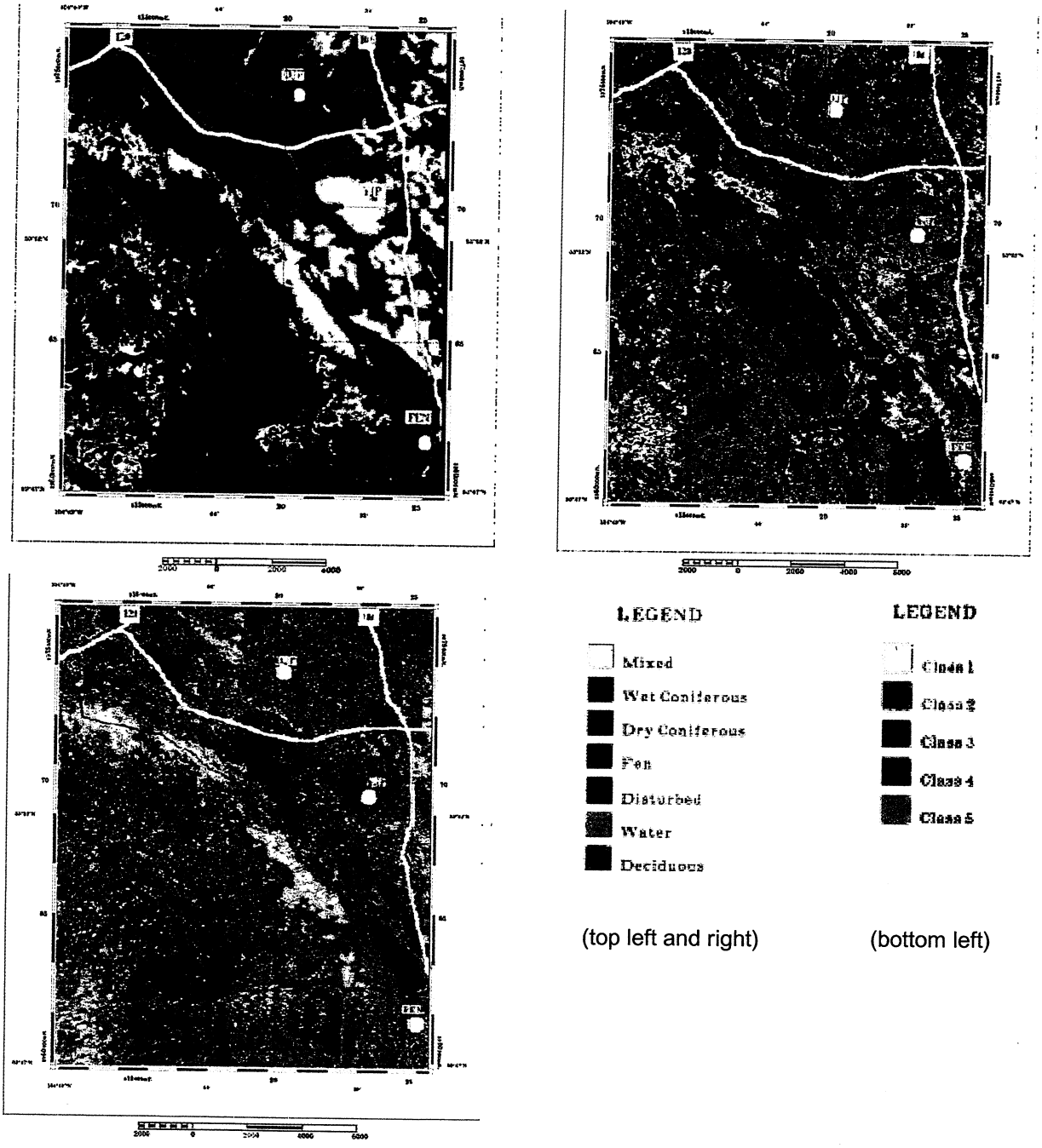

Figure 1. Land cover classes (aggregated into the 7 functionally-dominant landscape units) for the BOREAS Southern Study Area, based on polygon data from *Saskatchewan Environment and Resource Management* used as ground truth (top-left), land cover classification based on Landsat TM data and the physical modeling approach of Hall *et al.* (1995, 1997) (top-right), and classification using the red edge spectral parameters λ_p, λ_o, and σ based on CASI hyperspectral mosaic of the BOREAS SSA modeling grid, re-sampled to 30 m spatial resolution (Zarco-Tejada and Miller, 1999).

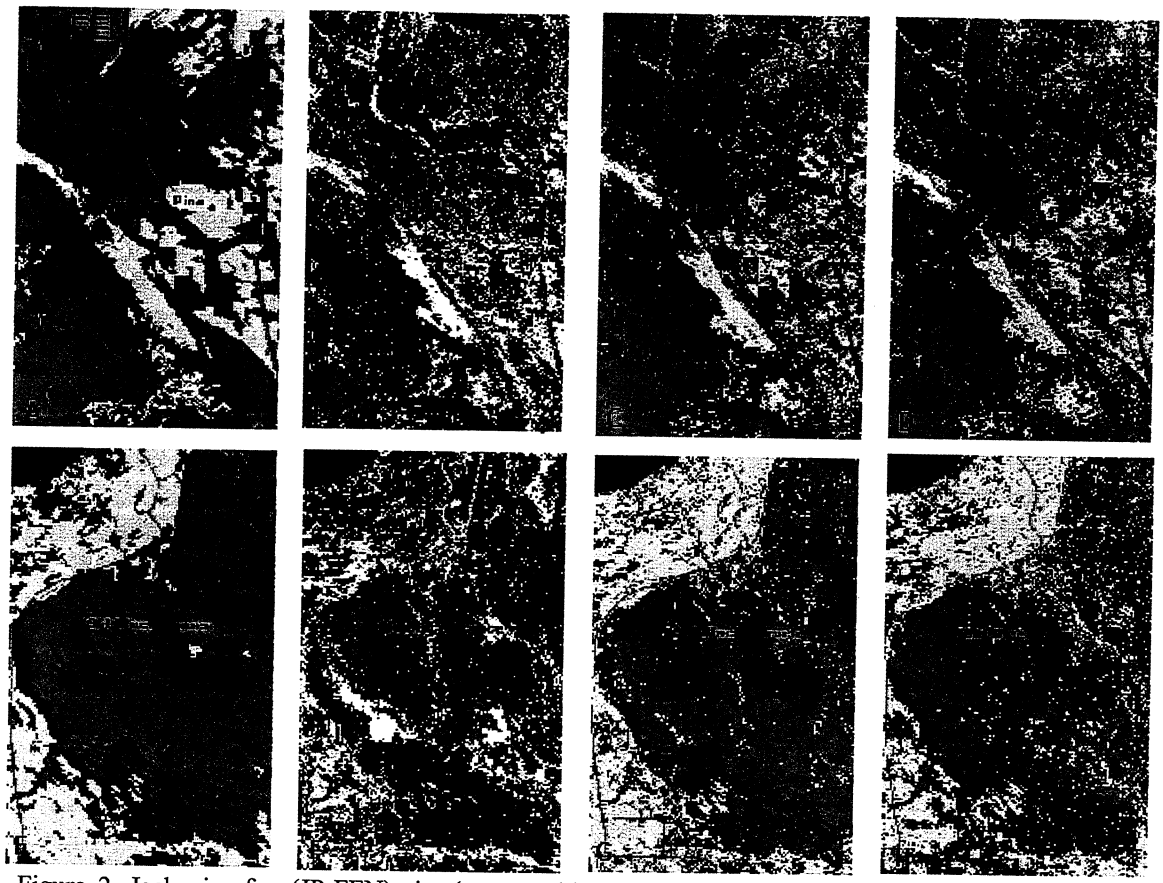

Figure 2. Jack pine-fen (JP-FEN) site (top panels) and Old black spruce (OBS) site (bottom panels). For the evaluation of classification accuracy, the SERM-FBIU (Gruszka, 1998; Panels A & E), obtained from the BOREAS Information System (BORIS), was assumed to be true. The Landsat TM physical classification (Hall, 1999; Panels B & F). The, AVIRIS leaf-based (Panels C & G) and index-based (Panels D & H) maximum likelihood classifications were derived from the July 21, 1994 overflight. (Fuentes *et al.,* in press).

3. Carbon estimates with multispectral coarse resolution remote sensing data

Global estimates of CO_2 dynamics using ecosystem models such as Simple Biosphere Model, SiB2 (Sellers *et al.*, 1986, 1996a,b) and CASA (Potter *et al.*, 1993; Field *et al.*, 1995; Randerson *et al.*, 1997) obtain input data from AVHRR-derived NDVI data to capture biophysical and ecological properties used in the models. NDVI is affected by both pigment absorption (blue and red) and the scattering of the medium (NIR), a function of the arrangement of elements of the canopy (structure). Moreover, it is well documented that NDVI saturates at leaf area index (LAI) values substantially below LAI in high productivity sites. Limitations of current methods for deriving canopy biophysical (LAI, structure) and leaf biochemical constituents (chlorophyll (chl_{a+b}), nitrogen (N), and water content (H_2O)) limits accuracy when estimating the significance of photosynthetic processes in regulating some components of the carbon cycle. Moreover, no current remote sensing approaches provide reliable estimates of other critically important ecosystem-level properties such as senescent vegetation (e.g., dry carbon loading) or canopy structural changes. Observations of these factors, which have been demonstrated from hyperspectral imaging systems, would provide a major step toward an improved understanding of the carbon cycle.

Widely used ecosystem models (Sellers *et al.*, 1986, 1996a,b) and CASA (Potter *et al.*, 1993; Field *et al.*, 1995; Randerson *et al.*, 1997) use remotely sensed data products for estimating carbon allocation, including new model advances such as a 6-layer soil submodel (Bonan, 1996, 1998). Explicit litter layer (Denning *et al.*, 1996),

new parameterizations of carbon and nitrogen allocation, growth and maintenance respiration and decomposition are obtained using new hybrid ecosystem models, e.g., incorporating SYLVAN (Kaduk 1996; Kaduk and Heimann 1996a,b). However remote sensing paramaterizations have not advanced and NDVI is used to simultaneously estimate LAI, evapotranspiration, photosynthesis, primary productivity and carbon cycling.

A number of studies have shown that the NDVI saturates at LAI of 3-4 (Sellers, 1986), while LAI exceeds this for most closed-crown crops and forests. NDVI saturation under-estimates the fluxes of CO_2 and H_2O, and this error feeds back into other physiological processes. One of the key driving variables used by CASA and SiB-2 models is the flux of absorbed PAR, with gross CO_2 uptake, NPP, and canopy conductance all scaled to NDVI. In theory, absorptance of PAR is proportional to NDVI but because both saturate most of the variability occurs at LAI values < 3. Canopies with large variations in LAI also exhibit large differences in total photosynthetic capacity and the quantity of nitrogen and other nutrients in the canopy are incorrectly inferred from an NDVI parameter. NDVI failed to track variation in pigment content, such as might occur under environmentally induced plant stress at study sites with high LAI values (Zarco-Tejada, 2000). Furthermore, maximum site LAI, governed by climate and site conditions is often reached at an early stage of growth while non-photosynthetic components of biomass (stems, roots) continue accumulation throughout the growing season. This biomass estimate saturates at relatively low levels of biomass, and causes NDVI to markedly under-estimate biomass in woody vegetation. Fluxes of CO_2 and H_2O, feed back into other physiological processes that are also under estimated. Figure 3 shows NDVI, red-edge spectral parameter λ_p, and estimated canopy water content, calculated from cotton fields using hyperspectral AVIRIS data. It can be seen that NDVI does not correspond to λ_p, which is highly correlated with pigment content, and functionally with canopy water content.

The accuracy of carbon model predictions in vegetation at higher spatial scales will improve estimates of biophysical parameters through more effective linkage between leaf and canopy radiative transfer models (RT) from hyperspectral data. Estimates of leaf chl_{a+b} and its relationship to N content, LAI, and canopy H_2O, are biophysical parameters that can be retrieved from hyperspectral canopy reflectance data by inversion of coupled leaf and canopy models.

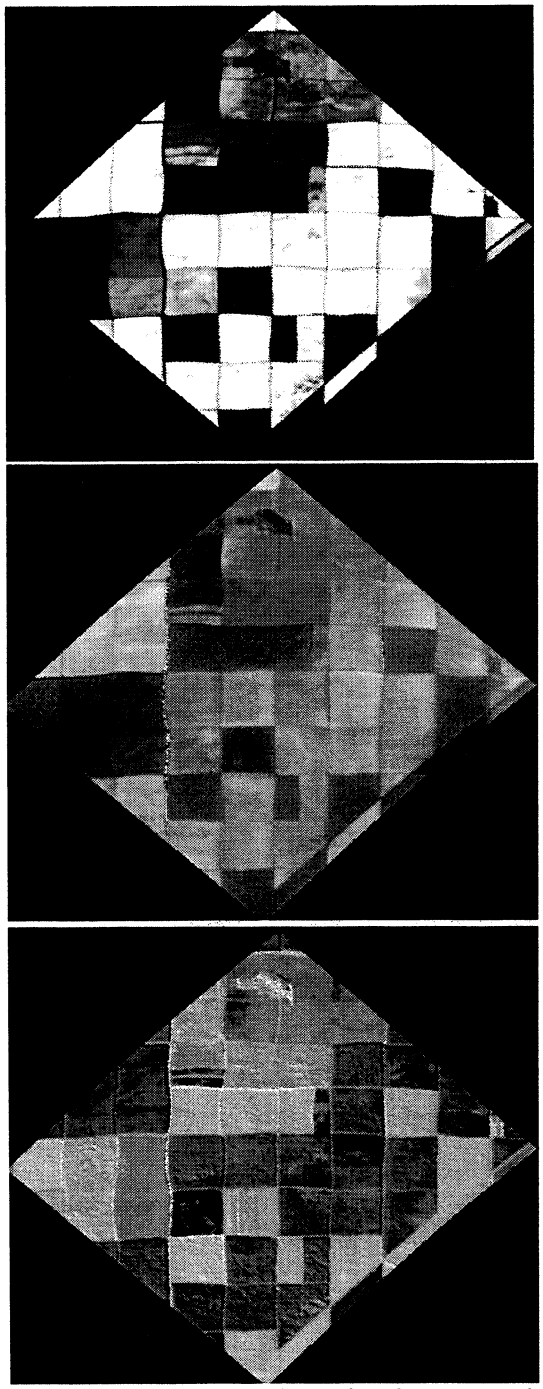

Figure 3. NDVI (top), red edge spectral parameter λ_p (middle), and canopy water content (bottom), calculated from the same cotton fields from AVIRIS data.

3.1. Estimation of other physiological variables using hyperspectral remote sensing

The carbon system is closely linked to the water and energy cycles through regulation of photosynthesis (Sellers *et al.*, 1992; Sellers and Schimel, 1993; Collatz *et al.*, 1991), and to the nitrogen cycle through metabolism (Schimel, 1995). Correctly predicting the linkages between the carbon, water, and nitrogen cycles is crucial to

predicting the changing Earth system and feedback to atmospheric concentrations of greenhouse gases and primary productivity of the biosphere (Schimel, 1995).

The global carbon cycle (i.e., through CO_2 uptake) is affected by alteration of the global N cycle through fertilizer use and air pollution (Schimel, 1995; Vitousek *et al.* 1997). Fertilization of agricultural crops and N deposition affect carbon storage, generate vegetation injury with prolonged N additions (Schultze *et al.*, 1989) and increase N losses by gaseous and solute pathways to the soil. Spatial estimation of N in forest and agricultural canopies is important to quantify interactions between the carbon and nitrogen cycles. Estimating leaf nitrogen content is obtained through total chlorophyll concentration, because the majority of leaf N is contained in the carbon-fixing enzyme, RUBP-carboxylase (Daughtry *et al.*, 2000; Yoder and Pettigrew-Crosby, 1995). Estimating chlorophyll content from canopies with different structural characteristics requires hyperspectral data to couple specific radiative transfer models with leaf models using red-edge indices in the merit function while minimizing the effects of canopy shadows, understory, and large variations of LAI (Zarco-Tejada *et al.*, in press; Zarco-Tejada, 2000). Therefore, accurate estimates of leaf chl_{a+b} at canopy levels with high spatial resolution hyperspectral reflectance data is critical for obtaining estimates of leaf N. Estimation of canopy concentrations of chl_{a+b} have been demonstrated by model inversion using hyperspectral remote sensing data (Jaquemoud, 1993; Jacquemoud *et al.*, 1995; Kuusk, 1998; Demarez and Gastellu-Etchegorry, 2000; Jacquemoud *et al.*, 2000; Zarco-Tejada, 2000; Zarco-Tejada *et al.*, in press). Specific results by Jaquemoud (2000) and Zarco-Tejada *et al.* (in press) using airborne hyperspectral data showed errors of RMSE = 3-8 $\mu g/cm^2$ for chl_{a+b} estimated by linking leaf radiative transfer model (PROSPECT) to infinite reflectance (Hapke, 1993; Yamada and Fujimura, 1991) and canopy reflectance models (SAILH, Kuusk, SPRINT) (Figure 4). These results show accurate estimates of leaf biochemical constituents from hyperspectral reflectance data for both crop and forest canopies (Figure 5).

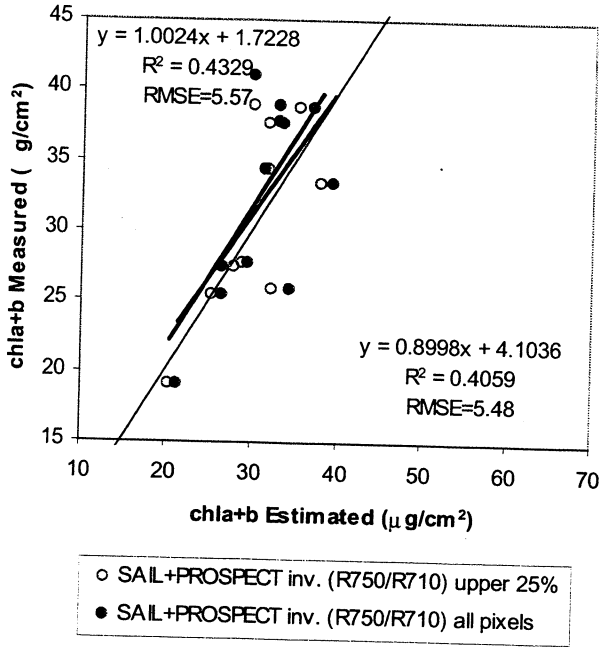

Figure 4. Estimation of leaf chl_{a+b} from canopy airborne hyperspectral data by inversion of SAILH+PROSPECT models using R_{750}/R_{710} optical index in the merit function. Using red edge optical indices in the merit function for model inversion avoids effects due to canopy structure and shadows (using all pixels from a study plot, labeled as *all pixels*), obtaining the same pigment estimates when targeting crowns (labeled as *upper 25%*) from 30x30 m study sites (Zarco-Tejada *et al.*, in press).

Many studies have demonstrated a direct relationship between the photosynthetic rate, light absorbance, leaf N, and dry matter production (Alt *et al.*, 2000). There appears to be a linear dependence of maximum photosynthetic capacity on leaf N to the point of species-specific optimality. The increases in photosynthetic capacity are strongly correlated with the distribution of Chl_{a+b} and N within crop canopies (Fontes *et al.* 1997). Canopy N distribution exhibits a phenological shift in the LAI (Yin *et al.* 2000). In addition, leaf N exhibits a linear relationship with increases in specific leaf mass (Garnier *et al.* 1999), which are associated with high N.

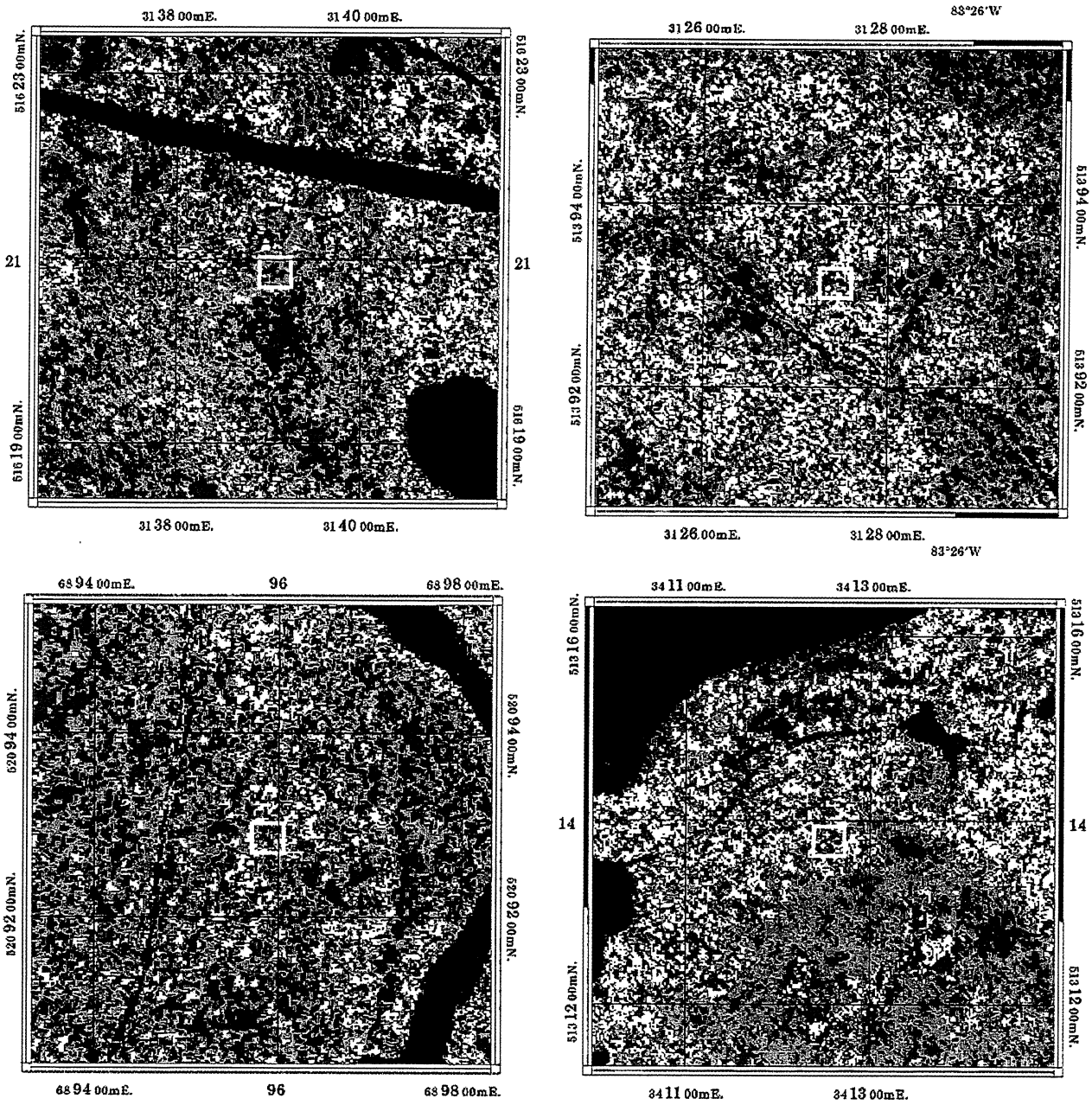

Figure 5. Chl_{a+b} estimation by radiative transfer model inversion from airborne hyperspectral data over 500m x 500m study areas with extreme values of chl_{a+b} measured in the field. Model estimates showed good agreement with ground truth assessment (RMSE=5.5 $\mu g/cm^2$) carried out in 30x30m sampling areas (white box), with chl_{a+b}=38.8 $\mu g/cm^2$ (upper left), chl_{a+b}=45.8 $\mu g/cm^2$ (lower left), chl_{a+b}=19.08 $\mu g/cm^2$ (upper right), and chl_{a+b}=26.58 $\mu g/cm^2$ (lower right) (Zarco-Tejada *et al.*, in press).

Leaf-level optical indices and ratios centered at the water absorption bands at 940nm and 1200nm show good correlations with ground-based measures of leaf water thickness (Ustin *et al.*, 1998; Gao and Goetz, 1995; Serano *et al.*, 2000) and therefore such indices can be used to map canopy water content. In contrast to NDVI, LAI estimated from canopy water content, remains linear to LAI $\geq$ 10 (Roberts *et al.*, 1998). Estimates of canopy water

content contribute information about carbon sequestration at low values and by extending the range of LAI estimates.

Dry carbon (C) stores, including woody stems and roots, and plant litter (i.e., dry leaves and stems) may indicate different ecosystem processes or conditions depending upon the specific setting (Ustin *et al.*, 1993; Asner 1998). In dense forest systems, an increase in plant litter follows disturbance or stresses and has been used in tropical forests to assess stress (Asner *et al.* in review). In drier forests, lower canopy cover allows detection of more plant litter on the ground and provides a spectral estimate of disturbance, physiological and biogeochemical processes. In sparsely vegetated shrublands and savannas dry plant litter and wood indicates fire fuel loading (Asner *et al.* 1998, Roberts *et al.* 1998), and thus becomes a critical observation for predicting wildfires and subsequent CO_2 emissions. Spatial and temporal variability of dry carbon in shrub and grassland ecosystems also indicates variations in climate forcing, such as in precipitation patterns. Asner *et al.* (2000) and Asner and Heidebrecht (in press) showed that dry carbon cover and content cannot be accurately estimated using multispectral observations such as from Landsat or MODIS.

Hyperspectral observations in the shortwave infrared (SWIR) are needed to measure dry C (Asner and Lobell 2000, Asner *et al.* 1998, 1999). The observed variation (Figure 6) in LAI (both chl_{a+b} and H_2O) and litter are highly non-linear mixing processes (Jacquemoud 1993, Jacquemoud *et al.* 1995, Asner *et al.* 1998). In nature, many factors co-vary, creating a highly complex volume mixing problem that is best understood using hyperspectral observations. For instance, while changes in LAI have the most pronounced effect on the VNIR between 0.4 – 1.3μm, dry C has its most pronounced effect in the SWIR from 2.0 -2.4 μm. Observation of the entire reflected solar spectrum (0.4 - 2.5 um) provides the best chance to estimate both the cover and volumetric content of leaf and dry plant litter in many vegetation types.

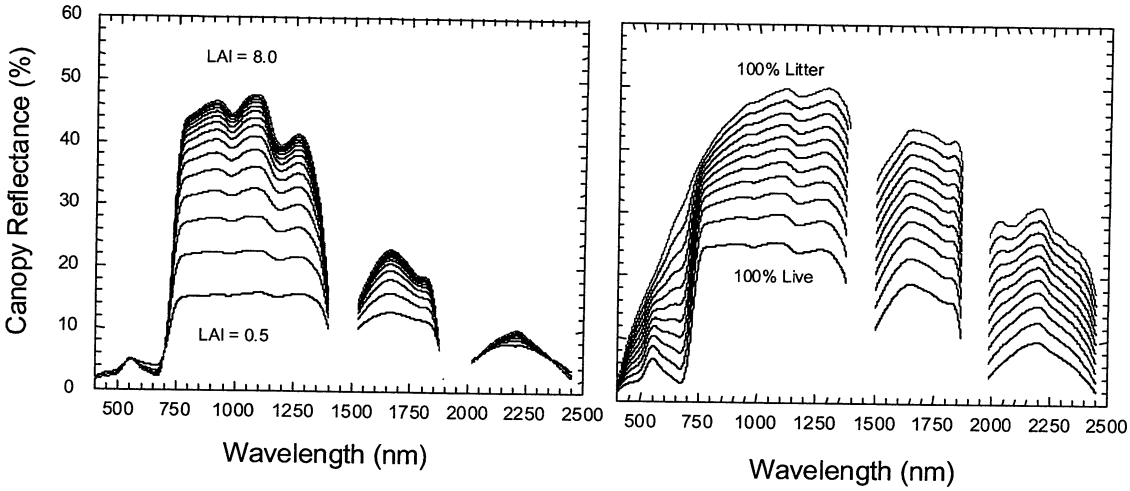

Figure 6. The non-linear effect of changing LAI (left panel) and dry C (right panel) on canopy or pixel-scale reflectance (Asner, 1998).

For example, in savannas, shrublands and woodlands, observed variations in AVIRIS hyperspectral signatures were highly indicative of the 3-dimensional variation in LAI and dry C (Figure 7). Simultaneous observation of both LAI and dry carbon area index (NPVAI) produced highly accurate maps of structural and functional vegetation types and of fire fuel load (Asner *et al.* 1998). Similarly, Asner *et al.* (1999) quantified live and senescent aboveground biomass in the central Amazon basin using hyperspectral observations. In most humid tropical ecosystems, the combination of LAI and NPVAI indicates nutrient limitations for both NPP and C storage (Asner *et al.* 1999). Observed hyperspectral variation in these parameters contributes to regional carbon fluxes and stocks.

Knowledge of soil properties and below ground C stores is limited. While optical sensors do not penetrate into the soil, some surface properties can be estimated. Ahn *et al.* (1999) used AVIRIS data to map soil surface properties, demonstrating the potential to map heterogeneity and identify localized characteristics, e.g., soil organic

carbon (SOC) and soil inorganic carbon (SIC). Palacios-Orueta and Ustin (1996) spectrally separated closely related agricultural soils and showed differences in SOC using AVIRIS and field data. In the Santa Monica Mountains AVIRIS methodologies were extended to mapping SOC and iron content (Palacios-Orueta and Ustin 1998; Palacios-Orueta *et al.*, 1999). Schreier *et al.* (1988) quantified the relationship of SOC to moisture, exchangeable Calcium and Magnesium cation exchange capacity, and soil color, with established procedures and reference reflectance libraries been developed from soil samples (Krishnan *et al.*, 1980; Henderson *et al.*, 1989; Henderson *et al.*, 1992; Kimes *et al.*, 1993; Wilcox *et al.*, 1994).

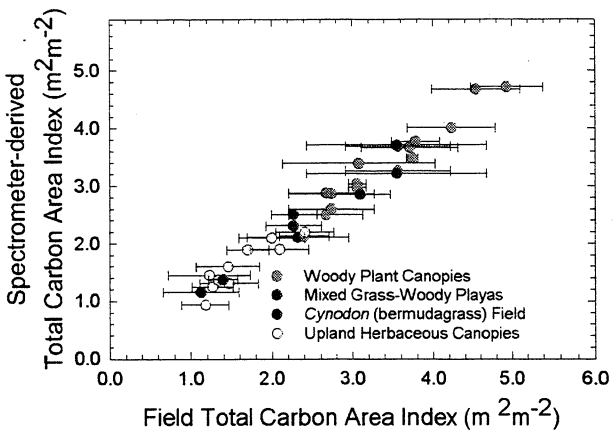

Figure 7. Comparison of field and AVIRIS-derived total carbon content of savanna woody and herbaceous vegetation canopies on the Rio Grande Plains of South Texas. Horizontal bars indicate uncertainty in field measurement techniques (Asner *et al.*, 1998).

4. Conclusions

Years of modeling and experimental research have shown that vegetation canopies are strongly under-determined remote sensing problems. Multiple combinations of vegetation structural and functional characteristics produce similar reflectance signatures, as have been observed in multi-spectral remote sensing instruments. Hyperspectral observations provide additional degrees of freedom that allow improved resolution of vegetation land cover maps and estimates of physiological properties e.g., LAI, fPAR, Chl_{a+b} and H_2O. Imaging spectroscopy opens the door to measurements that are directly indicative of ecosystem structure and functioning, such as chlorophyll concentration and dry C loading.

Hyperspectral data from a satellite platform can provide the best information, with current technology, on how the global carbon budget is changing. The design of a sampling instrument with pointing capability and Landat-type spatial resolution (30 m) and nadir repeat frequency (16 day), a 40-60 km swath (e.g., SPOT), and 200 spectral bands at AVIRIS quality signal-to-noise (e.g., 1000:1 in VNIR and 500:1 SWIR) would provide the information needed to significantly reduce uncertainties in the global carbon budget.

5. References

Ahn, C.-W., M.F. Baumgardner, and L.L. Biehl, Delineation of soil variability using geostatistics and fuzzy clustering analyses of hyperspectral data. *Soil Sci. Soc. Am. J.* 63:142–150, 1999.

Alt, C., H. Stutzel, and H. Kage, Optimal nitrogen content and photosynthesis in cauliflower (*Brassica oleracea* L. *botrytis*). Scaling up from leaf to whole plant *Annals of Botany* 85:779–787, 2000.

Asner, G.P., Biophysical and biochemical sources of variability in canopy reflectance. *Remote Sensing of Environment* 64:234–253, 1998.

Asner, G.P.; C.A. Bateson; J.L. Privette, N. ElSaleous, C.A. Wessman, Estimating vegetation structural effects on carbon uptake using satellite data fusion and inverse modeling. *Journal of Geophysical Research-Atmospheres*, 103(ND22):28839–28853, 1998.

Asner, G.P. and K.B. Heidebrecht, Spectral unmixing of vegetation, soil and dry carbon in arid regions: Comparing multi-spectral and hyperspectral observations. *International Journal of Remote Sensing*, in press.

Asner, G.P. and D.B. Lobell, A biogeophysical approach for automated SWIR unmixing of soils and vegetation. *Remote Sensing of Environment* 74:99–112, 2000.

Asner, G.P., A.R. Townsend, and M.C.M. Bustamante, Spectrometry of pasture condition and biogeochemistry in the Central Amazon. *Geophysical Research Letters* 26:2769–2772, 1999.

Asner, G.P., C.A. Wessman, and D.S. Schimel, Heterogeneity of savanna canopy structure and function from imaging spectrometry and inverse modeling. *Ecological Applications* 8:926–941, 1998.

Asner, G.P., C.A. Wessman, C.A. Bateson, and J.L. Privette, Impact of tissue, canopy and landscape factors on the hyperspectral reflectance variability of arid ecosystems. *Remote Sensing of Environment* 74:69–84, 2000.

Bonan, G. B., A land surface model (LSM version 1.0) for ecological, hydrological, and atmospheric studies: Technical description and User's Guide. NCAR/TN-417+STR, 1996.

Bonan, G. B., The land surface climatology of the NCAR Land Surface Model coupled to the NCAR Community Climate Model. *Jour. Clim.* 11:1307–1326, 1998.

BOREAS, Boreal Ecosystem Atmosphere Study Experiment Plan Version 3.0, P.J. Sellers *et al.* (eds.), NASA Goddard Space Flight Center, Greenbelt, MD, 4 volumes, 1994.

Benediktson, J. A., P. H. Swain, and O.K. Ersoy, Neural network approaches versus statistical methods in classification of multi source remote sensing data, *IEEE Trans. Geosci. and Remote Sens.*, 28:540–552, 1990.

Boardman, J.W., and R.O. Green, Exploring the spectral variability of the Earth as measured by AVIRIS in 1999. In Proc. 9th JPL Airborne Earth Science Workshop, Dec. 2000, R.O. Green (Ed.), pp. 55–64. JPL Publ. 00-18, 2000.

Cihlar, J., J. Beaubien, Q. Xiao, J. Chen, and Z. Li, Land cover of the BOREAS region from AVHRR and Landsat data, *Can. J. Remote Sens.*, 23:16–175, 1997.

Collatz, G. J., J. T. Ball, C. Grivet, and J. A. Berry, Physiological and environmental regulation of stomatal conductance, photosynthesis, and transpiration: a model that includes a laminar boundary layer, *Agric. and Forest Meteorol.* 54:10–136, 1991.

Daughtry, C.S.T., C.L. Walthall, M.S. Kim, E. Brown de Colstoun, and J.E. McMurtrey III, Estimating corn leaf chlorophyll concentration from leaf and canopy reflectance, *Remote Sensing of Environment*, 74:22–239, 2000.

DeFries, R., C. Field, A. Fung, C. Justice, S. Los, P. Matson, M. Matthews, H. Mooney, C. Potter, K. Prentice, P. Sellers, J. Townshend, C. Tucker, S. Ustin, P. Vitousek. Mapping the land surface for global atmosphere-biopshere models: toward continuous distributions of vegetation's functional properties. *J. Geophysical Research-Atmospheres* 100:20, 86–882,. 1995.

DeFries, R.S., C.B. Field, I. Fung, G.J. Collatz, and L. Bounoua, Combining satellite data and biogeochemical models to estimate global effects of human-induced land cover change on carbon emissions and primary productivity, *Global biogeochemical Cycles*, 13(3);803–815, 1999.

Demarez, V., and J.P. Gastellu-Etchegorry, A Modeling Approach for Studying Forest Chlorophyll Content, *Remote Sensing of Environment*, 71:226–238, 2000.

Denning, A. S., D. A. Dazlich, and D. A. Randall. Simulations of soil temperature, snowpack, and carbon fluxes with an atmospheric general circulation model. Presented at 1996 Fall Meeting of the American Geophysical Union A32D-2, 1996.

Duguay, C. R., and D. R. Peddle, Comparison of evidential reasoning and neural network approaches in a multi-source classification of Alpine Tundra Vegetation, *Can. J. Remote Sens.*, 22:433–440, 1996.

Field, C.B., J.T. Randerson, and C.M. Malmstrom, Global net primary production: Combining ecology and remote sensing, *Remote Sens. Environ.* 51:74–88, 1995.

Fontes, P., P. Pereiru, and R. Conde, Critical chlorophyll, total nitrogen, and nitrate-nitrogen in leaves associated to maximum lettuce yield. *J. Plant Nutrition* 20:1061–1068, 1997.

Fuentes, D.A., J.A. Gamon, H. Qiu, D.A. Sims, D.A. Roberts, Mapping Canadian Boreal Forest Vegetation Using Pigment and Water Absorption Features Derived From The AVIRIS Sensor, *Journal of Geophysical Research* (in press).

Gamon, J. A., and H.-L. Qiu, Ecological applications of remote sensing at multiple scales. pp. 805–846. In: Pugnaire, F. I., and Valladares, F. (eds). *Handbook of functional plant ecology*. Marcel Dekker, Inc., New York, 1999.

Gamon, J. A. and J.S. Surfus, Assessing leaf pigment content and activity with a reflectometer, *New. Phytol.* 143:105–117, 1999.

Gao, B.-C., NDWI - A normalized difference water index for remote sensing of vegetation liquid water from space. *Remote Sens. Environ.* 58:257–266, 1996.

Gao, B.C., and A.F.H. Goetz, Retrieval of Equivalent Water Thickness and Information Related to Biochemical-Components of Vegetation Canopies From AVIRIS Data, *Remote Sens. Environ.* 52:(3) 155–162 Jun 1995

Garnier, E., J.L. Salager, G.Laurent, and L. Sonie, Relationship between photosynthesis, nitrogen and leaf structure in 14 grass species and their dependence on the basis of expression. *New Phytologist.*143:119–129, 1999.

Gitelson, A. A. and M.N. Merzlyak, Signature Analysis of Leaf Reflectance Spectra: Algorithm Development for Remote Sensing of Chlorophyll, *Journal of Plant Physiology.* 148:494–500, 1996.

Gitelson, A. A. and M.N. Merzlyak, Remote estimation of chlorophyll content in higher plant leaves, *International Journal of Remote Sensing.* 18:2691–2697, 1997.

Green, R.O., and J. Boardman, Exploration of the relationship between information content and signal-to-noise ratio and spatial resolution in AVIRIS spectral data. . In *Proc. 9th JPL Airborne Earth Science Workshop*, Dec. 2000, R.O. Green (Ed.), pp. 195–206. JPL Publ. 00-18, 2000.

Gruszka, Fern, BOREAS Forest Cover Data Layers over the SSA-MSA in Raster, Available online at [http://www-eosdis.ornl.gov/] from the ORNL Distributed Active Archive Center, Oak Ridge National Laboratory, Oak Ridge, Tennessee, U.S.A, 1998.

Hall, F. G., Y. E. Shimabukuro, and K. F. Huemmrich, Remote sensing of forest biophysical structure using mixture decomposition and geometric reflectance models, *Ecological Applications,* 5:993–1013, 1995.

Hall, F. G., D. E. Knapp, and F. Huemmrich, Physically based classification and satellite mapping of biophysical characteristics in the southern boreal forest, *J. Geophys. Res.*, 102:D24, 29567–29580, 1997.

Hall F. G., BOREAS TE-18 Landsat TM Physical Classification Image of the SSA, Available online at [http://www-eosdis.ornl.gov/] from the ORNL Distributed Active Archive Center, Oak Ridge National Laboratory, Oak Ridge, Tennessee, U.S.A, 1999.

Hapke, B., *Theory of Reflectance and Emittance Spectroscopy,* Cambridge University Press, 1993.

Hare, E. W., J. R. Miller, and G. R. Edwards, Studies of the vegetation red reflectance edge in geobotanical remote sensing, in *Proceedings of the 9th Canadian Symposium on Remote Sensing*, pp. 433–440, Can. Remote Sens. Soc., Can. Aeronaut. and Space Inst., Ottawa, 1984.

Henderson, T.L., A. Szilagyi, M.F. Baumgardner, C.T. Chen, and D.A. Landgrebe, Spectral band selection for classification of soil organic matter content. *Soil Sci. Soc. Am. J.* 53:1778–1784, 1989.

Henderson, T.L., M.F. Baumgardner, D.P. Franzmeier, D.E. Stott and D.C. Coster, High dimensional reflectance analysis of soil organic matter. *Soil Sci. Soc. Am. J.* 56:865–872, 1992.

Intergovernmental Panel on Climate Change (IPCC), Climate Change 1995: The Science of Climate change, (Eds.) J.T. Houghton, L.G. Meira Filho, B.AS. Callander, N. Harris, A. Kattenberg, and K. Maskell, Cambridge University Press, Cambridge. 572 pp., 1996.

Jacquemoud, S., Inversion of the PROSPECT+SAIL canopy reflectance model from AVIRIS equivalent spectra: theoretical study, *Remote Sensing of Environment.* 44:281–292, 1993.

Jacquemoud, S., F. Baret, B. Andrieu, F.M. Danson, and K. Jaggard, Extraction of vegetation biophysical parameters by inversion of the PROSPECT+SAIL models on sugar beet canopy reflectance data. Application to TM and AVIRIS sensors, *Remote Sensing of Environment.* 52:163–172, 1995.

Jacquemoud, S., C. Bacour, H. Poilve, and J.P. Frangi, Comparison of four radiative transfer models to simulate plant canopies reflectance–Direct and inverse mode, *Remote Sensing of Environment,* 74:471–481, 2000.

Kaduk, J. (eds). Simulation der Kohlenstoffdynamik der Landbiosphäre mit SILVAN - Modellbeschreibung and Ergibnesse. MPI Für Meteorologie, 1996.

Kaduk, J., and M. Heimann, Assessing the climate sensitivity of the global terrestrial carbon cycle model SILVAN. *Physics and Chemistry of the Earth* 21:529–535, 1996*a*.

Kaduk, J., and M. Heimann, A prognostic phenology scheme for global terrestrial carbon cycle models. *Climate Research* 6:1–15, 1996*b*.

Kimes, D.S., J.R. Irons, E.R. Levine, and N.A. Horning, Learning class descriptions from a dat base of spectral reflectance of soil samples. *Remote Sens. Environ.* 43:161–169, 1993.

Krishnan, P., J.D. Alexander, B.J. Butler, and J.W. Hummel, Reflectance technique for predicting soil organic matter. *Soil Sci. Soc. Am. J.* 44:1282–1285, 1980.

Kuusk, A., Monitoring of vegetation parameters on large areas by the inversion of a canopy reflectance model, *International Journal of Remote Sensing.* 19:2893–2905, 1998.

Martin, M. E., S. D. Newman, J. D. Aber, and R. G. Congalton, Determining forest species composition using high spectral resolution remote sensing data, *Remote Sens. Environ*, 65:249–254, 1998.

Miller, J. R., E. W. Hare, and J. Wu, Quantitative characterization of the vegetation red edge reflectance I. An inverted-Gaussian reflectance model, *Int. J. Remote Sens.*, 11:121–127, 1990.

Miller, J. R., J. Wu, M. G. Boyer, M. J. Belanger, and E.W. Hare, Seasonal patterns in leaf reflectance red edge characteristics, *Int. J. Remote Sens.*, 12:1509–1524, 1991.

National Research Council (NRC), Global Environmental Change: Research Pathways for the Next Decade, http://stills.nap.edu/books/0309064201/html/, 1999.

Palacios-Orueta, A. and S.L. Ustin, Remote sensing of soil properties in the Santa Monica mountains. I. Spectral analysis. *Remote Sens. Environ.* 65:170–183, 1998.

Palacios-Orueta, A., J.E. Pinzon, S.L. Ustin, and D.A. Roberts, Remote sensing of soil properties in the Santa Monica Mountains. II. Hierarchical Foreground and Background Analysis. Remote Sensing of Environment. Remote Sensing of Environment. 68(2):138–151, 1999.

Peddle, D. R., F.G. Hall, E.F. LeDrew, and D.E. Knapp, Classification of forest land cover in BOREAS. II: Comparison of results from a sub-pixel scale physical modeling approach and a training based method, *Can. J. Remote Sens.*, 23:131–142, 1997.

Peñuelas, J., J. Piñol, R. Ogaya, and I. Filella, Estimation of plant water concentration by the reflectance Water Index WI (R900/R970 *Int. J. Remote Sens.* 18:2869–2875, 1997.

Peñuelas, J., and I. Filella, Technical focus:Visible and near-infrared reflectance techniques for diagnosing plant physiological status. *Trends In Plant Science*, 3(N4):151–156, 1998.

Potter, C.S., J.T. Randerson, C.B. Field, P.A. Matson, PM. Vitousek, H.A. Mooney, and S.A. Klooster, Terrestrial ecosystem production: A process-oriented model based on global satellite and surface data. *Global Biogeochem. Cycles*, 7:811–842, 1993.

Potter, C.S., E.A. Davidson, S.A. Klooster, D.C. Nepstad, G.H. De Negreiros, and V. Brooks, Regional application of an ecosystem production model for studies of biogeochemistry in *Brazilian Amazonia, Gloval Change Biology*, 4:315–333, 1998.

Randerson, J. T., M. V. Thompson, I. Y. Fung, T. Conway, and C. B. Field. The contribution of terrestrial sources and sinks to trends in the seasonal cycle of atmospheric carbon dioxide. *Global Biogeochemical Cycles* 11:535–560, 1997.

Roberts D.A., M.O. Smith, and J.B. Adams, Green Vegetation, Nonphotosynthetic Vegetation, and Soils In *AVIRIS Data. Remote Sensing of Environment*, 44(N2-3):255–269, 1993.

Roberts, D., K. Brown, R. Green, S. Ustin, and T. Hinckley. Investigating the Relationship Between Liquid Water and Leaf Area in Clonal Populus. *Proceedings of the Seventh Earth Science Airborne Workshop*, Jet Propulsion Laboratory, Pasadena, CA, January 12–14, 1998. JPL Publ. 97-21, vol. 1, p. 335–344, 1998.

Schimel, D., Terrestrial biogeochemical cycles: global estimates with remote sensing, *Remote sensing of environment* 51:49–56, 1995.

Schreier, H., R. Wiart, and S. Smith, Quantifying organic matter degradation in agricultural fields using PC-based image analysis. *J. Soil and Water Conserv.* 43:421–424, 1988.

Schulze, E.D., W. De Vries, and M. Hauhs, Critical loads for nitrogen deposition in forest ecosystems, *Water Air Soil Pollut.* 48:451–456, 1989.

Sellers, P.J., Y. Mintz, Y.C. Sud, and A. Dalcher, A simple biosphere model (SiB) for use within general circulation models, *J. Atmos. Sci.,* 43:505–531, 1986.

Sellers, P.J., J.A. Berry, G.J. Collatz, C.B. Field, and F.G. Hall, Canopy Reflectance, Photosynthesis, and Transpiration .3. A Reanalysis Using Improved Leaf Models and A New Canopy Integration Scheme. *Remote Sensing of Environment*, 42(N3):187–216, 1992.

Sellers, P.J. and D. Schimel, Remote sensing of the land biosphere and biogeochemistry in the EOS era: science priorities, methods and implementation, *Global and Planetary Change* 7(4):279–297, 1993.

Sellers, P.J., *et al.*, The Boreal Ecosystem-Atmosphere Study (BOREAS): An Overview and Early Results from the 1994 Field Year. *Bull. Am. Meteorol. Soc.,* 76:1549–1577, 1995.

Sellers, P.J., D.A. Randall, G.J. Collatz, J.A. Berry, C.B. Field, D.A, Dazlich, C. Zhang, G.D. Collelo, and L. Bounoua, A Revised land surface parameterization (SiB2) for atmospheric GCMs. Part I: Model formulation. *Journal of Climate*, 9:676–705, 1996*a*.

Sellers, P.J., S.O. Los, C.J. Tucker, C.O. Justice, D.A. Dazlich, G.J. Collatz and D.A. Randall, A Revised land surface parameterization (SiB2) for atmospheric GCMs. Part II: The generation of global fields of terrestrial biophysical parameters from satellite data. *Journal of Climate*, 9:706–737, 1996*b*.

Serrano, L. S.L. Ustin, D.A. Roberts, J.A. Gamon, and J. Penuelas, Deriving water content of chaparral vegetation from AVIRIS data. *Remote Sensing of Environment,* 74(N3):570–581, 2000.

Steyaert, L.T., T.R. Loveland, W.J. Parton, Land cover characterization and land surface parameterization research. *Ecological Applications*, 7(N1):1–2, 1997.

Townsend, A.R., G.P. Asner, and M.C.C. Bustamante. Unexpected changes in soil phosphorus dynamics following conversion of forest to pasture in humid tropical forests. *Journal of Geophysical Research*, in press.

Ustin, S.L. and Q.-F. Xiao, Mapping of forested ecosystems in interior central Alaska. *International Journal of Remote Sensing,* 22:1779–1797, 2001.

Ustin, S.L., M.O. Smith, and J.B. Adams. Remote Sensing of Ecological Processes: A strategy for Developing Ecological Models Using Spectral Mixture Analysis. In J. Ehlringer and C. Field (Eds.) Scaling Physiological Processes: Leaf to Globe. Academic Press, New York, p.339–357, 1993.

Ustin, S.L., Q.J. Hart, L. Duan, and G. Scheer. Vegetation mapping on hardwood rangelands in Califonia, *International Journal of Remote Sensing*, 17:3015–3036, 1996.

Ustin, S.L., D.A. Roberts, S. Jacquemoud, J. Pinzon, M. Gardner, G. Scheer, C.M. Castaneda, and A. Palácios. Estimating canopy water content of chaparral shrubs using optical methods. *Remote Sensing of Environment,* 65:280–291, 1998.

Veroustraete, F., J. Patyn, and R.B. Myneni, Estimating net ecosystem exchange of carbon using the normalized difference vegetation index and a ecosystem model, *Remote Sensing of Environment*, 58:115–130, 1996.

Vitousek, P.M., J.D. Aber, R.W. Howarth, G.E. Likens, P.A. Matson, D.W. Schindler, W.H. Schlesinger, D.G. Tilman, Human alteration of the global nitrogen cycle: Sources and consequences, *Ecological Applications*, 7(N3):737–750, 1997.

Wilcox, C.H., B.E. Frazier, and S.T. Ball, Relationship between soil organic carbon and Landsat TM data in Eastern Washington. *Photogramm. Eng. and Remote Sens.* 60:777–781, 1994.

Yamada, N. and S. Fujimura, Nondestructive measurement of chlorophyll pigment content in plant leaves from three-color reflectance and transmittance, *Applied Optics.* 30:3964–3973, 1991.

Yin, X., A. Schapendonk, M. Kropff, M. Van Oijen, and P. Bindraban, A generic equation for nitrogen-limited leaf area index and it application in crop growth models for predicting leaf senescence. *Annals of Botany* 85:579–585, 2000.

Yoder, B.J. and R.E. Pettigrew-Crosby, Predicting nitrogen and chlorophyll content and concentrations from reflectance spectra (400-2500 nm) at leaf and canopy scales, *Remote Sensing of Environment.* 53:199–211, 1995.

Zarco-Tejada, P.J. and J.R. Miller. Land Cover Mapping at BOREAS using red edge spectral parameters from CASI imagery. *Journal of Geophysical Research*, Vol. 104, No D22, pp. 27921–27933, 1999.

Zarco-Tejada, P.J., Hyperspectral remote sensing of closed forest canopies: Estimation of chlorophyll fluorescence and pigment content, Ph.D. Dissertation, *Graduate Program in Earth and Space Science*, York University, Toronto, 2000.

Zarco-Tejada, P.J., J.R. Miller, G.H. Mohammed, T.L. Noland and P.H. Sampson, Scaling-up and Model Inversion methods with narrow-band Optical Indices for Chlorophyll Content Estimation in closed Forest Canopies with Hyperspectral Data, *IEEE Transactions on Geoscience and Remote Sensing*, 39(7):1491–1507, 2001.

MAPPING ARID VEGETATION SPECIES DISTRIBUTIONS IN THE WHITE MOUNTAINS, EASTERN CALIFORNIA, USING AVIRIS, TOPOGRAPHY, AND GEOLOGY

C. Van de Ven* and S. B. Weiss**[1]

1. INTRODUCTION

1.1 Problem Statement

Our challenge is to model plant species distributions in complex montane environments using disparate sources of data, including topography, geology, and hyperspectral data. From an ecologist's point of view, species distributions are determined by local environment and disturbance history, while spectral data are "ancillary." However, a remote sensor's perspective says that spectral data provide picture of what vegetation is there, topographic and geologic data are "ancillary." In order to bridge the gap, all available data should be used to get the best possible prediction of species distributions using complex multivariate techniques implemented on a GIS.

Vegetation reflects local climatic and nutrient conditions, both of which can be modeled, allowing predictive mapping of vegetation distributions. Geologic substrate strongly affects chemical, thermal, and physical properties of soils, while climatic conditions are determined by local topography. As elevation increases, precipitation increases and temperature decreases. Aspect, slope, and surrounding topography determine potential insolation, so that south-facing slopes are warmer and north-facing slopes cooler at a given elevation. Topographic position (ridge, slope, canyon, or meadow) and slope angle affect sediment accumulation and soil depth. These factors combine as complex environmental gradients, and underlie many features of plant distributions. AVIRIS data, digital elevation models, digitized geologic maps, and 378 ground control points were used to predictively map species distributions in the central and southern White Mountains, along the western boundary of the Basin and Range province. Minimum Noise Fraction (MNF) bands were calculated from the visible and near-infrared AVIRIS bands, and combined with digitized geologic maps and topographic variables using Canonical Correspondence Analysis (CCA). CCA allows for modeling species "envelopes" in multidimensional environmental space, which can then be projected across entire landscapes.

1.2 Setting

The location for this study is the White Mountains, east of, and within the rain shadow of, the Sierra Nevada (see Figure 1). Elevation ranges from 1220 m in adjacent Owens Valley to 4330 m at White Mountain Peak. Geologic substrates include granitoids, metavolcanics, quartzites, argillites, phyllites, limestones, and dolomites. Vegetation includes desert shrubs, pinyon-juniper woodland, sagebrush meadows, subalpine bristlecone-limber pine forests, and alpine fell fields (Mooney 1973; Hall 1993).

[1] *Dept. of Geological and Environmental Sciences, Stanford University, Palo Alto, California; vandeven@pangea.stanford.edu
** Creekside Center for Earth Observations, Menlo Park, California 94025; StuBWeiss@netscape.net

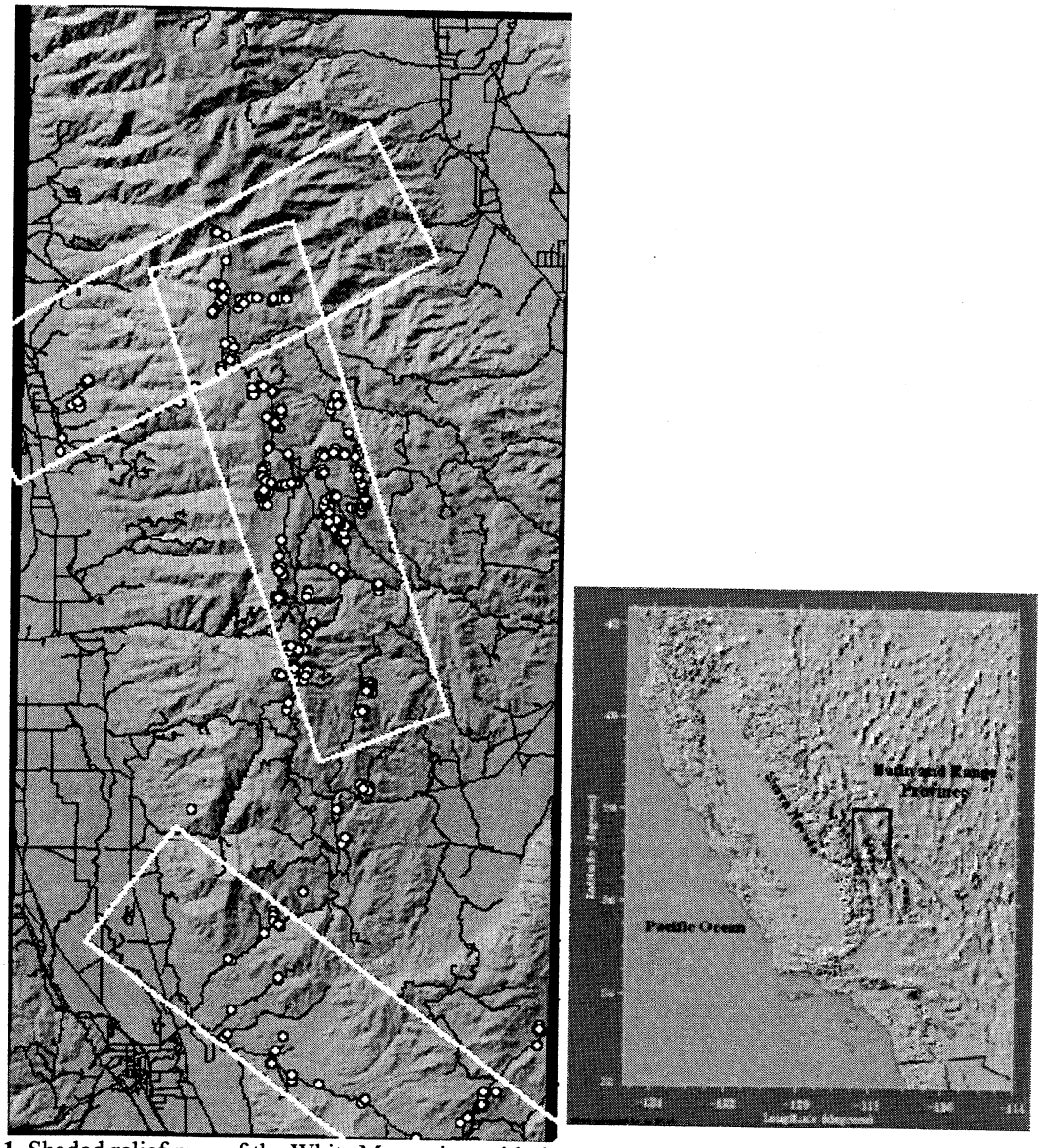

Figure 1. Shaded relief map of the White Mountains, with three October, 1996 AVIRIS flightlines (white boxes), roads and trails (black lines), and vegetation sites (white dots).

2. METHODS

2.1 Canonical Correspondence Analysis

Canonical Correspondence Analysis (CCA) is a direct gradient ordination that relates site/species and site/environment matrices (ter Braak 1998). It extracts synthetic axes that are linear combinations of environmental variables, indicated by bold names (topographic position, insolation, elevation, slope, and rock types – granite, quartzite, limestone, and dolomite) and numbers for MNF bands in Figure 1, that maximize separation of species and sites. Environmental variables were chosen by forward selection with Monte-Carlo significance tests. Six axes were extracted from 21 input variables. Each species has a centroid and tolerance (standard deviation) on each axis that defines its distribution envelope in canonical space as a multi-dimensional ellipsoid known as a species envelope whose centroids are indicated by abbreviated species' names in Figure 2. Maps of all six CCA axes were produced (four are shown in Figure 3). Statistical distances of each pixel to species centroid in six-dimensional

canonical space were calculated. Results were expressed in standard deviation units - closer to the centroid means higher probability of occurrence, and beyond three standard deviations was taken as absence. Axes maps show the spatial realization of the linear combinations of environmental variables. Each cell has six axis values that are then used to determine whether that cell falls into environmental envelopes of selected species based on the species' centroids and tolerances in six-dimensional canonical space.

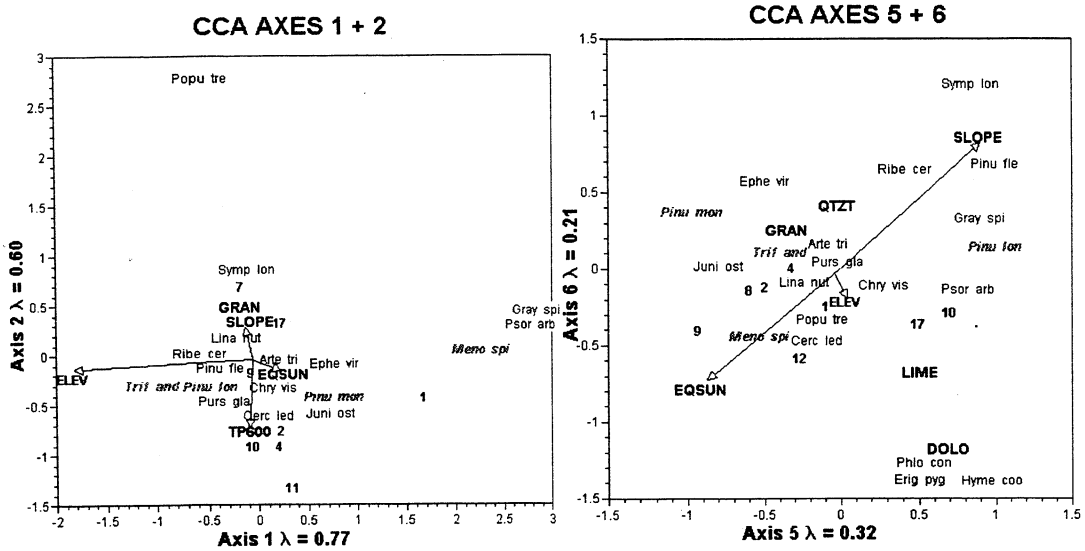

Figure 2 Left: Axis 1 is the long elevational gradient, running from desert shrubs on the right, to pinyon-juniper woodlands near the center, to subalpine bristlecone-limber pine forests, and alpine fell-fields to the left. Elevation is modified by EQsun; higher insolation lowers the effective elevation. Axis 2 is dominated by MNFs 11, 10, 4, 2, 7, and TP600 (topographic position) and strongly separates aspen (Popu tre) at the top of the diagram. Italicized, bold species are mapped in Figure 2. The eigenvalue (λ) for each axis is given next to the axis title.
Right: Axes 5 and 6 illustrate strong topographic effects (slope and EQsun) and geologic factors (the gradient from dolomite, limestone, through granitoid/quartzite). Lower eigenvalues for these axes indicate that fewer species (toward the edges of the diagram) are effectively separated, and gradients are relatively short. Three dolomite restricted herb species are shown lower right. MNF scores are more difficult to interpret, but their spread along these axes show that they add significant information to the axes.

2.2 CCA Methods

Axes and species parameters were derived from 202 calibration plots. 146 plots were used to evaluate presence/absence of 17 species. Projections were smoothed by 3x3 cell moving average (to account for registration errors between the different environmental and spectral grids). Kappa statistics were calculated for each species. Kappa is the relative increase in correct assignments over that expected by chance. A threshold standard deviation was chosen to maximize kappa.

Figure 4 shows the predicted distributions of four selected species overlain on the hillshaded DEM Because MNF bands derived from the AVIRIS data were included as variables, species predictions could only be made within the three flightlines. Darker red indicates a higher probability of occurrence (closer to the centroid of the species envelope). The predicted species distributions includes details beyond simple elevation limits or geologic affinities, but incorporates environmental, geologic, and spectral constraints derived from all the input variables.

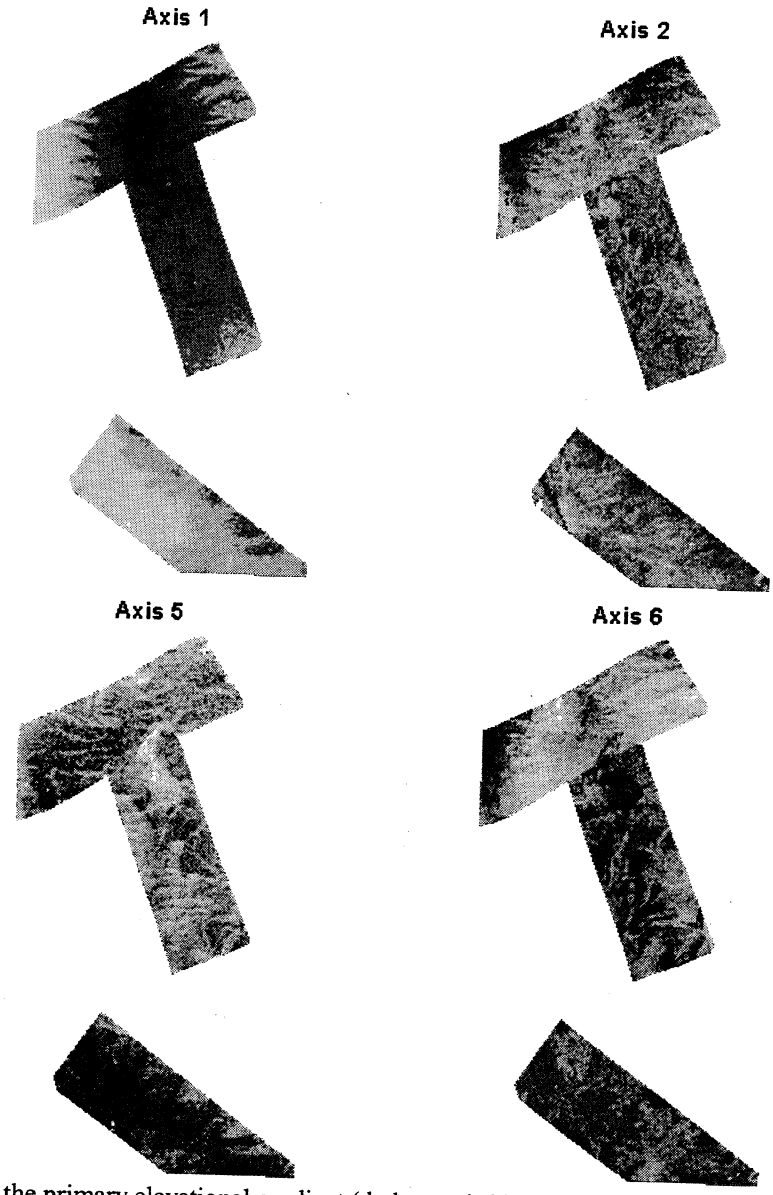

Figure 3: Axis 1 is the primary elevational gradient (dark gray is higher elevation), but the finer-scale variations include differences between the north and south sides of canyons. Axis 2 is more difficult to interpret, but is effective in separating out aspens. Axes 5 and 6 have large geologic components -- dolomite shows up particularly strong on Axis 6 as darker lighter gray at mid-elevations. Each cell has 6 axis values that are then used to determine whether that cell falls into environmental envelopes of selected species based on the species' centroids and tolerances in six-dimensional canonical space.

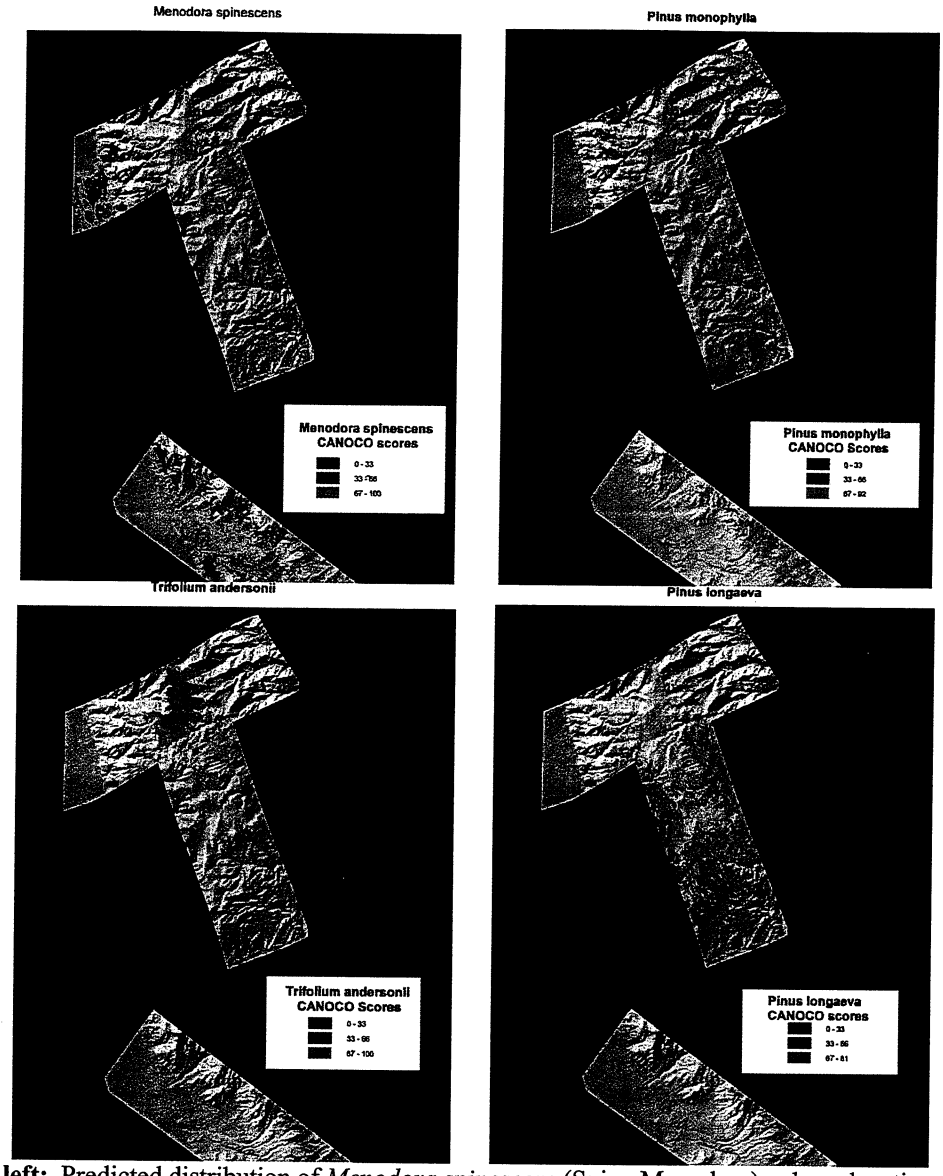

Figure 4 Top left: Predicted distribution of *Menodora spinescens* (Spiny Menodora), a low elevation desert shrub. *Menodora spinescens* occupies south-facing slopes at its extreme upper range limit (2300 m), all aspects at mid-elevations (1600-2000 m), and north-facing slopes at lower range limits (1300 m). The species has no obvious association with geology,

Top right: Predicted distribution of *Pinus monophylla* (Pinyon Pine) the lower timberline tree in the White Mountains. *Pinus monophylla* occupies south-facing slopes at its extreme upper range limit (3100 m), all aspects at mid-elevations (2300-2600 m), and north-facing slopes at lower range limits (1800 m). It also avoids dolomite, even in the middle of its elevation range.

Bottom left: Predicted distribution of *Trifolium andersonii* (Mono Clover), a common herb in the alpine-fell fields above timberline. *Trifolium andersonii* occupies south-facing slopes at its extreme upper range limit (4000 m), all aspects at mid-elevations (3700-3900 m), and north-facing slopes at lower range limits (3600 m). It has a preference for flat areas, and strongly avoids dolomite.

Bottom right: Predicted distribution of *Pinus longaeva* (Bristlecone Pine), the upper timberline tree and the most famous species from the mountain range. *Pinus longaeva* occupies south-facing slopes at its extreme upper range limit (3600 m), all aspects at mid-elevations (3100-3400 m), and north-facing slopes at lower range limits (2900 m). Bristlecone pine is found on all geologic substrates, contrary to the common perception of a tight association with dolomite.

3. EVALUATION AND RESULTS

Each species map can be considered a testable hypothesis, and the 146 evaluation plots provide an initial test. Our main evaluation criterion is the kappa statistic. As shown in Table 1, evaluation kappa ranged from 0.81 (a very good fit) for *Pinus monophylla* to 0.09 for *Purshia glandulosa*. Five of seventeen species models produced kappa > 0.60, a very satisfying value (Guisan et al. 1999). Five more were between 0.4 and 0.6, a moderate improvement over random. Seven species models produced poor fits (<0.40).

Table 1

Species	MaxKappa	Threshold	Absence	Presence	ProdAcc	UserAcc	OverallAcc
Pinus monophylla	0.81	87	136	10	0.7	1	0.98
Juniperus osteosperma	0.75	100	135	11	0.73	0.73	0.96
Trifolium andersonii	0.74	100	116	30	0.67	0.95	0.92
Pinus longaeva	0.72	81	123	23	0.78	0.75	0.92
Psorothamnus arborescens	0.67	100	126	20	0.6	0.86	0.93
Cercocarpus ledifolius	0.42	82	130	16	0.5	0.47	0.88
Pinus flexilis	0.41	93	127	19	0.79	0.38	0.81
Artemesia tridentate	0.41	100	37	109	0.72	0.91	0.73
Grayia spinosa	0.40	99	128	18	0.28	1	0.91
Linanthus nuttallii	0.40	69	108	38	0.5	0.59	0.78
Menodora spinescens	0.36	96	126	20	0.3	0.67	0.88
Ephedra viridis	0.35	79	127	19	0.47	0.41	0.84
Populus tremuloides	0.31	86	142	4	0.5	0.25	0.95
Symphoricarpos longiflorus	0.25	70	139	7	0.43	0.23	0.9
Chrythamnus viscidflorus	0.25	93	60	86	0.73	0.68	0.64
Ribes cereum	0.20	89	119	27	0.78	0.32	0.65
Purshia glandulosa	0.09	100	135	11	0.64	0.12	0.63

The species with good fits include 3 trees, 1 desert shrub, and 1 alpine herb. Species with well-defined environmental envelopes, and/or a well-defined spectral signature such as trees are naturally easier to model with these methods. Many of the poorer fits include shrub species that are disturbance-dependent (i.e. *Chrysothamnus viscidiflorus*), wide environmental tolerances (i.e. *Artemesia tridentata*), or have few occurrences for calibration and evaluation (i.e. *Populus tremuloides*). The quality of the models and evaluation data are strongly dependent on having many presences among the sample points.

Evaluation data provided an independent measure of fit (kappa). High evaluation kappas (>0.60) were obtained for 5/17 sample species, moderate kappas (0.4-0.6) were obtained for another 5 species, and the remaining 7 species with poor fits tended to be disturbance dependent or relatively rare. Combining hyperspectral imagery, topography, geology, and field data provide a powerful tool for understanding the major factors determining the distributions of specific plants in the arid White Mountains, but finding the correct method for effectively combining the data remains a research challenge.

The producer, user, and overall accuracies are strongly weighted by absence of species, and are misleadingly high. Kappa weights both omission and commission errors, and is a better-integrated measure of model success (or failure), and therefore is our primary evaluation criterion.

More than 60 species were abundant enough to model (> 2 sites present), but many had very few occurrences for both calibration and evaluation. For these species, any projected distribution is, at best, a broad hypothesis. Full evaluation of all species where it is appropriate is presently underway, and collection of more evaluation (and calibration) data is a priority for the upcoming field season.

4. DISCUSSION

The inclusion of topographic factors was effective in determining the fundamental temperature/moisture gradient. All species occupy proper elevational ranges, and major features of their microdistributions are captured. CCA Axis 1(the strongest axis) is primarily elevation but is influenced by insolation. Each additional MJ/m^2 of potential March 21 (equinox) insolation added approximately 30 meters to the effective elevation - the full range of insolation values from a steep north-facing slope to a steep south-facing slope (15 MJ/m^2) produces about a 500 m equivalent shift in elevation. Other topographic factors create more subtle patterns, but several species demonstrate distinct preferences for flats, steep slopes, canyons or ridgetops. However, many species depend on topographic features well below the resolution of the DEM, such as small depressions or rocky outcrops.

Geologic factors were important for many species. Some site-specific errors could be attributed to geology not digitized at a fine enough scale. Many of the formations and members described as quartzite for the purposes of this study actually contain distinct members, layers, or lenses of carbonates. These carbonate lenses frequently support very different vegetation than the surrounding clastic rocks, but are generally too small to appear on geologic maps, or, if mapped, were too numerous and discontinuous to be digitized separately. For example, the Wyman Formation contains significant carbonate layers, but was grouped with the quartzite units due to the greater proportion of that rock type. Many *Cercocarpus ledifolius* (Mountain Mahogany) sites in the Wyman Formation were actually on limestone lenses, surrounded by sagebrush-covered quartzites.

AVIRIS data (MNF bands) were highly significant in the CCA ordination for most of the tree species, and apparently contributed to species models, but were difficult to interpret except by visual inspection. Because the AVIRIS data was obtained in October, most of the vegetation had senesced. However, the tree species were still green, helping distinguish forested from unforested areas, although not perfectly due to topographic shading and spectral similiarity to green riparian grasses. One of the challenges in mapping mature bristlecone pine groves was the wide spacing between trees with minimal foliage on individual trees, making spectral identification of areas such as the Patriarch Grove (3500 m) difficult. While MNF data with environmental variables improved prediction of tree species, it did not improve the prediction of other species, and, in a few cases of low elevation shrubs (*Ephedra viridis* and *Menodora spinescens*) seemed to hinder accurate predictions. Low elevation shrubs grow sparsely on a variety of rock types, and, at the time of the AVIRIS imagery, was very dry, resulting in little vegetative cover to be detected within a 20 m pixel. Conversely, trees are considerably larger, frequently dense, and had a healthy vegetative spectral signature to be detected within the imagery.

The MNF data improved the predictions for four of six tree species (*Cercocarpus ledifolius*, *Juniperus osteosperma*, *Pinus longaeva*, and *Pinus flexilis*), and did slightly worse for *Populus tremuloides* and *Pinus monophylla*. The addition of the AVIRIS spectral (MNF) data did not significantly improve the prediction of shrub or herb species, and seemed to do particularly poorly for low elevation species. It is likely that the tree species were large enough, dense enough, and green enough to comprise spectrally distinct pixels from the smaller, drier shrub and herb dominated communities. *Populus tremuloides*, whose prediction was slightly worse with the addition of MNF data, was found in few sites, and may have been in different stages of senescing at different elevations. The low elevation shrubs did particularly poorly with the MNF data likely due to the fact that by October, when the AVIRIS data was obtained, the low elevation shrubs were completely dried and are sparsely distributed. Hence, the AVIRIS data primarily sees the geology at low elevations, rather than the vegetation. Inclusion of June 2000 AVIRIS flightlines may provide a better test of hyperspectral data inputs.

Using all three data sources (DEM derived products, AVIRIS data products, and digitized geologic maps) proved challenging, as registration accuracy becomes important. Some degree of data-smoothing was necessary - our predictions are at a scale of 90 meters (3x3 pixel window). Input data, especially AVIRIS MNF bands, may need to be smoothed as well to account for registration errors. At a broader scale, the obvious boundary on the MNF8 map corresponds to the flightline boundary, so stitching together scenes (even those taken within minutes of each other) may introduce artifacts.

5. CONCLUSIONS

Combinations of topographic, geologic, and hyperspectral data can provide good models for some individual species. Other species are more difficult to model; they are disturbance dependent, influenced by fine-scale or other unmapped ecological factors, or are not spectrally apparent (senescent in October or characteristically sparse cover).

These species-specific models go beyond coarse vegetation "communities" that can be determined from spectral data alone. Each type of data provides unique information. Spectrally similar species (i.e. pines) can be separated by elevation and geology; species at similar elevations may be separated by spectral data.

Predictions can be made for species with low cover. Spectral data alone can only map communities or large, "macroflora," while predictions can be made for nearly all species noted in field data based on non-spectral environmental variables. Each species projection is a testable hypothesis and may lead to insights into environmental controls on distribution, even in the absence of a high kappa values.

Topographic and geologic factors can be interpreted ecologically. Some MNFs can be interpreted, but many cannot due to incorporation of many visible (brightness or relief) and non-visible factors (water vapor or vegetation health).

6. NEXT STEPS

Mapping species distributions in complex mountain ranges is an inherently difficult problem. Many combinations of input data and analyses are possible. The MNF transformation may not be the ideal way to incorporate AVIRIS data. Spectral indices that relate directly to known features of vegetation (i.e. red-edge), or even standardized raw bands at key wavelengths may be more appropriate (and interpretable) spectral inputs. Because October is not an ideal month for vegetation (many species are senescent), the June 2000 AVIRIS data may provide better spectral information. AVIRIS flightlines are only 9 km wide but contain 224 spectral bands. Other imagery may also be used; LANDSAT images have coverage of entire range in different seasons, but only with seven spectral bands.

Further evaluation methods include black and white Digital Orthophoto Quads (DOQs) for broad-scale evaluation of tree cover. More field evaluation plots, especially where there are "interesting predictions," will allow for inclusion of more data into the calibration data set while still maintaining sufficient points for evaluation.

We have explored only one statistical method in this poster -- the use of CCA. There are many options within CCA itself. For example, running the ordinations with presence/absence data may provide a different picture (especially on higher order axes) because abundant species are downweighted. Species-specific General Linear Models (GLMs, Guisan et al. 1999), General Additive Models (GAMs), Regression Trees, Neural Networks, and other modeling techniques can be applied to this data set.

End member spectral classifications appear to work well for some species/communities (Van de Ven et al. 2000a and b), but inclusion of elevation/insolation (i.e. CCA Axis 1) as an input "band" may allow for a better representation of broad cover-types.

These sorts of analyses can be used to help understand implications for climate change on vegetation. Elevation and insolation, primary determinants of local temperature, are important variables in mapping present vegetation. For example, a 3 degree C rise in temperature is the equivalent of 500 meters elevation. Species may shift their elevation ranges, but the fine-scale patterns determined by insolation, slope, topographic position, and geology will still operate.

7. ACKNOWLEDGEMENTS

We gratefully acknowledge support from the White Mountain Research Station, Stanford University (McGee grant), NASA (grant NAG5-4888), Texaco (Exploration Technology and Production Dept.), the White Mountain Groupies, W. G. Ernst, R. J. P. Lyon, and the White Mountain Research Station chefs and staff.

8. LITERATURE CITED

Ernst, W. G., C. A. Nelson, and C. A. Hall, 1993, "Geology and metamorphic mineral assemblages of Precambrian and Cambrian rocks of the central White-Inyo Range, Eastern California," Map Sheet 46, California Division of Mines and Geology, Sacramento, California.

Guisan, A., S. B. Weiss, A. D. Weiss.1999, "GLM versus CCA spatial modeling of plant species distribution," Plant Ecology, vol. 143, pp. 107-122.

Hall, C. A. (ed.), 1991, Natural History of the White-Inyo range, Univ. of California Press, Berkeley, California.

Mooney, H. A. 1973, "Plant communities and vegetation," in Lloyd, R.M., and R.S. Mitchell (eds.), Flora of the White Mountains, California and Nevada, Univ. of California Press, Berkeley, California, pp. 7-18.

ter Braak, C. J. F., 1996, CANOCO 4 Users Manual, Waginegen Press, Netherlands.

Van de Ven, C. M., W. G. Ernst, and R. J. P. Lyon, 2000a, "Relationships between the geologic substrate and vegetation in the White-Inyo Mountains, Eastern California as determined from AVIRIS and field data," Proceedings of the Fourteenth International Conference Applied Geologic Remote Sensing, Veridian ERIM International, Ann Arbor, Michigan, pp. 36-43.

Van de Ven, C. M., W. G. Ernst, and R. J. P. Lyon, 2000b, "Analysis of the relationships between geologic substrate and vegetation in the White-Inyo Mountains, Eastern California," Proceedings of the Ninth JPL Airborne Earth Science Workshop, JPL Publication 00-18, Jet Propulsion Laboratory, Pasadena, California. Also available at http://www.makalu.jpl.nasa.gov/docs/workshops/toc.htm Last accessed November 2001.

ANALYSIS OF SUB-PIXEL MIXING IN HIGH-ALTITUDE AVIRIS DATA OVER VIRGINIA CITY, NEVADA, USING SYSTEMATIC FIELD-BASED OBSERVATIONS

R. Greg Vaughan, Wendy M. Calvin and James V. Taranik [1]

1. Introduction

In 1995 AVIRIS data were acquired over Virginia City, Nevada at a 20-km altitude above sea level. The average elevation of the scene is about 2 km, so the resultant size of a pixel is 18 x 18 m^2 - about the size of a tennis court. One of the important questions to ask about such remote sensing data is how the effects of sub-pixel scale mixing will affect the ability to create an accurate mineral map. Pixel-scale mineralogic heterogeneity results in a spectrum that is a function of all the different materials that make up that pixel. Additionally, heterogeneity at the hand-sample scale can be recognized with field spectrometer analyses in the field or in the laboratory. This report describes methods used for the systematic sampling of a field site and the results of modeling the spectra of a heterogeneous area with linear mixtures of measured end-member spectra.

2. Study Area and Data Set

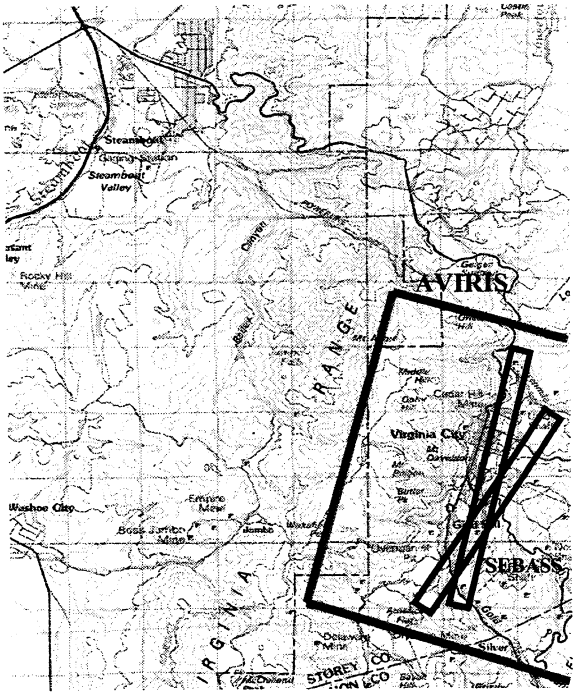

Figure 1. Location and data coverage.

Virginia City, Nevada is located on the east flank of the Virginia Range about 30 km southeast of Reno, Nevada (figure 1). Within the Virginia Range precious metal mineralization is associated with hydrothermal alteration of Tertiary volcanic and intrusive rocks. Virginia City, home of the historic Comstock Mining District and a source of Au, Ag and Hg since the 1850's, has been the focus of many geologic and remote sensing studies (Thompson and White, 1964; Whitebread and Hoover, 1968; Hudson, 1983; Hutsinpillar and Taranik, 1988; Vickre, 1998). As a result of ancient acid-sulfate style hydrothermal alteration, surface rocks now exhibit widespread propylitization, extensive bleaching, iron staining, kaolinitization, and alunitization.

High-altitude AVIRIS data were acquired over Virginia City in a group shoot in September 1995 (Kruse and Huntington, 1996). AVIRIS is an airborne imaging spectrometer that acquires data in 224 continuous spectral bands between 0.38 and 2.5 μm with a 10-nm spectral resolution. It uses a whiskbroom scanner with a FOV of 33° and an IFOV of 1 mrad, resulting in a swath of about 10.5 km (614 pixels) and a spatial resolution of 20 m when flown on the ER-2 platform at 20 km (Vane et al., 1993). Figure 1 shows the extent of the AVIRIS coverage.

1- Arthur Brant Laboratory for Exploration Geophysics, Mackay School of Mines, University of Nevada, Reno, (vaughan@mines.unr.edu)

3. Field Methods

The specific field area was chosen based on preliminary analysis of the AVIRIS data. Near the center of the image, just south of the Virginia City town site, there is an easily identifiable landmark: Wheeler Reservoir. Comparing the AVIRIS image to a Digital Orthophotoquad (DOQ) image with 1-m spatial resolution, it appears that the southwest corner of the reservoir is very nearly coincident with the corner of an AVIRIS pixel. Figure 2 shows a subset of the AVIRIS image and a DOQ of the same area.

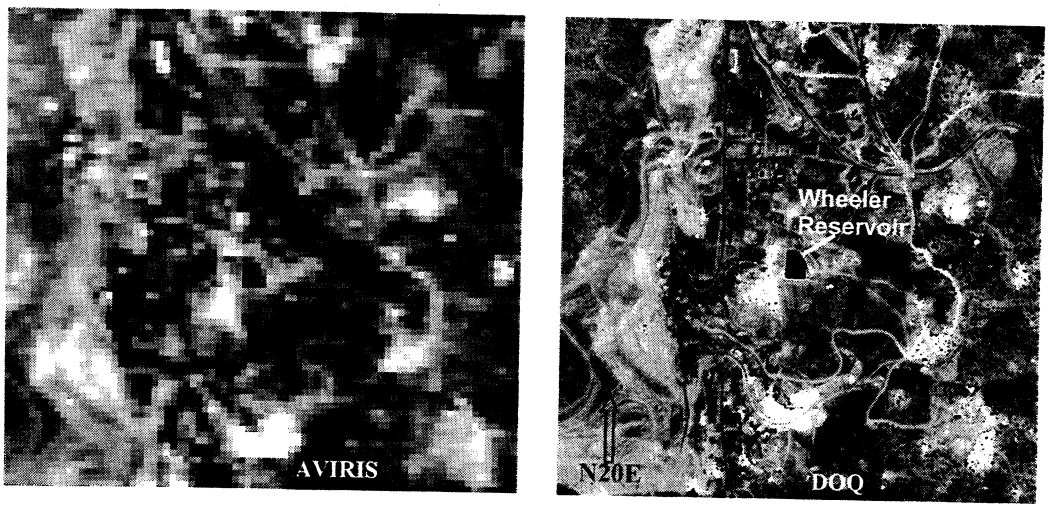

Figure 2. Comparison of spatial resolutions for AVIRIS (18-m) and DOQ (1-m). The SW corner of Wheeler Reservoir is coincident with the corner of an AVIRIS pixel.

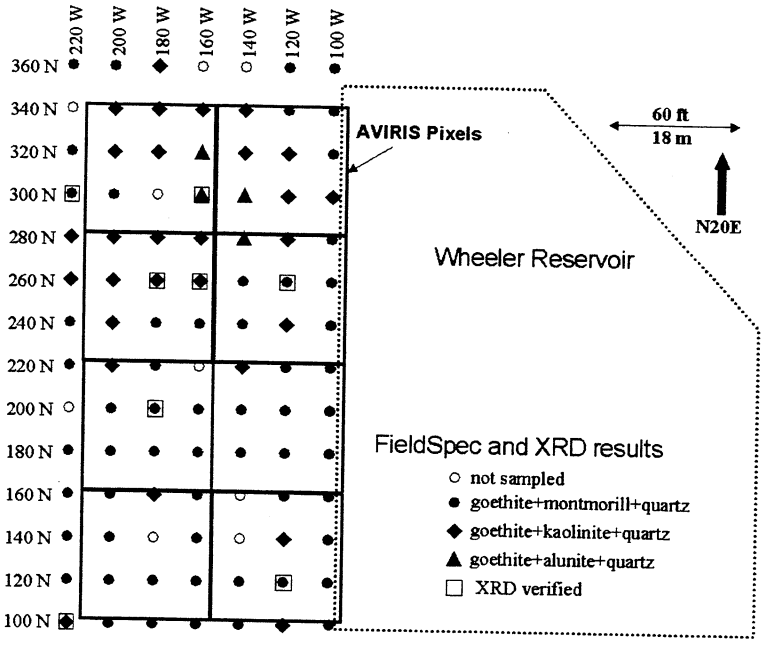

Figure 3. Diagram of field site with location of AVIRIS pixels, Wheeler Reservoir, and sample locations. Sample mineralogy identified with field spectrometer and XRD analyses are indicated with symbols.

In addition, the AVIRIS flight line is oriented in a N20E direction, parallel to the long dimension of the rectangular reservoir. Thus, the west edge of the reservoir coincides with the edges of 4 AVIRIS pixels. Figure 3 is a diagram of the field site indicating where AVIRIS pixels are relative to landmarks. In reality the pixels along the west side of the reservoir may receive some component of reflected radiance from the water. Starting at the southwest corner of the reservoir, using the west edge as a baseline, a grid was established with a 6-m (20-ft) spacing between stations (see figure 3). Surface samples were taken at each grid station over an area that evenly covered approximately 2600 m^2 (8 AVIRIS pixels), and the surface features were mapped in detail. 90 samples were taken and analyzed under laboratory conditions with an ASD field spectrometer for mineral identification. Samples that were identified as being representative of a unique surface cover type were analyzed with X-ray diffraction for verification of mineral identification. For each sample discussed here, XRD analyses agree with the field spectrometer mineral identification. Systematic mapping and sampling of the subset area provides a quantitative way of estimating the percentage that each unique surface cover class should contribute to a single AVIRIS pixel.

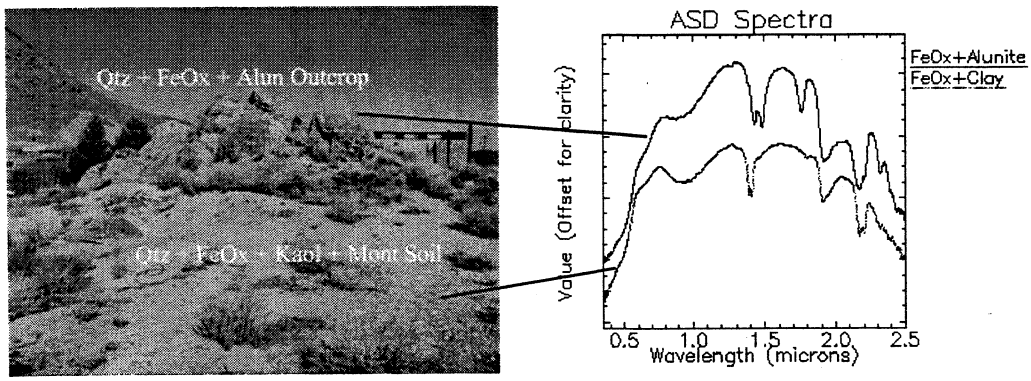

Figure 4. Spectra of selected field locations measured with ASD field spectrometer.

4. Image Processing

The raw AVIRIS data were calibrated to apparent reflectance using ATREM (ATmospheric REMoval program) and EFFORT (Empirical Flat Field Optimal Reflectance Transformation). ATREM is designed to retrieve "scaled surface reflectance" from hyperspectral image data. It uses an approximate atmospheric radiative modeling technique and corrects for scattering and absorption of atmospheric aerosols and gasses (H_2O, CO_2, O_3, NO, CO, CH_4, O_2). EFFORT is a routine that removes residual atmospheric and instrument artifacts from the apparent reflectance data. Numerous trial-and-error experimentation with the EFFORT routine suggests that if this smoothing algorithm is applied to the entire wavelength range together, some mineralogic spectral information is lost. Therefore, prior to applying the EFFORT transformation, certain wavelength regions are isolated to lessen the degradation of mineralogic absorption features. Extracting AVIRIS bands 1-29, 33-96 and 99-224 (0.383-0.657 μm, 0.663-1.268 μm and 1.273-2.509 μm, respectively) for the EFFORT transformation also eliminates the overlapping wavelengths between spectrometers inherent to the 1995 AVIRIS data sets. Finally, for the linear mixes, AVIRIS spectra are scaled to match the reflectance values of the sample spectra measured with the field spectrometer.

5. Linear Mixing

Natural surfaces are rarely composed of a single uniform material. Spectral mixing occurs when materials with distinct spectral properties are present within a certain area. Mineralogic heterogeneity can be present at many scales. At the scale of a tennis-court-sized AVIRIS pixel (18x18 m^2) different materials can be distributed over the area in a linear fashion, where each material can be examined

macroscopically, and a percentage contribution determined. At a microscopic scale mixing is more intimate, and can not be modeled as truly linear. However, such small-scale non-linear mixing tends to be a second order effect and linear unmixing techniques appear to work well for approximating spectrally mixed areas (Boardman and Kruse, 1994).

5.1 Micro-Scale Mixing

Sample #300-160 was taken from an outcrop of quartz-alunite in the northern part of the study area. The ASD-measured reflectance for this sample is shown in figure 4 (upper spectrum) and figure 5 (solid line). The sharp 1.76 and 2.32 μm absorption features, the broad 2.15 μm feature, and the doublet feature centered around 1.45 μm are all characteristic of alunite. In addition, the spectral structure between 0.5 and 1.0 μm is indicative of an iron oxide phase (goethite), and the 1.92 μm feature indicates the presence of a clay mineral (montmorillonite), or possibly adsorbed water on the sample.

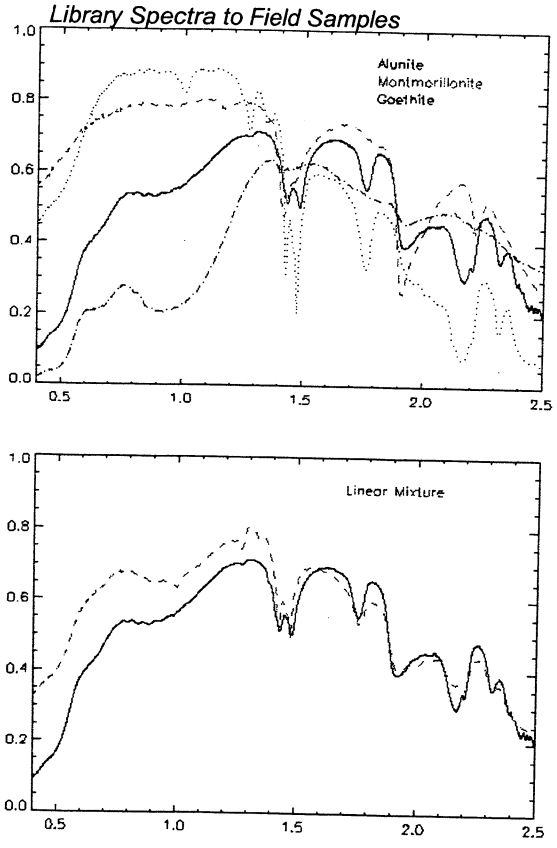

Figure 5. Weighted linear mixture of USGS library alunite (dotted), montmorillonite (dashed), and goethite (dash-dot) compared to ASD-measured spectra (solid line) for quartz + alunite field sample.

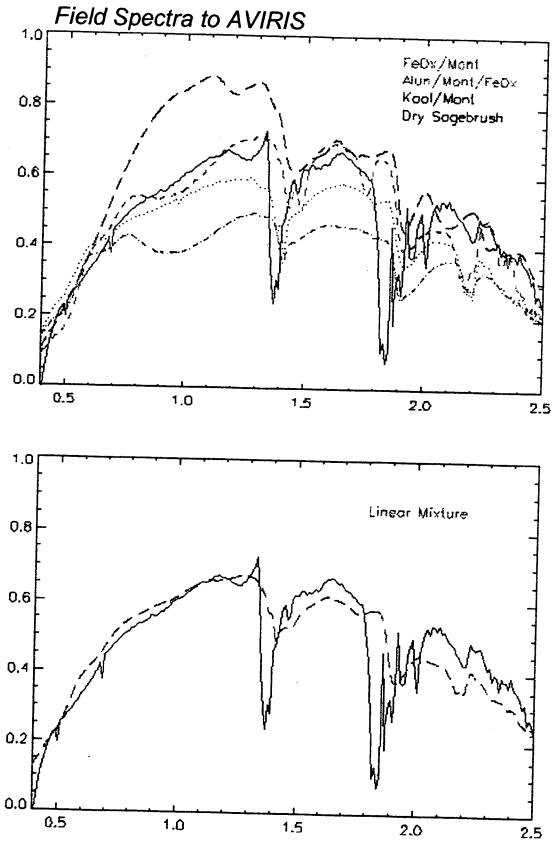

Figure 6. Weighted linear mixture of ASD-measured spectra of field samples FeOx/Mont (dash-dot), Alun/Mont/FeOx (dashed), Kaol/Mont (dotted), and USGS library dry sagebrush (long dashes) compared to AVIRIS spectrum for a single pixel (solid line).

Figure 5 shows 2 plots with the ASD-measured spectrum for this sample as a solid line. The upper plot also shows mineral end-member spectra extracted from the USGS spectral library for alunite, montmorillonite and goethite. The lower plot shows that a weighted, linear mix of these library spectra reproduces the ASD-measured spectrum very well. Band positions, shapes, and relative band depths match particularly well throughout the wavelength range. The only place the mixture doesn't match well is in absolute reflectance values at shorter wavelengths (below 1.5 μm).

5.2 Macro-Scale Mixing

The quartz-alunite outcrop is apparently divided by 2 AVIRIS pixels and spatially only covers about 15% of each. For one of the pixels that contains this outcrop (the one not bordered by the reservoir), a scaled linear mixture of measured spectra of samples from that pixel, yields a spectrum that fits the EFFORT-corrected AVIRIS spectrum for that pixel. Figure 6 shows 2 plots with the EFFORT-corrected AVIRIS spectra displayed as a solid line. The upper plot shows measured spectra of 3 rock samples from within the pixel and a spectrum for dry sagebrush extracted from the USGS spectral library. The lower plot shows a scaled, linear combination of these spectra (dashed line). The best match is produced by assigning weights to the "end-member" spectra in the mix, based on field mapping estimates of the percentage cover for each surface material. Approximately 40% of the pixel is covered with clay-rich (kaolinite + montmorillonite) gravel, 15% is iron oxide and clay-rich soil, 15% is oxidized quartz-alunite outcrop and 30% is covered with vegetation. In September, when the AVIRIS data were acquired, the vegetation was likely very dry, thus, it is important to include this component of the area because even sparse presence of dry vegetation can have a significant effect on the spectrum, particularly in the steepness of the spectral structure between 0.5 and 1.0 μm and in the suppression of the band depth of the 2.2 μm feature.

6. Conclusions and Future Directions

Linear mixing of library spectra appears to be successful in reproducing spectra measured of field samples particularly in matching band position, depth, and shape. Deviation in absolute reflectance at lower wavelengths (less than 1.5 μm) suggests a need for an intimate mixture model to account for albedo differences. At the scale of an AVIRIS pixel, linear mixing of spectra measured of field samples from within that pixel is successful in reproducing the EFFORT-corrected AVIRIS spectrum for that pixel. Weighting the sample spectra based on their fractional abundance mapped in the field and including the percentage of vegetation cover is important for producing the best matching result.

There are limitations to producing linear mixtures that accurately identify the contents of a pixel. The presence of at least 30% dry vegetation appears to degrade the spectral structure between 0.5 and 1.0 μm diminishing the ability of high-altitude AVIRIS to identify iron oxides. In addition, a notable outcrop like one composed of quartz-alunite mineralization will not contribute significantly to the spectra if the spatial extent is less than about 15% of the pixel. Low-altitude AVIRIS data, with finer spatial resolution, should be able to resolve such smaller features.

In the future, identification of sulfate minerals like alunite may be enhanced by the use of high-resolution hyperspectral thermal infrared (TIR) data in conjunction with hyperspectral VNIR/SWIR data. Sulfate minerals have abundant spectral absorption features throughout the VNIR/SWIR and TIR wavelength ranges. These features are diagnostic and exhibit measurable variations such as band shifts with cation substitution allowing for species identification. However, in the SWIR region, some non-uniqueness is introduced due to the overlap between the diagnostic spectral features of sulfates with those of clay minerals. In the TIR region, emissivity minima of sulfate and clay minerals are clearly separated in wavelength, and can be uniquely identified. The high spectral resolution images provided by AVIRIS and the Spatially Enhanced Broadband Array Spectrograph System (SEBASS) could be used as complementary data sets for the unambiguous identification of sulfates, clays and silicates.

7. References

Boardman, J.W. and F.A. Kruse, 1994, "Automated Spectral Analysis: A Geologic Example Using AVIRIS Data, North Grapevine Mountains, Nevada", in Proceedings, 10th Thematic Conference on Geologic Remote Sensing, Environ. Inst. of Michigan, Ann Arbor, MI, pp. I-407 - I-418.

Hudson, D.M., 1983, *Alteration and Geochemical Characteristics of the Upper Parts of Selected Porphyry Systems, Western Nevada*, Ph.D. Dissertation, Department of Geological Sciences, Univ. of Nevada Reno, 1983.

Hutsinpiller, A. and J.V. Taranik, 1988, "Spectral Signatures of Hydrothermal Alteration at Virginia City, Nevada, Bulk Mineable Precious Metal Deposits of the Western United States," Symposium Proceedings, GSN, Ed. Robert W. Schafer.

Kruse, F.A. and J.F. Huntington, 1996, "The 1995 AVIRIS Geology Group Shoot", AVIRIS 1996 Airborne Geoscience Workshop Proceedings, JPL, Pasadena, California.

Thompson, G.A. and D.E. White, "Regional Geology of the Steamboat Springs Area, Washoe County, Nevada," USGS Professional Paper 458-A, 52 p, 1964.

Vane, G., R.O. Green, T.G. Chrien, H.T. Enmark, E.G. Hansen and W.M. Porter, 1993, "The Airborne Visible/Infrared Imaging Spectrometer (AVIRIS)", Rem. Sens. Environ., v. 44, pp. 127-143.

Vikre, P.G., "Quartz-Alunite Alteration in the Western Part of the Virginia Range, Washoe and Storey Counties, Nevada," *Economic Geology*, Vol. 93, pp. 338-346, 1998.

Whitebread, D.H. and D.B. Hoover, 1968, "Preliminary Results of Geological, Geochemical, and Geophysical Studies in Part of the Virginia City Quadrangle, Nevada," USGS Circular 596, 20 p.

MAPPING MINERALS AT THE COPPER FLAT PORPHYRY, NEW MEXICO, USING AVIRIS DATA

Charles S. Verdel,[1] Daniel Knepper, Jr.,[2] K. Eric Livo,[2] Virginia T. McLemore,[3] Brian Penn,[4] and Randy Keller[5]

ABSTRACT

The Copper Flat porphyry is a Laramide copper deposit in southwest New Mexico. High-altitude AVIRIS data were acquired over the site in 1998. Limonite minerals, carbonates, some phyllosilicates, epidote, gypsum, and tremolite/talc have been preliminarily mapped based on AVIRIS data. The results indicate a fairly regular zonation of hydrothermal alteration minerals around the porphyry that is consistent with classic models of alteration from porphyry copper deposits. Verification of the preliminary results is on-going. X-ray diffraction analyses and laboratory spectral analyses will be performed on samples from the area in order to confirm the results of mineral mapping.

1.0 INTRODUCTION

The Hillsboro mining district is located in the Animas Mountains in Sierra County, New Mexico, approximately 180 miles south of Albuquerque (Figure 1). The district lies on the eastern edge of the Laramide Arizona-Sonora-New Mexico porphyry-copper belt. The district contains six types of mineral deposits: the Copper Flat porphyry, polymetallic fissure veins that radiate from the porphyry, carbonate replacement deposits, weakly mineralized skarn deposits, jasperoids, and placer gold deposits derived from the fissure veins.

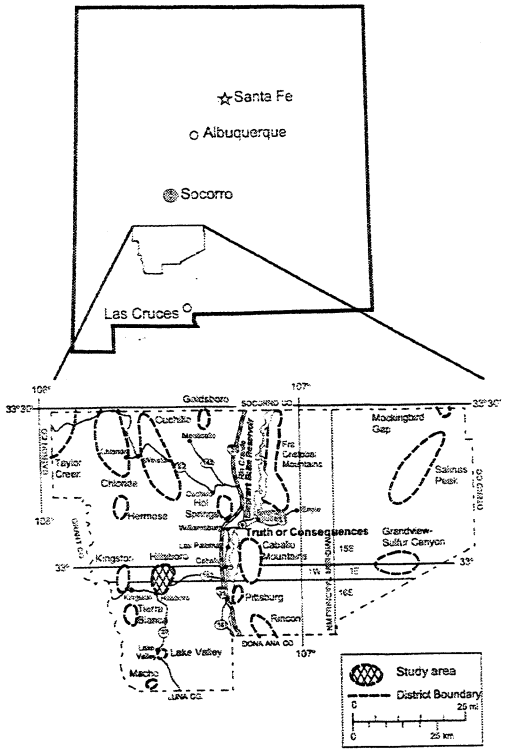

Figure 1--Location of the Hillsboro mining district (McLemore et al., 1999).

[1] Colorado School of Mines, Golden, Colorado (cverdel@mines.edu)
[2] U.S. Geological Survey, Mineral Resources Team, Denver, Colorado
[3] New Mexico Bureau of Mines and Mineral Resources, Socorro, New Mexico
[4] Autometric, Inc., Colorado Springs, Colorado
[5] University of Texas at El Paso

High-altitude Airborne Visible Infra-Red Imaging Spectrometer (AVIRIS) data were collected over the site during the summer of 1998. This type of remotely sensed data has a spatial resolution of approximately 17 meters and measures spectral radiance in 224 channels from 0.38 to 2.5 micrometers. AVIRIS data have been used with success many times in the past to produce maps of minerals occurring on the surface. The Hillsboro district provides a good location to study the use of AVIRIS data to map hydrothermal alteration because of the variety in deposit types and alteration types within the district.

2.0 RESEARCH OBJECTIVE

The objective of this research is to evaluate AVIRIS data as a tool for mapping hydrothermal alteration in the Hillsboro district. The research is aimed at answering two questions. The first is, what is the distribution of alteration minerals within the Hillsboro district? The second is, how well can this distribution be mapped from AVIRIS data?

3.0 GEOLOGY OF THE HILLSBORO MINING DISTRICT

Figure 2 is a generalized geologic map of the Hillsboro district. The Animas Mountains are composed of Cretaceous andesites erupted from the Copper Flat volcano. The Copper Flat quartz monzonite porphyry was emplaced in the vent of the volcano. The circular outcrop of andesite surrounding the porphyry measures approximately six kilometers in diameter and is at least 830 meters thick (Figure 2) (McLemore et al., 1999). Thirty-four latite dikes radiate outward from the porphyry into the andesite, many of which are associated with polymetallic veins. The circular andesite outcrop is surrounded by Paleozoic carbonates and alluvial deposits. Skarn deposits occur in the carbonates to the north and south of the andesite. In addition, jasperoid bodies, which replaced some of the carbonates, are found to the south of the andesite. The Warm Springs quartz monzonite intrudes the flank of the andesite to the south of Copper Flat, and there is another quartz monzonite in the northern part of the district (McLemore et al., 1999). Pliocene basalts cap some of the peaks in the region.

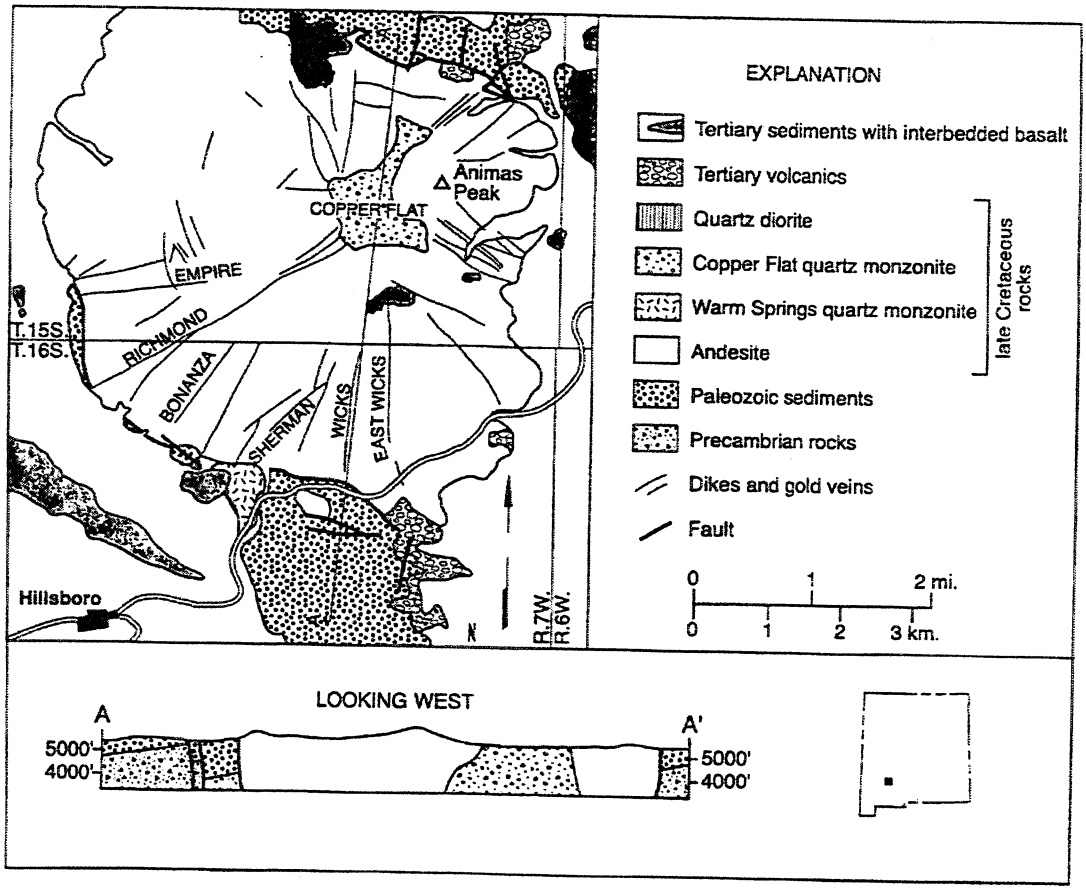

Figure 2--Generalized geologic map of the Hillsboro mining district (McLemore et al., 2000).

The andesite is composed of volcanic flows, flow breccias, and volcaniclastic rocks. It is usually dark gray to greenish gray and porphyritic. It is composed of plagioclase, orthoclase, hornblende, and magnetite, with lesser amounts of biotite, clinopyroxene, quartz, rutile, apatite, and zircon (McLemore et al., 1999). The andesite also contains epidote and is propylitically altered near the Copper Flat quartz monzonite and the polymetallic veins (Fowler, 1982).

The quartz monzonite is light gray to pinkish gray and contains large euhedral potassium feldspar crystals, euhedral to subhedral plagioclase, quartz, biotite, and hornblende (Fowler, 1982).

The dikes are gray to tan to white and vary in thickness from 1 to 38 m (McLemore et al, 2000). They contain feldspar phenocrysts in a groundmass of feldspar and quartz. Small amounts of biotite and hornblende are present locally. Three types of dikes have been mapped: quartz latite, latite porphyry, and latite (Fowler, 1982).

Skarns occur in the limestones to the north and south of the andesite. The skarns are small and contain garnet, epidote and magnetite. Carbonate replacement deposits, which are either Ag-Mn or Pb-Zn dominant, are developed in the Paleozoic limestones and dolomites (McLemore et al., 1999). Jasperoids have replaced large portions of the carbonates to the south of the andesite. The jasperoids are white to reddish brown and brecciated. They contain primarily quartz, iron oxide, and manganese oxide. Lesser amounts of weathered pyrite, dolomite, calcite, magnesite, sericite, fluorite, and altered feldspar are also present (McLemore et al., 2000).

4.0 HYDROTHERMAL ALTERATION

Alteration is a change "in the chemical or mineralogical composition of a rock, generally produced by weathering or hydrothermal solutions" (Bates and Jackson, 1984). Hydrothermal alteration assemblages within the Hillsboro district are prevalent, varied and well characterized. McLemore et al. (2000) summarized the alteration types as shown in Table 1.

Table 1--Summary of alteration types (McLemore et al., 2000)
[Minerals in boldface type may be identified with AVIRIS data.]

Host Rock/Mineral Deposit Type	Alteration Type	Alteration Mineral Assemblage
Quartz monzonite/porphyry copper deposit	Biotite-potassic	Biotite, K-feldspar, quartz, pyrite
	Potassic	K-feldspar, **chlorite**, quartz, pyrite
	Sericitic	**Sericite**, quartz, pyrite
Andesites adjacent to the latite dikes and polymetallic veins	Propylitic	**Epidote**, **chlorite**, **sericite**, pyrite, magnetite
	Argillic	**Sericite**, **calcite**, **chlorite**, quartz, pyrite
	Propylitic	**Chlorite**, **kaolinite**, **sericite**, **calcite**, quartz, pyrite
Latite dikes associated with the polymetallic veins	Propylitic	Quartz, K-feldspar, pyrite, **epidote**, **chlorite**
	Sericitic	Quartz, **sericite**, **chlorite**, pyrite
Limestones, dolostones	Skarn	Garnet, **epidote**, magnetite, quartz
	Marble	Marble, recrystallized limestone
	Jasperoid	Quartz, **iron oxides**, manganese oxide

A model for hydrothermal alteration around porphyry copper deposits was developed by Lowell and Guilbert (1970). In this model, alteration progresses outward from a central core of potassic alteration to a phyllic alteration zone, then to an argillic zone, and finally to a propylitic alteration zone along the periphery. Potassic alteration is characterized by biotite and orthoclase. Phyllic alteration consists of quartz, sericite and pyrite. Argillic

alteration minerals include kaolinite and montmorillonite. Typical propylitic alteration minerals include epidote, calcite, and chlorite. A schematic cross-section through an idealized copper deposit is illustrated in Figure 3.

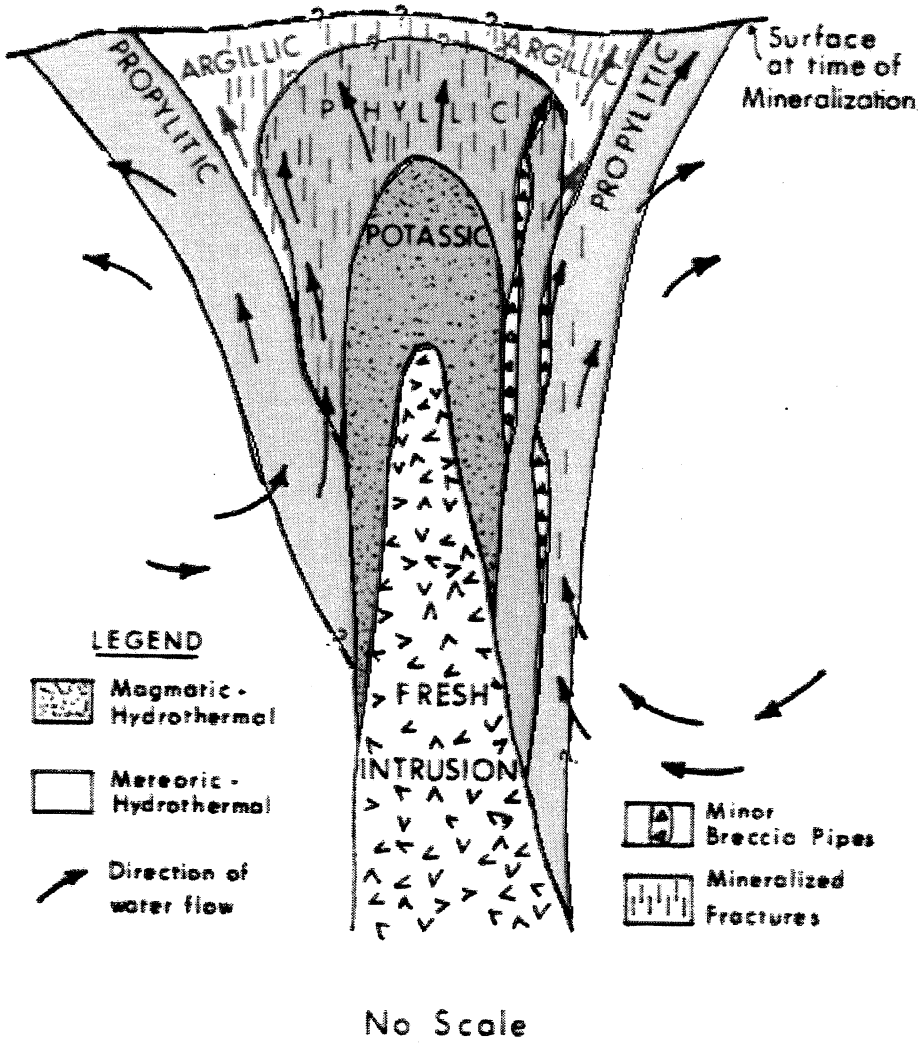

Figure 3--Model for hydrothermal alteration around a porphyry copper deposit. Modified from Hollister (1978).

In addition to hydrothermal alteration, deuteric alteration is also prevalent in the Hillsboro district. Deuteric is defined as "referring to reactions between primary magmatic minerals and the water-rich solutions that separate from the same body of magma at a late stage in its cooling history" (Bates and Jackson, 1984). In the Hillsboro district, deuteric alteration is responsible for the widespread replacement of feldspar phenocrysts by sericite, replacement of groundmass minerals by sericite and chlorite, and replacement of hornblende by biotite, hematite, and chlorite (McLemore et al., 2000).

5.0 METHODOLOGY

This research project consists of four steps:

1. Preparation of mineral maps from AVIRIS data;
2. Field checking of mineral maps combined with field mapping of alteration in critical areas such as the porphyry itself and an anomalous area in the andesite to the northwest of the porphyry;
3. X-ray diffraction (XRD) analysis of samples to support the identification of clay minerals;
4. Laboratory spectral measurements and analysis of samples.

The AVIRIS data were calibrated to spectral reflectance by personnel at the Mineral Resources Team at the USGS in Denver. Additional pre-processing is unnecessary. The image is georeferenced, facilitating combination with other geospatial data sets, such as geochemical or geophysical data. The data scene encompasses the six mineral deposit types within the Hillsboro district.

Mineral maps of the Hillsboro district have been prepared with ENVI® software using the continuum removal/spectral feature fitting™ technique. This procedure begins by selecting diagnostic electromagnetic absorption features for the minerals being mapped. These absorption features were obtained from the USGS Tetracorder 3.5 command file. Spectra from the USGS Digital Spectral Library (Clark et al., 1993) have been used as references.

The spectral range of an absorption feature is isolated in every pixel within the scene by spectrally subsetting the image. Individual features from various pixels must then be normalized in order to compare them to the reference spectrum. The normalization process consists of (1) drawing a straight line between the endpoints of a given absorption feature (the straight line is referred to as a "continuum") and (2) dividing the value of the reflectance spectrum by the value of the continuum at many points along the line.

Following continuum removal of both the reference spectrum and the image spectra, absorption features in the reference spectrum can be compared with spectra from the image. This is the "spectral feature fitting" portion of the procedure. Two statistics are calculated that indicate how well the spectrum of an individual pixel matches an absorption feature in the reference spectrum. The first is dubbed "RMS" and is simply the root mean square error between the spectrum of an individual pixel and the reference spectrum. Low RMS values indicate pixels with spectra that have shapes similar to the reference spectrum in the spectral range of the absorption feature being considered. Theoretically, the RMS value can be used to determine the presence or absence of the material.

The second statistic is called the "scale." It is a measure of the depth of the absorption feature seen in individual pixels. A pixel with a high scale value has a strong absorption in the spectral range being considered. Theoretically, the scale value is proportional to the abundance of the material within the pixel.

A third statistic, the "fit," can be derived from the two calculated statistics. The fit is simply the scale value divided by the RMS value. A high scale value and low RMS value (both indicative of a good match with the absorption feature seen in the reference spectrum) will result in a high fit value. For mapping purposes, the fit statistic is particularly useful, because it highlights those pixels in which the material is not only present, but is also abundant.

Mineral maps are prepared by selecting a threshold value for the fit statistic. All pixels with fit values greater than the cutoff are classified as containing the mineral being mapped. This process is subjective, because different individuals will probably choose different thresholds. They would therefore produce different mineral maps. Selection of the threshold values is the most difficult, and probably the most important, step in the mineral mapping process. A seemingly effective approach to creating reliable mineral maps is to field map critical areas to verify the remote sensing results. For minerals that may not be readily identified with the naked eye, e.g., many clay minerals, samples collected in the field can be analyzed with a technique other than spectroscopy, e.g., XRD, to support the spectroscopic results. The results of analyses from these samples will provide control areas within the image where certain minerals are known to be present or absent. The areas may help in determining appropriate threshold values and may facilitate the refinement of mineral maps.

6.0 RESULTS

Mineral maps have been prepared for limonite minerals, carbonates, some phyllosilicates, epidote, gypsum and tremolite/talc. Figure 4 illustrates the distribution of sericite, kaolinite-montmorillonite, montmorillonite, epidote, chlorite, gypsum, and tremolite/talc. This map indicates that the distribution of hydrothermal alteration minerals immediately surrounding the Copper Flat porphyry is similar to the zonation pattern illustrated in Figure 3. Potassic alteration has not been mapped, however, because of the indistinct spectra of the characteristic minerals biotite and potassium feldspar. A propylitic alteration assemblage, consisting of epidote, chlorite and calcite, has been mapped around the porphyry. This assemblage is also prevalent in the andesite to the northwest of the porphyry. Sericite alteration adjacent to the polymetallic veins has been mapped from AVIRIS data. Gypsum has

also been mapped; it is actively precipitating from the pond in the center of the porphyry. This map has been only priminarily field checked, and additional work will be aimed at verifying and improving the remote sensing results.

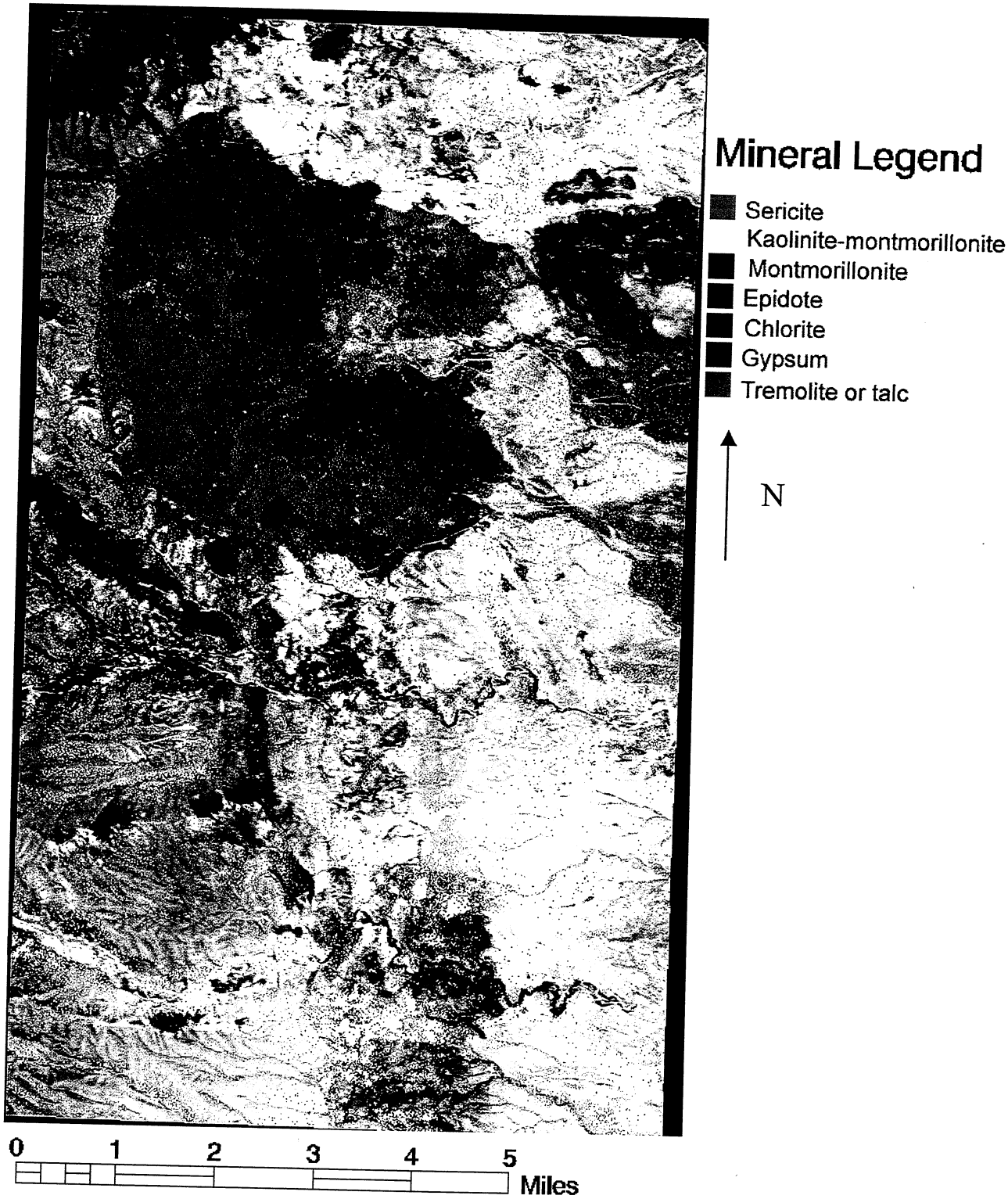

Figure 4--Preliminary map of selected minerals in the Hillsboro mining district.

7.0 REFERENCES

Bates, R.L., and Jackson, J.A., eds., 1984, Dictionary of geological terms (3rd ed): New York, American Geological Institute, 571 p.

Clark, R.N., Swayze, G.A., Gallagher, A.J., King, T.V.V., and Calvin, W.M., 1993, The U.S. Geological Survey Digital Spectral Library: Version 1: 0.2 to 3.0 microns: U.S. Geological Survey Open-file Report 93-592, 1340 p.

Fowler, L.L., 1982, Brecciation, Alteration, and Mineralization at the Copper Flat Porphyry Copper Deposit, Hillsboro, New Mexico (M.S. thesis): University of Arizona, Tucson, 133 p.

Hollister, V.F., 1978, Geology of the porphyry copper deposits of the western hemisphere: New York, Society of Mining Engineers of the American Institute of Mining, Metallurgical, and Petroleum Engineers, 219 p.

Lowell, J.D., and Guilbert, J., 1970, Lateral and vertical alteration mineralization zoning in porphyry ore deposits: Economic Geology, v. 65, No. 4.

McLemore, V.T., Munroe, E.A., Heizler, M.T., and McKee, C., 1999, Geochemistry of the Copper Flat porphyry and associated deposits in the Hillsboro mining district, Sierra County, New Mexico, USA: Journal of Geochemical Exploration, v. 67, p. 167-189.

McLemore, V.T., Munroe, E.A., Heizler, M.T., and McKee, C., 2000, Geology and evolution of the mineral deposits in the Hillsboro district, Sierra County, New Mexico *in* Cluer, J.K., Price, J.G., Struhsacker, E.M., Hardyman, R.F., and Morris, C.L., eds., Geology and Ore Deposits 2000: The Great Basin and Beyond: Geological Society of Nevada Symposium Proceedings, Reno/Sparks, May 2000, p.643-659.

SPECTRAL BAND CHARACTERIZATION FOR HYPERSPECTRAL MONITORING OF WATER QUALITY

Stephanie C. Vermillion,[†] Rolando Raqueño,[‡] Rulon Simmons[†]

1. INTRODUCTION

1.1 Motivation

A method for selecting the set of spectral characteristics that provides the smallest increase in prediction error is of interest to those using hyperspectral imaging (HSI) to monitor water quality. The spectral characteristics of interest to these applications are spectral bandwidth and location. Three water quality constituents of interest that are detectable via remote sensing are chlorophyll (CHL), total suspended solids (TSS), and colored dissolved organic matter (CDOM). Hyperspectral data provides a rich source of information regarding the content and composition of these materials, but often provides more data than an analyst can manage. This study addresses the spectral characteristics need for water quality monitoring for two reasons. First, determination of the greatest contribution of these spectral characteristics would greatly improve computational ease and efficiency. Second, understanding the spectral capabilities of different spectral resolutions and specific regions is an essential part of future system development and characterization. As new systems are developed and tested, water quality managers will be asked to determine sensor specifications that provide the most accurate and efficient water quality measurements. We address these issues using data from AVIRIS and a set of models to predict constituent concentrations.

1.2 Background

Hyperspectral data has been used for a number of applications including geology, vegetation mapping, and atmospherics. We believe that hyperspectral imaging holds the potential for remotely monitoring important water quality constituents. This area has previously received little attention compared to the other applications listed above. Water quality monitoring is an important issue for communities everywhere. There is a myriad of agencies at the local, state, national, and international levels actively involved in this issue. Monitoring concerns range from phosphorous to organic sediments and animal water run-off. Water quality monitoring is an area where a significant amount of conventional and surface surveying and monitoring work has already taken place. Furthermore, an area could greatly benefit from improved information regarding where to take a reduced set of local field samples and a means to interpolate and extrapolate results over a much larger study area. Thus, HSI is seen as a cost-effective solution for surveying water quality over large areas.

1.3 Proposed Contribution

This study performs two minimization studies using 30 AVIRIS bands, ranging from 419nm to 683nm. First, a band averaging method is used to determine the maximum bandwidth obtainable with no significant increase in constituent prediction accuracy. Spectrally degraded AVIRIS bands were used with the prediction models to show error as compared to field measurements. Results are presented based on the prediction error degraded resolution provides when compared to the 30-band AVIRIS data. Second, a principal component analysis is used to rank modeled reflectance values at each AVIRIS bandpass according to their correlation with the first principal component. The method then tracks the error between the constituent components predicted using the ranked bands and field measurements. The results of the study show the error in prediction as a function of the number of bands, given the chosen rank ordering.

2 METHODOLOGY

2.1 Simulation Tools

HydroMod is a computer-aided tool that models the complex radiometry of aquatic systems including the impact from clouds, wind speed, and the scattering characteristics of water. This model builds upon past work by Bukata *et al.* (1995) and ongoing work at RIT to link bio-optical models of air-water interface models and atmospheric radiative transfer models (Berk, 1989). HydroMod is used with the HydroLight water radiance propagation model (Mobley, 1994) to simulate water-leaving spectral radiance above and below the water's surface for varying values of water quality parameters. Spectral measurements can then be compared with this family of predicted water-leaving spectral radiance output to find the best match and subsequently the associated water quality

[†] Eastman Kodak Company (stephanie.vermillion@kodak.com)
[‡] Rochester Institute of Technology

parameters used to generate the matching. The optimization algorithm that was used is a downhill simplex algorithm called *AMOEBA* (Press, 1992).

2.2 Test Data

The AMOEBA algorithm requires two inputs to create the constituent concentration maps: a library of constituent spectra and an image to classify. For this study, the signature library used is a HydroMod look-up-table (LUT) that contained 640 spectral signatures. The 640 signatures were created using between eight and ten different concentration levels of each constituent and all of their combinations. The water quality constituents are measured in units of scalar carbon[1] (CDOM), mg/m^3 (CHL), and g/m^3 (TSS). The LUT available for this study was generated with more samples at lower concentration levels to best represent the sampling needs of the littoral coastal environment. In order to make the results of this study applicable to multiple environments, an even sampling of all concentrations is required. To estimate the spectrum of any combination of constituents not specifically specified in the original LUT, a piecewise trilinear interpolation is used. The interpolation selects the closest fit for the desired spectrum by interpolating simultaneously over each of the three water constituent's reflectance values. Table 1 shows the concentration levels used in this study and the values contained in the original 640 signature library. The input images were band subsets of a 30-band (419-683nm) reflectance calibrated AVIRIS image. Reflectance calibration was performed using a three point Empirical Line Method (ELM).

Table 1. Listing of the constituent concentrations used for this study and the LUT values from which they were interpolated. Study concentrations were selected by fixing the start and end values and dividing the remaining range evenly to create ten equally spaced levels.

Constituent	LUT Concentrations (8-10 Uneven Levels)	Study Concentrations (10 Even Levels)
CDOM	0.0, 0.015, 0.030, 0.145, 0.550, 2.0, 8.0, 30.0	0, 3.33, 6.66, 9.99, 13.32, 16.65, 19.98, 23.31, 26.64, 30
TSS	0.0, 0.015, 0.030, 0.145, 0.550, 2.0, 8.0, 30.0	0, 3.33, 6.66, 9.99, 13.32, 16.65, 19.98, 23.31, 26.64, 30
CHL	0.0, 0.03, 0.30, 0.525, 0.750, 2.0, 5.0, 13.0, 85.0, 33.0	0, 9.44, 18.88, 28.32, 37.76, 47.2, 56.64, 66.08, 75.52, 85

2.3 Band Averaging

The narrowest bands obtainable may not be the best choice for all remote-sensing applications. Broader bandwidths provide the sensor the capability to collect more photons, increasing the signal to noise ratio. Spectral signatures for detectable targets vary greatly within a class. Some of those variations may have a low frequency of spectral change. If the signatures are "smooth," then coarser resolutions (broader bands) will provide sufficient information as finer resolutions, with minimal addition of noise. Determining the widest bandwidth possible for the measurement of water quality constituents is needed to provide the most efficient means of data collection.

An understanding of the bandwidth requirements needed for accurate water quality measurements can be determined by analyzing adjacent bands. We explored coarser data sets by averaging the AVIRIS data (9nm channels). We selected new bandwidths by dividing the range of the 30-band data by the number of new bands. New band centers are designated by the wavelength value halfway between the average bandwidth and the initial wavelength (419nm). Additional bands are then evenly spaced based on the average bandwidth. The AMOEBA algorithm error for each of these new data sets is then calculated with respect to the original 30-band data (Table 2). Error is measured by calculating the root mean square (RMS) error between each simulated data map and the 30 band "truth" maps.

2.4 Band Selection

Ideally, a band selection study consists of an examination of all possible band combinations and their interactions effects. Given the high dimensionality of hyperspectral data, a thorough search for spectral uniqueness would be a substantial computational effort. The spectral richness of hyperspectral data further complicates analysis due to the high correlation of the bands. Often conclusive statistical decisions are unobtainable because it is difficult

[1]NOTE: Because the presence of CDOM cannot be directly detected by the hyperspectral sensor, measurements must be related to the absorption curve as a proportional indicator, and all other concentrations were scaled to that curve.

Table 2. Bandwidths used for the study (all fall within 419-683nm).

Number of Spectral Bands	Bandwidth
30	9nm
25	11nm
20	13nm
15	18nm
10	27nm
5	53nm

to select obvious thresholds or determine significant differences. Transforming hyperspectral data to a lower dimensional space addresses each of these issues.

We propose a method that determines the minimum number of bands needed for water quality measurements based on a Principal Component Analysis (PCA) and an error minimization process. PCA is commonly used in remote sensing as a data reduction technique. A PCA involves transforming the raw sensor data into a new space of uncorrelated components with certain ordered variance properties (Singh and Harrison, 1985). Our PCA method follows the steps proposed by Short (1982) and uses the spectral statistics from the HydroMod predicted reflectance.

The process of the PCA begins with the decomposition of the covariance matrix, **K**, of the concentration reflectance values according to

$$\mathbf{K} = (\mathbf{E}^{\mathrm{T}})^{-1}\mathbf{\Lambda}\mathbf{E}^{-1} \equiv \{\mathbf{k}_{ij}\}$$

where $\mathbf{\Lambda}$ = diag $\{ \lambda_1, \lambda_2, \ldots \lambda_n \}$ contains the N eigenvalues of **K**, **E** holds the eigenvectors associated with $\lambda_1, \ldots \lambda_n$, and N represents the number of hyperspectral bands. Specifically, $\mathbf{E} = \{\mathbf{e}_{ij}\} = [\mathbf{e}_1 \vdots \mathbf{e}_2 \vdots \cdots \vdots \mathbf{e}_N]$, where $\mathbf{e}_{ij}$ is the contribution of band *i* to component *j*.

The eigenvalues can be used to calculate the percent of total variance explained by each component *j* using Equation 1. Usually, the first transformed component describes the majority (over 80%) of the spectral variability in a data set (Jensen, 1996). We propose that bands with the highest contribution to the first principal component will be the most valuable as spectral input to the AMOEBA algorithm.

$$\text{Percent of variance described} = \frac{100\lambda_i}{\mathbf{tr}(\mathbf{K})^{\mathrm{T}}} \qquad \text{(Equation 1)}$$

The contribution of each spectral band to the first component is determined using Equation 2. The band "loading" is calculated by computing the correlation between each band and each component. The loading values from the original data can then be used to rank each band's importance to the first component, and subsequently their importance to the AMOEBA algorithm. The loading of band *i* unto the j_{th} principal component is

$$\beta_{ij} = \mathbf{e}_{ij}\,[(\lambda_j)/(\mathbf{k}_{ij})]^{1/2} \qquad \text{(Equation 2)}$$

Our error minimization process incorporates the information gained from the band ranking as established by their loading to the first component. Once the band ranking is determined, band subsets are tested for prediction accuracy. We begin with the 30-band image and create 29 new band subsets, each time eliminating the band with the lowest ranking. Removal of the least valuable band for every trial allows for tracking of the prediction error through the band rankings. Next, we input each band subset into the AMOEBA algorithm, resulting in 29 error measurements. The single band subset can not be tested because the AMOEBA algorithm requires at least two points to make a concentration prediction. A reference data set is available for 11 points in the AVIRIS scene. At each reference point, we collected water samples (constituent concentrations), geo-location data, and field spectrometer reflectance measurements. We calculated the root-mean-square (RMS) error between the concentration trials and the 11 field measurements and averaged samples to provide one RMS value. This error measurement is used to indicate which bands between 400-700nm are the most useful for hyperspectral water quality monitoring. Because this method of analysis considers all three constituents simultaneously, the RMS results for each of the constituents was averaged to provide a total prediction error.

3. EXPERIMENTAL RESULTS

3.1 Band Averaging

The RMS error for each simulated data set verses the 30-band "truth" images is listed in Table 3. The control error was calculated by running the AMOEBA algorithm on the LUT spectra (instead of the pixel reflectance) and comparing those results to the known LUT concentrations. This provides a reference for the analysis of error for the band-simulated data sets. Figures 1-3 have been provided to better visualize the trends in the error by constituent.

Table 3. RMS Error for the averaged band simulated data sets.

Number of Bands	CHL	TSS	CDOM
5	4.43	1.40	3.29
10	2.81	0.48	1.50
15	2.32	0.37	1.25
20	1.90	0.33	1.09
25	1.93	0.34	1.12

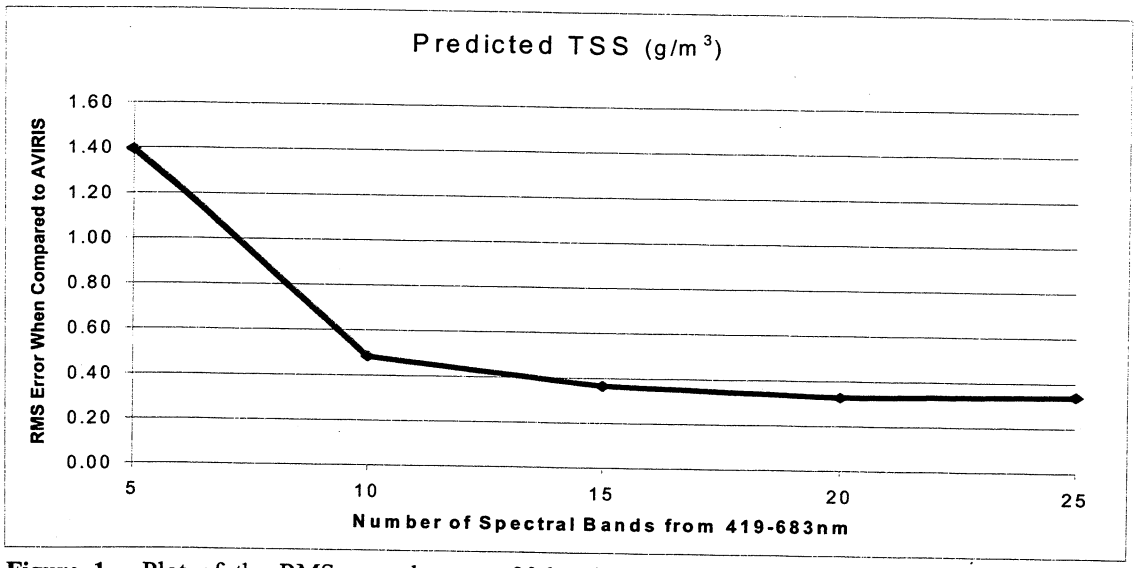

Figure 1. Plot of the RMS error between 30-band AMOEBA results and the spectrally degraded simulated images for TSS.

For all water constituents, as spectral resolution decreases, the algorithm error increases. There does not appear to be a significant change in the error for any of the constituents between 20 and 25 spectral bands. Using this method, analysts may choose to use as few as 15 bands, with errors comparable to 0.37 g/m^3 (TSS), 1.25 scalar carbon (CDOM), and 2.32 mg/m^3 (CHL). TSS was the least affected by changes in spectral resolution, having the smallest error between resolutions ($\overline{x} = 0.26$) as well as the smallest range of error (1.07). The error ranges for CDOM and CHL were 2.19 and 2.52 respectively.

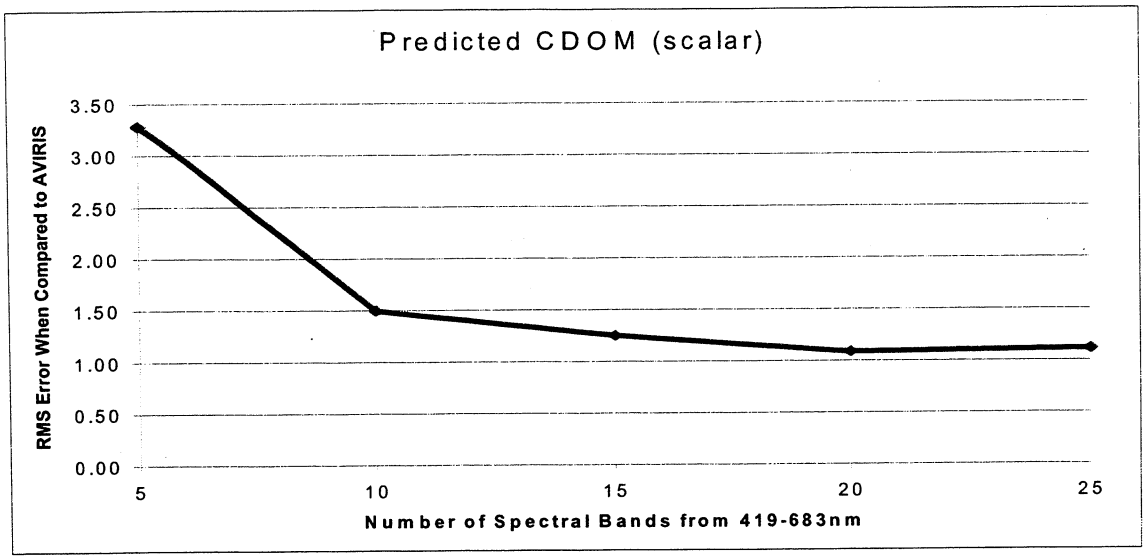

Figure 2. Plot of the RMS error between 30-band AMOEBA results and the spectrally degraded simulated images for CDOM.

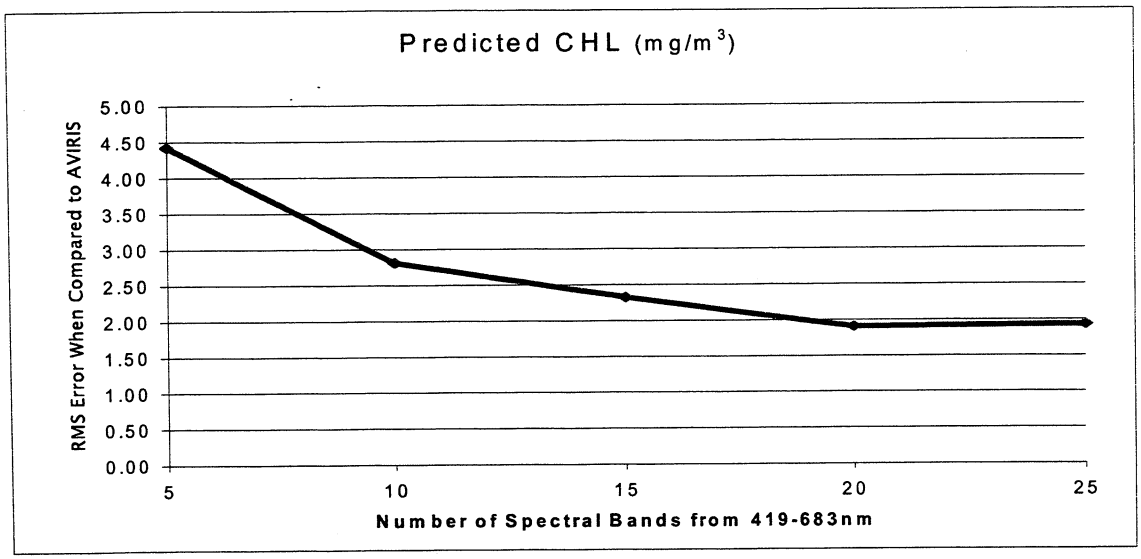

Figure 3. Plot of the RMS error between 30-band AMOEBA results and the spectrally degraded simulated images for CHL.

3.2 Band Selection

A PCA was used to transform the 30-band modeled reflectance data. The first principal component accounted for 89.68% of the spectral variance in the data set. Components 2 and 3 accounted for and additional 10% of the variance, and the components greater than three provided mostly noise. A list of the entire band loading is provided in Table 4. The highest band loading for the first component were for bands 5,10, and 4 (6.20, 3.55, and 3.38 respectively). The lowest loading was from bands 21 (0.25), 30 (0.15), and 28 (0.14). This indicates that the blue region (400-500nm) may be contributing the most to the variance in the data set. The red region (600-700nm) bands are contributing the least to the data set variance.

Table 4. Band loading for the first principle component of the 30 band transformed image.

Band Ranking	Band Number	Wavelength	Loading	Band Ranking	Band Number	Wavelength	Loading
1	5	439.63	6.1983	16	23	616.42	0.9266
2	10	488.74	3.5467	17	27	655.71	0.9242
3	4	429.81	3.3780	18	1	400.35	0.8184
4	9	478.92	3.0948	19	13	518.20	0.7565
5	7	459.27	2.7986	20	24	626.24	0.7070
6	8	469.10	2.4987	21	14	528.02	0.6485
7	12	508.38	2.2926	22	3	419.99	0.6365
8	11	498.56	2.2885	23	20	586.95	0.5556
9	15	537.85	1.9302	24	17	557.49	0.5293
10	2	410.17	1.7560	25	29	675.35	0.4588
11	19	577.13	1.5819	26	16	547.67	0.4160
12	6	449.45	1.4907	27	25	636.06	0.3142
13	26	645.88	1.0129	28	21	596.78	0.2454
14	22	606.60	0.9502	29	30	683.90	0.1517
15	18	567.31	0.9447	30	28	665.53	0.1371

The results of the band selection method are summarized in Figure 4. The overall error trend shows a decrease in prediction error as more bands are added. The error ranges from 4.09 to 37.84 with a minimum at 30 bands and a maximum at three bands. There are two substantial drops in the error, one at 12 bands and one at 23. Areas where there are large drops in error may indicate thresholds for the selection of the minimum number of bands required for water quality monitoring. To make the best decision as to the bands to select, an understanding of these three error regions is essential. It is important to note that although the individual constituent errors assist with the analysis of this study, the objective was to provide a recommendation for the best bands to predict all three constituents simultaneously.

The bands loading the variance the most are the first 11 bands in the ranking (see Table 3). Upon individual examination of those bands, we see that the TSS average spectrum has a much higher reflectance than both the CHL and the CDOM. This may be why the error using the first 11 bands is low for TSS, and higher for CDOM and CHL (Figure 5). More specifically, the 11 bands being used by the AMOEBA algorithm are the bands that provide the best fit for TSS spectra, not necessarily the best fit for CDOM and CHL (increasing the individual errors).

The next region of interest is between the bands ranked 12 to 22. These bands are ranked higher because the variance among all three constituents is high. When the 12th band is added to the first 11, the individual errors for CDOM and CHL demonstrate opposite trends. At this band, the CDOM error drops considerably (61.84 units) and the CHL error increases 7.47 units. The CHL error continues to fluctuate and rise to a maximum of 36.10. This increase in the CHL error may be due to reflectance confusion between the CHL and TSS data. After 550nm, CHL and TSS exhibit similar average spectral curves. An examination of the reflectance curves for both constituents shows an overlapping of values as the concentrations change. Although the TSS signatures dominated the first 11 bands, all three constituents were separable. For this region, the algorithm has difficulty fitting CHL pixel values because it may not be able to separate a low concentration of TSS from a high concentration of CHL. The CDOM error improves here because it is not confused with TSS or CHL. The TSS error is unchanged most likely because it is still weighting the variance more then the CHL spectra.

The third region of interest is the bands ranked greater than 22. This region is created when the error drops significantly at the band ranked 23. This effect is related to the confusion described in the previous section. The bands ranked 23-25 provide improved error for the CHL spectra. At those bands, the variance from the CHL spectra becomes separable enough from the TSS spectra that the algorithm can provide a better spectral fit. Two of these bands fall within the algorithm weighting region of CHL, and one (683nm) falls where there is little spectral overlap between CHL and TSS.

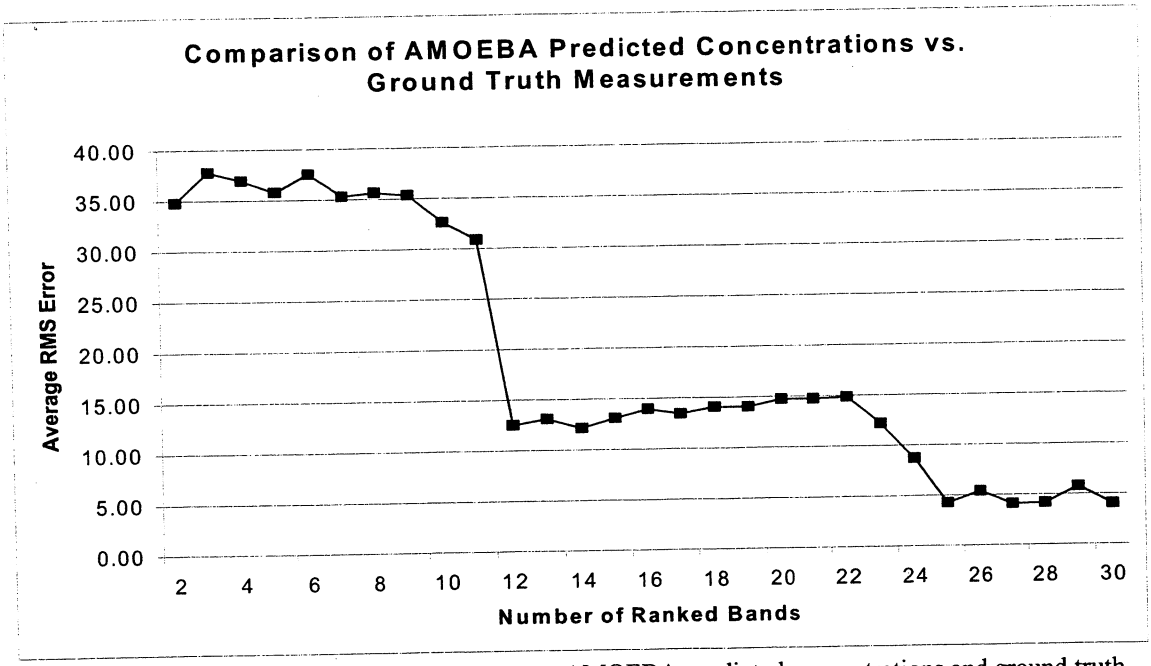

Figure 4. Plot of the average RMS error between AMOEBA predicted concentrations and ground truth measurements for all three constituents.

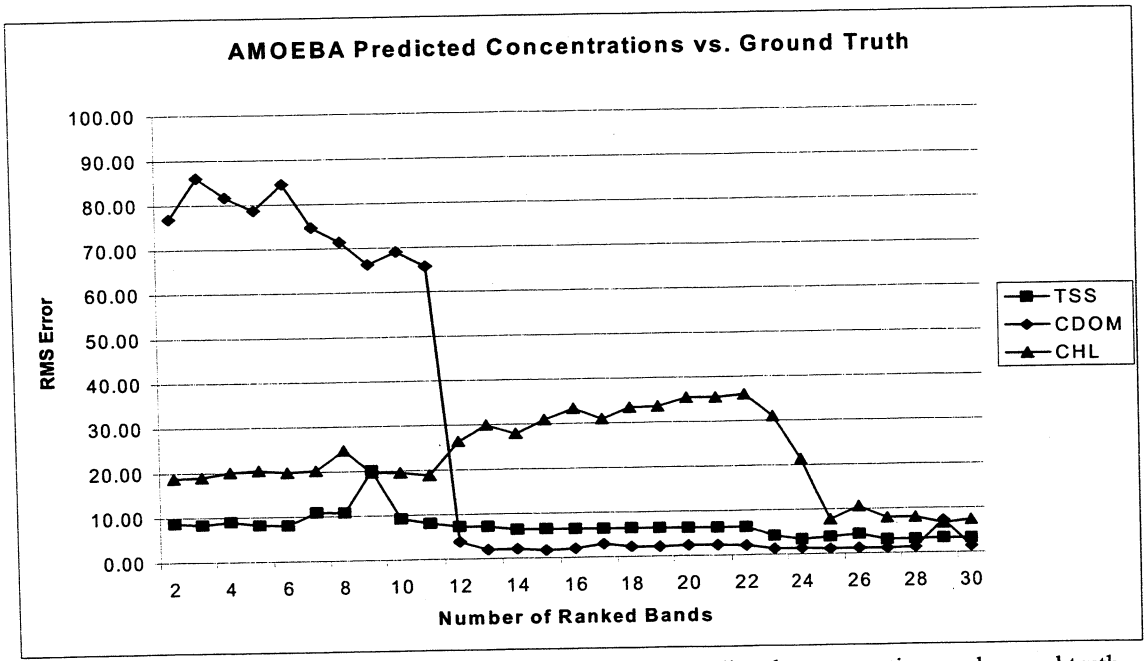

Figure 5. Plot of the average RMS error between AMOEBA predicted concentrations and ground truth measurements for all three constituents listed individually.

Given this understanding of the trends in prediction error, bands can be selected to reduce the raw data set with minimal addition of measurement error. The 30-band data set can be reduced to 23 bands with an error increase of.8.15 units for a total error of 12.24. Of primary interest, however, is the effect of reducing the data set to 12 bands. At the 12-band threshold, the total predicted error is 12.56 (an increase of 8.47 units). This error may be

well within the acceptable limit for some water quality applications. However, before the 12-band ranked subset can be recommended, the analysts must understand how the water quality information is being separated in this region.

Although the TSS signatures dominate the spectral variance in the first band region, this region can be used for the prediction of all three constituents together. This is because there is little overlap across the concentration range of all three constituents. Spectral overlap occurs between TSS and CHL for almost every concentration level, indicating that separation of these constituents may be difficult. However, how and to what degree these spectra are overlapping may contradict that assumption. CDOM is separable at all concentration levels from the other two constituents, and is not of concern for spectral overlap.

4. CONCLUSIONS AND FUTURE WORK

Given this optimization strategy, this study provides a set of 12 spectral bands that can be used for the prediction of water quality constituents with a RMS error of 12.56. This is an 8.47 unit error increase from using the maximum amount of data available across the 400-700nm spectral range. Of those 12 bands, nine fall within the blue spectral region (400-500nm) and 3 fall within the green range (500-600nm). Using the highest spectral resolution data currently available (AVIRIS), the best prediction error the AMOEBA algorithm provides is a RMS of 4.09. These are small units when considering the 20-meter sample pixel of AVIRIS. It does not seem likely that an error of +8 units will make a substantial difference when mapping water constituents over large areas. For most purposes, spectral data with 13nm channels (20 bands, 400-700nm) can be utilized with no significant addition of error. Analysts may chose data with 18nm bandwidths with some additional error; however, the impact of that error on water quality results will depend on the acceptable error associated with a specific task.

Although this is one of the better strategies for spectral characterization, we understand its limitations. First, PCA does not consider the spectral separability of the constituents. More specifically, it assumes that there is an even contribution from all of the constituents to the reflectance of the entire scene. This is rarely the case. Often one signature may have a much higher reflectance than the other components at the same band. For that band the variance will be biased towards the dominant signature. Another limitation of our method this that we have limited our analysis to the first principal component. Although that component describes the vast majority of the variance in the data set, there may be a significant contribution in the remaining components. Finally, our method uses models for our error measurements that are experimental in nature. It is important to note that determining the accuracy of the AMOEBA algorithm is beyond the scope of this study. A complete discussion of the simulation tools used for this study can be found in the final report for the NASA EOCAP contract NAS13-98080. The models used for this study are recently developed tools designed to fulfil an immediate need in the water quality community. Further refinement is required before they are fully implemented for water quality monitoring.

This study indicates that both the width and the placement of spectral bands are important to water quality monitoring. As new systems are developed and tested, water quality managers will be asked to determine sensor specifications that provide the most accurate and efficient water quality measurements. As studies such as this one develop, it may become clear that existing sensors may be adequate for water quality monitoring. If so, determining the best spectral characteristics becomes useful not only to increase computational ease, but also to assist with the sampling issues that plague the water quality community. Sensitivity studies similar to this one can provide an indication of the amount of error to be expected given varying spectral conditions. If hyperspectral data was not available given certain acquisition parameters (i.e., cloud cover), it may be acceptable to collect data from a broad band sensor given an understanding of the inherent error at that resolution. For example, animal water run-off measurements are often event-driven collections. If for some reason samples cannot be collected using one of the methods some other method may be better then no data at all. Understanding how the error in the prediction of water quality constituents is related to the spectral characteristics of remotely sensed data is a valuable reference for the water quality community.

To answer the question of required system specifications most accurately, a functional measure that is two-dimensional (width and location) in nature is required. This study was developed as part of a larger project to design and test hyperspectral algorithms for the monitoring of water quality. The resources were not available for an extensive joint minimization study, but future exploration of this topic is encouraged.

5. ACKNOWLEDGEMENTS

The work associated with this paper was funded under the NASA EOCAP project NAS-98080 and was completed co-jointly at the Eastman Kodak Company and the Rochester Institute of Technology in Rochester, NY. We thank Jim Coss and Jason Hamel for their assistance with data processing as well as Shiloh Dockstader and Mike Heath for their technical advisement and support.

6. REFERENCES

Berk, A., L.S. Bernstein, and D.C. Robertson, 1989, "MODTRAN: a moderate resolution model for LOWTRAN 7," GL-TR-89-0122, Spectral Science, Burlington, MA.

Bukata, R.P., J.H. Jerome, K.Ya. Krondratyev, and D.V. Pozdnyakov, 1995, "Optical Properties and Remote Sensing of Inland and Coastal Waters," New York: CRC Press, ISBN 0-8493-4754-8, 362 pages.

Jensen, J.R., 1996, "Introductory Digital Image Processing: A Remote Sensing Perspective," Upper Saddle River, NJ: Prentice Hall, ISBN 0-13-205840-5, pp. 172-179.

Mobley, C.D, 1994, "Light and Water: Radiative Transfer in Natural Waters," Boston, Academic Press, ISBN 0-12-502750-8, 592 pages.

Press, W.H., 1992, "Numerical Recipes in C: The Art of Scientific Computing," Cambridge University Press, pp. 408-412.

Short, N., 1982, "Principles of Computer Processing of Landsat Data," Appendix A in The Landsat Tutorial Workbook, Publication 1078. Washington: National Aeronautics and Space Administration, pp. 421-453.

Singh, A. and A. Harrison, 1985, "Standardized Principal Components," International Journal of Remote Sensing, vol. 6, pp. 883-896.

AN APPROACH TO APPLICATION VALIDATION OF MULTISPECTRAL SENSORS, USING AVIRIS DATA

Amanda Warner,* Slawomir Blonski,* Gerald Gasser,* Robert Ryan,* and Vicki Zanoni**

1. INTRODUCTION

High spatial resolution multispectral/hyperspectral sensors are being developed by private industry with science/research customers as end users. With an increasingly wide range of sensor choices, it is important for the remote sensing science community and commercial community alike to understand the trade-offs between ground sample distance (GSD), spectral resolution, and signal-to-noise ratio (SNR) in selecting a sensor that will best meet their needs. High spatial resolution hyperspectral imagery and super resolution multispectral charge-coupled device imagery can be used to develop prototypes of proposed data acquisition systems without building new systems or collecting large sets of additional data. By using these datasets to emulate proposed and existing systems, imaging systems may be optimized to meet customer needs in a virtual environment. This approach also enables one to determine, a priori, whether an existing dataset will be useful for a given application.

NASA's Earth Science Applications Directorate at the John C. Stennis Space Center (SSC) supports state and local governments, commercial companies, agricultural-related users, and researchers: all of whom have finite financial resources. The Applications Directorate assists these organizations, which in some cases have no background in remote sensing science, in selecting the imagery that will best meet their needs. The need to simulate other sensors lies in the tradespace between cost and utility. The number of pixels, number of bands, spectral coverage, and SNR all drive the cost of conducting an image survey. When planning a mission, the altitude of the plane can have serious coverage, cost, and usefulness impacts. While it might be less costly to fly higher and to cover a larger area, the subsequent data might not carry the information needed to make informed decisions.

In this study, we performed spatial synthesis and spectral integration, and we applied noise to AVIRIS-LA (low altitude) imagery to parametrically simulate the performance of example sensors. AVIRIS data were selected as the source data to use in these simulations because of the system's high SNR, excellent radiometric performance, and very high spatial and spectral resolution. With these characteristics, we may simulate larger GSD, lower SNR, and lower spectral resolutions by aggregating pixels, by binning spectral bands, and by adding random noise. AVIRIS data may also be used to more fully understand the limitations of spaceborne hyperspectral systems. The recent launch of the Hyperion hyperspectral instrument on the EO-1 platform has served to reinforce the fact that although hyperspectral instruments are finally making it into space, spatial resolution and SNR are not at the level of airborne hyperspectral sensors. For scientific usage, the limitations and advantages of these sensors need to be understood.

As aerial and satellite systems evolve, both the government and the private sector will benefit from improved requirements analysis. A preliminary set of tools now exists to address many related questions. Previous studies have examined the impact of GSD, spectral resolution, and noise on hyperspectral image analysis (Table 1). Our approach was to develop a set of tools that creates simulated datasets from AVIRIS-LA and that will parametrically vary GSD, spectral resolutions, noise characteristics, and additional platform characteristics to better understand the utility of present and planned commercial systems. The Applications Research Toolbox currently in development at SSC will be used in collaboration with industry partners to help define future systems. This paper demonstrates some of the technology that will be present in this toolbox and performs preliminary analysis on simulation metrics.

* Lockheed Martin Space Operations – Stennis Programs, John C. Stennis Space Center, Mississippi (Principal contact: Robert.Ryan@ssc.nasa.gov)
** National Aeronautics and Space Administration, John C. Stennis Space Center, Mississippi

Table 1. Previous studies on the impact of GSD, spectral resolution, and noise on hyperspectral image analysis.

Impact Factor	Previous Studies
GSD	Green and Boardman, 2000; Kruse, 2000; Perry et al., 2000; Smailbegovic et al., 2000; Chabrillat and Goetz, 1999; Goetz and Kindel, 1999; Rockwell et al., 1999; Shen, 1997; Teillet et al., 1997; Goetz and Kindel, 1996; Price, 1997; Justice et al., 1989.
Spectral Resolution	Asner and Heidebrecht, in press; Boardman and Green, 2000; Kruse, 2000; Warner et al., 2000; Kokaly and Clark, 1999; Price, 1997; Shen, 1997; Teillet et al., 1997; Swayze and Clark, 1995.
Noise	Green and Boardman, 2000; Kruse, 2000; Okin and Roberts, 2000; Goetz and Kindel, 1999; Kokaly and Clark, 1999; Shen, 1997; Clark and Swayze, 1996; Swayze and Clark, 1995; Curran et al., 1991.

2. METHODS

2.1 Simulation

We began our simulation process by selecting an image that represented a wide variety of landcover to observe the results of simulation on a variety of surface features. The primary site selected was a subscene of 1999 AVIRIS-LA Yellowstone National Park imagery. This scene contains riparian features, roads, exposed soil, senescensed and live vegetation, and water. The first step in the simulation process was to use the scale factors provided by the AVIRIS team to bring the data into non-scaled radiance units. Although this step is not necessary for all processing scenarios, using radiometric units does allow the user the option of comparing the finalized simulation product to other data sources if desired. Following this step, the data were either kept at the original AVIRIS wavelengths or mapped to the Landsat ETM+ channels by integrating the AVIRIS data over the ETM+ filter response functions. Landsat ETM+ filter response functions were used in these simulations because many commercial and government systems use similar bands. The next step after spectral resampling was spatial aggregation. Pixels were aggregated in this study through block averaging using the IDL routine *rebin*. Pixels were scaled by 5, 10, 15, and 20 times the original resolution. See Figure 1 for processing flow.

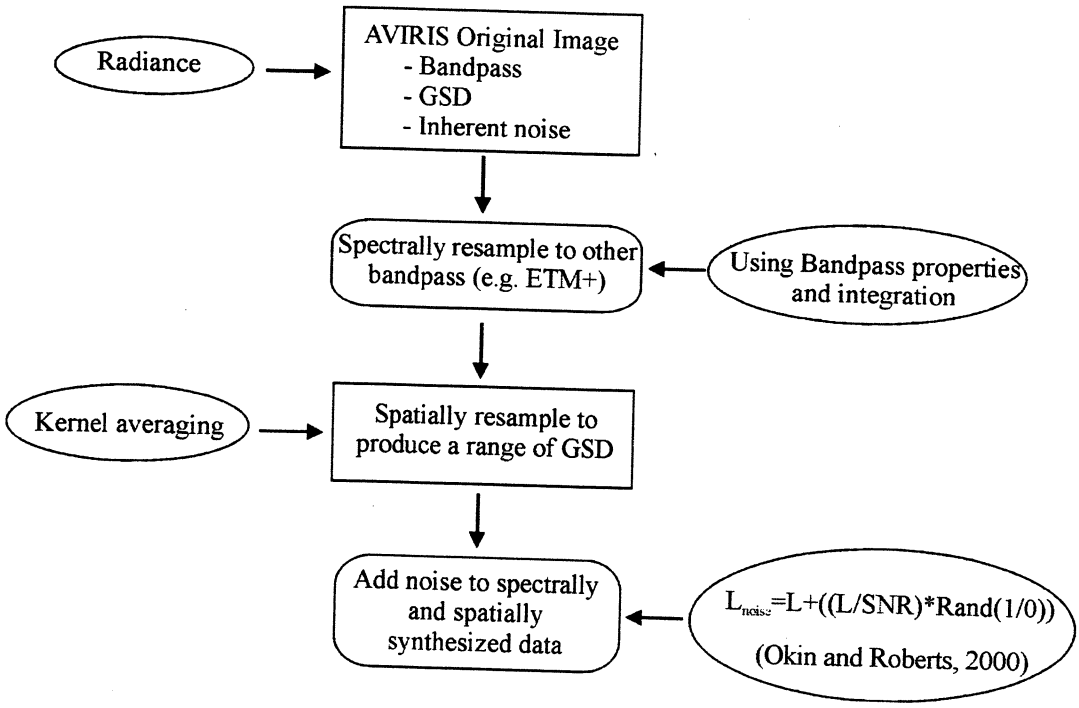

Figure 1. Flowchart of simulation process.

The last step prior to analysis was to add random noise to the dataset to simulate various SNR levels. This step was performed using equation 1 from Okin and Roberts (2000):

$$L(\lambda)_{noise}=L(\lambda)+((L(\lambda)/SNR)*Rand(1/0)) \quad (1)$$

Where:

Lnoise	=	Resulting radiance with noise added
L	=	Original radiance values with system inherent noise
SNR	=	Signal to noise value used; i.e., 100, 25 etc.
Rand(1/0)	=	Normally distributed random number with a mean of zero and a standard deviation of 1.

This method applies noise that is based on the radiance of each band but does not include detector-specific noise characteristics. The above expression is valid when the input scene SNR is much higher than the simulated SNR. This approach adds random noise without separating the individual sources of noise, which holds after spatial and spectral integration.

2.2 Noise Considerations

Sensor designs often must incorporate tradeoffs between SNR and GSD. Decreasing the GSD without compensating the optical throughput (i.e., lengthening the telescope and narrowing the aperture to achieve a smaller GSD) will reduce the SNR. In other words, for a fixed telescope diameter and detector size, the number of photons reaching the detector for a smaller GSD will be reduced and the SNR will be lower. Improving the spatial resolution may result in poor quality but high spatial resolution data. Most systems are limited by a combination of photon and detector noise. For our simulations, we simply added random (Poisson) noise, which accounts for both of these processes. Sources of coherent noise, such as striping and power supply noise, were not considered here but might be selected for simulation in the Application Research Toolbox.

2.3 Simulated Product Assessment

Following the simulation process, the data were displayed to examine visual effects from the synthesis. The images were transformed into eigenspace to appraise the effects of the simulation on eigenvectors. Principal Component Analysis (PCA) or eigen analysis is a routine widely used to assess the variance of an image. Image bands are orthogonally projected to determine axes of maximum variance. The coefficients to rotate each band into these new axes are the eigenvectors. Eigenvectors are ranked in order of maximum variance (the first principal component) to the dimension of least variance (the last component). PCA results can be used as input into classifiers because some surface features are more apparent when taken into PC space. The appearance of noise in eigenvectors is indicative of reduced data dimensionality. By looking at the eigenvectors of degraded data, we can see when noise and spatial resolution begin to change the dimensionality of an image relative to the original dataset.

3. RESULTS

Normalized Difference Vegetation Index (NDVI) was computed using the simulated images to show the effects of the reduced spatial resolution. While this step is quite simple, the product can have a large impact on users who need to determine the GSD necessary to observe phenomena. Evaluating the effects of various GSD on NDVI can aid in the development of the user's spatial requirements for applications such as precision agriculture. In Figure 2, it is clear that while 17.0 m images still show the road and features of the creek, the utility of these images for geographic information system work would be limited compared to the utility of the 8 m images, where feature boundaries are more defined. For example, Warfighter/Orbview 4 might be able to detect features spatially where Hyperion would not. A simulated product such as this would be valuable to users whose imagery can be acquired at varying altitudes to determine how GSD affects their ability to resolve surface features of interest.

Eigenvector analysis proved to be very useful for determining the effects of noise and degraded spatial resolution. While the NDVI images with 100:1 signal to noise added do not visually look different than the images with higher SNR, the eigenvectors with higher noise levels clearly show how noise influences the dimensionality of an image (see Figure 3, panel c, eigenvectors 9 and 10). When eigenvectors are no longer coherent and are

dominated by noise, the subsequent rotation of the original image by the noisy eigenvector is a noisy PC image that shows little about the original scene. When higher-order eigenvectors are not dominated by noise, the subsequent image data from the rotation can be used to identify more spectrally subtle features. The effect of lower SNR on dimensionality has been studied with historical AVIRIS data (Kruse, 2000). Through eigen analysis we can observe the effects of SNR on proposed systems and determine at what noise level features of interest are lost.

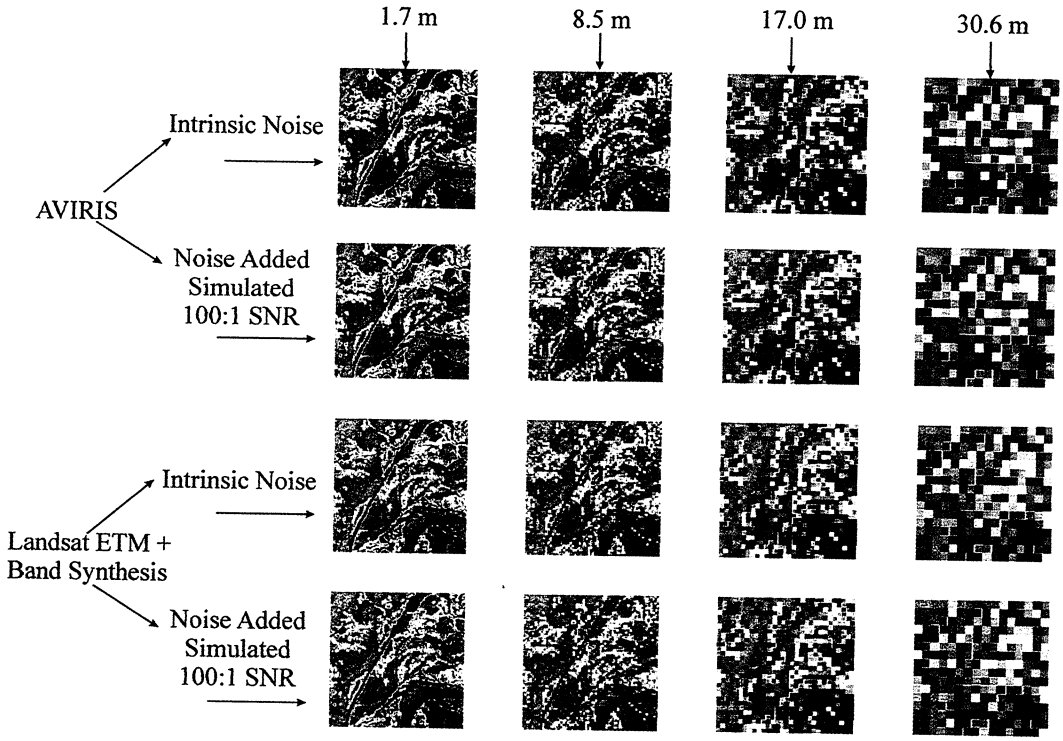

Figure 2. NDVI images with varying spatial resolution, spectral resolution, and noise levels. Visually, spatial resolution is more important than SNR when SNR for NDVI bands is greater than or equal to 100:1.

The eigenvector plots of Figure 3 also show that while noise reduces the dimensionality of a scene, larger GSD changes the shape of high-order eigenvectors. Starting with the fourth eigenvector for all noise levels, the shape of the eigenvectors for all increased GSD departs from that of the original spatial resolution. This change shows that although noise levels influence the dimensionality, the spatial resolution can greatly affect the type of information that may be extracted from the image. The coefficients for rotation would be changed and the eigenvectors with larger GSD would highlight different materials. These results are significant to researchers and commercial users alike who have several options for GSD to accomplish their mapping objective. Using eigen analysis enables visualization of the noise levels and spatial resolution where the detection of scene components is diminished.

We also performed noise addition and eigen analysis on the spectrally synthesized AVIRIS data (Figure 4). AVIRIS data were mapped to Landsat ETM+ filter response functions in this scenario. The results from this process are not as intriguing in respect to dimensionality as were the hyperspectral data because of the greatly reduced number of bands. The eigenvectors from the mapped data do show that with larger spectral resolution, the effects of noise and reduced GSD are not as noticeable in principal component analysis. The second eigenvector of the simulated data departs from the shape of the original resolution eigenvector at all noise levels. The PC images for this eigenvector are shown in Figure 5. Although the eigenvectors for the 2nd principal component are different, the overall shape is preserved and similar features are highlighted in the PC image. Lowered SNR and reduced spatial resolution do not affect eigenvectors as much with multispectral data as with hyperspectral data.

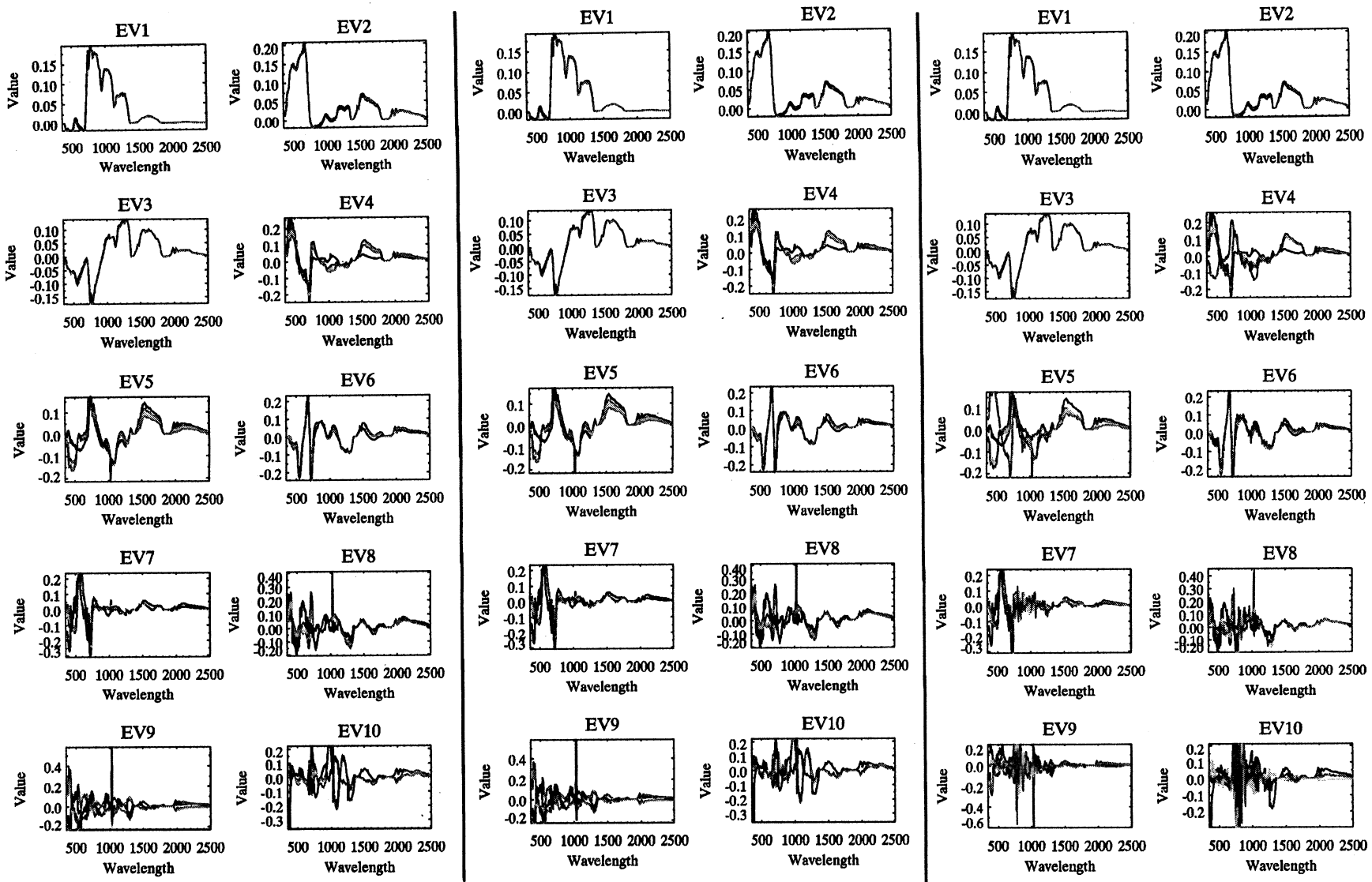

Figure 3. Eigenvectors for spatial resolutions of 1.7 m—, 17 m—, 25.5 m—, and 34 m—; noise levels are indicated beneath each panel.

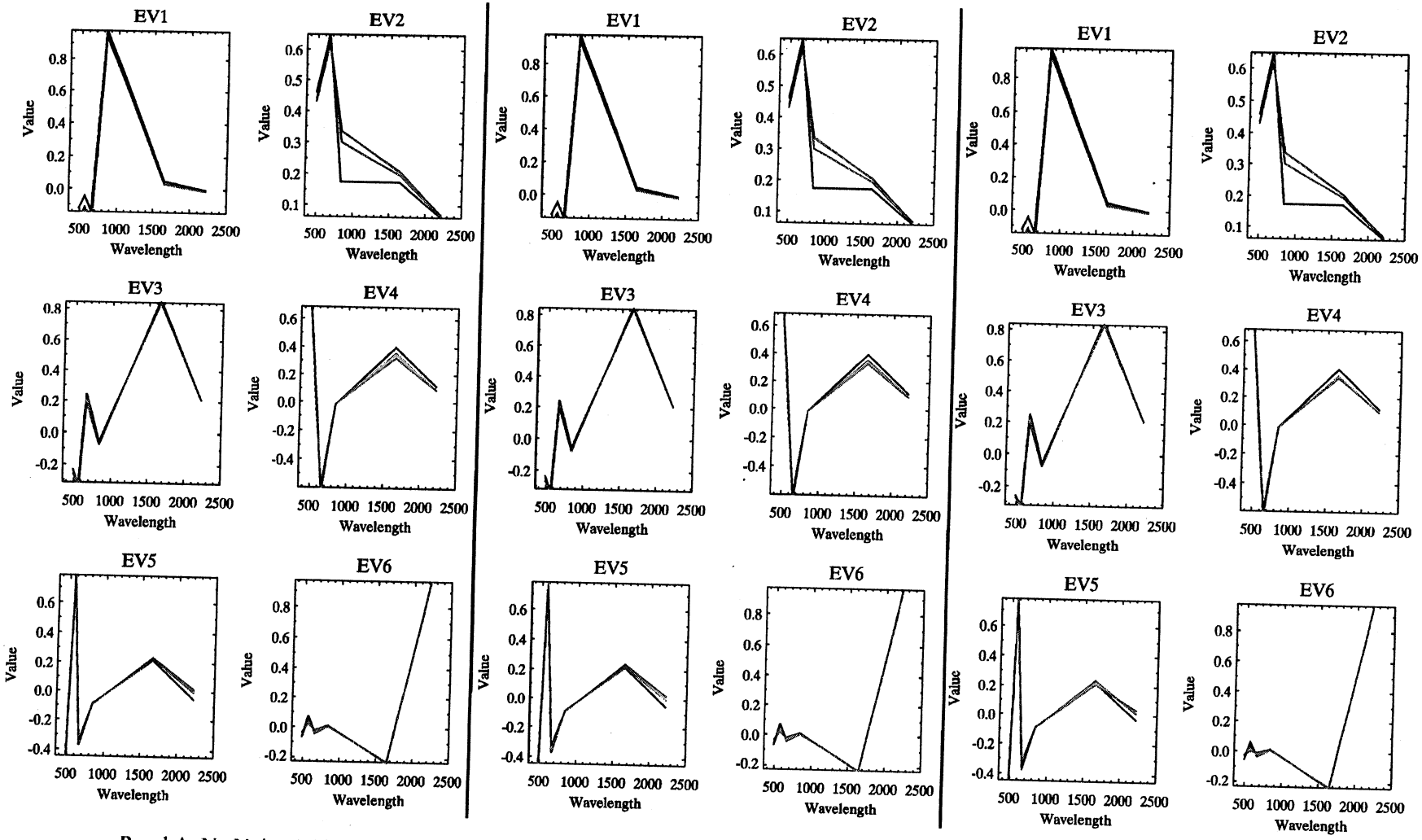

Figure 4. Landsat ETM+ spectral resolution eigenvectors for spatial resolutions of 1.7 m—, 17 m—, 25.5 m····, and 34 m—; noise levels are indicated beneath each panel.

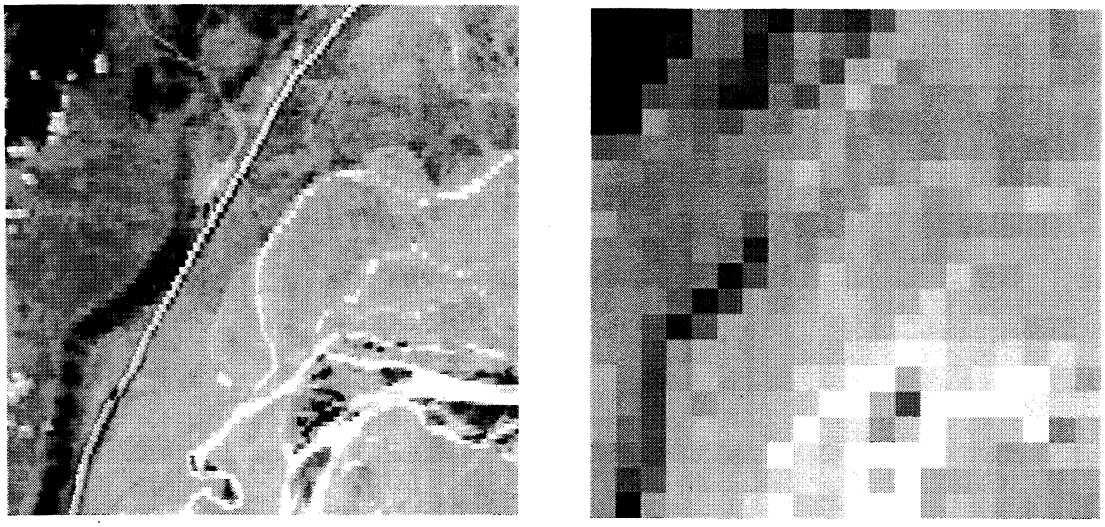

A B

Figure 5. Landsat ETM+ convolved 2nd PC bands.

Figure 5a is the 2nd PC band of the scene convolved to Landsat ETM+ bands with no additional noise added and at the original spatial resolution. Figure 5b is the 2nd PC band of Landsat convolved data at 25.5-m spatial resolution with no noise added. The departure seen in the second eigenvector in Figure 5 is difficult to attribute to a surface feature since the very dark and very light areas in each scene correspond to each other. The departure is most likely related to spatial degradation's diluting the intensity of components.

4. CONCLUSIONS

Simulations produced by parametrically varying GSD show that SNR of 100:1 might not visually affect results (e.g., NDVI), but its effects can be better quantified by looking at eigenvectors. Changes observed in eigenvectors shapes at lower SNR are more due to spatial effects than added noise. This result is significant and should be investigated for a variety of scenes to determine the effects of spatial dilution on principal components. Continued work is needed to develop more robust noise models that will more realistically include the multiple sources of noise found in aircraft and satellite imagery as well as the overall level. Further analysis of the spatial properties of images could be analyzed as well for the contribution that the point-spread function of a sensor plays in principal component analysis. We hope to further parameterize these simulations to fit future and present systems in an effort to show the effects of data characteristics on applications. As both aerial and satellite systems evolve, both the government and the private sector will benefit from improved requirements analysis. A preliminary set of tools now exists to address this issue. Analysis will continue to define the "right questions" and to develop relevant metrics for data evaluation.

5. ACKNOWLEDGEMENTS

The authors wish to thank Greg Terrie for his helpful review of this paper as well as Marcia Wise, Lee Estep, Joe Spruce, and Judith Berglund for helpful comments along the way. This research was supported by the NASA Earth Science Applications Directorate under contract number NAS 13-650 at the John C. Stennis Space Center, Mississippi.

6. REFERENCES

Asner, G. P., and K. B. Heidebrecht, in press, "Spectral Unmixing of Vegetation, Soil and Dry Carbon Cover in Arid Regions: Comparing Multispectral and Hyperspectral Observations," International Journal of Remote Sensing.

Boardman, J. W., and R. O. Green, 2000, "Exploring the Spectral Variability of the Earth as Measured by AVIRIS in 1999," 2000 Proceedings from the Airborne Earth Science Workshop, JPL Publication, online at http://makalu.jpl.nasa.gov/docs/workshops/00_docs/Boardman_web.pdf

Chabrillat, S. and A. F. H. Goetz, 1999, "The Search for Swelling Clays Along the Colorado Front Range: The Role of AVIRIS Resolution in Detection," 1999 Proceedings from the Airborne Earth Science Workshop, JPL Publication, online at http://makalu.jpl.nasa.gov/docs/workshops/00_docs/Boardman_web.pdf

Clark, R. N., and G. A. Swayze, 1996, "Evolution in Imaging Spectroscopy Analysis and Sensor Signal-to-noise: An Examination of How Far We Have Come," 1996 Proceedings from the Airborne Earth Science Workshop, JPL Publication, online at http://makalu.jpl.nasa.gov/docs/workshops/96_docs/7.PDF

Curran, P. J., J. L. Dungan, and G. M. Smith, 1991, "Increasing the Signal-to-Noise Ratio of AVIRIS Imagery Through Repeated Sampling," 1991 Proceedings from the Airborne Geoscience Workshop, JPL Publication, online at http://makalu.jpl.nasa.gov/docs/workshops/91_docs/22.PDF

Goetz, A. F. H., and B. Kindel, 1999, "Comparison of Unmixing Results Derived from AVIRIS, High and Low Resolution, and HYDICE images at Cuprite, NV," 1999 Proceedings from the Airborne Earth Science Workshop, JPL Publication, online at http://makalu.jpl.nasa.gov/docs/workshops/99_docs/25.pdf

Goetz, A. F. H., and B. Kindel, 1996, "Understanding Unmixed AVIRIS Images in Cuprite, NV Using Coincident HYDICE Data," 1996 Proceedings from the Airborne Geoscience Workshop, JPL Publication, online at http://makalu.jpl.nasa.gov/docs/workshops/96_docs/15.PDF

Green, R. O., and J. W. Boardman, 2000, "Exploration of the Relationship Between Information Content and Signal-to-noise Ratio and Spatial Resolution in AVIRIS Spectral Data," 2000 Proceedings from the Airborne Earth Science Workshop, JPL Publication, online at http://makalu.jpl.nasa.gov/docs/workshops/00_docs/Green_Explor_web.pdf

Justice, C. O., B. L. Markham, J. R. E. Townsend, and R. L. Kennard, 1989, "Spatial Degradation of Satellite Data," International Journal of Remote Sensing, 10:1539-1561.

Kokaly, R. F., and R. N. Clark, 1999, "Spectroscopic Determination of Leaf Biochemistry Using Band-depth Analysis of Absorption Features and Stepwise Linear Regression," Remote Sensing of Environment, 67:267-287.

Kruse, F. A., 2000, "The Effects of Spatial Resolution, Spectral Resolution, and Signal-to-noise Ratio on Geologic Mapping Using Hyperspectral Data, Northern Grapevine Mountains, Nevada," 2000 Proceedings from the Airborne Earth Science Workshop, JPL Publication, online at http://makalu.jpl.nasa.gov/docs/workshops/00_docs/Kruse_web.pdf

Okin, G. S., and D. A. Roberts, 2000, "Linear Unmixing of Simulated, Noisy Spectra: Vegetation Detection Limits in Areas of Low Cover," 2000 Proceedings from the Airborne Earth Science Workshop, JPL Publication, online at http://makalu.jpl.nasa.gov/docs/workshops/00_docs/orkin_web.pdf

Perry, E. M., M. Gardener, J. Tagestad, D. Roberts, P. Cassady, J. Smith, and D. Nichols, 2000, "Effects of Image Resolution and Uncertainties on Reflectance-derived Crop Stress Indicators," 2000 Proceedings from the Airborne Earth Science Workshop, JPL Publication, online at http://makalu.jpl.nasa.gov/docs/workshops/00_docs/perry_web.pdf

Price, J. C., 1997, "Spectral Band Selection for Visible-Near Infrared Remote Sensing: Spectral-Spatial Resolution Tradeoffs," IEEE Transactions on Geoscience and Remote Sensing, 35(5):1277-1285.

Rockwell, B. W., R. N. Clark, K. E. Livo, R. R. McDougal, R. F. Kokaly, and J. S. Vance, 1999, "Preliminary Materials Mapping in the Park City Region for the Utah USGS-EPA Imaging Spectroscopy Project Using Both High and Low Altitude AVIRIS Data," 1999 Proceedings from the Airborne Geoscience Workshop, JPL Publication, online at http://makalu.jpl.nasa.gov/docs/workshops/99_docs/51.pdf

Shen, S. S., 1997, "Multiband Sensor System Design Tradeoffs and Their Effects on Remote Sensing and Exploitation," SPIE Imaging Spectrometry III, 3118:296-307.

Smailbegovic, A., J. V. Taranik, and F. Kruse, 2000, "Importance of Spatial and Radiometric Resolution of AVIRIS Data for Recognition of Mineral Endmembers in the Geiger Grade Area, Nevada, U.S.A.," 2000 Proceedings from the Airborne Geoscience Workshop, JPL Publication, online at http://makalu.jpl.nasa.gov/docs/workshops/00_docs/smailbegovic_web.pdf

Swayze, G. A., and R. N. Clark, 1995, "Spectral Identification of Minerals Using Imaging Spectrometry Data: Evaluating the Effects of Signal to Noise and Spectral Resolution Using the Tricorder Algorithm," 1995 Proceedings from the Airborne Geoscience Workshop, JPL Publication, online at http://makalu.jpl.nasa.gov/docs/workshops/95_docs/42.PDF

Teillet, P. M., K. Staenz, and D. J. Williams, 1997, "Effects of Spectra, Spatial, and Radiometric Characteristics on Remote Sensing Vegetation Indices of Forested Regions," Remote Sensing of Environment 61:139-149.

Warner, A. S., A. F. H. Goetz, K. B. Heidebrecht, and E. L. Johnson, 2000, "Measuring the Ability of Landsat 7 to Map Vegetative Fractions Using a Near-simultaneous AVIRIS Underflight," 2000 Proceedings from the Airborne Earth Science Workshop, JPL Publication, online at http://makalu.jpl.nasa.gov/docs/workshops/00_docs/warner_web.pdf

CORRELATING AVIRIS IMAGERY TO FIELD SAMPLING AND SPECTROMETER MEASUREMENTS FOR INORGANIC SOIL CARBON

Michael L. Whiting and Susan L. Ustin*

1. INTRODUCTION

The AG2020 USDA and NASA program sponsors the advancement of remote sensing and other spatial technologies to enhance precision farming and sustainability. This affiliated study in the San Joaquin Valley (http://www.ag2020.net) is through the leadership of the National Cotton Council and the cooperating farm manager. Both contribute funding support and in-kind services. The majority of support is from the 23+ investigators who volunteer time and their own research funding for this collaborative effort. The list of cooperating organizations includes: NASA-JPL through AVIRIS and other imagery contributions; USDA – Agricultural Research Service, at Shafter Research Field Station, studying the use of hyperspectral imaging for the detection of plant stress and disease through their own airborne multispectral scanner and contracting of additional hyperspectral imagery and analysis from Opto-Knowledge Systems, Inc. (OKSI). The University of California Cooperative Extension, and UC Department of Agriculture and Natural Resources, and Kings County Farm Advisor have contributed staff in nutrient status and ground measurements. The University of California, Davis facility in the Departments of Agronomy and Range Science, and Land, Air and Water Resources are studying soil and plant nutrient through remote sensing, and amendment and fertilizer trials. Many investigators have joint studies among these organizations, including Center for Spatial Technology and Remote Sensing (CSTARS), joining in remote sensing of soil quality and plant stress. This report is a brief description of one field study, soil surface spectra and sampling conducted in July 2000. The status of lab and image data, and initial findings in the relationships between soil chemical analysis and spectra for the study site, are also discussed.

Of the several measures of soil quality, salinity/alkalinity is of particular importance to sustaining semi-arid and arid agriculture. Farmers worldwide face declining productivity where there is a lack of adequate drainage in both irrigated and non-irrigated lands. Without proper drainage management, soils accumulate salts near the surface due to parent materials abundant in salt and/or imported with irrigation water. Salinity is due to high contents of carbonate, and some chloride salts, $CaCO_3$, $MgCO_3$ and NaCl, and will raise the soil pH to less than 8.5. Salinity creates moisture and nutrient uptake difficulties for less tolerant crops. Sodicity, proper term for alkalinity, is due to the soil solution containing greater than a 13:1 ratio of sodium to calcium and magnesium contents. This is generally from sodium chloride, and can raise the pH far beyond pH 9. These soils are toxic to nearly all crops. The mixture of saline and sodic soils varies spatially and temporally due to subsurface hydrology, generally appearing on the surface as spotty and random.

At high pH's the cation retention sites on the clay particles are overwhelmed by calcium and sodium cations. Ca^{++} and Na^{+} replace magnesium, potassium, and important micronutrients, which are then lost through leaching. In a very basic environment, H^{+} is limited to that extruded from the plant roots. In sodium dominated soil-water solutions, farmers apply lime, gypsum or dolomite as amendments to overcome deficiency in calcium and magnesium and replace the Na^{+} on the clay exchange site. Applications of elemental sulfur or sulfuric acid are far more efficient and less expensive in reducing the pH, but do not contribute the necessary cations Ca and Mg. Overtime, sulfate amendments, even the fertilizer ammonium sulfate (NH_4SO_4), will help acidify the soil.

Growers have preserved and improved the soil productivity through adjusting cropping practices, such as salt tolerant crops, installing drainage systems, additional irrigation applications, and reclamation amendments. Just as precision farming techniques have increased the efficiency and economic return in the application of fertilizers

* Center for Spatial Technologies and Remote Sensing (CSTARS), Department of Land, Air and Water Resources, University of California, Davis, California 95616 (mwhiting@ucdavis.edu)

and pesticides, there is potential to increase the efficiency of amendments and additional irrigation applications. A one percent $CaCO_3$ content in the soil is equivalent to approximately 40 tons of most agricultural grade calcium amendments, or $1800/acre of gypsum. Remotely sensed image maps that identify salt types and contents in the soil surfaces are essential to developing precision farming practices. The image derived map of salt contents is one of the layers in the precision farming prescription used by the tractor computer to meter acid or sulfur, and placement of lime and gypsum amendments.

In the laboratory, full range spectrometry techniques have demonstrated the ability to accurately estimate many of the soil parameters, such as salinity, texture, organic matter and associated components (Ben-Dor and Banin, 1994; Condit, 1972; Csillag et al., 1993; Stoner and Baumgardner, 1981; Stoner et al., 1980). A few important studies have transferred these techniques of soil characteristic identification to airborne and satellite images (Metternicht and Zinck, 1996; Palacios-Orueta and Ustin, 1996).

Important work related to carbonate identification was reported by Ben-Dor and Banin in the last decade (1995; 1990; 1994). The carbonate region of the spectrum is 2230 – 2270nm and 2310 – 2330nm for calcite (Ben-Dor et al., 1999). Nearby, the attached hydroxyl groups (–OH) and cations provide the identifying features to clay content measured near 2200nm. Sulfates, such as gypsum (hydrated calcium sulfate), with absorption at 2250nm (Clark, 1999) are another common group of soil compounds near the carbonate spectral features. While their work is based on laboratory analysis of near pure mineral samples, Ben-Dor and Banin (1990) developed the near infrared analysis (NIRA), a regression of the wet lab chemistry of the soil samples compared to the first derivative of both the 2230 – 2270 and 2310 – 2330 nm spectra curves. They achieved a standard error of prediction within 15%, dried soil. When the samples were super heated to 650° C to evolve the bound water, the standard error of prediction improved.

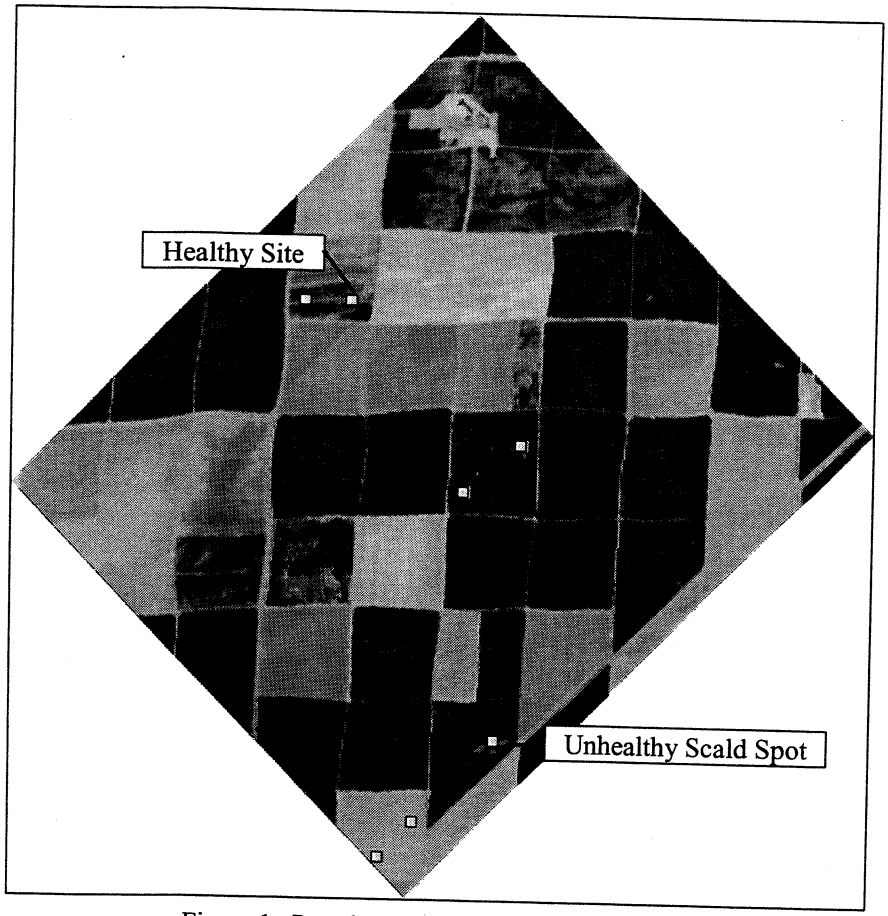

Figure 1. Pseudo-CIR from AVIRIS, 8/28/99

The promise of precision farming techniques can be negated by the high costs of field mapping. Identifying the type of salt and the areal extent is routinely mapped by field sampling using transects and grids, based on aerial photos of crop conditions. Due to the mapping and chemical analysis expense, reclamation recommendations are generally field-wide. Remote sensing of the salt type and content through hyperspectral imagery is a promising alternative. The challenge is to un-mix the varying salt concentrations spatially.

2. STUDY SITE

The AG2020 site in Kings County, California, is on the northwest edge of the Tulare Lake basin, at the southern end of the San Joaquin Valley. These highly fertile, clayey soils have naturally accumulated salts, over the millenniums, in the bottomland and on the rim of this ancient closed basin. In most areas, high value crops of garlic, beans, tomatoes, and cotton, made farming economical. As prices and production decline, the producers are forced to reclaim the poor producing areas within their fields. Conventional farming is practiced, after summer and fall harvests, they plow under the residues leaving little residue on the surface at fall planting time. This is a benefit for this study in reducing the cellulose on soil surface for summer and fall images.

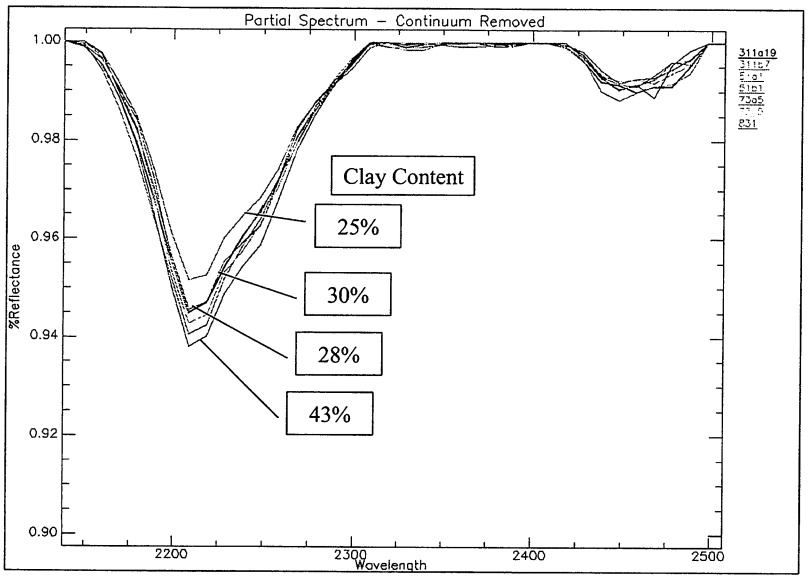

Figure 2. Representative samples of varying clay contents compared to adsorption depths, after continuum removal process.

On August 28, 1999, high altitude, and on July 19, 2000, low altitude AVIRIS flights covered the main project area, a block of 13 km^2 (approximately 3 miles square) containing 23 quarter section fields. In the high altitude image (figure 1) exposed soils appear after the harvest of wheat, garlic, garbanzo beans and within the young pistachio orchard. The strong infrared reflectance (red) in the image are from the cotton fields. Cooperating agronomists and other production scientists are also using this flight for vegetation vigor studies (Greenberg et al., 2001).

For the low-altitude overflight, sample sites were selected within the available bare soil fields. Plant vigor expressed in the pseudo-CIR image from the August 28, 1999 high-altitude AVIRIS flight (figure 1) was used to select areas of non-/slightly saline and highly saline soils. The sample sites are within large areas, and with ample saline surface characteristics. The pseudo-CIR image was sufficient to find the positions in the fields. GPS coordinates were used to geo-positions during sampling.

Seven sites were selected. At each site, nine sample points were taken, in a 3 by 3 grid, approximately 10-m apart. The sampling proceeded in a north to south direction through the points. Approximately 500-g of the first 3-cm of tilled soil surface was collected at each point. The soil surface was a mix of loose material from less than 1-mm up to clods 6-cm in size. Crop residues were removed by hand. Standing to the north of each point, three spectral measurements were taken approximately 1-m apart in the SE, S, and SW directions. Soil spectra were collected with an Analytical Spectral Devices, Inc. full range (FR) field spectrometer. The optical cable tip was held approximately 2-m from the surface using an extension pole, gathering a 1.2-m radius ground view area in nadir. The field spectra measurements are not presented in this paper.

3. METHODS AND RESULTS

3.1 Soil Chemistry, Mineralogy and Laboratory Spectra

Presented here is a preliminary review of the soil spectra, chemistry and mineralogy in this study. The Division of Natural Resources and Agriculture laboratory, UC Davis, laboratory conducted the chemical analyses on the 63 soil samples. The laboratory spectra was collected using a LabSphere diffusion sphere attachment to a Cary 5 laboratory spectrophotometer (Varian Inc.), at the Center for Spatial Technology and Remote Sensing, UC Davis (CSTARS). The soil samples were prepared by lightly grinding in a mortal and pestle, then removing remaining

plant materials with 2-mm sieve. Samples were put in small petri dishes loosely, and graded flat across the top with a spatula without packing. ENVI (Research Systems, Inc.) software was used for image and endmember spectral analysis.

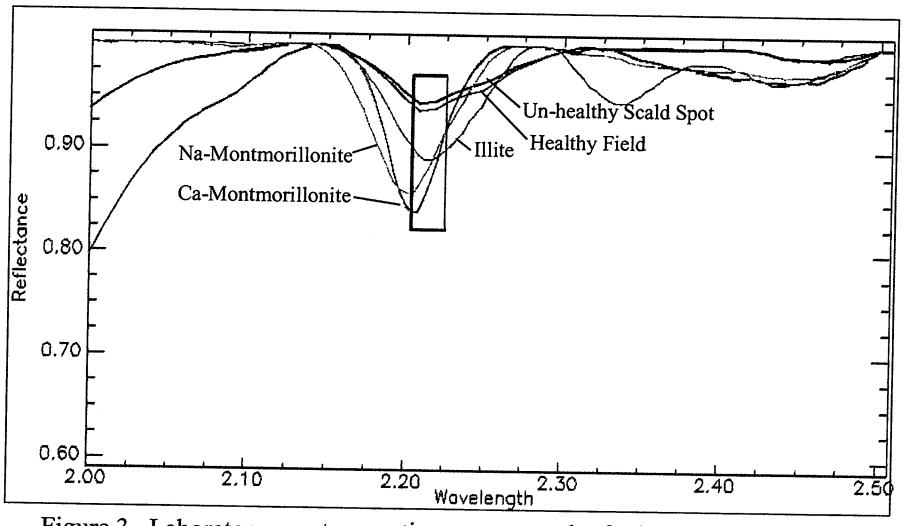

Figure 3. Laboratory spectra, continuum removed, of mixed mineralogy and soils.

Hydrometer and sieve analyses were conducted for soil texture measurements. The soil texture varied significantly in sand and clay content. Since, soil albedo is sensitive to clay and sand contents (Stoner and Baumgardner, 1981), and to moisture contents (Bowers and Hanks, 1965), the continuum removal technique (Clark and Roush, 1984) was used to remove the albedo in all the laboratory and image spectra shown in the following figures. The sand content varied from 10 to 40% of the texture. The sum of the clay and silt content within the samples varied from 60 to 90% of the dry texture, in approximately equal proportions. In figure 2, the absorption depth in the clay bands, near 2200-nm, of laboratory spectra are closely related to the amount of clay found in hydrometer analysis for a subset of samples from the project.

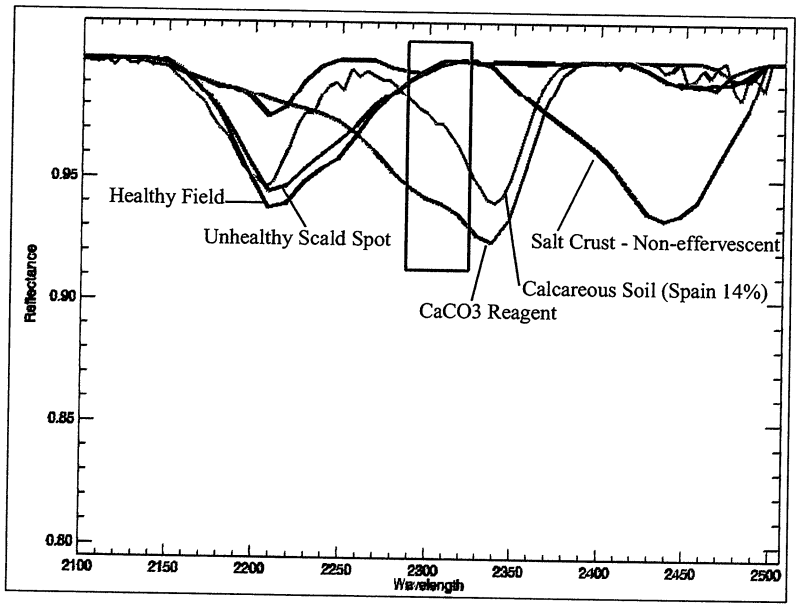

Figure 4. Comparison of soils of varying carbonate contents, continuum removed.

In figure 3, laboratory spectra of the samples from the Unhealthy and Healthy sites are displayed with USGS spectral library samples for Na- and Ca-montmorillonite and illite. Illite is commonly found as a silt and clay size mineral, a mix of dioctahedral and trioctahredral layered silicate minerals (Dixon and Weed, 1989). In a mix with the montmorillonites, illite would shift the clay absorption upwards slightly away from the Na- and Ca-montmorillonite, a 2:1-layered silicate secondary minerals. For the Kings County Soil Survey (USDA, 1978), laboratory analysis describes the soil as a mixed mineralogy of illite and montmorillonite clays. The soils include fine-loamy, mixed (calcareous), thermic Typic Torriorthents, and fine, montmorillonitic, thermic Typic Natrargrids. Because the full-range spectrum of sodium chloride is nearly featureless, one thought for quantifying the sodium salt is to use the cation dominance on the clay lattice. This may not be feasible since a variable mix of mineral types will confound the separation of cation dominance on the clay.

In this project, the salinity and sodicity is a function of the sodium chloride contents. Sodium and the other cations will be analyzed in the future. The sulfate contents ranged from 22 to greater than 400 ppm, probably due to

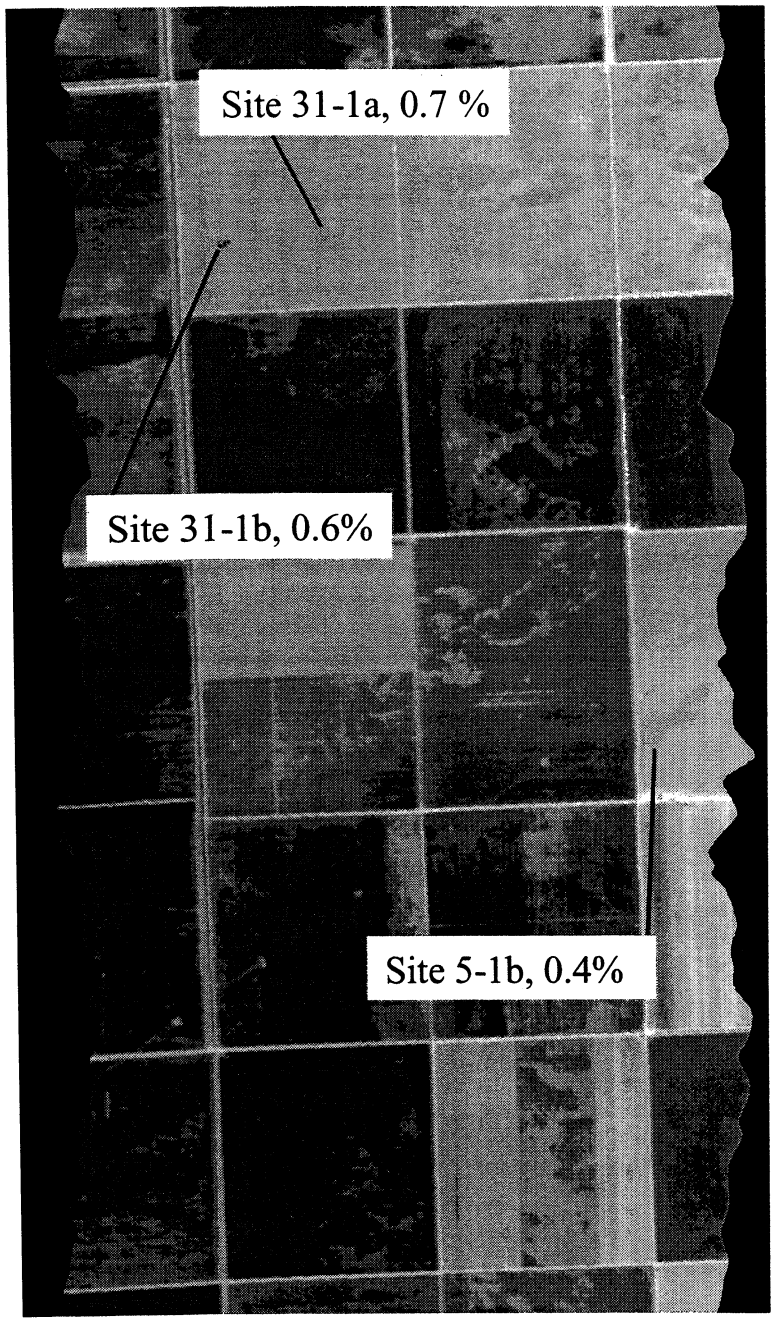

Figure 5. Low-altitude AVIRIS, 8/2000, RGB 2360, 2340, 2320-nm, Gaussian stretch.

application of gypsum. Sulfates, such as gypsum (hydrated calcium sulfate) absorption, at 2250nm (Clark, 1999), are in close proximity to the carbonate absorption bands. This may effect the accuracy of the carbonate spectral measurement. Gypsum is an amendment commonly used by this grower.

For the entire dataset, soil carbonates varied from 0.4 to 1.2 % of the oven dry soil. In terms of salinity, these levels of carbonate are considered very low. A comparison of texture and carbonate contents showed no clear relationship. As many samples with higher carbonate contents had similar textures as those with lower carbonate contents. In figure 4, continuum removal process curves are used to compare: finely ground regent grade calcium carbonate; a calcareous soil from La Mancha, Spain, (approximately 14% $CaCO_3$); an acid non-effervescent salt crust sample of San Joaquin Valley (predominately NaCl); and the Healthy and Unhealthy samples. The strong absorption features in the carbonate range for the calcium carbonate specimen and the Spanish soil demonstrate the spectral separation is possible. The salt crust also shows little absorption difference from the project samples, and the three show little or no adsorption within the carbonate range.

3.2 AVIRIS Image Spectra

To evaluate the potential of the near infrared analysis (Ben-Dor and Banin, 1990), spectral samples, figure 6, were extracted from regions of interest in the 1999 high altitude AVIRIS image at sites described as "Health" and "Unhealthy" soil areas (figure 1). The regions of interest represent the extremes in vegetative health; vigorous cotton and saline affected areas denude of vegetation within cotton field. The continuum removal process (Clark and Roush, 1984) was used to reduce the effect of varying moisture. The Unhealthy soil spectrum from the AVIRIS pixels has a much stronger slope, and deeper absorption within the carbonate range (2350-nm), indicating the greater carbonate content. The absorption features from the Healthy sample are broader, with greater depth in the clay band (2200-nm). Further work is needed to understand the absorption derivative and depth, and the effect of a 10-nm spectral resolution of the AVIRIS instrument.

Pictured in figure 5 is a portion of the project site from July 19, 2000 low altitude AVIRIS image. This RGB is composed of three bands in the carbonate region, 2360, 2340, 2320-nm, respectively. It was enhanced with

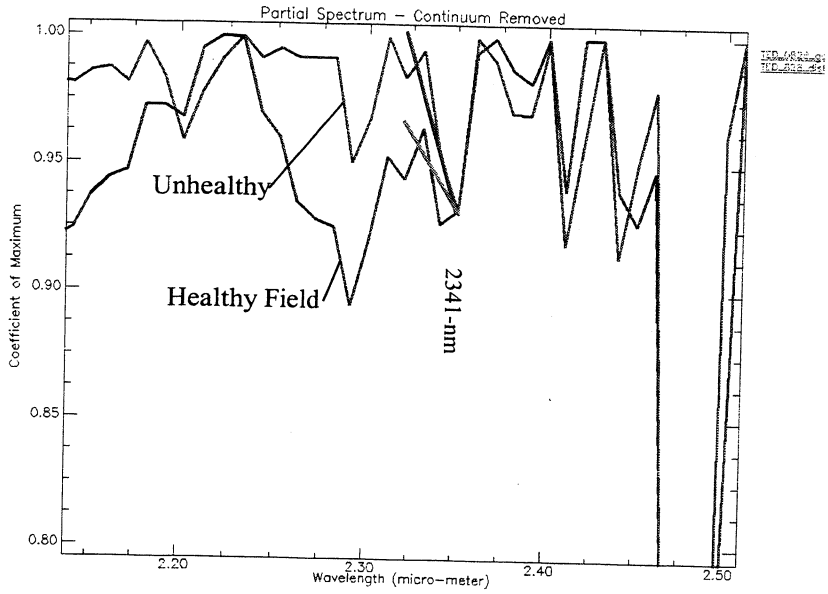

Figure 6. AVIRIS, 1999, spectral plots comparing carbonate bands, in continuum removed.

a Gaussian stretch. The average carbonate content of the nine samples within the sites of 31-1a and 31-1b vary substantially from the average for the 5-1b site, 0.7, 0.6, and 0.4%, respectively. Though all are very low in carbonates, these regions of interest are spatially very consistent. The regions of interest were allowed to "grow" within 0.5 standard deviation for the 2360nm band (band of the maximum absorption depth) within a distance of 4 pixels. Visually the growth is very small. Average spectra for these expanded regions of interest, with continuum removal, are shown in figure 7. Additionally, the spectra for 31-1a and b samples were averaged for a "31-1 field" spectrum. The grouping of the 31-1 field samples spectra and their separation from the 5-1 field spectra indicate the potential to separate small concentrations of carbonate. Further work will be conducted to isolate other influences on the spectral differences.

4. CONCLUSION

The evaluation of the high and low altitude AVIRIS imagery, soil chemistry, field and laboratory spectral analysis has just begun. These preliminary results indicate the potential use of AVIRIS images, both high and low altitudes, and other spectrometer measurements for quantifying carbonate in the soil surface. More work is ahead, including analysis of soils having a broad range of carbonate levels to evaluate the robustness of the methods.

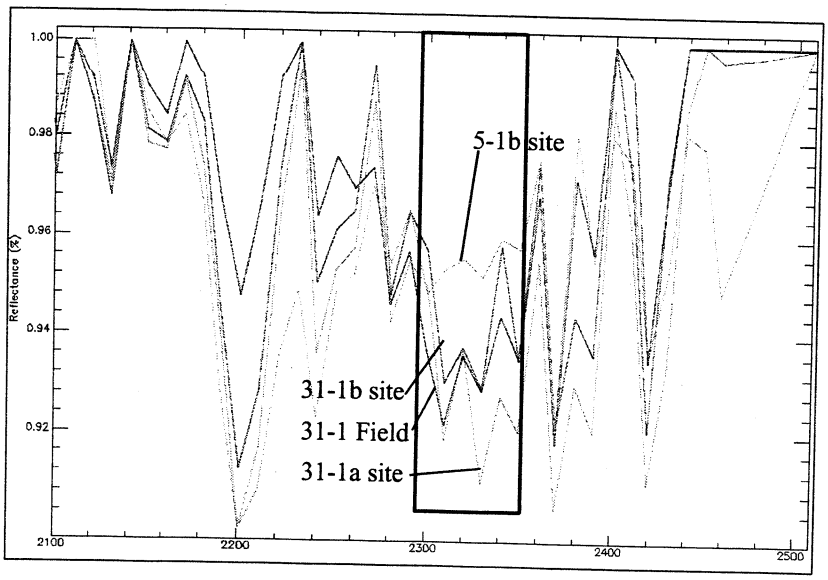

Figure 7. AVIRIS, 2000, low altitude, spectra for areas in figure 5.

To understand the affects of variable soil moisture, due to irrigation and precipitation, we need to develop a relationship model of moisture content to spectral adsorption by carbonates and soil mixtures. This will evaluate the effectiveness of continuum removal process for studies such as this. The light absorption in the 2200 – 2400-nm range may not be linearly proportional to the change in hydration of both the clay and carbonate.

Soil samples are still being analyzed for other cations to explain the spectral features in the carbonate and other wavelength regions. The outcome of this analysis will provide a carbonate map to improve to precision applications and the efficiency of lime, gypsum and acid.

5. REFERENCES

Ben-Dor, E. and Banin, A. 1995. "Near infrared analysis (NIRA) as a method to simultaneously evaluate spectral featureless constituents in soils," Soil Science, vol. 159, no. 4, pp. 259-270.

Ben-Dor, E. and Banin. A. 1994. "Visible and near-infrared (0.4-1.1 MU-M) analysis of arid and semiarid soils," Remote Sensing of Environment, vol. 48, no. 3, pp. 261-274.

Ben-Dor, E., and Banin, A. 1990. "Near-infrared reflectance analysis of carbonate concentration in soils," Applied Spectroscopy, vol. 44, no. 6, pp. 1064-1069.

Ben-Dor, E., Irons, J. R., and Epema, G. F. 1999. "Soil Reflectance," Remote Sensing for the Earth Sciences: Manual of Remote Sensing, A. N. Rencz, ed., John Wiley & Sons, Inc.

Bowers, S. A., and Hanks, R. J. 1965. "Reflection of radiant energy from soils." Soil Science, vol. 100, pp. 130-138.

Clark, R. N. 1999. "Spectroscopy of rocks and minerals, and principles of spectrocopy," Remote Sensing for the Earth Sciences: Manual of Remote Sensing, A. N. Rencz, ed., John Wiley & Sons, Inc, pgs. 3-58.

Clark, R. N., and Roush, T. L. 1984. "Reflectance spectroscopy: Quantitative analysis techniques for remote sensing applications," Journal of Geophysical Research, vol. 89, no. B7, pp. 6329-6340.

Condit, H. R. 1972. "The spectral reflectance of American Soils," Photogrammetric Engineering, vol. 36, pp. 955-966.

Csillag, F., Pasztor, L., and Biehl, L. L. 1993. "Spectral band selection for the characterization of salinity status of Soils," Remote Sensing of Environment, vol. 43, pp. 231-242.

Dixon, J. B., and Weed, S. B. 1989. Minerals in Soil Environments, Soil Science Society of America, Madison, WI.

Greenberg, J., Scheer, G., Whiting, M., and Ustin., S. 2001. "Analysis of water and chlorophyll features in cotton agriculture," Tenth JPL Airborne Visible Infrared Imaging Spectrometer (AVIRIS) Workshop, Jet Propulsion Laboratory, California Institute of Technology, Pasadena, CA.

Metternicht, G. I., and Zinck, J. A. 1996. "Modelling salinity-alkalinity classes for mapping salt-affected topsoils in the semiarid valleys of Cochabamaba (Bolivia)," ITC Journal, vol. 2, pp. 125-135.

Palacios-Orueta, A., and Ustin, S. L. 1996. "Multivariate classification of soil spectra," Remote Sensing of Environment, vol. 57, no. 2, pp. 108-118.

Stoner, E. R., and Baumgardner, M. F. 1981. "Characteristic variations in reflectances of surface soils," Soil Science Society of America Journal, vol. 45, pp. 1161-1165.

Stoner, E. R., Baumgardner, M. F., Biehl, L. L., and Robinson, B. F. 1980. "Atlas of soil reflectance properties laboratory for application of Remote Sensing," Purdue University Research Bulletin 962.

USDA, NRCS. 1986. "Soil Survey of Kings County, California," USDA Soil Conservation Service in cooperation with University of California Agricultural Experimental Station, Hanford, CA.

CHLOROPHYLL *a+b* CONTENT ESTIMATION THROUGH TURBID-MEDIUM AND MONTE-CARLO RT MODEL INVERSION FOR FOREST CANOPIES, USING HYPERSPECTRAL DATA

Pablo J. Zarco-Tejada,[1,6] John R. Miller,[1,2] John Harron,[1,7] Baoxin Hu,[2,3] Thomas L. Noland,[4] Narendra Goel,[5] Gina H. Mohammed,[4,8] and Paul H. Sampson[4]

1. Introduction

This paper reports on progress made within the Bioindicators of Forest Sustainability Project (Mohammed *et al.,* 1997; Sampson *et al.,* 1998) to develop links between physiologically-based bio-indicators (e.g., pigment concentrations, chlorophyll fluorescence) from field and laboratory data and optical indices from hyperspectral remote sensing data for assessing forest condition.

Predictions of chlorophyll content (chl_{a+b}) or any other canopy biophysical parameter from airborne or satellite canopy reflectance are generally carried out through four different methodologies: i) directly studying the statistical relationships between ground-measured biochemical data and canopy-measured reflectance (Johnson *et al.,* 1994; Matson *et al.,* 1994); ii) applying the leaf-level relationships derived between optical indices and the pigment content directly to canopy-measured reflectance (Peterson *et al.,* 1988; Yoder and Pettigrew-Crosby, 1995; Zagolski *et al.,* 1996); iii) *scaling-up* the leaf-level relationships based on optical indices related to pigment content through models of canopy reflectance or infinite reflectance (Zarco-Tejada *et al.,* 1999a; 1999b; 2000); and iv) inverting the observed canopy reflectance through a canopy reflectance or infinite reflectance model coupled with a leaf model to estimate the optimum pigment content (Jacquemoud *et al.,* 1995; Kuusk, 1998; Demarez and Gastellu-Etchegorry, 2000; Weiss *et al.,* 2000; Jacquemoud *et al.,* 2000).

Traditional statistical methods have demonstrated successful retrievals of pigment content from hyperspectral reflectance, such as from multivariate analysis between Airborne Visible InfraRed Imaging Spectrometer (AVIRIS) reflectance and total nitrogen, lignin, starch, chlorophyll content and LAI (Johnson *et al.,* 1994) and with nitrogen and chlorophyll (Matson *et al.,* 1994) through application of a stepwise multiple-regression procedure using the AVIRIS spectral bands. Nevertheless, statistical leaf-level relationships applied to canopy reflectance for pigment estimation are site and species specific (Chappelle *et al.*, 1992; Gitelson and Merzylak, 1997) and therefore require relationship parameterization that is a function of the canopy structure and viewing geometry at the time of remote sensing data collection. Therefore, the statistical relationships derived at leaf level need to be parameterized in order to be useful for estimation at the canopy level, due to the differences between the two media: one where the relationship is derived (leaf) and the other where it is applied for estimations (forest canopy). Although significant correlations are found when statistical approaches are used, no prediction capabilities can be inferred from either one of these research results since the locally-derived relationships are affected by species, canopy structure, LAI, canopy openings, shadows and understory.

Scaling-up methods using coupled leaf-level statistical relationships and radiative transfer (RT) models (Zarco-Tejada, *et al.,* 1999a, 1999b; Zarco-Tejada, 2000), and RT model inversion techniques coupling leaf and canopy models (Jacquemoud *et al.,* 1995; Kuusk, 1998; Demarez and Gastellu-Etchegorry, 2000; Jacquemoud *et al.,*

[1] Centre for Research in Earth and Space Science, York University, 4700 Keele Street, Toronto M3J 1P3, Canada.
[2] Department of Physics and Astronomy, York University, Toronto M3J 1P3, Canada.
[3] Canadian Space Agency, 6767 Route de L'Aéroport Saint-Hubert, Québec J3Y 8Y9, Canada.
[4] Ontario Forest Research Institute, OMNR, Sault Ste. Marie P6A 2E5, Ontario, Canada.
[5] Department of Computer Science,Wayne State University Detroit, Michigan 48202 USA.
[6] Now at Center for Spatial Technologies and Remote Sensing (CSTARS), Department of Land, Air, and Water Resources (LAWR), University of California, Davis, CA 95616 – 8671 USA - pzarco@ucdavis.edu
[7] Now at Spectral Applied Research Inc., 10 North Rivermede Rd. Concord, Ontario L4K 2H2, Canada.
[8] Now at P&M Technologies, 66 Millwood St., Sault Ste. Marie, Ontario P6A 6S7, Canada.

2000; Zarco-Tejada *et al.*, 2001a; 2001b) allow consideration of the canopy structure, with leaf RT simulation using leaf biochemical constituents as input to model leaf reflectance and transmittance that is in turn used as input for the canopy reflectance model. This paper reports on progress made to estimate leaf chlorophyll content by radiative transfer model inversion techniques. The study was carried out at forest sites of *Pinus strobus* L. and *Acer saccharum* M. in Ontario, Canada, where field measurements and hyperspectral CASI imagery were collected between 1997 and 2000 in airborne deployments. PROSPECT, SAILH, and SPRINT radiative transfer models were used for numerical inversion using red edge spectral indices to build the merit function used in the optimization procedure. Individual tree samples were collected at each site for biochemical analysis and measurement of leaf chlorophyll, carotenoid concentrations, as well as reflectance and transmittance of broad leaves and needles. The model inversion techniques were tested using CASI data of 72 and 288 channels and 0.5 and 2 m spatial resolution.

2. Hyperspectral Data Collection

Data collection was carried out in 18 study sites of *Pinus strobus* L. and *Acer saccharum* M. in Ontario (Canada), where field data and airborne hyperspectral data were collected with the *Compact Airborne Spectrographic Imager* (CASI) sensor. Airborne data were collected in the 400-950 nm spectral range, with spatial resolution varying from 0.5 to 5m and with CASI modes of operation of 72 and 288 bands with 7.5 and 2.5 nm spectral resolution, respectively. Field campaigns were carried out in summer of 1997, 1998, 1999 and 2000, collecting LAI, canopy cover, using hemispherical photography and PCA-LiCor 2000. A total of 440 leaf samples per year were collected from 12 deciduous sites and 84 groups of needles from the 6 conifer sites. Leaf and needle samples were used for measuring chlorophyll $a+b$ and carotenoids as described in Zarco-Tejada *et al.* (2000). Reflectance (r) and transmittance (t) from each broad leaf and needle sample were obtained with a LiCor integrating sphere attached to a 7.5 nm bandwidth fibre spectrometer in the 400-900 nm range. Raw CASI data were calibrated to radiance and atmospherically corrected using CAM5S model using aerosol optical depth at 550nm collected over the area at the time of airborne data collection. Airborne data were geocoded using onboard GPS and two-axis gyro.

3. Leaf-Level Radiative Transfer Modelling for Broad Leaves and Needles

Accurate determination of the optical properties of leaf samples is critical for development and validation of leaf RT models. The PROSPECT model (Jacquemoud and Baret, 1990), has been widely used and validated in broadleaves for numerical inversion to estimate chlorophyll content. Nevertheless, development and validation of leaf models to simulate needle reflectance and transmittance has not been that successful due to existing difficulties to measure the optical properties of needles associated with their shape and size.

The method of Daughtry *et al.* (1989) for needle r and t was adapted by Harron and Miller (Harron, 2000) through the use of a carrier to support the needles avoiding gaps between samples. Using the carrier-based method the effect of the specular-scattered light is eliminated completely, therefore avoiding errors made in the meticulous measurement of the gap fraction between the needles presented at the exit port. Besides, Harron and Miller's method avoids the influence of specular scattered light from the curved needle surface which in previous methods escapes from the sphere in the reflectance measurements and is introduced into the sphere in the transmittance measurements. This new method considerably improved the measurement of needle optical properties (Harron, 2000) and allowed successful application of PROSPECT model to simulate needle r and t. Figure 1 shows needle reflectance and transmittance spectra measured with Harron and Miller's method using a carrier in the Li-Cor integrating sphere, and simulated by PROSPECT leaf model using chl_{a+b} and N values obtained by model inversion. The close agreement obtained between measured and simulated reflectance and transmittance spectra in needles from the study areas, and the extensive validation of PROSPECT in the literature prompted our adoption of the traditional PROSPECT for the needle simulations presented in this paper.

The 84 reflectance and transmittance spectra were used for estimation of the leaf structural parameter N and the total chlorophyll pigment chl_{a+b} using the PROSPECT model. The model inversion was performed by iteration, varying N from 2 to 5 as the first step, with the root mean square error (RMSE) function $\xi(N)$ to be minimized using both r and t in the NIR (780-800 nm), where structural effects dominate significantly over pigment effects in reflectance and transmittance [Equation 1].

$$RMSE = \xi(N, chl_{a+b}) = \sqrt{\frac{\sum_{\lambda}[(r_{PROSPECT} - r_m)_{\lambda}^{2} + (t_{PROSPECT} - t_m)_{\lambda}^{2}]}{n}} \quad [1]$$

where r_m and t_m are r and t measured from the needle samples with the Li-Cor and fibre spectrometer. In the second step, with N estimated, chl_{a+b} was varied from 40 to 100 μg/cm^2 and the function $\xi(N, chl_{a+b})$ minimized by calculating the RMSE over the 450-700 nm range. Following the above procedure, the assessment of chl_{a+b} estimation by PROSPECT model inversion yielded r^2=0.4.

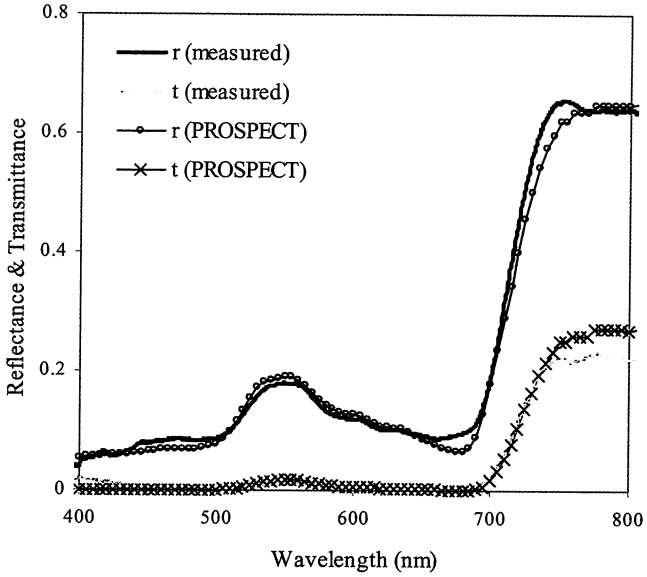

Figure 1. Needle reflectance and transmittance spectra measured with Harron and Miller's method using a carrier in the Li-Cor integrating sphere, and simulated by PROSPECT leaf RT model. Measured chl_{a+b} in the shoot of the set of needles used for optical measurement of this plot was 60.2 μg/cm^2 (after conversion using nominal thickness and FLA). Plotted simulated reflectance and transmittance with PROSPECT was carried out with chl_{a+b} = 68.5 μg/cm^2 and N=3.5, obtained previously by numerical inversion of the leaf model.

4. Estimation of Chlorophyll *a+b* by RT Model Inversion from Airborne Hyperspectral Data in Deciduous and Conifer Canopies

Canopy simulation modeling was carried out using two radiative transfer models, SAILH for closed deciduous canopies, and SPRINT for conifers. The use of turbid-medium models such as SAILH in deciduous canopies was carried out by building a merit function based on spectral transforms to minimize the forest canopy structure, shadows and openings. Building merit functions based on spectral transforms or vegetation indices (Zarco-Tejada, 2000; Zarco-Tejada *et al.*, 2001a) are found effective when they are based on optical indices that are related with the variable subject to estimation, such as chl_{a+b}. The use of optical indices in the merit function has not been reported in any of the validation work found in the literature, although it appears that there is significant inherent potential of this approach in remote sensing application. Reflectance values measured from airborne or satellite sensors are a function of illumination, canopy structure, and atmospheric condition at the time of data collection. On the other hand, estimation of biophysical parameters through optical indices enable the sensitivity to such biophysical parameters to be maximized, normalizing external effects due to atmosphere, illumination conditions, and viewing geometry (Running *et al.*, 1994; Huete and Justice, 1999).

The iterative-optimization numerical model-inversion technique to estimate chlorophyll content by using a coupled leaf model and a canopy model requires the error calculation by comparison of estimated canopy reflectance r^* to the at-sensor measured reflectance r_m. Error calculation consists of determination of a set of parameters $P=(N, Chl_{a+b}, C_w, LAI, \theta_s...)$ which minimizes a merit function Δ^2 over the whole spectrum [Equation 2].

$$\Delta^2 = \sum_n [r_m(\lambda_i) - r^*(\lambda_i, P)]^2 \quad [2]$$

where, $r_m(\lambda_i)$ is the measured canopy spectral reflectance; and $r^*(\lambda_i, P)$ is the modelled canopy spectral reflectance with a set of P parameters. Equation [3] presents the merit function used in this study when the red-edge spectral parameter R_{750}/R_{710} is used for pigment estimation:

$$\Delta^2 = \left[\left(\frac{R750}{R710} \right)_m - \left(\frac{R750}{R710}, P \right)_* \right]^2 \quad [3]$$

where $R750/R710_m$ is the optical index calculated from measured canopy reflectance, and $R750/R710_*$ is the optical index calculated from modelled canopy reflectance, for a given set of input parameters P. Zarco-Tejada *et al.* (2001a) demonstrated that forest canopy shadows and heterogeneity are minimized when a red edge optical index is used in the merit function used for error assessment in the coupled PROSPECT+SAILH RT models. This methodology was used for model inversion in deciduous and coniferous study sites, using PROSPECT+SAILH for deciduous and PROSPECT+SPRINT for coniferous sites. Structural parameters and viewing geometry values for RT modeling (Figure 2) were measured in the field at the time of data collection, with specific pine values extrapolated from field measurements made earlier (Fox, 1991). The structural values from both species were used for model simulation, using the following for *Pinus strobus*: tree density, 1100 trees/ha; Poisson distribution of trees; irregular ellipsoidal crown shape, height of trunk, 8.5 m; height of tree, 15.0 m; trunk radius, 8.3 cm; crown radius, 2.0 m; spherical leaf angle distribution; shoot area, 0.0008 m^2; canopy effective LAI, 2.5; and leaf area density, 0.4171 /m. whereas for *Acer saccharum* parameters were: LAI=3.5, plagiophile leaf angle distribution function (LADF), soil reflectance data derived from CASI imagery, and model-estimated skylight irradiance fraction based on conditions during airborne acquisitions. Estimated versus measured leaf pigment content results from the 12 study sites of *Acer saccharum* yielded r^2=0.4, RMSE=5.5 µg/cm^2 (years 1999 and 2000), and r^2=0.4, RMSE=8.1 µg/cm^2 for *Pinus strobus* (year 2000).

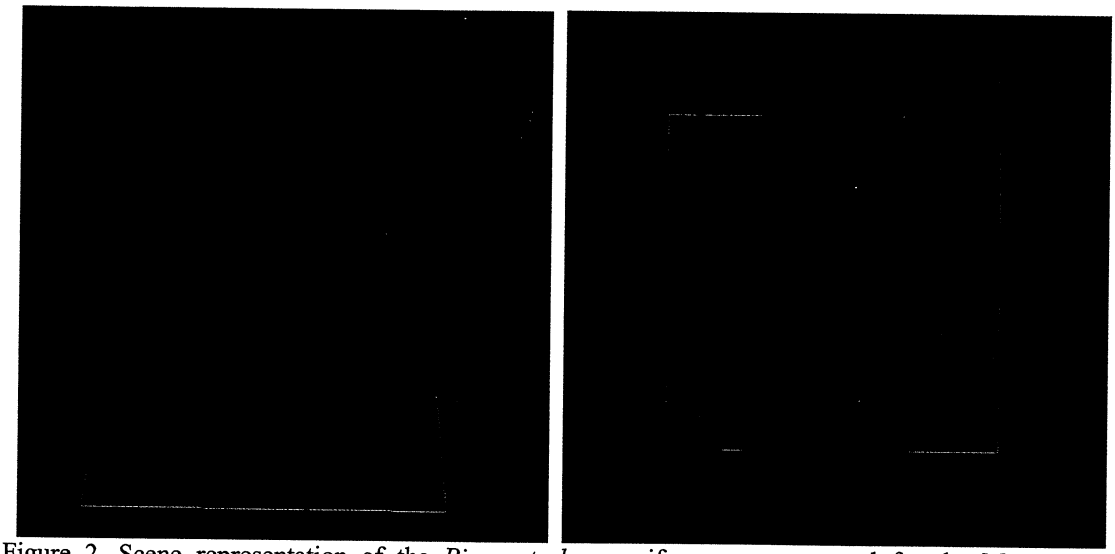

Figure 2. Scene representation of the *Pinus strobus* coniferous canopy used for the Monte-Carlo radiative transfer simulation with SPRINT model (30° viewing angle, left; nadir view, right). Structural parameters and viewing geometry values were measured in the field at the time of data collection for *Pinus strobus*: tree density, 1100 trees/ha with Poisson distribution; irregular ellipsoidal crown shape, height of trunk, 8.5 m; height of tree, 15.0 m; trunk radius, 8.3 cm; crown radius, 2.0 m; spherical leaf angle distribution; shoot area, 0.0008 m^2; canopy effective LAI, 2.5; and leaf area density, 0.4171 /m.

5. Conclusions

This paper demonstrates that radiative transfer model inversion techniques can be applied successfully to forest canopies with different structural characteristics, such as *Acer saccharum* and *Pinus strobus*. The new approach of Harron and Miller for measuring the optical properties of needles using a carrier method, enabled the validation of PROSPECT leaf model for pigment content estimation by inversion in needles. Estimation of chlorophyll content in closed deciduous canopies was successfully carried out using a turbid-medium model (SAILH) coupled to PROSPECT, and building the merit function with a red edge optical index R750/R710. It was previously demonstrated that a turbid-medium model could successfully be used in closed forest canopies when a red edge index is used in the merit function used for minimization. Red edge indices such as R750/R710 used as merit function minimizes shadows and canopy openings, therefore enabling the use of less complicated RT models such as SAILH in forest canopies. The same approach was carried out for the coniferous canopies, coupling PROSPECT to SPRINT Monte-Carlo RT model and using the same red edge index to build the merit function. Results obtained from the 12 study sites of *Acer saccharum* were r^2=0.4, RMSE=5.5 μg/cm^2 (1999 and 2000 campaigns) and r^2=0.4, RMSE=8.1 μg/cm^2 for *Pinus strobus* (2000 campaign), showing that RT model inversion methods can be used with success over forest canopies to estimate chlorophyll content.

6. References

Chappelle, E. W., Kim, M. S. and McMurtrey, J. E. I. (1992), Ratio analysis of reflectance spectra (RARS): an algorithm for the remote estimation of the concentrations of chlorophyll *a*, chlorophyll *b*, and carotenoids in soybean leaves. *Remote Sensing of Environment.* 39:239-247.

Daugherty, C. S. T., Biehl, L. L., and Ranson, K. J. (1989), A new technique to measure the spectral properties of conifer needles, *Remote Sensing of Environment*, 27:81-91.

Demarez, V., and Gastellu-Etchegorry, J.P., (2000) A Modeling Approach for Studying Forest Chlorophyll Content. *Remote Sensing of Environment*, 71:226-238.

Fox, B. (1991), Silvicultural demonstration areas of the Kirkwood Forest. Ministry of Natural Resources, Cent. Ont. For. Tech. Dev. Unit. Blind River, ON, COFTDU Rep. No. 16. 85 pp.

Gitelson, A. A. and Merzlyak, M. N. (1997), Remote estimation of chlorophyll content in higher plant leaves. *International Journal of Remote Sensing.* 18:2691-2697.

Harron, J. W. (2000), Optical properties of phytoelements in conifers, M. Sc. Thesis, *Graduate Program in Earth and Space Science*, pp193, York University, Toronto, December, 2000.

Huete, A., and Justice, C., (1999), MODIS Vegetation Index (MOD 13) Algorithm Theoretical Basis Document, Greenbelt: NASA Goddard Space Flight Centre, http://modarch.gsfc.nasa.gov/MODIS/LAND/#vegetation-indices, 129pp.

Jacquemoud, S. and Baret, F. (1990), Prospect: A model of leaf optical properties spectra, *Remote Sensing of Environment.* 34:75-91.

Jacquemoud, S., Baret, F., Andrieu, B., Danson, F. M. and Jaggard, K. (1995), Extraction of vegetation biophysical parameters by inversion of the PROSPECT+SAIL models on sugar beet canopy reflectance data. Application to TM and AVIRIS sensors. *Remote Sensing of Environment.* 52:163-172.

Jacquemoud, S., Bacour, C., Poilve, H., and Frangi, J.P., (2000) Comparison of four radiative transfer models to simulate plant canopies reflectance–Direct and inverse mode, *Remote Sensing of Environment,*74:471-481.

Johnson, L. F., Hlavka, C. A. and Peterson, D. L. (1994), Multivariate analysis of AVIRIS data for canopy biochemical estimation along the Oregon transect. *Remote Sensing of Environment.* 47:216-230.

Kuusk, A. (1998), Monitoring of vegetation parameters on large areas by the inversion of a canopy reflectance model. *International Journal of Remote Sensing.* 19:2893-2905.

Matson, P., Johnson, L., Billow, C., Miller, J. and Pu, R. (1994), Seasonal patterns and remote spectral estimation of canopy chemistry across the Oregon transect. *Ecological Applications.* 4:280-298.

Mohammed, G.H., Sampson, P. H., Colombo, S. J., Noland, T. L., y Miller, J. R. (1997), Bioindicators of forest sustainability: *Development of a forest condition rating system for Ontario*, OFRI, ON, Canada.

Peterson, D. L., Aber, J. D., Matson, P. A., Card, D. H., Swanberg, N., Wessman, C. and Spanner, M. (1988), Remote sensing of forest canopy and leaf biochemical contents. *Remote Sensing of Environment.* 24:85-108.

Running, S.W., Justice C.O., Solomonson, V., Hall, D., Barker, J., Kanfmann, Y.J., Strahler, A.H., Huete, A.R., Muller, J.P., Vanderbilt, V., Wan, Z.M., Teilletland, P. and Carneggie, D., (1994), Terrestrial Remote Sensing and Algorithms Planned for EOS/MODIS, *International Journal of Remote Sensing*, 15(17):3587-3620.

Sampson, P.H., G.H. Mohammed, S.J. Colombo, T.L. Noland, J.R. Miller and P.J. Zarco-Tejada, 1998. *Bioindicators of Forest Sustainability Progress Report, Ontario Forest Research Institute*, Sault Ste. Marie, ON, Canada.

Weiss, M., Baret, F., Myneni, R.B., Pragnere, A. and Knyazikhin, Y., (2000) Investigation of a model inversion technique to estimate canopy biophysical variables from spectral and directional reflectance data, *Agronomie* 20:3-22.

Yoder, B. J. and Pettigrew-Crosby, R. E. (1995), Predicting nitrogen and chlorophyll content and concentrations from reflectance spectra (400-2500 nm) at leaf and canopy scales. *Remote Sensing of Environment.* 53:199-211.

Zagolski, F., Pinel, V., Romier, J., Alcayde, D., Fotanari, J., Gastellu-Etchegorry, J. P., Giordano, G., Marty, G., and Joffre, R. (1996), Forest canopy chemistry with high spectral resolution remote sensing. *International Journal of Remote Sensing.* 17:1107-1128.

Zarco-Tejada, P. J. (2000), Hyperspectral remote sensing of closed forest canopies: Estimation of chlorophyll fluorescence and pigment content, Ph.D. Dissertation, *Graduate Program in Earth and Space Science*, York University, Toronto.

Zarco-Tejada, P. J., Miller, J. R., Mohammed, G. H., Noland, T. L. and Sampson, P. H. (1999a), Canopy Optical Indices from Infinite Reflectance and Canopy Reflectance Models for Forest Condition Monitoring: Application to Hyperspectral CASI data, In *IEEE 1999 International Geoscience and Remote Sensing Symposium, IGARSS'99*, Hamburg (Germany).

Zarco-Tejada, P. J., Miller, J. R., Mohammed, G. H., Noland, T. L. and Sampson, P. H. (1999b), Optical Indices as Bioindicators of Forest Condition from Hyperspectral CASI data, In Proceedings 19th Symposium of the European Association of Remote Sensing Laboratories (EARSeL), Valladolid (Spain).

Zarco-Tejada, P. J., Miller, J. R., Mohammed, G. H., Noland, T. L and Sampson, P.H. (2000). Chlorophyll Fluorescence Effects on Vegetation Apparent Reflectance: II. Laboratory and Airborne Canopy-Level Measurements with Hyperspectral data, Remote Sensing of Environment, 74(3).

Zarco-Tejada, P.J., J.R. Miller, G.H. Mohammed, T.L. Noland and P.H. Sampson, *Scaling-up* and *Model Inversion* methods with narrow-band Optical Indices for Chlorophyll Content Estimation in closed Forest Canopies with Hyperspectral Data. *IEEE Transactions on Geoscience and Remote Sensing, Special Issue on Hyperspectral Remote Sensing,* in press (2001a).

Zarco-Tejada, P.J., J.R. Miller, Harron, J., Hu, B., Noland, T.L., Goel, N., Mohammed, G.H., and P.H. Sampson, Needle Chlorohyll content estimation through model inversion using hyperspectral data from Boreal Conifer Forest Canopies. *Remote Sensing of Environment,* BOREAS Special Issue III (submitted, 2001b).